WE 122
An assisted data-driven procedure to select functionally connected brain regions in fMRI

Pierre Bellec[1,3], Guillaume Marrelec[1,3,4], Carine Posé[1,2,3], Odile Jolivet[1,3], Mélanie Pélégrini-Issac[2,3], Julien Doyon[1,4], Habib Benali[1,3]
[1]INSERM U494, Paris, France, [2]INSERM U483, Paris, France, [3]IFR 49, Orsay, France, [4]Université de Montréal, Montréal, Canada

Introduction
Functional connectivity, based on the correlation between mean time courses (TCs) of brain regions, is thought to reflect functional interactions (1). To carry out such analyses, a network of regions is usually selected on the basis of conventional activation maps. However, correlation maps, which are derived by correlating the mean TC of a single seed region with TCs of other brain voxels (1), often show that the network of regions connected to an activated seed comprise non-activated regions. Thus, these new regions need to be taken into account in functional connectivity analyses, yet their automatic selection remains a problem, because presence, localization and extent of correlation peaks vary from maps to maps. To identify the whole network of regions that are functionally connected, we propose a new method, which combines a rough manual initialization and an iterative clustering algorithm.

Methods
Five healthy volunteers were included in our study. Five functional runs of 70 T_2^*-weighted volumes (Bruker 3 T scanner; TR: 3,500 ms; TE: 35 ms; voxel size: 3*3*3 mm^3; 42 slices) were acquired while subjects were continuously executing a motor adaptation task at asymptotic level of performance (3). Activated regions were determined using SPM99 in a fixed-effect group study, and were used as seeds to compute correlation maps. A rough manual delineation around correlation peaks, common for all correlation maps, was then performed. Because accuracy of such segmented areas are highly expertise-dependent, final selection of the cluster in each area was achieved with a clustering algorithm CAMIS (2) based upon TCs homogeneity using a data-driven approach. CAMIS is an iterative algorithm. Starting from all voxels, clusters were merged at each step with respect to a similarity measure defined as the mean correlation between TCs for any pair of voxels; each voxel belonging to one cluster. Clusters were accepted when their extent was larger than 15 voxels, and the most homogeneous one was selected, as measured by the mean correlation over the TCs of any pairs of voxels in the cluster.

Results
Activated regions were located in the cerebellum, motor cortex, and visual areas (figure 1). Correlation maps using these regions as seeds allowed identification of many non-activated regions (figure 2). For each area manually delineated, the cluster selected by CAMIS was found relevant anatomically (figure 3). Although the TCs of functionally connected, but non-activated regions (e-g- thalamus or precuneus) was uncorrelated to the stimulus, these regions were nevertheless fundamental from a connectivity viewpoint, because they could be used as modulatory regions, or relays. Our method allows, in a context of noisy images, to perform an objective and data-driven selection of the relevant regions for functional connectivity analysis of fMRI data.

References
(1) Lowe et al, Neuroimage 7, 119-132 (1998) ;(2) Benali et al, Proc. SPIE 2299, 336-347 (1994); (3) Doyon et al. this issue.

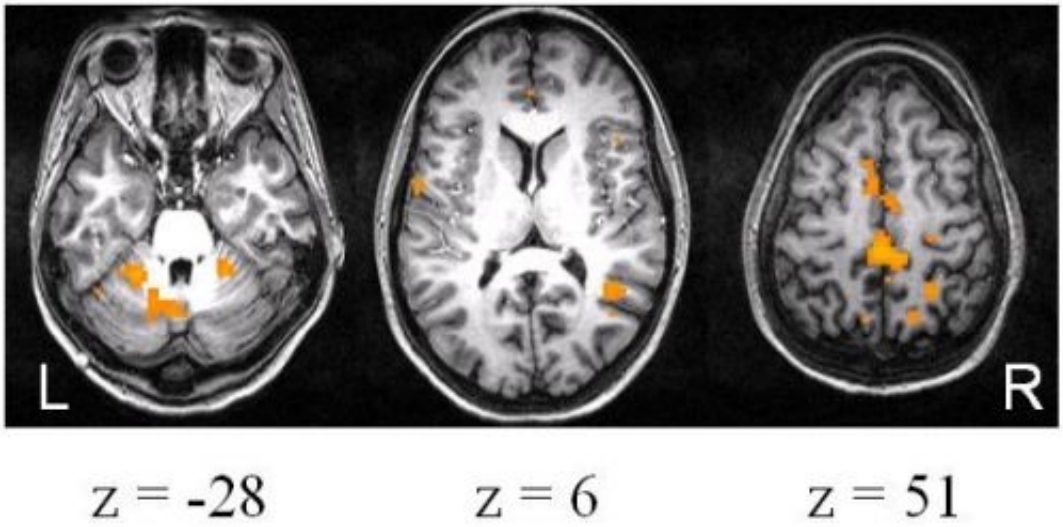

Activation maps (threshold: p < 0.01 uncorrected), superimposed on the corresponding axial slice. Z-coordinate refers to Talairach template.

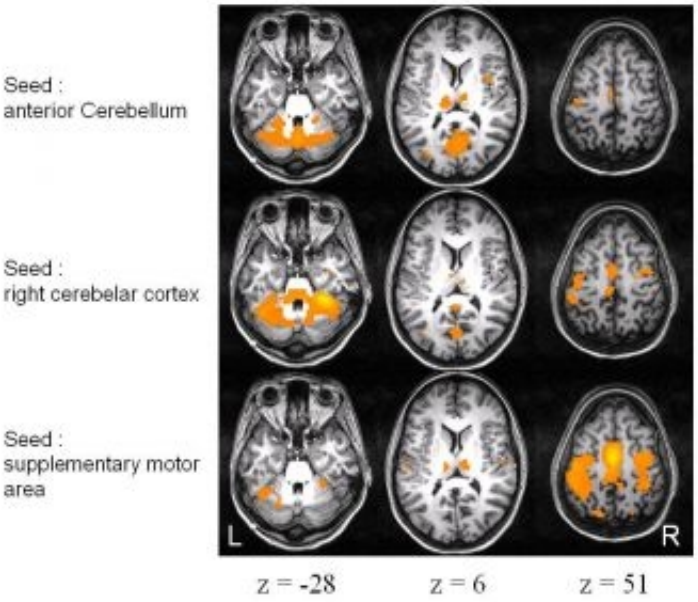

Correlation maps (threshold: p < 0.05 uncorrected), superimposed on the corresponding axial slice. Z-coordinate refers to Talairach template. Note that the thalamus was present on three maps, even though it was not activated. Localization and presence of peaks varied from maps to maps.

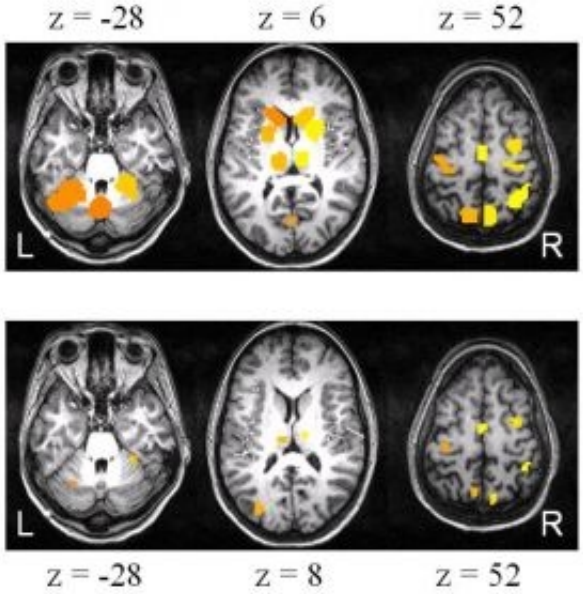

Top: manual delineation of areas where at least one correlation peak has been observed. The resulting network is larger than the one shown on figure b because all correlation maps to an activated region were taken into account. Bottom: resulting clusters after application of CAMIS. The region are 3-dimensional, so that all 15 voxels for each region do not appear on a single slice.

WE 123
Statistical Analysis of Simultaneous EEG-fMRI Data

Sumitra Purkayastha[1], **Robin I. Goldman**[2], **Keith J. Worsley**[3]
[1]Theoretical Statistics and Mathematics Unit, Indian Statistical Institute, Kolkata, India, [2]Hatch Center for MR Research, Columbia University, New York, U.S.A., [3]Department of Mathematics and Statistics, McGill University, Montreal, Canada

The functional significance of the alpha rhythm in humans is not known definitively. Alpha band activity has been used as an indirect measure of brain activation because increased activity in the frequency range is considered to be corresponding to decreased functional activity in underlying cortex. The identification of generator regions using scalp EEG alone, however, is challenged by the fundamental difficulties in localizing sources in a conductive volume from only surface information. In order to address this problem of localization, a current trend is to look at data collected simultaneously from EEG and some modality of medical imaging. This work reports findings of one such investigation on a simultaneous EEG-fMRI experiment.
We recorded simultaneous EEG and fMRI on subjects (eleven in number; mean age 30, age 23--43, five females) while they were at rest with their eyes closed. No visual or auditory stimuli were presented at any time during functional scanning.
EEG was recorded from 16 scalp sites of the international 10-20 system in a hard-wired bipolar montage (Fp2-F8, F8-T4, T4-T6, T6-O2, O2-P4, P4-C4, C4-F4, F4-Fp2, Fp1-F7, F7-T3, T3-T5, T5-O1, O1-P3, P3-C3, C3-F3, F3-Fp1). The functional scans were obtained on a General Electric 3T imager with Echo planar imaging (EPI) capability provided by Advanced NMR systems. The functional EPI gradient-echo scans in six adjacent slice planes, with the second most inferior slice oriented through the anterior commissure-posterior commissure (AC-PC) line to ensure consistency of slice plans across subjects (1,2).
The statistical analysis consists of fitting a linear model to the fMRI time-series for every voxel, with the powers in the alpha band corresponding to all the 16 channels as covariates. In particular, we explore the contribution of EEG data corresponding to each channel to the fMRI data, and compare these contributions. The magnitudes of the regression coefficients and also their dependence on the distance between the locations of electrodes used in collecting EEG data and voxels associated with the fMRI data are of special importance. We report these findings. We use the software fMRIstat (www.math.mcgill.ca/keith/fmristat) heavily in our work.

References

(1) Goldman, R.I. et al. Clinical Neurophysiology, 2000, 111:1974-1980.
(2) Goldman, R.I. et al. NeuroReport, 2002, 13:2487-2492.

WE 124
Investigating directed influences between activated brain areas in fMRI in a motor-response task

Birgit Abler[1], Alard Roebroeck[2], Annett Höse[1], Carlos Schönfeldt-Lecuona[1], Günther Hole[3], Henrik Walter[1]
[1]Dep. of Psychiatry, University of Ulm, Ulm, Germany, [2]Dep. of Cognitive Neuroscience, Maastricht University, Maastricht, The Netherlands, [3]Ravensburg, Germany

Introduction
Functional neuroimaging is very well suited to investigate the localization of certain brain functions. However information about functional interactions as well as information about the direction of these interactions is crucial for a deeper understanding of brain function. We applied vector autoregressive modeling in the context of Granger causality as a method to analyze directed connectivity [1] in a standard event-related fMRI study using a simple auditory-motor paradigm. The basic idea is to use temporal information in stochastic time series of a brain region in order to predict signal time courses in other brain regions. As causes precede their effects in time these predictions can be related to causal influences rather than to only correlational relations between brain regions. In our paradigm a simple motor action was triggered by an auditory command. Thus, we predicted that the method should demonstrate indirect causal influence of the auditory cortex on primary motor cortex.

Methods
11 right-handed healthy female subjects were studied in an event-related fMRI paradigm using a 1.5 Tesla Siemens Symphony Scanner (TR=2.44 sec, TE=40 msec). Subjects were instructed to press a ball with either their left or their right hand when hearing the command 'right' or 'left' (n=20 each) in the scanner. Data were analyzed using BrainVoyager (BrainInnovation, Maastricht). First, a standard model with regressors for left and right was calculated. Then, regions of interest (ROIs) were defined centered on the individual subjects' peak motor activity for left and right motor cortex. Finally, inhouse programs written in MATLAB (Natick, MA) were used to map Granger causality over the imaging volume for the selected ROIs [1] for each subject individually. The resulting Granger Causality Maps (GCMs) can be used to make inference on 1) Granger causality from the ROI to the rest of the brain, 2) Granger causality from other regions in the brain to the ROI. Bootstrapping was used to assign significance to the GCMs.

Results
Granger causality to the left motor cortex was found from bilateral auditory cortex as well as from the supplementary motor area (SMA) in 9 of 11 subject at a significance level of 0.001 uncorrected. Granger causality to the right motor cortex existed from bilateral auditory cortex in 5 and from SMA in 6 subjects.

Conclusion
Analysis of data with Granger causality in a standard event related fMRI paradigm was able to demonstrate that the time course in motor cortex can be predicted by past signal time courses in two areas which are known (by experimental design) to causally influence motor cortex. Evidence for directed connectivity was clearer for left motor cortex corresponding to the dominant hand. Our findings in a simple task show that even under sub-optimal circumstances (a relatively long TR) Granger causality can be a useful tool to explore effective connectivity. Temporally optimized scanning should increase that potential.

Reference
[1] R. Goebel, A. Roebroeck, D. Kim, E. Formisano. Investigating directed cortical interactions in time-resolved fMRI data using vector autoregressive modeling and Granger causality mapping. Magnetic Resonance Imaging 21 (2003) 1251-1261.

WE 125
Fully automatic lobe delineation for regional lesion load quantification in large a scale study

Faiza Admiraal-Behloul[1], Nicole Schmitz[2], Dominique MJ van den Heuvel[2], Hans Olofsen[1], Johannes HC Reiber[1], Mark A van Buchem[2]
[1]Leiden University Medical Center, Division of ImageProcessing, Leiden, The Netherlands, [2]Leiden University Medical Center, Department of NeuroRadiology, Leiden, The Netherlands

Fully automatic lobe delineation for regional lesion load quantification in large a scale study

Introduction

In a previous study, [1] we developed a semi-automated method to quantify white matter lesion (WML) load. It has been successfully used in a large study in geriatric subjects and produced clinically relevant results [2]. The main goal of the present work was to develop a software tool that allows the quantification of WML load in anatomical regions (lobes and cerebellum), for further correlation analyses with cognitive information in geriatric patients. A fully automatic template-based approach has been implemented and evaluated on 1054 scans. The software showed very high reliability.

Methods

MR images of 527 subjects, scanned twice (1054 scans), were acquired on a 1.5 Tesla system (Philips Medical Systems, Best, The Netherlands), and comprised dual fast spin-echo imaging (TE 27/120ms, TR 3000 ms, echo train length factor 10, 48 contiguous 3mm slices, matrix 256x256, FOV 220). These images have been, in previous work[1,2], semi-automatically segmented. For each subject the Intra cranial (IC) and WML masks, among others, were saved.

Three experts have delineated manually the lobes on a single T1 high-resolution image resized and co-registered to the Montreal Neurological Institute (MNI) brain template (109 slices, voxel size 2x2x2 mm, see figure1.a). The delineation is labor-intensive (10 hours). The 3D distance of every voxel to each lobe was then computed and every voxel of an IC prior probability map (from MNI) was assigned to the closest lobe (see figure 1.b). The obtained template-like image was used for a fully automatic IC and lobe delineation in a template-based approach, which combined affine registration, fuzzy clustering and mathematical morphology. Using the previously segmented WML masks, the system generates for each lobe and the cerebellum the respective WML load (see fig.2a). For quality control purposes, the software generates a mosaic view per subject, showing selected slices for visual inspection (see figure 2.b). Furthermore, a flag is automatically put on scans that did not co-register correctly to the template (using the value of the cost function of the registration).

Results and conclusion

Since it is very labor-intensive to manually delineate brain lobes, we used the total intra-cranial mask, semi-automatically delineated, to evaluate the automatic delineation. Out of the 1054 scans, 941 were automatically flagged as successfully segmented and the rest as possible failure. We compared the volumes of the semi-automatic IC and fully automatic IC masks (union of the 4 lobes and cerebellum) using intra class correlation coefficient (ICC), with one-way random effect model. We obtained an ICC of 0.949. The mean degree of overlap was 97% ±15%; The lobe delineation was evaluated visually using the mosaic images in the 941 successfully segmented subjects. Only 1% cases were marked as non-accurate delineation. Our automatic approach is therefore a valid and reliable tool for use in large-scale studies. The 1054 scans were processed fully automatically within 15 hours on a Pentium4.

References

1. F. Admiraal Behloul et al., ISMRM, 2003 .
2. D. v.d. Heuvel et al., ISMRM, 2003.
3. R.P. Woods et al., J CAT, 1998, vol. 22, pp 153-165.

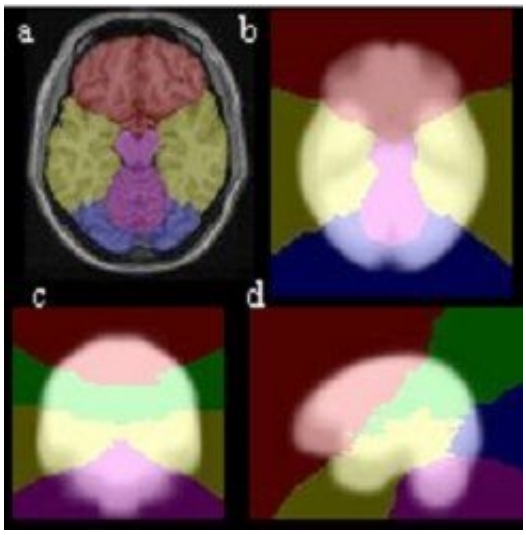

Fig 1. a: manually de lineated lobes. b: distance map on IC prior probabilities in axial view. c: in coronal view and d: in sagittal view.

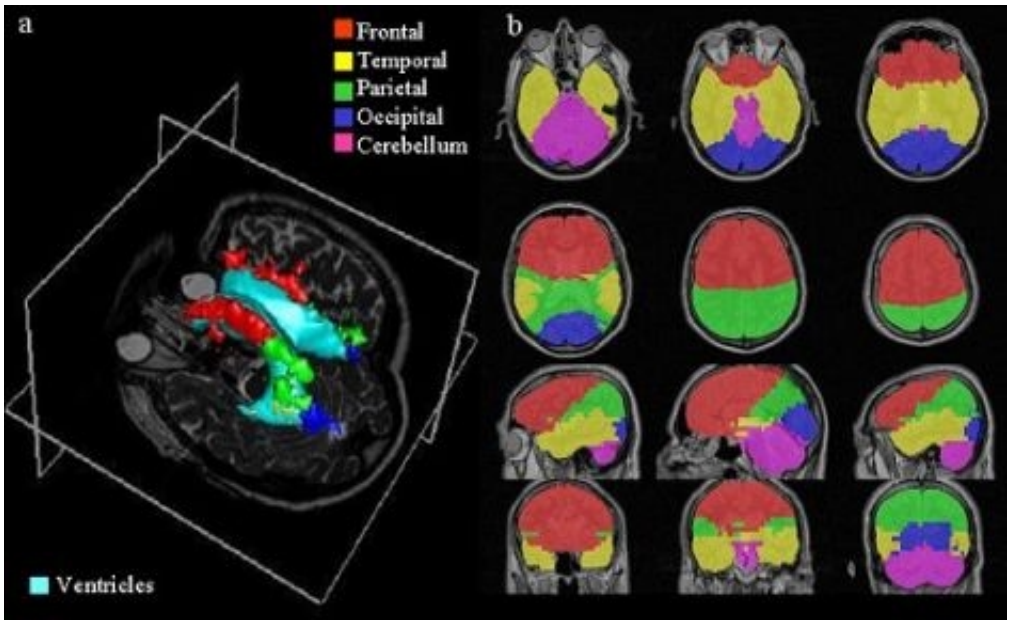

Fig 2 (a) WML assigned to intersecting lobes. (b) Mosaic view for quality control

WE 126
Application of Coherence Spectra to fMRI Connectivity Studies

Alexandre Andrade[1], Jean-Baptiste Poline[2], Jean-Luc Anton[3], Matthew Brett[4]
[1]IBEB/FCUL, Lisbon, Portugal, [2]CEA/SHFJ, Orsay, France, [3]fMRI Center, CHU La Timone, IFR 131, Marseille, France, [4]University of California, Berkeley, USA

BACKGROUND
Connectivity studies using fMRI rest state data have achieved significant popularity in the latest years (e.g. [1]). Typically, the data are temporally filtered, and correlation coefficients are computed between a reference time series and the remaining brain voxels. The physiological phenomena underlying this approach are poorly understood. Besides, several practical aspects are often overlooked: for instance, optimal temporal sampling is required, to avoid contamination by aliased cardiac and breathing components [2]. In the present study, we look into the frequency specificity of across-brain correlations, using coherence spectra. The purpose is twofold: a) to provide better grounds for correlation studies (to ascertain to what extent breathing and cardiac components contribute to correlations); b) to contribute to a better understanding of the spatiotemporal behaviour of fMRI noise.
METHODS
450 seconds of rest state data were acquired from one subject (Bruker 3 T, EPI, TR=303 ms, TE=27.5 ms, 64x64 matrix, 3x3x4 mm voxels, 6 slices + 2 mm gap). Simultaneous measurement of pulse and respiratory rhythm was performed. The scans were realigned, corrected for slice acquisition timing and spatially smoothed, using SPM99 [3]. Frequencies significantly different from white noise (including pulse and breathing frequencies) were classified as frequencies of interest (FOIs). ROIs were defined in structures often involved in imaging studies (e.g. striate cortex), and served as reference for the estimation of coherence maps for the FOIs. Correlation patterns of very low frequencies (< 0.08 Hz) were also computed, following the established low pass filtering approach.
RESULTS
The results indicate that both breathing and pulse (especially the latter) related components have the potential to confound correlation estimations, whenever aliasing occurs. For instance (see Figure), coherence patterns using anterior cingulate gyrus as a reference show marked frequency related differences (0.05 Hz: posterior cingulate, cuneal and precuneal regions involved; pulse frequency: contralateral insular cortex and ventricles). Overall, the coherence patterns centered at frequencies in the range 0.02-0.08 Hz were cognitively meaningful, and more sharply defined than correlation patterns of low pass filtered data. Careful choice of parameters allowed to probe the spectral fine structure of low frequency interactions.
CONCLUSIONS
The low pass filter approach has important limitations, and much can be gained by using a full frequency domain method instead. Coherence spectra are a powerful tool to probe frequency specific spatiotemporal interactions across the brain. Moreover, they allow rigorous statistical evaluation, and they are not phase sensitive (allowing detection of time lagged interactions). In this work, it was shown that contamination of the frequency spectrum by aliased pulse related components should indeed be a concern. Work in the near future should be directed towards optimization of the spectral estimation parameters (e.g. windowing), application of time-frequency methodologies (e.g. wavelets), and tackling possible non linearity of the interactions [4].
REFERENCES
(1) Hampson et al. (2002), Human Brain Mapping, 15:247-262
(2) Lund (2001), Magnetic Resonance in Medicine, 46:628
(3) www.fil.ion.ucl.ac.uk/spm/
(4) Lahaye et al. (2003), NeuroImage, 20:962-974

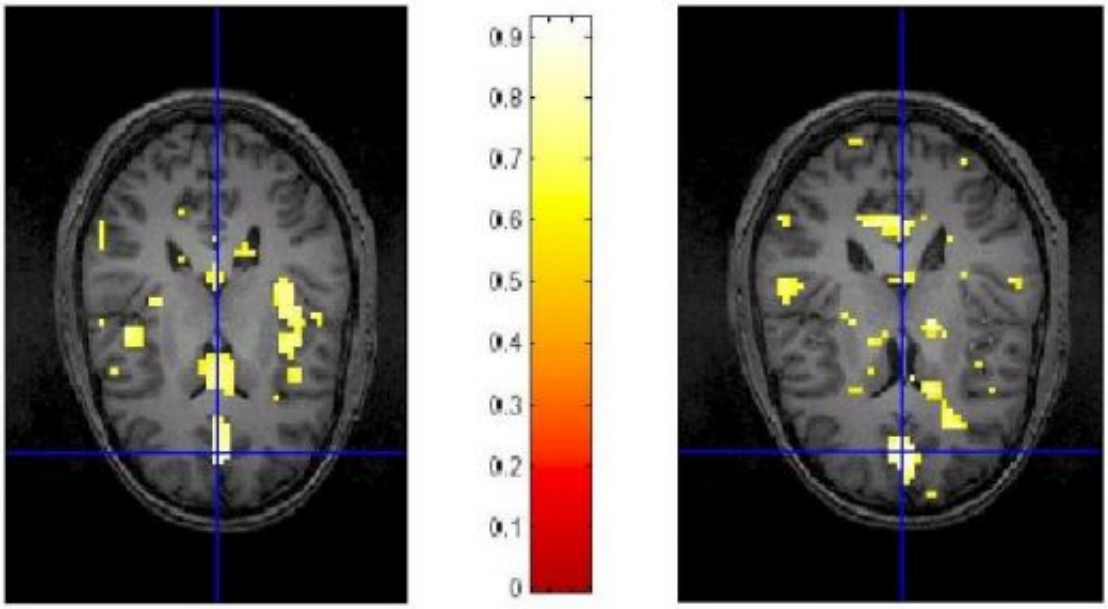

Thresholded coherence patterns at pulse frequency (left) and at 0.05 Hz (right)

WE 127
Segmentation by Integrating Intensity-based Classification and Template Matching

John Ashburner , Karl J Friston
Functional Imaging Laboratory, London, UK.

Many investigators currently use the tools within SPM for a technique that has become known as "optimized" VBM [1]. VBM performs region-wise volumetric comparisons among populations of subjects. It requires the images to be spatially normalized, segmented into different tissue classes, and smoothed, prior to performing statistical tests. The "optimized" pre-processing strategy involves spatially normalizing subjects' brain images to a standard space, by matching gray matter in these images, to a gray matter reference. The historical motivation behind this approach was to reduce the confounding effects of non-brain structural variability on the registration.
Tissue classification in SPM requires the images to be registered with tissue probability maps [2]. After this registration, these maps represent the prior probability of different tissue classes being found at each location in an image [3]. Bayes rule can then be used to combine these priors with tissue type probabilities derived from voxel intensities, to provide the posterior probability.
However, this procedure is inherently circular, because the registration requires an initial tissue classification, and the tissue classification requires an initial registration. This has been resolved by combining several components into a single large generative model. This model also includes parameters that account for image intensity non-uniformity, although it is now fairly standard to include intensity non-uniformity correction in segmentation [4] and registration [5] methods. Estimating the model parameters (for a maximum a posteriori solution) can then be done by repeatedly alternating among classification, bias correction and registration steps [6]. This iterative approach will provide better results than simple serial applications of each component (e.g. N3 [7], ANIMAL and INSECT [8]).
The classification component of this scheme involves updating class means, variances and mixing proportions, accounting for the current estimates of the intensity non-uniformity and warps for overlaying the prior probability maps. It uses the usual expectation-maximization strategy for fitting a mixture of Gaussians model.
The non-uniformity is re-estimated by holding the warps and mixture parameters fixed, and updates of the warps are made by fixing the bias and mixture parameters. A Levenberg-Marquardt optimization scheme is used for both these steps, requiring the first and second derivatives of the log-probability objective function to be computed with respect to the parameters.
Operational details, examples and improvements in relation to existing schemes will be presented.
References
[1] C. D. Good et al. NeuroImage 14:21-36 (2001).
[2] J. Ashburner and K. J. Friston. NeuroImage 6:209-217 (1997).
[3] A. C. Evans et al. NATO ASI Series A, Life Sciences 264:263-274 (1994).
[4] W. M. Wells III et al. IEEE TMI 15:429-442 (1996).
[5] K. J. Friston et al. Hum. Brain Mapp. 2:165-189 (1995).
[6] S. Warfield et al. Chap. 4 of "Brain Warping" (1999).
[7] J. G. Sled et al. IEEE TMI 17:87-97 (1998).
[8] D. L. Collins and A. C. Evans. Chap. 8 of "Brain Warping" (1999).

WE 128
Full Bayesian Analysis of the MEG Inverse Problem with lp-norm Priors

Toni Auranen[1], Aapo Nummenmaa[1], Matti S Hämäläinen[2], Iiro P Jääskeläinen[1,2], Jouko Lampinen[1], Aki Vehtari[1], Mikko Sams[1]

[1]Laboratory of Computational Engineering, Helsinki University of Technology, Espoo, Finland, [2]Massachusetts General Hospital - Massachusetts Institute of Technology - Harvard Medical School, Athinoula A. Martinos Center for Biomedical Imaging, Charlestown, MA, USA

Introduction

The well-described minimum-norm and minimum-current estimates (MNE and MCE) [1, 2] are widely used in estimating sources of MEG/EEG responses. In Bayesian interpretation, these models are members of the lp-norm prior family with a Gaussian likelihood for the measurements. MCE corresponds to the l1-norm source priors and produces rather focal estimates whereas MNE corresponds to l2-norm prior and results in more diffuse estimates. However, the choice between these two solutions is more or less arbitrary as any value of the lp-norm order *p* between 1 and 2 could be used. In Bayesian sense, the choice of the norm order *p* is subject to uncertainty and, since it is not *a priori* known, it can be treated as an additional unknown variable. Similarly, the width of the prior distribution, the regularization parameter, is not known. Here, we performed a full Bayesian analysis of the lp-norm prior model, using Markov chain Monte Carlo methods, to obtain numerical samples from the joint posterior distribution of the parameters (neural currents) and hyperparameters (lp-norm order *p* and the prior width).

Methods

A single-compartment MRI-based boundary-element model was utilized in the forward field calculations with source locations restricted to the cortical mantle. Furthermore, the source orientations were constrained to be normal to the cortex [3]. Simulated source and Gaussian noise was used to generate MEG signals. Slice sampling [4] was used to obtain numerical samples from the joint posterior distribution.

Results

5000 samples were drawn from the posterior. Convergence diagnostics and time series analysis was used to verify that the convergence of the sampler was plausible. Figure 1 shows a simulated source and the respective inverse estimate, which reflects the posterior expectation value of the currents integrated over the hyperparameters. The posterior distributions of the hyperparameters are also shown.

Discussion

Slice sampling was chosen to improve mixing of the Markov chain suffering from correlations between the parameters and the prior width. The method is computationally heavy but it is fairly automatic as it requires only little or no tuning of the sampling parameters. In this approach, all parameters and hyperparameters are estimated from the data without manual interaction. Notably, the distribution of *p* is somewhat diffuse, which suggests that fixing this hyperparameter to some *ad hoc* value (*e.g.*, 1 or 2) leads to overfitted estimates. At the present stage, for computational reasons, the source space consists of 1500 source locations. With cortical orientation constraint this may be too limited for empirical investigations. We are currently implementing methods to accelerate the computational procedure.

References

[1] Hämäläinen, M. S., and Ilmoniemi, R. J. *HUT Report TKK-F-A559,* 1984.
[2] Uutela, K. *et al. Neuroimage,* **10**:173180, 1999.
[3] Dale, A. M., and Sereno, M. I. *Journal of Cognitive Neuroscience,* Vol 5, **2**:162176, 1993.
[4] Neal, R. M. *The Annals of Statistics,* Vol 31, **3**:705767, 2003.

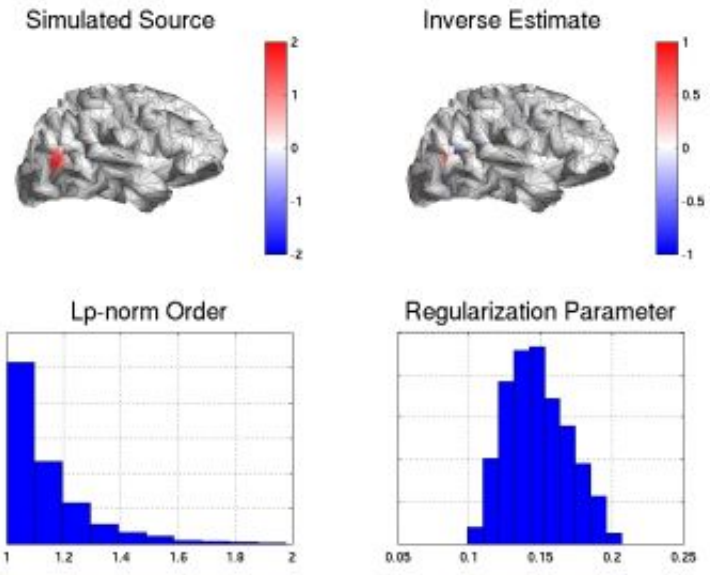

Figure 1. Top row: A simulated source and the corresponding inverse estimate. The surface represents gray-white matter boundary and it is viewed directly from the right side of the brain. Bottom row: The posterior distributions of the lp-norm order, *p*, and the prior width, regularization parameter, respectively.

WE 129
Multimodal Integration Of EEG And fMRI For The Estimation Of The Cortical Connectivity During A Finger Tapping Movement

Fabio Babiloni[1], Claudio Babiloni[1,2], Filippo Carducci[1,3], Febo Cincotti[4], Alessandra Basilisco[1], Laura Astolfi[1], Paolo Rossini[2,3,5], L. Ding[6], Y. Li[6], J. Cheng[6], K. Christine[6], J. Sweeney[6], Bin He[6]
[1]Dip. Fisiologia umana e Farmacologia, Univ. "La Sapienza", Rome, Italy, [2]AFAR, Ospedale Isola Tiberina, Rome, Italy, [3]IRCCS FBF San Giovanni di Dio, Brescia, Italy, [4]IRCCS Fondazione Santa Lucia, Rome, Italy, [5]Cattedra di Neurologia , Università Campus Bio-Medico, Roma, Italy, [6]University of Illinois, Chicago, USA

Aim. Recently, it has been demonstrated that the multimodal integration of high resolution EEG and fMRI recordings improves the estimation of the cortical activity. By using the cortical estimated waveforms and appropriate signal processing techniques, it is also possible to estimate the dependence of the activity in one cortical region of interest (ROI) from the activity generated in other ROIs. Here, we will use the Directed Transfer Function (DTF) technique to estimate the pattern of cortical connectivity subserving the finger tapping movements of the left hand finger from high resolution EEG and fMRI recordings in normal subjects.
Methods. High resolution EEG and fMRI recordings were performed in a group of normal subjects during a finger tapping task performed with the left hand. Realistic cortical and head models were used to estimate the cortical activity from these recordings with linear inverse methodologies. Cortical activity was estimated in particular regions of interest (ROI) coincident with the Brodmann areas. The estimation of the cortical connectivity patterns subserving the different phases of the task has been performed by using the DTF technique. The statistical significance of the observed pattern of cortical connectivity was assessed by generating an empirical distribution for the DTF values with surrogate EEG data. The analyzed patterns of cortical connectivity were discussed only if they were statistically significant at the 5%, corrected for multiple comparisons. The connectivity patterns were estimated in two time intervals, lasting 300 msec before and after the onset of muscular activity (EMG onset).
Results and Conclusions.
Different patterns of connectivity were observed during the task. The first one involves posterior parietal (B.A. 5) and the premotor-prefrontal areas in almost all the frequency bands examined and in the two time periods considered. Another one was observed in the alpha frequency band (8-12 Hz) after the movement begins, linking the primary somatosensory and motor area of both hemispheres. This last connectivity pattern is related to the actual performance of the movement, while the first one could be related to the general allocation of the attentional resources for the task performed. In the case of the connectivity patterns generated by the cortical estimation performed with the use of hemodynamic priors we noted a change with respect those already presented in the case of only EEG. The inclusion of the fMRI priors elicited the premotor-prefrontal clusters that were hidden in the analysis based on the EEG only

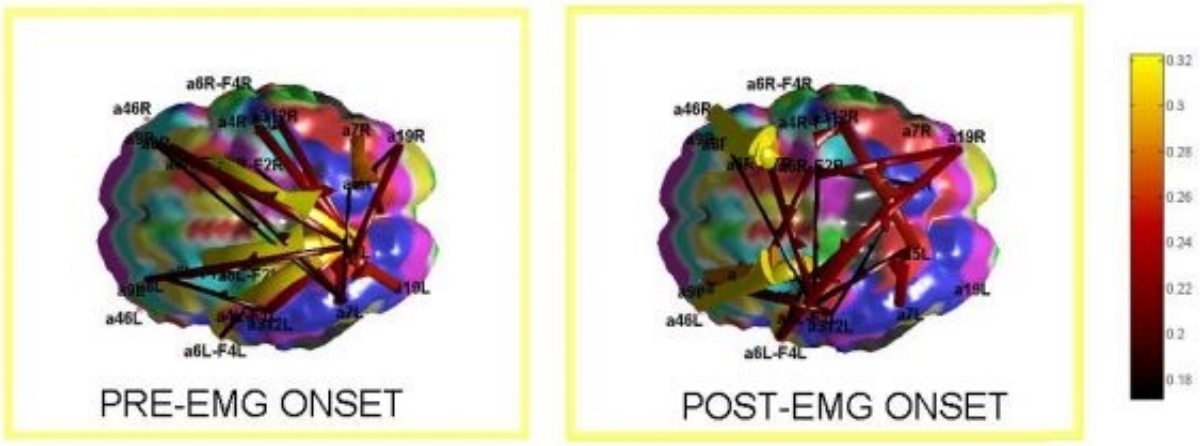

Figure presents a pattern of cortical connectivity estimated by the application of the DTF to the ROI waveforms, in a frequency band from 8 to 12 Hz, in a time period from -300 ms to the occurrence of the EMG trigger onset. The bar codes the values of DTF in colors. The labels represent the name of the ROIs in which statistically significant activity has been assessed

WE 130
The feasibility of real-time functional MRI analysis using computational grids

Epifanio Bagarinao[1], Kayako Matsuo[1], Yoshio Tanaka[2], Toshiharu Nakai[1]
[1]Life Electronics Laboratory, National Institute of Advanced Industrial Science and Technology, Osaka, Japan,
[2]Grid Technology Research Center, National Institute of Advanced Industrial Science and Technology, Tsukuba City, Ibaraki, Japan

Introduction
In [1], we reported a system for the real-time analysis of functional MRI time series using a dedicated PC cluster. The system exploits the advantages of parallel computing to attain fully real-time analysis of whole-brain fMRI data. In this study, we investigate the feasibility of employing remote resources via computational grids [2] to process functional magnetic resonance (fMRI) data in real time. The effect of two critical time factors, namely, data transfer time and analysis time, to the overall system performance is examined. The former is strongly influenced by the speed of the used network transport while the latter is dependent on the employed computational resources.

Implementation
Figure 1 shows the schematic representation of the prototype grid-enabled real-time system composed of an MR imaging subsystem and several analysis servers (PC clusters) and their interconnection via the Internet. Physically, the system may span several sites, which are geographically separated from each other. System integration is accomplished by the accompanying software component. The series of operations can be summarized as follows. After an image volume is acquired, the volume is immediately sent to the remote analysis server for immediate processing. The analysis server processes the received data using the approach in [3]. The updated results are sent back to the analysis workstation, which then updates its displayed activation map. These steps are repeated until all volumes are processed.

Results
One of the critical factors in the real-time analysis of fMRI time series is the analysis time. The results obtained demonstrated that a PC cluster with 16 processors was already sufficient to process a 64x64x30 image volume within a given TR (3 s). The bulk of the processing time was spent on image realignment (1.034 s per volume) whereas statistical analysis took around 23 ms per image volume. On the other hand, the time required to transfer the data from the analysis workstation connected to the MR scanner to the remote analysis servers varies from site to site. In one site, the transfer rate was around 17.69 ms per slice (16096 bytes). In another site, the transfer rate was around 11.28 ms per slice. This timing, however, depends on several factors including the number of users logged into the system, time of the day, network traffic, among others.

Discussion and Conclusion
Performing real-time analysis using computational grids imposes additional constraint in the overall performance of the system. The data transfer time introduces extra time in the overall analysis and is strongly affected by the unpredictable behavior of the network. In spite of this, the results indicated that real-time analysis is still possible with the activation map becoming available a few minutes after the last volume is acquired. Moreover, further performance improvement can be achieved using high-speed network connectivity.

References
[1] Bagarinao E, et al. Mag Res Eng 19B, 14-25 (2003)
[2] I. Foster and C. Kesselman, *The Grid: Blueprint for a Future Computing Infrastructure.* San Francisco: Morgan Kaufmann Publishers, Inc, 1999.
[3] Bagarinao E, et al. NeuroImage 19, 422-429 (2003)

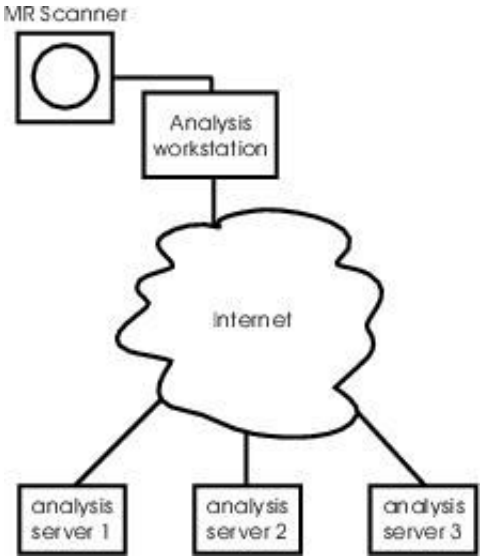

Figure 1. Schematic representation of a grid-enabled real-time analysis system. The MR scanner subsystem and the analysis servers can be geographically separated from each other interconnected only via the Internet.

WE 131
A NEW TECHNIQUE FOR SIMULTANEOUS STUDY OF PHYSIOLOGICAL AROUSAL AND BRAIN IMAGING

Matthew J. Barton[1,2], David Alexander[3], Evian Gordon[1,3], Leanne M. Williams[1,3,4]
[1]The Brain Dynamics Centre, Westmead Hospital, Westmead, NSW 2145, Australia, [2]Department of Psychological Medicine, University of Sydney, NSW 2006, Australia, [3]The Brain Resource International Database, Ultimo, NSW 2007, Australia, [4]School of Psychology, University of Sydney, NSW 2006, Australia

Introduction

At a time when advances in functional neuroimaging are providing increasingly precise techniques for mapping neural activity, the value of concurrent recording of autonomic variables, such as skin conductance (SC), remains often overlooked. Autonomic measurements can be used (i) to augment traditional analyses by providing both a continuous index of physiological arousal and a discrete and objective index of phasic responses to the significance, novelty and/or emotional valence of stimuli, and (ii) to measure potential sources of confound due to habituation or fatigue. The integration of brain and body measures has already shown considerable promise in functional MRI studies where subaveraging by simultaneous SC responses (SCRs) has revealed more precise brain network activity in both healthy and clinical samples [1,2]. Here we present two recent developments in this area from the Brain Resource International Database; an MRI-compatible SC recording system, and a new algorithm for analysing SC data.

Method and Results: Data Recording

Despite the challenges of developing non-standard MRI-compatible recording systems for autonomic data, reliable systems for recording SC and electrooculography have been developed [3,4]. We have designed and built an MRI-compatible system for recording multiple channels of autonomic data including heart and respiration rate, as well as SC. The system has been used to record interference-free data, requiring no post-processing, from over 100 subjects using a 1.5 T scanner. The SC channel consists of shielded, and radio-frequency filtered, Ag-AgCl finger electrodes placed on the medial phalanges of digits III and IV of the non-dominant hand. A constant 0.5 V_{DC} excitation across the fingers is provided by a SC adapter whose output is optically isolated, amplified and sampled at 10 Hz.

Method and Results: Data Analysis

Algorithms for auto-scoring SCRs have typically used peak-and-trough detection. This strategy is adequate for isolated SCRs (in long inter-stimulus interval, ISI, paradigms), but is unable to correctly score the compound (potentially overlapping) SCRs often seen in short-ISI cognitive paradigms. We previously used an algorithm based on a sigmoid-exponent model developed specifically to handle overlapping SCRs [1,2]. Here we report on a new technique that uses capacitance equations to decompose compound SCRs. The algorithm operates by extracting peak-containing segments to which an inverse capacitance equation is applied to generate an approximation to the individual SCR responsible for the observed peak. The reconstructed SCR is then scored for amplitude, latency and rise time. Analysis of 100 subjects with the new algorithm has shown increased robustness and accuracy over the previously used curve-fitting technique.

Conclusion

The simultaneous recording of fMRI with autonomic measures is a growing area of research which allows brain function to be probed more precisely. Such research however necessitates the development of both MRI-compatible recording apparatus and analysis techniques which facilitate the combining of fMRI-ANS data, as described here for SC.

References

1. Williams LM, et al. *NeuroImage* **14**, 1070-1079 (2001).
2. Williams LM, et al. *Am. J. Psychiatry* (In Press).
3. Shastri A, et al. *J. Magn. Reson. Imaging* **14**, 187-193 (2001).
4. Knuttinen MG, et al. *NeuroImage* **17**, 977-987 (2002).

WE 132
Multimodal fusion methodology applied to a categorisation task

Sebastien Basan , Cyril Pernet , Xavier Franceries , Pierre Celsis
INSERM U455, Neurological Department, CHU Purpan, 31059 Toulouse, France

Introduction
Categorization is a dynamic process of perception that reduces the complexity of our environment. One major topic in visual cognition is to understand, spatially and temporally, how our brain binds stimuli that differ in their physical features to produce categories. In the present study, neural spatio-temporal correlates of categorisation task were investigated using a combined fMRI and ERP interactive approach.
Materiel and Method
One subject performed a same/different task, responding for items that differ and not responding for identical stimuli. The categorisation task consisted in deciding whether items belong to the same category. For functional MR imaging studies, blood oxygen level-dependent (BOLD) imaging was performed using a T2*-weighted single-shot EPI sequence (64x64x16 matrix, FOV = 230 mm, 5 mm slice thickness). Functional images were processed with SPM2 (available at www.fil.ion.ucl.ac.uk) with a threshold p= 0.0001 and an extend threshold of 20 voxels. EEG data were obtained with a 64-electrode montage and were processed with Scan 4.2 (Neuroscan, USA) to compute ERP data. In addition, electrodes locations were acquired with a digitizer (Fastrak, Polhemus). A realistic boundary element model (BEM) was derived from 3D anatomical MRI and used to solve the inverse problem. In a first step, an ICA filtering was done to filter noise and enhance SNR (figure 1). In a second step, because of the poor EEG spatial resolution, ERP source localisation was computed with a distributed source algorithm (L2-norm) at fixed latencies to obtain a first estimation of source locations. Only source locations corresponding to the highest 5% part of intensity distribution were retained. In a third step, a direct comparison between distributed sources and fMRI data was performed to estimate co-location of ERP sources and fMRI activation loci. Finally, a dipolar model constrained spatially by fMRI data and in source number by distributed source reconstruction was computed for each latency previously analysed in order to validate the spatiotemporal modelling of our data.
Results
Five components were identified. N1 component (156ms) was modelled with 2 dipoles in occipital regions, one dipole in the left precuneus and in the right fronto-temporal area. P2a (210ms) exhibited 3 dipoles in the right fusiform gyrus, in the left cuneus and the right mid-dorsolateral prefrontal cortex. P2b (272ms) involved two dipolar sources in the left precuneus and the right fronto-temporal cortex. N2 component (360ms) was associated with a right mid-dorsolateral dipole and one left precuneus dipole, 1 left inferior occipital and 1 right fusiform dipole. Finally, P3 (420ms) was modeled with 3 dipoles in the left inferior occipital, the right fusiform dipole and the right mid-dorsolateral cortex. Categorisation task exhibited low residual variance (table 1) although generally modelled with few dipoles.
Discussion
Future research would make use of this new combined approach to elaborate spatiotemporal models at the group level, by identifying temporal and spatial differences from ERP and fMRI data and by combining multiple individual dynamic models.

Table 1

N1	P2a	P2b	N2	P3
1.12	1.48	4.59	3.98	3.23

Residual variance of each component

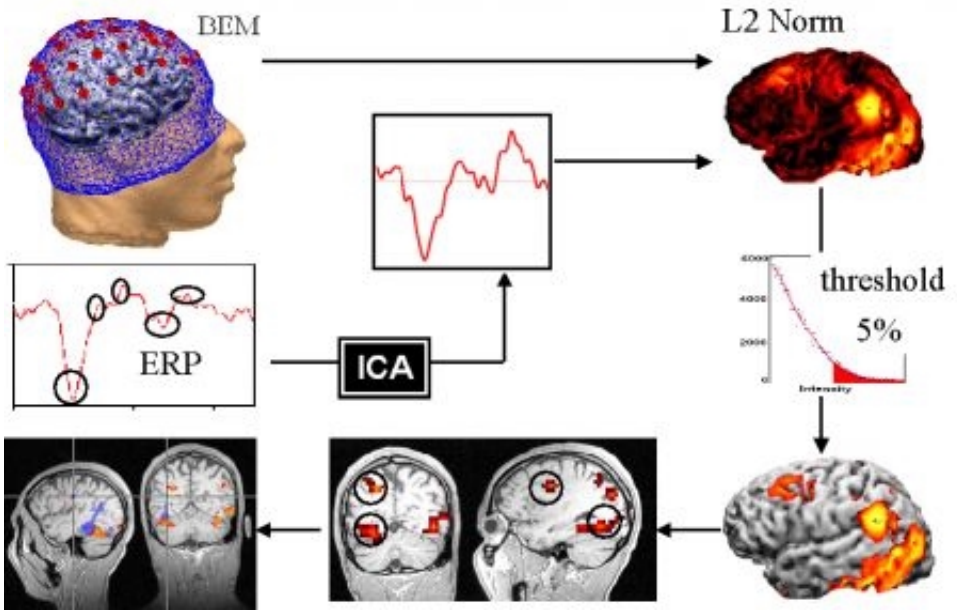

Figure 1 : Schematic representation of the methodology used in multimodal fusion

WE 133

Tensorial extensions to Independent Component Analysis for Multi-Subject/Session FMRI data

Christian F. Beckmann , Stephen Smith
FMRIB Centre - University of Oxford, U.K.

Abstract

We discuss the analysis of multi-subject/ multi-session FMRI data by extending standard bilinear models to higher dimensions and present a method for an iterated rank-1 tensor ICA decomposition based on a generalisation of a 3-way parallel factor analysis (PARAFAC) model [1].

Method

The three-way PARAFAC technique is characterised by the following generative model:

$$x_{ijk} = \Sigma_r \, a_{ir} b_{jr} c_{kr} + \varepsilon_{ijk},$$

where the data at time point *i*, voxel location *j* and session (or subject index) *k* is given by the sum of *R* products from vectors that characterise processes in time ($\boldsymbol{a}_r$), space ($\boldsymbol{b}_r$) and across subjects/sessions ($\boldsymbol{c}_r$).

This gives rise to expressions for the individual 2-D subsets of the 3-D data $\boldsymbol{X}$:

$$\boldsymbol{X}_{..k} = \boldsymbol{A}\mathrm{diag}(\boldsymbol{c}_k)\boldsymbol{B}^t + \boldsymbol{E}_{..k}; \; k=1,2,...,K,$$

(similarly for $\boldsymbol{X}_{.j.}$ and $\boldsymbol{X}_{i..}$). These can be expressed as

$$\boldsymbol{X}_{IK*J} = (\boldsymbol{C}|*|\boldsymbol{A})*\boldsymbol{B}^t + \boldsymbol{E}, \quad (1)$$

where $\boldsymbol{X}_{IK*J}$ denotes the matrix formed by concatenating all *K* different data sets and $(\boldsymbol{C}|*|\boldsymbol{A})$ denotes the *Khatri-Rao* product of $\boldsymbol{A}$ and $\boldsymbol{C}$ (*K* stacked copies of $\boldsymbol{A}$ scaled by $\mathrm{diag}(\boldsymbol{c}_k)$ [2]).

Optimising for statistical independence in the spatial domain, the matrices $\boldsymbol{A}$, $\boldsymbol{B}$ and $\boldsymbol{C}$ can be identified by iterating the following steps:

(i) treating eqn. (1) as a 2-D problem with $(\boldsymbol{C}|*|\boldsymbol{A})$ as the 'mixing matrix' $\boldsymbol{M}$ and finding spatially independent maps $\boldsymbol{B}^t$ and a new estimate of $\boldsymbol{M}$ as in [3].

(ii) identifying $\boldsymbol{a}_r$ and $\boldsymbol{c}_r$ from $\boldsymbol{M}$ via a rank-1 SVD of each column *r*, reshaped into *I*K* matrices $\boldsymbol{M}_r$ and collecting eigenvectors and loadings into $\boldsymbol{A}$ and $\boldsymbol{C}$.

Model order selection is treated as in [3] and final spatial maps are thresholded using a Gaussian/Gamma mixture model [4].

Example

The data consist of 10 sessions under the motor paradigm from [5]: right-handed male; block design with 24.6s on/off periods, right index finger tapping at 1.5 Hz. Figure (1) shows GLM mixed-effects results, generated by fixing both the temporal signal characteristics (design matrix) and the assumed response over sessions. In contrast, Figure 2 shows tensor-ICA results (*R=19*), where the signal characteristics in space, time and across sessions is estimated from the data. The spatial maps correspond closely, with fig. 2 showing larger clusters especially in bilateral secondary somatosensory areas (both maps thresholded using mixture modelling [4]). The estimated session response corresponds closely to observed variation in individual post-threshold first level cluster sizes. While this presentation only deals with the single group case, the approach can be extended to multiple groups.

Conclusion

The Tensor-ICA approach provides a conceptually attractive decomposition of multi-subject/session FMRI data into sets of characteristic spatial/temporal and session modes. Simulations on artificial and real FMRI data suggest that Tensor-ICA is able to accurately identify underlying signals and extract plausible modes in 3-way data.

Acknowledgements
UK MRC and GSK for finacial support and D. McGonigle for data.

References

[1] Harshman, R. et al (1994) *Comp. Statistics and Data Analysis*, 18:39-72
[2] Bro, R. *PhD Thesis* (1998)
[3] Beckmann, C.F. et al (2003) *Proc. 4th Int. Symp. ICA & BSS*, 301--306
[4] Beckmann, C.F. et al (2003) *Proc. HBM*, 985
[5] McGonigle, D. et al (2000) *NeuroImage*, 11:708-734

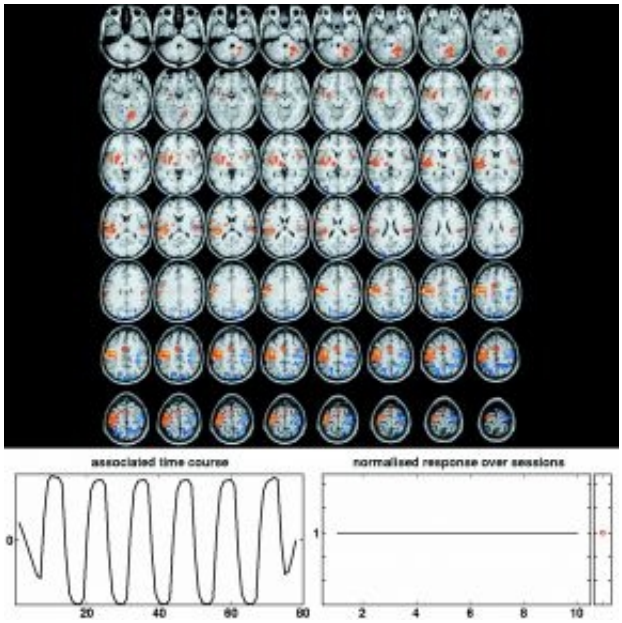

GLM mixed-effects results

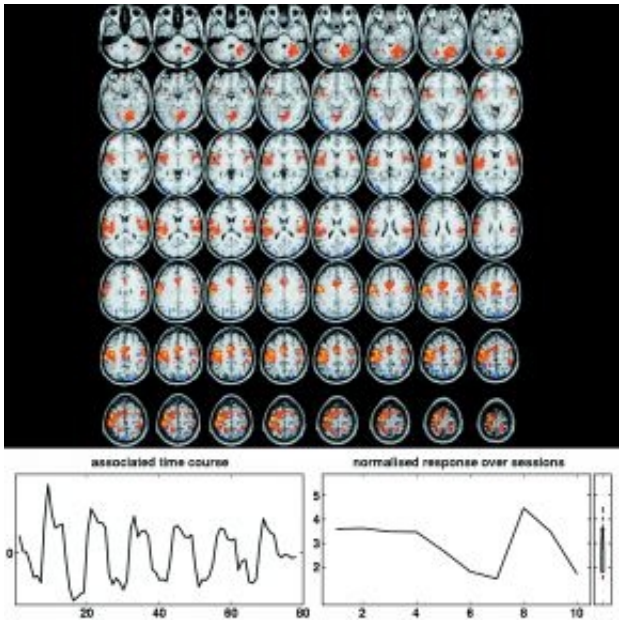

Tensor ICA spatial map, time course and session response

WE 134

Reordering diffusion-based connectivity matrices to define anatomical networks in the human brain.

T E J Behrens[1,2], H Johansen-Berg[1], S M Smith[1], J M Brady[2], P M Matthews[1], D J Higham[3]
[1]FMRIB Centre, University of Oxford, UK, [2]Dept. Engineering Science, University of Oxford, UK, [3]Dept. Mathematics, University of Strathclyde, Glasgow, UK

Introduction

The anatomical connectivity pattern of a brain region determines its function. Brain areas with distinct functions have different connectivity patterns. Conversely, regions with similar functions have similar connectivity patterns and are highly interconnected. A defining feature of such hierarchical networks is that their connectivity matrices may be reordered (by simultaneous permutation of rows and columns) such that blocks of high connectivity appear around the leading diagonal [1]. Here we use diffusion imaging of the human brain to provide pairwise connectivity information between all areas of the human visual system and submit these data to a spectral matrix reordering routine to test the hypothesis that they may be organised into a hierarchical form.

Methods

Diffusion-weighted data were acquired with an optimised method [2] based on echo planar imaging, implemented on a General Electric 1.5 T Signa Horizon scanner with a standard quadrature head-coil and maximum gradient strength of 22 mT /m. 60 diffusion weighted volumes were acquired with diffusion gradients isotropically distributed in angular space, with a maximum b-value of 1150 smm^{-2}. Cardiac gating was applied to minimize artefacts due to CSF pulsatile flow.

Probabilistic tractography was carried out from each seed voxel in structural space, according to [3]. Connectivity values were stored from each seed voxel to every other voxel in the visual system (seed/target masks were resampled to a coarse resolution of $10x10x10mm^3$). Log connectivity information was arranged in a matrix, **A**. Symmetry was imposed on this matrix by computing $\mathbf{C}=(\mathbf{A}+\mathbf{A}^T)/2$ (figure 2 (right)). The nodes in this matrix were then permuted using a spectral reordering algorithm [4]. This algorithm looks for the node reordering which minimises the sum of element values multiplied by the squared distance of that element from the diagonal, hence forcing large values to the diagonal. The algorithm does not search for clusters in the matrix. Clusters that emerge are due to organisation in the data.

Results

Figure 2 shows the connectivity matrix in its original form (A) and after spectral reorganisation (B). The matrix was divided by eye into 3 dominant clusters (horizontal coloured bars in Fig 2(right)). These clusters were then mapped back onto their anatomical location (Figure 3). The first cluster (blue) included lateral parietal lobe corresponding to putative dorsal visual stream. The second cluster (yellow) included inferior occipital lobe and inferior temporal lobe corresponding to putative ventral visual stream. The third cluster (red) included medial occipital lobe corresponding to putative primary visual cortex (V1). Clusters are consistent across subjects.

Discussion

Applying a spectral reordering routine to a matrix of connectivity values between brain voxels revealed hierarchical network organisation. Clusters of nodes emerge in the reorganised matrix. When mapped back into anatomical space, these clusters appear to correspond well with the ventral and dorsal processing streams in the visual system and primary visual cortex.

References

[1]Hilgetag et al. Philos Trans R Soc Lond. 2000 355, 91-110. [2]Wheeler-Kingshott et al. ISMRM 10, 1118 2002 [3]Behrens et al. MRM. 2003 50,1077-88 [4]Higham J. CA Math., 158, 2003, 61-74

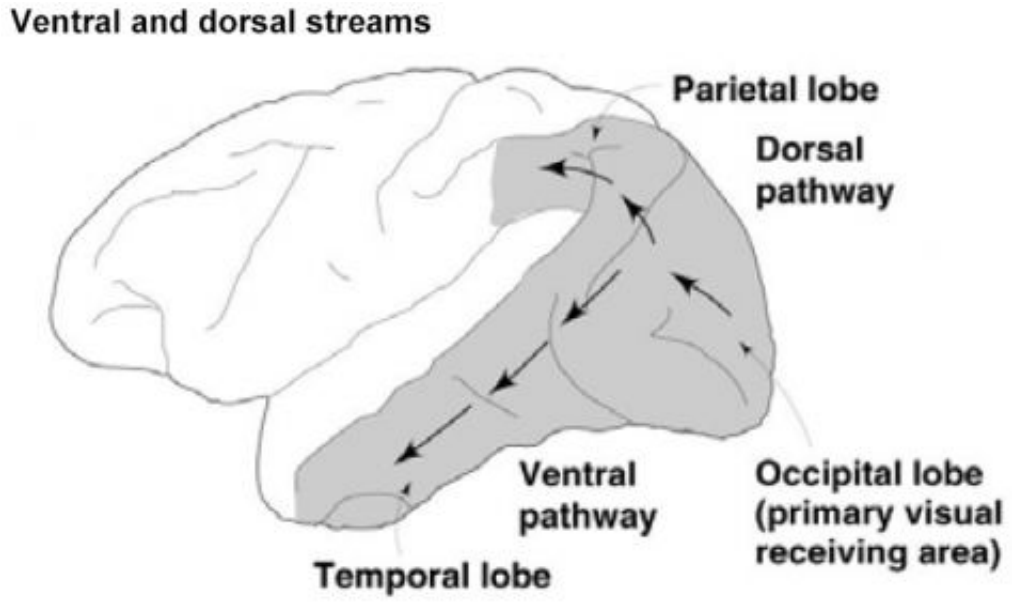

Visual information is sent from primary visual cortex (V1) along 2 broadly parallel processing streams [2] . The ventral pathway processes object form information and includes projections to inferior temporal lobe. The dorsal pathway processes information on object motion and includes projections to posterior parietal cortex.

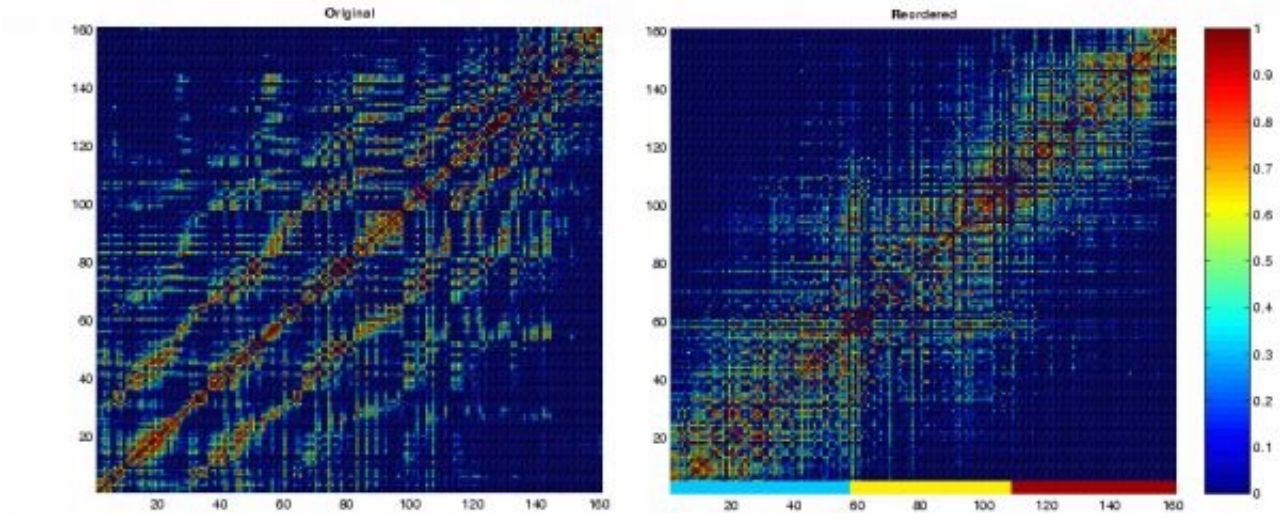

Connectivity Matrices. Original (left) and reordered according to spectral reordering.

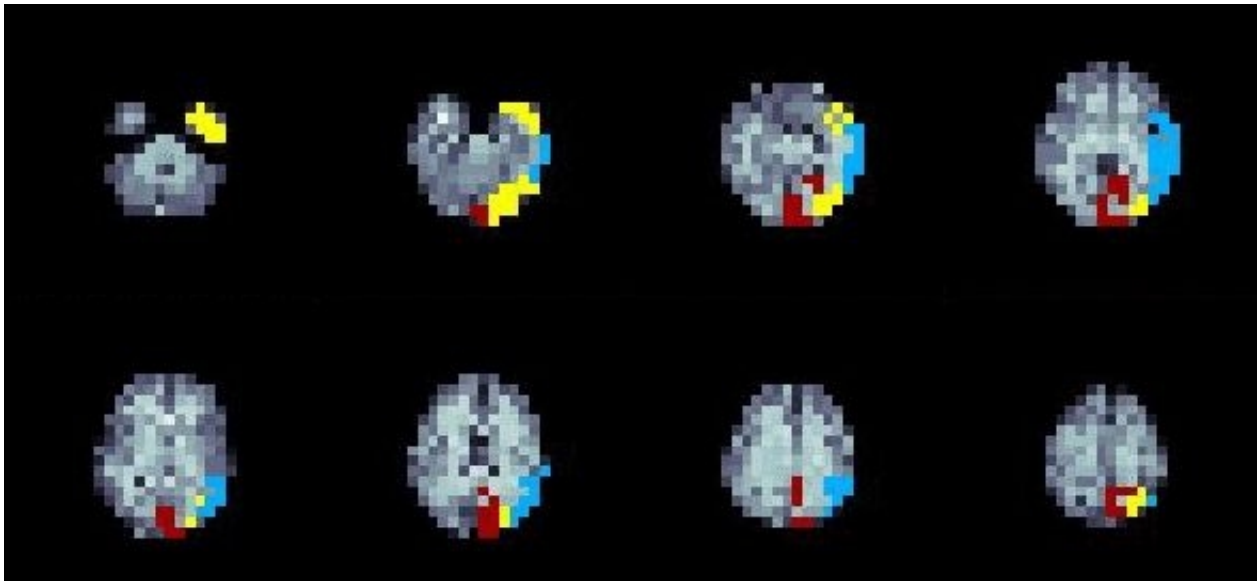

Clusters recovered from connectivity matrix reorganisation of the visual system. Colours correspond to coloured clusters at the bottom of the right hand matrix in figure 2.

WE 135
A new Algorithm for Detection of Coherent Brain Areas working with MEG data

Paolo Belardinelli[1,2], Luca Ciancetta[1,2], Vittorio Pizzella[1,2,3], Cosimo Del Gratta[1,2,3], Gian Luca Romani[1,2,3]
[1]Department of Clinical Sciences and Biomedical Imaging - University of Chieti, Italy, [2]Institute of Advanced Biomedical Technologies - Fondazione Università G. DAnnunzio, Chieti, Italy, [3]INFM - GC Chieti, Italy

The study of spontaneous activity and coherence between different regions in the brain is an issue of growing importance in recent neuroimaging studies. Starting from the work of Gross et al. with MEG data, we conceived an algorithm the application of which is independent from a particular external reference signal. This may be done by integrating the original algorithm with additional tools for the identification of an internal reference signal.
The description of the procedure follows. A discrete isotropic 3D grid is placed inside a spherical model of the brain. The sphere is fitted to the reference points on the real head. A set of tomography localization tools (derived from Loreta and SAM) was developed to detect the areas characterised by the strongest activity. The maximum of electric activity is considered the starting point for the detection of coherent areas. When the areas of interest have been localized, a map of the coherence degree between the different areas of the brain is obtained to study further kinds of interactions (phase locking, directionality).
The possible applications of this procedure are numerous, especially in the field of cognitive studies where many different brain areas are activated in complex sequences. As an example, we are currently working on MEG data recorded during sexual arousal, where the interplay of many brain districts, such as thalamus, hypothalamus, hippocampus, amygdala, anterior cingulate, insula, is expected.

WE 136
Calibrating BOLD fMRI Response Latencies Using Gd-DTPA Bolus Washout Dynamics

Rasmus M Birn[1], Karen E Bove-Bettis[2], Peter A Bandettini[1,2]
[1]Laboratory of Brain and Cognition, National Institute of Mental Health, [2]Functional MRI Facility, National Institute of Mental Health

Introduction:
Mapping the relative timing of brain activation with functional magnetic resonance imaging (fMRI) is at present difficult, since the latency of the blood oxygenation level dependent (BOLD) response is dominated by spatial heterogeneity of the vasculature. This heterogeneity gives rise to variations in response latency of several seconds, clearly dominating underlying neuronal timing variations. The goal of this study is to estimate the vascular contribution to the spatial variation in the latency of the BOLD response by measuring the dynamic signal changes following a bolus injection of a susceptibility contrast agent, gadopentetate dimeglumine (Gd-DTPA). More specifically, it is hypothesized that the Gd-DTPA washout time is reflective of the transport of blood from the microvasculature in cortex through the draining veins, and would therefore be correlated with the latency of the BOLD response. This estimate is then applied to a hemi-field visual stimulation paradigm, to test whether this calibration technique can improve the estimation of subtle differences in the onset of neuronal firing.
Methods:
Several series of axial echo-planar MR images were acquired through the visual cortex. In two runs, subjects viewed a contrast reversing checkerboard for periods of 10s alternated with fixation periods of 10s. The checkerboard in the one visual hemi-field was turned on either 500ms or 1s before the checkerboard in the other hemi-field. In two runs, subjects viewed no stimulus and received a bolus injection of Gd-DTPA after 1 minute of scanning.
Functional areas were identified by correlating the measured response with an ideal reference function. Signal time-courses measured during the Gd bolus were fit on a voxel-wise basis to Gamma-variate functions. The latency of BOLD and Gd-DTPA responses were also computed by finding the peak of the correlation function of the time-course with an ideal response. BOLD latency maps from the hemi-field stimulation paradigm were calibrated by subtracting the washout time of the Gd-DTPA bolus.
Results:
A Gamma-variate function provided a good fit to the Gd-DTPA-induced signal change. This fit was repeatable across runs. The latency of the BOLD response was only slightly correlated with the onset of the Gd-DTPA bolus (average correlation-coefficient = .23). A better correlation was found between the BOLD latency and the Gd-DTPA washout time constant (average CC = 0.36). Using this estimate to calibrate the BOLD latency estimate resulted in a small improvement in the delineation of underlying neuronal latency differences, but considerable variability remains.
Discussion & Conclusion:
Attempts at correcting variations in the BOLD latency by comparing the timing to dynamics of a Gd-DTPA bolus have been performed previously, but these studies have focused only on the onset latency of the Gd-DTPA induced signal decrease, a time constant that is influenced by variations in the arrival time of the bolus from the site of injection to the arteriolar sphincters. As shown here, the washout time of the Gd-DTPA, is more predictive of BOLD latencies. Remaining variability can be due to a variety of sources, and may be improved by more accurate modeling of the hemodynamic time constants.

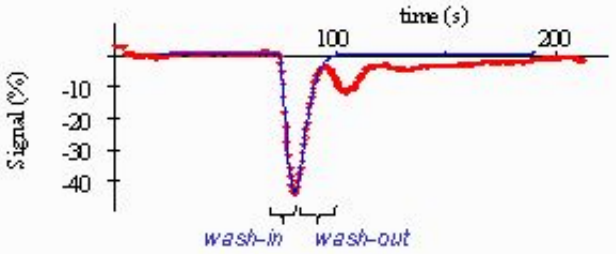

Figure 1: Average signal intensity time course showing signal decrease following a bolus injection of Gd-DTPA. Red points = data; blue line = gamma-variate fit

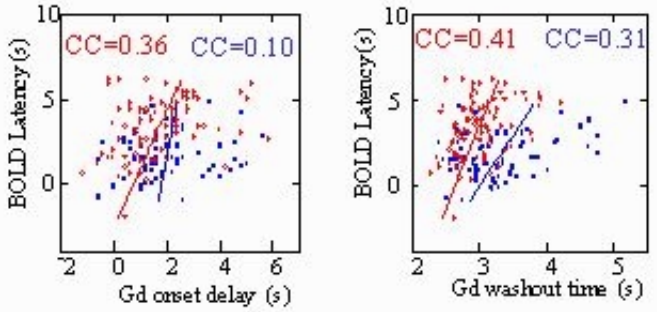

Figure 2: Correlation of the BOLD response latency with a) the Gd onset delay and b) the Gd washout time. Red points = left hemisphere, blue=right hemisphere. BOLD latency is more correlated with Gd washout time.

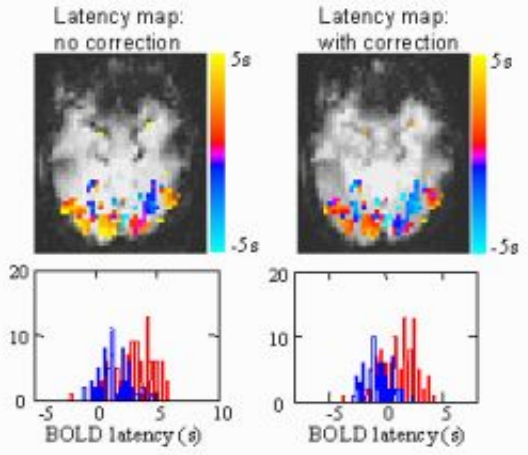

Figure 3: latency of BOLD response (left) before and (right) after correction, performed by subtracting the washout time estimated from the Gd bolus.

WE 137
When is a conjunction not a conjunction?

Matthew Brett[1], Tor Wager[2], Jean-Baptiste Poline[3], Tom Nichols[4]
[1]CognAc lab, Psychology department, University of California, Berkeley, CA 94720, USA, [2]Department of Psychology, Columbia University, New York, NY 10027, USA, [3]SHFJ/CEA/INSERM, Orsay, France, [4]Department of Biostatistics, University of Michigan, Ann Arbor, MI 48109, USA

Neuroimaging experiments can require conjunction inference (Price and Friston 1997). For example, it may be interesting to find brain areas that are commonly activated across different tasks. Imagine a study on working memory (WM), with a verbal WM task (task A) with a verbal control (task B), and a spatial WM task (C) with a spatial control (D). If there are areas of activation that are common to the two subtractions [A-B] and [C-D], these areas may be involved in WM independent of modality. This is a test of logical AND, finding areas where both [A-B] AND [C-D] are activated.

Price and Friston suggested the following way of getting at this problem; find areas where ([A-B] + [C-D]) is statistically significant (main effect), then remove all areas where [A-B] - [C-D] is significant (interaction effect). This was the 'interaction' conjunction test implemented in SPM96.

This method had problems. It equated the lack of statistical significance for the interaction with no effect; for example, if [A-B] is large and [C-D] is small, it is possible to have a significant main effect but not a significant interaction, and hence for the test to be positive. Alternatively both [A-B] and [C-D] could be very large but different in magnitude, giving a significant main effect and interaction, and a negative test.

In 1999, Worsley and Friston proposed a Minimum Statistic Test (MST) for conjunction. Imagine a brain region where [A-B] gives a t statistic of 1.5 and [C-D] gives a t statistic of 1.6. Alone, neither t value is convincing, but the fact that both values are quite high suggests there may be a real effect. This intuition can be formalized by taking the minimum t value from ([A-B] and [C-D]), here 1.5, and testing if this value is unexpectedly high for the minimum of two random t values under the null hypothesis. If so, we conclude there is some effect over [A-B], [C-D]. SPM99 and SPM2 use the MST for conjunction analysis.

Researchers usually interpret the MST as a test of logical AND in the sense described in Price and Friston (1997). Unfortunately this is incorrect. The problem arises because the null hypothesis for the MST is that *none* of the tasks have activated, which can be refuted if *any* task activates. Consider the t values for a single prefrontal voxel across 5 tasks, 4 WM tasks and a flashing checkerboard (FC) task. All WM tasks give a high prefrontal t value; by chance the FC gives a prefrontal t slightly less than 0. The 5% uncorrected threshold for one Z is 1.64, but the 5% uncorrected threshold for the minimum of 5 Z's is -0.12, so the MST is significant even if the minimum value is less than 0. If we interpret the MST as a test of AND, we must conclude that FC activates prefrontal cortex, although this is clearly false.

In fact we show that a test for activation in every comparison needs to use the standard thresholds for each single comparison. Readers and reviewers should consider screening for problems related to MST.

WE 138
Component-Wise Model of the BOLD Response in the Human Primary Visual Cortex

Emma S. Buneci[1], Kenneth C. Roberts[2], Rachael Brady[1], Allen W. Song[3], Xiaobai Sun[1], Marty G. Woldorff[2]
[1]Department of Computer Sciences, Box 90129, Duke University, Durham, NC 27708, [2]Center for Cognitive Neuroscience, Box 90999, Duke University, Durham, NC, 27708, [3]Brain Imaging and Analysis Center, Duke University Medical Center, PO Box 3918, Durham, NC 27710

Introduction

We report our investigation in characterizing and modeling the relationship between stimulus duration and the hemodynamic response (HDR) in the human primary visual cortex.

Materials

A 4.0 Tesla GE scanner was used with a Nova Medical surface coil. Visual stimuli were displayed via a LCD goggle system. We acquired 22 slices per time point (TR=1sec) that were centered on and parallel to the calcarine fissure (2D inverse spiral pulse sequence, 64x64 matrix, 3.75mm isotropic voxels). Subjects fixated on a central cross while a series of visual stimuli were presented. There were two different types of visual stimuli, presented in random order: 1) a frequent regular stimulus (83.33%), which was a black/white radial checkerboard pattern and 2) an infrequent target stimulus (16.67%), which was the same as the regular stimulus except it contained a color change during the last 30ms. The stimulus was displayed to the subject at 9 different durations from 50ms to 1500ms. Subjects were instructed to press a button at each occurrence of the target stimulus. The stimulus onset asynchrony (SOA) was constant at 16s.

Methods

Data analysis consisted of four steps: 1) preprocessing, 2) time-locked averaging within the primary visual cortex 3) testing of the linear transform model for the averaged event responses 4) modeling of the HR using a newly proposed component-wise model, C-WISE. In preprocessing, the SPM99 package was used for slice timing correction, motion correction, co-registration of functional with anatomical images, smoothing with a Gaussian filter of FWHM=8mm, and high pass filtering to remove low frequency drifts. Correlation analysis was used for signal detection and for the formation of activation maps. Our C-WISE model describes the observed HDR as the integration of three component hemodynamic responses triggered by two types of neuronal activations. The activations from onset and offset transient neurons are assumed to respond immediately and relatively briefly to the stimulus onset and offset, respectively. The response due to the activities of sustained neurons is proportional to the stimulus duration. The model specifies also additional constraints based on physiological conditions and expectations. The model parameters were estimated using nonlinear programming techniques.

Results

We found that across the duration range of the stimuli used here (<1.5s), a linear model breaks down. This finding is in agreement with other studies showing nonlinearity in the BOLD response. Both linear and nonlinear behaviors are captured in the model components: onset, sustained and offset. Figure 1 illustrates a very good fit (R^2=0.968) between the data (solid traces) and the model (dotted traces). Figure 2 shows in detail the estimated components for each of the stimulus durations. We note that both the offset and sustained neuronal activations begin to contribute to the HDR at around 200-400ms duration and both increase in amplitude as the duration increases, a pattern consistent with studies from the ERP and single-unit literature.

Conclusion

C-WISE represents a novel approach to modeling the HDR. It offers a physiologically structured mapping between component hemodynamic responses and activities associated with different neuronal populations.

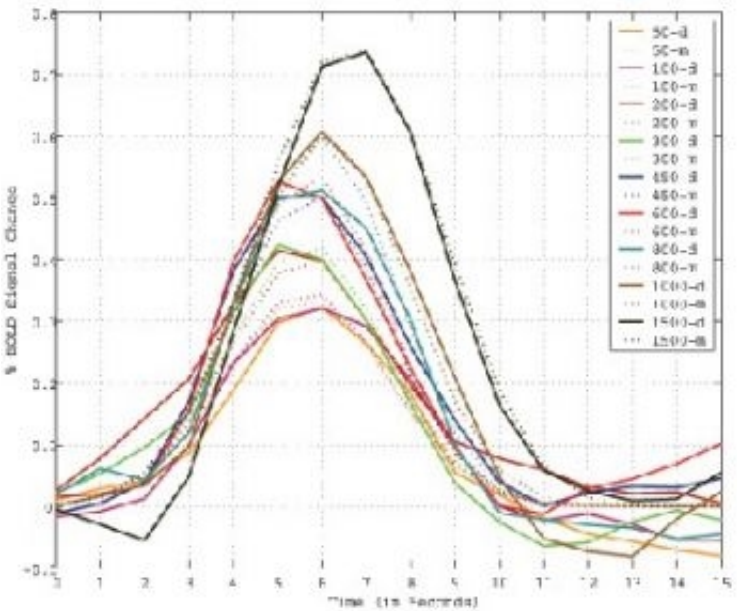

Figure 1: Data and Model Fitting of the C-WISE model.

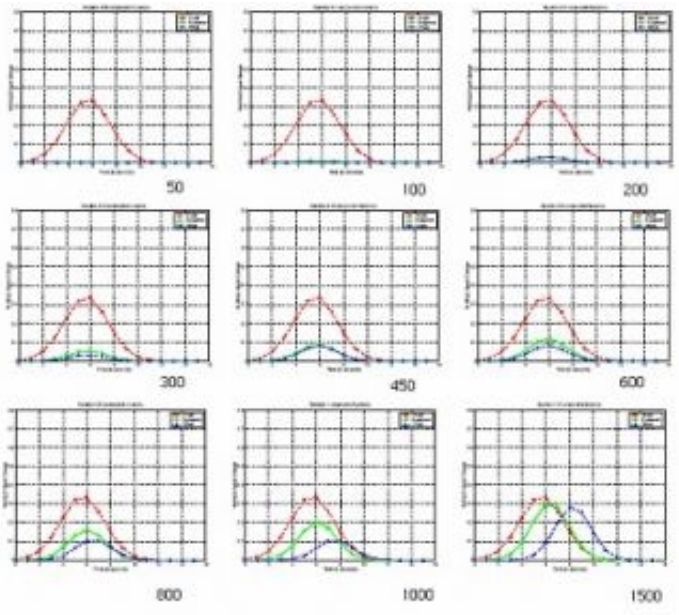

Figure 2: Individual response decomposition to an onset, sustained and offset component. Red Curve: Onset Component, Green Curve: Sustained Component, Blue Curve: Offset Component for the C-WISE proposed model.

WE 139
FMRI Analysis with the General Linear Model: Removal of Latency-Induced Amplitude Bias by Incorporation of Hemodynamic Derivative Terms

Vince D Calhoun[1,2,3], Michael Stevens[1,2], Godfrey D Pearlson[1,2,3,], Kent Kiehl[1,2]
[1]Olin Neuropsychiatry Research Center, Hartford, CT, [2]Yale University Dept. of Psychiatry, New Haven, CT, Johns Hopkins University, [3]Dept. of Psychiatry and 4Dept. of Radiology, Baltimore, MD

Introduction: FMRI data are often analyzed by employing a hemodynamic model. Model mismatches can be caused by spatially varying delays or slice-timing differences. It is common practice to desensitize the analysis to such delays by incorporation of the hemodynamic model plus its temporal derivative. However, amplitude bias can occur due to the use of only the non-derivative portion of the model in the final test for significant amplitudes. We propose instead testing an amplitude value which is a function of both the non-derivative and the derivative terms of the model. Using simulations, we show that the proposed amplitude test does not suffer from delay-induced bias and that a model incorporating temporal derivatives is a more natural test for amplitude differences.
Methods: We generated a synthetic fMRI model waveform consisting of events modeled as delta functions spaced fifteen seconds apart and convolved with the default hemodynamic response function in SPM99 [1]. Simulated MRI data with different delays were created by adding Gaussian noise and shifting this model relative to the model waveform. We then compared the amplitude estimates obtained by using either the non-derivative term only or both terms as proposed.
100 subjects (50 female) completed two 8 minute runs of an auditory oddball task. Imaging was performed on a GE 1.5T scanner (TR/TE 3000/40 ms, flip angle 90, FOV 24 x 24 cm, 64 x 64 matrix, 29 5 mm slice). Images containing standard or derivative corrected amplitude estimates were then entered into a second level analysis (random effects).
Results: The simulations show that as the delay increases, the amplitude estimate for the non-derivative terms decreases below the true value, with significant decreases occurring even for delays as small as one second. For delays of three seconds the amplitude estimate is reduced by a factor of three from the correct value (fig 1). When utilizing both terms the amplitude estimate is much closer to the true response even for a three second delay. Differential maps of [targets (with both terms) targets (with non-derivative term)] [novels (with both terms) novels (with non-derivative term)] were also calculated (fig 1). The largest amplitude differences occur in motor, supplemental motor, and basal ganglia regions consistent with areas that may have delayed hemodynamic response functions.
Discussion: This work has important implications for both within- and between-subject fMRI analyses. Spatially varying delays can be present between voxels due to hemodynamic differences, (uncorrected) slice timing differences and also potentially between groups of subjects (e.g. young and old). Both main effect and differential effect estimates can be affected by these spatially varying delays since as the actual delay differs from the assumed (modeled) delay the amplitude of the non-derivative term will decrease (the affect of delay upon amplitude is also true when the temporal derivative is not modeled). Using both a simulated data set and actual fMRI data we demonstrate the effect of amplitude bias.
References: 1. Worsley K and Friston K, Neuroimage 2:173-181 (1995)

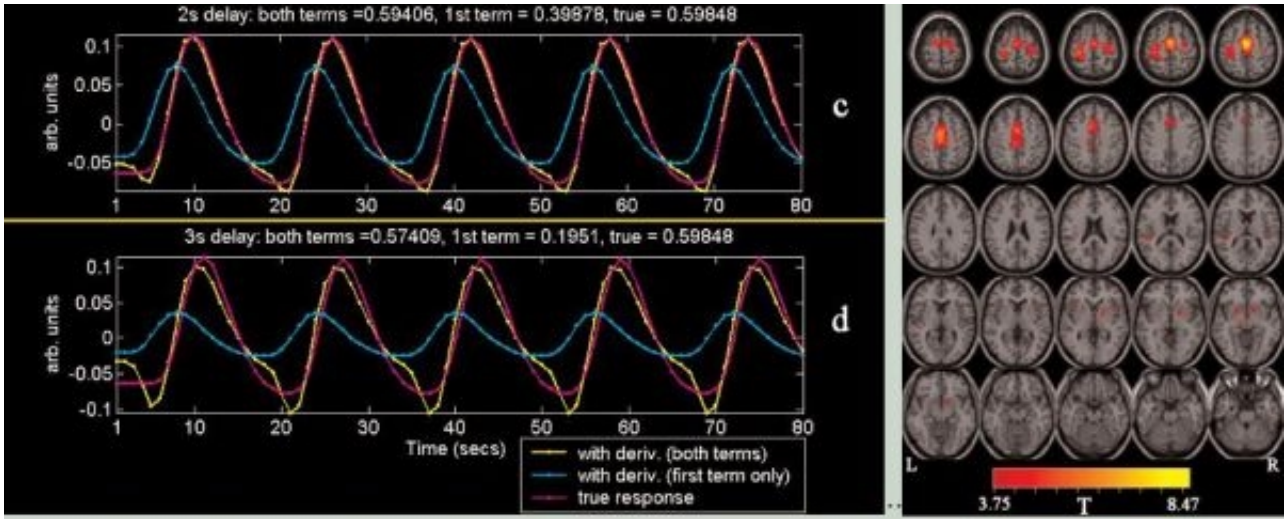

Figure 1: Simulation results (left) and fMRI results indicating regions exhibiting amplitude bias.

WE 140
Modeling the structure of the visual system based on structural connectivity and spike onset data

Michael Capalbo[1], Eric Postma[2], Rainer Goebel[1]
[1]Cognitive Neuroscience Section, Dept. of Psychology, University of Maastricht, the Netherlands, [2]Computer Science Section, Dept. of General Sciences, University of Maastricht, the Netherlands

Introduction
In the 1950s Hubel and Wiesel suggested that a *serial scheme* could account for the progressive increase in the complexity of receptive field properties in the visual cortex. Felleman & Van Essen [1] have recently taken this notion further, by a method called *hierarchical* analysis. Goodale & Milner [2] propose another, complementary, organizational principle by claiming the visual system is organized in *two pathways*, the Vision for perception and the Vision for action pathways respectively. If we take these theories together we arrive at the currently popular *serial, hierarchical, dual pathway model* of the organization of the visual system.
Recent single-cell data by Schmolesky [3] suggests that a serial and hierarchical model does not suffice to explain onset latency effects. They found that there was a functional sequence in the ventral stream wherein several modules demonstrated successively longer latencies. In contrast, there was simultaneous onset of firing in the modules of the dorsal stream. The dorsal pathway is dominated by the fast magno cells and the ventral pathway consists of mixed cell types, but the resulting speed difference [4] alone cannot account for the size of the effects. This means these effects cannot be attributed to different cell propagation speeds alone and therefore show a shortfall of the currently held beliefs. We modeled the structure of the visual system based on these single cell response data, constrained by a database (CoCoMac) of the known anatomical connectivity of the macaque brain [5].

Methods
The building blocks of our model are the functional modules of the visual system that were described by Felleman & Van Essen [1] and measured by Schmolesky [3]. With these blocks we generated semi-randomly all possible architectures by gradually increasing the probability of a connection existing between two modules. This was constrained by what connections are possible given the known connections in the brain as collected in the CoCoMac database [5]. We then measured the characteristic path length [6] and congestion robustness [7] of the generated architectures, to characterize and compare them. Finally we tested the architectures to see which architectures would fit the onset latency data best, by feeding activity to the input modules and propagating the activity through the model.

Results and Conclusion
The results show that for a dual pathway model to explain the current spike onset data in the visual system, the two pathways must have a different organization to attain different throughput speeds. Generated models that show the best fit have smaller path lengths, and higher congestion robustness in the dorsal system. These different characterizations show that speed might be an important design consideration in the architecture of the visual system.

1. Felleman & Van Essen, 1991, Cerebral Cortex
2. Goodale & Milner, 1992, Trends in Neuroscience
3. Schmolesky et. al., 1998, Journal of Neurophysiology
4. Bolz, Rosner and Wassle, 1981, Journal of Physiology
5. Stephan et al., 2001, Proceedings of the Royal Society
6. Watts and Strogatz, 1998, Nature
7. Dodds & Watts, 2003, PNAS

WE 141
Evaluation of human cortical sites underlying International 10-10 System scalp electrodes. An MRI study.

Filippo Carducci[1,3], Claudio Babiloni[1], Fabio Babiloni[1], Febo Cincotti[1], Cosimo Del Gratta[4,5], Antonio Ferretti[4], Paolo Nalin[1], Gian Luca Romani[4,5], Paolo Maria Rossini[2,3,6]

[1]Dipartimento di Fisiologia Umana e Farmacologia, Università La Sapienza, Roma, Italy, [2]IRCCS S Giovanni di Dio, Via Pilastroni, Brescia, Italy, [3]AFaR.- Dip. di Neuroscienze, S. Giovanni Calibita, Fatebenefratelli Isola Tiberina, Roma, Italy, [4]ITAB Università di Chieti, Chieti, Italy, [5]Istituto Nazionale di Fisica della Materia, UdR LAquila, Italy, [6]Clinica Neurologica, Campus Biomedico, Università di Roma-Italy

Electrodes placed on the subjects scalp according to the International 10-10 System (S.I. 10-10), an extension of the S.I. 10-20 (Jasper, 1958) that considers percentage curvilinear distances instead of absolute ones, take into account inter-subjects differences in skull size and shape (Jasper, 1958; Penfield et al., 1958), and show a stable neuro-anatomic correlation with underlying brain cortical areas (Jasper, 1958, Penfield et al., 1958, Kagawa et al., 1962; Hellstrom et al., 1964; Silverman, 1965; Torres et al., 1968; Blume et al., 1974; Morris et al., 1986; Homan et al., 1987; Myslobodsky and Bar-Ziv, 1989; Steinmetz et al., 1989, Myslobodsky et al., 1990; Grzeszczuk et al., 1990; Jack etal., 1990; Givens and Illes, 1991; Van den Elsen and Viergever, 1991; Largelund et al., 1993, Barnet et al., 1993, Towle et al., 1993). Until now, only a small amount of crude studies have tried to investigate and to evaluate this neuro-anatomic correlation, involving too few subjects and considering a very small subset of scalp electrode sites, and not giving any reliable and complete evaluation of this correlation. In this study, we evaluated neuro-anatomical correspondence of all S.I. 10-10 scalp electrodes.

On 35 realistic MRI-constructed head models (including the one reconstructed from the set of averaged MRIs of 152 subjects coming from the Montreal Neurological Institute, MNI), describing scalp and brain surfaces, the positions of S.I. 10-10 electrodes were determined over the scalp surface by means of an automatic procedure (Echallier et al., 1992). Then, these electrode positions were perpendicularly projected onto the corresponding brain surface, that is referred to the Talairach stereotaxic space. Talairach coordinates of the projected electrodes were recorded. Brodmann areas (BA) associated to these projections were identified using Talairach atlas.

WE 142
Content-Based Retrieval of Structural MRI

Monica P. Carley-Spencer , Kenneth P. Smith , John K. Dixon , Jeffrey P. Woodard , Jeffrey C. Hoyt
The MITRE Corporation

Augmenting our MRI management platform, we will present our progress toward the development of querying capability over image content. The goals of our research are to provide users the ability to (i) present an example image (e.g., a slice of an MRI volume) and automatically retrieve similar images from an archive, (ii) provide feedback on the relevance of retrieved "matches", (iii) examine the attributes of subjects having similar image characteristics, and (iv) automatically filter requested scans based on image quality metrics. The first three capabilities would support virtual hypothesis-testing. For example, a researcher might notice that a particular anatomical structure has an unusual shape in one individual’s scan and want to know if it correlates with a certain attribute such as handedness or perhaps a disease. Hypothesizing that it is a distinguishing structural characteristic of people with this attribute or condition, the researcher would query the system for archived scans of other subjects with the same unusual shape. The system would then retrieve the requested attributes of the subjects, thus enabling the researcher to test the hypothesis over an existing set of data.
We will present a system architecture, our progress in identifying and developing similarity metrics for query-by-example, and the software tools we are developing for users to interact with the proposed system and visualize query results.

WE 143
Functional Connectivity Excluding Extreme-Low-Frequency: A BOLD fMRI study

Chia-Fang Chen , Chang-Wei Wu , Jyh-Horng Chen
Interdisciplinary MRI/MRS Lab, Dept. of Electrical Engineering, National Taiwan University, Taipei, Taiwan

Introduction

Low frequency fluctuations in functional connectivity MRI (fcMRI) were used to detect neural connections among local regions in human brain, which were claimed during 0~0.1 Hz avoiding respiratory and cardiac effects [1, 3]. However, the observation range has not been officially determined. Wang reported that BOLD show markedly increased power in extreme-low-frequency (ELF, corresponding frequency: 0 ~ 0.01Hz) comparing with perfusion data and Biswal demonstrated functional connectivity map exists in perfusion imaging [2]. Therefore, it was reasonably hypothesized that the source of ELF is from noise irrelevant to neural connectivity. Here we compared resting-state dataset of low frequency with ELF (0~0.1 Hz) and without ELF (0.01~0.1 Hz) in the fcMRI research.

Materials & Methods

Experiments were performed on Bruker MedSpec 3T system (Bruker, Ettlingen, Germany) with quadratic birdcage head coil. Two subjects were conducted in two experiments: visual task and resting. Block-designed visual task with 8 Hz checkerboard (20 sec on, 20 sec off, 4 blocks) were applied to subjects by LCD goggle. Both task and resting images were acquired by gradient-echo echo planar imaging with 64x 64 matrix size,4 slices with slice thickness of 7mm, 2mm gap, 25.6-cm FOV, and TE of 35 ms; task images with TR of 2000 ms, 80o flip angle while resting images with TR of 400 ms, 45o flip angle. Two seed voxels were selected from the task data with largest correlation coefficient values in each subject. Resting-state data were low-pass filtered at the cutoff frequency 0.1 Hz, and then filtered by band pass filter from 0.01 Hz to 0.1 Hz. Resting time courses of seed voxels were analyzed by cross-correlation (CC, threshold >0.7) to resting-state data of whole dataset. Comparison was made between the low-pass results and band-pass results.

Results & Discussion

Figure 1 shows the power spectrum profiles of BOLD with ELF and without ELF of single subject. Corresponding fcMRI maps were shown in Figure 2 and 3. As Table 1 shows, resting dataset without ELF has both more correlated voxels and stronger correlation coefficients in contrast to that with ELF. Therefore, we can presume that ELF signal is unconcerned with neural connectivity. However, even though the power spectrum of BOLD without ELF is similar to that of perfusion, the functional mappings from BOLD without ELF and perfusion are quite different. It was speculated that this phenomenon is mainly caused by physiological differences of BOLD and perfusion images, resulting in mismatches of activated area and correlation coefficients.

References

[1]. Jiongjiong Wang et al., Empirical analyses of null-hypothesis perfusion FMRI data at 1.5 and 4 T, NeuroImage 19 (2003) 1449-1462.
[2]. Biswal B et al., Simultaneous Assessment of Flow and BOLD Signals in Resting-State Functional Connectivity Maps, NMR in
Biomedicine, vol. 10, 165-170 (1997).
[3]. Cordes D. et al., Mapping Functionally Related Regions of Brain with Functional Connectivity MR Imaging, AJNR Am J Neuroradiol 21:1636-1644, October 2000.

Comparison of activated voxel numbers and correlation coefficient between BOLD signals with and without ELF

	BOLD with ELF (0 ~ 0.1 Hz)	BOLD with ELF (0 ~ 0.1 Hz)	BOLD without ELF (0.01 ~ 0.1 Hz)	BOLD without ELF (0.01 ~ 0.1 Hz)
	Activated Number	Correlation Coefficient	Activated Number	Correlation Coefficient
Subject #1	90.75±13.20	0.79±0.02	229.75±12.71	0.80±0.01
Subject #2	17.25±7.14	0.77±0.01	26.75±14.77	0.79±0.02

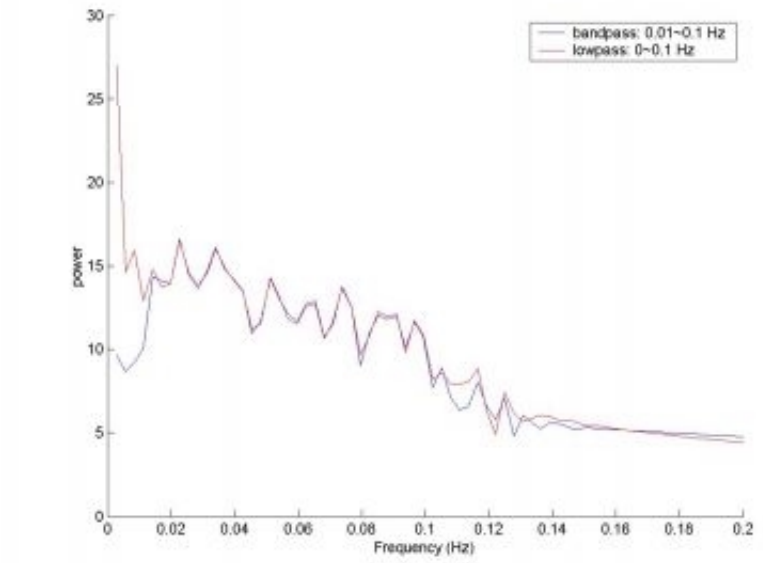

Power spectrum of BOLD signal with ELF (0~0.1Hz, red) and without ELF (0.01~0.1Hz, blue)

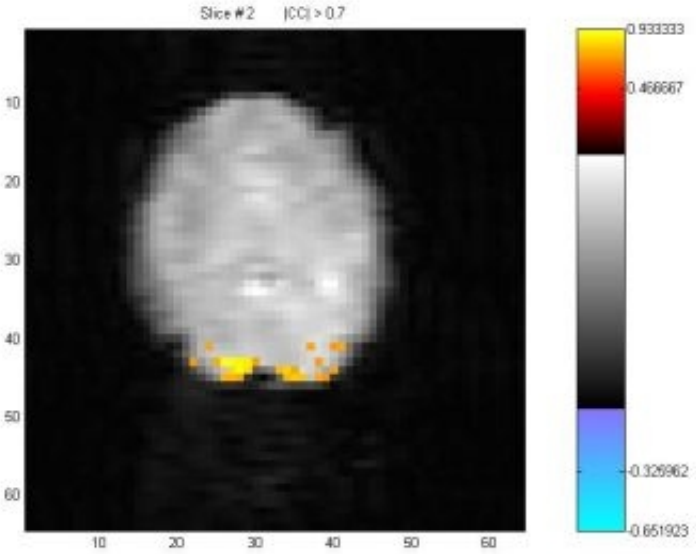

fcMRI map with ELF (0~0.1 Hz)

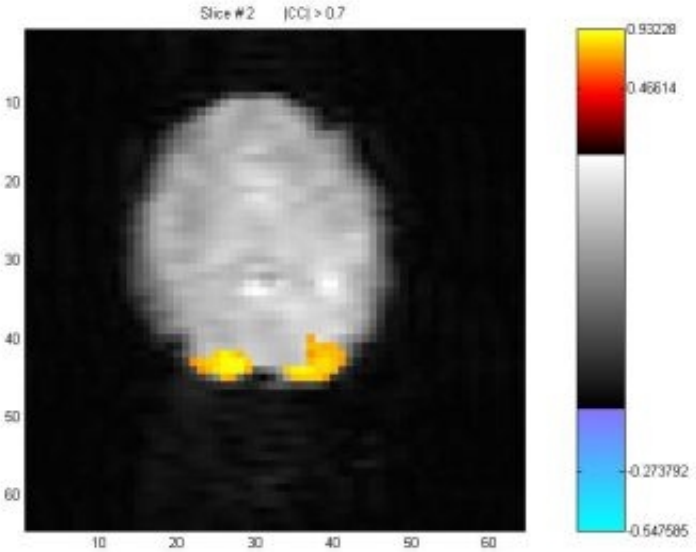

fcMRI map without ELF (0.01~0.1 Hz)

WE 144

Mutual information based approach for detecting cortical connectivity during self-paced finger lifting tasks

Chun Chuan Chen[1], Yu-Te Wu[1,2], Po-Lai Lee[1], Shyan-Shiou Chen[1], Yz-Te Wu[1,3], Li-Fen Chen[1,4], Tze-Chen Yeh[1,3], Jen-Chuen Hsieh[1,3,4]

[1]Integrated Brain Research Unit, Taipei Veterans General Hospital, Taiwan, [2]Institute of Radiological Sciences, National Yang-Ming University, Taiwan, [3]Institute of Neuroscience, School of Life Science, National Yang-Ming University, Taiwan, [4]Faculty of Medicine, School of Medicine, National Yang-Ming University, Taiwan

Introduction

In this study, we exploit the mutual information (MI) method to elucidate the functional connections between cortical regions in MEG study, especially the participation of SMA and ipsilateral sensorimotor area. Contrary to the conventional coherence method using the second-order covariance, the MI method utilizes the entropy to take the high-order statistics among data into account. Results of MI method were compared with that of conventional coherence method to demonstrate its effectiveness.

Materials and Method

Eight healthy and right handed subjects were recruited for this study. All subjects gave written informed consent for the experiment. Subjects were asked to perform repeatedly self-paced brisk index finger movement with a period about 8 ~15 seconds inside the magnetic shielding room. To avoid the movement-related vibration contaminated into the ipsilateral hemisphere, the left hand was put on a pillow. The brain magnetic signals were continuously recorded during the movement by using the 306 channel whole-head MEG device with 1000 Hz sampling rate and downsampled to 250 Hz. The surface EMG signals were simultaneously recorded for verification the movement of index finger. The number of trials is more than 100 for each subject.

The time-frequency maps of measured MEG trials were created and averaged across trials and across pre-specified passbands (16 ~ 25 Hz; beta band). A channel exhibited the strongest oscillatory power in the vicinity of sensorimotor area, and another arbitrary (task non-related) channel were respectively selected as the channel of interest (COI). The mutual information of averaged temporal-frequency powers between COI and other channels were then computed. The 95% confidence limit of t-distribution was used as a threshold to determine the significant regions.

Results

We superimposed the thresholded MI values (obtained in the sensor space) on top of individual MRI to facilitate the visualization (Fig.1). When the COI was task-related, the involved regions included mesial frontocentral cortex, likely supplemental motor area (SMA) and primary sensorimotor areas (SM I), and premotor area (PM), which were in line with previous fMRI or PET studies. Table 1 summarized the MI result. The SMA and ipsilateral SM I were detected consistently in all subjects, even the signal-to-noise level was low. In addition, significantly functional relevance between left and right senserimotor areas, which was not resolved by the conventional coherence method, was manifested. When the COI was arbitrary, the MI results exhibited much less connectivity than the coherence results (Fig. 2). These results demonstrated that MI method is superior not only in detecting the event-related regions but also in discriminating the event-related regions from the event-non-related regions.

Conclusion

In this study, we have developed a MI method to detect the functional connectivity between cortical regions in MEG study. The results show that MI method is a promising tool to appraise inter-regional neural network and to probe the unknown dynamics of brain function.

Table 1 The summary of MI result

area	A	B	C	D	E	F	G	H	Average
SM I [1]	B(C) [3]	B(C)	B(C)	B(C)	B(C)	B(C)	B(C)	B(C)	8/8
Pre-motor	C [4]	C	B(C)	C	C	C	B(C)	B(C)	8/8
SMA [2]	B(C)	I	C	B(C)	B(C)	B(C)	B(C)	C	8/8
Parietal lobe	X	X	C	C	C	C	X	C	5/8

1: primary sensorimotor area ; 2: supplemental motor area ; 3: bilateral activation with contralateral side dominat; 4: contralateral side only; 5: ipsilateral side only; X : no significance

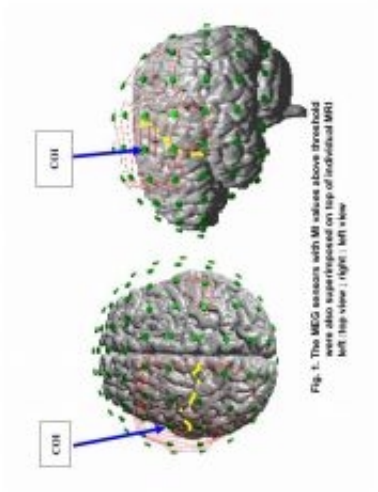

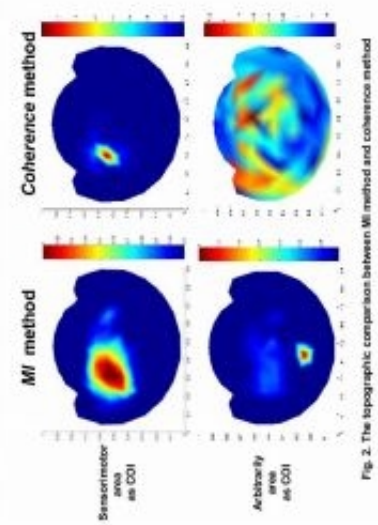

WE 145
Gaussian Convolution Model of the BOLD response of functional MRI

Huafu Chen , Dezhong Yao
School of Life Science & Technology, School of Applied Math., University of Electronic Science and Technology of China, Chengdu 610054, PR China

Introduction
Blood oxygenation level dependent (BOLD) contrast based functional magnetic resonance imaging (fMRI) has been widely utilized to detect brain neural activities and great efforts are now stressed on the hemodynamic performances of different brain regions activated by a stimulus. The focus of this work is the convolution model of a BOLD signal (Miller et al, Human Brain Mapping, 2001,13:1). We extended this model by replacing the kernel function with a Gaussian function, and newly added a baseline term.
Model and Methods
In the original model (Miller, et al 2001), the convolution was between the perfusion function of the neural response to a stimulus and a Gamma function that is the response of a single neuron. Since a BOLD signal is the collective response of a neural cluster, and based on the law of large numbers in probability, we suggested using a Gaussian function to replace the original Gamma function. Meanwhile, for simulating the background activities, a baseline term was newly included, too. The final model is
$X(t)=n(t)*gauss(t)+(1+t.a).baseline +noise$ (1)
Here the BOLD signal x(t) was expressed by the convolution between the perfusion function of the neural response n(t) to stimulus and a Gaussian function gauss(t) of Cerebral Blood flow (CBF) hemodynamic change of a neural cluster. (1+a.t).baseline was introduced to represent the background activities. The baseline was a constant, and the time dependence was assumed being a linear function a.t.baseline with a baseline shift factor a. The noise represented various additive noise. The parameters of the model were estimated by a nonlinear least-squares optimal algorithm for fMRI data collected in a visual stimulus experiment.
Results
Figure 1 shows the relative errors (RE) of the new model and the original Gamma model, they are calculated over a totally 12 BOLD signals in ROIs in the left and right primary visual cortexes. The maximum RE of the Gaussian model is 0.0333, and its average is 0.0243, minimum is 0.0135. However, the maximum RE of the Gamma model is 0.0453, and its average is 0.0283, minimum is 0.0144.
Conclusions
Our results show the new Gaussian convolution model is better than the original Gamma convolution model in fitting the curves of the fMRI signals with a much smaller relative error. As for the available spatial resolution of fMRI, any measurable signal is due to neuronal cluster which means that the BOLD response is a macroscopic response (Gaussian response), not a response of a single neural cell (Gamma response), and so the foundation of the new Gaussian convolution model is theoretically stronger than the Gamma model.
Acknowledgement The work was supported by NSFC(No.90208003 and 30200059) and the China 973 Project (No. 2003CB716106).

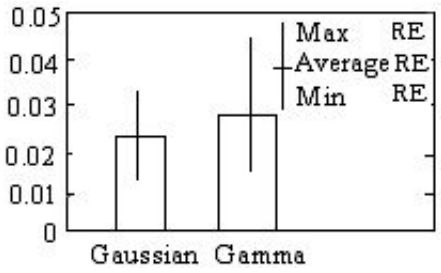

Figure.1 Relative errors (RE) of the models, they are calculated over a totally 12 BOLD signals in ROIs in the left and right primary visual cortexes.+

WE 146
Comparison of Activation Detection Methods for fMRI using ROC Curves

Xu Chen[1], Pulapura Sujit[2], Lars K Hansen[3], Jane Zhang[4], Jon R Anderson[1], Stephen C Strother[1,5]
[1]Department of Neurology,University of Minnesota, USA, [2]Department of Electrical Engineering,University of Minnesota, USA, [3]Informatics and Mathematical Modeling, Technical University of Denmark,DK, [4]Department of Health Information,University of Minnesota, USA, [5]Department of Radiology,University of Minnesota, USA

INTRODUCTION. Several frequency domain activation-detection methods based on multi-taper spectral estimation[1] were evaluated using fMRI simulation data and a normalized partial ROC index within the NPAIRS framework. The results were also compared with univariate *Bayesian* and GLM techniques, as well as multivariate Canonical Variates Analysis (CVA) in the time domain.
METHODS. Data Simulation: The simulation data were generated using a brain-mask volume(64*64*32) from one subject for a 1.5T fMRI experiment in which every volunteer was asked to perform two runs of a static force task alternating six rest and five force periods/run (44s/period, TR=4s). Four artificial Gaussian blob (FWHM=1,1.5,2,4 pixels) activations, each restricted to a 7*7 square, were added to different locations in a single slice. To form the simulated time sequence, the blobs were then multiplied by 1) Block: the on-off reference function for two parametric static force runs; 2) a sinusoidal wave of 0.011 Hzthe fundamental block frequency; both were convolved with a *Poisson* shaped (λ=7.3) HRF. After adding white noise to the sequence and normalizing the SNR at the blobs centers to be 1, two sets of simulation data (Block & Sinusoidal) were obtained. Finally the spectra of the time series corresponding to each voxel were estimated using multi tapers[1] (MTM, the number of *Slepian* sequences K=3, timehalf band width product NW=2, the *Rayleigh* frequency N=128).
Analysis: In frequency domain: 1) Harmonic F test; 2) regression with reference F test; 3) CVA (each frequency component corresponding to a group, total group number=N/2); 4) Complex Singular Value Decomposition (SVD) was performed over the MTM spectral data [2]. In time Domain: 1) GLM; 2) *Bayesian* Detection [3]; 3) 2 Class CVA; 4) 11 class CVA. All of the above 8 methods were implemented in the NPAIRS framework [4] with consensus, reproducing Z-score images as the final results for each data set. The normalized area under a partial ROC curve (*pAUC*) with FPRs ranging between 0 and 0.1 was calculated as the performance measurement.
RESULTS/CONCLUSIONS. The figures illustrate the *pAUC* trends as a function of Gaussian blob threshold only the voxels in the Gaussian Blob with values no less than the threshold were treated as truly activated for the 8 detection methods applied to the Sinusoidal and Block simulated data sets. Our conclusions require further justification using real fMRI data: 1) GLM performs the worst of all methods tested; 2) Time domain CVA, whether 2 class or 11 class, performs the best; 3) the *Bayesian* method dramatically outperforms all other univariate methods because it takes maximum advantage of prior information; 4) Among frequency domain methods, complex SVD performs the best; 5) Regression with reference F test uses the 0.011Hz priori frequency and therefore performs better than the harmonic F test.
REFERENCES.[1] Mitra PP, et al, Biophysical Journal 76: 691-708, 1999; [2] Sujit KP, master thesis, UMN2757487, 2003; [3] Hansen LK, et al, AIM 25: 35-44, 2002;[4] Strother SC, et al, NeuroImage 15, 747-771, 2002.
ACKNOWLEDGEMENTS. This work is supported in part by NIH grant MH57180.

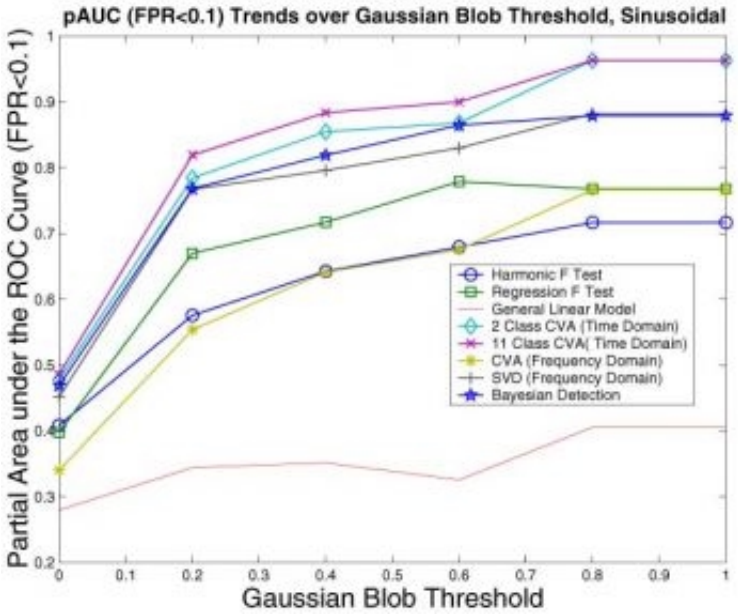

Fig.1 pAUC trends over Gaussian Blob Threshold, Sinusoidal

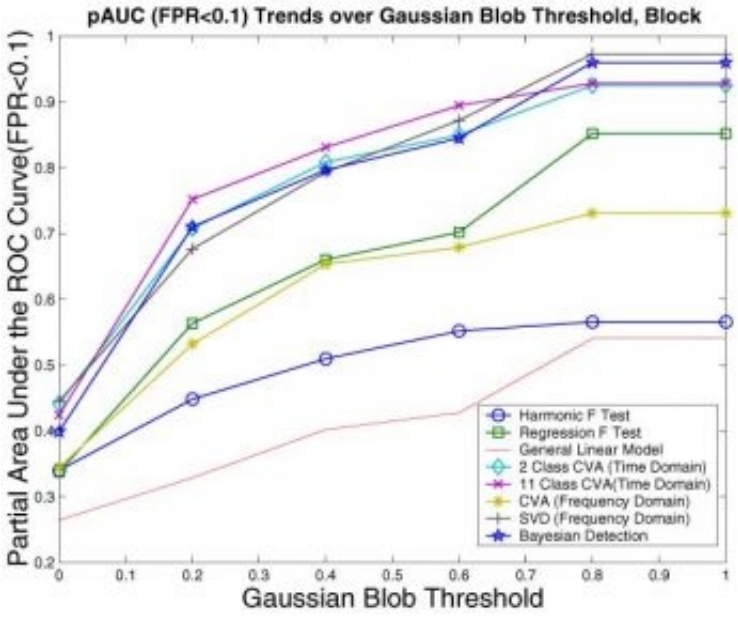

Fig.2 pAUC trends over Gaussian Blob Threshold, Block

WE 147

Detection of cortical activity asymmetries from non invasive EEG recordings for Brain Computer Interface applications

Febo Cincotti[1], Donatella Mattia[1], Marco Mattiocco[1], Alessandro Timperi[1], Giorgio Campani[1,2], Serenella Salinari[2], Maria Grazia Marciani[1,3], Fabio Babiloni[4]

[1]Fondazione Santa Lucia, Roma, Italy, [2]Dip. di Informatica e Sistemistica, Univ. La Sapienza, Roma, Italy, [3]Dip. di Neuroscienze, Univ. Tor Vergata, Roma, Italy, [4]Dip. Fisiologia umana e Farmacologia, Univ. La Sapienza, Roma, Italy

Objectives. To analyze whether the use of the cortical activity estimated from non invasive EEG recordings could be useful to detect mental states related to the imagination of limb movements.
Methods. Estimation of cortical activity was performed on high resolution EEG data related to the imagination of limb movements gathered in six normal healthy subjects by using realistic head models. Cortical activity was estimated in Region of Interest associated with the subjects Brodmann areas by using depth-weighted minimum norm solutions. Comparisons between surface recorded EEG and the estimated cortical activity were performed.
Results. The estimated cortical activity related to the mental imagery of limbs in the six subjects is located mainly over the contralateral primary and supplementary motor areas. The unbalance between brain activity estimated in contralateral and ipsilateral cortical areas appears greater than those obtained in the scalp EEG recordings.
Conclusion. Results suggest that the use of the estimated cortical activity for the motor imagery of upper limbs could be potentially superior with respect to the use of surface EEG recordings. This is due to a greater unbalance between the activity estimated in the contralateral and ipsilateral hemisphere with respect to those observed with surface EEG. These results are useful in the context of the development of a non invasive Brain Computer Interface.

WE 148
A Permutation Multiple Hypothesis Procedure based on the Weighted Sum of Test-Statistics

Marco Congedo[1], Livio Finos[2], Federico Turkheimer[3]
[1]IRISA (Institute for Research in Informatics and Random Systems), Rennes, France, [2]Department of Statistics, The University of Padova, Italy, [3]Neuropathology Department, Imperial College London, UK

We introduce a new test procedure for multiple hypothesis testing based on the permutation space of the sum of test-statistics (t-sum). The underlying combining function is shown to be an instance of a family to which it also belongs the well-known combining function based on the maximum of test-statistics (t-max). After discussing the family-wise error rate and the false discovery rate, two common neuroimaging approaches to the control of the type I error in multiple testing, we consider two further error rates, the stochastic family error and the mean square error model fit estimator. By means of a large set of simulations we show that besides controlling the family-wise error rate in the weak sense, the t-sum procedure also controls the stochastic family error and generally considerably outperform the t-max procedure in power and mean square error in experiments with low degrees of freedom.
The t-sum procedure is suitable for pilot and exploratory studies in neuroimaging and in other experimental contexts in which the sample size/number of hypotheses ratio is low, the data correlation is moderate, and the proportion of false hypothesis is possibly large. We end the discussion outlining possible investigations of the more general form of combining function (weighted sum) with the aim of data-driven selection of an optimal power combining function.

WE 149
Investigating the Reliability of ICA Sources Obtained After PCA Preprocessing

Dietmar Cordes , Rajesh Nandy
Department of Radiology, University of Washington

Introduction
Independent Component Analysis (ICA) is a promising technique for analyzing fMRI data [1]. Unfortunately, the size of fMRI datasets often renders this technique as being computationally intractable, and certain compromises must be made to perform the analysis. One such compromise is to project the full dataset onto a lower-dimensional subspace that, in some well-defined sense, captures the essence of the data. The most common method for achieving this aim is Principal Component Analysis (PCA). PCA is used for two reasons in ICA, for computational efficiency and to prevent ICA from splitting components into multiple groups. In our investigation we focus on the first aspect by using pseudo real and simulated data.
Methods
All scans were done on a GE 1.5 Tesla MRI scanner (20 slices, 64 x 64 resolution, 7mm slice thickness, 2mm gap, TR 2 s, bandwidth, +/-62.5 kHz, TE 40ms, flip angle 82°, 165 time frames). Standard resting-state data and motor activation data (30 second on/off task, repeated 5 times) were collected with experienced volunteers. ICA was carried out using FastICA with and without PCA preprocessing [2]. Two types of simulations were performed. In the first simulation, an ICA motor component (obtained from an activation study) was added to the resting-state data set using different mixing amplitudes to provide different SNRs. The simulated data set was then reduced by PCA to different dimensions and analyzed by ICA. In another simulation we investigated the dependence of the ICA component extracted (after PCA preprocessing) as a function of the shape of the source distribution. We assumed that the source activation pattern can be parameterized by an exponential power family with a free parameter α describing the shape of the distribution. For a fixed value of α [0.3,2.5] in steps of 0.1 we generated 20,000 independent identically distributed points from the distribution. The generated numbers represent a spatial intensity pattern that was then multiplied with a hypothesized hemodynamic response function and added to resting-state data with different amplitudes as before.
Results and Conclusion
To obtain accurate ICA sources using PCA reduction in a preliminary step, the strength of the signal sources and their spatial distribution play a major role. Indeed, in both the pseudo-real and simulated data, PCA-preprocessed ICA can be beneficial if the signal is strong (≥1% relative amplitude) but can also fail to detect all the activations associated with the paradigm when the dimension was reduced too aggressively (< 50) or the relative amplitude was low (< 1%).
References
[1] McKeown et al. Analysis of fMRI data by blind separation into Independent Spatial Components. 1998. Human Brain Mapping 6:160-188.
[2] Hyvärinen et al. 1997. A fast fixed-point algorithm for Independent Component Analysis. Neural Computation 9(7):1483-1492.

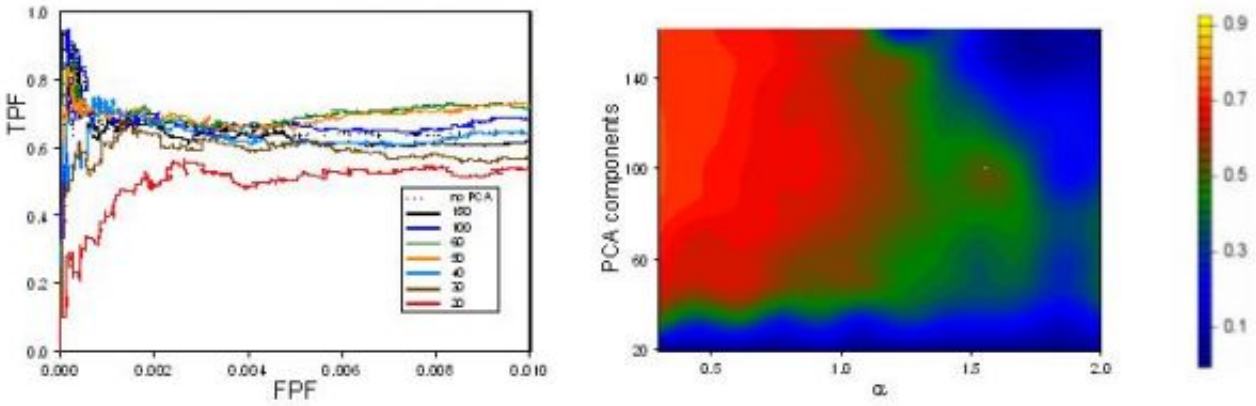

Fig. 1. Modified ROC curves for an ICA source using simulated data processed by ICA with different degrees of PCA reduction for 1% activation (left: resting-state plus activation pattern from real motor data, right: TPF at FPF=0.005 for resting-state plus an activation pattern from an exponential power family parameterized by α.

WE 150
A (Sort of) New Image Data Format Standard: NIfTI-1

Robert W Cox[1], John Ashburner[2], Hester Breman[3], Kate Fissell[4], Christian Haselgrove[5], Colin J Holmes[6], Jack L Lancaster[7], David E Rex[8], Stephen M Smith[9], Jeffrey B Woodward[10], Stephen C Strother[11]
[1]NIMH/NIH/DHHS/Bethesda, [2]FIL/London, [3]Brain Innovation/Maastricht, [4]U Pittsburgh/Pittsburgh, [5]MGH/Charlestown, [6]SGI/Mountain View, [7]RIC/UTHSCSA/San Antonio, [8]LONI/UCLA/Los Angeles, [9]FMRIB/Oxford, [10]Dartmouth College/Hanover, [11]U Minnesota/Minneapolis and **DFWG Chair**

The problem of interoperability of neuroimaging data analysis software is being addressed by the NIfTI (Neuroimaging Informatics Technology Initiative) task force. The Data Format Working Group (DFWG) within NIfTI was chartered to deal with the particular issue of *data* interoperability; that is, making it simpler to interchange image (etc.) data between analysis packages.

The DFWG decided to proceed in two phases: near- and long-terms. Since the ANALYZE™-7.5 file format (.hdr/.img file pairs) is simple, widely used, and contains some unused/little-used fields, for the first phase we decided to modify this format to add features that the DFWG agreed were highly desirable for FMRI analysis purposes. In outline, new features include:

(1) *Two* affine coordinate definitions relating voxel index to spatial location:
 → one orthogonal transform, to indicate orientation/location of data in scanner coordinates;
 → one general affine transform, to indicate mapping to a "normalized" space;
 → global coordinates are +*x*=Right, +*y*=Anterior, +*z*=Superior.
(2) Codes to indicate spatial normalization type (e.g., MNI-152).
(3) Codes to indicate units of spatial and temporal dimensions.
(4) Codes to indicate temporal and spatial acquisition ordering for MRI.
(5) "Complete" set of 8..128 bit data type codes.
(6) Standardized way to store vector-valued datasets (e.g., a matrix at each voxel).
(7) Affine data scaling (i.e., true-data-value≡α*data-in-file+β; α, β stored in header).
(8) Codes and parameters for data "meaning" (e.g., values are *t*-statistics with 23.7 DOF):
 → 21 types of statistics are encodable; parameters can be global or voxel-dependent.
(9) "Magic" string indicates if header is NIfTI-1 compliant:
 → i.e., contains "extra" data not defined in ANALYZE™-7.5.
(10) Single or dual file storage (**.nii** or **.hdr**/**.img**).

The NIfTI-1 format has been carefully designed so that unmodified FMRI analysis programs that read ANALYZE™-7.5 files are likely to work with NIfTI-1 files; for example, the NIfTI-1 header is still 348 bytes long. Another goal was to reduce the uncertainty about diverse ANALYZE™-7.5 extensions used in this community. The developers of Brain Voyager, FSL, SPM, and AFNI have agreed to adapt their codes to read and write NIfTI-1 files; other sites (including those represented by the DFWG committee) have also agreed to support this format.

The complete definition of the NIfTI-1 format (as a heavily-commented C .h file) is available at the Web site **nifti.nimh.nih.gov**. In addition, sample C source code for reading and writing NIfTI-1 files is available at this site; Matlab code is planned.

The primary goal of NIfTI-1 is to foster near-term data interchangeability between FMRI analysis and visualization tools. The format is simple, and programs already using the ANALYZE™-7.5 format should be easily adapted to use NIfTI-1. We are aware that many desiderata are missing from this format; work is underway to define and agree upon a more ambitious and extensible NIfTI-2 format.

Acknowledgments: NIfTI and the DFWG are sponsored by NINDS and NIMH. Mark Jenkinson of the FMRIB aided significantly in formulating some aspects of NIfTI-1. The Mayo Foundation granted permission to use components of the ANALYZE™-7.5 header dbh.h.

WE 151
Mapping of binding parameters in the human brain using artificial neural network based noise attenuation

Zsolt Cselényi , Hans Olsson , Johan Lundberg , Christer Halldin , Lars Farde , Balázs Gulyás
Department of Clinical Neuroscience, Karolinska Institutet, S-171 76 Stockholm, Sweden

PET images obtained after injecting radioligands of different neuroreceptors can be used to map the binding properties of different brain regions. Despite the existing several techniques, due to the highly noisy nature of these PET images, the most stable approach to date still remains the calculation of binding parameters on user-defined regions of interests (ROIs). The ROI-based analysis builds on the idea of removing noise in 4D PET images by averaging the time-activity curves (TACs) of voxels belonging to a given region of interest. This proved to be an efficient way to overcome the effects of noise.
However, the approach has some major disadvantages. (i) As it takes the average value of an area, the information on sub-regional distribution of the signal is lost. (ii) If the regions are inappropriately placed on the image, voxels with inhomogeneous kinetic behaviour may appear in the same ROI, and the resulting kinetic analysis may be misleading. (iii) ROIs with small volume lead to insufficient removal of noise and, consequently, incorrect results.
Our aim was to create a method which (i) builds upon the same principles as the ROI-based approach and (ii) is able to produce a 3D map of binding parameters, i.e. which diminishes the effects of noise by averaging individual TACs of voxels. In contrast to the ROI-base technique, however, this approach does not average the TACs of spatially adjacent voxels but that of voxels with a similar shape of the TAC, i.e. it classifies voxels into a number of groups.
This is performed by using an artificial neural network model called the growing adaptive neural gas (GANG), which belongs to the family of self-organizing maps (SOM). This network model is capable of classifying the input into a large number of similarity-groups, called neighborhoods, in arbitrary dimensional data-space. This classification is used to obtain the average TACs of voxels in the same neighbourhood. Kinetic calculation is then performed on these average TACs and the resulting binding parameters are back-projected to the spatial locations of the voxels they emanate from according to the classification of the voxels. Thus the technique yields 3D parametric maps of binding parameters. Since the entities of the kinetic calculation are noise-attenuated TACs, any method of estimating binding parameters may be applicable that one can use in the classic ROI-based approach.
The calculations were performed on PET images obtained with [11C]FLB 457 and [11C]WAY-100635, high affinity D2- and 5-HT1A-receptor ligands, respectively.
The results indicate that the approach based on the classification of individual voxel TACs is an efficient way to remove noise. The parametric maps created are highly detailed enabling us to visualise anatomical structures of only one voxel in diameter (e.g. the tail of the caudate nucleus or the raphe nuclei). Comparing the parametric values with results obtained using the classic ROI-based approach or previously validated voxel-based techniques indicates a high accuracy of the approach.

WE 152
EEG/MEG data-driven cortex parcelling

Jean Daunizeau[1,2,4], Jérémie Mattout[1,3,4], Bernard Goulard[2], Jean-Marc Lina[1,2,4], Habib Benali[1,2,4]
[1]Imagerie Médicale Quantitative, U494 INSERM, Paris, FRANCE, [2]Centre de Recherches Mathématiques, Université de Montréal, CANADA, [3]Wellcome Department of Imaging Neuroscience, Institute of Neurology, London, UK, [4]IFR 49 de Neurosciences, Orsay, FRANCE

Introduction

Reconstructing the cortical sources of the EEG/MEG activity constitutes an ill-posed inverse problem that requires constraints from additional information. In the context of distributed source model, regularization is all the more needed since the problem is highly under-determined. Several types of priors such as anatomical, functional or mathematical constraints have been yet evaluated [1,2].

As a complement to such needed regularization approaches, we propose a pre-processing tool which aims at optimizing the source model, using the EEG/MEG data to be analyzed. This method consists in dividing the cortical surface into a few anatomically connex but also functionally coherent parcels. Those parcels might be then exploited for constraining any source reconstruction algorithm.

Method

The proposed approach involves the two following priors.

- An anatomical smoothness prior: the shorter the cortical distance between two putative sources, the higher their prior correlation,
- A data-driven functional prior: a source covariance matrix is estimated from the EEG/MEG data itself, using the Multivariate Source Prelocalization approach [3].

It then consists in a clustering procedure which successively involves the three following steps.

Defining seeds:

The sources that anatomically correspond to a local maximum of the prior covariance matrix are defined as seeds. These seeds are easily constrained to be homogeneously distributed over the cortical surface. They are then used as starting points in an iterative cluster-growing procedure. The initial number of seeds thus determines the final number of clusters.

Iterative clustering:

Driven by the priors, anatomically and functionally coherent clusters are grown from the seeds. This process ends when no single source is left.

Determining the optimal parcelling order:

The initial number of seeds is the hyperparameter of the process. It can be optimized *a posteriori*, by minimizing a between-cluster contrast criterion. The optimal clustering is the one which both guarantees high within parcel homogeneity and high between parcel heterogeneity.

Application

Two active extended sources were randomly chosen on a true cortical surface, made of 3,400 dipoles. Corresponding ERP data were simulated on 59 channels and corrupted by an additive white Gaussian noise so that SNR = 20 dB (cf. Figures 1 and 2).

Due to the prior types, the initialization itself and the simultaneous growing of the regions, the final clusters are homogeneous in size.

Conclusion

This systematic and data-driven clustering approach is currently under extensive evaluation. Using synthetic data, the quality of the clustering itself can be assessed by quantifying a distance between the true simulated sources and the obtained most intersecting parcels.

Such a methodology would be very useful for constraining some recent inverse approaches that explicitly requires an anatomically and functionally coherent cortex parcelling [4,5].

References

[1] Baillet et al. IEEE Sign. Proc. Mag. 18:14-30 (2001)
[2] Pascual-Marqui IJBEM 1:75-86 (1999)
[3] Mattout et al. NeuroImage 13:S196 (2001)
[4] Mattout et al. IPMI'03 536-547 (2003)
[5] Amblard et al. IEEE Trans.biomed. Eng. (accepted)

Figure 1. Cortex upper view : the two simulated sources.

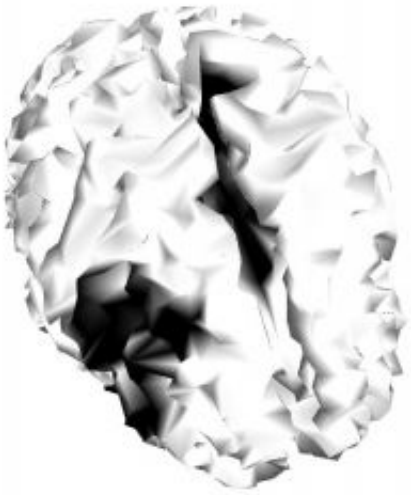

Figure 2. The two most intersecting parcels estimated by the optimal clustering procedure.

WE 153
Modelling event-related potentials in cortical hierarchies

Olivier David , Karl J. Friston
Wellcome Dept. of Imaging Neuroscience, UCL, WC1N 3BG, London, UK

The aim of this work was to evaluate the dependence of event-related potentials (ERPs) on the biophysical attributes of stimulation (e.g. amplitude) and the network engaged by perceptual and cognitive processing (i.e. its connectivity). We used a neural mass model that is a slightly modified version of the model used previously to study oscillatory dynamics (1).
In our model, each cortical area comprises three interacting neuronal populations (inhibitory and excitatory interneurons, excitatory pyramidal cells). Bottom-up processes between areas are enacted by connections from the pyramidal cells of one area to the excitatory interneurons of a higher area. Top-down processes are mediated by connections from pyramidal cells of one area to pyramidal cells and inhibitory interneurons of a lower area. Extrinsic inputs model incoming stimuli and act on synaptic activity of excitatory interneurons (spiny stellate cells) of the lowest area. The ensuing architecture allows us to construct hierarchical, realistic neuronal models of ERPs.
We were primarily interested in the effects, on ERPs, of the strength of extrinsic inputs and connections (bottom-up and top-down), and how these effects changed with the hierarchical level. The results show that when extrinsic inputs are strong enough to induce nonlinear saturation in neuronal outputs, the forms of the ERPs change. The role of connectivity is central. For instance, strong top-down connections render the system unstable and promote oscillatory dynamics. Finally, the level in the hierarchy, from which recordings are made, is a key factor in determining the form of the observed ERP.
To conclude, the ERP is a phenomenon that depends on multiple factors that are often difficult to disentangle. Explicit generative or forward models, that are neuronally plausible, are essential for a mechanistic understanding. The comparison of real ERPs with model predictions (2) should help to better characterise the relevant biophysical mechanisms that generate these waveforms.
(1) O. David et al., NeuroImage, 20(3): 1743-1755, 2003.
(2) C.J. Rennie et al., Biol Cybern, 86(6):457-471, 2002.

WE 154
3D Structural Parcellation of the Human Cerebral Cortex Using *in vivo* high-resolution MR Images

Rhodri H Davies[1,2], Chris Adamson[1,3], Nathan Walters[1], John Watson[1], Gary Egan[1,2]
[1]Howard Florey Instituite, University of Melbourne. Australia, [2]Centre for Neuroscience, University of Melbourne. Australia, [3]Electrical Engineering, University of Melbourne. Australia

1. Introduction
The human cerebral cortex has distinct cytoarchitectural and myeloarchitectural regions, discernible via traditional histological methods. Techniques have been developed to objectively parcellate the cortex (e.g. [4,5]), but these approaches have some major limitations. In particular, it is generally very difficult to obtain functional results form the same subject prior to post-mortem analysis, preventing the study of structure-function correlations in the human cortex.
We have shown recently [6] that *in vivo* high-resolution T1-weighted MR images contain sufficient information to discriminate between different cortical areas, predominantly based on myeloarchitectonic information [2]. We have also successfully applied automated 2D parcellation techniques to *in vivo* images [6]. Here, we describe a more robust approach to parcellation that requires minimal human intervention.

2. Method
High-resolution T1-weighted MR images (0.28mm*0.28mm*0.35mm) were obtained as described elsewhere [6]. The grey matter-white matter and grey matter-cerebrospinal fluid interfaces were segmented and converted into a pair of triangulated surfaces, one for each interface. Intensity profiles, sampled across the cortex, were used to represent the laminar structure. The start- and end-points of these profiles were defined using an adaptation of an existing method [3], which involves a solution to Laplaces equation, between fixed values at the two interfaces. The tangent field of this solution was traced from one surface to the other, giving a one-to-one correspondence, and thus the start- and end- points of our profiles. The image intensity was interpolated along the profiles at fixed positions with the distance between sample points on a profile chosen to be comparable to the distance between adjacent profiles. Profiles were then grouped together into similar classes using a mixture of Gaussian models. The model parameters were optimised using the EM algorithm [1].

3. Results
Figure 1 shows a high-resolution T1-weighted MR coronal section of the human V5 area in the occipito-temporal cortex. Five distinct parcellated areas were found by the algorithm.
The method was also applied to an image of a histological section (figure 2), where the finer resolution (<10μm) allows a visual confirmation of the results of this parcellation algorithm. Three distinct parcellated areas were determined on the delineated cortex, with the area boundaries shown by the arrows.

4. Conclusions
High-resolution *in vivo* MR imaging now allows sub-millimetre investigation of structure-function correlations in the human brain. The intrinsic 3D nature of the images necessitates the development of automatic tools for robust cortical extraction and parcellation.
Whilst our recent developments are promising, the lack of ground truth represents a significant challenge. Future work will involve validation with a 3D phantom and volumetric post-mortem data.

References
[1] Bishop, *Neural Networks for pattern recognition*, OUP
[2] Eickhoff *et al.*, *Neuroimage*, **19**: p S:659
[3] Jones *et al.*, *Human Brain Mapping*, **11**: 12-32
[4] Schleicher *et al.*, *Neuroimage*, **9**: p 165-177
[5] Schmit *et al.*, *Neuroimage*, **19**: p 42-63
[6] Walters *et al.*, *Proceedings National academy science*, **100**: 2981-2986

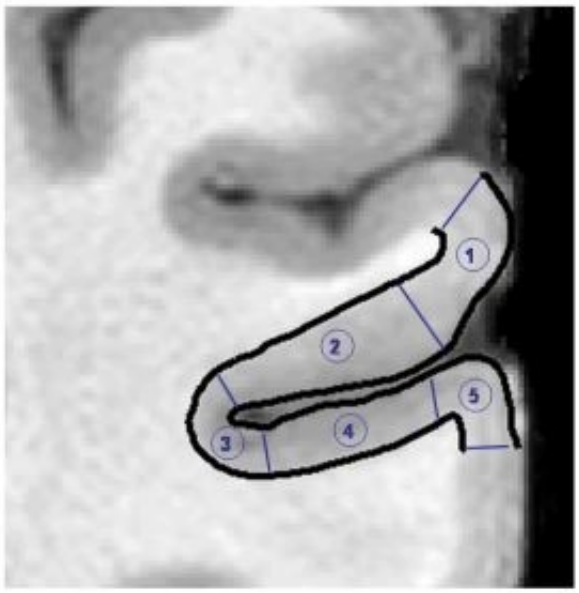

Figure 1

Figure 2

WE 155
Verifying the use of Non-parametric Statistics for fMRI Analyses

Patrick A. De Mazière , Marc M. Van Hulle
Laboratorium voor Neuro- & Psychofysiologie, Medical School, Campus Gasthuisberg O & N, K.U.Leuven, B-3000 Leuven, Belgium

Introduction

Many attempts have been reported to improve the detection of active brain areas with *functional Magnetic Resonance Imaging* (fMRI). Most statistical fMRI analysis tools rely on the assumptions of Gaussianity and linearity despite the fact that this can be debated [1]. Building on previous experience, we further developed the non-parametric statistics behind our fMRI analysis tool.

Implementation

Previously, reservations were made concerning the use of non-parametric statistics as it would not take into account, *e.g.*, multiple comparisons [2] or serial correlations (autocorrelations). The former concern is dealt with by adopting proper non-parametric statistics and with the False Discovery Rate [3], the latter by a new technique that allows us to analyse fMRI time series by means of non-parametric rank tests which are based on the *empirical signal distribution function* (EDF). For this purpose, the time-series are splitted in parts according to their estimated autocorrelation lag.

Finally, after applying the proposed statistical procedures, a simple clustering algorithm is used which guarantees that the detected active voxels are spatially grouped in a consistent manner.

Results

Given these improvements, we examined two types of non-parametric statistics, namely the *Mann-Whitney* and the *Cramer-von Mises* tests. Both are EDF-based, the former is used to test for a difference in median, the latter to test for a difference in distributions. FMRI monkey data were used to compare the two approaches. In general, they yielded similar results, with a small superiority of the Mann-Whitney test over the Cramer-von Mises test with respect to its sensitivity. Furthermore, we performed a number of comparisons with SPM99 by verifying the accordance between the local maxima of the significantly active regions of SPM99 and the non-parametric statistic. A very high degree of correspondence was found.

Using non-parametric statistics, one no longer has to rely on the assumption of Gaussianity and linearity. The necessary correction for the haemodynamic response is resolved by discarding the transitional scans. Besides the theoretical advantages offered by non-parametric statistics, we also noted a decreased sensitivity for variations in the haemodynamic delay (which varies over space and even over time [4]) and for variations in the timing of the different stimuli. The result is a more robust method for the detection of activations.

References

[1] T. Gautama, D.P. Mandic, and M.M. Van Hulle.
Signal nonlinearity in fMRI: A comparison between BOLD and MION.
IEEE Transactions on Medical Imaging, 22(5):636--644, 2003.
[2] G.K Aguirre, E. Zarahn, and M. D'Esposito.
A critique of the use of the Kolmogorov-Smirnov (KS) statistic for the analysis of BOLD fMRI data.
Magnetic Resonance in Medicine, 39(3):500--505, 1998.
[3] Y. Benjamini and D. Yekutieli.
The control of the false discovery rate in multiple testing under dependency.
The American Statistician, 29(4):1165--1188, 2001.
[4] Z.S. Saad, K.M. Ropella, R.W. Cox, and E.A. De Yoe.
Analysis and use of fMRI response delays.
Human Brain Mapping, 13(3):74--93, 2001.

WE 156
Conditional Granger Causality for Exploratory Connectivity Analysis of fMRI data

Filip Deleus , Temujin Gautama , Patrick A. De Mazière , Marc M. Van Hulle
Laboratorium voor Neuro- en Psychofysiologie, Medical School,, Campus Gasthuisberg, K.U.Leuven, B-3000 Leuven, Belgium

Introduction
Traditional approaches for connectivity analysis of fMRI data are SEM [Buechel and Friston, 1997] and DCM [Friston, 2003]. These approaches are confirmatory since they start from a predefined network topology of nodes and connections and they only quantify the strengths of the given connections. We introduce an exploratory method, which precedes the previous ones, to discover the network *topology* for a set of given nodes.

Method
We apply the principle of causal networks [Pearl, 2000] to reveal the unknown network topology. Causal networks rely on the Markov condition which states that each node x_i in the network is independent of all its nondescendants, given its parents PA_i. Hence, in a causal network indirect or spurious connections are not modelled by a direct edge but are only represented by an indirect path in the network. This principle can be implemented by an algorithm which tests for the conditional independencies between the nodes in the network. To test for the conditional independencies between the (fMRI) time series, we apply the principle of conditional Granger causality. The traditional approach for testing the conditional Granger causality from *x* to *y* given a set of nodes *z* is to compare the performance of a restricted model, which predicts the current fMRI signal value of *y* from previous values of *y* and *z*, to that of an unrestricted model, which predicts the current signal value of *y* from previous values of *y*, *z* and *x*. We have extended this principle (and accordingly the causal search algorithm) by also taking the current value of *x* into account such that not only delayed or lagged connections but also instantaneous connections between brain regions can be considered.

Results
We applied our method on fMRI data from a macaque motion experiment, described in [Vanduffel *et al.*, 2001]. Stimuli of moving and stationary dots were presented in blocks of 66.4 seconds (TR 3.321s) alternated with a uniform gray screen, and each of the 15 runs consisted of 256.7 seconds. Data are analysed using SPM99. Nodes for connectivity analysis are selected by looking for local minima in the p-values of the all stimuli versus rest-contrast and by smoothing the time series of these voxels with those of the neighbouring voxels. Seven regions were selected in the right hemisphere of the macaque: V1,V2,V3 and MT in the occipital lobe; FST in the temporal lobe; and MST, VIP in the parietal lobe. The discovered network topology has been shown in the figure 1.

References
Buechel, C. and Friston, K. (1997). *Cerebral Cortex*, **7**: 768-778.
Friston, K. (2003). *Neuroimage*, **19**(4): 1273-1302.
Pearl, J. (2000). Causality: Models, Reasoning and Inference, Cambridge University Press.
Vanduffel, W. *et al.* (2001). *Neuron*, **32**(4): 565-577.

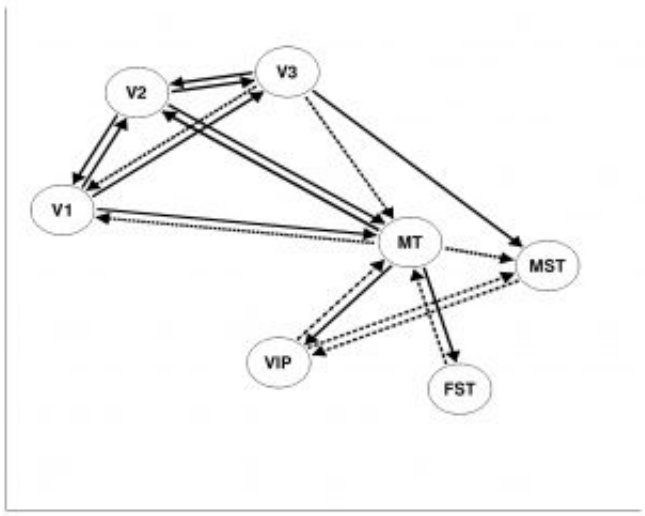

Connection pattern during the presentation of moving random dot pattern. Full lines represent connections with instantaneous and delayed influence; dashed lines represent delayed connections; dot-dashed lines represent instantaneous connections.

WE 157

Neuronal activity vs. fMRI : estimation of the Balloon Model parameters using extended Kalman filter

Thomas Deneux , Olivier Faugeras
Odyssée lab., INRIA, Sophia-Antipolis 06 902 CEDEX, France

ABSTRACT
We give a new method to estimate the parameters of the Balloon Model using an extended Kalman filter. We present our experimental results on macaques involving two modalities : single cells measure and contrast-enhanced MRI.

INTRODUCTION
BOLD signal is admitted to be a combination of blood vessels volume and their deoxyhemoglobin content measures. Buxton and al. (1998) proposed the so-called 'Balloon Model' to describe the metabolic processes involved in these hemodynamic changes due to neuronal activity.
Friston and al. (2000) formalized that model, and described the hemodynamic filter as a 4-hidden states dynamical system. The system is determined by 6 physiological parameters that need to be estimated if we want to introduce the model in latter fMRI analysis.

METHODS
We introduce an innovative noise in the system, that can be interpreted as physiological noise. The extended Kalman filter is a useful tool for such a non-linear dynamical system : provided we know the input of the system (the neural activity), and its output (the BOLD signal, which is a noisy measure of a combination of volume and deoxyhemoglobin), we can estimate simultaneously the 4 hidden states time courses and the 6 parameters.
We present numerical simulations of such estimations.

EXPERIMENTAL DATA
Experimental data where acquired at the Laboratorium voor Neuro- en Psychofysiologie. K.U.Leuven, Belgium (Prof. G.A. Orban, director). Kinetic gratings were presented to a Macaque. The same stimuli were used for single cells and for MION-enhanced MRI acquisitions. These measures were used respectively as the input and output of the 'Balloon Model', to feed the estimation of its physiological parameters.
It is important to note, first, that we used real neural activity measures as the input instead of the mere experimental paradigm ; and secondly, that in the case of this experience, the Balloon Model was simplified, since the MION-enhanced MRI is a measure of the solely blood volume. These two points reduce the incertitude in the parameters estimation, compared to former studies.

IMPLICATIONS
The better understanding of the hemodynamic filter and the BOLD response that we get through such validations of the Balloon Model will allow better fMRI analysis and even open the door to the fusion between fMRI and other modalities, like electro-physiological measurements (EEG, MEG) for example.

REFERENCES
[1] Buxton R.B., Wong E.C. and Frank L.R. 1998. Dynamics of blood flow and oxygenation changes during brain activation : The Balloon model. MRM 39: 855-864
[2] Friston K.J., Mechelli A., Turner R. and Price C.J. 2000. Non-linear responses in fMRI : The Balloon model, Volterra kernels and other hemodynamics. NeuroImage 12: 466-477

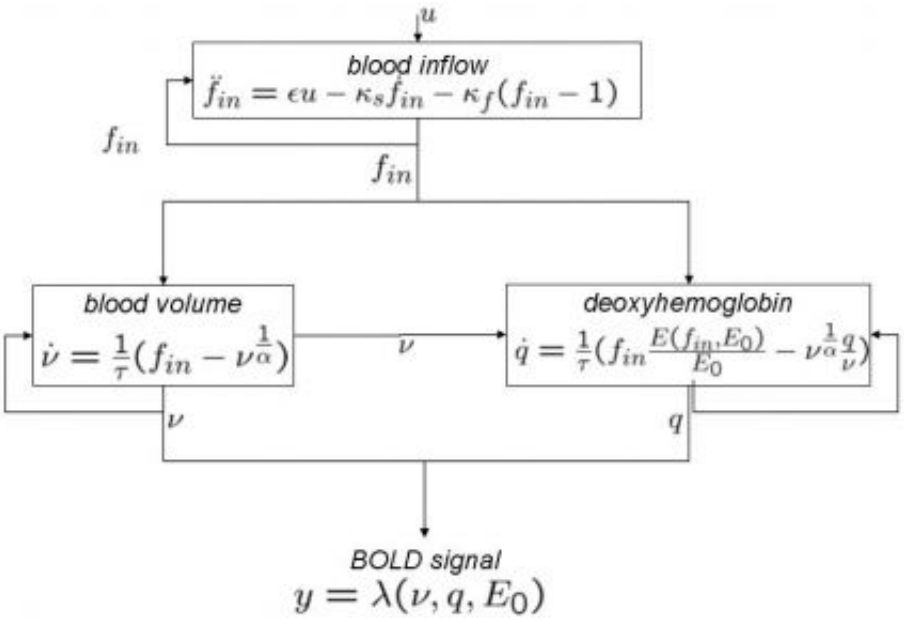

The Balloon model

WE 158
An automated processing pipeline for anatomical and functional MRI data

James Dias , James T. Voyvodic
Duke-UNC Brain Imaging and Analysis Center , Duke University, Durham NC, USA

Functional MRI scanning generates large datasets (typically hundreds of Mbytes) that need to be efficiently and reliably transferred from the scanner to data analysis computers and archival media. Processing of these data sets also typically involves some routine image processing procedures, which can be time consuming because of the amount of data involved. In clinical cases where rapid processing of fMRI data is important, many potentially useful processing steps may often be omitted to save time. In order to make these routine data manipulation steps more efficient and more reliable, therefore, we have implemented a fully automated data processing pipeline that detects MRI data as soon as it is acquired on the scanner and takes care of the initial critical aspects of the analysis.

The automated pipeline consists of two custom-built software programs written in Perl: 1) a transfer daemon that runs on each scanner computer, and 2) a processing daemon that runs on a separate analysis computer. Each scanner data file contains an experiment ID code, which is used to guide that file through the processing pipeline. The transfer daemon detects raw functional MR data files (k-space files on our GE scanners) and copies those files across the computer network to the analysis computer (currently a Linux PC). After verifying successful transfer, the scanner raw data file is deleted to make space for more data. Anatomical images acquired by the scanner are also sent (using GEs automatic image transfer option) as DICOM files to the analysis computer.

The second program in the pipeline is a processing daemon running on the analysis computer. Raw k-space data files are automatically reconstructed to images using pulse-sequence appropriate reconstruction programs for spiral or echoplanar data. An XML-based metadata descriptor file is also generated for each scan series (including DICOM anatomical images). These XML headers provide a common data description that can be used by all subsequent processing steps; they also contain a history of what processing steps have occurred.

Our processing daemon can then carry out any of the following optional analysis steps (depending on parameters entered for that experiment ID): motion correction using AIR (Woods et al., 1998) or SPM (Friston et al. 1995), TR alignment using SPM, motion and intensity stability quality assurance plots using fScan (Voyvodic, 1999), and/or spatial smoothing using SPM. After all of the optional processing steps have completed, the resultant data are all transferred across the network to the user directories specified for that experiment ID. All original k-space and DICOM data files are also copied to tape storage.

This automated pipeline has dramatically reduced the incidence of lost MRI data and has greatly increased the efficiency and reliability of the initial data processing steps routinely performed in fMRI analysis.

This work was supported by US PHS grant IP01NS41328.

References:

Friston KJ, et al. (1995) Human Brain Mapping, 2:189-210
Voyvodic JT (1999) NeuroImage, 10:91-106.
Woods RP, et al. (1998) Journal of Computer Assisted Tomography, 22:139-152.

WE 159

Applying the Target Field Method to Transcranial Magnetic Stimulation Coil Design.

Stephen J Dodd[1], Jack L Lancaster[2], Peter T Fox[2]
[1]Laboratory for Functional and Molecular Imaging, NINDS, NIH, [2]Research Imaging Center, University of Texas Health Science Center at San Antonio

Introduction

Transcranial magnetic stimulation (TMS) involves the application of a rapidly changing magnetic field next to the skull and inducing an electric field in the tissue below, thereby forcing neurons to fire. Here we adapt some of the magnetic coil theory, typically used in gradient coil design for MRI systems, namely the target field method (1,2), to the task of magnetic stimulation.

Method

The target field method of Martens et al. (2) for design of low inductance bi-planar gradient coils has been modified for TMS coil design. For the moment we have only considered the situation where there is a homogeneous media, i.e. for the moment we have neglected the effect of tissue boundaries, and so the electric field may be calculated using the time derivative of the vector potential. This E-field may then be substituted for the B-field in the design process, eventually leading to a solution for a continuous planar current density. This current density may be split into discrete loops providing the coil pattern. The accuracy of the design is then dependent on the number of loops chosen to approximate the continuous current density. The inductance may be estimated using $W = 0.5*L.I^2$, as the energy, W, is used in the current density calculation. The design may be checked by summing the electric field components of discrete coil sections. Estimates of the effect of placing the coil next to spherical tissue boundaries may be determined using the method of Eaton (3).

Results

An example of a coil resulting from the design method is shown in Figure 1. The electric field was constrained at three positions to the values listed in Table 1. These constraints were defined to be similar to the field profile of a Cadwell B-shaped coil. The algorithm determined a current of 1382 A was required produce 96.8 V/m, or 1427 A at 100 V/m. This is compared to a required current of 1714 A for the B-shaped coil to produce a maximum of 100 V/m. An operating frequency of 5 kHz was assumed and that the coil lies on the z=0 plane. The inductance was estimated to be 23 μH compared to ~27 μH for the B-shaped coil. The spatial extent of the target field design may be reduced to a certain extent without affecting the field significantly (2).

Conclusion

A method for more efficient TMS coil designs with a planar geometry has been proposed. The lower inductance coils provided by the target field method allow for greater efficiency (by allowing more turns for the same inductance). Alternatively, a coil with a narrower E-field profile may be designed using the same current as, say, a B-shaped coil.

References

Turner, R. *J. Phys. E: Sci Instrum.* 21:948-952, 1988
Martens, M. et al. *Rev. Sci. Instrum.* 62:2639-2645, 1991
Eaton H. *Med BiolEng Comp* 30:433?440, 1992

Table 1. Electric field (y-component) constraints and calculated results for coil shown in Figure 1.

x (cm)	y (cm)	z (cm)	Defined E-field (V/m)	Figure 1 Coil (V/m)
0.0	0.0	3.0	100.0	96.8
3.0	0.0	3.0	50.0	48.2
0.0	4.5	3.0	50.0	47.8

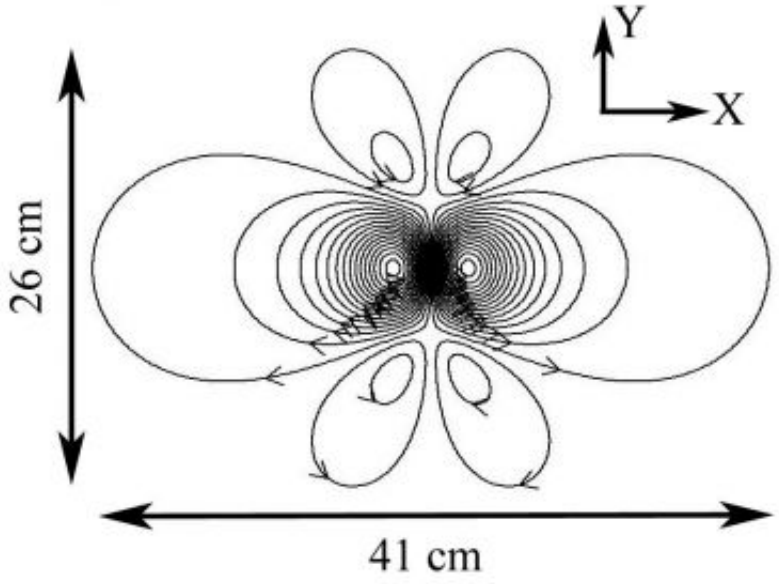

Figure 1. Target coil field example. The coil is lying in the z=0 plane.

WE 160
How functional connectivity is influenced by physiology

Silke Dodel[1], Jean-Baptiste Poline[1], Jean-Luc Anton[2], Matthew Brett[3]
[1]UNAF/SHFJ Orsay, France, [2]IFR 45, [3]MRC Cognition and Brain Sciences Unit, Cambridge, United Kingdom

Functional connectivity in fMRI has been investigated most often using resting state data, i.e. the subject is lying in the scanner without any specific task or stimulus. In this case no external reference is available to validate the results. Therefore it is particularly important to distinguish signals reflecting functional activity from purely physiological signals. To attain this goal we investigate functional connectivity in resting state data where in addition to high rate MRI we simultaneously acquired data from respiratory and cardiac influences (henceforth called physiological effects). We cleaned the data from the latter and compared the resulting functional connectivity networks (Fig.1) [1].
For the networks we found essentially that they were slightly smaller after effect removal than before and that effect removal led to the appearance of very small new parts of the network as well. To understand this we investigated more closely how correlation is affected by effect removal. We quantified the influence of physiological effects on a voxel by the variance ratio of the signal (ratio of the variances after and before removal of the effect). The lower the variation ratio, the stronger the voxel is influenced by the respective effect (Fig.2).
Our main results are:
1) Voxels highly influenced by physiology are localized consistently at similar identifiable regions. (Fig.2)
2) Respiration has less influence on the variance of the signals than cardiac effects (Fig.2).
3) High variance loss does not go along with high correlation loss. (Figs. 1, 3)
4) The risk of false positive connections is particularly high for voxel pairs where one voxel is weakly and the other strongly influenced by physiology (Fig.3d).
Fig. 3 shows representative results for correlation changes by effect removal (here: cardiac) for 10% of the voxels showing, respectively, the strongest and the weakest influence by the effect. As one might expect we find essentially no difference in correlation before and after effect removal among weakly influenced voxels (Fig.3b). For strongly influenced voxels effect removal spreads out the correlations with a tendency towards zero (Fig.3c). For pairs of strongly and weakly influenced voxels effect removal has a slight tendency to enhance the absolute value of correlations (Fig 3d). This might lead to spurious connections, which could be the reason for the persistence of the connectivity networks in regions that are highly influenced by non-functional physiology (Fig.1).
We are able to explain our findings within a theoretical framework that investigates how the correlations are affected by various effects. However this framework assumes linear influence of the effects. Furthermore correlation as a measure of functional connectivity is linear as well. We have shown that linear removal of the physiological effects is not enough to avoid spurious connectivity. It is therefore of great interest to investigate nonlinear measures of functional connectivity as well as a possible nonlinearity of the physiological effects [2].
[1] S. Dodel et al., "Functional connectivity by cross-correlation clustering", Neurocomputing, vol. 44-46, 2002
[2] Pierre-Jean Lahaye et al., ‘‘Functional Connectivity: Studying Nonlinear, Delayed Interactions between BOLD Signals’’, NeuroImage 20(2), 2003

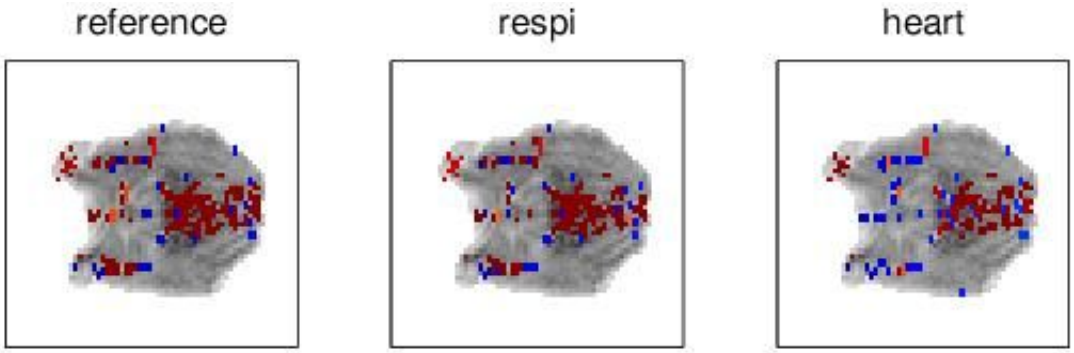

FIG. 1 – Functional connectivity networks before effect removal (reference) and after removal of respiratory (respi) and cardiac (heart) effects. Note that respi means *removal* of respiratory effects and heart means *removal* of cardiac effects

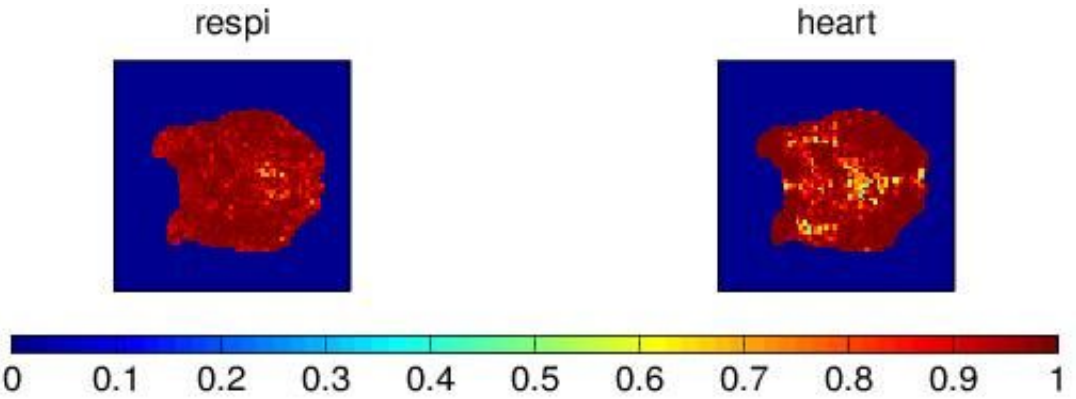

FIG. 2 – Variance ratio before and after effect removal of respiratory (respi) and cardiac (heart) effects.

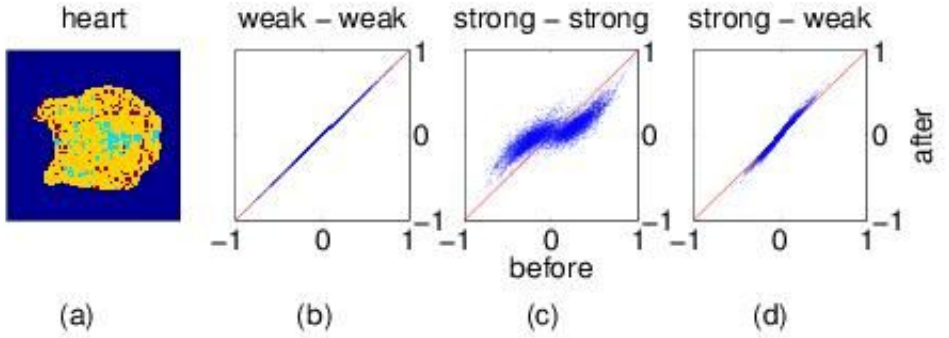

FIG. 3 – Representative results for correlation changes by effect removal. (a) 10% of the voxels that are most strongly (blue) and most weakly (red) influenced by cardiac effects. (b) Scatter plot of the correlations between the *red* voxels before and after effect removal. (c) The same for the *blue* voxels. (d) The same for the correlations between *red* and *blue* voxels.

WE 161
BOLD SINGLE-TRIAL VARIABILITY AND MODEL SELECTION

Sophie DONNET[1], Marc LAVIELLE[1], Jean-Baptiste POLINE[2,3], Philippe CIUCIU[2,3]
[1]Laboratoire de Mathématiques, Université Paris-Sud, 91405 ORSAY, France, [2]SHFJ/CEA 4, Place du Général Leclerc, 91406 Orsay, France, [3]IFR 49, Institut d'Imagerie Neurofonctionnelle, Paris, France

The mechanisms coupling neuronal activity and the BOLD response (Blood Oxygen level Dependent)[1] observed with fMRI are still poorly understood. Changes in the BOLD contrast can by characterized by the Hemodynamic Response Function (HRF). A precise estimation of the HRF may help to quantify neuronal activity. Advances have been made on the non parametric estimation of HRF[2,3]. Smoothness constraints due to neurovascular environment can now be taken into account. However, recent works have addressed the non parametric estimation of the HRF under the assumption of stationarity in time. In other words, previous works have assumed that each occurrence of a given experimental condition evoked a response constant in shape and in magnitude. Recently, it was suggested that this might not always be the case[4]. Consequently, we propose to test a more flexible model that allows for the variation of the magnitude of the HRF with time in specific brain areas. This model is tested against a model with a fixed magnitude using maximum likelihood procedures.
The model assumed to hold between the stimuli and the fMRI data is a standard convolution model within a bayesian framework that allows the inclusion of prior information. To enforce the positivity of the BOLD response that occurs in many paradigms (\eg motor, visual responses), we introduce prior information about the magnitudes through the definition of a relevant probability density function. The parameters of interest (event magnitudes, HRF shape) are estimated using a stochastic version of the Expectation Maximization algorithm, the SAEM[5].
We tested this model on fMRI data acquired on eight subjects during a paradigm involving eight types of events, (right and left button click and visual stimuli that may involve motor preparation). 3D scans were acquired with a 3 Tesla Brucker scanner. Data from the left motor cortex were extracted and filtered to remove low frequency drift.
Results show that the hypothesis of a variable BOLD response is usually validated for button click and often rejected for visual stimuli. It is possible that motor responses are not well controlled for their intensity and duration, while visual stimuli are sensory conditions which may generate more stable responses. These findings suggest that, in some cases at least, the model selected should allow for the variation of the HRF magnitude across events occurrences. This may have important implications for comparing different kinds of events since it reveals a new variance component ignored so far.
References

[1] S.Ogawa, &al ‘‘Brain magnetic resonance imaging with contrast dependent on blood oxygenation’’, Proc.Natl.Acad.Sci. USA, 1990.
[2] P.Ciuciu, &al ‘‘Unsupervised robust non-parametric estimationof the hemodynamic response function for any fMRI experiment’’, IEEE Trans. Medical Imaging, 2003.
[3] G.Marrelec &al, ‘‘Estimation of the hemodynamic response function in event-related functional MRI: Directed acyclic graphs for a general Bayesian inference framework’’, Proc. 18th Int.Conf.onInfo.Proc.in Med.Imaging
[4] JR.Duann, &al ‘‘Single-trial variability in event-related bold signals’’, Neuroimage, 2002.
[5] B.Delyon &al, ‘‘Convergence of a stochastic approximation version of the EM algorithm’’,Ann.Statist., 2002.

WE 162

FMRI simulation and its application in modelling the interaction of motion and B0-inhomogeneities

Ivana Drobnjak , Mark Jenkinson
FMRIB Centre, University of Oxford, UK

Introduction

B_0-inhomogeneities occur at interfaces of materials with different magnetic susceptibilities, such as tissue-air interfaces. These differences lead to distortion in the local magnetic environment, causing signal loss and geometric distortion of the image. Current methods for modeling and correcting these artifacts involve acquiring a field map (i.e. an image of the perturbed field) and then transforming the image by warping from the distorted to undistorted voxel positions. However, acquiring field maps at each time point is not practical in fMRI. Hence a more quantitative and analytical approach is needed to examine the interaction of B_0-inhomogeneities and motion[1].

Methods

A C++ MRI simulator was constructed to solve the Bloch equations for each object element (small rectangular voxels). The perturbed field $B_z^{(1)}$ was calculated from a known susceptibility distribution using a perturbative solution of Maxwell's equations[2]. To model general object motion, a rigid-body coordinate transform, R(t), relating the object and scanner coordinate systems is specified as a function of time; i.e. $x_{sc}=R(t)x_{ob}$. Motion parameters are specified at discrete time points via an input file and interpolated between these points. Integrating the magnetization vector in time for each tissue type separately in a voxel element (in object space) gives the MR signal as shown in Equation 1, where M_0 is the transverse magnetization after RF excitation,ρ is the average spin density of the tissue type in this voxel, $\mathbf{G}_{sc}(t)$ is the applied gradient vector (in scanner coordinates). $B_{z,sc}^{(1)}(t)$ is the perturbed field (in scanner coordinates) evaluated according to Equation 2, where $B_p^{(1)}(\mathbf{q})$ is the field in object coordinates calculated in the p direction (x, y or z) from an applied field $B^{(0)} = \mathbf{q}$ (being either **x**, **y**, or **z**). The total signal is calculated as the sum of the contributions from each voxel.

Results/Discussion:

Figure 3 shows an image acquired by simulating an EPI pulse sequence and using the BrainWeb partial volume tissue estimates[3]. It shows effects of the B_0-inhomogeneities, where the biggest distortion is in the frontal lobe as it is close to a large air/tissue boundary. The interaction of B_0 artifact and motion is also significant and larger than spin-history or interpolation artifacts in frontal regions for typical movements. Numerical measurements of relative motion artifact levels for various movements are now available.

We have quantitatively simulated the effects of B_0-inhomogeneities with and without motion effects, using a theoretical model for the B0 changes[2]. Future work will seek to implement time varying signals of a physiological nature (e.g. BOLD) to provide a realistic method of generating simulated data (see [1]) that includes motion effects where the ground truth is known. This will be valuable for testing and validation of statistical analysis methods.

Acknowledgments

UK-EPSRC (MIAS-IRC) for support.

References:

[1] MIDAS consortium, HBM 2004
[2] M. Jenkinson, J. Wilson and P. Jezzard, ISMRM 2002
[3] R.K.S. Kwan, A.C. Evans and G.B. Pike, IEEE TMI 1999, 18(11)

$$S_{\text{voxel}} = \iiint_{\text{voxel}} M_0 \rho \exp\left(-\frac{t}{T_2}\right) \exp\left(j\gamma \int \mathbf{G}_{sc}(t) R(t) \mathbf{x}_{ob}\, dt\right) \exp\left(j\gamma \int B_z(t)\, dt\right)\, d\mathbf{x}_{ob}$$

Equation 1

$$B^{(1)}_{z,sc} = [0\ 0\ 1]\, R^{-1} \begin{bmatrix} B^{(1)}_x(1,0,0) & B^{(1)}_x(0,1,0) & B^{(1)}_x(0,0,1) \\ B^{(1)}_y(1,0,0) & B^{(1)}_y(0,1,0) & B^{(1)}_y(0,0,1) \\ B^{(1)}_z(1,0,0) & B^{(1)}_z(0,1,0) & B^{(1)}_z(0,0,1) \end{bmatrix} R \begin{bmatrix} 0 \\ 0 \\ 1 \end{bmatrix}$$

Equation 2

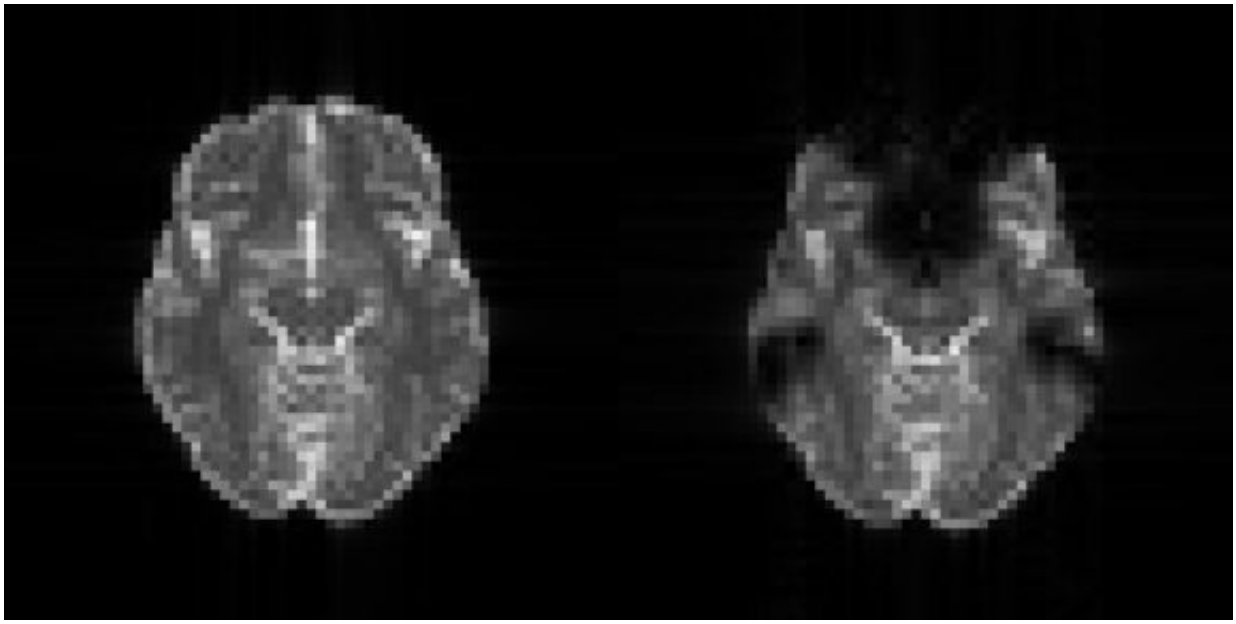

SImulated EPI without (left) and with (right) B0 distortion

WE 163
Consistent task-related BOLD activity during simultaneous EEG/fMRI recording

Jeng-Ren Duann[1,2], Tzyy-Ping Jung[1,2], Frank Haist[3], Luca Finelli[1,2], Andrey Vankov[1], Terrence J. Sejnowski[1,2], Scott Makeig[1]

[1]Swartz Center for Computational Neuroscience, Institute for Neural Computation of University of California San Diego, La Jolla CA, USA, [2]Computational Neurobiology Lab., the Salk Institute for Biological Study, La Jolla CA, USA, [3]Department of Psychiatry, University of California San Diego, La Jolla CA, USA

Introduction

Here, we demonstrate the result of fMRI data acquisition and analysis obtained from simultaneous EEG/fMRI recording experiments. Makeig et al. (2002), pointed out that the biophysical mechanisms linking BOLD and EEG signals, while potentially very important, are still unknown. To investigate the linkage between these two, we have customized our MR-compatible EEG system and have successfully acquired 15 experimental sessions recording 71 EEG channels during continuous BOLD scanning at 1.5-Tesla. Here, we report the fMRI results. EEG results will be reported separately in Jung et al. (HBM 2004).

Methods

Fifteen healthy young adults participated in this study. The subjects were fitted with 73 custom tin EEG electrodes before the fMRI sessions and were asked to perform 3 6-min bouts of a two-back working memory task intersperced with 2 bouts of a simple eyes closed/open paradigm (Finelli, HBM 2004). EEG and fMRI signals were recorded simultaneously. Working memory task bouts consisted of 5x40-s "on" alternating with 6x20-s "off" periods. During "on" periods, a series of letters (’A’ through ’E’) was displayed at screen center in random order. Subjects were asked to press a thumb button when the letter displayed was the same as the one presented two back in the series. Each letter was displayed for 200 ms with an inter-stimulus interval of 1 s. Data was analyzed with methods (preprocessing, infomax ICA, and visualization) implemented in FMRLAB (Duann et al., http://sccn.ucsd.edu/~fmrlab). For each subject, the fMRI data from the 3 working-memory bouts was concatenated. After preprocessing and ICA decomposition, the time course of each independent component was compared to a reference function based on the experimental paradigm. The component with maximum correlation was selected as the task-related component(s) of interest.

Results

EEG data recording produced no noticeable deleterious effects on the fMRI signals. For each subject, we found one independent component whose region of activity (ROA) comprised bilateral dorsal and lateral prefrontal plus inferior parietal cortices and whose time course was highly correlated with the reference function. This ROA was reproduced near-exactly in each subject.

Discussion

As is commonly known, EEG and fMRI data collection can interfere with each other during simultaneous EEG/fMRI recordings. It is thus essential to make sure that the interference does not contaminate the data quality and degrade the data analysis. Our EEG acquisition system did not degrade our fMRI recordings or noticeably interfere with the ICA data analysis. ICA analysis methods allowed estimation of the stability of BOLD regions of activity ’ (ROAs) within and between individuals. ICA, applied to these data, found the same brain areas to be involved in the two-back working memory task in each of the 15 subjects, without data smoothing, averaging or lumping.

WE 164
Guessing the Sex from the Shapes of Cortical Folds

E Duchesnay , A Roche , D Rivière , D Papadopoulos-Orfanos , Y Cointepas , J.-F. Mangin
Service Hospitalier Fréedéric Joliot, CEA, Orsay, France. Institut d'Imagerie Neurofonctionnelle (IFR 49), Paris, France

Recent advances in neuroimaging have led to an increasing recognition that certain neuroanatomical structures may be preferentially modified by particular cognitive skills, genes or diseases. This recognition has mainly resulted from the recent design of automated morphometric methods [1] relying on deformable atlases that enable point-to-point comparisons of the local amounts of grey or white matter. Another approach (structural morphometry [2]) is to extract "stable" cortical landmarks such as sulci, and compare the latter across subjects in order to show morphometric differences in the cortical shapes of two different populations.
We propose to go beyond the latter goal, by addressing a second level issue: is it possible to design a classifier that will learn to distinguish two population based on their cortical sulci morphometric features? While the final aim is automatic diagnostic, this abstract focuses on distinguishing males and females from a large set of measures on the shapes of the cortical sulci.
These sulci were first automatically identified in T1-weighted MR images using a pattern recognition system described previously [3]. A set of 116 different sulci were identified in each brain of the database (that contains 60 females and 83 males). Each sulcus is described by 27 attributes:
(i)pure shape: surface, maximum and minimum depth;
(ii)localization: extremity and center of mass coordinates in a reference system;
(iii)orientation: sulcus surface averaged normal, sulcus outer line averaged direction;
(iv)structural: number of connected components in the sulcus and maximal gap between these components.
Preliminary experiments have shown that the two populations can usually not be differentiated from a single feature. Using all features together (116*27=3132), however, leads to a curse of dimensionality preventing a good generalization power of the classifier. Therefore, the first goal was to reduce the huge amount of morphometric data to a small set of features allowing good classification performance.
The data reduction is performed in two step :
(i)*Feature selection*: a greedy algorithm [4] explores the feature space in order to select the most discriminant attributes.
(ii)*Feature generation*: because the previous subset of features may be too big and may cause over-fit problems: a single new feature is generated for each sulcus, as a linear combination of the selected features.
Three different classifiers are then built upon the previous extracted features: linear discriminant analysis, one hidden layer perceptron and support vector machine. After evaluating the classifiers' performances using a bootstrapping technique, the result of the best classifier is used to drive the next feature selection.
The algorithm stops when all available features have been discarded or selected. The final discriminant model (subset of features, linear projectors, and a classifier) is then validated with a leave-one-out technique.
As a conclusion, the best classifier built from an optimal set of 54 morphometric features
achieves a 96% correct generalization rate during a leave-one-out procedure.
[1] Ashburner et al, NeuroImage, vol. 11, pp. 805--821, 2000
[2] Mangin et al, Artificial Intelligence in Medicine, 2003, in press
[3] Rivière et al, Medical Image Analysis, vol. 6, no. 2, pp. 77--92, 2002
[4] Pudil et al, Pattern Recognition Letters, vol. 15, pp. 1119--1125, 1994

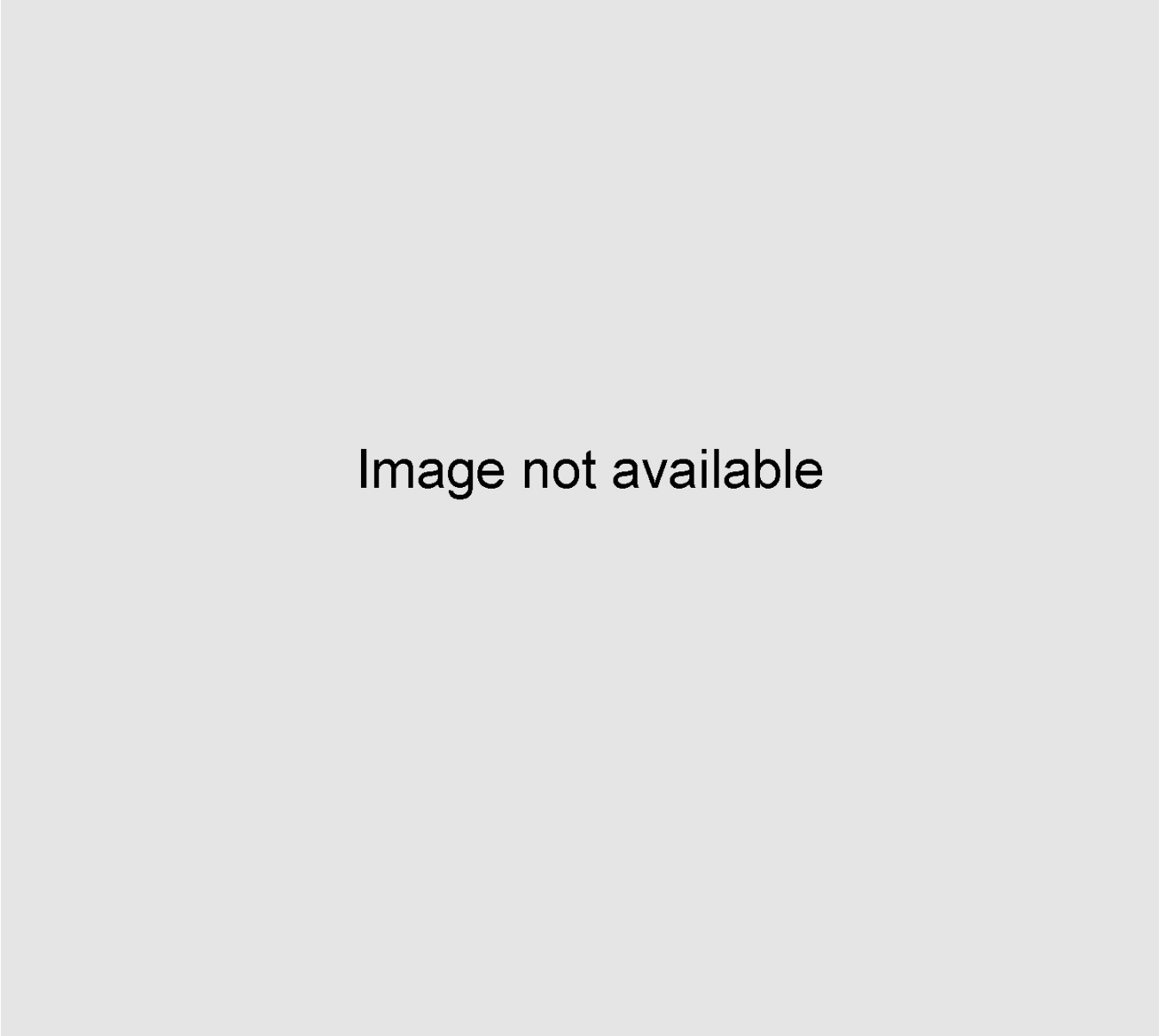

System overview

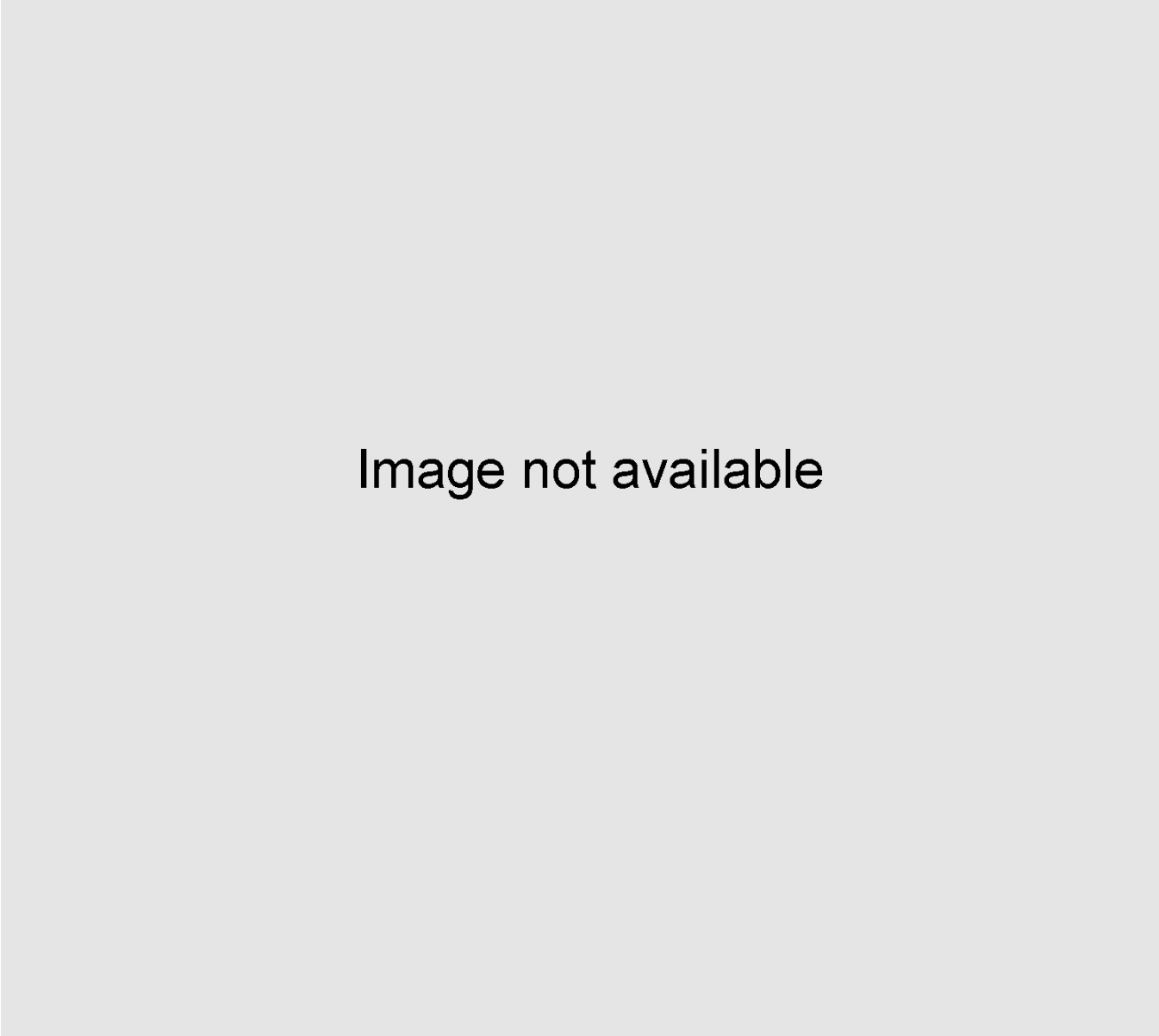

The design of the classifier

WE 165
Convolutive ICA (c-ICA) captures complex spatio-temporal EEG activity.

Mads Dyrholm[1], Lars K Hansen[1], Li Wang[2], Lars Arendt-Nielsen[2], Andrew CN Chen[2]
[1]Informatics and Mathematical Modelling, Technology University of Denmark, Denmark, [2]Human Brain Mapping and Cortical Imaging Laboratory, Aalborg University, Denmark

[Background]
Independent Component Analysis (ICA) is a useful tool for removing electroencephalographic (EEG) artifacts such as eye-blink or eye-movement. Artifact activity that is spatially-separable and temporally independent from other EEG activity will, in a successful ICA decomposition, appear in a separate component. The ICA method is advocated because the obtained artifact components can be excluded from the EEG by a linear projection. Hence it is possible to clean EEG in its full length without loosing contaminated data segments. However, this approach still requires an expert judgment to determine which of the obtained ICA components are wanted or unwanted. In this work we show how Convolutive ICA (c-ICA) can capture more complex spatio-temporal behavior in a single component than is possible with conventional ICA. This creates components with more realistic temporal structure and furthermore assists the component inspection procedure by reducing the number of components to inspect. Convolutive ICA of EEG data has been studied by Makeig et al (2002,2003) in the complex frequency domain, here we apply a temporal un-mixing c-ICA approach which does not require windowing or frequency based representation of data.
[Methods]
The data used for the analysis was a 124 channel EEG recorded at 204.8Hz sampling rate. Electric pulses were generated at approximately 2Hz and applied to the subjects little-finger as stimulus. An eighty seconds long recording was obtained with approximately 150 stimulation epochs. DC components and slow drift were eliminated from each channel separately by high-pass filtering with a 0.2Hz transition-band around 1Hz cutting frequency. Five principal component features were extracted from the resulting data matrix for convolutive independent analysis (fig. 1).
ICA algorithm: Maximum-Likelihood instantaneous ICA (Bell & Sejnowski, 1995). Convolutive ICA algorithm: Maximum-Likelihood (Dyrholm & Hansen, 2003). The number of convolutive lags was set to fifty samples (0.25 sec).
[Results]
The ICA and c-ICA algorithms each resulted in five components. We illustrate the difference between the two ICA approaches by analysis of the components with the maximum correlation with the stimulus delivery. In Fig. 2 and 3 we show time series for the conventional and c-ICA for the five spatial variance components. The conventional ICA time series all follow a stereotypical time-course, hence appear as being completely time synchronized. While the c-ICA time series show non-trivial delay structure between the five spatial patterns, hence, can give rise to time variant scalp contours of activity. This is an important advantage for c-ICA because it directly, within a single component can capture delayed correlations across the features and locations. In Fig. 4 we show the cross-correlation between time series associated with two of the spatial variance features. The cross-correlation function shows two off-center peaks characteristic of two symmetrically delayed signal components. The conventional ICA algorithm captures only the average behavior, while the c-ICA component captures the delayed presence of one of these components.
[Conclusion]
Convolutive ICA (c-ICA) offers a more flexible representation with non-trivial temporal structure of the component time series, highly relevant for EEG analysis.
Acknowledgement: supported by the Danish Technological Council

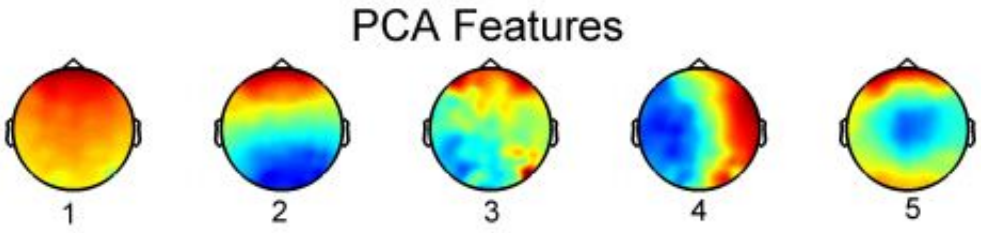
PCA Features
1
2
3
4
5

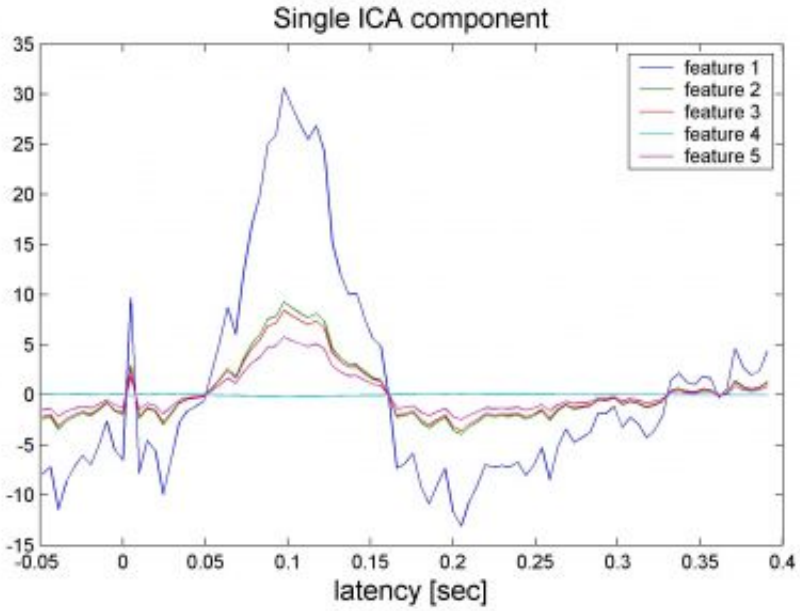
Single ICA component
feature 1
feature 2
feature 3
feature 4
feature 5
latency [sec]

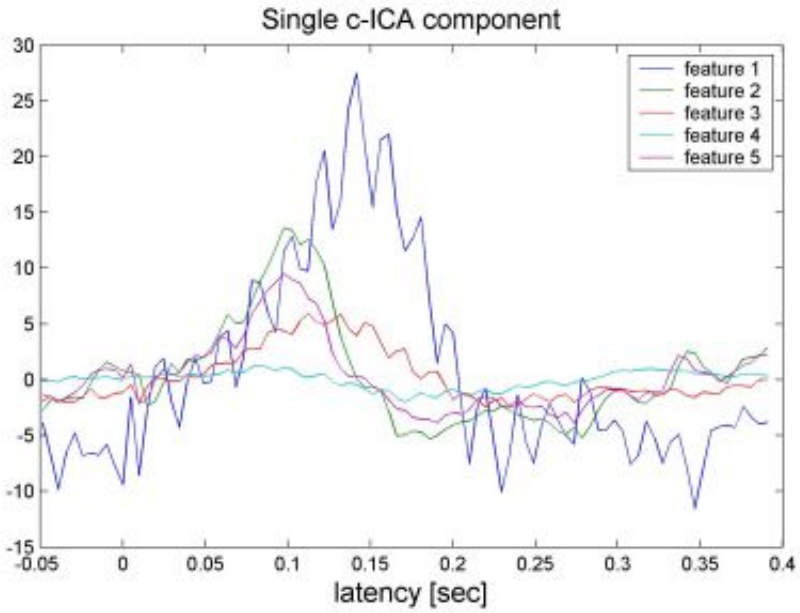
Single c-ICA component
feature 1
feature 2
feature 3
feature 4
feature 5
latency [sec]

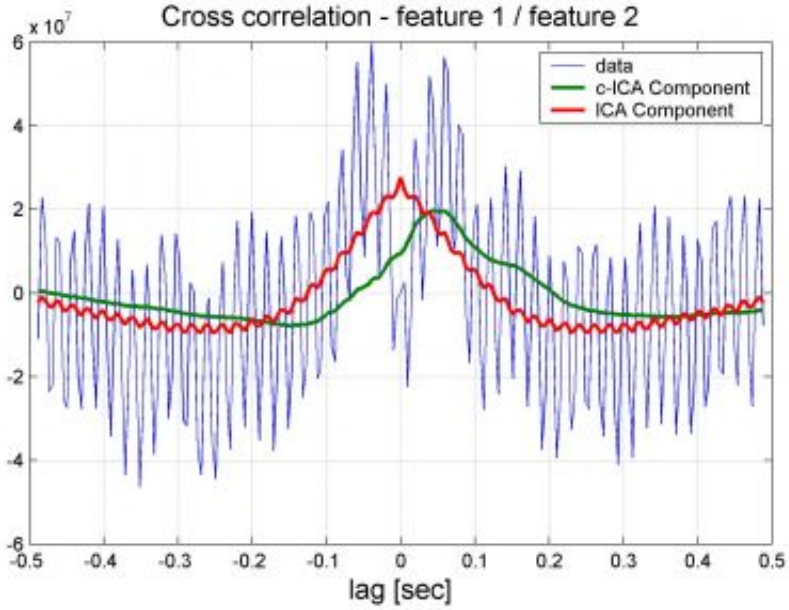
Cross correlation - feature 1 / feature 2
x 10^7
6
4
2
0
-2
-4
-6
-0.5
-0.4
-0.3
-0.2
-0.1
0
0.1
0.2
0.3
0.4
0.5
lag [sec]
data
c-ICA Component
ICA Component

WE 166
Whole head measurement NIRS system

Hideo Eda[1], Tsutomu Murata[1], Satoru Kohno[5], Akira Takatsuki[1,2], Akitoshi Seiyama[1,3], Toshio Yanagida[1,2,3,4]

[1]Brain Information Group, CRL, [2]Graduate School of Engineering Science Osaka University, [3]Osaka University Graduate School of Medicine, [4]Graduate School of Frontier Biosciences Osaka University, [5]Medical Systems Division, Shimadzu Corporation

Introduction

Light in the near infrared (NIR) region around 800nm wavelength can penetrate human tissue. Optical measurements at multiple NIR wavelengths enable a spectroscopic technique that calculates haemoglobin parameters such as changes in oxygenated haemoglobin and deoxygenated haemoglobin. These parameters are related to changes in blood volume resulting from neural activity in the brain. NIR spectroscopic (NIRS) imaging system detects signals with a high time resolution and it is now widely applied for human brain mapping. The system requires a probe holder that connects optical fiber pairs to the scalp. It is very important to attach holder at the appropriate head location because measurement areas are limited by the holder. Especially for higher brain function experiment, such as perceptual rivalry [1], several brain areas activate and their interaction will be discussed. We need to measure different brain areas precisely. In order to improve NIRS imaging system we here introduce a whole head measurement system. It consists of two major discussions. One is the measurement system with a whole head holder, the other is the data analysis with the optical path length.

Whole head holder for NIRS

Figure 1 shows NIRS measurement with Soft vinyl based whole head holder during perceptual rivalry experiment. Measurement areas had been determined before the experiment. Figure 2 shows an experimental setup with FLexible Adjustable Surface Holder (FLASH). This was developed by Shimadzu Corporation [2]. FLASH completely fits surface of human heads, and keeps the same measurement distance between a radiation and detection.

Phase shift measurement system for the optical path length

Haemoglobin parameters are calculated based on the modified Lambert-Beers law which assumes tissue homogeneities. Unit of the calculated parameters is not pure concentration (mM), but concentration multiplied by distance (mM cm). The distance is defined as the optical path length. According to the brain structural differences, it may vary from each portion of the head. If we want to discuss quantitative aspect of haemoglobin changes, we have to correct the parameter by the optical path length. To know the optical path length, other measurement system, a time resolved measurement system or a phase detection system, is needed. Figure 3 is a scheme of a phase detection system. A radiation fiber connected to a light source is placed on the object a few centimeters apart from a detection fiber connected to a detector. Modulation frequency of the light source changes from 10MHz to 1000MHz. Phase shifts are detected at every modulation frequencies. By fitting the frequencies and phase shifts to the analytical solution of the optical diffusion equation, we can get two optical properties; absorption coefficient and reduced scattering coefficient. The optical path length can be calculated by these optical properties.

References

1 T.Murata et al., Discrete stochastic process underlying perceptual rivalry, NeuroReport, Vol.14, No.10, 1347-1352, 2003

2 S.Kohno et al., Development of FLASH (FLexible Adjustable Surface Holder) in functional near infrared spectroscopic imaging system, HBM2004 (abstract)

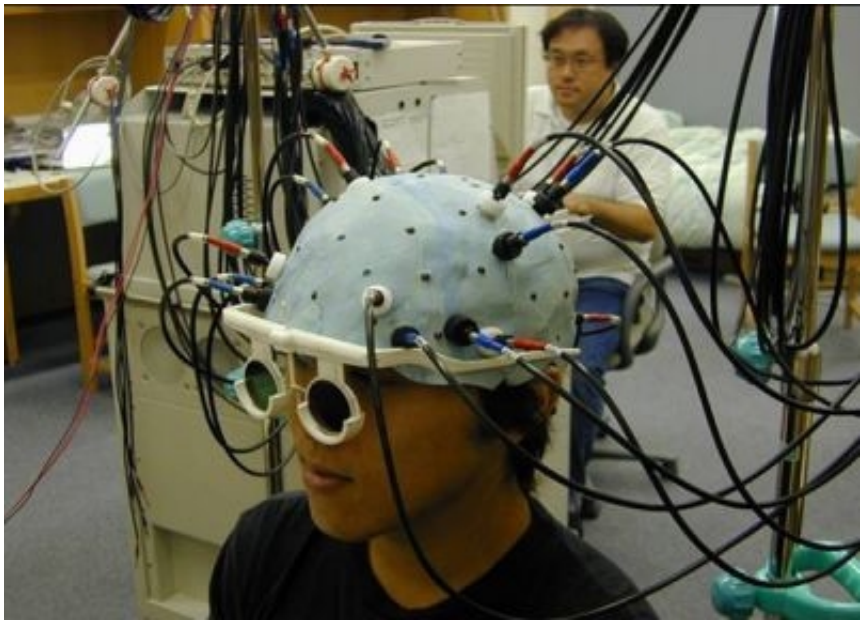

Fig.1. Soft vinyl based whole head holder

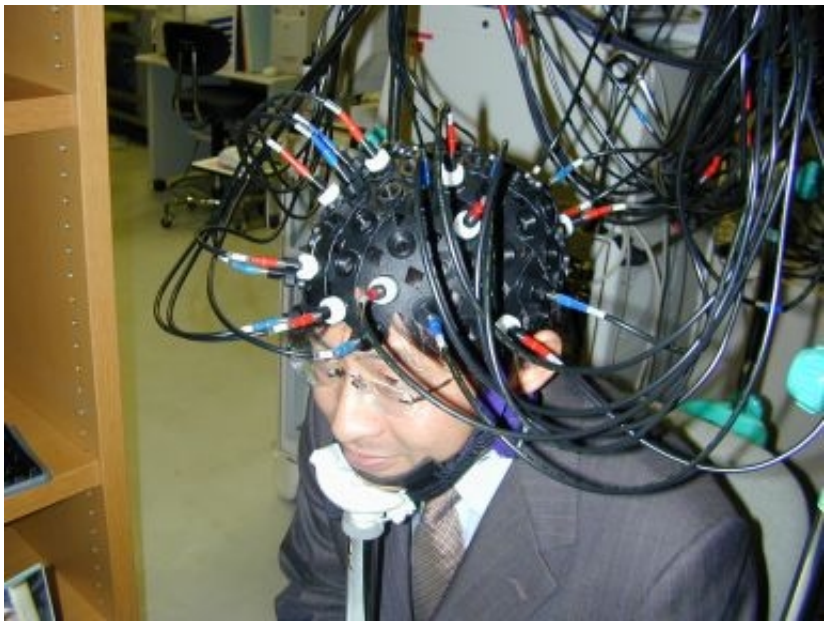

Fig.2. FLexible Adjustable Surface Holder (FLASH)

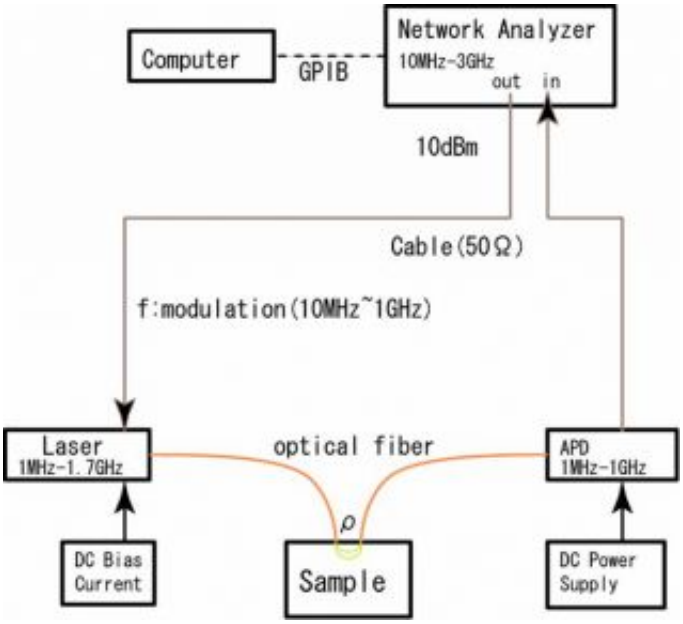

Fig.3. Phase shift measurement system

WE 167
A new SPM toolbox for the combined analysis of fMRI data and probabilistic cytoarchitectonic maps

Simon Eickhoff[1,2], Hartmut Mohlberg[1], Klaas E. Stephan[3], Gereon R. Fink[1,4], Karl Zilles[1,2], Katrin Amunts[1]
[1]Institut für Medizin, Forschungszentrum Jülich, Jülich, Germany, [2]C. & O. Vogt Institut für Hirnforschung, Düsseldorf, Germany, [3]Wellcome Dept. of Imaging Neuroscience, University College London, UK, [4]Neurologische Klinik, Universitätsklinikum Aachen, Germany

The analysis of the relationship between structure and function of the human brain is one of the major goals in neuroscience. Since the microstructural organization of the cortex constrains its functions1, architectonically defined areas represent the appropriate topographical reference for activations obtained in functional imaging studies. In contrast to classical cytoarchitectonic maps (e.g.[2]), probabilistic cytoarchitectonic maps provide stereotaxic information about the location and variability of cortical areas[3]. They have already successfully been applied for studying different cognitive functions, e.g. somatosensory processing and language[4,5]. The maps are now available in MNI space[6,7], which is used as spatial reference system in SPM.
We here introduce a new SPM toolbox providing a convenient user-interface for structural-functional analyses. At the beginning of a session, a summary map of the relevant probabilistic maps is calculated. This map defines the most likely anatomical area at each voxel (maximum probability map). It therefore allows the definition of non-overlapping volumes of interest for several areas, comparable to conventional brain atlases. The cytoarchitectonic maps are now ready for analysis:
1) Cluster labeling can be used to allocate functional clusters of activation to cytoarchitectonic areas (e.g. 70% of the volume of the cluster was located in BA44, 15% in neighboring BA45).
2) Local maxima labeling gives cytoarchitectonic information with respect to the statistical peak of an activation (e.g. the maximum showed a probability of 60% of lying in BA45, and only of 10% of lying in BA44).
3) The extent of the activation of a cortical area can be quantified (e.g. 30% of BA 44 was activated).
4) The relative percent signal change as the result of a certain experimental condition within a cytoarchitectonic area can be calculated. Thus, functional data can be assessed based on a-priori anatomical knowledge, by evaluating the relative involvement (defined by the percent signal change) of a given area at different conditions.
We have implemented this software as a new toolbox to the SPM2 software package (www.fil.ion.ucl.ac.uk/spm). This integration into this widely used functional analysis software enables a user-friendly and routine use of probabilistic cytoarchitectonic maps as anatomical references.
The probabilistic maps are available under www.bic.mni.mcgill.ca/cytoarchitectonic. A beta-release of the toolbox can be can be obtained via S.Eickhoff@fz-juelich.de.
This Human Brain Project/Neuroinformatics research was funded jointly by the NIMH, NINDS, NIDA, the NCC, the DFG and the Volkswagenstiftung.
1. Luppino,G. at el. J. Comp Neurol. 311, 463-482 (1991).
2. Brodmann,K. Vergleichende Lokalisationslehre der Großhirnrinde. Barth, Leipzig (1909).
3. Zilles,K. et al., Brain Mapping, the methods. Mazziotta,J. & Toga,A. (eds.), pp. 573-602 (Elsevier,2002).
4. Amunts,K. et al. Neuroimage (2004, in press).
5. Bodegard,A. et al. Neuron 31, 317-328 (2001).
6. Evans,A.C. et al.. Neuroimage 1, 43-53 (1992).
7. Mohlberg,H. et al., HBM 2003, Poster 905

WE 168
Functional Correlation Index: a useful parameter for characterizing functional correlation

Miklós Emri[1], Zsolt Lengyel[1], Dóra Glaub[2], Roland Berecz[2], István Degrell[2], Lajos Trón[3]
[1]University of Debrecen, PET Center, [2]University of Debrecen, Department of Psychiatry, [3]PET Study Group of the Hungarian Academy of Sciences

Introduction
One of the most self-evident methods to analyze human brain networks is based on the cross-correlation analysis of voxels. The efficacy of this kind of analysis can be dramatically increased by eliminating voxels in correlation with only few other voxels. For this purpose a functional correlation index FCI(x,y,z) is introduced reporting on the number of voxels correlated with the reference voxel (x,y,z) by $R>R_0$ and being further away then distance D_0. This index can be calculated by voxel or cluster-based methods, although the latter one requires computing capacity of GRID or a computer-cluster.
Here we present a method to the voxel-based calculation of the FCI-maps and investigate its applicability in a cognitive brain activation study.

Methods
Calculation and analysis of the FCI-map
Adjusted rCBF-values to generate Student-T map in the SPM were used as input data of the FCI-map calculation. FCI data were separately evaluated by a developed iterative FCI-map evaluation algorithm for voxel pairs of positive and negative correlation. This algorithm generates a map containing only voxels of $FCI>FCI_0$ and fulfilling $R>R_0$ and $D>D_0$ conditions. An additional 3D cluster-analysis can result in size of the clusters of the map, the locations of local minima, the minimum and maximum FCI-values within the clusters and a list rendered to the ith cluster indicating any jth cluster in correlation with the ith one. These lists characterize the clusters from the point of view of correlation multiplicity and are useful in the further analysis of these regions as well.
Application of the FCI-analysis
Changes in rCBF, induced by a cognitive "odd-ball" paradigm, were analysed by PET in nine healthy volunteers. The subjects underwent four reference and four "odd-ball" tasks. Activated areas were localised by SPM analysis, and $^{+}$FCI_ref, $^{-}$FCI_ref, $^{+}$FCI_odd, $^{-}$FCI_odd (Figure 1) maps were generated.

Results
Areas of high correlation multiplicity (parietal gyrus, bilateral insular regions, cingular gyrus, frontal superior, medial and inferior gyrus, parahippocampal/enthorinal region) identified by FCI-analysis met the expectation based on neurobiology data indicating the usefulness of FCI to characterize the functionally correlated areas in the human brain.

This project is supported by NKFP-1A/0010/2002 (National Research and Development Program), and IKTA-00006/2001 (Info Communications Technologies and Applications Program) projects.

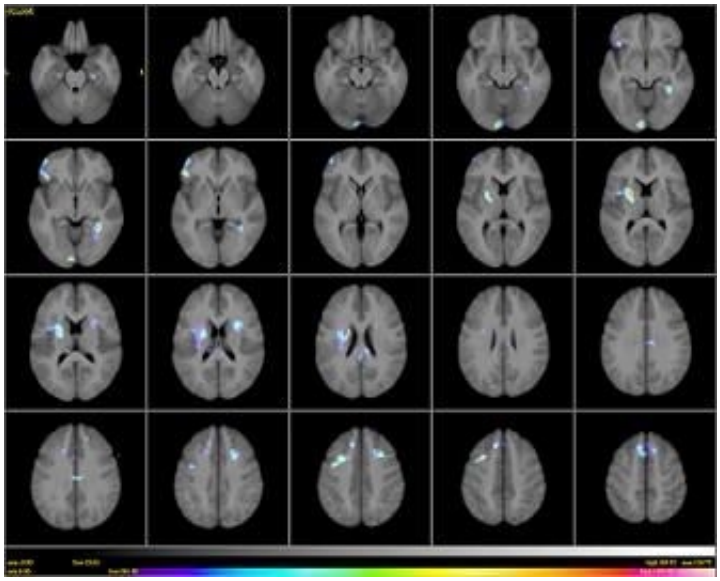

Negatively correlated FCI-map generated from adjusted rCBF-values of

WE 169

EEG / EOG - fMRI Cold head artifact removal

Eric Featherstone , Oliver Josephs , Ralf Deichmann
Wellcome department of Imaging Neuroscience, London, United Kingdom.

Introduction

In fMRI studies it is often desirable to record EEG or EOG data during the scanning process. However, the scanners cold-head refrigerant pump often causes problematic interference. EOG eye-blink signals are sufficiently large that they can be seen despite the interference. Eye movement EOG signals and EEG signals are typically much smaller and can be obscured. The interference is repetitive lending itself to being modelled and subtracted from the data. Several techniques have been described; active noise cancellation (1-2), subtracting mean noise (1,5). Here we describe a new method based on dividing the data into blocks of a suitable length and applying high-pass filtering. This method works even if there is a slow drift in pump timing.

Method

Apparatus : EOG signals were recorded from a subject inside a Siemens Allegra 3T MRI scanner. The scanner was not operating. The EOG leads were connected via an MRI compatible EEG amplifier system (1) to a CED 1401 (3) and PC running Spike (3) data acquisition software. The sampling rate was 5000/s to allow the interfering signals to be characterised. One recording run of approximately two minutes was made whilst the subject blinked normally.

Processing : The data was exported from Spike into Matlab (4) for processing. The data was divided into blocks of 5012 samples (twice the cold-head pump period) and reformed into a matrix with the blocks vertical. The array was high-pass filtered in the horizontal direction. The filter parameters were chosen by trial to best remove the interference. The data was then reformed into a time series.

Results and Discussion

Figure 1 (top trace) shows a typical EOG recording. Eye-blinks are clearly identified as large negative spikes in a background of interference and eye movement EOG signals. Closer inspection (figure 2, top trace) shows that the artefact from the pump consists of short duration pulses with a frequency of ~30Hz, occurring every 500ms. Figure 3 shows the EOG data as greyscale intensity after being divided into blocks of 5012 samples. The pump artefact is now evident as horizontal stripes, two cycles of the pump can be seen clearly. Eye-blinks show as black points. The artefact drifts slightly in time, up-to ~15ms. Filtering removes almost all trace of the pump artefact (figure 4). The eye-blinks are still clearly visible. Reforming the data into a time series (figure 1, bottom trace) shows eye-blinks as before against a smaller background of noise. Close inspection (figure 2, bottom trace) shows that the pump artefact has been successfully removed with little effect on the low level EOG or larger eye-blink signals.

Conclusion

This method allows the reduction of interference artefacts caused by the cold head pump from the EOG signals, revealing clearly the eye movement signals. This method works even where there is a very slow drift of the cold head pump timing.

References

1. Allen, PJ et al. Neuroimage. 2000 Aug; 12(2):230-9
2. Featherstone, E et al. Proc. Intl. Soc. Mag. Reson. Med. 9 (2001):1226
3. Cambridge Electronic Devices, www.ced.co.uk
4. Mathworks Inc, www.mathworks.com
5. Josephs, O & Turner, R. Neuroimage. 1998; (7):s590

Figure 1 : EOG & filtered EOG time series

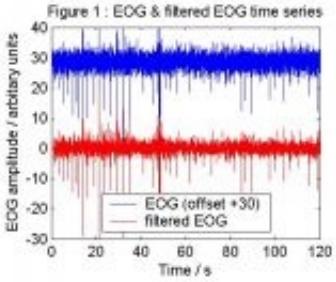

Figure 2 : Highlighting two eye blinks

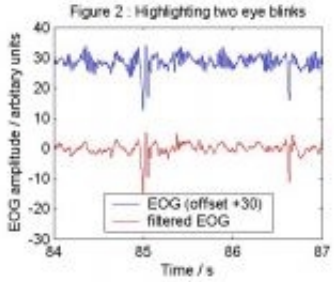

Figure 3 : EOG time series buffered in 1s blocks

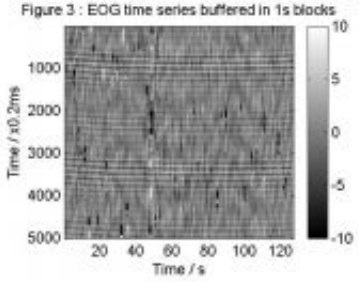

Figure 4 : Filtered EOG time series buffered in 1s blocks

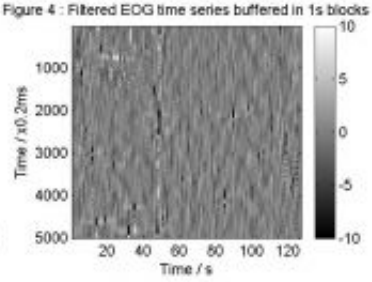

WE 170
Multi-subject anatomo-functional classification for activation studies

Guillaume Flandin[1,2,4], Xavier Pennec[1], Alexis Roche[2,4], Will Penny[3], Nicholas Ayache[1], Jean-Baptiste Poline[2,4]

[1]Epidaure project, INRIA Sophia Antipolis, France, [2]Service Hospitalier Frédéric Joliot, CEA, Orsay, France, [3]Wellcome Department of Imaging NeuroScience, UCL, UK, [4]IFR 49, Institut d'Imagerie Neurofonctionnelle, Paris, France

One of the fundamental goals of functional neuroimaging is to extract relevant information on the brain functional organization across several subjects. Mainstream methods use standard normalization procedures to pool data from several subjects in the same anatomical space and these results are analyzed through statistical hierarchical models in this standardized space (Friston et al, Smith et al).

However, this (most useful) approach presents several fundamental limitations. First, the procedure to place various subject anatomy in a single space suffers from the specific subject anatomical variability. Second, the functional organization of the brain is not exactly similar across subjects, and indeed is a research topic in itself. Third, experimental protocols often include several experimental conditions to better distinguish the various components of brain organization. Current methods to analyze data from group of subjects are not well adapted to take into account these limitations.

We therefore propose a method that can complement current procedures. The method is based on the classification of functional and anatomical data and does not require the exact voxel per voxel match between subjects. First, a standard SPM procedure is applied on each subject, and several conditions or contrasts of interest that summarize the pertinent functional results are selected such that a vector of typically 5 to 10 functional coordinates is defined for each voxel. Second, anatomical coordinates are included, that can be simply Talairach coordinates, or more interestingly could be geodesic distances to anatomical landmarks labelled subject per subject (Riviere et al). These coordinates are then classified using a Gaussian mixture model and an Expectation Maximization algorithm is used to estimate the model parameters.

We exemplify this method on an fMRI protocol consisting of 6 pairs of Condition-Control acquired on 10 subjects (Simon et al, Neuron, 2003) . Results show striking differences between the spatial representation of clusters between subjects for some clusters, and very reproducible results for others. For instance, clusters with a high representation of motor task are found reproducible (although their spatial extend may vary between subjects) while other conditions are only represented on a few subjects. Figure 1 presents a reproducible functional cluster detected across subjects

(shown on 5 subjects on a sagittal slice for visualization purpose) with high values of motor response contrast in the parietal cortex. Interestingly, the size of the cluster is variable between subjects and its location not exactly similar, showing how this method takes into account inter individual variability. These results are further compared to the standard SPM analysis.

This approach provides a new perspective on group analyzes of functional MRI data that may lead to a better understanding of the inter subject anatomo-functional variability.

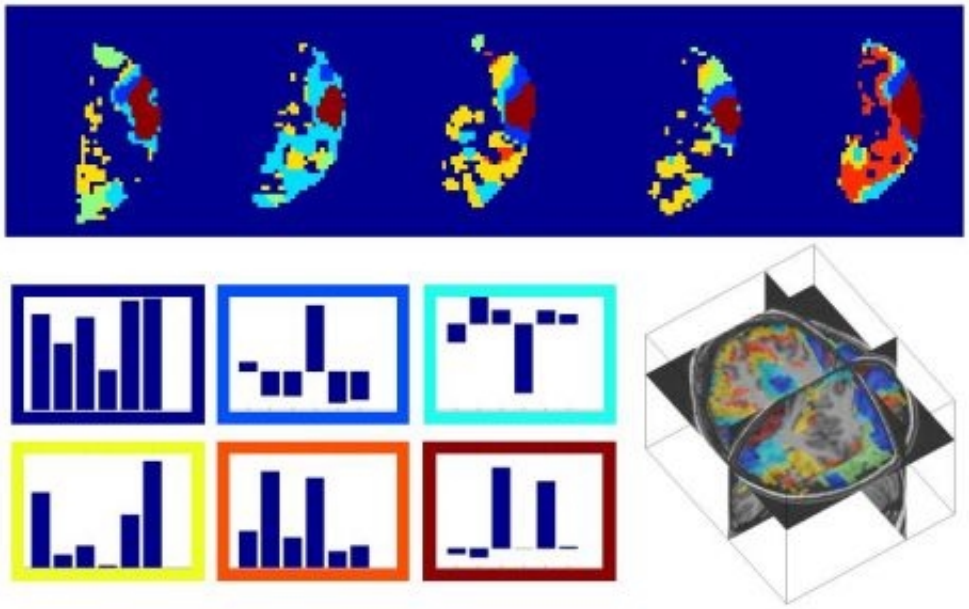

Upper panel shows functional clusters (one color per cluster). The brown cluster is located in the parietal cortex and the amount of activity for each experimental condition is represented on the left bottom panel. The brown cluster shows high activity for grasping and pointing tasks. Right bottom pannel indicates the orientation of the slice displayed.

WE 171

Classification of fMRI-independent components in a multidimensional feature space using least-square support vector machines.

Elia Formisano[1], Federico De Martino[1,2], Francesco Gentile[2,1], Marco Balsi[2], Fabrizio Esposito[3], Francesco Di Salle[4], Rainer Goebel[1]

[1]Department of Cognitive Neuroscience, Faculty of Psychology, Maastricht Universiteit, The Netherlands, [2]Dipartimento di Ingegneria Elettronica, Università, [3]Second Division of Neurology, Second University of Naples, Napoli, Italy, [4]Department of Neuroradiology, Università

Introduction

Independent component analysis (ICA) is being increasingly employed in fMRI[1]. It has the distinctive property of not requiring *a-priori* specification of the temporal profile of the effect(s)/artifacts.
Spatial ICA decomposition of fMRI time-series typically produces a large (up to the number of time-samples) set of spatial maps and associated time-courses (independent components or ICs). As there is not an intrinsic,'meaningful' relation between ICs, the experimenter is confronted with the problem of selecting interesting subsets from the large set of ICs, for each subject. This problem has been rarely addressed[2] and solutions proposed so far are often based on strongly constraining hypotheses on IC-time-courses.
Here we describe a novel approach that allows the inspection and classification of 'interesting' ICs without any strong constraint. It is based on: 1) a representation of the ICs in a multidimensonal space of features and on 2) a least-square support vector machine(LS-SVM) classifier [3]. SVMs are kernel-based learning algorithms which are often used for classification problems.

Methods

FMRI data sets are decomposed using spatial ICA. Each IC is associated with its *fingerprint*, i.e. with a representation in a multidimensional space of components-descriptive parameters (Figure). These parameters characterize spatial distribution and layout (kurtosis, skewness, entropy, degree of clustering) as well as temporal and spectral properties (one-lag autocorrelation, entropy, power contribution of different frequency-bands) of the ICs. This multidimensional space represents the input space for the LS-SVM. ICs-classification proceeds as it follows: Initially, classes of ICs relative to a subset of data (e.g. one functional run) are specified by visually inspecting the corresponding *fingerprints*. Together with simulated data this initial classification is used to define the optimal kernel parameters and train the LS-SVM. After training, the LS-SVM is used to classify automatically the ICs obtained on all remaining data-sets (i.e. on the same subjects or other subjects new data).

Results

We tested this approach on data from a visual experiment using structure from motion stimuli[4]. The multidimensional representation of ICs presented a high intra- and inter-subject consistency. Classes of *fingerprints* corresponding to expected (visual, task-related) and unexpected (transient) activations as well as to head-motion and other artifacts showed characteristic, distinctive and well-reproducible features (Figure), even across functional runs having different stimulation conditions.
After training on a small subset (30) of ICs from one subject, the LS-SVM automatically and correctly classified ICs obtained from different runs of the same subject and in other subjects.

Conclusion

Our new method of inspection and classification of fMRI-ICs can be used in any experiment, is largely independent of a priori knowledge of the experimental protocol and thus preserves the richness and peculiarity of information about brain processes that ICA provides.
The LS-SVM classifier we used has the potential to recursively improve its performance and to 'transfer' learned knowledge of spatio-temporal structure of ICs across subjects and experiments.

References

1.McKeown et al.(2003)CONB
2.Formisano et al.(2002)Neurocomputing
3.Suykens et al.(1999)Neural Processing Letters
4.Kriegeskorte et al.(2003)J.Neuroscience

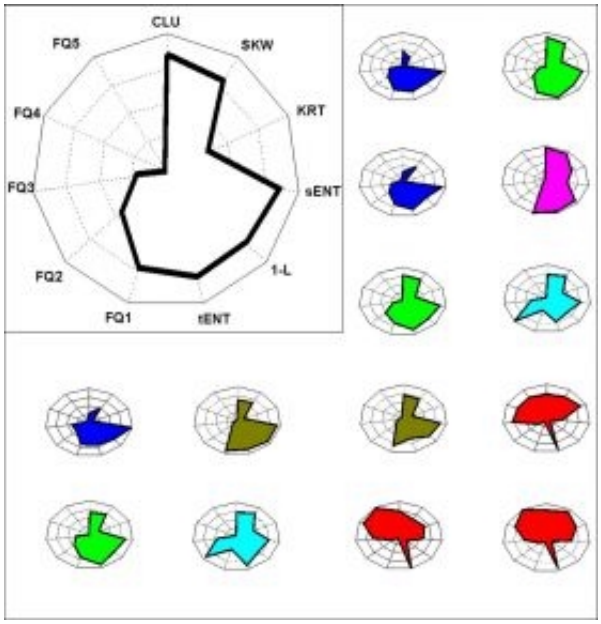

Figure1. (Up) An example of IC-fingerprint. Each axis of the plot represents an IC-descriptive (spatial, temporal or spectral) parameter (see text). The remaining part of the figure shows a sample of the results of the LS-SVM classification on one subject. Each color corresponds to a different class (purple: highly task-related activation, green: weakly task-related activation, blue: spatially distributed noise, red: high temporal frequency noise, brown movement-related artifacts, light blue: large vessels). Consistent results were obtained in other subjects.

WE 172

Insights into Multi-Site FMRI Repeatability: Scanner Differences in Sensitivity and Spatial Smoothness

Lee Friedman[1], Stefan Posse[1], Functional BIRN[2]
[1]The MIND Institute, Albuquerque, NM, [2]www.nbirn.net

Introduction:
The FIRST-BIRN (FBIRN) project is composed of a team of 11 universities studying brain dysfunction with fMRI in schizophrenia. One goal of the project is to characterize the quality and sensitivity of fMRI data at the 11 sites and to study the impact of possible inter-site differences on group studies. We have evaluated the sensitivity (to the BOLD effect) and spatial smoothness (spatial correlation) of the fMRI images. Below, we report substantial, highly significant inter-site differences in sensitivity and smoothness. Site differences in smoothness may, in part, be related to site differences in sensitivity.
Methods:
The ten FBIRN sites reported on here have a variety of MRI scanners, and field strengths (5@1.5T, 4@3.0T, 1@4.0T, Siemens-4, GE-5 and Picker-1). They employ several different functional acquisition sequences (6 EPI, 3 spiral, 1 double echo EPI). Five volunteers traveled to 10 sites and had identical fMRI studies performed. All the sites used a 3000 msec TR with 35 axial slices. The TE for 1.5T was 40 msec and for 3T and 4T was 30 msec. The (nominal) voxel size was 3.44 X 3.44 X 4.00 mm. The sensorimotor paradigm (85 TRs, 5 TRs rest, 5 TRs active,...) included a finger tapping component designed to activate primary motor cortex. The data were analysed in a conventional manner with AFNI (slice-time corrected, motion-corrected, detrended, correlated with a square wave convolved with a canonical HRF).
To measure sensitivity for the motor cortex ROI, we determined the correlation threshold (Pearson r) for each study to optimally match a canonical motor cortex activation pattern. The threshold at which each study best matched this pattern was considered an index of BOLD sensitivity for that study. Pearson r's were converted to a linear scale prior to statistics.
Smoothness was measured on unaltered functional images with the AFNI program 3dFWHM. It measures the extent of spatial correlation corresponding to each axis as a Gaussian FWHM (Forman et al., 1995). We present data only on the FWHM for the Y-axis.
Results:
There were highly significant differences between the sites in the index of BOLD sensitivity effect in the motor cortex (Fig 1) ($F = 22.4$, $df = 8, 32$, $p < 0.0001$). There were also inter-site differences in spatial smoothness of the raw functional images (Figure 2, A and B same subject, different 1.5T scanners) and in measured smoothness (FWHM Y) (Fig 3) ($F = 590.4$, $df = 8, 45$, $p < 0.0001$). There was a significant relationship between smoothness and sensitivity across sites (Fig 4)($F(linear) = 5.5$, $df, 1, 83$, $p = 0.02$; $F(quad) = 3.84$, $p = 0.0535$).
Discussion:
There are important "site" differences in sensitivity to the motor cortex BOLD effect. These differences will have to be taken into account before data from the sites can be merged. There are also marked site differences in smoothness of raw functional images from the 10 fBIRN sites. These differences may be related to imaging method (EPI vs. spiral), gradient performance, image reconstruction method, reconstruction filter settings, and field strength. There is a significant curvilinear relationship between smoothness and sensitivity across the sites. The possibility of reducing inter-site differences in sensitivity by smoothing the functional images to an equal level is under examination.
References: Forman SD et al. Magn Reson Med, 33:636-47, 1995;

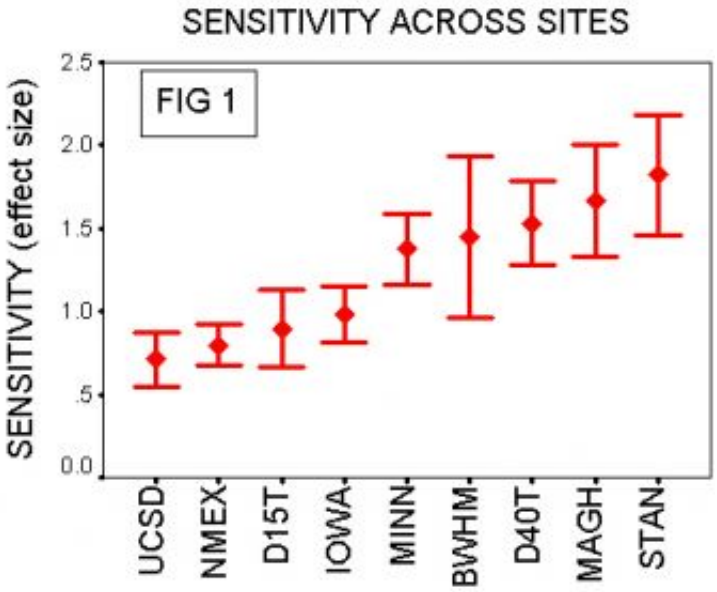

Sensitivity Differences across Sites

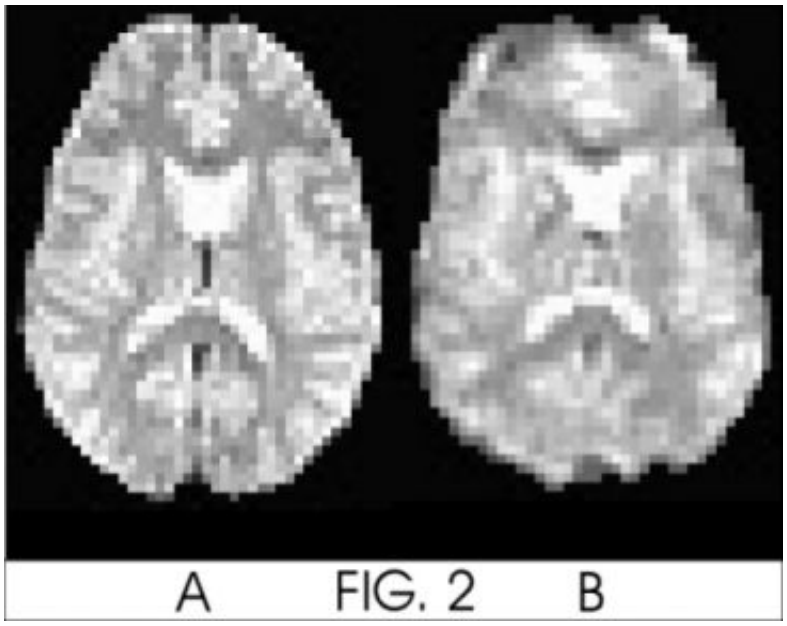

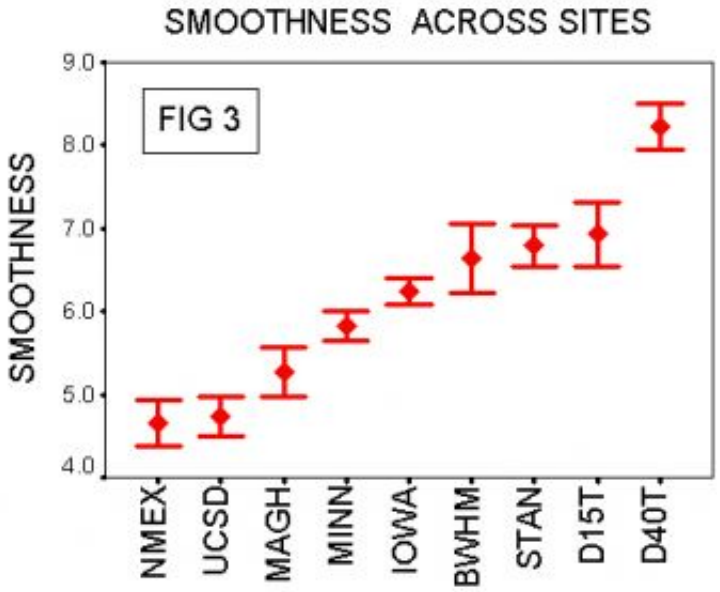

Smoothness Differences across Sites

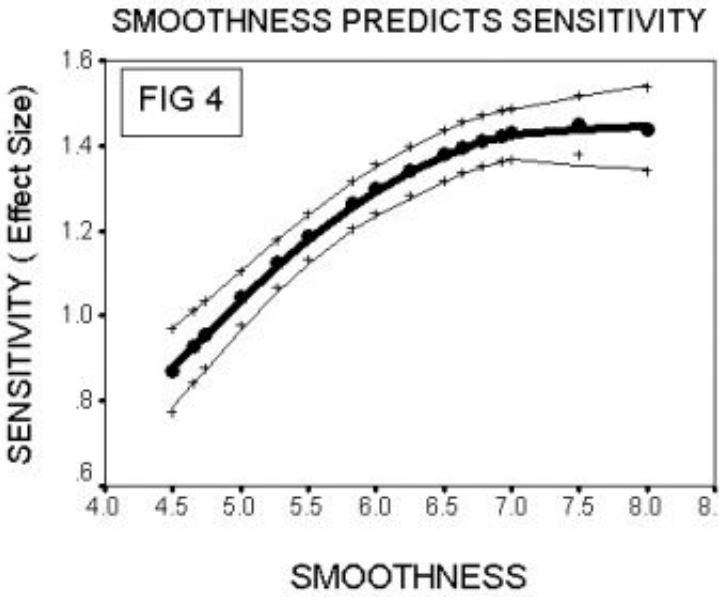

Relationship between Smoothness and Sensitivity

WE 173
SNR-limited Confidence Ranges of Dipole Source Reconstructions

Manfred Fuchs , Michael Wagner , Joern Kastner
Compumedics / Neuroscan Germany, Lutterothstr. 28 e, 20255 Hamburg

Equivalent dipole models are widely used in Electro-Encephalo-Graphic (EEG) and Magneto-Encephalo-Graphic (MEG) source reconstruction. Despite their point-like definition, the best-fit solutions have a certain probability volume depending on the source position and orientation as well as on the actually used sensor set-up and the Signal-to-Noise-Ratio (SNR). In order to avoid the misleading impression of exact localization results, a measure of the standard deviation of the dipole localization is desirable.
This measure can be obtained by performing a deviation scan around the best-fit positions, where the explainable field is determined and compared to the best-fit field. Using a linear approximation, confidence ellipsoids can then be computed and their axes and volumes can be determined by relating the field differences to the noise of the measured data.
Test-dipoles inside of a three spherical shells volume conductor model were used to simulate EEG- and MEG-data with sources of known positions, orientations, and noise levels. Confidence ellipsoids were computed for these test-dipole solutions and deviation scans around the best-fit dipole positions were performed in order to compare the size and the shape of the confidence ellipsoids with the real error hyper-surface. Standard deviations of repeated dipole localizations at different depths were computed to show the validity of the linear approximation over the whole eccentricity range.
The size of the axes of the confidence ellipsoids is inversely proportional to the SNR of the measured data, thus the confidence volume is inversely proportional to the third power of the SNR. Good agreement between standard deviations of repeated dipole localizations and the confidence ellipsoids was found for both EEG- and MEG-cases. The new method adds a new and important dimension to dipole source reconstruction results by characterizing their reliability. It is also very helpful in deciding how many dipoles are necessary to explain the measured data, since superfluous dipoles exhibit rather large confidence volumes.

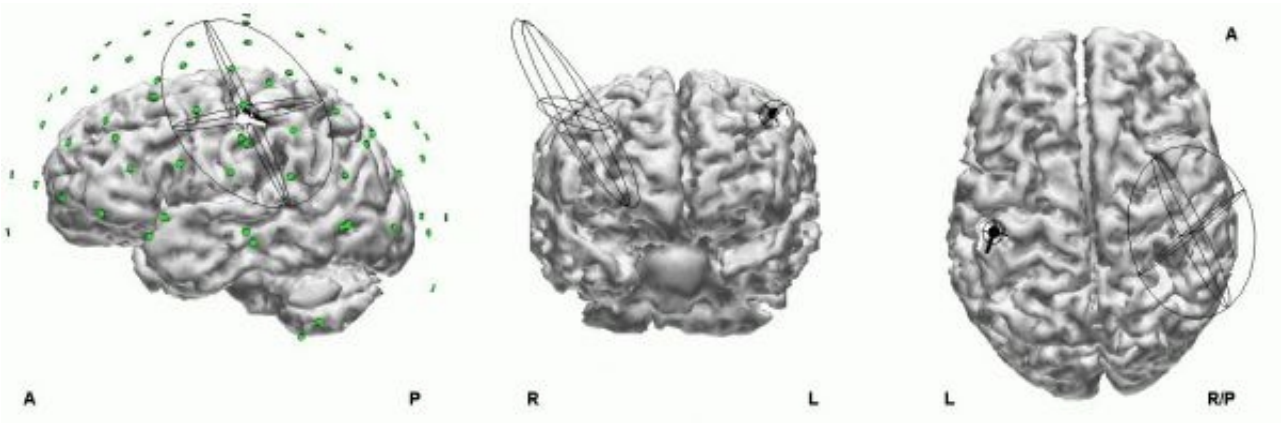

Somatosensory Evoked Potentials (SEP) experiment: electric Medianus nerve stimulation. N20 single equivalent dipole reconstruction (white pole/ellipses) and two mirrored dipoles (black poles/ellipses). The fit quality of the two-dipole reconstruction is slightly better due to increased number of parameters (1.1% versus 0.8% residual variance). However, the second, mirrored dipole shows a large confidence ellipsoid, whereas the first dipole, that is really needed to explain the measured data, stays well described in left central sulcus area. Dipoles are shown as white / black poles together with their confidence ellipsoids, electrodes (left side view) and a rendering of the cortical surface.

WE 174
An XML-based Data Access Interface for Image Analysis and Visualization Software

Syam Gadde , Charles R. Michelich , James T. Voyvodic
Duke-UNC Brain Imaging and Analysis Center , Duke University, Durham NC, USA

Constructing a robust image analysis pipeline from several, often disparate, software elements is not a trivial process. Many valuable software tools have arbitrary data format requirements. Combining such software tools in analysis requires data conversion steps that may slow down processing and introduce errors.
We have defined a general data access interface in the form of a structured text file, written in XML (Extensible Markup Language). This XML file provides instructions on how to extract image data from files in any uncompressed data format, without explicit conversion of data. This interface supports data of arbitrary dimensionality, data type, and byte order, and is applicable to most MR image formats, physiological and stimulus data. The XML file is placed alongside the data it "encapsulates", and points to the raw data files by reference.
The XML markup language provides several advantages over simpler plain text formats. Because XML is merely structured text, it is easily parsed and used as a common access interface for image dimensions, subject information, acquisition parameters, or transformations between image and world coordinate systems. The XML structure itself is extensible using XML namespaces, facilitating the integration of additional metadata modules.
We have created subroutine libraries to provide software support for the XML file format for C, C++, and MATLAB. These libraries employ XML tools based on platform- and language-independent standards such as XPath and DOM. Incorporating these library tools into existing analysis programs allows those programs to read images of many types (e.g. DICOM, GE Signa 5.x, Analyze 7.5/SPM, MINC, etc.) via the XML file, and makes them forward-compatible with future data formats that can be encapsulated within this XML specification. Conversely, any image files with an associated XML file, regardless of the underlying format, are automatically readable by all XML-aware applications that support this interface. The XML interface allows existing software to take advantage of the additional information and data formats the metaheader supports. For example, our analysis tools that formerly required users to manually specify orientation, position, and image dimensions now obtain this information from the XML files.
We also use this approach to support legacy software. Using an XML-based metaheader as the common intermediary greatly simplifies our conversion software; conversions between N formats require only 2N software components, rather than the N^2 required by a direct format-to-format approach. Moreover, the XML file maintains the image metadata we might otherwise lose when converting from a richly annotated data format (e.g. DICOM) to one that is sparsely annotated (e.g. Analyze 7.5).
This general framework, implemented as the BIAC XML Header (BXH), has been in wide use at the Duke-UNC Brain Imaging and Analysis Center since late 2002. It has also been adopted as a component of the XML schema developed by the Biomedical Informatics Research Network (BIRN).
This work was supported by US NIH grants IP01NS41328 and 3M01RR00030.

WE 175
Innovation approach to extracting connectivity information from fMRI time series

Andreas Galka[1,2], Tohru Ozaki[2,3], Jorge Bosch-Bayard[4], Okito Yamashita[3], Jorge Riera-Diaz[5], Norihiro Sadato[6]

[1]Institute of Applied Physics, University of Kiel, Kiel, GERMANY, [2]Institute of Statistical Mathematics, Tokyo, JAPAN, [3]Department of Statistical Science, Graduate University for Advanced Studies, Tokyo, JAPAN, [4]Cuban Neuroscience Center, Havana, CUBA, [5]Advanced Science and Technology of Materials, NICHe, Tohoku University, Sendai, JAPAN, [6]National Institute of Physiological Sciences, Okazaki, JAPAN

Data sets obtained by functional magnetic resonance imaging (fMRI) represent both spatial and temporal aspects of the hemodynamics of the human brain. Whereas usually in the analysis of fMRI data sets the focus lies on spatial aspects, the temporal dimension has been receiving less attention. In this contribution we show that by fitting spatiotemporal dynamical models to fMRI data sets information about the long-distance connectivity structure of the investigated brain can be obtained.

The dynamical models are chosen from the class of linear multivariate autoregressions; extensions to nonlinear model classes are straightforward. Stimulation terms can be explicitly included into the model. The spatial aspect is limited to local neighbourhoods, i.e. to interactions between neighbouring voxels. This approach is equivalent to fitting partial differential equations to the data. Model selection and parameter estimation are performed by a modified maximum-likelihood approach.

The connectivity structure can be quantified by estimating Mutual Information (MI) for each pair of voxels. Presence and absence of a fast connection between two voxels correspond to two different dynamical models, which can compared within the likelihood framework. MI is estimated not for the pure data directly, but for the time series of residuals (or *innovations*) which are provided by these modelling steps. This deviation from the usual procedure has the advantage that the distribution of the residuals will be close to that of white Gaussian noise, such that error-prone nonparametric estimation of probability distributions can be avoided; instead MI can be obtained directly from the difference of the log-likelihoods.

The modelling step implements a whitening filter which removes most spatial and temporal correlations from the data; for this reason even weak correlations in the innovations (i.e. in the noise process driving the dynamics) can be detected. This method is capable of producing useful results also from short single-trial time series.

Examples for the application of this method to simulated data and to real fMRI data from healthy subjects will be shown.

WE 176
TurboFIRE: Real-Time fMRI with Automated Selection of Regions for ROI-Analysis based on Standardized Neuro-Anatomical Atlas

Kunxiu Gao[1], Stefan Posse[2]
[1]The MIND Institute, Albuquerque, NM, USA, [2]Dept. of Psychiatry, University of New Mexico School of Medicine, Albuquerque, NM, USA

Introduction:
Quantification of brain activation in standardized neuro-anatomical space during the ongoing scan is desirable for real-time fMRI. Based on our methodology for real-time spatial normalization with integrated Talairach Daemon database (1), we developed a reverse process to automatically select neuro-anatomically defined regions for ROI analysis during the ongoing scan.

Methods and Results:
Our spatial normalization methodology with integrated Talairach Daemon database (1) assigns anatomical structural information for voxels in non-normalized EPI or multi-echo EPI data (subject space), which requires a coordinate-lookup table from subject space to normalized space (S2N). While generating the lookup table S2N using affine and nonlinear transformations derived from SPM99 (2), an inverse lookup table (N2S) can also be created, which allows mapping from normalized space to subject space. To do automated ROI analysis in real-time, neuro-anatomical regions have to be selected from a list (e.g., BA 18, Amygdala, etc.). By scanning anatomical information for every voxel in normalized space, contained in the Talairach Daemon database (3), we can determine the corresponding voxels in normalized space for the selected region. Coordinates of all these voxels are transformed back to MNI space using Mathew Brett's formula (4) and the resulting coordinates are searched through lookup table N2S to determine their corresponding coordinates in subject space, and thus identify the region (Fig.1). Not all voxels in normalized space have a direct correspondence in subject space due to nonlinear transformations. In these cases a weighted neighborhood search is performed. Subsequent time course and cluster analysis of activated brain areas can be automatically limited to the selected region(s). When integrated into the TurboFIRE real-time analysis tool (1), 10 Brodmann Areas could be selected within less than a second (on average) using a 1.7 GHz Pentium M laptop.

Discussion:
The ability to select neuro-anatomically defined ROIs in subject space facilitates interpretation of activation maps under the time constraints of real-time fMRI. Quantifying spatial extent of activation in relation to neuro-anatomical boundaries may also help to increase the specificity of classifying activation patterns and to perform group studies. The precision of spatial mapping, which is limited by digital resolution and ambiguity in voxel mapping due to nonlinear transformation, could be increased by interpolation at the expense of real-time performance.

Acknowledgments:
Supported by NIH NIBIB 1 R01 EB002618-01. We thank Siemens Medical Systems (Erlangen, Germany), Jack Lancaster and Peter Kochunov (UTHSCSA - Research Imaging Center), Karl Friston and John Ashburner (FIL, U. London, UK) for software support and source codes.

References:
1. Gao, K., Posse, S. *Human Brain Mapping*, 2003, 838
2. Friston, K.J., et al., *Human Brain Mapping*, 2, 165, 1995
3. Lancaster, J.L., et al., *Human Brain Mapping* 10:120, 2000
4. *http://www.mrc-cbu.cam.ac.uk/Imaging/mnispace.html*

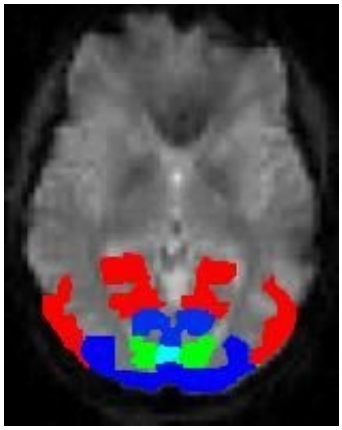

Figure 1: An example of visual regions mapped onto an individual's non-normalized EPI using automated ROI selection (green: BA 17, blue: BA 18, red: BA19)

WE 177
TurboFIRE: Real-Time fMRI with Online Generation of Reference Vectors

Kunxiu Gao[1], Stefan Posse[2]
[1]The MIND Institute, Albuquerque, NM, USA, [2]Dept. of Psychiatry, University of New Mexico School of Medicine, Albuquerque, NM, USA

Introduction:
Fixed reference vectors limit the application of real-time fMRI in situations where subject responses cannot be predicted before the scan starts or where physiological variables measured during the scan are required for baseline detrending or for modeling covariates of interest. Here we show feasibility of creating multiple reference vectors during the ongoing scan in a task design controlled by the subject at will.

Methods and Results:
For online reference vector creation, correlation analysis is implemented such that once the reference vector is modified it is immediately used for the next available volume to update the correlation map The analysis is initiated with a zero reference vector and no activation map is initially generated, while data are accumulated. The reference vector can be modified anywhere during the current TR period while data are being acquired. Up to four independent reference vectors can be defined online. When integrated into the TurboFIRE real-time analysis tool (1) the delay between modifying the reference vector and updating the correlation map was less than one TR period. As an example of the application of this method, a healthy subject performed a self-controlled interleaved left/right index finger tapping with eyes open during tapping and closed during rest in a Siemens Sonata 1.5T scanner using whole brain EPI. A control experiment with a fixed paradigm design was performed in which right index finger tapping and open/closing the eyes was externally paced with an auditory cue. Two independent reference vectors for the left and right finger movement were defined online in real time based on the subject's willed movements and two correlation maps were updated online (Figs.1,2). A third reference vector which represents the combination of the two online created reference vectors revealed a network of frontal regions including anterior cingulate (Fig.3), which was not present in the control experiment (Fig.4).

Discussion:
The results show feasibility of monitoring brain activation during self-generated movement in real-time. Generating the reference vector online in neurocognitive experiments requires knowledge of subject dependent delays in response time relative to neuronal activation. Taking these delays into account may require retardation of online processing or retrospective modification of the reference vector to maximize sensitivity. Adaptation of online reference vector generation for General-Linear-Model analysis, which has already been implemented into TurboFIRE using a modification of (2), is being investigated.

Acknowledgments:
Supported by NIH NIBIB 1 R01 EB002618-01. We thank Siemens Medical Systems (Erlangen, Germany) for software support.

References:
1. Gao, K., Posse, S. *Human Brain Mapping*, 2003, 838
2. Bagarinao, E. et.al., *NeuroImage*, 19 (2003) 422-429

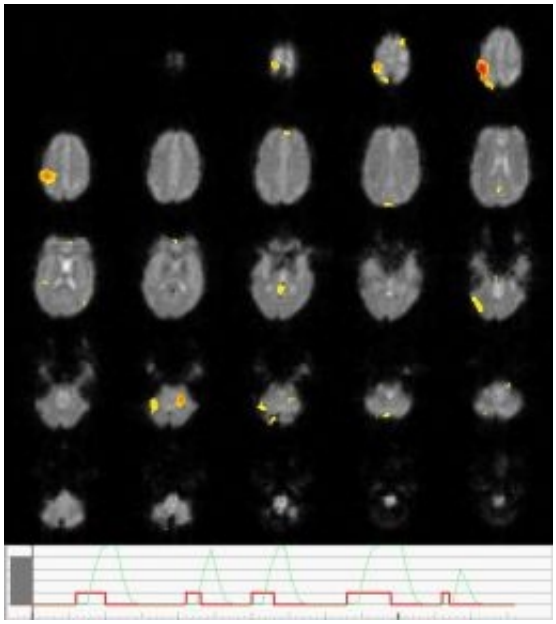

Figure 1: Activation map for left finger tapping using online creation of reference vector based on a paradigm time course controlled by the subject.

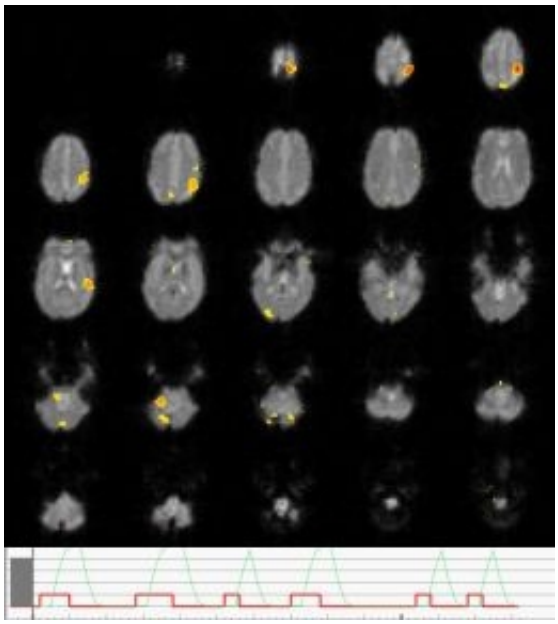

Figure 2: Corresponding activation map for right finger tapping in the same experiment as Figure 1.

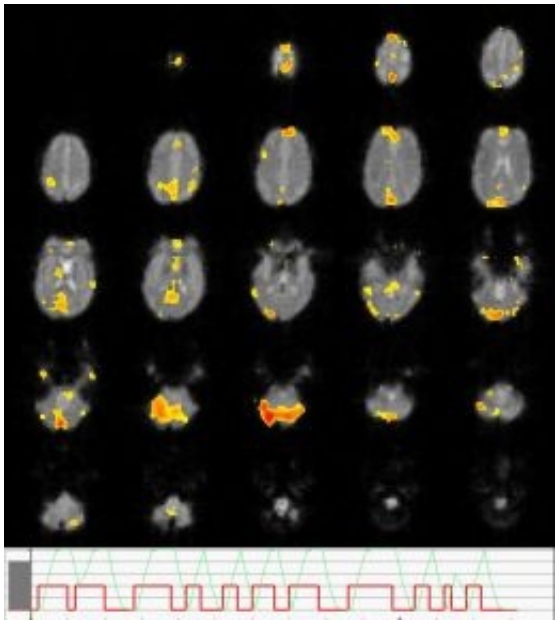

Figure 3: Activation map for combined reference vector highlights a network of frontal regions.

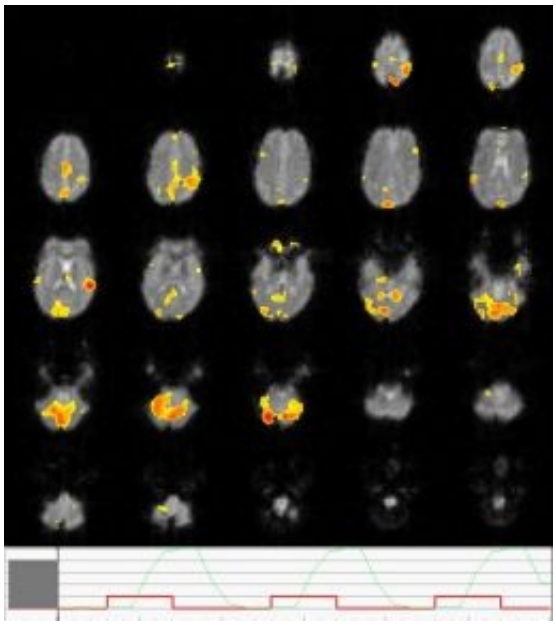

Figure 4: Activation map for right finger tapping using a fixed paradigm design.

WE 178
Low-frequency coherent fluctuations in BOLD activity : a preliminary report

Gaëtan Garraux[1,2], Guido Nolte[2], Mark Hallett[2]
[1]Cyclotron Research Center, University of Liège, Belgium, [2]Human Motor Control Section, NINDS, NIH, USA

Background
Low frequency (<0.1Hz) fluctuations originating from blood flow and oxygenation have been observed in the brain by different groups (Golanov et al. 1994; Biswal.et al. 1995). The goal of this study was to use BOLD fMRI to characterize coherent fluctuations in those low frequencies between spatially distant brain regions.
Methods
Thirteen right-handed subjects were studied using blocked-design BOLD fMRI at rest and as they performed sequential finger movements at a slow rate (~0.5 Hz) with their right hand. Serial acquisitions of EPI images were obtained at 3T using a single-shot 2D gradient-echo echo-planar imaging sequence. Data were processed and analyzed using standard procedures implemented in the statistical parametric mapping software (SPM2). Temporal profile of brain activity in 6 predefined regions (left S1M1, right S1M1, SMA, left thalamus, right cerebellum and CSF) were extracted on a subject-by-subject basis using the VOI tool in SPM2. After deconvolution (Gitelman et al. 2003), time series data representing movement and resting conditions were concatenated to create 2 within-condition time-series. After subtracting the mean over all epochs from each epoch, the (complex) coherency was calculated in the 5 lowest frequency bins with a frequency resolution of 1/17.5Hz (0, 0.05, 0.11, 0.17, 0.23 Hz). Real and imaginary parts of coherency, representing correlation and correlation of phase-shifted signals, respectively, were analyzed separately. Coherency was computed independently for each region pairs and each subject. Significance was defined as $p<0.05$ Bonferroni corrected for multiple comparisons.
Results
The main finding was the presence of coherent fluctuations in BOLD signal mainly in the lowest frequencies for (almost) all regions. The real part of coherency was equally pronounced during the movement and rest conditions. The only exception was a larger coherence during rest than during the task condition in the lowest frequencies between left and right S1M1. We could not find any significant imaginary part of coherency indicating that the time delays between dependent neural activations are negligible compared to the inverse frequencies under study. Partialling out the data in any of the regions did not have any significant impact on coherence map. Importantly, there was no evidence of coherent activity between any of the brain regions and CSF in any of the frequency bands.
Discussion
BOLD signal recorded during different behavioral steady-states showed very similar coherent fluctuations for all regions pairs studied mainly in the lowest frequencies. Those results are in good agreement with electrophysiological recordings in monkeys in which high coherence in band-limited power of local field potential signals have been reported at very low frequencies (<0.1Hz) (Leopold et al. 2003). In that study, coherence patterns were also highly similar under distinctly different behavioral states. Task-independent coherence in lower frequencies may be related to whole brain slow synchronous oscillations whose significance remains to be elucidated.
References
Golanov et al. (1994). Am J Physiol. 266; R204-214.
Biswal et al. (1995). Magn Reson Med. 34; 537-541.
Gitelman et al. (2003). NeuroImage. 19; 200-207.
Leopold. et al. (2003). Cereb Cortex. 13; 422-433.

WE 179
BOLD contrast signal history contribution to the auditory cortex functional connectivity in resting state fMRI data

Maria Gavrilescu[1,2], Geoffrey W Stuart[1,2], Alex A Sergejew[1,2], David Copolov[1,2], Gary F Egan[1,2,3]
[1]Mental Health Research Institute, Melbourne, Australia, [2]National Neuroscience Facility, Melbourne, Australia, [3]Howard Florey Institute, Melbourne, Australia

Introduction
The BOLD contrast signal history determined by lagged linear correlation has a significant contribution to functional connectivity in activation data sets (1). Moreover, Cordes (2,3) demonstrated that in resting state BOLD contrast data, the major contribution to synchronous correlation between functionally connected areas arises from low frequencies contributions (< 0.1Hz) with physiological noise having a negligible contribution in auditory and visual cortices. We have investigated the within subject across sessions reproducibility of low frequency and signal history contributions to the functional connectivity in auditory cortex in resting state fMRI data.

Methods
Two fMRI sessions consisting of 96 T2* weighted images were recorded for three healthy male subjects while lying at rest with their eyes closed in a 3T scanner (acquisition parameters TR/TE/FA=3sec/40msec/60, and 1.88x1.88x5mm spatial resolution). The images were motion corrected and spatially normalised to the EPI template using spm2 (www.fil.ion.ucl.ac.uk/spm). Two regions of interest were defined in one subject using WFU_PickAtlas (4) in the primary auditory cortex (PAC-BA41) in the left and right hemispheres. The time courses of the voxels in these regions were averaged and the inter-regional correlation coefficient (r) was computed separately for each session. The signal history contribution to r was estimated by computing the lagged correlations between the signal in the left PAC y(t) and the lagged signal in the right PAC x(t-nTR) where n=0,1,2,3,4 (3). The spectral decomposition of r was performed for each lag according to (1) to obtain the frequency content of the correlation coefficient. For each session a 2D map was constructed by plotting the spectral decomposition of r for each lag (Fig.1 and 2). The spatial correlation (r_map) of these 2D maps was then investigated in the raw and denoised data. Data denoising was performed using an ICA decomposition as implemented in Melodic (www.fmrib.ox.ac.uk/fsl/melodic) to identify and remove components highly correlated with the motion parameters (r>0.5) and other obvious artifacts (slice dropout, drifts, ghosting).

Results and discussion
The r values were significant for both sessions in raw and denoised data with larger values for denoised data (raw data: session1 r=0.45, session 2 r=0.59; denoised data: session 1 r=0.57, session 2 r=0.77).
However, correlation map value (r_map showing the reproducibility of history and frequency contribution to correlation coefficient r across sessions) was significant only for the denoised data (raw data: r_map=0.072, p=0.211; denoised data: r_map=0.59, p=0.000). Similar results were obtained for r_map limited to frequencies<0.08 (raw data: r_map=-0.13, p=0.239; denoised data: r_map=0.74, p=0.000). Signal history contributions from n=0 and n=1 lags were significant and positive in all situations while the contributions from n=2,3,4 lags were not always significant and switched sign across runs and preprocessing methods.
These results replicate the findings of Lahaye et al.(1) that signal history should be taken into account when studying functional connectivity in fMRI data. Our study suggests that even when data denoising has a relatively small impact on zero-lag temporal correlations it may significantly improve the reproducibility of signal history effects for the functional connectivity of auditory cortex. This has important consequences for studying the involvement of auditory cortex in schizophrenic patients experiencing auditory hallucinations.

References
1.Lahaye,2003,NeuroImage,20:962-974
2.Cordes,2000,AM J Neuroradiol,21:1636-1644
3.Cordes,2001,AM J Neuroradiol,22:1326-1333
4.Maldjan,2003,NeuroImage,19:1233-1239

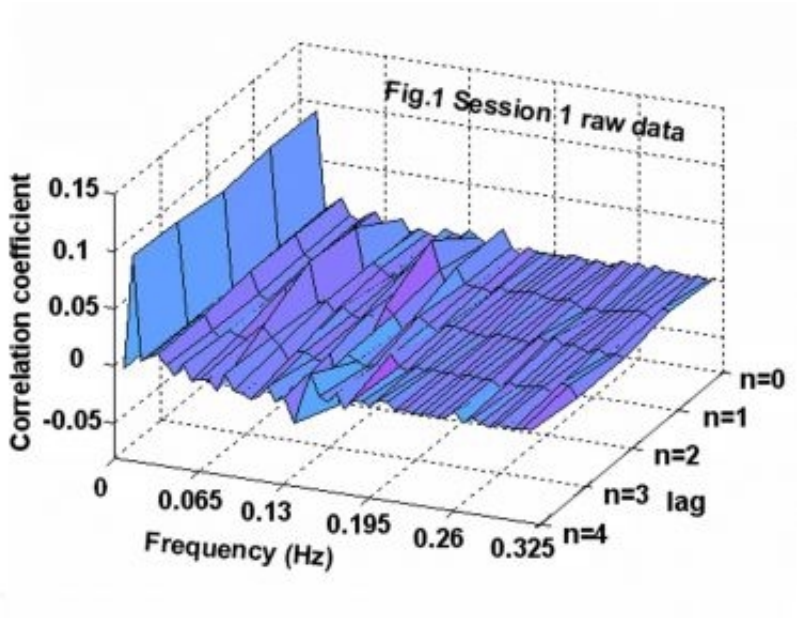
Fig.1 Session 1 raw data
Correlation coefficient
0.15
0.1
0.05
0
-0.05
0
0.065
0.13
0.195
0.26
0.325
Frequency (Hz)
n=0
n=1
n=2
n=3
n=4
lag

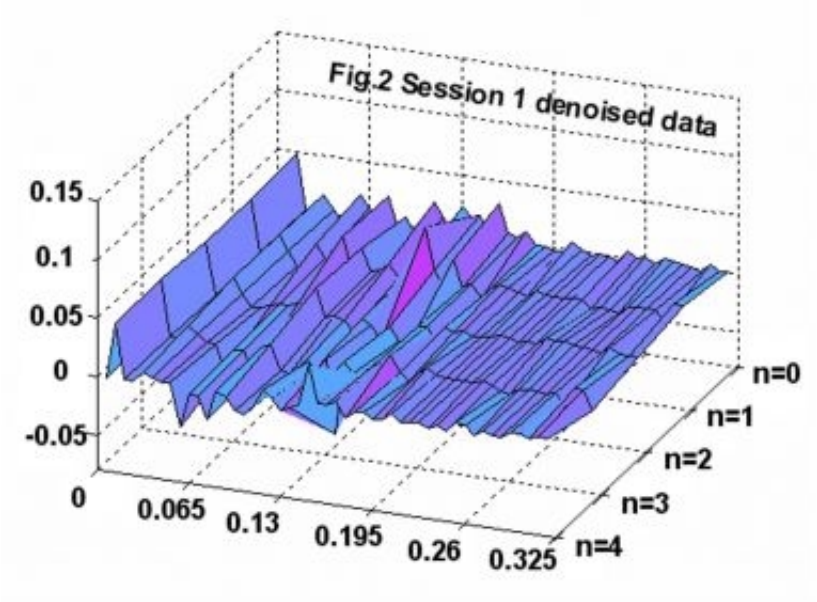
Fig.2 Session 1 denoised data
0.15
0.1
0.05
0
-0.05
0
0.065
0.13
0.195
0.26
0.325
n=0
n=1
n=2
n=3
n=4

WE 180

The reproducibility of frequency content and signal history contributions to functional connectivity in fMRI data acquired during an orthographic lexical retrieval task

Maria Gavrilescu[1, 3], Geoffrey W Stuart[1, 3], Anthony Waites[2], Graeme Jackson[2], Gary F Egan[1,3,4]
[1]Mental Health Research Institute of Victoria, Melbourne, Australia, [2]Brain Research Institute, Austin Repatriation Center, Melbourne, Australia, [3]National Neuroscience Facility, Melbourne, Australia, [4]Howard Florey Institute, Melbourne, Australia

Introduction

There is significant interest in investigating functional connectivity beyond temporal correlation between spatially separated neurophysiological measurements (1). We have investigated whether data denoising may improve the across subject reproducibility of signal history (1) and frequency contributions (2) to the correlation coefficient between brain regions activated by an orthographic lexical retrieval (OLR) task.

Methods

Twelve subjects were scanned using a 3T scanner while performing an OLR task (TR=3.6sec,see (4) for details). During the task period the subjects were asked to silently generate as many words as possible starting with a letter presented on a screen every 18 seconds. The task was presented in a block design with a period of 72 seconds. In the rest condition the subjects were asked to fixate on a crosshair at the center of the screen. Beginning with rest nine alternating block were presented (10 volumes/block).

For three subjects the images were motion corrected, smoothed with a 3x3x3mm Gaussian kernel and the statistical analysis was performed using spm2 (www.fil.ion.ucl.ac.uk/spm). Two activated regions of interest were defined as 4mm radius spheres in the left inferior frontal gyrus (LIFG) and anterior cingulate (AC) based on the t maps (fdr<0.05).

Data denoising was performed using an ICA decomposition as implemented in Melodic(www.fmrib.ox.ac.uk/fsl/melodic) to identify and remove components highly correlated with the motion parameters (r>0.5) and other obvious artifacts (slice dropout, drifts, ghosting). The task related component was identified based both on the time course correlation with the experimental paradigm and on the number of voxels in ROIs (5). After denoising, the images were reanalysed with spm2 with the same settings as for raw data.

The correlation coefficient (r) between the average time courses of the two regions was estimated within subject for the residuals obtained after removing the task defined as: 1) a boxcar (boxcar); 2) a boxcar convolved with the hrf function (hrf), and 3) task related component as identified by ICA (ICA). The average r value was then calculated across subjects.

The signal history contribution to r was estimated by computing the lagged correlations between the signal in LIFG y(t) and the lagged signal in AC x(t-nTR) where n=0,1,2,3,4 (3). The spectral decomposition of r was performed for each lag according to (1) to obtain the frequency content of the correlation coefficient. For each subject a 2D map was constructed by plotting the spectral decomposition of r for each lag. The spatial correlation (r_map) of these 2D maps was then estimated for each pair of subjects in the raw and denoised data. An average value for r_map was obtained as the mean of pair-wise values.

Results and discussion

While preprocessing and task removal methods had only a relatively small impact on the r values (Fig 1), r_map values were significant and positive only for denoised data with the highest value for the ICA task-removal method (Fig 2).

These results suggest that for more sophisticated functional connectivity measures, data denoising may significantly improve the reproducibility across subjects.

References

1.Friston, 1993,J.Cereb.Blood Flow Metab,13:5-14
2.Lahaye, 2003,NeuroImage,20:962-974
3.Cordes, 2000,AM J Neuroradiol,21:1636-1644
4.Wood, 2001,NeuroImage,14:162-169
5.Esposito, 2003,NeuroImage,20:2209-2224

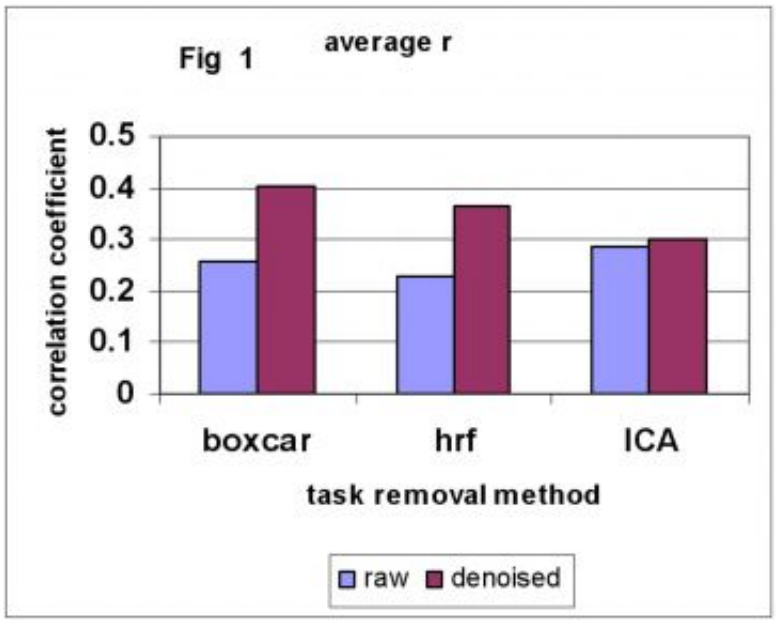
average r
correlation coefficient
0.5
0.4
0.3
0.2
0.1
0
boxcar
hrf
ICA
task removal method
raw
denoised

Fig 1

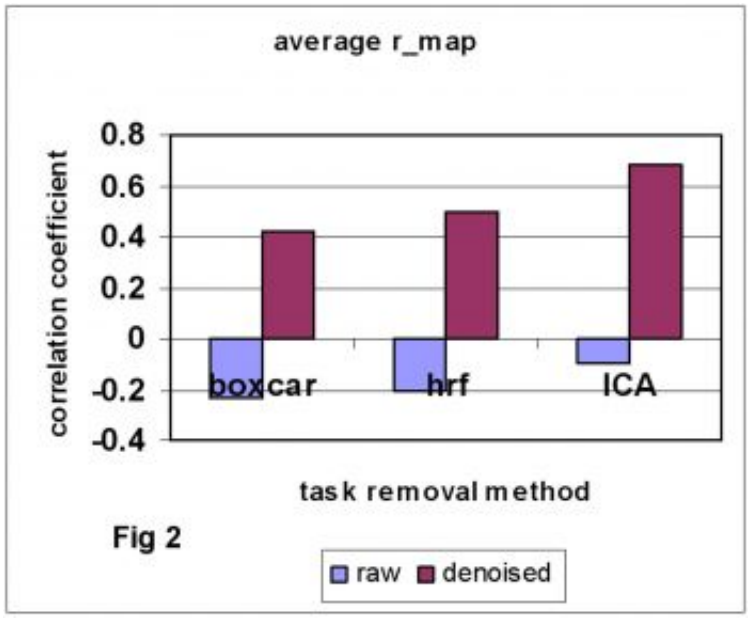
average r_map
correlation coefficient
0.8
0.6
0.4
0.2
0
-0.2
-0.4
boxcar
hrf
ICA
task removal method
raw
denoised

Fig 2

WE 181
Influence of fMRI Smoothing Procedures on Replicability of Fine Scale Motor Localization

Alexander Geissler[1], Andreas Gartus[1], Markus Barth[2], Rupert Lanzenberger[1], Denny Milakara[1], Amir Tahamtan[1], Thomas Foki[1], Gregor Meller[1], Roland Beisteiner[1]
[1] Study Group Clinical fMRI at the Departments of Neurology, [2] Department of Radiology

A comparison between results of smoothed data using SPM99 and a non smoothed correlational analysis (risk-map technique4) was performed to investigate the influence of smoothing procedures on localization replicability of essential motor cortex areas.

Methods:

11 healthy right handed subjects (mean age: 25.3 years; 7 males / 4 females) and one right handed patient suffering a left postcentral-tumor (male, age 37) participated in this study. We compared the localizations of the most active hand motor voxel (i.e. the voxel with the highest probability to represent a true positive) within two conditions: opening and closing of (1) the dominant hand (condition hand isolated), and (2) both hand and jaw movements simultaneously (condition hand simultaneous).

fMRI acquisition: 3T BRUKER Medspec scanner using a single shot EPI-sequence (TE/TR = 55.5/4000ms, 128x128 matrix, 230x230 FOV, 25 axial slices, slice thickness 3mm, sinc-pulse-excitation). Individual plaster helmets1 were applied for optimised head fixation.

The movements were self-initiated and self-paced at a subjective convenient frequency. One run consisted of 4 rest and 3 movement phases with 20s duration each. Prior to further analysis, all volumes of every subject were realigned to the first volume of the first run using AIR2.

We performed two different spatial smoothing analysis with a 4mm and a 8mm FWHM Gaussian smoothing kernel using SPM993 All scans of a condition were analyzed together. The smoothed data were calculated with a fixed response Box-car function shifted by 8 seconds. No cluster criterion was applied for generating t-value maps ($p < 0.001$, corrected $p < 0.05$ for multiple comparisons). Based on SPM T-maps, the voxel with the highest t-value within the primary sensorimotor cortex was determined as the most active one.

For the correlational risk-map analysis4 the same reference function and the same ROIs as in SPM were used. The hand motor center was defined as the voxel with the largest minimum correlation coefficient over all runs. This corresponds to a voxel with 100% reliability at the highest possible correlation threshold.

For each subject and both data analysis technique (SPM, risk-map) 3D localization difference (Euclidean distance: $\sqrt{((x1-x2)^2+(y1-y2)^2+(z1-z2)^2)}$ of the hand motor center between conditions was (x1, y1, z1 and x2, y2, z2 are the Cartesian- coordinates of the hand motor center in the simultaneous and isolated conditions respectively).

Results and Discussion:

The localization differences of the movement representation centers for isolated and simultaneous movements are depicted in table 1. Here, identical movement representation centers were found in 6/12 subjects for the risk-Map analysis, 2/12 for the SPM 4mm kernel and 1/12 for the SPM 8mm kernel smoothed analysis. As presented in figure 1, the localization variability between isolated and simultaneous movements was larger with smoothed compared to non-smoothed data. Table 2 shows the appropriate Wilcoxon tests indicating a significant decrease in localization replicability with smoothed data analysis techniques (fig. 2). There is no significant difference between both smoothed data analysis techniques. Our results show a significant decrease in localization replicability due to smoothing procedures

	Difference Risk Map				Difference SPM 4mm			
	Hand isolated vs. Hand simultaneous				Hand isolated vs. Hand simultaneous			
Subject	ml	ap	si	3D dist	ml	ap	si	3D dist
BJ	0	0	0	0	1.8	0	0	1.8

GS	-1.8	3.6	0	4.025	-1.8	1.8	0	2.55
HP	0	0	0	0	5.4	-7.2	6	10.8
KI	0	0	0	0	0	0	0	0
LR	0	0	0	0	0	0	3	3
SC	-1.8	0	0	1.8	0	-1.8	0	1.8
AM	0	-1.8	-6	6.3	0	3.6	6	7
LuR	0	0	0	0	-9	19.8	3	22
MG	-1.8	1.8	0	2.546	-1.8	0	0	1.8
SL	-1.8	0	0	1.8	-1.8	3.6	0	4.02
TN	0	1.8	0	1.8	-1.8	0	-3	3.5
TH	1.8	3.6	0	4.025	0	0	0	0

Difference SPM 8mm

Hand isolated vs. Hand simultaneous

Subject	ml	ap	si	3D dist
BJ	1.8	-1.8	0	2.55
GS	0	0	0	0
HP	0	-9	9	12.7
KI	0	-3.6	3	4.69
LR	0	-1.8	0	1.8
SC	7.2	-7.2	0	13.6
AM	-3.6	0	0	3.6
LuR	-3.6	14.4	0	14.8
MG	3.6	0	3	4.69
SL	-1.8	5.4	0	5.69
TN	0	1.8	0	1.8
TH	3.6	27	0	27.2

Individual localization differences of motor centers between isolated and simultaneous hand movements. The ml = medio-lateral, ap = anterior-posterior, si = superior-inferior axis and the 3D distances are given in mm. Pixel dimensions: 1.8mm x 1.8mm x

Acknowledgement:
This study was supported by the Ludwig Boltzmann Institute for Functional Brain Topography (head: Prof. Dr. L. Deecke) and by the Austrian Science Foundation (FWF P15102)."

References

1.) Edward V, Windischberger C, Cunnington R, et al.
Human Brain Mapping 2000;11(3):207-213.
2.) Woods R. P., Grafton S. T., Holmes, C. J., et al
Comput. Assist. Tomogr., 22:141-154 (1998)
3.) Members & collaborators of the Wellcome Department of Cognitive Neurology
Statistic Parametric Mapping Available at: http://www.fil.ion.ucl.ac.uk/spm/ .
Accessed September 3, 2002.
4.) Beisteiner, R. Lanzenberger, R. *et al.*,
Neuroscience Letters, Volume 290, Issue 1, 18 August 2000, Pages 13-164.

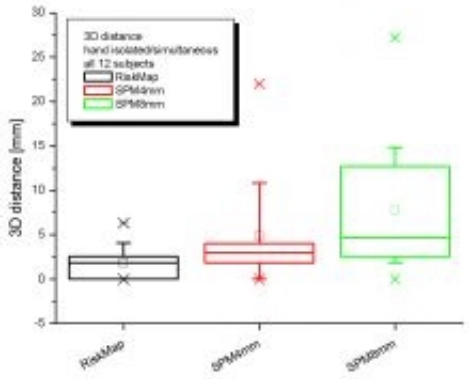

Fig. 1 Box Plot illustration of the mean 3D distances of the motor centers for isolated and simultaneous hand movements.
The box stretches from the lower hinge (defined as the 25th percentile) to the upper hinge (the 75th percentile), the range of the whiskers is from the 5th to the 95th percentile. Median: line across the box; mean: little square; the crosses indicate outliers; small sized straight lines: minimum and maximum value.

	RiskMap/SPM99 4mm	RiskMap/SPM99 8mm	SPM99 4mm / SPM99 8mm
Double sided significance	0.021	0.028	0.480

Table 2: Wilcoxon results testing for significant increases in 3D differences between non-smoothed and smoothed analysis techniques.

3D Distance	Mean	Standard deviation
RiskMap	1,333	1,57482
SPM4mm	4,85583	6,18152
SPM8mm	7,76	7,89033

Table 3: Mean 3D distances per analysis method in mm.

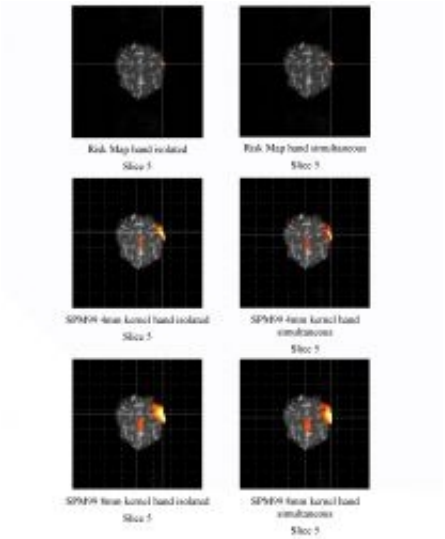

Fig 2: Comparison of the position of the motor hand center voxel for the isolated and simultaneous hand movement condition (subject SI.). Subjacent slice is the original functional image and not smoothed. The crossbair at the center voxel indicates larger localization differences with the smoothed than the non-smoothed data analysis techniques.

WE 182
Spatial semivariance analysis of fMRI data

Yulia Gel[1], Rajesh Nandy[2], Dietmar Cordes[2]
[1]George Washington University, USA, [2]University of Washington, Department of Radiology

Introduction The overall objective of this research is to adapt spatio-temporal methods of geostatistics to fMRI analysis and to develop spatio-temporal models for fMRI data. Our current focus is on the spatial pattern of the data.

Theory and methods In first, we apply a segmentation based approach to isolate gray matter, white matter and CSF, which makes each individual segment more homogeneous. Then we investigate the spatial dependency of the signal by semivariance analysis. We fit a variogram curve with an exponential covariance function and estimate spatial covariance parameters such as variance (sill), range (degree of correlation of signal at neighbor pixels), and nugget (the level of microscale variability) for CSF, white and gray matter separately. We repeat our experiments for a number of healthy subjects. The research addresses the following questions: a) How to identify pathological areas in the brain? In fact, assuming that we accumulate a sufficient database of covariance parameters, we can check whether the parameters of the new subject fall within certain confidence interval. If not, we can subdivide the brain into local subareas and identify a region with the unusual covariance parameters and hence suggest a further medical examination of this part of the brain. Such an approach might open the possibility to identify even a tumor with significantly small size. b) How to achieve an image of high resolution from the data of low resolution i.e. is kriging a useful approach for fMRI data? c) How do the covariance parameters evolve in time, i.e. how does the brain change over age?

Results We apply our analysis to 4 normal subjects and 4 subjects with dyslexia. In Figures 1 and 2, we provide the estimated density functions of the sill ã2, the range r and the nugget â for white matter (WM) and gray matter (GM) for normal subjects and subjects with dyslexia, respectively. The normal subjects show tendencies to bimodal behavior of range parameter in WM and more significant small-scale variability (nugget variability) for GM. Inter-subject variability for the sill ã2 appears to be less for normal subjects. However, such patterns may be due to outlier influence or lack of data. Although the results are preliminary, the plots show the relative consistency of fitting the exponential covariance function to the spatial data, and we found this approach to be promising. To test our method further, we plan to apply the method to a higher number of normal and affected subjects.

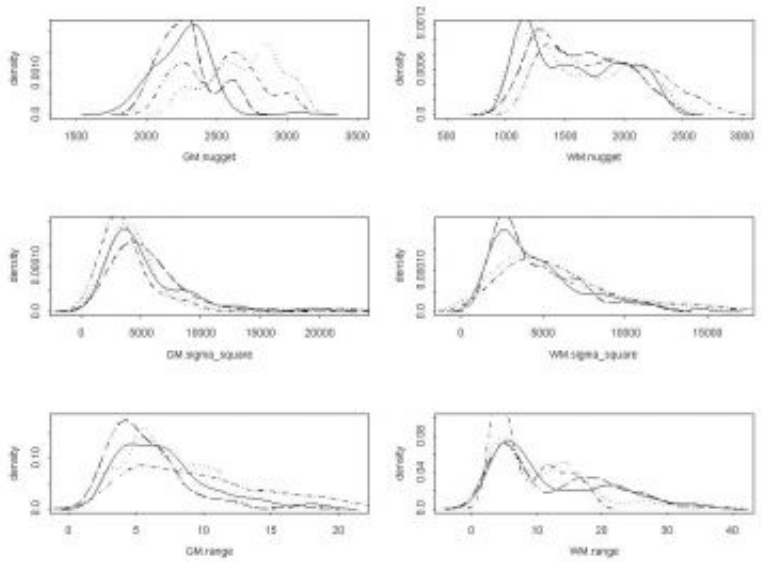

The density functions of covariance parameters for normal subjects

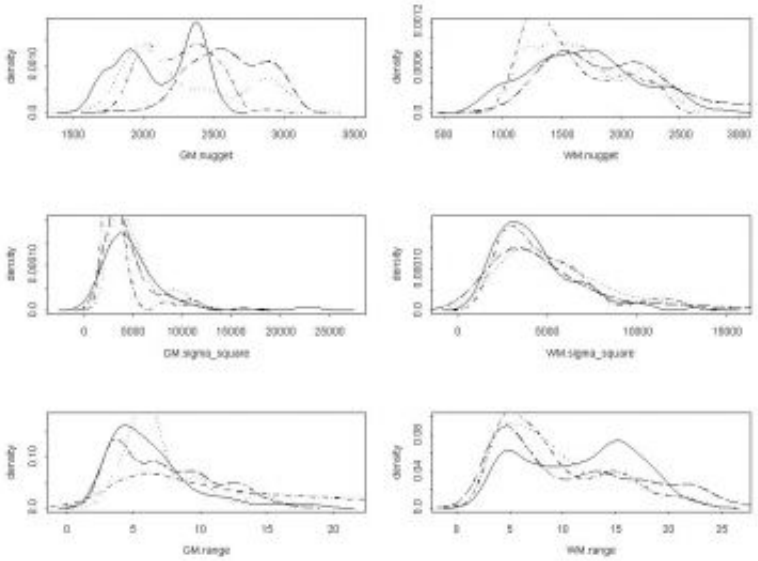

The density functions of covariance parameters for dyslexic subjects.

WE 183

Repeatability of Brain Tissue Volume Quantification using Magnetic Resonance Images

Juan D. Gispert , Santiago Reig , Javier Pascau , Juan J. Vaquero , Manuel Desco
Medicina y Cirugía Experimental. Hospital General Universitario Gregorio Marañón. Madrid, Spain.

INTRODUCTION

The conventional way to characterize MR tissue measurements has been to assess accuracy and precision (or repeatability) (i.e. systematic and random errors). Sources of error (contributing to both inaccuracy and imprecision) arise both in the data collection procedure and in the image analysis procedure. Two main sources of systematic error in data acquisition are B1 non-uniformity and partial volume effects. Precision may have a large biological component because of the significant intra-subject biological variation. Besides, patient positioning and movement contribute to random errors (Tofts, 2003). Accuracy of MR quantification methods has received greater attention than precision. However, systematic errors do not mask differences in group comparisons whilst imprecision decreases the statistical power of the statistical test. Early works that measured the reproducibility of MRI analysis procedures have little practical value, since patient positioning was not considered and can be a major source of variation (Gawne-Cain et al., 1996; Tofts, 1998).

The aim of this work is to study the repeatability of brain tissue volume quantification achieved by different MRI segmentation methods. We have quantified the variance components associated to different sources, considering both data acquisition variability (including biological, scanner and positioning variability) and image post-processing variability (introduced by intensity inhomogeneity and segmentation algorithms). We have also measured the reproducibility of eight different MRI tissue segmentation algorithms under different acquisition and post-processing conditions by calculating the standard deviation of the repeated measurements (absolute variability, in cm3) and the coefficient of variation (CV) (relative variability, in percentage).

MATERIAL AND METHODS

Two experiments were conducted using an MR dataset consisting in a total of 24 MR images of 4 different subjects, acquired in 2 different MR scanners of different static field (0.5 and 1.5 Tesla) and repeating the acquisition in each scanner 3 times. All these images were then corrected for intensity inhomogeneities with the N3 algorithm. Both the corrected and uncorrected images were segmented by using eight different MRI segmentation algorithms, selected on the basis of being representative of the use of partial volume modeling (Santago and Gage, 1995; Laidlaw et al., 1998; Grabowski et al., 2000; Ruan et al., 2000) or the use of statistical templates (Ashburner and Friston, 1997; Van Leemput et al., 1999). Images were also segmented by a baseline reference algorithm which does not implement any partial volume modeling nor uses statistical templates (Wells et al., 1996).

RESULTS

Figures 1 to 3 show the percentage of variance explained by the 5 sources of variability considered and Table 1 the reproducibility of the 8 segmentation algorithms under the different measurement conditions.

CONCLUSIONS

Our results indicate that the explicit modeling of partial volume effects improves the MRI segmentation repeatability. The inclusion of spatial information by using anatomical templates and spatial normalization techniques enables a greater improvement in the repeatability, although it is very sensitive to eventual registration errors.

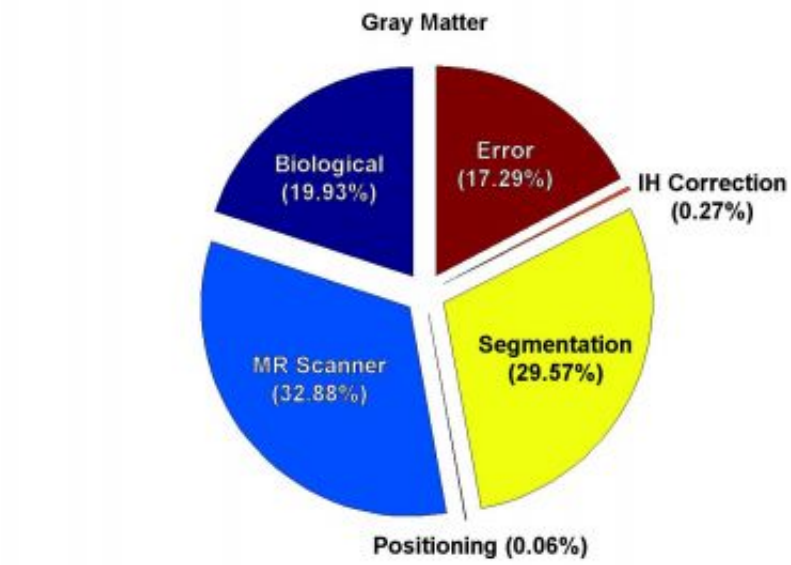

Figure 1: Percentage of variance explained in Gray Matter quantification by the different factors: Subject (Biological variability), MR scanner, Positioning (nested in MR scanner), Intensity inHomogeneity Correction and Segmentation Algorithm

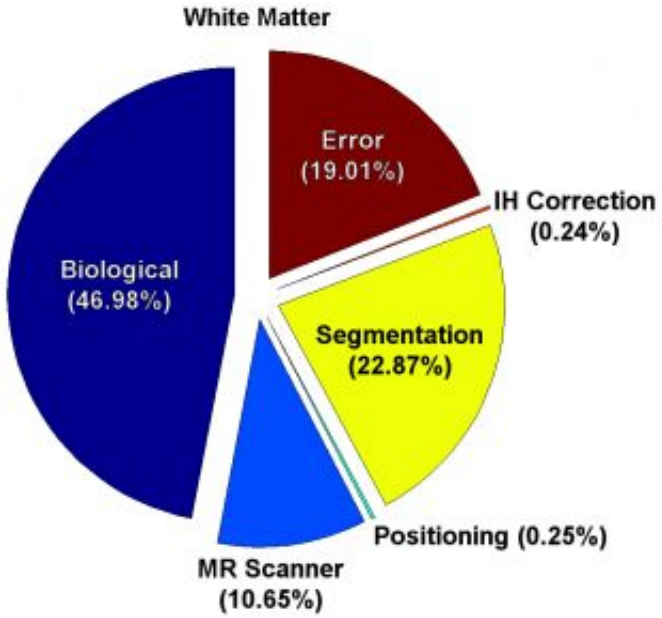

Figure 2: Percentage of variance explained in White Matter quantification by the different factors: Subject (Biological variability), MR scanner, Positioning (nested in MR scanner), Intensity inHomogeneity Correction and Segmentation Algorithm

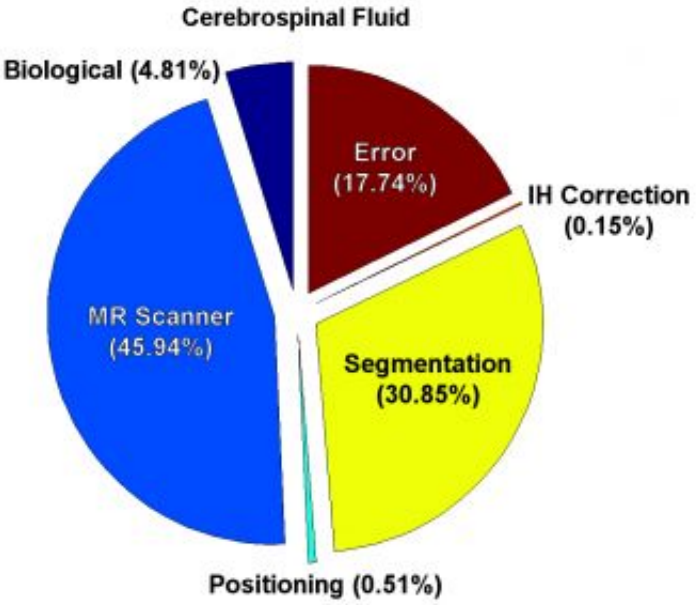

Figure 3: Percentage of variance explained in Cerebrospinal Fluid quantification by the different factors: Subject (Biological variability), MR scanner, Positioning (nested in MR scanner), Intensity Inhomogeneity Correction and Segmentation Algorithm

MR Scanner	0.5 T				1.5 T			
IH Correction	N3		None		N3		None	
	Abs. (cm^3)	Rel. (%)	Abs. (cm^3)	Rel. (%)	Abs. (cm^3)	Rel. (%)	Abs. (cm^3)	Rel. (%)
Gray Matter								
Wells	38.77	4.47	36.85	4.65	88.62	10.08	96.69	9.40
Santago	20.45	2.10	22.77	2.09	22.13	2.14	48.66	3.77
Laidlaw	15.35	1.46	19.57	1.90	27.00	2.53	31.88	3.00
Ruan	18.26	1.73	38.36	3.38	19.96	1.87	34.72	3.57
Grabowski	13.25	1.38	20.71	2.06	51.24	4.37	58.31	4.95
SPM	7.21	0.92	9.16	0.87	6.16	0.68	3.88	0.42
EMS	8.00	1.18	8.13	1.17	68.47	9.74	69.27	9.76
EMS+MRF	11.63	1.49	10.23	1.33	58.30	8.54	56.16	8.27
White Matter								
Wells	13.45	2.72	11.74	2.31	30.30	7.03	38.45	7.29
Santago	16.68	3.36	13.60	2.65	19.55	4.92	39.52	7.53
Laidlaw	14.80	3.28	15.58	3.63	19.14	4.79	26.19	6.67
Ruan	21.81	2.98	29.24	5.02	15.73	3.07	27.35	5.75
Grabowski	11.96	2.81	15.83	3.40	23.12	5.61	28.67	7.19
SPM	5.16	0.87	4.90	0.81	4.07	0.74	3.84	0.69
EMS	18.41	2.21	18.76	2.25	120.44	14.27	120.55	14.28
EMS+MRF	7.42	0.93	8.36	1.08	70.15	8.04	71.95	8.26
Cerebrospinal Fluid								
Wells	26.23	5.49	29.54	6.63	61.99	23.91	62.25	24.11
Santago	11.80	3.55	14.11	3.59	3.70	2.03	10.24	4.66
Laidlaw	9.38	3.24	8.42	3.12	9.98	5.77	8.33	5.32
Ruan	11.08	3.13	13.62	3.53	5.74	2.82	13.28	5.03
Grabowski	10.45	2.69	10.54	2.73	34.69	9.94	37.28	11.33
SPM	5.03	1.27	6.60	1.71	3.54	1.19	3.12	1.26
EMS	12.52	10.97	12.60	11.20	57.29	58.35	55.45	57.99
EMS+MRF	15.67	9.68	15.02	9.47	67.23	43.04	66.02	42.83

Table 1: Mean values of the standard deviation (Abs., in cm3) and the coefficient of variation (Rel., in %) of the tissue volumes estimated using 0.5 T and 1.5 T MR scans and with and without intensity inhomogeneity correction (N3, None).

WE 184
Asymmetry Analysis Along Cingulum Using Diffusion Tensor Imaging

Gaolang Gong[1], Tianzi Jiang[1], Chaozhe Zhu[1], Yufeng Zang[1], Yong He[1], Sheng Xie[2], Jiangxi Xiao[2], Xuemei Guo[2]

[1]National Laboratory of Pattern Recognition, Institute of Automation, Chinese Academy of Sciences, Beijing 100080, P. R. China, [2]Department of Radiology, Peking University First Hospital, Beijing 100034, P. R. China

Introduction
So far, analysis of diffusion tensor imaging (DTI) is often based on region of interesting (ROI) in image dataset, which is specified by user. However, this method is not always reliable because of the uncertainty of manual specification. Here, we introduce an improved fiber-based scheme rather than ROI-based analysis to study asymmetry of the cingulum in DTI dataset, which is the most prominent white matter fiber tract of the limbic system. The present method can automatically extract the quantitative anisotropy properties along the cingulum bundles from tractography.

Method
Thirty-one healthy, right-handed volunteers with informed consent were scanned on a 1.5-Tesla MR scanner (GE Signa 1.5T Twinspeed), The diffusion sensitizing gradients were applied along 25 non-collinear directions with b-value=1000 s/mm^2, together with an acquisition without diffusion weighting. Totally 12 slices were gathered with the most caudal slice passing through the genu of corpus callosum to cover most cingulum bundles as possible. The acquisition parameter was as follows: TR=4000ms; TE=80ms; matrix=128x128; FOV=24x24cm; number of excitation (NEX)=3; slice thickness=3mm without gap. Total scan time for DTI sequence was 5 minutes 20 seconds. Moreover, high-resolution 3D T1-weighted image (TR=11.3ms, TE=4.2ms, FOV=24x24mm, matrix=128x128, slice thickness=2.4mm, NEX=2) was also obtained.

The cingulum bundle was first reconstructed by fiber tracking algorithm. All traced fibers with the common origin were then parametrized by arc-angle. In this case, the plane passing the anterior commissure (AC) point and perpendicular to the anterior commissure-posterior commissrue (AC-PC) line was assigned as the reference plane, in which seed ROI for cingulum bundle tracking can be specified. The left-right line passing AC point was assigned as the axis of rotation, then all traced fibers were parameterized by arc-angle automatically in the new polar coordinates. After such anatomical correspondence of cingulum of subjects was established, paired t-test was then employed to access the difference of FA value along the cingulum.

Result and conclusion
Averaged FA value of the 31 subjects corresponding to arc-angle in bilateral cingulum was shown in Fig.1, and standard deviations for FA distribution were also presented. Significant difference in FA distribution between left and right was found with a left-greater-than-right asymmetry pattern in the most segment of cingulum, except extreme posterior portion. And such asymmetry pattern was verified by the P-value distribution in Fig.2, where significant difference ($P<0.05$) was approximately distributed in -50°~40°.

References
[1] Cao Y et al. (2003) Human Brain Mapping, 20:8290. 54:11711180
[2] Fillard P et al. (2003) MICCAI2003
[3] Kubicki M et al. (2003) Biol Psychiatry
[4] Lazar M et al. (2003) Human Brain Mapping 18: 306 321

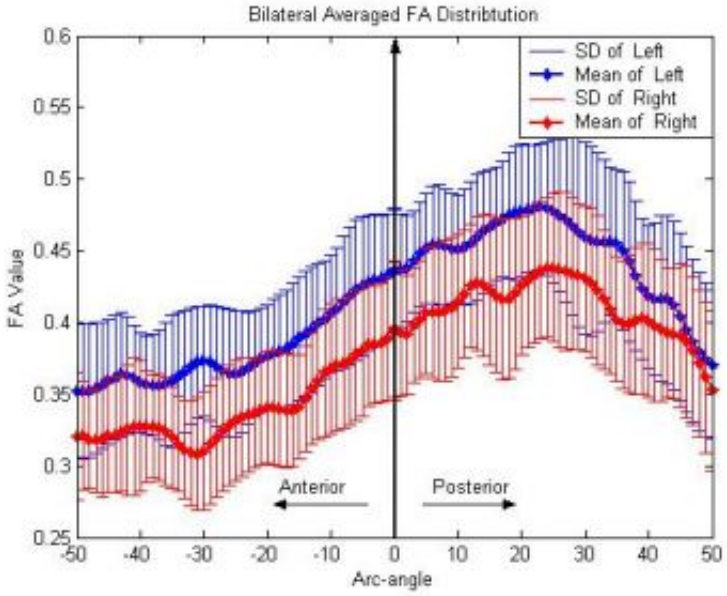

Fig. 1. FA Value distribution along the cingulum for the 31 subjects, blue denotes left side and red denotes right side.

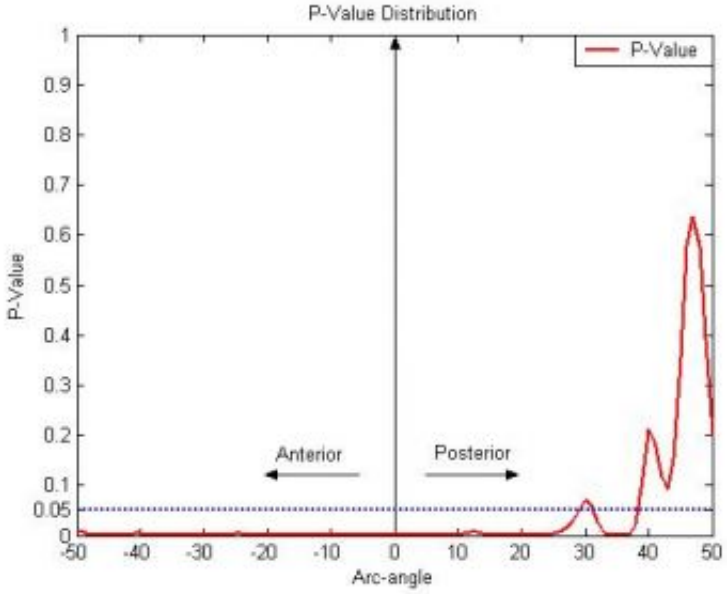

Fig. 2. Corresponding P-value distribution

WE 185
Application of Voxel-Based Group Analysis in a small group of former professional deep-sea divers

Renate Grüner[1,3], Karsten Specht[2,1], Lars Ersland[3,1], Gunnar Moen[3,1]
[1]University of Bergen, Norway, [2]Research Center Jülich, Germany, [3]Haukeland University Hospital, Norway

Introduction

The mechanism by which divers damage their brain, is still unknown. Polkinghorne et.al.[8] showed by fluoresceinangiography that the capillary density in the retina among divers was reduced. They also found dilated arteriolas and microaneurysms in the retinal vessels of divers. Their conclusion was that most of these findings could be explained by vascular obstructions.

From a major ongoing study (N=120) on former professional deep-sea divers, the perfusion maps from ten randomly selected and the ten youngest controls, were selected for group analysis using statistical voxel-by-voxel comparison. This method for group analysis has recently been applied in morphometrical data ([1]-[7]), but to our knowledge never to parametric perfusion images (blood flow, blood volume and mean transit time).

Acquisition and Analysis

Echo-planar contrast perfusion imaging were performed (Siemens Vision 1.5T,TR/TE=1500/60.7ms, FoV=240x240,Matrix=128x128). Parametric images were computed using the ICE (Image Control and Evaluation) software from NordicNeuroLab AS.

The transformation matrix, obtained from normalising the pre-contrast echo-planar images to a standard EPI-template, was used to normalise the parametric images from each diver to the same reference image. Then, a template was created for each parametric image in an iterative manner by averaging the normalised parametric images and using the averaged images to create a new, more accurate, template, which again was used to normalise the original parametric images. Based on the resulting normalized images, an ANCOVA analysis of variance (implemented in SPM2, voxel threshold $p<0.01$, mimimum cluster size 100 voxels) was performed between the diver group and the defined control group.

Results

Results from the group comparison show distinct clusters, where values of flow are significantly different between the two groups. Several of these areas correlate with findings in cerebral blood volume and mean transit time. Most prominent were the differences in mean transit time and blood flow in the right frontal lobe (Fig.1). Also, mean transit time differences were seen bilaterally in the amygdala and subcortical areas, left and right to the ventricles.

Discussion and Conclusion

The statistical voxel-based procedure presented in this study is a valuable tool when performing group analysis in perfusion studies. One of its major strengths is the ability to identify areas of significant changes without prior assumptions.

Preliminary results indicate a predilection of flow disturbances in certain areas in the brain of divers. In our opinion these localized disturbances in blood flow, blood volume, and mean transit time among divers, reflect areas of more vulnerable vessels to injuries related to diving. Further validation of these findings will be achieved when all divers (N=120) and normal controls are investigated.

Acknowledgement

We are thankful to the Norwegian Health Department for financial support. The authors would like to acknowledge Schering for their generous contribution of Gadovist, and Tore Gamborg for his continuous support.

References

[1] Ashburner J.et.al.,Neuroimage 11:805-821(2000)
[2] Ashburner J.et.al.,Neuroimage JID-9215515 14:1238-1243(2001)
[3] Good C.D.et.al,Rev.Neurol.JID-2984779R 157:797-806(2001)
[4] Good C.D.et.al,Neuroimage JID-9215515 14:685-700(2001)
[5] Good C.D.,Neuroimage JID-9215515 14:21-36(2001)

[6] Salmond C.H.et.al.,Neuroimage.17:1027-1030(2002)
[7] Specht K.et.al.,Arch.Neurol.60:1431-1435(2003)
[8] Polkinghorne PJ.et.al.,Lancet-ii,1381-1383(1988)

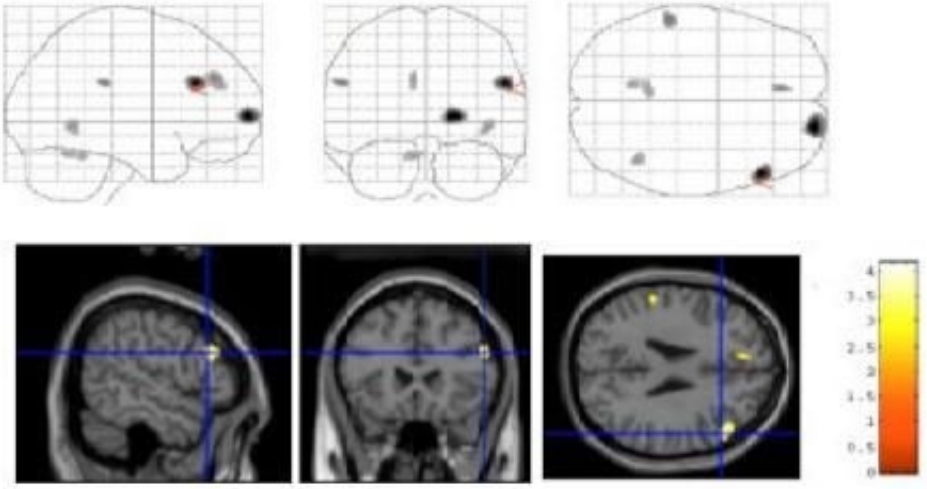

Fig. 1: Significant differences in cerebral blood flow. The color bar to the right indicates t-score values.

WE 186
Evaluation of fMRI Sensitivity Across Multiple Sites

Douglas N. Greve , Nathan S. White , Anders M. Dale
Martinos Center for Biomedical Imaging, Department of Radiology, Massachusetts General Hospital, Harvard Medical School

INTRODUCTION: The Functional Imaging Research in Schizophrenia testbed Biomedical Information Research Network (FIRST-BIRN) project is one part of an NIH-NCRR initiative that aims to bring advances in computer sciences and informatics to biomedical science. The FIRST-BIRN project links eleven collaborating sites together with high speed internet and shared hardware and software to database, share and analyze fMRI data collected at the participating sites for the purpose of overcoming technical and sociological obstacles to performing multi-institutional large-scale fMRI studies of schizophrenia. The first step toward this goal is to characterize the sources of variability in the fMRI data introduced by collection across sites. These include differences in field strength (1.5T, 3T, 4T), echo time, readout time, k-space trajectory (spiral and EPI), k-space reconstruction strategies, and scanner manufacturer (GE, Siemens, Picker). This abstract begins to characterize variation in the sensitivity of fMRI data collected across the FIRST-BIRN sites (see also HBM abstract by Zou, et al, for a related analysis).
METHODS: Five subjects were scanned with the same protocol twice at each site. Each visit consisted of ten fMRI runs (TR=3s, 85 time points, 64x64x35, 3.4x3.4x5mm). In two of the runs, there was no task (REST). In two other runs, the subject performed a periodic breath hold (BH) task. Each run was motion corrected and smoothed at 5mm. The BH and REST were analyzed using a Fourier model, and each voxel was assigned a significance (no temporal
whitening performed). The True-Positive Rate (TPR) was assessed by examining cortical grey matter voxels [1,2] from the BH task under the assumption that breath holding activates all grey matter [3]. The False-Positive Rate (FPR) was assessed by examining the same voxels from the REST condition. The significances for a site were pooled across all subjects, visits, and runs (BH and REST separately pooled) in order to compute the FPR and TPR for that site. The Receiver-Operating Characteristic (ROC) was then determined by plotting the TPR vs the FPR for each member of the consortium.
RESULTS AND DISCUSSION: the FPR, TPR, and ROC curves are shown in Figures 1, 2, and 3. As can be seen, there is a wide range of sensitivities across the sites. For all three figures, the ranking of the sites is almost perfectly predicted by field strength, with stronger fields, in general, being more sensitive but with higher FPR. Increasing FPR with field strength is expected because there is more temporally correlated noise relative to white noise. The variation may also be explained by other factors, including inherent spatial smoothness and misregistration with the cortical ribbon due to B0 distortion.
REFERENCES:
[1] Kwong, et al, MRM, 33: 448-452, 1995.
[2] Dale, et al, NeuroImage, 9: 179-194. 1999.
[3] Fischl, et al, NeuroImage, 9: 195-207. 1999.
Acknowledgments: NCRR FIRST-BIRN (P41RR14075).

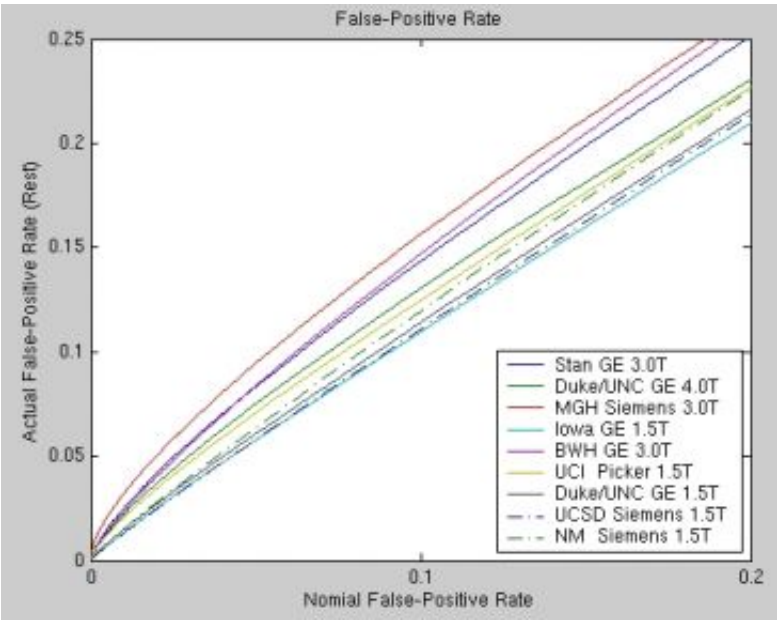

False Positive Rate

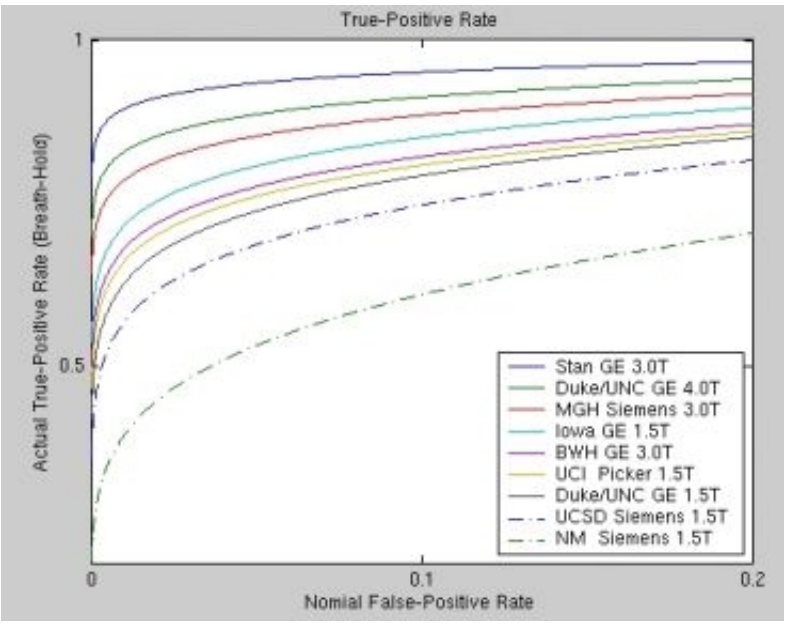

True Positive Rate

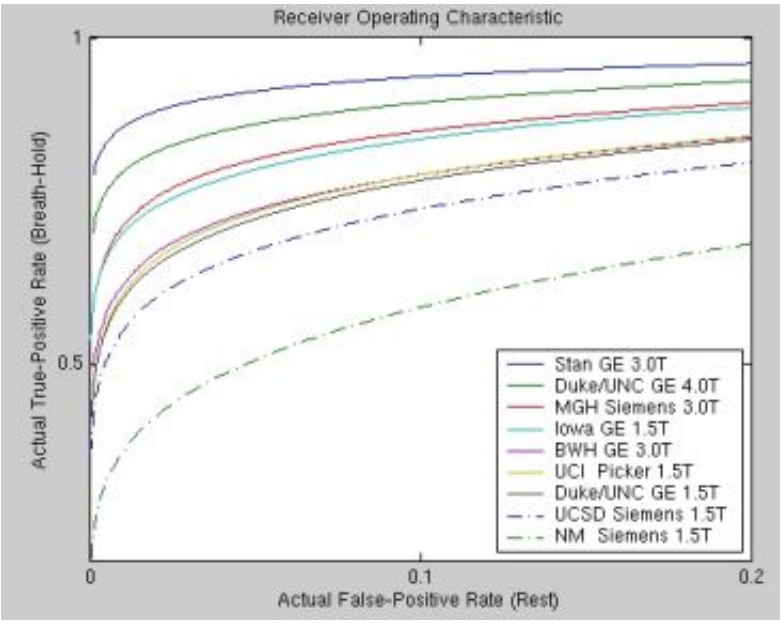
Receiver Operating Characteristic
Actual True-Positive Rate (Breath-Hold)
Actual False-Positive Rate (Rest)
1
0.5
0
0.1
0.2
Stan GE 3.0T
Duke/UNC GE 4.0T
MGH Siemens 3.0T
Iowa GE 1.5T
BWH GE 3.0T
UCI Picker 1.5T
Duke/UNC GE 1.5T
UCSD Siemens 1.5T
NM Siemens 1.5T

ROC

WE 187
Spatial distribution of the respiratory component of the fMRI magnitude and phase

Mark P Griffin , Bruce Pike
Montreal Neurological Institute, McGill University

Respiratory artifacts are a significant source of noise in fMRI. The exact nature of their origin (often attributed to bulk susceptibility changes) is still unclear. Previous work has focused on the respiratory component of the signal magnitude (hereafter referred to as the magnitude-correlated component), and was limited since these components appear only in regions of large signal intensity variation (tissue boundaries) [1]. The MR phase also contains a strong respiratory component [2]. This abstract describes the generation of three-dimensional phase-correlated images, which reveal information not seen in magnitude-correlated images. These respiratory models were incorporated into the MIDAS fMRI simulator [3].

Four multi-slice resting-state complex EPI data sets were collected for each of ten healthy volunteers (TR/TE/flip angle = 2.12s/53ms/90). In addition a single-slice data set and an anatomical T1-weighted volume were collected. During each scan, a respiratory belt measured the subject's breathing patterns. Following acquisition, the phase of each image was unwrapped and low frequency drift removed. The magnitude and phase of the MR signal were then viewed against the temporally-matched externally-measured respiratory time-course (see Figures 1a and 1b). The size of the respiratory component was described by the slope of the straight line fitting these data-points. This component was then extracted as the product of the slope with the externally measured time-course. The standard deviation (STD) of the respiratory component within each voxel was hence determined for both the magnitude and phase images. Figures 1c and 1d shows the T1-weighted scan from a representative subject. Figures 1e through 1h show the STD's of the different respiratory components. As has been previously reported [1], the component from the magnitude images (1e and 1f) generally appears only in regions where there is a large signal intensity gradient. In contrast the component from the phase images (1g and 1h) possesses a fairly smooth appearance across the brain.

The goal of this work was to characterize the spatial nature of the respiratory artifacts for simulation purposes and to provide some insight into their physical origin. Magnitude-correlated images were produced where their information content was localized to regions of large signal intensity gradients. In contrast the three-dimensional, phase-correlated images had a regular structure across the brain. There was roughly linear intensity gradient along the z-direction. For both the magnitude and phase images shown, the STD of the respiratory component within each voxel was determined. A straight line was then fit to the mean of the STD in each slice. This produced a respiratory component STD of 0.05 radians in the bottom slice and 0.02 radians in the top slice. This fall off strongly supports the hypothesis that respiratory artifacts are caused by bulk susceptibility as opposed to head motion. This work may also have implications for the use of navigator echoes with segmented EPI as a means of determining the phase of the respiratory cycle for each MR acquisition.

[1] Windischberger, MRI, 20(8), 2002.
[2] Hu, MRM, 34(2), 1995.
[3] Boada, HBM, 2004 (submitted to these proceedings).

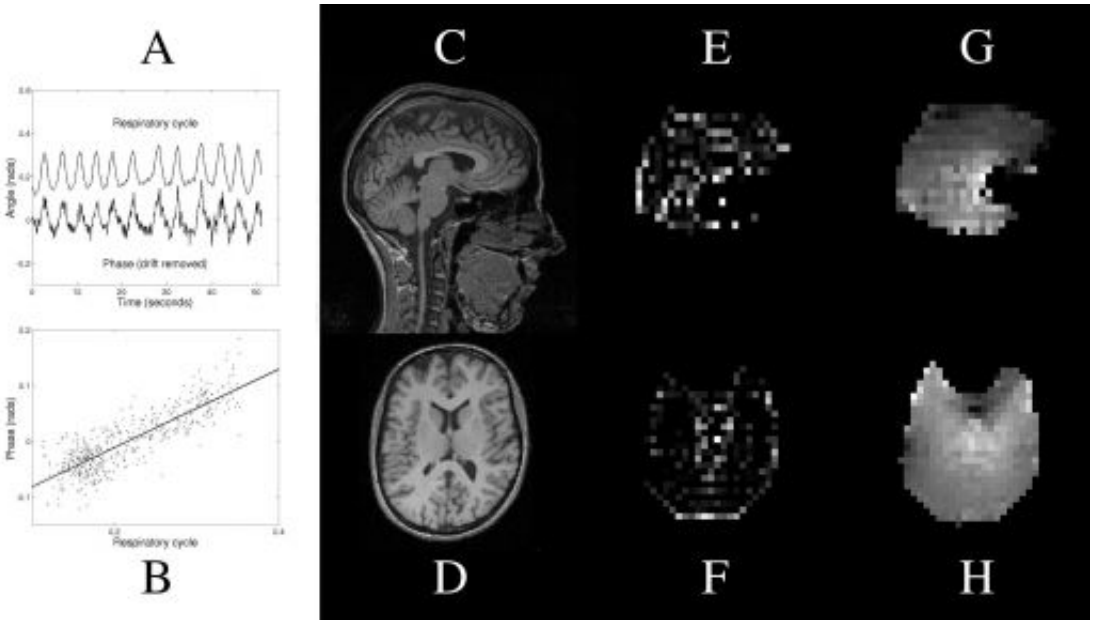

Fig. 1. (a) the respiratory time-course and the phase from a single voxel, (b) the correlation between the phase and the respiratory time-course, (c) and (d) the anatomical T1 image, (e) and (f) the amplitude of the respiratory component in the signal magnitude, (g) and (h) the amplitude of the respiratory component in the signal phase.

WE 188
A probabilistic atlas of the human inferior frontal gyrus

Alexander Hammers[1,2], Chi-Hua Chen[1], Richard Allom[1], Spyridon Vossos[1], Samantha L Free[2], Ralph Myers[3], Louis Lemieux[2], Tejal N Mitchell[2], David J Brooks[1], Matthias J Koepp[1,2], John S Duncan[2]
[1]MRC Clinical Sciences Centre and Division of Neuroscience, Faculty of Medicine, Imperial College, Hammersmith Hospital, DuCane Road, London, [2]Department of Clinical and Experimental Epilepsy, Institute of Neurology, UCL, Queen Square, London, and National Society for Epilepsy MRI Unit, Chalfont St Peter, [3]Hammersmith Imanet., MRC Cyclotron Building, Hammersmith Hospital, London

Background:
We have previously presented the concept and implementation of manually constructed brain atlases for use with Statistical Parametric Mapping (SPM) (Hammers A et al., Hum Brain Mapp 2002; 2003). These atlases did not contain lobar subdivisions of the frontal lobe.
Interest in the human inferior frontal gyrus (IFG) is due to its main functions, including expressive language, particularly on the left (Brocas area), verbal working memory, semantic generation, and selecting and comparing information (Petrides M 1995, Cabeza R et al. 2000).
Methods:
High resolution MRIs were acquired in 30 normal healthy subjects, 15 women (median age 31 years, mean ±SD 31.3±7.9 years) and 15 men (30 / 30.7±7.9 years), nonuniformity corrected and reorientated along the anterior-posterior commissure (ACPC) line. Using Analyze AVW 5.0, the IFGs were delineated following a written algorithm, utilizing orthogonal planes and three-dimensional rendering. The resulting 30 individual maps and their grey matter contributions (Lemieux et al. 2002) were spatially transformed (normalized) into standard stereotactic space, using standard software (SPM99) and a widely used template (MNI/ICBM 152).
We evaluated volume data for all IFGs both in native space and after spatial normalization and used the normalized superimposed atlases to create a probability map (Figure 1).
Results:
There was no side-to-side difference in IFG volume. In native space, the IFG was an average of 5%, and the GM portion of the IFG 12% larger in women; the latter was significant ($p<0.04$). After normalization to stereotaxic space (effectively correcting for brain size), the IFG was on average 17% larger in women and the GM contribution 22% larger ($p<0.001$).
In native space, the medial border of the right IFG was situated on average 1.34 mm more lateral than the left, and the lateral border of the right IFG 1.34 mm further lateral ($p<0.002$); in stereotaxic space, these differences were 2.20 mm and 1.97 mm ($p<0.0003$).
Overlap of IFGs in standard stereotaxic space was similar on the left and right; the volume occupied by at least 95% of IFGs was 7870 mm3 on the left and 8492 mm3 on the right; corresponding to 15% of the volume occupied by at least 5% in both cases.
The area occupied by at least 50% of IFGs was similar to the mean values (in brackets), 24898 (26319) mm3 on the left and 24537 (26937) mm3 on the right.
The anterior and superior extent of the IFG were more variable than the posterior and inferior extent (Figure 1).
Discussion and Conclusions:
We have shown subtle differences in IFG volume, composition and extent between men and women and right and left sides. Applications for this knowledge about IFG volume and position in stereotaxic space include probabilistic determination of location in group activation studies, automatic labeling of new scans, and detection of anatomical abnormalities in patients.

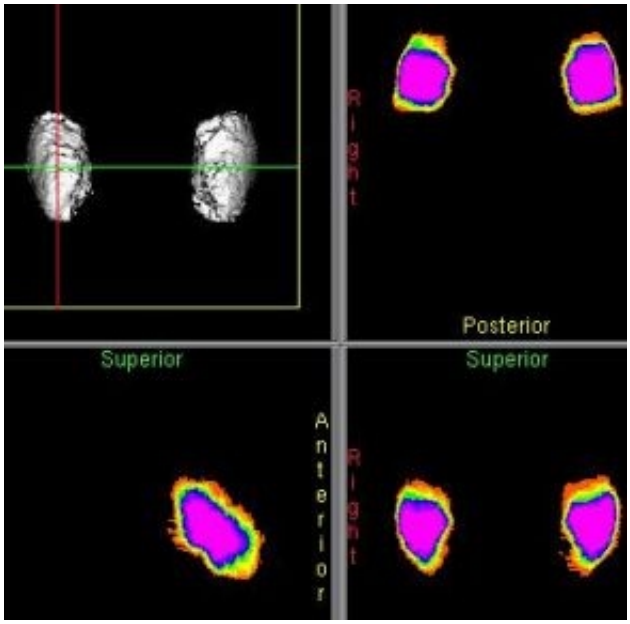

Probabilistic atlas of the human IFG. 3D render (top left), transverse (top right), sagittal (bottom left) and coronal slices (bottom right). The colourscale indicates increasing probabilities (10% steps) of encountering IFG in a given voxel.

WE 189

STRUCTURAL EQUATION MODELING AND MARKOV CHAIN MONTE CARLO IN ASSESSING BRAIN INTERACTIVITY

Stephen Hanson , Toshihiko Matsuka , Adi Zaimi , Catherine Hanson , Yaroslav Halchenko
RUMBA Labs, Psychology Department, Rutgers University

Graphical linear statistical modeling approaches, such as path analysis and structural equation modeling (Jennings, McIntosh, Kapur, 1998; McIntosh & Gonzalez-Lima, 1994), have been used with some success to investigate relations among brain areas that are active during the processing of a task. In general, these types of statistical technique are used to confirm a priori assumptions about a model, and the success of a given model is evaluated by how well the empirical covariance matrices can be reproduced. However, because these modeling approaches are not exploratory in nature, the potential role of brain areas that are not specified a priori is unknown. For fields with many uncertainties, such as neuroscience, analyses that are more exploratory could be very beneficial.In the present study, we conducted exploratory graphical modeling analyses without having any a priori assumptions or theories about relations among neural regions. In particular we investigated the activity of neural regions in a series of fMRI studies in which subjects were engaged in a task that would likely engage many perceptual and cognitive functions interactivtly. The task involved having subjects watch videos of action sequences and respond when they believed an event boundary had occurred. A cluster analysis of the fMRI data revealed 13 clusters common to all the subjects watching one sequence and 15 clusters common to subjects watching the other video sequence. Based on observed covariance matrices using the nine (out of 13 or 15) most activated neural regions, we created and evaluated 362880 (i.e., 9!) graphical causal models for each condition. We kept only the (directed) links that were statistically significant (Figure 3).The canonical model (based on the 1000 best models defined in terms of $\chi 2$ statistics) for neural activities observed for one video sequence is shown in Figure 4. In a second analysis, we fitted fully connected graphical models using an MCMC (Markov Chain Monte Carlo) method in order to compare to the exhaustive search and to fit larger networks efficiently. This method may be promising for the unbiased analysis of brain interactivity.

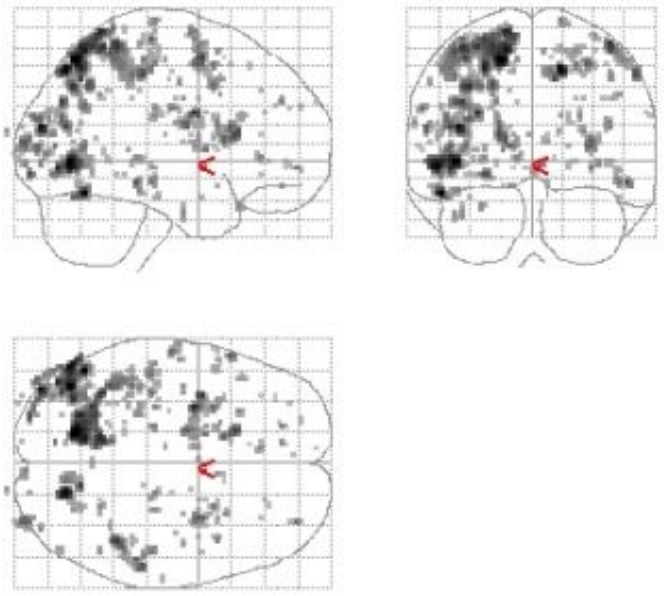

Brain map for Event Perception

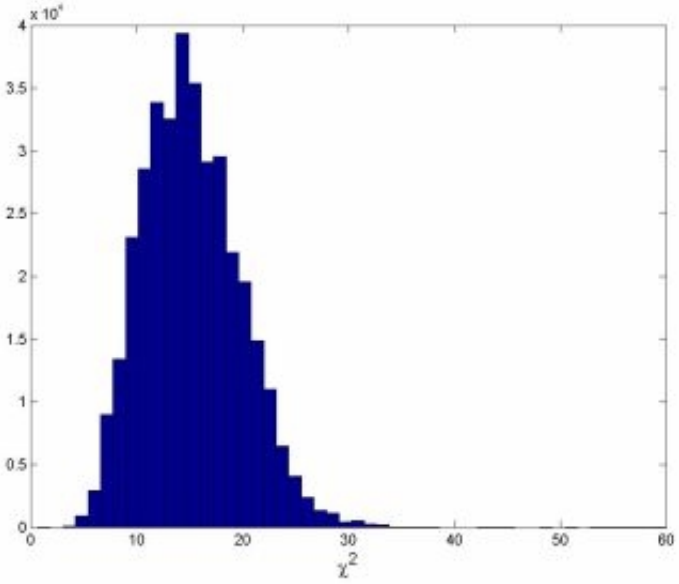

Chi Square fit Distribution to Covariance

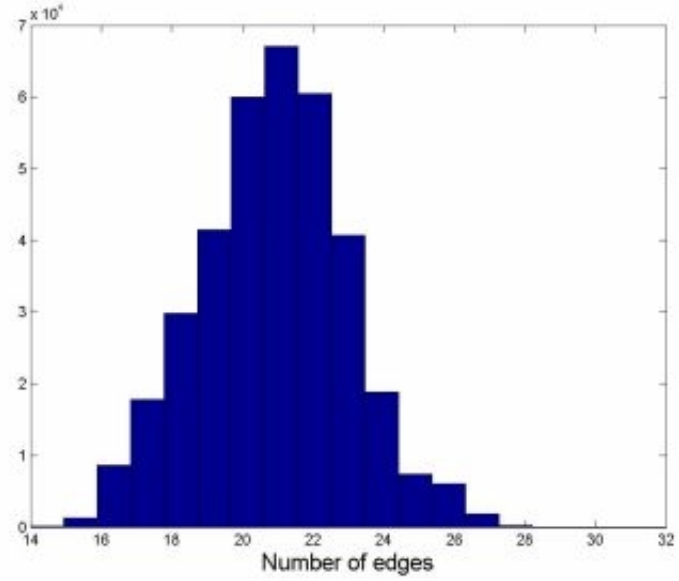

Network Edge distribution over 1000 fit networks

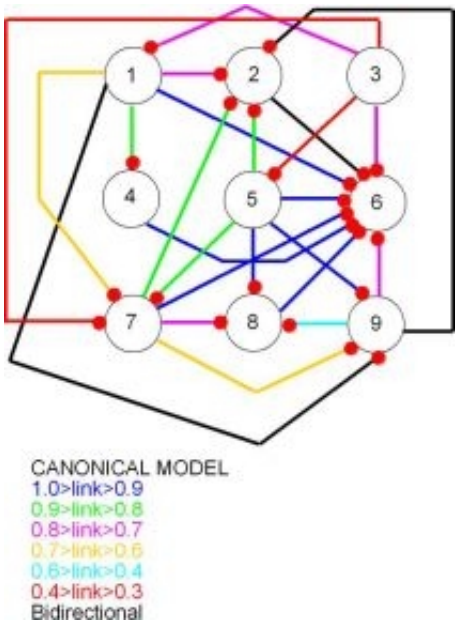

Canonical Network Fit to Event Perception Brain Map

WE 190
Bayesian Estimation of complex neuronal dynamics

Lee M Harrison , Olivier David , William Penny , Karl Friston
Wellcome Department of Imaging Neuroscience, Queen Square, London

Motivation
We have generalized Dynamic Causal Modeling (DCM) (1) to deal with arbitrary nonlinear dynamic systems. The aim is to extend the estimation procedure to cover models of ERP generation, which can then be used as observation models. This should enable estimation of meaningful biophysical parameters of neuronal architectures.
Background
DCMs have recently been used to model inter-regional interactions from fMRI time-series (1). DCMs parameterize interactions among regions of interest in terms of time constants of influence (coupling) among regions, using hemodynamic signals. This is achieved by modeling neuronal interactions in terms of differential equations and using a Bayesian estimation scheme to identify a sufficient model that explains the data. This constitutes a principled way of introducing assumptions and priors into the estimation procedure. The method can be generalized to any dynamic system and therefore DCMs of electrophysiological recordings are possible.
Method
Synthetic data generated from the nonlinear neuronal model (2), shown in figure 1, was used to estimate posterior densities over model parameters, which were compared to the actual values. The states x and y are coupled to each other through excitatory and inhibitory connections (where $\sigma(x)$ and $\rho(y)$ are sigmoid functions) and exogenous input drives the system into one of its dynamic regimes. These regimes depend on model parameters ($\Phi=\{\tau x, \tau y, a,b,c,d\}$) and include stable nodes and spirals, bistability and limit cycles. The parameters define the systems architecture and include time constants and coupling strengths.
Figure 2 shows the trajectory of the system about a stable spiral equilibrium point. Input to state x evokes a response in both states, which relax back to equilibrium through several oscillations. Noise has been added to this signal and is shown in figure 3.
A Bayesian estimation scheme uses priors over parameters ($p(\Phi)$)to be estimated and the likelihood of the data given the parameters ($p(D|\Phi)$) to calculate a posterior density over the parameters ($p(\Phi|D)$).
$p(\Phi|D) \sim p(D|\Phi)*p(\Phi)$
The posterior densities can then be used to make inferences based on the probability that the parameters are above a certain threshold. Priors on Φ were chosen within a physiological range with low precision.
Results
Posterior and prior densities compared well to actual values used to generate the data in figure 4. This accuracy was achieved using 256 data points in 33 iterations.
Discussion
The current study demonstrates a Bayesian estimation scheme for the system identification of nonlinear dynamics. Electrophysiological data can be modeled in terms of nonlinear oscillations and this work will be extended to include models of ERP generation (3). These models can be used as forward models of interactions among neurophysiological variables to account for observed ERPs.
Reference List
1. Friston, K.J. Bayesian estimation of dynamical systems: an application to fMRI. NeuroImage 16, 513-530 (2002).
2. Gillies,A., Willshaw,D. & Li,Z. Subthalamic-pallidal interactions are critical in determining normal and abnormal functioning of the basal ganglia. Proc. R. Soc. Lond B Biol. Sci. 269, 545-551 (2002).
3. David,O. & Friston,K.J. A neural mass model for MEG/EEG: coupling and neuronal dynamics. NeuroImage. 20, 1743-1755 (2003).

Model and schematic of interactions

$$\tau_x \dot{x} = -x + a\sigma(x) - c\rho(y) + I_x$$
$$\tau_y \dot{y} = -y - b\rho(y) + d\sigma(x) + I_y$$

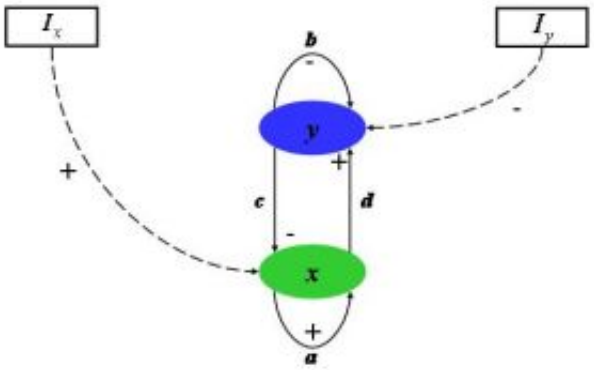

Nonlinear model used to generate synthetic data

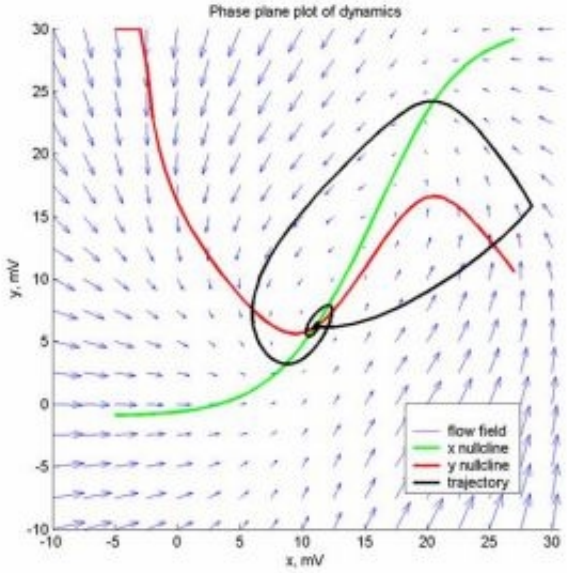

Trajectory of system through state space evoked by input to x

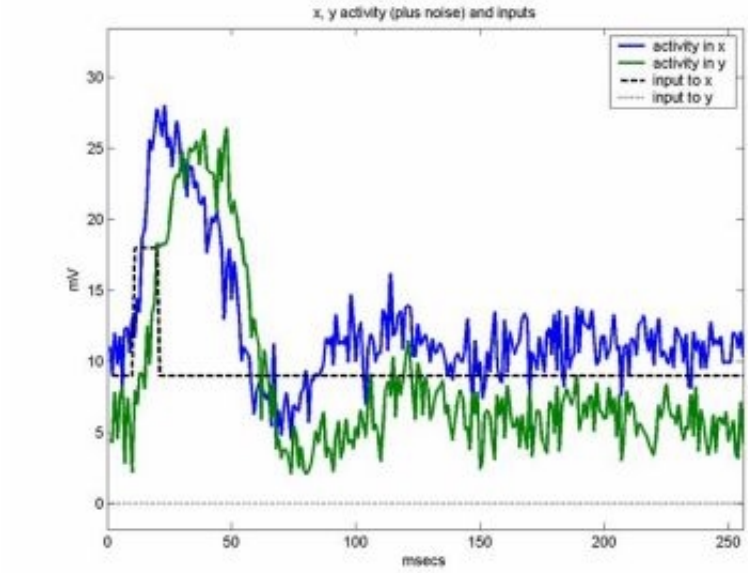

Time series of activity in x and y with additive noise

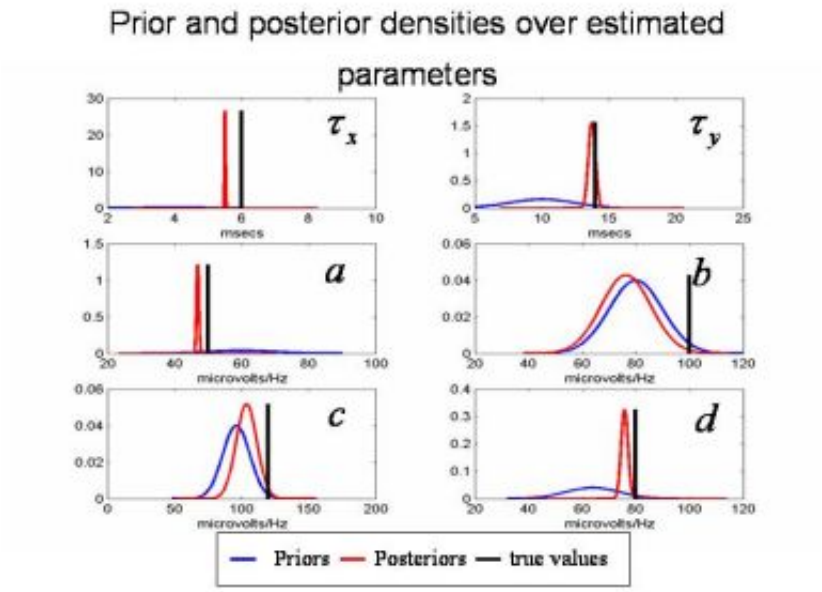

Comparison of prior and posterior densities with true parameter values

WE 191

Combining Voxel Intensity and Cluster Extent with Permutation Test Framework

Satoru Hayasaka[1], Thomas E Nichols[2]
[1]MR Unit, University of California, San Francisco / VA Medical Center, USA, [2]Department of Biostatistics, The University of Michigan, Ann Arbor, USA

Introduction: In a massively univariate analysis of fMRI data, statistical inference is based on intensity or spatial extent of signals. The former provides great sensitivity for high intensity signals, whereas the latter is sensitive to spatially extended signals. To benefit from the strengths of both, the intensity and extent information can be assessed jointly [1,2]. In this work, we study general methods for intensity-extent inference using combining functions [3] and permutation framework [4]. Furthermore, we propose meta-combining which combines combining functions and incorporates strengths of these functions into a single statistical test.

Methods & Materials: From a permutation test [4], corrected p-values for the peak intensity and extent of each cluster, P_i^t and P_i^s respectively, are obtained. Then three combining functions are calculated: Tippet $W_i^T = 1-\min(\log P_i^t, \log P_i^s)$, Fisher $W_i^F = -2(\log P_i^t + \log P_i^s)$, and cluster mass W_i^M [2]. The Tippet function is suitable when either P_i^t or P_i^s is significantly small, while the Fisher and cluster mass functions work well when both P_i^t and P_i^s are sufficiently small. Each of these combining functions is used as a test statistic in a permutation test, and corrected p-values are calculated for the Tippet, Fisher, and cluster mass combining functions as P_i^T, P_i^F, and P_i^M respectively. We additionally consider a meta-combining function $W_i^A = 1-\min(\log P_i^T, \log P_i^F, \log P_i^M)$ to be used as a test statistic in a permutation test.

The combined and meta-combined tests are applied to a second-level fMRI data set on working memory [5]. For each of 12 subjects, 528 images are acquired during working memory tasks, then a contrast image for item recognition versus control is calculated. The resulting 12 contrast images are analyzed in a one-sample t-test using the combining and meta-combining functions explained above.

Results: The critical regions from the different combined tests, as well as that of the voxel and cluster size tests are shown in Figure 1. Figure 2 shows the five activation clusters, including Clusters 1-4 in areas associated with working memory tasks [5]. For Clusters 1-3 where both intensity and extent are large, the Fisher and cluster mass tests have increased sensitivity (see Figure 3). Only the extent is significantly large for Clusters 4-5, and the Tippet test is the most sensitive of the three. The meta-combined test is sensitive to all of these clusters.

Conclusion: With a use of combining functions and permutation framework, we are able to develop tests sensitive to both high intensity and large extent signals. Though none of our combining functions dominate over the other, our meta-combining function is able to incorporate the strengths of individual combining functions into a single valid statistical test.

Acknowledgment: The authors would like to thank Dr Christy Marshuetz for providing the data set.

Reserences:

[1]Poline et al. NeuroImage 5:83-96(1997)
[2]Bullmore et al. IEEE Trans Med Img 18:32-42(1999)
[3]Pesarin. Multivariate Permutation Tests. Wiley.(2001)
[4]Holmes et al. JCBFM 16:7-22(1996)
[5]Marsheutz et al. J Cog Neuro 12(S2):130-144(2000)

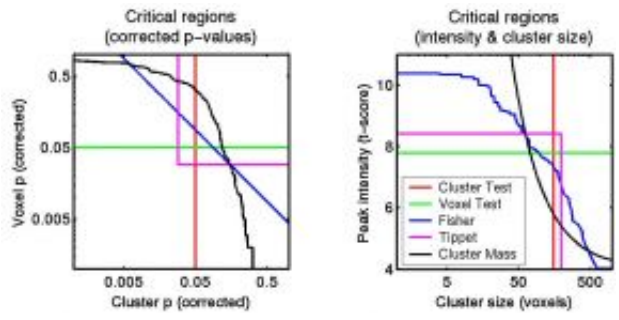

Figure 1 Critical regions for the three combined tests, as well as that of the voxel and cluster size tests. The left panel shows the regions in terms of p-values, while the right panel shows in terms of intensity and cluster size. Though all these critical regions have 0.05 significance level, they apportion this 0.05 probability differently.

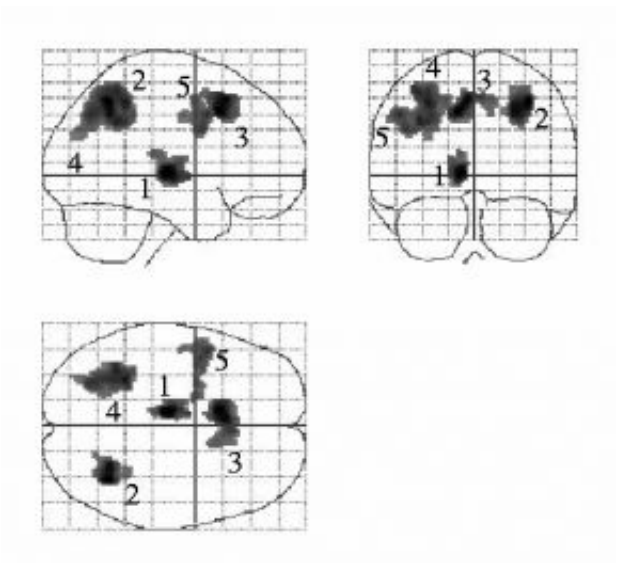

Figure 2: Results from the data analysis. Activations are found in the bilateral posterior parietal (2,4), left thalamus (1), and anterior cigulate (3) regions which are typical of working memory studies, as well as in the left pre-motor region (5).

Cluster	Size (voxels)	p-values Cluster	Fisher	Tippet	Mass	Meta	Peak	T^*
1	345	0.010	0.001	0.001	0.003	0.001	0.001	13.15
2	529	0.005	0.002	0.009	0.001	0.001	0.007	10.19
3	520	0.005	0.002	0.009	0.002	0.003	0.012	9.37
4	1138	0.001	0.004	0.001	0.001	0.001	0.083	7.36
5	436	0.006	0.021	0.011	0.012	0.016	0.208	6.31

Figure 3: P-values from the various tests in the working memory data analysis

WE 192
Mapping Functional Connectivity Network in the Cerebellum with Resting State MR Images

Yong He[1], Yufeng Zang[1], Tianzi Jiang[1], Xuemei Guo[2], Jiangxi Xiao[2], Sheng Xie[2]
[1]National Laboratory of Pattern Recognition, Institute of Automation, Chinese Academy of Sciences, Beijing 100080, P. R. China, [2]Department of Radiology, Peking University First Hospital, Beijing 100034, P. R. China

Introduction
So far, resting state functional connectivity (RSFC) has been performed mainly by seed voxel correlation analysis (SVCA). In these studies, the seeds are usually selected on the basis of prior anatomical information [1] or previously performed activation maps [2]. Here, we propose a novel way to select the desired seeds by taking the natures of resting state data into account. The proposed approach is based on the measurement of regional homogeneity (ReHo) of brain regions [3]. Using this technique, we identify the seeds located in the cerebellum and ascertain their RSFC patterns.

Method
FMRI studies of 34 healthy, right-handed volunteers (25 males; age range 22-40, mean 26.2) were performed with a 1.5-Tesla GE Signa scanner. Each subject was scanned for 400s in a resting state. Functional images were acquired axially using the following parameters: 2000/40 ms (TR/TE), 20 slices, 5-mm-thickness, and 1-mm gap. First, image preprocessing [realignment, spatial normalization, spatial smoothing and temporal filtering above 0.08 Hz] was carried out by using spm2 and AFNI package. Next, Kendalls coefficient of concordance (KCC) is used to measure ReHo of a cluster [3]. Individual KCC maps were obtained on a voxel by voxel basis and then entered into a random-effect model. The resulting t-map was used to identify the seeds located in the cerebellum. Finally, the seeds were used to map RSFC network of the cerebellum by SVCA. The differences of connectivity patterns between the bilateral cerebellums were explored by a paired t test.

Results and Conclusions
In this study, the bilateral anterior-inferior cerebellum (AICb) showed higher ReHo (Fig.1) and served as the seeds for RSFC analysis. Fig.2 shows RSFC network of the right AICb, including the left AICb, the bilateral thalamus, the bilateral hippocampus, the posterior cingulated cortex, the bilateral precuneus and the temporal lobe. Fig.3 indicates the differences of RSFC patterns between the bilateral AICb. The right AICb showed more significant connectivity with the bilateral temporal lobe, the medial prefrontal cortex, the right precentral gyrus and the left postcentral gyrus, while the left AICb showed more with the bilateral thalamus and the right superior frontal gyrus.

Here, we successfully mapped RSFC network of the cerebellum using a novel approach, the most prominent feature of the approach distinguished from the existing counterparts is that it fully utilizes valuable information resulting from resting state data during selecting the seeds.

References
[1] Stein T et al. (2000): Am J Neuroradiol. 21:13971401.
[2] Biswal B et al. (1995) Magn Reson Med 34:537541.
[3] Zang YF et al. (2004) NeuroImage, in press.

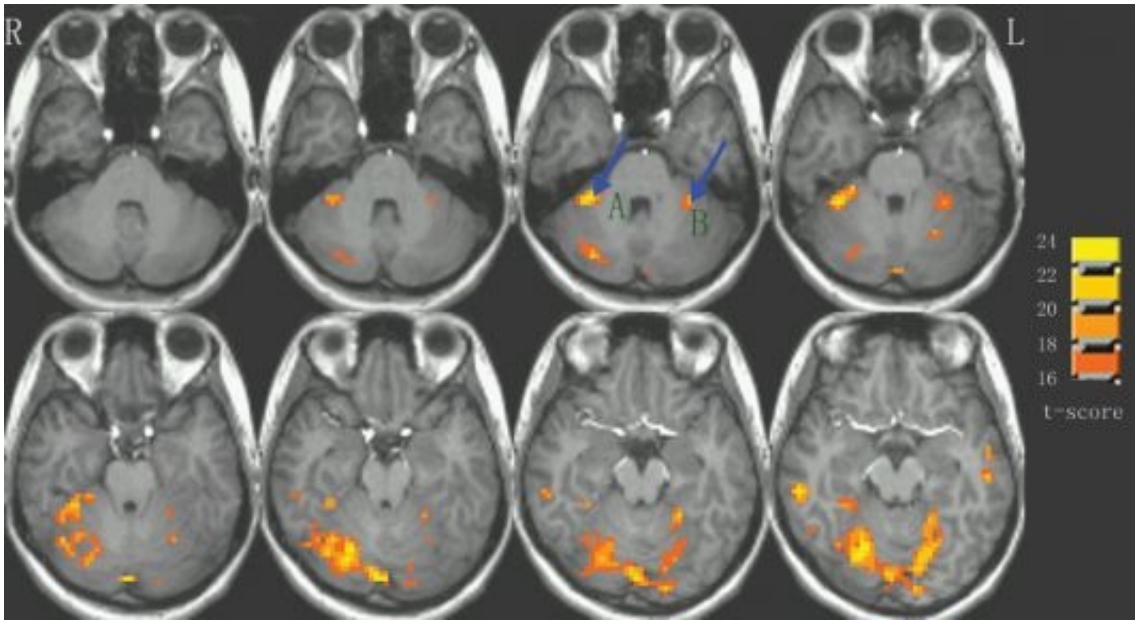

Fig.1 A group t-map based on the KCC maps (t>15.52, P<10^{-16}).

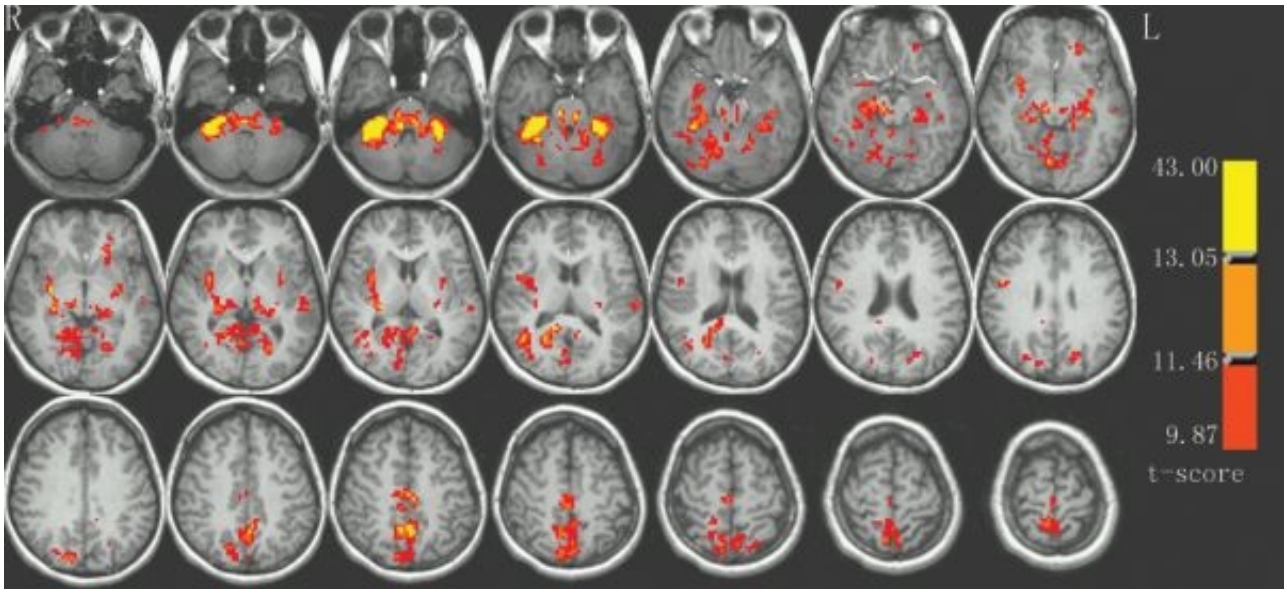

Fig.2 RSFC network of the right AICb (t>9.92, P<10^{-11}).

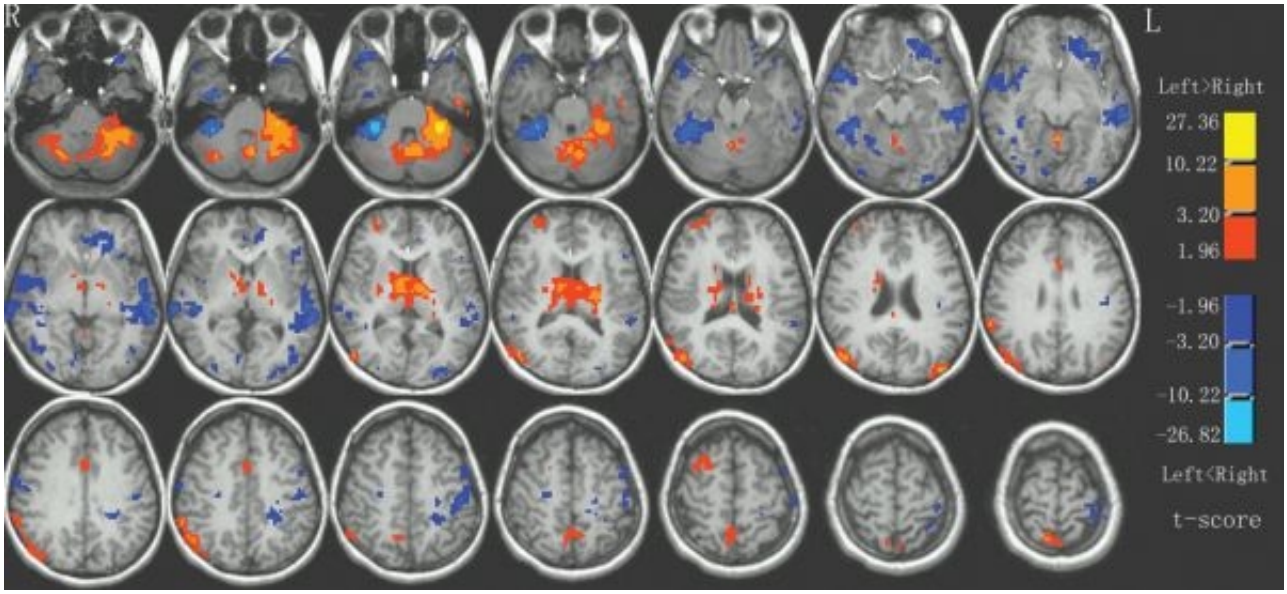

Fig.3 Paired t-test for the difference of RSFC patters between the bilateral AICb (|t|>2.04, P<0.05).

WE 193
NeuroLens: an integrated visualization and analysis platform for functional and structural neuroimaging

Richard Hoge , Anthony Lissot
A.A. Martinos Center for Biomedical Imaging, Charlestown MA USA

We have developed an interactive program for image display and analysis using an object-oriented approach, based on the 'Model-View-Controller' (MVC) design pattern [1]. This strategy has facilitated support of multidimensional image data stored in arbitrary file formats. It also allows highly interactive analysis sessions, with rapid user feedback of results, as well as incorporation of interactively designed analysis steps into automated processing pipelines. One of the primary design goals was to provide flexible and immediate display of unprocessed image data, with addition of higher level functionality in a modular, layered fashion using a plugin architecture. The application was implemented in Objective-C for Apple computers based on the G4 (Motorola Inc.) and G5/970 chipsets (International Business Machines) running the MacOSX operating system and using Apple's Cocoa frameworks (formerly NeXTStep).

The core NeuroLens application handles loading, management, and display of multidimensional datasets represented using a simple but carefully designed 'data model' that is file-format independent. Any number of disk storage formats may be supported by subclassing the data model object class and providing custom read methods (currently this approach has been used to support DICOM, MINC, AFNI, COR, bshort, and Analyze formats). Datasets containing two, three, or more dimensions of scalar or vector image values are seamlessly integrated into the data model and visualization layer, while all processing operations are encapsulated outside the core application as plugin modules.

Through aggressive optimization of analysis modules using the vector processing unit (AltiVec) present on the G4 and G5 chips used in Apple computers, it was possible to accelerate the processing steps required for generation of functional activation maps to the point where motion-correction, 3D spatial smoothing, and generalized linear model (GLM) fitting can be performed on an image series containing 180 time points and 24 slices on a 64x64 matrix in under 30 seconds (dual 2GHz G5, 2GB RAM) with immediate visualization of intermediate results in a concise display format. To compare performance with other analysis implementations and platforms, we wrote an AltiVec-based implementation of the motion correction algorithm used in AFNI [2] and compared execution times to a non-AltiVec (scalar) version on an Apple dual 2GHz PowerPC G5 running MacOSX 10.3.1 and a dual 2.8GHz Pentium Xeon system running RedHat Linux (kernel 2.4.18). Execution times for the reference dataset described above (with moderate motion) were 8.3s (AltiVec/G5), and 13.8s (scalar/Xeon), 17.2s (scalar/G5). Single-threaded versions were used here, to focus on the relationship between processor model and speed; multi-threaded implementations yielded slightly less than a factor of two increase in speed, due to overhead. Increases in speed with the AltiVec-enabled version were significant on older Apple systems; time to align the reference dataset on an 800MHz single-G4 PowerBook using AltiVec-based code was 34s, compared to 54s using the scalar implementation on the same machine.

References:

1) E. Gamma, R. Helm, R. Johnson, and J. Vlissides. Design Patterns. Addison-Wesley (1995).
2) R. Cox and A. Jesmanowicz. Real-Time 3D Image Registration for Functional MRI. Magn. Reson. Med. 42:1014 (1999).

WE 194
Identification of Brain Activity in a Visual Simulation Task --An Adaptive ICA Approach for fMRI Data

Baoming Hong[1], Godfrey D. Pearlson[1,2,3], Eric. A. Egolf[1], Vince D. Calhoun[1,2,3]
[1]Olin Neuropsychiatry Research Center, Institute of Living, Hartford, CT 06106, [2]Dept. of Psychiatry, Yale University, New Haven, CT 06520, [3]Dept. of Psychiatry, Johns Hopkins University, Baltimore, MD 21205

Introduction: Independent component analysis (ICA) has become a popular tool for fMRI data analysis. Typical ICA models assume that the independent sources have similar distributions. For example, the probability density functions of the underlying sources are usually assumed as highly kurtotic and symmetric [1,2]. This assumption is inconsistent with the real situation of fMRI data for analysis of event-related task [3,4]. There have been some efforts to modify underlying assumptions in ICA to be more suitable for fMRI data analysis [3,4,5,6]. However, these modified ICA approaches still use fixed contrast functions. Due to source differences and individual variability, using fixed contrast functions may not be optimal for the fMRI data analysis. In this paper, we propose an adaptive density estimation-based ICA method for application to the fMRI data processing.
Methods: The central idea of our method is to use a three-stage separation process: 1) Standard Infomax ICA for initial statistically independent source estimates; 2) Kernel estimator for estimation of the probabilistic density of these sources; 3) Source density-based optimal nonlinearities for the final separation. Different channels can have different nonlinearities for source separation. We use hyperbolic tangent as the nonlinear function for modeling symmetric distributions and the Log Weibull distribution as a model family for skewed distributions. For different sources, the distribution parameters are calculated from the initial ICA signal estimate for all channels. These parameters are subsequently used in the proposed algorithm such that an optimal contrast function is used in the corresponding channel for the final source estimation stage. For the fMRI data, the source images of interest containing local features such as vascular activity usually occupy very little part on the homogeneous background. To emphasize the importance of these local features, we further introduce a histogram enhancement transformation [7] on the located region of interest obtained by the initial ICA algorithm.
Results: The experimental data included eight participants with left/right/fixation visual checkboard experimental paradigms scanned on a 1.5T Philips scanner [8]. Figure 1 shows the result from one subject for the proposed algorithm and standard infomax ICA. The correlation between the ICA time courses and standard models shows the proposed method has a higher correlation value and a bigger activation region relative to infomax ICA.
Discussion: It is clear that flexible modeling approaches are useful for understanding fMRI data. The potential of ICA methods can be fully realized by incorporating physiologically realistic prior information (e.g., skewed distribution [3,4]). We demonstrate that an adaptive ICA method improves performance compared to the infomax ICA method.
References: 1. McKeown M, *et al., Pro. Natl. Acad. Sci. USA* 95:803-810 (1998), 2. Calhoun V, *et al., HBM* 13:43-53 (2001), 3. Suzuki K, *et al., HBM* 15:54-66 (2001), 4. Stone J, *et al., NeuroImage* 15:407-421 (2002), 5. Nakada T, *et al., Neurosci Res.* 37:237-244 (2000), 6. Biswal B, *et al., J. Comput Assist Tomogr* 23:265-271 (1999), 7. Gonzalez R, *et al.*, Digital Image Processing, Pearson Education, Inc. 8. Calhoun V, *et al., HBM* 14:140-151 (2001)

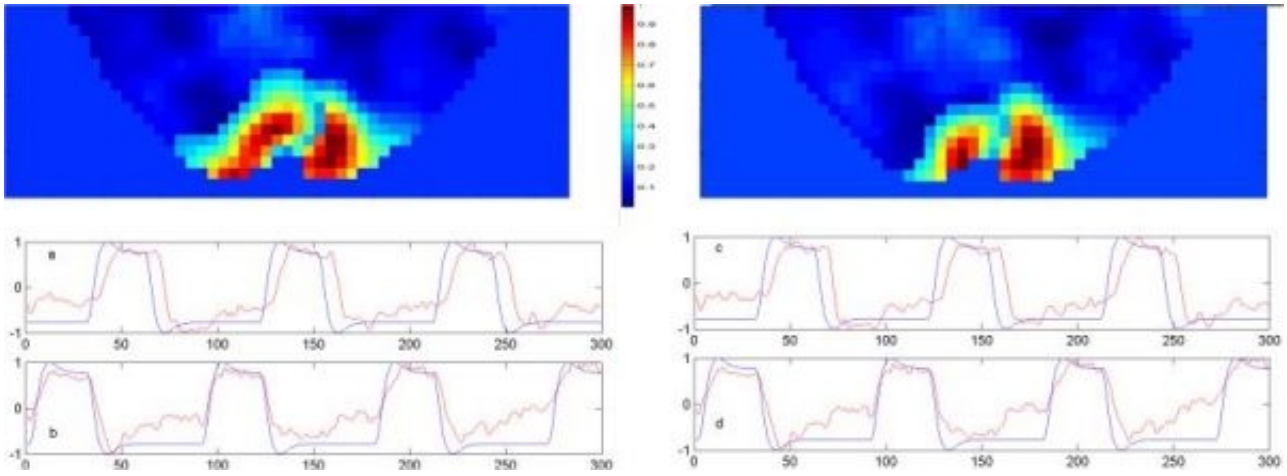

Figure 1: Areas and time courses identified by ICA on a single slice in occipital cortex (left: Adaptive ICA; right: Infomax ICA). The correlations between ICA fitting models (denoted in red) and standard models (denoted in blue) in the left and right visual hemifield are respectively 0.8580 and 0.9400 (for adaptive ICA) and 0.8514 and 0.9210 (for standard ICA).

WE 195
The Neurobiological Substrates of fMRI Functional Connectivity

Barry Horwitz[1], Brent Warner[1], Julia Fitzer[1], M.-A. Tagamets[2], Fatima T. Husain[1], Theresa W. Long[1,3]
[1]Brain Imaging & Modeling Section, NIDCD, NIH, Bethesda, MD USA, [2]Psychiatric Research Center, Univ. Maryland School Medicine, Baltimore, MD USA, [3]Imagenet, Inc., Williamsburg, VA USA

Viewing cognitive functions as mediated by networks of interacting brain regions has begun to play a central role in interpreting neuroscientific data, and studies evaluating functional and effective connectivity are becoming staples of the neuroimaging literature. The neurobiological substrates of functional and effective connectivity, including their relation to anatomical connectivity, are, however, uncertain. Functional connectivity for fMRI, determined by correlating fMRI activities between two regions, provides information about how hemodynamic/metabolic activity in one region influences activity in other regions. Although it is often discussed in terms of the interrelationship between neural activities, to do this requires knowing the neurobiological substrate of fMRI functional connectivity. We have constructed large-scale, biologically realistic, neural models for visual and auditory object processing with multiple interconnected brain regions that perform delayed match-to-sample (DMS) tasks; the simulated electrical activities in each region are similar to those found in single-cell monkey data, and the simulated integrated synaptic activities match human brain imaging data. We used these models to investigate how neurobiological parameters affect the interregional functional connectivity between fMRI timeseries.

The simulated experimental conditions are a matching task (visual shape or tonal pattern) with a delay period, and a control task using noise stimuli. The regions comprising the model represent the object processing stream: primary and secondary cortex, anterior temporal cortex (IT or STG) and prefrontal cortex (PFC). The models basic neural element is an excitatory-inhibitory interacting pair of units representing a cortical column, with intra- and inter-regional connections based on primate neuroanatomical data. Instructions as to what task to perform are mediated via an attentional unit making diffuse synapses onto PFC units, which in turn have feedback connections to posterior cortex. The fMRI response is simulated by temporally and spatially integrating the absolute value of the synaptic activity in each region over the time needed to acquire a slice of data (50 msec) and convolving this with a hemodynamic response function. To generate functional connectivity, variability is included in the models as subject-to-subject differences in the strengths of anatomical connections, scan-to-scan changes in the level of attention, and trial-to-trial interactions with nonspecific neurons processing noise stimuli.

Under optimal conditions, timeseries correlations between integrated synaptic activities between IT (or STG) and PFC were smaller during the control task than during the DMS task. These results were less clear when the integrated synaptic activity was hemodynamically convolved to generate simulated fMRI activity. As the strength of the anatomical connectivity between IT (or STG) and PFC was weakened, so too was the strength of the corresponding functional connectivity. Thus, for two anatomically linked brain regions, the strength of the functional connectivity between them depends on the strength of their anatomical connectivity (as embodied in the synaptic weights), and also on the extent to which the circuit in which the two regions are nodes is being utilized. These simulation results hence provide a partial validation for using fMRI functional connectivity to assess brain interregional relations.

WE 196
A Temporal Comparison of Simultaneously Acquired BOLD fMRI and Near-Infrared Spectroscopy (NIRS) Hemodynamic Response Functions

Ted J. Huppert , Rick D. Hoge , Maria Angela Franceschini , David A Boas
Athinoula.A. Martinos Center for Biomedical Imaging. Massachusetts General Hospital. Harvard Medical School, Building 149 13th St. Charlestown, Massachusetts 02129 USA.

1. Introduction:
In recent years, a number of studies have been published comparing hemoglobin concentration changes measured with NIRS and BOLD-fMRI signals in humans [1-3]. While all theoretical studies to date support the expectation of a strong correlation between deoxy-hemoglobin and BOLD, due to insufficient temporal resolution and low SNR in both the NIRS and fMRI signals, this issue remained experimentally controversial. In some publications, better temporal correlation between oxy-hemoglobin and BOLD had been reported [1,4], while others [3] showed better correlation between BOLD and deoxy-hemoglobin. In this study, an event-related finger-tapping paradigm was used to present a large number of stimuli, which allowed improvement of the SNR over previous studies. Additionally, the brief activation periods allowed for better temporal comparisons showing a strong correlation of BOLD with deoxy-hemoglobin.
2. Methods:
Acquisition:
In this study, healthy subjects (ages 18-64) were examined. During data acquisition, subjects were instructed with a visual cue to sequentially tap their thumb and fingers on their dominant hand at a self-paced rate (approximately 2-3Hz) for duration of 2 seconds. NIRS optical measurements were made using the CW4 system [5]. In these experiments, a rectangular geometry probe consisting of 8 detector and 4 source positions was used. Laser wavelengths were chosen to minimize cross-talk between the two hemoglobin species (690nm; 830nm) [6]. Source-detector separation distance was 2.9cm. BOLD fMRI measurements were taken using a Siemens Allegra MR scanner (2.9T). Data was taken with a gradient echo EPI sequence [TR=500ms; TE=30ms; è=90o].
Data processing:
Optical data, collected at 40kHz, was low-pass filtered below 10Hz using a custom iirfilter. Changes in optical density for each source-detector pair were then calculated using a 1/60 Hz high-pass filtered drift correction and further converted to change in concentration using the modified Beer-Lambert relationship. Individual subject data was deconvolved against the impulse train and averaged across runs. Region of interest averages were then taken from all active source-detector channels across subjects. Functional MRI data were motion corrected as described in [7], spatially smoothed using a 6mm FWHM Gaussian filter, and deconvolved within the motor cortex ROI.
3. Results:
Figure 1 shows the typical hemodynamic response recorded via both modalities. The response functions begins within 1-3 seconds following the start of subject finger tapping, with the expected increase in oxy-hemoglobin preceding deoxy-hemoglobin by approximately 1.5 seconds. This temporal delay had been previously reported [8,9] and is associated with the transit time from arteries to veins. A cross-correlation comparison between normalized BOLD and optical response profiles showed significant for the period 0-15 seconds post-stimulus and yielded R-values of 0.781, 0.976, and 0.636 for the zero-lag coefficients between HbR/BOLD, HbO/BOLD, and HbT/BOLD respectively [p-values = 3.47e-7; 5.52e-20; 1.65e-4]. The BOLD response was also shifted by the same 1.5 seconds relative to the onset of the oxy-hemoglobin response and aligned fully with the deoxy-hemoglobin profile.
[1] Neuroimage 17: 719 (2002).
[2] J Cereb Blood Flow Metab. 16: 817 (1996).
[3] Med Phys. 28:521 (2001).
[4] J Appl Physiol. 90:1657 (2001).

[5] Psycophysiology. 40:548 (2003).
[6] Neuroimage. 18:865 (2003).
[7] Magn Reson Med. 42:1014 (1999).
[8] Neuroimage. 20:479 (2003).
[9] Neuroimage 16:704 (2002).

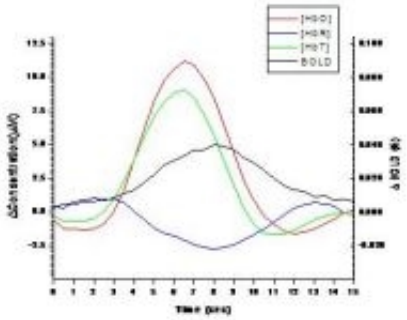

Figure 1: The response functions of hemoglobin concentrations and BOLD for event-related finger tapping as measured through simultaneously acquired fMRI-BOLD and NIRS optical recordings of the primary motor cortex.

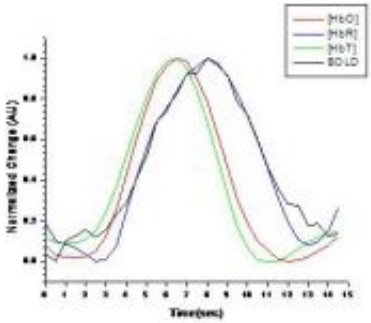

Figure 2: Normalized and rescaled response functions for the event-related finger tapping to allow visualization of the four variables on the same linear scale. The deoxy-hemoglobin data has also been inverted.

WE 197
Automated Topological Correction of Cortical Surfaces

Monica K. Hurdal
Department of Mathematics, Florida State University, Tallahassee, FL 32306-4510, U.S.A.

Locations and patterns of functional brain activity are difficult to compare across subjects because individual differences in cortical folding and functional foci are often buried within cortical sulci. Cortical flat mapping can address these problems by taking advantage of the two-dimensional sheet topology of the cortical surface and may facilitate the recognition of structural and functional relationships that were not previously apparent. Many flat mapping algorithms have been applied to cortical data [1-4]. All require a topologically correct two-manifold (i.e. a topological sphere or disc) triangulated mesh representing the cortical surface. Few algorithms produce topologically correct surfaces and widely used algorithms, such as marching cubes/tetrahedra algorithms, produce surfaces with topological errors. Thus, there is a need for methods that detect and repair topological problems in surfaces. Algorithms which meet this need are presented here.

Methods

A piecewise flat, topologically correct triangulated surface consists of flat triangular faces connected along edges. Each edge is an interior edge (contained in exactly two triangles) or a boundary edge (contained in exactly one triangle). If there are no boundary edges, the surface is a topological sphere; if the boundary edges form a single closed boundary component, the surface is a topological (closed) disc. Typical topological problems include non-manifold edges (i.e edges which occur more than two times), holes (i.e. more than one boundary component), handles and multiply-connected components.

A surface's Euler characteristic is defined by $\chi(S) = v - e + t$; the genus of a surface, g(S), yields the number of handles and satisfies $\chi(S) = 2 - 2g(S) - m(S)$, where v, e, t and m(S) are the numbers of vertices, edges, triangles and boundary components of the surface respectively. If a surface is topologically correct, then it is a topological sphere if and only if $\chi(S) = 2$; it is a topological disc if and only if $\chi(S) = 1$. This paper presents algorithms that detect and repair topological problems by using these topological invariants. The algorithm for correcting non-manifold edges examines the surface complex; surface components are detected using a region growing algorithm and surface handles are detected by examining how the Euler characteristic changes during the region growing algorithm. Surface holes are detected and repaired by examining the extra boundary components.

Results and Conclusions

This paper presents algorithms which have been developed for automatically detecting and correcting topological errors in triangulated surfaces. These algorithms have been used successfully on cortical surfaces generated from a variety of algorithms. Software is available that can read in and output surfaces in a variety of file formats (including byu, obj, vtk, CARET and FreeSurfer). Applying these algorithms to cortical data will speed up the processing pipeline for creating surfaces which are topologically correct.

References

[1] Drury, H.A. *et al.* 1996. *J. Cog. Neuro.* **8:**1--28.
[2] Fischl, M.I. *et al.* 1999. *Neuroimage* **9:**195--207.
[3] Goebel, R. *Neuroimage* **11:**S680.
[4] Hurdal, M.K. *et al.* 1999. *Lecture Notes in Computer Science* **1679:**279-286.

Acknowledgments

This work is supported in part by NSF grant DMS-0101329 and NIH grant P20 EB02013.

WE 198
Parallel design and implementation for cortical surface inflation on a Linux cluster system

Ki-Ho Im , Jong-Min Lee , In-Young Kim , Sun-Il Kim
Department of Biomedical Engineering, Hanyang University, Seoul, Korea

Background:
The surface of the human cerebral cortex is a highly folded sheet with the majority of its surface area buried within folds. The cortical surface inflation has been suggested for visualization and analysis of structural and functional properties of the cerebral cortex (B. Fischl et al, 1999). The surface inflation can also provide the feature of brain surface which can be used for cortical surface registration. The inflation process that optimizes a cost function spends a lot of computation time. In order to reduce the execution time and facilitate the analysis, we have parallelized inflation algorithm using Message Passing Interface (MPI) that is practicable on a Linux cluster.
Materials and Methods:
In this study, surface model was generated by ASP algorithm (D. McDonald et al, 2000). In optimization process to inflate the surface model, the computation of cost function spent about 90% of the execution time approximately. Computing cost function was parallelized as a SPMD (Single Program Multiple Data) model. Every node in the cluster holds the model data and executes the same computation but just computation of cost function is distributed to each node (Fig 1). Parallelization was designed not only to prevent communication overhead but also to minimize load unbalance using block distribution method.
Results:
We have parallelized inflation process with two types of surface model, which are 20,480 triangles model and 5,120 triangles model. The parallel computing has been performed on an IBM Linux cluster 1350 with 9 nodes, which are IBM eServer xSeries 335 model. Speedup as s= T1/Tp was measured, where Tp is the time it takes using the parallel algorithm on p processors. The efficiency is defined as e=s/p. In case of 20,480 triangles model on 8 nodes, the results showed that parallelized inflation process was performed within 8.5 hours whereas a sequential process took 45 hours. Speedup was 5.4 and efficiency was 0.68.
Conclusion:
The parallel processing achieved the result of surface inflation successfully and effective speedup and efficiency. Speedup increased as the number of computing nodes and the size of model data increased. By means of Amdahls law (G. Amdahl, 1967), the parallelized actual fraction of inflation process was 0.93 for 20,480 triangles model and was nearly equal to the theoretically expected fraction of 0.9. It means that the inflation process which takes a great deal of computing time was parallelized efficiently without load unbalance and communication overhead nearly. Reducing the execution time of cortical surface inflation facilitates the research of analyzing structural and functional properties and acquiring the feature of brain surface. The feature of brain surface can be used for cortical surface registration, which helpful for surface-based analysis. In addition, the inflation process is similar to the concept of the deformable model that can extract cortical surface. The extraction of cortical surface also takes a very long time. It is possible and useful to apply parallelization to the deformable model algorithm in the future.

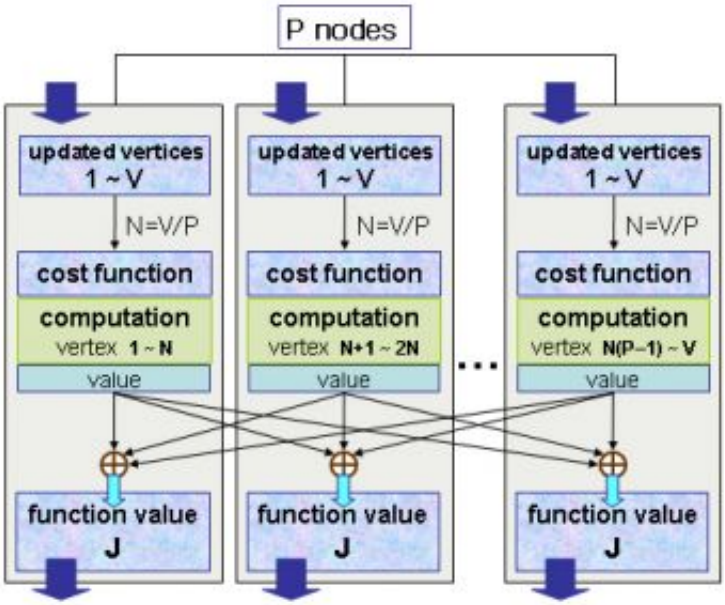

Fig. 1: ***Parallelization of computing cost function***

WE 199
A bottom-up approach for fMRI and NIRs fusion. II- Application to real data

Kazuki Iwata[1,2], Jorge Riera[1,2], Ryuta Kawashima[2]
[1]LBC Research Center, Tohoku University 21st Century Center of Excellence Program in Humanities, Japan,
[2]New Industry Creation Hatchery Center, Tohoku University, Japan

Introduction
The simultaneous recording of fMRI and NIRs represents nowadays an advanced technique to explore brain activations, which make best use of high temporal-spatial resolution. However, due to complexity and cost it is far from practical use. Additionally, there is a dilemma related to methodological and technological restrictions that resided in the physical basis of BOLD signal acquisition and in the inverse problem rising from the optical tomography. Therefore, in this paper, a new methodology to properly use data obtained from separated observation of BOLD and optical signals is proposed on the basis of: a)- a ROI selection criterion based on images standardization, b)- non-linear regression to remove signal drifts, c)- the introduction of a factor that control the effective transparency of capillary bed and d) finally, using of a bottom-up model for a common non-linear dynamics, where physiological parameters are fitted by using LL filter strategy.

Methods
Eight right-handed normal volunteers participated in the study. Each subject was asked to perform visually cued right-hand movement tasks as indicated in the figure (a). The task was repeated 4 times guarantying a counterbalance among subjects. For each task, different opening/closing frequencies (0.5, 1.0, 1.5, or 2.0 Hz) were allocated. NIRs (ETG-100, Hitachi Medical Corp.) and fMRI (1.5-T, Siemens Vision) data were obtained on separate occasions while subjects perform exactly the same task.
Individual fMRI and T1-anatomical/brain images were co-registered and normalized using both linear and nonlinear transformations provide by SPM99. T-test statistical mappings were obtained for each experimental condition after specifying the appropriate design matrix to assess the hemodynamic responses and applying the GLM and Gaussian fields theory (Fig. d). Low-frequency drifts were removed from BOLD signals using SPM. In order to determine the ROI in the primary motor area (M1), the correlation between brain activation and movement frequency was examined. A sphere with 10mm-diameter and centered at hot-spot in M1 region represents the ROI (Fig. b). The BOLD signals were averaged in the ROI for each subject/task condition.
The optical probes were fixed on the scalp, covering the expected M1 area based on the results of fMRI. The positions of probes were measured by a 3D-digitizer (Polhemus Isotrack II) and projected on each normalized T1-anatomical/brain image (Fig. b). The HbO and dHb topographs for each task condition were constructed by spatially-interpolating the mean value of HbO and dHb concentration data. A normalized 2D-topographic map of HbO and dHb, virtually projected on the cortex, were obtained for each subject/condition (Fig. d). The nearest middle point (transmitter/receiver pair-probes) to the ROI was selected for each subject. The drift, which was significant for NIRs data, was removed using non-linear polynomial regression (Fig. c).

Results and conclusion
The BOLD and HbO Signals were significantly correlated to movement frequency as shown in the figure (d). It was found that BOLD and HbO signals followed very similar temporal-patterns. The factor of capillary visibility and other physiological parameters were estimated from data fusion using the LL filter.

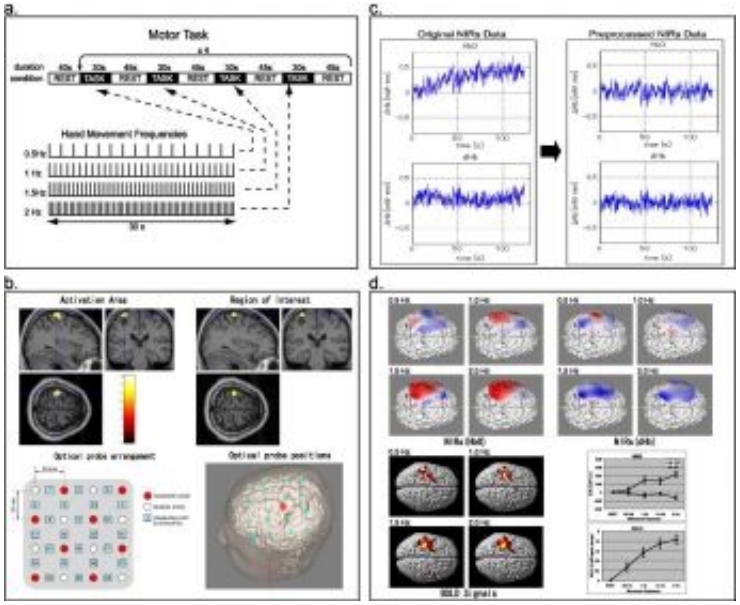
a.
Motor Task
Hand Movement Frequencies
0.5 Hz
1 Hz
1.5 Hz
2 Hz
30 s
b.
Activation Area
Region of Interest
Optical probe arrangement
Optical probe positions
c.
Original HRRs Data
Preprocessed HRRs Data
d.

WE 200
Non-linear hemodynamics: The spatial distribution of Balloon model parameters

Daniel J. Jacobsen[1], Lars Kai Hansen[1], Thomas Deneux[2], Olivier Faugeras[2]
[1]Technical University of Denmark, Denmark, [2]INRIA Sophia Antipolis, France

Background
Understanding the hemodynamic response is fundamental to fMRI-based neuroimaging. Buxton et al. proposed the Balloon model (Buxton et al., 1998) which represents the BOLD response in a non-linear state-space form. The model parameters can be estimated from data. Various parameter estimation approaches have been pursued including Volterra kernels (Friston et al., 2000) and Kalman filters (Riera et al, 2003). The main focus has been to investigate the response to given stimuli, locate the activated regions, and understand the global distribution of the hemodynamic parameters. In this communication we are interested in the spatial distribution of Balloon model parameters, their identifiability and possible interdependency.
Methods
We analysed a visual stimulus fMRI BOLD contrast data set acquired by Dr. Egill Rostrup, Hvidovre Hospital, (TR=333ms, see Hansen et al .1999 for more details of this data set), using the Kalman Filter implementation of Nørgaard et al. (2000, http://www.iau.dtu.dk/research/control/kalmtool.html). The Balloon model non-linearity is handled approximately using the so-called extended Kalman filter using first derivatives. The Kalman filter estimates the six parameters of the Balloon model based on the measured pixel time course and a 0-1 input activation reference function.
Results
In Figure 1. we show the spatial distribution of the six Balloon model parameters averaged over four runs of the baseline-activation-baseline paradigm. The slice is paraxial and aligned with the calcarine sulcus. Extended regions in the visual areas show parameter estimates deviating from the values found in the other parts of the slice, except for the signal decay parameter which appears independent of the activation. The strong effects of activation on five of the six parameters in the Balloon model may be due to lack of identifiability or overfit. In Figure 2. we show the slice-global distribution of the parameters. Note that these values are from the whole slice, not from activated regions as in Friston et al. (2000). To further illustrate the dependency of the parameter estimates we show in Figure 3 scatter plots of the transit time vs. neuronal efficacy and the oxygen extraction fraction vs. the signal decay parameter. The first pair is seen to be highly correlated, while the latter pair seems rather uncorrelated in line with the visual impression of Figure 1. Future study will be devoted to investigate whether this dependency is induced by the activation or is a function of the model parameterization.
Conclusion
Using State-of-the-Art estimation tools it is possible to estimate parameters pixel by pixel of non-linear hemodynamics in large samples. Five of six Balloon model parameters show high correlation in the specific example.
Acknowledgement
This work is supported by NIH Human Brain Project Grant P20 MN57180 and by the Danish Research Councils

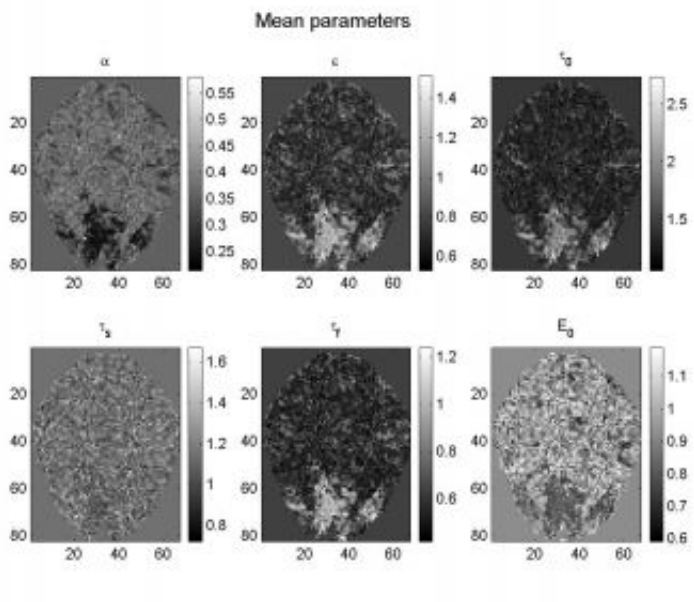
Mean parameters
α
c
τ0
τs
τγ
E0

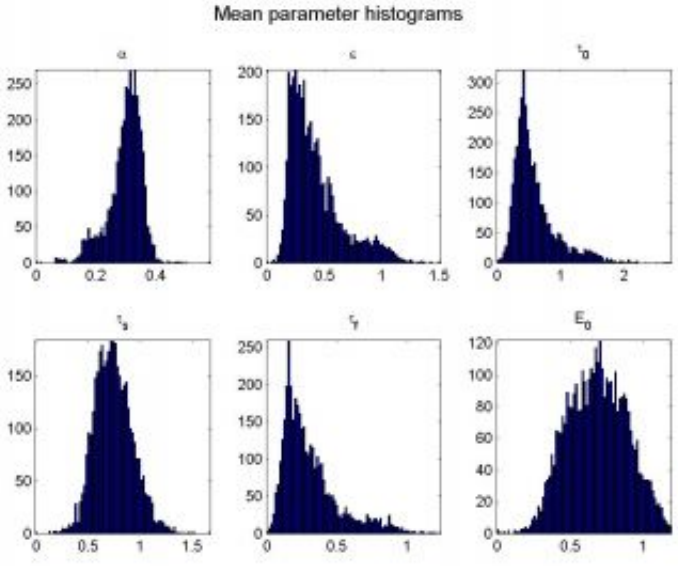
Mean parameter histograms
α
c
τ0
τs
τγ
E0

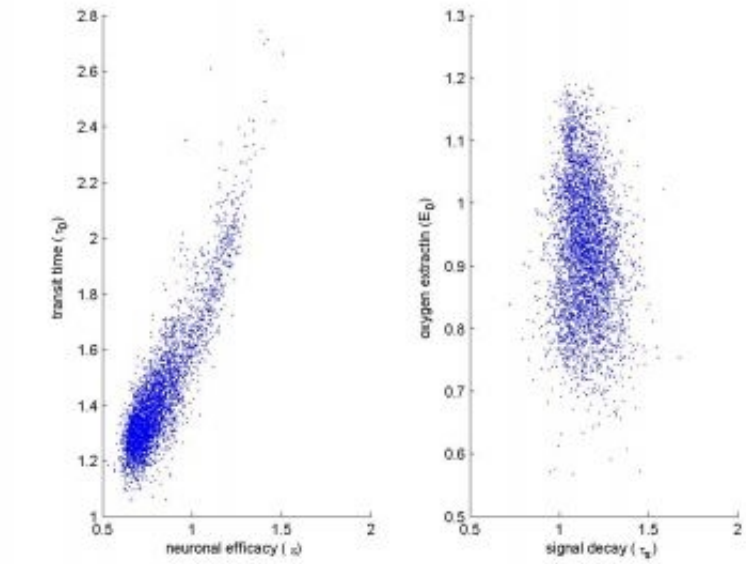
transit time (τ_0)
neuronal efficacy (ε)
oxygen extraction (E_0)
signal decay (τ_s)

WE 201
Method for rapid event related functional MRI allowing detection and seperation of first and second order stimulus effects

J Martijn Jansma[1], Peter van Gelderen[1], Jacco A de Zwart[1], Masaki Fukunaga[1], Peter Kellman[2], Jeff H Duyn[1]
[1]Advanced MRI section, LFMI, NINDS, National Institutes of Health, Bethesda, MD, USA, [2]Laboratory of Cardiac Energetics, NINDS, National Institutes of Health, Bethesda, MD, USA

Background. Conventional analysis methods for rapid-event related fMRI experiments typically assume a linear relationship between a stimulus, neuronal activation and the resulting BOLD response. However, this assumption may not always hold, due to interaction effects (for instance extinction effects, attention level changes) or non-linear BOLD effects. Here, a rapid event-related fMRI design is presented that overcomes this limitation, by allowing for separation of first and second order (interaction) effects. The method was tested using two simulations.
Method. The simulations use 2 stimuli (s1, s2) presented in interleaved fashion (see figure 1). A binary m-sequence [1] (63 length) was used to control stimulus presentation. Advantages of using an m-sequence above random stimulus presentation are: 1) m-sequences have zero correlation at non-zero shift, 2) multiplication of two shifted m-sequences yields another shifted version of the original m-sequence [2]. In the simulation, s2 is controlled by the same m-sequence as s1, but with a shift of 9. Therefore, each first and second order effect of s1 and s2 is correlated to the original m-sequence, but with a specific shift (see table 1). Trials were assumed to last 4 s, and were sampled by two scans, resulting in an experiment with 63 trials (126 scans). Two simulations (sim1, sim2) were performed: in sim1 there are only first order effects, in sim2 various interactions terms were added (see table 1). The resulting signals were convoluted with a simulated BOLD curve (black line in figure 3). Analysis is based on a cross-covariance between the simulated activation and the input m-sequence. This results in a function with distinct peaks for the first and second order effects of s1 and s2. As interaction effects in sim2 are not symmetric (they are only present when both stimuli are on), the added interaction terms in sim2 not only results in second order peaks, but also affects the first order peaks. The unaffected activation of s1 and s2 (without interaction effects) can be derived by adding the second order peaks at the proper shift.
Results. Figure 2 shows the distinctive peaks related to first and second order (interaction) effects. Results of sim1 (red line) show the original activation of s1 and s2 as expected at shifts 0 and 19. In sim2, s1 appears to be stronger than s2, due to the interaction effects. If peak A and B are corrected for the interaction effects, the resulting peaks are identical to peaks A and B of sim1, and to the simulated input BOLD function (figure 3).
Discussion. Results of the simulation show the advantages of using a m-sequence for stimulus presentation opposed to random presentation. The paradigm allows for complete separation of first and second order activation effects. Strength of interactions can be determined, as well as the stimulus activation corrected for interactions. Experiments using a rapid event related designs in which an interaction between stimuli can be expected could benefit from using m-sequence based stimulus presentation instead of random stimulus presentation order.

Table 1: stimulus and interaction effects for sim1 and sim2 and corresponding m-sequence (ms)

effect	sim1	sim2	MSshift	shift (scan)	peak
s1	0.5	0.5	MS0	0 (0)	A
s2	1	1	MS0*MS9	9 (19)	B
s1->s2	-	-0.5	MS0*MS1	38 (76)	C
s2->s1	-	1	MS1*MS2	47 (95)	D
s1->s1	-	-0.2	MS0*MS2	45 (90)	E
s2->s2	-	-0.5	MS9*MS11	54 (111)	F

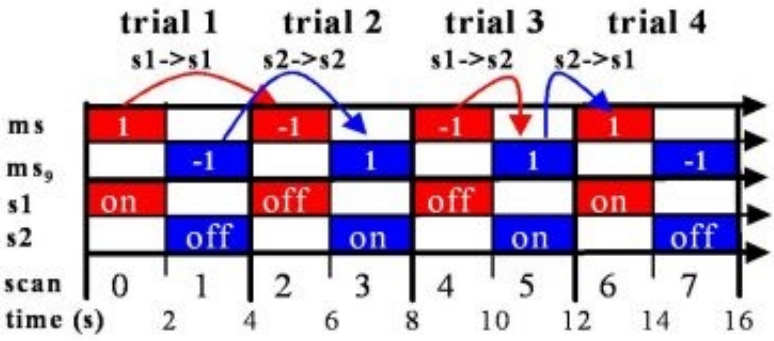

Figure 1: experimental design

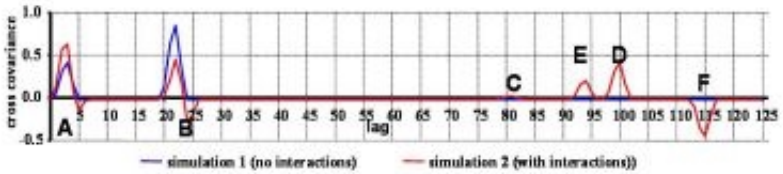

Figure 2: cross-covariance graph of m-sequence with simulated activation

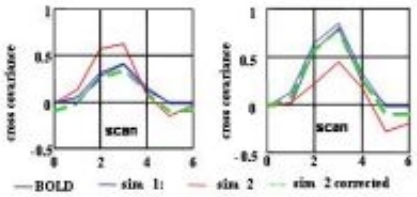

Figure 3: first order BOLD curves

WE 202
Improving the Registration of B0-disorted EPI Images using Calculated Cost Function Weights

Mark Jenkinson
FMRIB Centre, University of Oxford

Introduction
B0 inhomogeneities induce geometric distortion and signal loss in EPI images making registration with structural images particularly difficult. Geometric distortion can be compensated for by measuring a field map and using this to unwarp (pixel-shift) the image prior to registration[1][2]. Unfortunately measuring signal loss is difficult using such maps[2] as estimated gradients are very sensitive to noise and partial volume effects. Therefore simple intensity correction for signal loss is insufficient.
Cost function weighting can minimize such effects by down-weighting (during registration) areas where signal loss occurs. This work seeks to show how these weights can be calculated from field map values and used to improve registration quality.

Methods
Simulated B0 field maps and EPI images (both 64x64x25 voxels) were generated using an anatomical model and MRI simulator[3][4]. From these, estimated intensities and signal loss factors (S) were calculated, which showed dependence on both noise and partial volume effects. The signal loss factor is:
$S=\mathrm{sinc}(\gamma\, te\, Lz\, dB0/dz)$
where γ=gyromagnetic ratio, Lz=voxel dimension in z, dB0/dz=estimated z-gradient of B0 and te=echo-time.
Variation in S was estimated numerical by simulating 1000 image sets (SNR=100). This variation was (approximately) an inverse sigmoid function of S. Therefore the intensity correction factor (1/S) will induce large unwanted intensity fluctuations. The cost function weighting must deweight such regions and so the weight value was chosen to be inversely proportional to the variation:
$Weight=1/(1+\exp(-30(S-0.95)))$.
Registration of the simulated EPI with a simulated T1 image from the same phantom data[5] was performed (using FLIRT[6]) both with and without applying cost function weighting as well as with and without pixel-shift unwarping (using FUGUE[6]).

Results
Figure 1 shows ventricular registration quality. Red lines are taken from ventricle edges in the realigned EPI images. It can be seen that there is an improvement of several millimeters between the first case (no weighting or unwarping) and the last (both weighting and unwarping). Quantitative results on registration accuracy also show an average improvement of several millimeters across the entire brain.

Discussion
It is difficult to accurately calculate signal loss from experimental B0 maps containing noise and partial volume effects. The weighting values given here are derived from simulations and suppress large variations (on average) in the intensity correction. It is not the only candidate function, although it successfully acheives a compromise between de-weighting areas that are too large (losing image features) and areas that are too small (leaving behind artifact). Note that errors also exist in the pixel-shift estimation, but these are less sensitive as no gradients are needed.
In summary, a method for calculating a cost function weighting from a B0 map is proposed that improves global registration accuracy (together with geometric unwarping) by several millimeters.

Acknowledgments
UK-EPSRC (MIAS-IRC) for funding.

References
[1] Cusak et al, NeuroImage 18(1), 2003.
[2] Jenkinson, HBM 2001
[3] Drobnjak and Jenkinson, HBM 2004
[4] MIDAS consortium, HBM 2004
[5] Kwan et al, IEEE TMI 1999, 18(11)
[6] FSL - www.fmrib.ox.ac.uk/fsl

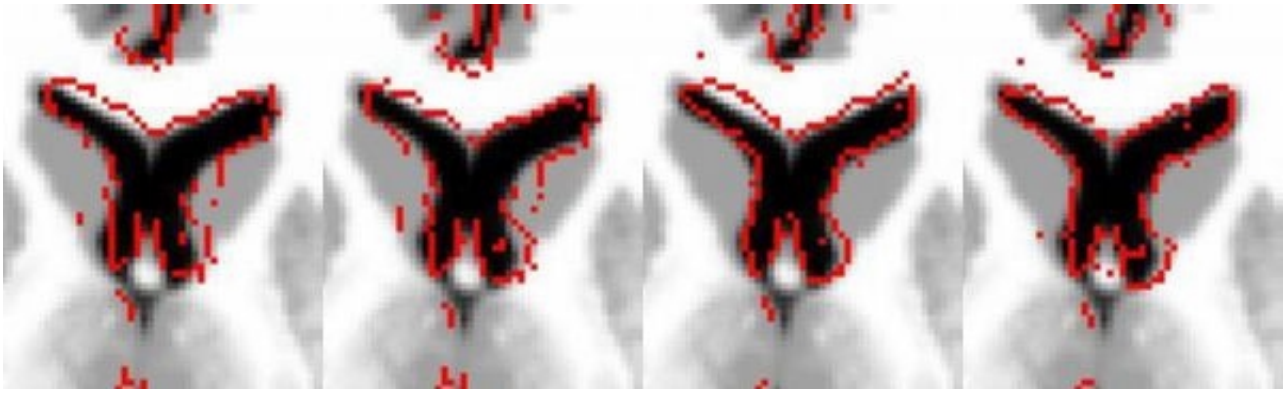

Figure 1: Results of registration near ventricles with (from left to right): (a) no unwarping or weighting; (b) unwarping but no weighting; (c) weighting but no unwarping; (d) both unwarping and weighting.

WE 203
Fast Determination of Optimal Classification Spaces for fMRI Pattern Classification

Sunil Jeswani[1], Stefan Posse[1,2]
[1]Department of Psychiatry and Behavioral Neurosciences, Wayne State University School of Medicine, Detroit, MI USA, [2]Dept. of Psychiatry, University of New Mexico School of Medicine, Albuquerque, NM, USA

Introduction:
Pattern classification of fMRI is a new area of research (1) and holds the potential for many applications, especially for real-time fMRI. Several learning algorithms have been employed such as Artificial Neural Networks and Support Vector Machines (SVM). The common approach is to build a multi-dimensional classifier space in which voxels of the brain (dimensions) that are most similar among the two classes are removed to increase generalization performance of the classifier (1,2). In this study, we attempt to further expand this approach by quickly finding optimal spatial resolutions of fMRI which give the most separability between two classes being classified, and minimize the dimensionality of the classification space.

Method:
It is expected that different sets of two classes have different sets of optimal resolutions. To avoid running the classifier on all possible spatial resolutions (N) we introduce a simple figure of separability (3) that quickly estimates the separability of two classes in each resolution in O(N) time by computing the overlap of two hyperspheres, where each hypersphere contains cluster of points from one class plotted in n-dimensional space and n is the resolution.
FMRI data were acquired on 11 healthy subjects using a 1.5T Siemens Sonata scanner and an interleaved randomized visual/motor/auditory/cognitive paradigm (4). Data were processed with SPM99 (5) using interpolation to 180x220x180 voxels. Tables with location, extent, and t-scores of each activated cluster were entered into the classifier. The four distinct activation patterns resulted in six different classifications when using a two way classifier. Different resolutions were then constructed by spatially averaging across voxels. The classifier was built using an SVM with a linear kernel (2). At each resolution, the accuracy of the classifier was recorded. The correlation between the figure of separability and accuracy of the classifier at each resolution was computed.

Results and Discussion:
Each of the six classifications had a different range of resolutions in which classifier accuracy was high (top 5% of highest accuracies across all resolutions, typically > 95%). This suggests that finding optimal resolutions for each classification problem may be more effective than using a standard resolution. Additionally, for all six classifications there was a positive correlation between the figure of merit and classifier accuracy. This suggests that the figure of separability can find optimal resolutions, and since the operation is computable in O(N), optimal resolutions can be found quickly, possibly even in real-time. Based on these results, we also propose a classifier architecture in which the k best resolutions based on their figure of merit are used, resulting in k different SVM classifiers. Multi-classifier fusion techniques can then be employed to produce a net classification output (3).

Acknowledgment:
Supported by NIH NIBIB 1 R01 EB002618-01 and State of Michigan (Joe Young Sr. Foundation).

References:
1. Cox, D.D., Savoy, R.L. *Neuroimage* 19, 261-270, 2003
2. *http:/ /www.ecs.soton.ac.uk/~srg/publications/pdf/SVM.pdf*, 1998
3. Braun, J., Jeswani, S. *Proceedings of SPIE* Vol. 5099, 13-23, 2003
4. Fitzgerald, D., Posse, S. *Neuroimage*, 2003, 663
5. Friston, K.J., et al., *Human Brain Mapping*, 2, 165, 1995

WE 204
Medical Image Classification Using Support Vector Machine

Ye Ji[1,2], Hongbo Liu[1,2], Xiukun Wang[1], Bo Li[1], Yijun Liu[3], Yiyuan Tang[2]
[1]Department of Computer, Dalian University of Technology, Dalian, 116023, China., [2]Institute of Neuroinformnatics, Dalian University of Technology, Dalian 116023, China., [3]Departments of Psychiatry & Neuroscience, McKnight Brain Institute, University of Florida, USA

Introduction

In medicine, acquired images such as MRI, Xray and CT images have increased rapidly over the last few years. An important problem in the development of medical systems is how to classify the enormous images by computer efficiently and precisely. Fortunately, the technique of CBIR (content-based image retrieval) offers new opportunities for image classification. It is necessary to depict an image in terms of a representation that best matches its information content. According to the characteristics of medical images, we choose both the texture and edge descriptor as the features of image representation, and employ the polynomial SVM(support vector machine) framework for image classification.

Methods

Image texture means a kind of change of pixels' intensity (or gray) in some neighborhood, which is spatially a statistical relative. It comprises two elements, texture unit and its arrangement. In our case the size of the neighborhood is 3*3 pixels. According to the concept of texture spectrum proposed by Karkanis S, et al. [1], we find the method to describe the medical image texture histogram. The 265 texture bins are created through this histogram.

Edge in the image is treated as another important feature to represent the content of the image. Edge features for image perception is important for medical image classification, too. Park [2] proposed a local edge histogram descriptor. The normative part of the edge histogram descriptor consists of 80 local edge histogram bins, 5 global bins and 65 semi-global bins.

After obtaining the features of texture and edge from an image, the two parts of features are combined into one vector. We employ support vector machine which is a well-known pattern classification method. Since the linear kernel doesn't work well, we use the polynomial kernel function to map the input train vector into high-dimension feature.

Results and Discussion

We find that the combined histogram is more accurate and precise than either texture histogram or edge histogram alone. It is a good method for medical image retrieval. However, the image is described by too many features (256 for texture and 150 for edge), it influences the time of calculation. How to decrease the features and increase accuracy and precision of classification is our further work.

References

[1] Karkanis S, Galousi K, Maroulis D. Classification of endoscopic images based on texture spectrum. In: Workshop on Machine Learning in Medical Applications. Chania, 1999. 63~69.

[2] Park DK, Jeon YS, Won CS. Efficient use of local edge histogram descriptor. In: Proceedings of the ACM Workshops on Multimedia. Los Angeles, 2000. 51~54.

Acknowledgements

This work is supported by the MOST (2100CCA00700) and MOST International Program, NSFC (30170321) and MOE (KP0302).

WE 205
Connectivity-based anatomical parcellation of cortical grey matter

Heidi Johansen-Berg[1], Timothy EJ Behrens[1], Ivana Drobnjak[1], Stephen M Smith[1], Paul M Matthews[1], Des J Higham[2]
[1]Centre for Functional MRI of the Brain, University of Oxford, John Radcliffe Hospital, Oxford, OX3 9DU, UK, [2]Department of Mathematics, University of Strathclyde, Glasgow, G1 1XH, Scotland, UK

Abstract
A goal of neuroimaging is to make inferences about brain structure and function in terms of cytoarchitecture. However, cytoarchitectonic boundaries do not correspond well to landmarks, such as sulci, that are visible *in vivo*. Regions that differ in cytoarchitecture will, however, have distinct patterns of anatomical connectivity. Diffusion tractography provides connectivity information *in vivo* in the human brain. Here, we test whether functional-anatomical cortical boundaries can be detected using diffusion data.
Medial area 6 consists of two cytoarchitectonically distinct regions in monkey[1] and two[2] or three[3] in human. In non-human primates there is a change in connectivity along medial frontal cortex: pre-SMA connects to prefrontal/anterior cingulate cortex whereas SMA proper connects to sensorimotor regions[4]. We tested whether we could detect this connectivity change *in vivo* and use it to anatomically parcellate the medial frontal cortex.
Methods
Diffusion-weighted data[5] and a T1-weighted image were acquired in 11 subjects. Each re-aligned T1-weighted image was used to define a medial frontal mask on a single axial slice (MNI Z=56). Probabilistic tractography was run from all voxels in this seed mask[6]. Probabilities of connection from each seed voxel (at $1.2mm^3$ resolution) to every other voxel in the brain (re-sampled to $5mm^3$) were binarised and stored in a matrix, **A**, whose cross correlation matrix, **B**, was found. The nodes in **B** were permuted using a spectral reordering algorithm[7] that finds the reordering that minimises the sum of element values multiplied by the squared distance of that element from the diagonal, hence forcing large values to the diagonal. If the data contains clusters (representing seed voxels with similar connectivity), then these clusters will be apparent in the re-ordered matrix and break points between clusters will represent locations where connectivity patterns change.
Results
In 8/11 subjects the re-ordered connectivity matrix could be easily divided (by eye) into 2 clusters whereas in 3/11 subjects there were 3 clusters apparent (figure 1). In all subjects, when clusters were mapped back onto the brain, they appeared as distinct regions along the anterior-posterior axis (figure 1). Clusters from the 8 subjects in whom two clusters were identified were overlaid to define a probabilistic putative pre-SMA/SMA-proper (figure 2).
Conclusions
A change in connectivity along medial frontal cortex was detected by identifying clusters in reordered connectivity matrices. Mapping these clusters back onto the brain defines a boundary that we hypothesise corresponds to a functionally relevant cytoarchitectonic border. Future imaging studies will test how well this border co-localises with a functional boundary.
Our approach is based solely on detecting *changes* in connectivity and is therefore able to define grey matter boundaries even when connectivity targets cannot be accurately defined or connectivity information is incomplete.
This provides a novel means for parcellating cortical grey matter *in vivo* using information that is directly relevant to function.
References
1. Vogt & Vogt (1919) J Psychol Neurol, 2. Zilles et al (1996) Adv Neurol. 3. Vorbiev et al (1998) Eur J Neurosci. 4. Wheeler-Kingshott et al (2002) Proc ISMRM. 5. Behrens et al (2003) MRM. 6. Higham (2003) J Computational & Appl Maths

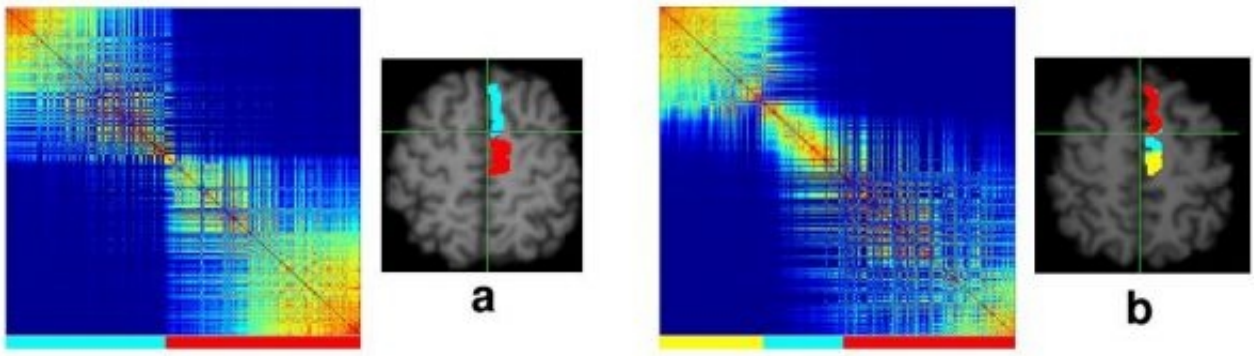

Figure 1: Reordered cross correlation matrices and clusters mapped back onto the brain for two example subjects. A) Example in which two clusters could be differentiated in the reordered matrix. The coloured bars under the matrix represent the clusters that were determined by eye. These clusters are mapped back onto the brain in the axial slice. B) Example from a subject in which 3 clusters were apparent in the reordered matrix

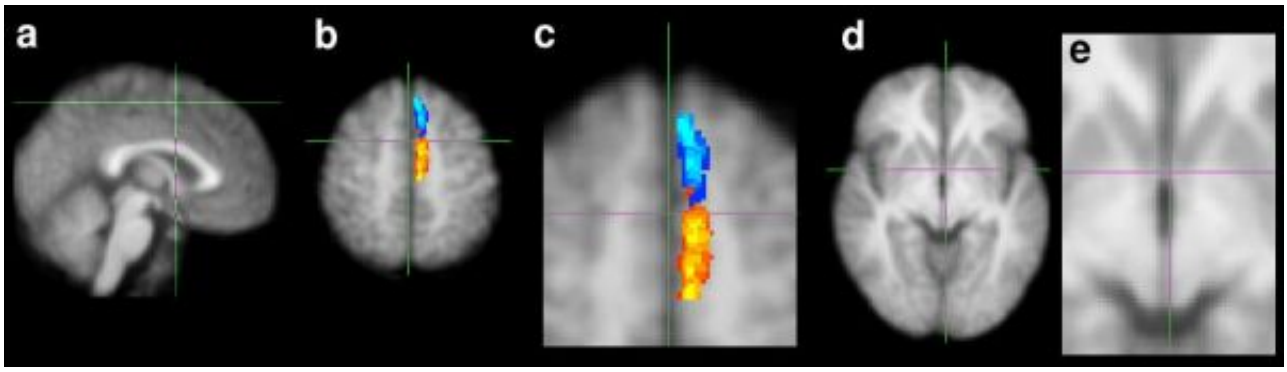

Figure 2: Probabilistic SMA/pre-SMA determined from group data. A) Sagittal view showing VAC line, which has been proposed to lie close to the SMA/pre-SMA border in the human brain. B,C) Axial slice showing group maps for pre-SMA (in blue-turquoise) and SMA-proper (in red-yellow). Colours represent numbers of subjects and clusters are thresholded at 3/8 subjects. The line across the y-axis corresponds to the VAC line and runs through the border between these two regions. D,E) Identification of AC on group average T1-weighted image.

WE 206
Reliability in Multi-Site Structural MRI Studies: Effects of gradient non-linearity correction on volume and displacement of brain subcortical structures

Jorge Jovicich[1], Elizabeth Haley[1], Douglas Greve[1], David Kennedy[1], Randy L Gollub[1], Bruce Fischl[1], Anders Dale[1], Brain Morphometry BIRN[2]
[1]Martinos Center for Biomedical Imaging, Massachussets General Hospital, [2]www.nbirn.net

Introduction: In studies where morphological MRI data is pooled across sites it is extremely important to characterize and minimize site-specific MRI image distortions factors to allow accurate cross-site comparisons of morphometry results. In previous work (Jovicich et al. 2003), a phantom study showed how non-linearities in the imaging gradient fields cause strong geometric distortions (displacements), which vary widely across FOV and across gradient models/vendors, and also showed how these distortions can be significantly reduced thereby improving multi-site reproducibility. Here we extend our work to study the effects of distortion correction on brain subcortical data. Specifically, we performed both a prediction and an empirical study of how distortion correction affects the volume and displacement of subcortical brain structures in a group of subjects scanned at multiple sites.
Methods: Image distortion characteristics [GE Signa (3-sites) and Siemens Sonata (1-site), all 1.5T] are accurately characterized by manufacturer-supplied spherical harmonics coefficients of the MR gradient fields (Jovicich et al. 2003). Prediction Study: An arbitrary volume (segmented hippocampus from a healthy volunteer) was used to predict the magnitudes of the volume changes and displacement effects introduced by the distortion correction, as a function of the location of the volume within the FOV. For each of the 4 sites investigated, the volume was parametrically moved within the FOV of the characteristic displacement field. At each position the volume was distortion corrected and the resulting correction multiplicative factor and mean magnitude of the volumes post-correction displacements were mapped. Empirical Study: 6 normal controls were scanned at the 4 sites (3D-spoiled gradient echo, TR=20ms, TE=6ms, 256x192, 1.5mm thick 124 sagittal slabs, flip angle=300). Subcortical brain segmentations were obtained from the original MRI data (Fischl 2002). Volume correction factors and mean displacements were calculated from the characteristic displacement fields for each corresponding site. An ANOVA was performed to test for site, session and structure effects.
Results and Discussion: The prediction study shows that, within the space where the head may be positioned in the gradient field, a structure like hippocampus can have up to 10% error in its uncorrected volume, with a post-correction mean displacement of up to 4 mm. Both magnitudes increase fairly rapidly moving away from the gradients iso-center. The empirical study shows that for most subcortical structures the volume correction errors were of the order of 3%, with displacements under 1mm. Strong site and subject effects were observed, directly related to how far away from the iso-center the imaging session was. Preliminary results show that distortion correction reduces the group variance in the volume estimates (up to 8% improvement for hippocampus). This work will continue to evaluate test-retest reproducibility.
References:
Jovicich J, et al; Biomedical Information Research Network: Characterization and Correction of Image Distortions in Multi-Site Structural MRI, HBM 2003.
Fischl B. et al; Whole brain segmentation: Automated labeling of neuroanatomical structures in the human brain. Neuron. 2002; 33(3): 341-355
Acknowledgements: Mark Vangel, NCRR BIRN Morphometry Project (BIRN004)

WE 207
Evaluation of Three Cortical Surface Flattening Methods

Lili Ju[1], Monica Hurdal[2], Kelly Rehm[3], Bill Wood[2], Kirt Schaper[4], Josh Stern[4], David Rottenberg[3,4]
[1]Institute for Mathematics and its Applications, University of Minnesota, Minneapolis, MN 55455, USA, [2]Department of Mathematics, Florida State University, Tallahassee, FL 32306, USA, [3]Department of Radiology, University of Minnesota, Minneapolis, MN 55455, USA, [4]Department of Neurology, University of Minnesota, Minneapolis, MN 55455, USA

Intoduction

FreeSurfer (FS) [1], a popular software package for cortical surface flattening, explicitly minimizes metric distortion of the flattened surface. In contrast, LSCM [3] and CirclePack (CP) [2] are quasi-conformal flattening methods that preserve angles locally; however, spherical maps generated by these methods can be normalized by a Moebius transformation that minimizes metric distortion among the auomorphism group. All three methods can flatten user-defined patches as well as an entire cortical surface.

Methods

Topologically-correct triangulated surfaces of the left hemisphere were extracted from two high-resolution T1 MRI brain volumes (MNI, PENN) that had been parcellated by an expert neuroanatomist; parcellation of the extracted cortical sheet was guided by the volume parcellation using in-house software (ParcelMan [4]). For each brain, the left hemispheral cortex (equivalent to a topological sphere) and four lobar cortical patches (equivalent to topological discs) were flattened using FS, LSCM, and CP to create the corresponding spherical or planar maps. Measurements of angular and metric distortion of the flattened surfaces [3], which are invariant under the similarity transformations were used to describe the quality of resulting maps.

Results and Conclusions

Measurements of angular and metric distortion for the three methods, two brains, and five surfaces (the left hemispheral cortex and four lobar patches) are presented in Table 1, and frequency histograms of angular and metric distortion for the MNI left hemispheral cortex are illustrated in Figure 1. For the lobar patches FS clearly outperforms both conformal methods with regard to the preservation of metric information; however, for the MNI left hemispheral cortex FS and LSCM produce similar results for mean metric distortion: 31.72% and 36.07%, respectively. For all five surfaces LSCM is superior to the other methods with regard to the preservation of angular information, and CP and LSCM perform similarly with regard to metric distortion. Thus, by preserving angular (shape) information and adequately preserving metric information, LSCM may offer advantages to methods such as FS, which preserve only metric information, for flattening hemispheral cortical surfaces.

References

1. Fischl B., et al., Neuroimage **9**:195-207, 1999.
2. Hurdal M.K., et al., LNCompSci, **1679**:279-286, 1999.
3. Ju L.L., et al., NeuroImage **19**:S864, 2003.
4. Rehm K., et al., HBM2004, submitted.

Acknowledgements

This work is supported in part by NIH grant MH57180 and NSF grant DMS101339.

Table 1. Angular (degrees) and metric (%) distortion of flat maps generated by FS, LSCM and CP.

		MNI surface					PENN Surface				
Flat Maps		S	F	O	P	T	S	F	O	P	T
FS	MAD	18.76	11.38	11.82	7.27	27.49	18.99	15.12	14.02	13.32	23.14
	MMD	31.72	18.14	18.81	15.24	25.79	24.47	22.60	22.29	20.73	30.46
LSCM	MAD	4.65	1.80	2.06	1.57	2.35	7.21	3.02	3.25	2.55	2.70
	MMD	36.07	34.94	32.38	29.14	36.19	40.70	36.10	36.59	39.45	41.93
CP	MAD	16.39	11.27	11.25	11.28	11.17	15.73	11.93	10.67	10.95	11.29
	MMD	40.18	31.51	31.69	24.23	39.98	41.42	32.81	35.32	30.74	45.20

MAD, mean angular distortion; MMD, mean metric distortion; S, spherical map of the left hemispheral cortex; F,O,P,T, planar maps of frontal, occipital, parietal and temporal patches, respectively.

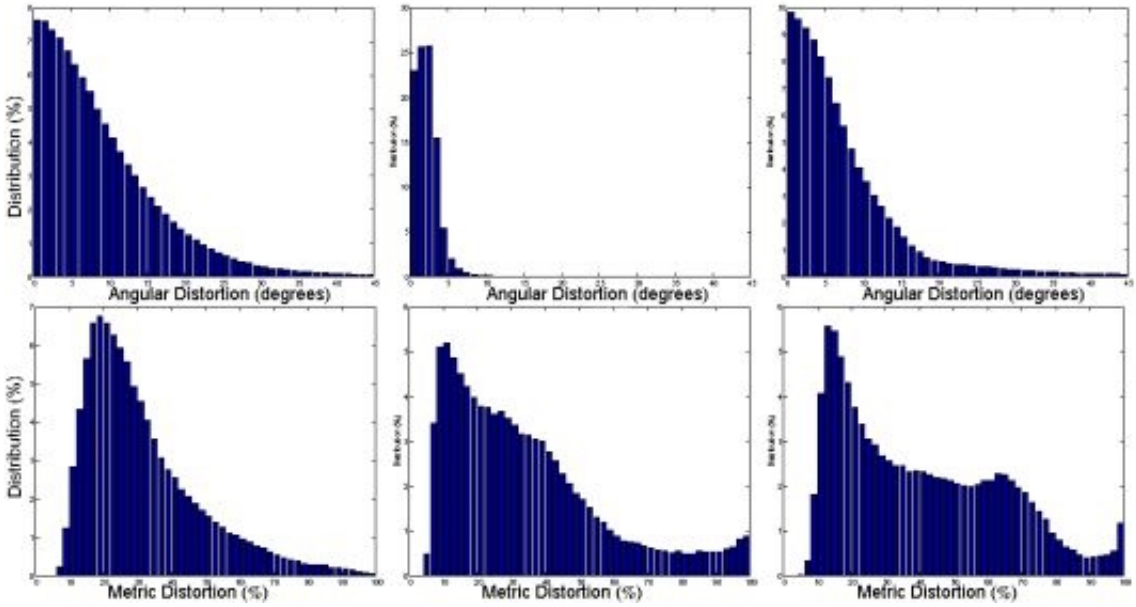

Figure 1. Frequency histograms illustrating the angular and metric distortion of spherical maps of the MNI left hemispheral cortex generated by FS (left), LSCM (middle) and CP(right). Top row, angular distortion; bottom row, metric distortion.

WE 208
Dipole Analysis on Spatiotemporal MEG signals using Bayesian Inference

Sung C Jun , John S George , Juliana Pare-Blagoev , Sergey M Plis , Doug M Ranken , David M Schmidt , Chris C Wood
Biological & Quantum Physics Group, MS-D454, Los Alamos National Laboratory, Los Alamos, New Mexico, USA

We have recently extended earlier applications of Bayesian Inference to the EEG/MEG inverse problem by using numerical techniques to estimate the full posterior probability distributions for the problem [1, 2; see related work by Bertrand et al. in 3]. Unlike other approaches to the inverse problem, these approaches do not result in a single "best" solution to the problem. Rather, they yield a probability distribution of solutions upon which all subsequent inferences are based. References [1] and [3] focused on the analysis of data at a single point in time, and demonstrated the utility of Bayesian inference both for including pertinent prior information (anatomical location and orientation, sparseness of regions of activity, limitations on current strength and spatial correlation, and etc.) and for yielding robust results in spite of the under-determined inverse problem. Reference [1] used an extended region model for neural activity while reference [3] used a multi-dipole model. Reference [2] extended their work to a spatiotemporal Bayesian inference analysis of the full spatiotemporal MEG/EEG data set, using their extended region model for neural activity.

Here we present a spatiotemporal Bayesian inference analysis using a dipole model of neural activity that is (A) relatively ast, (B) does not require the use of the subject’s anatomical information, (C) does not require the pre-set determination of the number of dipoles, and (D) yields quantitative probabilistic inferences that are one of the hallmarks of the Bayesian inference approach. At each active location, neural dipole current is now a function of both space and time. The unknown parameters are number of dipoles and for each dipole: location, moment time course, direction, and active time range. We added a current time prior probability distribution for the correlation of one time point with another that allows us to include the temporal correlation at nearby latencies. In addition we have incorporated the ability to handle much more complex and realistic estimates of the background noise [4] that reduce the effects of under-modeling this noise. We used Markov Chain Monte Carlo (MCMC) to sample the many possible likely solutions. The spatiotemporal Bayesian analysis is demonstrated using both simulated and empirical whole-head MEG data.

[1] Schmidt, D.M. , George, J.S., Wood, C.C., Hum. Brain Mapp., 1999, 7: 195-212.
[2] Schmidt, D.M., George, J.S., Ranken D.M. and Wood, C.C., Biomag2000, Proc. 12th Int. Conf. on Biomagnetism, 2001, 671--673.
[3] Bertrand C. et. al., IEEE Trans. Biomed. Engin., 2001, 48: 533-542.
[4] Plis S. et. al., Private Communication.

WE 209
Optimal linear basis for Statistical Parametric Mapping of event-related potentials/fields

Stefan J Kiebel , Olivier David , Karl J Friston
Wellcome Dept. of Imaging Neuroscience, UCL, WC1N 3BG, London, UK

Introduction We described Statistical Parametric Mapping (SPM) for the analysis of event-related potentials and fields (ERP/ERF) data (1). In the temporal domain, we specify a two-level hierarchical linear model with multiple error covariance components, at both levels, to account for non-sphericity of the data. For making inferences in fixed or random effects analyses, we use classical t- or F-statistics, based on [Restricted] Maximum Likelihood estimates, to compute p-values for temporally localized effects in peri-stimulus time or in the time-frequency domain. With this temporal model, we analyze reconstructed ERP/ERF time series, over voxels, in a mass-univariate fashion. P-values, corrected for multiple comparisons, are estimated using results from Gaussian Random Field theory (2).
This approach allows tests on (population) effects, which are expressed in terms of a multidimensional characterization of ERPs, defined by a basis set. As a result, in the same model, one can test conventional hypotheses (differences in amplitude), but also test time-frequency hypotheses, i.e. differences in power in a specific frequency range in some peri-stimulus time window.
Critically, the precision of the parameter estimates, at the second level, depends on the choice of the first-level ERP basis set. In general, complex models lead to imprecise parameter estimates. Ideally, the basis set should afford the least complex model that retains interesting variations. Such a parsimonious model engenders the most sensitive tests. Moreover, in a two-stage procedure (1), the full second-level error covariance matrix of first-level parameters can be estimated efficiently. We employed four different basis sets to model ERP/ERF data and compare their relative usefulness.
Methods The first basis set was the identity matrix, which is the implicit model used in classical ERP research. The second was a truncated discrete wavelet transform (DWT) set used typically for time-frequency analyses. The third comprised the eigenvectors of the sample covariance matrix of the ERPs. The fourth consisted of basis functions derived from a neural mass model for EEG data (3).
Results We found that all basis sets could be used for response detection in ERP/ERF data. The eigenvector and the neural mass model basis sets appeared best for time-frequency analyses because of their sparse representation of ERP data (typically 6 to 18 parameters per ERP). The (naive) use of the DWT does not lead to a sparse representation per se and is only useful, for time-frequency analyses, with additional assumptions. An example of such an assumption is that all or some of the correlations between wavelet coefficients, at the second level, are zero.
Conclusion We found that the best linear basis sets for analyses of ERP/ERF data, in the time-frequency domain, obtain by incorporating prior knowledge from either (i) other ERP data or (ii) from a generative model. In practice, other, less informed, basis sets can only be used for conventional ERP/ERF analyses or need further constraints.

References

(1) S.J. Kiebel and K.J. Friston., submitted to Neuroimage, 2004.
(2) K.J. Worsley et al., Human Brain Mapping, 8:98-101, 1999.
(3) O. David and K.J. Friston, Neuroimage, 20: 1743-1755, 2003.

WE 210
Evaluation Study of Korean-specific Tissue Probability Map with ICBM Tissue Probabilistic Atlases: A Probabilistic Similarity Index

J.H. Kim[1], J.M. Lee[1], U.C. Yoon[1], I.Y. Kim[1], J.S. Kwon[2], S.I. Kim[1]
[1]Department of Biomedical Engineering, Hanyang University, Seoul, Korea, [2]Department of Psychiatry, Seoul National University, Seoul, Korea

Probabilistic atlases of neuroanatomy are more representative of population anatomy than single brain atlases. In general, a group-specific probabilistic atlas was somewhat different from the existing probabilistic atlas, which could not reflect the characteristics of the group, such as Tissue Probabilistic Atlases of International Consortium for Brain Mapping (ICBM-TPA). In addition, since inter-ethnic differences of inter-subject variability were present, Korean-specific tissue probability map (KTPM) had been needed for domestic neuroimage analysis (Zilles et al, 2001). In this paper, we introduced the sequential procedures of KTPM and compared with ICBM-TPA using a newly proposed measure.

Generating KTPM procedure is as follows.

- Skull-stripping using the region growing method
- Affine transformation to the representative subject
- Tissue classification
- Estimation of probability in a given voxel position
- Affine transformation to ICBM-TPA for comparison (SPM99)

Although most of previous studies had used the similarity index for quantitative evaluation of segmentation results, we intended the probabilistic similarity index (PSI) because probabilistic results were compared, not binary one. Also, for clarity of the evaluation, it is desirable to have a general measure that represents the accuracy of probability map as a whole. The PSI is defined as in Fig. 1.

The PSI showed almost identical results expect for CSF 0.735 (CSF), 0.952 (Gray matter, GM), 0.937 (White matter, WM). However, the difference images between KTPM and ICBM-TPA showed that subjects that were consisted of KTPM were more variable than ones of ICBM-TPA in occipital and parietal lobe (Fig. 2).

Because our skull-stripping procedure approximated the outer CSF using morphological operation, PSI of CSF showed lower value than one of GM or WM. Therefore, additional researches for restoration of outer CSF must be continually followed. One of several factors that resulted in differences of KTPM and ICBM-TPA might be the number of subjects. In case of KTPM, T1-weighted magnetic resonance images of 50 healthy volunteers were acquired from Seoul National University Hospital (male/female = 34/16, 26.22±5.25 years). Subjects of ICBM-TPA were consisted of 452 young normal subjects (262/190). It was needed supplementary subjects for the improvement of probabilistic map. Finally, the occipital and parietal lobe in which variability of group was higher than any other region were regions coincident with previous literature that referred oriental races is relatively shorter, but wider than occidental (Zilles et al., 2001).

We evaluated KTPM with ICBM-TPA using the PSI which is reflected spatial variability and probability per voxel. Since inter-ethnic differences of inter-subject variability are present as described above, we expect that segmentation using KTPM as a prior knowledge might be better than using ICBM-TPA for the domestic neuroimages.

$$PSI = \frac{2 \times \sum \sqrt{P_{ICBM-TPA \cap KTPM}}}{\sum P_{ICBM-TPA} + \sum P_{KTPM}} \quad (0 \le \mathrm{PSI} \le 1)$$

With:

$\sum P_{ICBM-TPA}, \sum P_{KTPM}$: Sum over all probabilities in each probability map,

$P_{ICBM-TPA \cap KTPM}$: Product of probabilities of corresponding voxels in each probability map

Fig. 1: ***The definition of PSI***

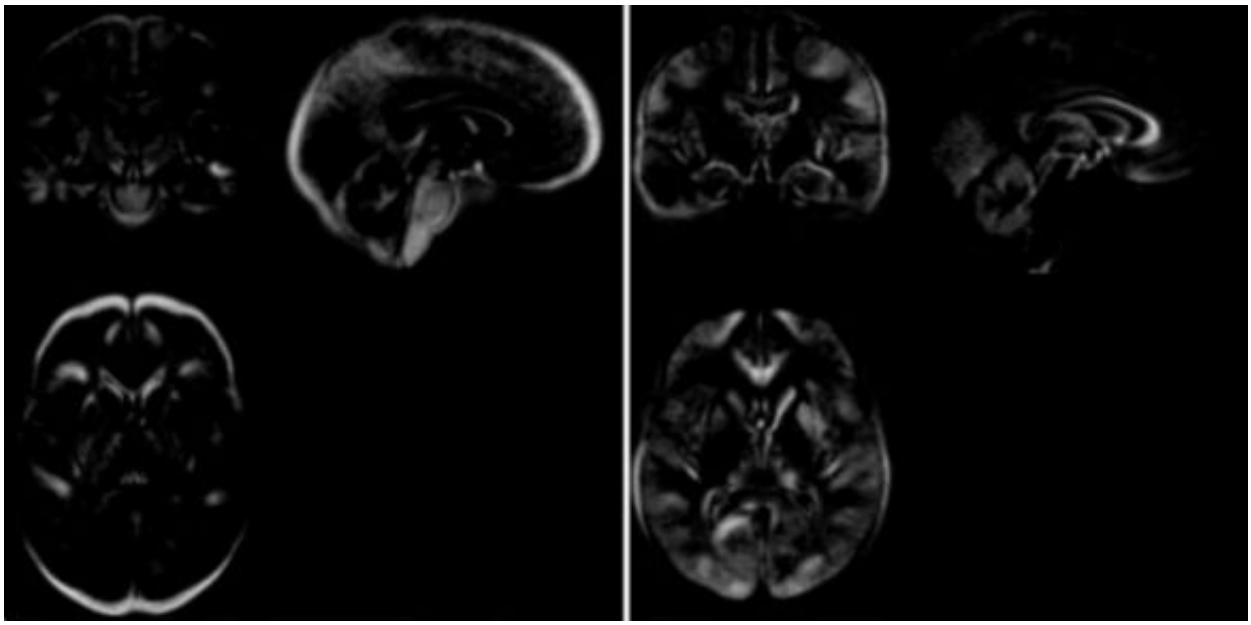

Fig. 2: ***Difference images between KTPM and ICBM-TPA (Gray Matter), (Left: ICBM-TPA > KTPM, Right: ICBM-TPA < KTPM)***

WE 211
Regional Specificity of Hemodynamic Response Function Analyzed by a New Method : HAW

Syoji Kobashi[1], Yuri T. Kitamura[2], Sayaka Imaeda[1], Katsuya Kondo[1], Yutaka Hata[1], Toshio Yanagida[2]
[1]Graduate School of Engineering, Himeji Insitute of Technology, [2]Graduate School of Frontier Biosciences, Osaka University

Objective:
Hemodynamic response (HR) characterized by functional MRI (fMRI) will be varied among cerebral regions. This study examines the variability of HR delays within activation sites of interest and differences of HR delays among the activation sites using a new fMRI analyzing method; HAW (Hemodynamic Response Analysis Using Wavelet Transform).
Subjects:
Ten healthy male volunteers (ages 22.9 ± 2.5 years) were recruited for this study. Nine were right-handed and one was left-handed. The handedness of each subject was confirmed using the Edinburgh inventory test for handedness. They all gave informed consent according to the guidelines approved by the local Ethical Committee of the Himeji Institute of Technology. For each subject, we acquired a few event related (ER)-fMRI datasets on different acquisition days between June 5 and Nov. 11, 2001. The activation task was the right-hand gripping and the left-hand gripping tasks.
Method:
Our method, called HAW, detects activation sites and estimates the HR function for each activate site, simultaneously. This method is based on wavelet transform, and the degree of activation is computed by statistically estimating the distribution of wavelet coefficients. Using the proposed method, we examine the variability of HR delays across three activation sites: the supplementary motor area (SMA; Brodmann area (BA) 6), primary motor cortex (M1; BA4), and primary visual area (V1; BA17). The variability is evaluated within a subject, across subjects within the same activation site, and across data acquisition days within a subject.
Results:
The distributions of the HR delays at the SMA, M1 and V1 for a subject are shown in Fig. 1. The datasets were obtained on four days between June 5 and Nov. 11, 2001. Comparison of the HR delays among subjects is shown in Fig. 2.
Discussion:
At each activation site, we found no significant difference across the data acquisition days using one-way analysis of variance (ANOVA) at a significance level of ≤ 0.01. The mean HR delays were 4.75 ± 0.50 s at the SMA, 5.43 ± 0.51 s at the M1 and 8.42 ± 0.65 s at the V1. The HR delays among the SMA, M1, and V1 were significantly different (significance level ≤ 0.01). In addition, in all cases, the HR delay was in the order V1 > M1 > SMA.
At each activation site, the inter-subject variance (i.e., the differences among subjects) was significantly larger than the intra-subject variance (temporal differences in one subject) by using ANOVA at a significance level of ≤ 0.01. This shows that HR delays are stable within the same subject in comparison with the variance among subjects.
Conclusion:
We have proposed a novel method for analyzing ER-fMRI data. With respect to the variability of the HR delays obtained with HAW, we found (1) HR delays are stable at a given activation site (i.e., M1, SMA and V1) in a given subject over a period of a few days, and HR delays vary among subjects at the same activation site, and (2) The HR delay at the SMA differs from that at the M1 within a subject.

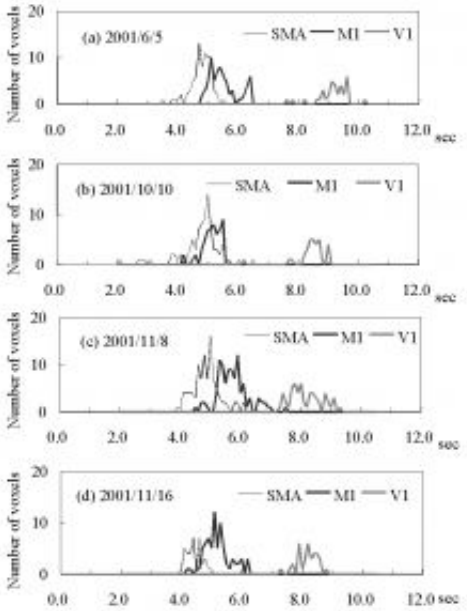

HR delay distribution at the SMA, M1 and V1 in the same subject (Subject 1, right-hand gripping).

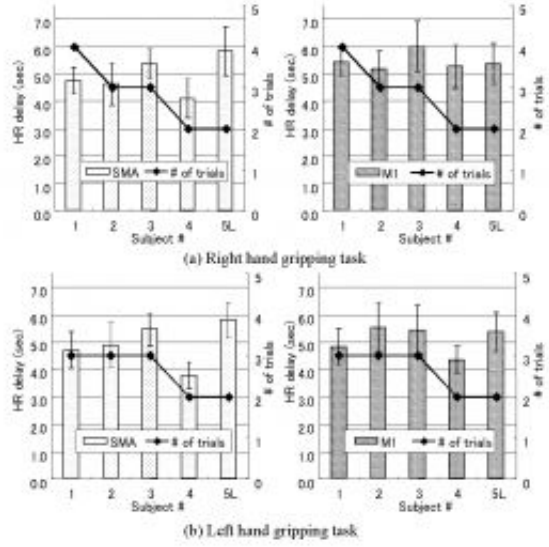

Variability of HR delay at the SMA and M1 in the same subject.

WE 212

Development of FLASH (FLexible Adjustable Surface Holder) in functional near infrared spectroscopic imaging system

SATORU KOHNO , AKIHIRO ISHIKAWA , SYOICHI TSUNEISHI , TAKASHI AMITA , KOJI SHIMIZU
Medical Systems Division, Shimadzu Corporation

Introduction

A holder cap fabricated from thermoplastic resin has been used to hold the probes of the functional near infrared spectroscopic (fNIRS) imaging system because the distance between a light source probe and a detector probe needs to be constant. However it can't fit the various head of all subjects because of differences among individuals. Then it results in the deterioration of signal-to-noise ratio and possessing lower reliability on the data. We developed a novel FLexible Adjustable Surface Holder (FLASH) to solve these problems.

Theory

From Gauss-Bonnet theorem, the following formulas are derived.

$\theta1+\theta2+\theta3=\pi+KA1$ (in the case of triangle on curved surface)

$\theta1+\theta2+\theta3+\theta4=2\pi+KA2$ (in the case of quadrangle on curved surface)

where K=Gaussian curvature, $\theta1\sim\theta4$=angle of triangle or quadrangle on curved surface, A1=area of triangle on curved surface and A2=area of quadrangle on curved surface. These formulas say that the sum of interior angles of a triangle or quadrangle on the curved surface changes according to the Gaussian curvature .

Method

The basic structure of FLASH consists of some slides and some nodes which are sockets to hold probes of a triangle or a quadrangle. Their slides are made of non-stretchable and flexible material. The sum of the interior angles can be changed by allowing the rotation of the slides at the position of the sockets in accordance with the flexible slides. Therefore FLASH can hold any curved surfaces by holding the interior angles using sockets (Fig.1). We developed a partial-head FLASH and a whole-head FLASH and evaluated their fitting performance using different sized balls and head mannequins.

Results and Discussion

The partial-head FLASH and the whole-head FLASH could completely fit different sized balls (20cm and 13cm in diameter) and different sized head mannequins respectively (Fig.2). FLASH may solve many problems due to unfitting.

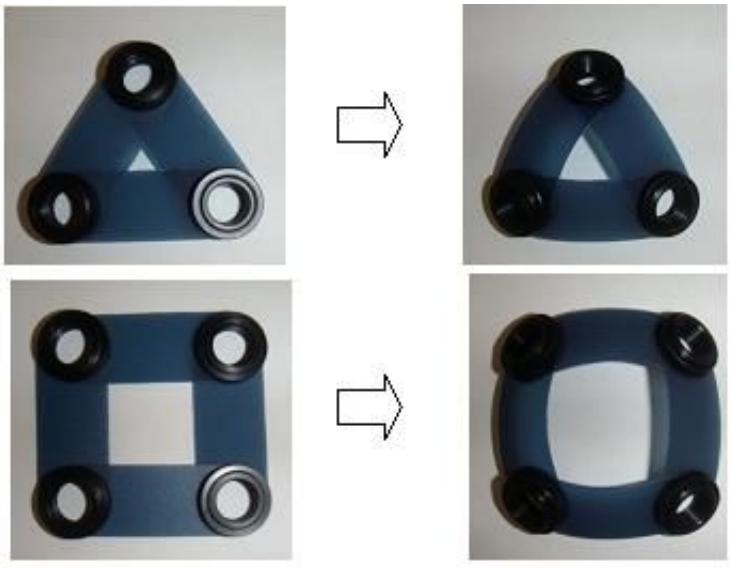

Fig.1 The basic structure and mechanism of FLASH

Fig.2 The whole-head FLASH fitted different sized head mannequins

WE 213

Analysis of near infrared spectroscopic signals during human locomotion using independent component analysis

SATORU KOHNO[1], SHIGEKI KAJIHARA[2], ICHIRO MIYAI[3], ICHIRO ODA[2], AKIHIRO ISHIKAWA[1], SHOICHI TSUNEISHI[1], TAKASHI AMITA[1], KOJI SHIMIZU[1]

[1]Medical Systems Division, Shimadzu Corporation, [2]Technology Research Laboratory, Shimadzu Corporation, [3]Neurorehabilitation Research Institute, Bobath Memorial Hospital

Introduction

It has been pointed out that the brain functional data obtained using functional near-infrared spectroscopic (fNIRS) imaging system possibly include the signal changes related to pulsation or breathing in addition to those related to brain activities. We investigated whether signals from the skin blood flow are superposed on those related to brain activities during walking tasks using Independent Component Analysis (ICA).

Measuring methods

In healthy human subjects, signal changes during locomotor tasks on the treadmill were simultaneously recorded using the fNIRS imaging system (OMM-2001 SHIMADZU CORPORATION) and the laser tissue blood flowmeter (FLO-C1 OMEGA WAVE INC.). The fNIRS system consisted of 24 optodes including 12 light source fibers and 12 detector fibers resulting in 36-channel simultaneous recording. Interoptode distance was set to 3.0cm. The light source fiber next to the posterior one in the center row was located in the Cz portion. The sensor of the laser tissue blood flowmeter was located on the forehead. The locomotor tasks at various speeds (3km/h, 5km/h and 9km/h) were performed using block designs (30s rest-90s walking or running-30s rest).

Analysis methods

The oxy-hemoglobin data obtained from fNIRS system was analyzed by using ICA algorithm by Molgedey and Schuster (1994). The cross correlation coefficients between the each independent component data and the skin blood flow data from the laser tissue blood flowmeter were calculated. Furthermore, we introduced new statistics values which are expressed as Absolute values of Coefficient of Standard Deviation (ACSD:$\sigma/|ave(x)|$) of the each component from the mixing matrix. We compared the original cortical activation mappings based on task related oxy-hemoglobin changes with those after removing the independent component data regarded as the skin blood flow.

Results

The independent component wave of which ACSD is the smallest was conspicuously similar to the skin blood flow wave and the cross correlation coefficient was 0.724. In case of the locomotor task at 3km/h, the cortical activation mapping after removing the independent component data with the smallest ASCD was more localized to the medical sensorimotor areas compared to the original mapping.

Discussion

ICA can possibly separate the skin blood flow data from the oxy-hemoglobin data obtained from fNIRS system. In addition, ACSD might be a useful statistics value for finding the skin blood flow component without using the laser tissue blood flowmeter.

References

[1] L.Molgedey and H.G.Shuster Separation of a mixture of independent signals using time delayed corrections, Phys. Rev. Lett. Vol.72 No23 3634-3637 1994

[2] Ichiro Miyai et al. Cortical Mapping of Gait in humans. A Near Infrared Spectroscopic Topography Study, NeuroImage 14 1186-1192 2001

WE 214

Evaluation of Reference Tissue-Based Analyses for Measurement of Brain Acetylcholinesterase Activity Using *N*-[^{11}C]Methylpiperidin-4-yl Propionate and Positron Emission Tomography

Sato Koichi[1, 2], Fukushi Kiyoshi[1], Shinotoh Hitoshi[1], Nagatsuka Shin-ichiro[1], Tanaka Noriko[1], Ota Tsuneyoshi[1], Shiraishi Tetsuya[1, 2], Hirano Shigeki[1], Tanada Shuji[1], Iyo Masaomi[2], Irie Toshiaki[1]
[1]Depatment of Medical Imaging, National Institute of Radiological Sciences, [2]Department of Psychiatry, Graduate School of Medicine, Chiba University, Chiba, Japan

Background: Because of the requirement of arterial blood sampling and considerable technical expertise, the standard analysis to estimate the brain regional acetylcholinesterase (AChE) using *N*-[^{11}C]methylpiperidin-4-yl propionate ([^{11}C]MP4P) may restrict the widespread use of this method in daily clinical practice. In this study, the applicability of internal reference tissue-based analyses without arterial blood sampling was evaluated in healthy subjects.
Methods: Twelve healthy subjects (aged 56±17 years, mean±SD, range 32±86 years; 9 men and 3 women) participated. Injected radioactivity ranged from 10.8 to 20.6 mCi. A sequence of 16 scan time frames was acquired over 60 min in the two-dimensional mode. A simplified analysis of the ratio of target tissue radioactivity relative to reference tissue radioactivity developed by Herholz and co-workers [1], as well as a linear least squares analysis derived from Blomqvist's equation [2], was examined as a reference tissue-based analysis. To evaluate these analyses, the standard analysis using arterial blood sampling was also carried out.
Results: The standard compartment analysis provided reliable quantification of k_3 (an index of AChE activity) estimates in regions with low (neocortex and hippocampus), moderate (thalamus) and high (cerebellum) AChE activity with a coefficient of variation (COV) of less than 20%. However, precise k3 in the striatum, where AChE activity is the highest, was unable to be obtained. The striatum was used as an internal reference, since its time-radioactivity curve was proportional to the time integral of the arterial input function. Reliable k_3 estimates were also obtained in regions with low to moderate AChE activity with a COV of less than 20% by striatal reference analyses, though not obtained in the cerebellum. In comparison with the standard analysis, a moderate overestimation of k_3 in the linear analysis and a moderate underestimation in the Herholz method were observed, which were appropriately explained by the results of computer simulation. As the third reference tissue-based analysis, a full non-linear calculation of the operational equation was also investigated.
Conclusions: Striatal reference analyses are practical and useful for the routine analysis of clinical [^{11}C]MP4P studies and should be almost as effective as the standard analysis for detecting regions with abnormal AChE activity.
[1] Herholz *et al.* (2001) *Eur J Nucl Med* 28: 472-477
[2] Nagatsuka *et al.* (2001) *J Cereb Blood Flow Metab* 21: 1354-1366

WE 215

Quantitative comparison study using of Korean probabilistic atlas and MNI SPAM: a rationale for constructing group specific probabilistic brain atlas

B.B. Koo[1], J.M. Lee[1], J.S. Kim[1], J.S. Lee[2], I.Y. Kim[1], J.J. KIm[4], D.S. Lee[2], J.S. Kwon[3], S.I. Kim[1]
[1]Department of Biomedical Engineering, Hanyang University, Seoul, Korea, [2]Department of Nuclear Medicine, Seoul National University, Seoul, Korea, [3]Department of Psychiatry, Seoul National University, Seoul, Korea, [4]Department of Psychiatry, Yonsei University, Seoul, Korea

- Backgrounds

Probabilistic atlases for human brain structure are more representative of population anatomy than single brain atlases. This approach allows localizing of the functional neuro-images with the consideration of morphological variability, anatomical labeling of the results of group studies in stereotaxic space, automated anatomical labeling of individual brain imaging datasets, and the statistical assessment of normal ranges for structure volumes and extents. From the point of view, we hypothesized a group-specific, i.e., ethnic, gender, age, or disease, probabilistic atlas showed differences from others which could reflect the characteristics of the group.

- Materials and Methods

Seventy six normal brains underwent T1-weighted spoiled gradient echo magnetic resonance imaging on a 1.5-T GE SIGNA scanner to construct a Korean probabilistic brain atlas. An anatomical definition of 89 regions of interest (ROI) was performed by a trained anatomist and the developed tools such as standard brain selection, spatial normalization and a nonlinear registration. Then, the occurrence of each region was calculated in each voxel. For assessing the difference between Korean probabilistic atlas and MNIs, which was developed for the functional labeling in the Montreal Neurological Institute, template matching between two probabilistic atlas was performed by using maximizing intensity similarity algorithm and re-sampling technique. After the spatial normalization process, corresponding ROIs between two atlases were extracted by two separate neuroanatomically trained operator. Then, the three factors, such as measurement of volume above the probability thresholds, Euclidian distance of center of mass and correlation factor, measured from each pairs of extracted ROIs were used for quantitative comparison between two probabilistic templates.

- Results

Korean SPAM showed similar degree of variability and shape with MNIs in the inner structure such as Basal ganglia, but also showed very disparate variance patterns in many other regions. Although this result can not indicate the ethnic difference directly because of slight difference in the constructing tools, it can be a proper demonstration of group specific probabilistic atlas. (Fig.1)

- Conclusion

In this study, we developed Korean probabilistic brain atlas, which was intensity based probabilistic atlases for volumetric studies of neuroanatomical structures, and compared it with the probabilistic atlas of Montreal Neurological Institute (MNI). This study can give a preliminary result on the group difference and suggest a novel approach to investigate the group specific atlas in the future study.

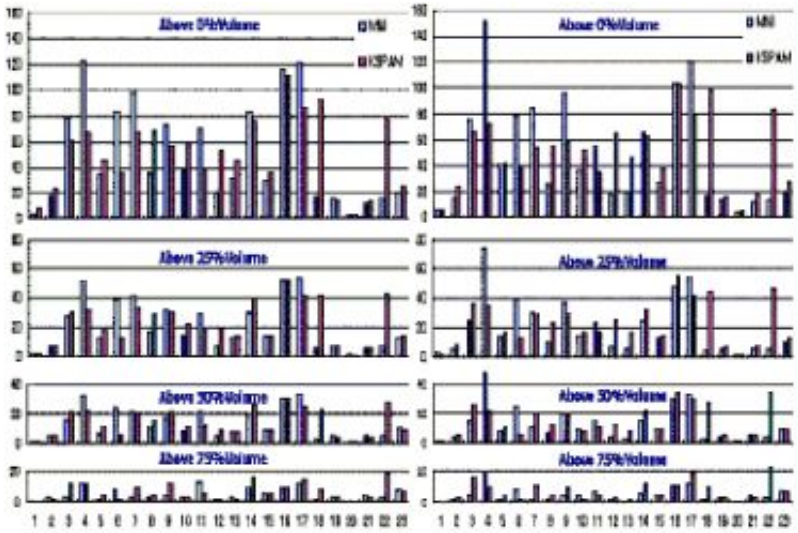

Number	Region of Interest
1	Amygdala gyrus
2	Hippocampal Formation
3	Inf. Temporal gyrus
4	Mid. Temporal gyrus
5	Parahippocampal gyrus
6	Sup. Temporal gyrus
7	Precuneal gyrus
8	Supramarginal gyrus
9	Sup. Parietal lobe
10	Cuneus
11	Lingual gyrus
12	Precuneus
13	Inf. Occipital gyrus
14	Inf. OccipitoTemporal gyrus
15	Insula
16	Mid. Frontal gyrus
17	Sup. Frontal gyrus
18	med. FrontoOrbital gyrus
19	caudate nucleus
20	Globus Pallidus
21	Putamen
22	Cingulate
23	Thalamus

Figure 1: ***Comparison result of volume measured by probabilistic thresholding***

WE 216
Functional connectivity of cortico - basal ganglia circuitry

Pierre-Jean Lahaye[1], Christine Delmaire[2], Emmanuel Gerardin[3], Stephane Lehéricy[4], Jean-Baptiste Poline[1]
[1]CEA/SHFJ, Orsay, France, [2]Department of Neuroradiology, CHU Salpêtrière, Paris, France, [3]CHU C Nicolle, Rouen, France, [4]CMRR/University of Minnesota, Minneapolis, USA

Introduction. Anatomical studies in non-human primates have shown that cortico-striatal connections are organized in segregated circuits (1-4). The sensorimotor cortex projects toward the posterior putamen. The premotor cortex projects toward more anterior parts of the putamen. The associative prefrontal cortex projects toward the caudate nucleus and large parts of the rostral putamen. In humans, these circuits have been evidenced using diffusion tensor imaging (5). This study aimed at determining the functional connectivity of cortical and basal ganglia areas, using a task allowing differentiating the motor, premotor and prefrontal circuits.
Materials and Methods. Nine right-handed volunteers were studied with EPI BOLD contrast at 3T. EPI axial slices (140 volumes) were acquired (TR/TE/ flip angle = 2 s / 40 ms / 90°, voxel size = 3.4x3.4x5mm3). Subjects were presented with a series of visual stimuli instructing them to prepare during a variable delay (4, 6 or 8 s) and execute a button press with either the left or the right hand (Go). The side of the movement was either selected by the subject (Selection) or specified by the instruction cue (Preparation). No-go signals also occurred at varying intervals. Data analysis was performed with SPM99. Clusters were considered significant at $p<0.05$ corrected. The connectivity analysis was performed on signals of 6 ROIs defined on anatomical images (Table 1). The amplitude of the response was estimated for all single events of each condition using a GLM model. For each condition and subject, the correlation between response amplitude found in different regions was calculated.
Results. **SPM analysis**. Movement selection was associated with activation in the associative prefrontal cortex, the rostral preSMA, and the caudate nucleus. Movement preparation was associated with significant signal changes in the preSMA, the primary sensorimotor cortex and adjoining parts of the lateral premotor cortex, and in the anterior part of the putamen. Movement execution was associated with activation in the primary sensorimotor cortex, the medial premotor cortex, the inferior parietal cortex, the posterior part of the putamen, and the thalamus.
Functional connectivity analysis. The correlations found for responses to all types of events are given in Table 1.
All 3 diagonal relations (CN-DLFPC, AP-PMC, PP-SMA) strongly increased in the 'Go' condition (coefficients of correlation of 0.54, 0.42, 0.54, respectively) relative to the 'No-go' condition (coefficients of correlation 0.46, 0.35, 0.46, respectively). Moreover, the CN-DLFPC correlation was stronger during the 'Selection' condition relative to the 'Go' and 'Preparation' conditions (0.61 versus 0.57 and 0.51), while the AP-PMC and PP-SMA correlations were stronger for the 'Preparation' condition (respectively 0.54 and 0.56 for 'Preparation' and 0.47, 0.41 and 0.49, 0.48 for 'Selection' and 'Go' conditions)
Conclusion. These results suggest that mental processes associated with movement selection, preparation, and execution are represented differentially within distinct rostro-caudal cortico-basal ganglia circuits. They also suggest that the functional relationship between anatomically connected cortical and subcortical areas is enhanced when these areas are actively recruited to perform the task.
References. (1) Alexander GE et al. Prog Brain Res. 1986 ; (2) Flaherty and Graybiel, 1993; (3) Inase et al., 1996; (4) Selemon and Goldman-Rakic, 1985; (5) Lehéricy et al. Ann Neurol, 2004.
Acknowledgments. This study was supported by grant ACI 6503H.

Table 1. Amplitude of correlations for all conditions

Correlation	Dorsolateral prefrontal cortex (DLFPC)	Lateral premotor cortex (PMC)	Supplementary motor area (SMA)
Caudate nucleus (CN)	0.47	0.37	0.44
Anterior putamen (AP)	0.41	0.38	0.47
Posterior putamen (PP)	0.36	0.34	0.46

WE 217
The BOLD/ EEG relationship and data fusion from simultaneous EEG/fMRI recordings

Pierre-Jean Lahaye[1,3], Jean-Baptiste Poline[1,3], Sylvain Baillet[2,3], Denis Schwartz[2,3], Laurent Hugueville[2,3], Jacques Martinerie[2,3], Line Garnero[2,3]
[1]CEA/SHFJ, Orsay, France, [2]CNRS/LENA, Paris, France, [3]IFR49, Paris, France

Introduction
Recent findings in animal electrophysiology suggest a linear relationship between evoked electrophysiological activity (esp. LFPs) and the amplitude of the corresponding BOLD response [1]. In parallel, it has been found that event-related fMRI recordings may elicit variable amplitude of single BOLD responses to identical stimuli [2]. In this work, we tested the hypothesis that the 'neural' activity as seen in EEG may explain variability observed in BOLD event related response, which could shed light on the origin of the BOLD signal and lead to better models. In a second step, the electro-metabolic coupling is locally detected using EEG/fMRI conjoint recordings. This coupling is then included in a fusion model to improve the localization and temporal separation of source reconstruction.

Methods
Protocol
We used an evenemential visual paradigm [5] composed of expanding rings stimuli (75 stimuli of duration 1.2s, rings moving at a 5Hz frequency during the 1.2 s). Events occurred randomly outside gradient switching periods in an interleaved acquisition design (1.5s acquisition - 1.5s pause). Two sessions were recorded from several healthy subjects.
Analysis
After pre-treatments, these data were analyzed in 3 steps.
(1) Data from each modality were separately analyzed for VEPs and BOLD activation maps, using BrainAmp Vision Analyzer and SPM.
(2) The energy of EEG signals at the 5Hz frequency (the stimulus frequency) was convolved by the canonical HRF to form additional regressors included in a new SPM model. The areas where EEG modulates BOLD response are compared to the classical activation map.
(3) A new EEG/fMRI fusion method [3] is applied. The local correlations between electrical source energies and BOLD response amplitudes [4] across events are detected, and then used where significant to inform and improve EEG source reconstruction.

Results
Following the analysis methods above,
(1) VEPs exhibit 5Hz oscillations at the frontal and occipital electrodes for all subjects. A fronto-occipital activation network is found in fMRI data in single subject and fixed effect analyses (frontal medial, V1, V5, $p<10^{-3}$, uncorrected).
(2) We show that a positive reproducible relation is found between EEG power (5 Hz, O1/O2) and BOLD response at sites in V5 and the frontal cortex for all subjects considered (p

-3, uncorrected). In V1, the EEG/BOLD relation is statistically significant ($p<10^{-3}$, uncorrected) but its sign varies across subjects. Modulation seems located at sites specifically activated by the paradigm.
(3) Local correlation between source energies and BOLD response
amplitudes has been found in occipital and frontal cortices on the first subjects analyzed (0.3 maximum correlation). The fusion step has been validated on simulation data [3] and is currently being carried out on this dataset.

References
[1] N. Logothetis et Al. Nature 412, 2001.
[2] J.-R. Duann et Al. Neuroimage, april 2002.

[3] P.-J. Lahaye, S. Baillet J.-B. Poline and L. Garnero, Proc. IEEE ISBI, 2003, accepted.
[4] P. Ciuciu, J.-B. Poline et Al. IEEE Trans. Medical Imaging, Oct. 2003.
[5] O. David, D. Cosmelli et Al. Neuroimage 2003, accepted.

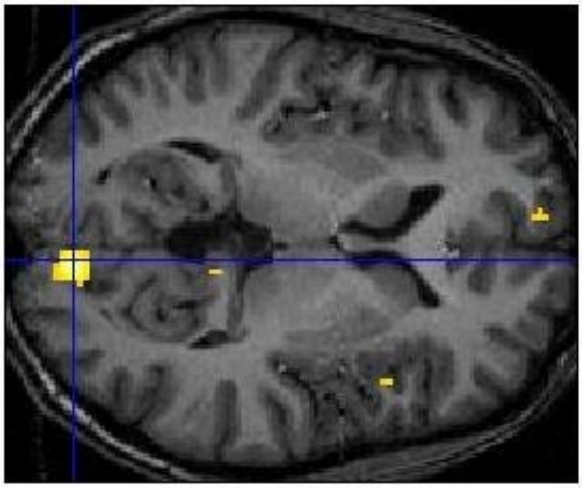

Modulation of BOLD response by EEG power

WE 218
BrainMap: An Environment for Meta-Analysis in Functional Neuroimaging Research

Angela R. Laird , Jack L. Lancaster , Peter Kochunov , Peter T. Fox
Research Imaging Center, University of Texas Health Science Center San Antonio

BrainMap is an online database and content-based neuroinformatics tool for the human functional brain mapping literature that has been under development for the last ten years. The purpose of BrainMap is to provide rapid, comprehensive access to the literature and its data in a manner facilitating the understanding of study design and results. In addition, BrainMap promotes quantitative meta-analysis of related studies. To this end, a multi-dimensional, multi-level indexing scheme for the context and content of brain-mapping studies has been developed. Papers described in BrainMap are coded by a team of scientists at the Research Imaging Center in San Antonio; however, submissions are accepted from both authors who seek higher visibility for their results or researchers interested in performing meta-analyses. Any published or in-press functional-mapping study in a peer-reviewed journal is eligible for submission.

The java-based application, Submit, is used to create an entry to BrainMap, while the Search&View application is used to view the entries in the BrainMap database. BrainMap currently contains 1,967 experiments, an experiment defined by the production of a statistical parametric image (SPI). Experiment information includes detailed descriptions of the behavioral conditions contrasted to create the SPI and the coordinate addresses of all reported activations, to facilitate meta-analysis. The present experimental corpus (1,967 entries) was drawn from 480 publications and reports 16,963 focal activations. Current rate of data entry is 1200-1600 experiments per year. The database is anticipated to grown at this rate (or faster) until the complete volume of literature is entered. Information is rapidly retrieved from the database using to a highly structured system of keywords. Once the studies of interest are downloaded into the Search&View workspace (Figure 1), they may be filtered to include or exclude experiments of interest. Search&View has been redesigned with a split panel workspace to aid paper viewing, wherein information about each paper may be viewed in the bottom panel of the workspace, and experiments are selected for plotting in the top panel. The Search&View plot panel (Figure 2) maps the activation locations for similar experiments on a Talairach template. Plotted locations for each paper are displayed in a different color and numbers are placed next to the foci to distinguish experiments within a paper.

Many new features have been added to Search&View, including: plot options dialog to enhance user control of each experiment, color dialog GUI (added sliders and changed defaults), option to export coordinates to text file, and notification of active locations/total locations in workspace and plot options dialog. In addition, it is now possible to search by anatomical label assigned by Talairach Daemon, and to filter plots by anatomical labels and ROIs. Lastly, the capability for creating a behavioral histogram profile has been added, an analysis tool that can characterize the behavioral aspects of a collection of experiments. Future work will involved the incorporation of advanced meta-analysis tools into the Search&View environment. Complete information about the BrainMap database and free software may be found at www.brainmap.org.

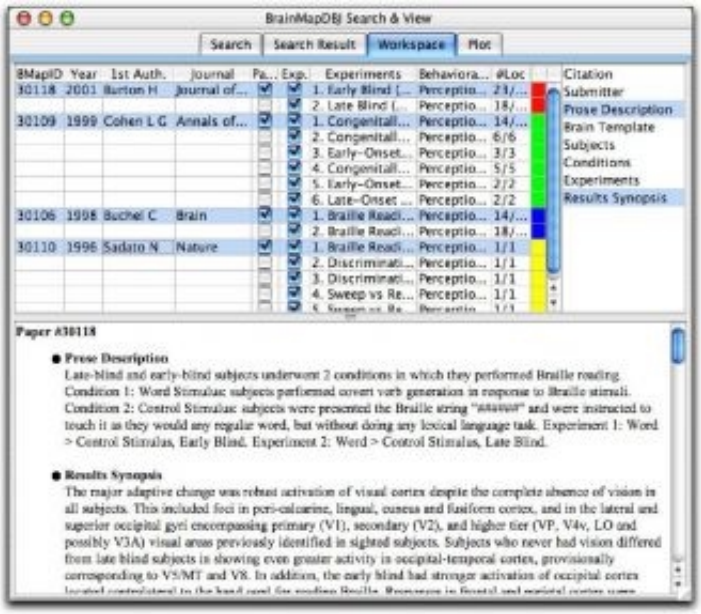

The BrainMap Workspace.

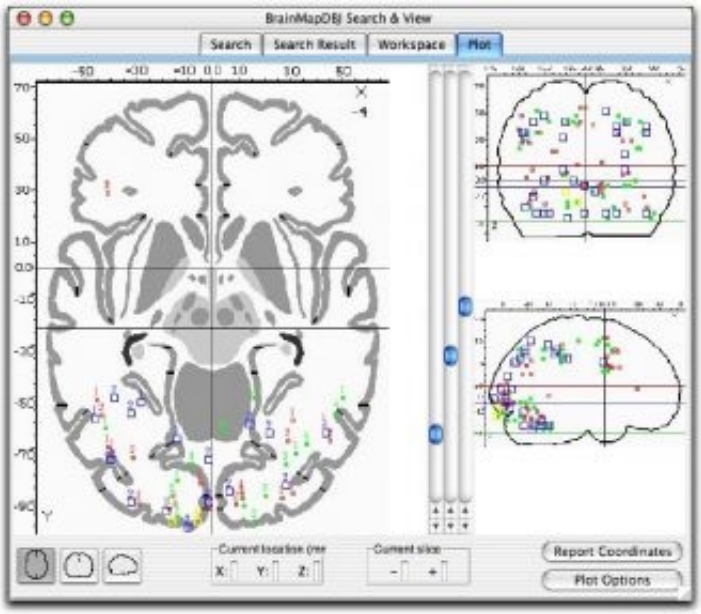

The BrainMap Plot Panel.

WE 219
Magnetoencephalographic Signals in Brain-Computer Interfaces

Laura Laitinen[1], Tommi Nykopp[1], Mikko Sams[1], Riitta Hari[2]
[1]Laboratory of Computational Engineering, Helsinki University of Technology, Finland, [2]Brain Research Unit, Low Temperature Laboratory, Helsinki University of Technology, Finland

Introduction: A brain-computer interface (BCI) records brain activity and classifies it into different categories that can be associated with computer commands to operate, *e.g.* a neural prosthesis. Currently, the nonexpensive and portable EEG is the best option for practical non-invasive BCIs. However, EEG signals are blurred by extracerebral tissues, which is not the case with MEG [1]. We therefore studied the use of MEG signals of the sensorimotor cortex as an input to a BCI. Specifically, we tested how different feature sets influence classification of the signals.
Methods: Four right-handed healthy adults participated in the whole-head MEG study. Subjects performed brisk index finger extensions, either left- or rightsided or bilateral according to their own choice after a tone presented once every 3 s. About 80 trials were collected for each movement, and the experiment was repeated once. A human expert selected a frequency band (centered on peak frequency, width 10 Hz) and a subset of MEG sensors (12 channels around the maximum signal) for each individual; this selection of feature sets was based on amplitude spectra and time-frequency representations of averaged movement-related sensorimotor signals.
The BCI classification utilized the postmovement rebound of 20-Hz activity occurring 0.51.5 s after movement onset [2]. The strength of the rebound, defined in frequency domain separately for each single trial with respect to a 0.5-s premovement baseline, was used as an input to a radial-basis-function classifier which was taught with the first data set and tested with the second; features were selected from the first data set only. No trials were rejected.
Results: Before and during finger movements, the motor-cortex 20-Hz activity was suppressed bilaterally in all subjects, followed by a contralaterally-dominant rebound seen in the single trials (Fig. 1) and very clearly in the averaged data (Fig. 2). The peak frequencies of signals used in the classification varied from 18 to 23 Hz in different subjects. The MEG signals related to the left- and right-sided movements were separated with an accuracy of 83%, 83%, 89%, and 90% in the four subjects.
Conclusions: The classifications were encouragingly good, suggesting that single MEG trials from the sensorimotor cortex can provide accurate information for BCIs.
[1] Hämäläinen et al., Rev. Mod. Physics 1993
[2] Salmelin and Hari, Neurosci. 1994

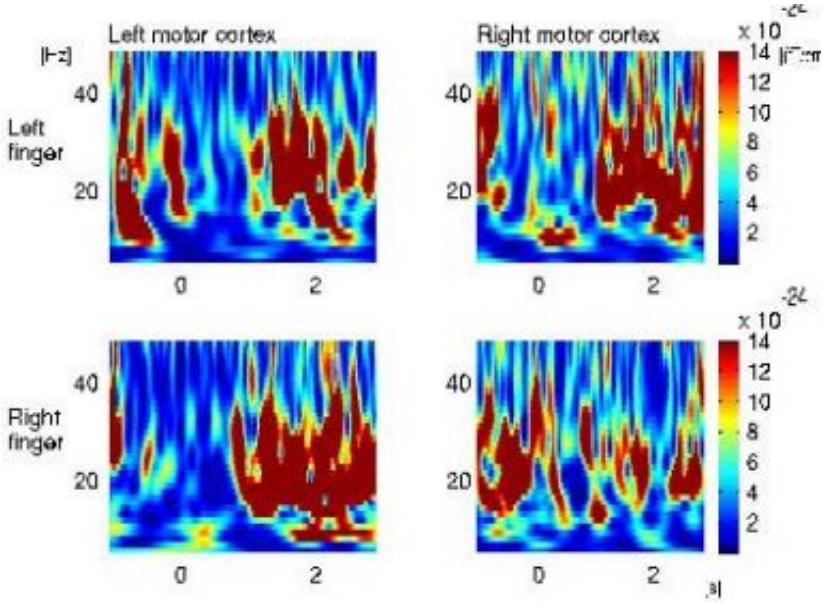

Figure 1: Time-frequency representations of 20-Hz rebound calculated from a single trial

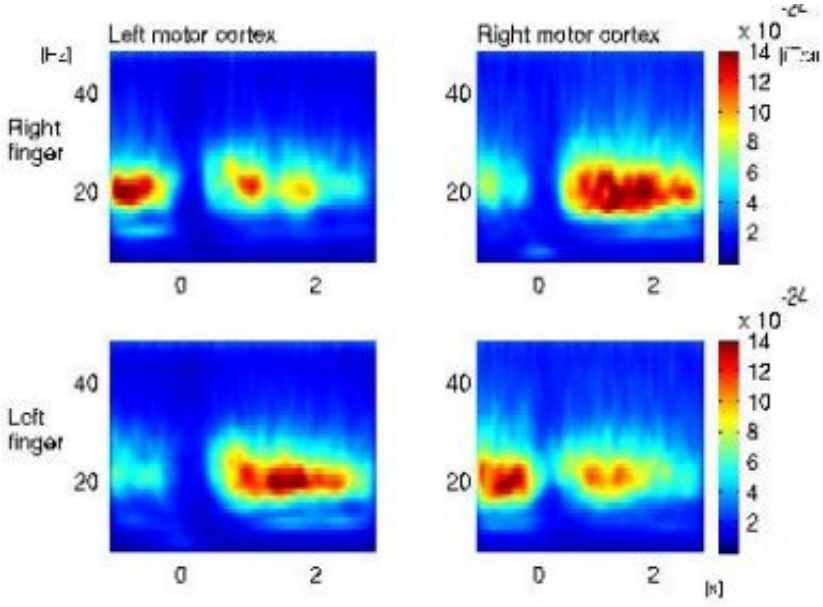

Figure 2: Time-frequency representations of 20-Hz rebound calculated from averaged trials

WE 220
Automatic generation of cortical surface model estimating deep sulci with partial volume effect

Jun-Ki Lee[1], Jong-Min Lee[1], Jun-Sik Kim[2], In-Young Kim[1], Sun-Il Kim[1]
[1]Department of Biomedical Engineering, Hanyang University, Seoul, Korea, [2]Montreal Neurological Institute, Montreal, Canada

Purpose:
The surface of the human cerebral cortex is a highly folded sheet. So, it is difficult to obtain an accurate and explicit representation of the cortical surface. Especially, PVE (Partial Volume Effect) causes vague boundary, between GM(gray matter) and CSF (cerebrospinal fluid), which results in the inaccurate surface representation. The iterative morphing methods such as ASP[1] overcome this problem partly with some model constraints. But, those constraints also cause inaccurate results in outer cortical surface. This paper presents a methodology for extracting accurate parametric representations of the cortical surface. We applied new forces to CLASP[2] for the accurate estimation of cerebral deep sulci which has the vague boundaries caused by PVE.
Method & Data:
The deformable surface is processed as the objective function is minimized. The objective function is devised to measure how closely a particular surface or set of surfaces simultaneously approximates the image data and adheres to a set of model constraints. This process produces two surfaces representing gray/white and gray/CSF interfaces respectively. The method we present was basically constructed on ASP. The forces which were used for the surface deformation are composed of two kinds of forces. Ones are from the distance fields estimating sulcul area with PVE. The others are from CLASP which is a kind of deformable surface model algorithms modified from conventional ASP. For the correct estimation of deep sulci with the PVE, two kinds of distance fields were generated and added to the objective function of original ASP as forces which pulling the surface into the center of sulcus area. One is the distance map between the inner and outer boundaries of the brain cortex. And the other is the distance map generated from the bottom of the sulcul area of the GM. To find the seeds for the second distance field, we generated single-seeded distance field and found the voxels with local-maximum value in this field. The algorithm was validated on 20 normal datasets which randomly selected from ICBM normal brain datasets from MNI (Montreal Neurological Institute, Montreal, CA).
Results:
To evaluate our method, we used GM volume comparison. We compared the tissue-classified GM obtained by INSECT with surface-masked GM obtained by ASP, CLASP, and the method we proposed respectively. In the volume based evaluation, the accuracies (True-Positive) of the surface models generated by ASP, CLASP, and our methods were 58%, 71%, 68% respectively. This result showed the improvement of the accuracy compared with conventional ASP. The method also could estimate deep sulci with PVE which couldnt be found by ASP or CLASP.

WE 221
Evaluation of MRI gradient noise effects on EEG source localization

Soo Y. Lee , Jae Y. Han , Tae S. Park , Min H. Cho
Graduate School of East-West Medical Science, Kyung Hee University, Korea

In the combinatory study of EEG and fMRI, the EEG source localization can provide high temporal resolution information while fMRI giving accurate spatial information about the brain activities. However, the gradient field switching during fMRI scans causes serious noise in the simultaneously measured EEG data. Considering the previous successful developments of gradient noise reduction techniques, it is expected that combinatory studies of EEG source localization and fMRI will be increased to a great extent in the near future.
In this work, we have evaluated the effects of the gradient noise on EEG source localization. Since the gradient noise has strong non-gaussianity, we have evaluated the effects using a real phantom on which an array of EEG electrodes was placed to pick up the gradient noise inside the MRI magnet as shown in figure 1. The phantom consists of two hollow hemispheres that can be joined to form a hollow sphere. Inside the sphere phantom filled with NaCl solution, we placed three electric current dipoles (ECDs) connected with external waveform generators. The 32 channel electric potential signals picked up at the electrodes were fed to an MRI compatible EEG amplifier. The spherical EEG phantom was placed in the center of the whole body 3.0 Tesla MRI system. The electric potential signals were measured during gradient echo single-shot EPI scans. The EPI scans were performed with the echo time of 36 ms, the gradient rise time of 160 ms, the image matrix size of 128 128, and the sampling time of 4ms. For EEG source localizations, we have used the simulated annealing method with the annealing temperature determined by the evolution strategy. In figure 2, we have shown examples of the measured potential signals with and without the gradient noises. Figure 2(a) and (b) show the potential signals when the gradient-noise power ratios relative to the sinusoidal potential signal power are 0 % and 29 %, respectively. The gradient noise waveform was found to have a super-gaussian distribution with the kurtosis as high as 18.6. This implies that the gradient noise effects should be analyzed with the real noise waveform. In figure 3, we have shown the localization errors in the EEG source localization with the electric potential data corrupted with the gradient noise and the simulated gaussian noise. As can be noticed from figure 3, the gradient noises and the gaussian noises have similar effects on the source localization when the gradient noise power ratio is below 20%. However, the gradient noise has much bigger negative effects than the gaussian noise when the gradient-noise power ratio is high.
As far as the present experimental results are concerned, it seems that the EEG data measured during fMRI scans can be used for the EEG source localization if the gradient-noise power ratio can be sustained below 15-20% by proper gradient-noise-reduction techniques.

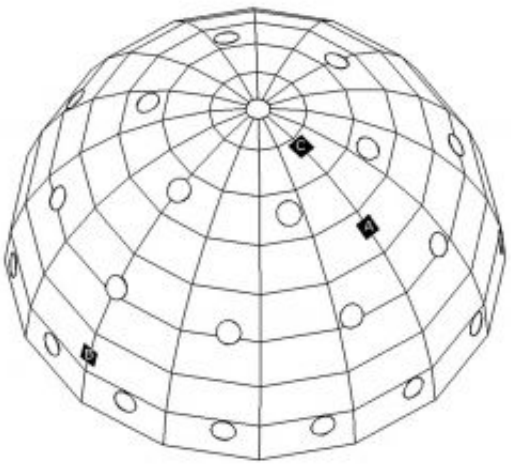

The upper part of the spherical EEG phantom

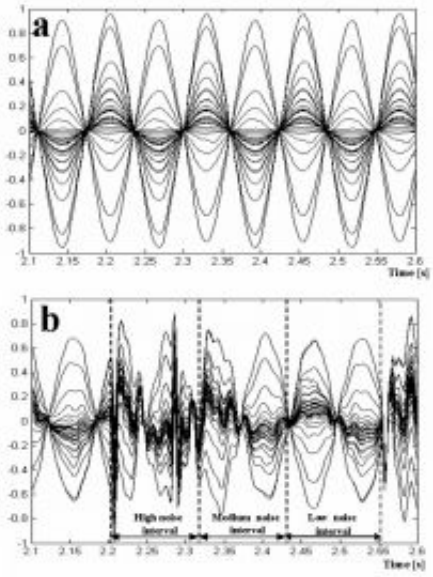

The potential signals (a) without the gradient noise and (b) with the gradient noise

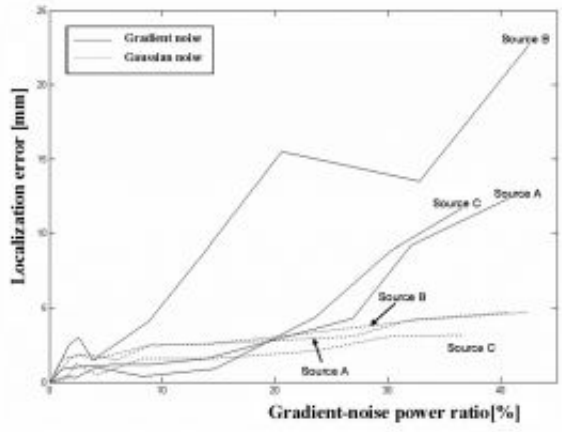

The localization errors caused by the gradient noise and the gaussian random noise

WE 222
Anatomical Connectivity Mapping Inferred from DTI-based White Matter Geometry

Christophe Lenglet , Rachid Deriche , Olivier Faugeras
Odyssee Lab, INRIA Sophia Antipolis, France

Introduction:
Diffusion MRI is the unique non-invasive technique capable of probing and quantifying the anisotropic diffusion of water molecules in biological tissues. Motivated by the potentially dramatic improvements that knowledge of anatomical connectivity would bring into the understanding of functional coupling between cortical regions [2], the study of neurodegenerative diseases, acute brain ischemia detection or tumor growth quantification, various methods have been proposed to tackle the issue of cerebral connectivity mapping. Local approaches [1,4] provide fast algorithms and can be augmented to incorporate natural constraints such as regularity, stochastic behavior or local non-gaussianity. Global algorithms [5] were proposed in order to resolve ambiguities related to false planar or spherical tensors in regions of fibers crossings. We derive a novel approach to white matter tractography, through the use of stochastic processes and differential geometry, which yields physically motivated distance maps in the brain seen as a 3D manifold. We also propose efficient and accurate numerical schemes to estimate neural fibers connecting pairs of voxels of interest.

Methods:
We have established [3] a rigorous link between Brownian motion and diffusion MRI by using the Laplace-Beltrami operator. It can be shown that the sole knowledge of the diffusion properties of water molecules is sufficient to infer the geometry of the manifold. Having access to that metric through our measurements, we propose a novel level set formulation to approximate the distance function generated by a Brownian motion. We actually solve the 3D anisotropic eikonal equation constrained by the fractional anisotropy *FA*. On that basis, a rigorous numerical scheme using the exponential map is derived to estimate the geodesics i.e. the diffusion paths of water molecules. Our dataset* consists of 30 diffusion weighted images and one T2 image. They were obtained on a GE 1.5T Signa Echospeed with a maximum gradient strength of 22mT/m. The echoplanar images were acquired in 56 evenly spaced axial planes with 128 x 128 pixels in each slice. Voxel size is 1.875 x 1.875 x 2.8mm. 6 gradient directions, each with 5 different b-factors and 4 repetitions were used. Imaging parameters were: b values between 0 and 1000s/mm^2, TR = 2.5s, TE = 84.4ms and a square field of view of 24cm [6].

Results, Conclusion:
Numerical experiments conducted on our dataset (Figure 1) in the splenium of the corpus callosum show that the algorithm estimates the best connection in terms of our distance function and is not influenced at all by locally isotropic regions. This global approach enforces coherence into DTI data and naturally handles ambiguities affecting local tractography, thus resulting in consistent tracking in crossings areas.

* kindly provided by J.F. Mangin and J.B Poline, CEA-SHFJ/Orsay, France

References:
[1] P.J. Basser et al, MRM 44:625-632, 2000
[2] M. Guye et al, NeuroImage, 19:1349-1360, 2003
[3] C. Lenglet et al, INRIA Research Report 4983, 2003
[4] S. Mori et al, Ann. Neurology, 45:265, 1999
[5] L. O'Donnell et al, MICCAI, LNCS 2488 459-466, 2002
[6] C. Poupon, PhD Thesis, ENST, Paris, 1999

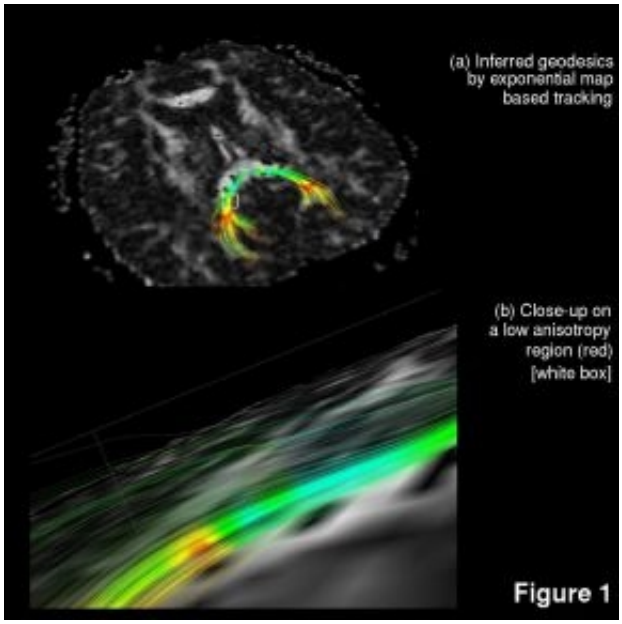
(a) Inferred geodesics by exponential map based tracking
(b) Close-up on a low anisotropy region (red) [white box]
Figure 1

WE 223
Evaluation of a landmark curve matching technique in brain mapping based on the level set method

A.D. Leow[1], H.D. Protas[2], S.C. Huang[2], P.M. Thompson[1]
[1]Laboratory of Neuroimaging, Department of Neurology, UCLA School of Medicine, [2]Department of Biomathematics and Department of Molecular and Medical Pharmacology, UCLA

Introduction
The level set method using implicit representation has recently been developed and shown to be capable of matching all types of geometric objects. The method was evaluated in this study for its ability to perform brain surface warping subject to landmark curve constraints. This key step in brain mapping allows multiple subjects' data to be compared after adjusting for gyral differences. Other methods that match equidistant landmark points on the curves via point matching do not allow relaxation along the curves. Moreover, it is difficult to incorporate these techniques into other methods due to the non-variational nature of point constraints. The method we use incorporates the level set method into image warping, offering a unifying approach for different types of feature-based matching. A diffeomorphic, one-to-one, and onto mapping can be generated using this approach subject to different kinds of feature constraints.
Methods
The brain surfaces of 4 normal individuals were flattened to the unit square in which a flattened brain surface of an average human template was defined. Nine sulcal curves (the central, precentral, postcentral, middle frontal, primary intermediate, collateral, and olfactory sulci, an olfactory control line and the Sylvian fissure) were chosen for testing our curve based warping method. Each sulcal curve was represented by the intersection of two level set functions. The resulting transformation was interpolated and applied to warp the brain surface, thus establishing a mapping between the individual and the average human brain. A set of coupled PDEs was used to guarantee a diffeomorphic mapping. As a measure of the adequacy of the method, the deviation of warped subjects' data from the average template was evaluated using the partial Hausdorff distance between individual and average sulcal curves. The partial Hausdorff distance is defined as the maximal value of the distance from any point on the individual curve to the corresponding average curve. The value was averaged over all selected sulci for each individual and then the maximum deviation over the four individuals was reported.
Results
The level-set based method was successful in curve matching for all subjects. To compute the partial Hausdorff distance, we discretized each curve to 100 points and evaluated the distance function of the average curve at the warped positions of these 100 points. The partial Hausdorff distance was then approximated by the maximum of these 100 values. The distances were similar among all 9 pairs of sulci, and consistent among 4 individuals with a maximal value of 0.3 pixel size. Fig. 1 shows the brain surface of one individual with the identified landmark sulcal curves. Fig. 2 shows the same brain surface on the flattened space with the average sulcal curves while Fig. 3 shows the warped brain surface. Fig. 4 shows the computed deformation for mapping the brain surface.
Conclusion
The level set method is capable of warping brain surfaces to a population average, which allows brain images from multiple subjects to be compared. The method is also expected to be useful for monitoring disease progression and for evaluation of treatment.

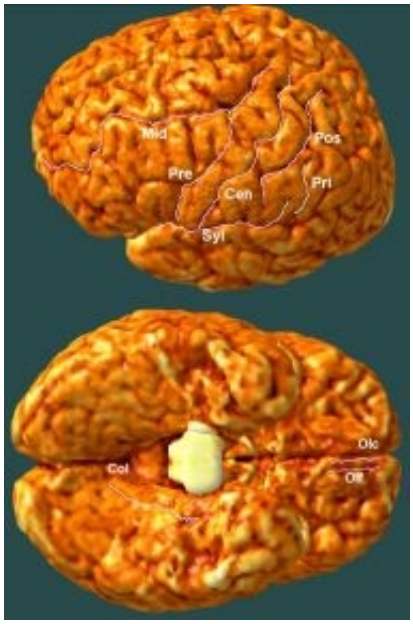

Figure 1: The brain surface of a normal individual with the nine sulcal curves chosen for surface warping

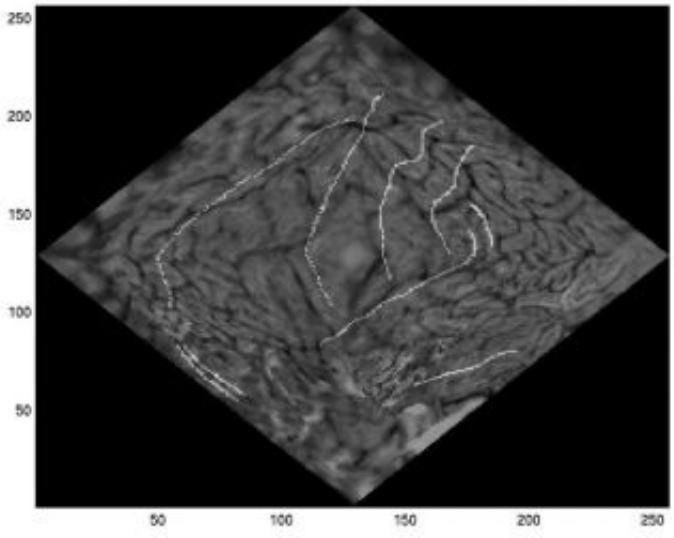

Figure 2: The flattened brain surfae in Fig. 1 overlaid with the landmark curves of the average human brain template

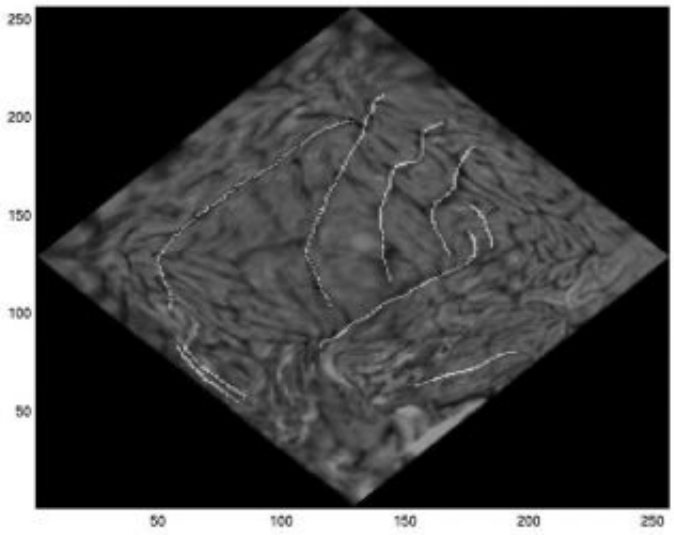

Figure 3: The brain surfae in Fig. 2 after warping overlaid with the landmark curves of the average human brain template

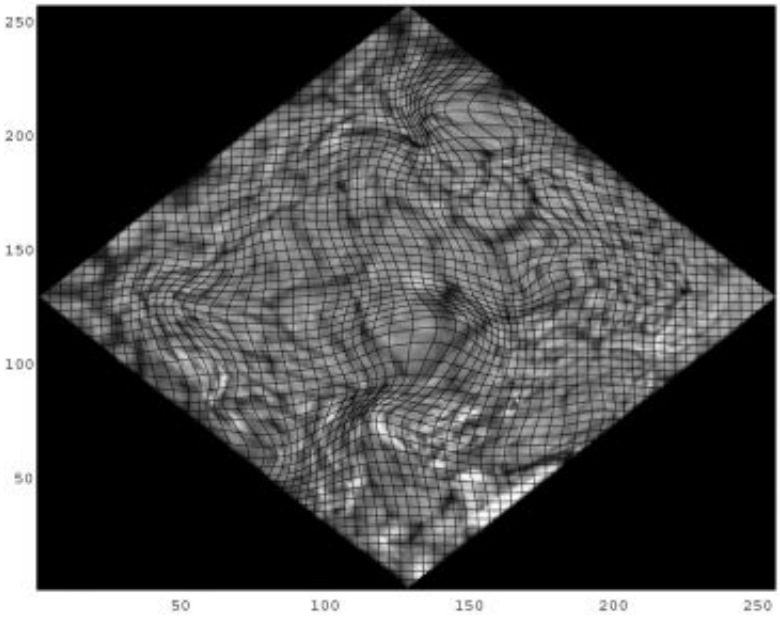

Figure 4: The warped brain surface in Fig. 3 overlaid with the underlying grid deformation

WE 224

Effective Drift Alleviate Algorithm in fMRI Time Series

Xingfeng Li[1], Jie Tian[1], Xiaoxiang Wang[1], Jianping Dai[2], Lin Ai[2]
[1]Medical image processing group, Institute of Automation,Chinese Academy of Sciences, [2]Department of radiology, Tiantan Hospital,Chinese Capital Unversity of Sciences

Modeling & Analysis

Abstract

Introduction

Quite often fMRI data contain low frequency drift with the signal intensities of certain voxels slowly rising or falling during the whole imaging series. The low frequency is very useful for functional connectivity study during the rest state, but it is harmful to active region detection when using block design method. To alleviate the baseline drift effect in the temporal fMRI signals, several groups applied a linear regression procedure with the least-square estimation as a pre-processor. Their method, however, is based on the assumption that the drift is linear and stable. These assumptions are often not satisfied. We present a new method for drift remove. The approach can be utilized to alleviate the low frequency drift effectively.

Materials and Methods

Imaging was performed on a 3.0-T GE Signa system (General Electric, Milwaukee WI, USA) with a standard head coil. Ten healthy subjects (7 men, mean age 35 years) participated in a hand flexing and extending experiment. The following methods for image acquisition were employed in the hand flexing and extending experiment. The whole scan took 5 min 12 seconds. The control and experimental conditions were alternated every 30 s (10 scans) and repeated so that each condition would occur 5 times. Each hand flexing and extending data set comprised 100 volumes. For each block, we calculate the maximum values and minimum of each block. For the maximum values, we employed the spline method to interpolate the curve as the up envelope. In the same way, we interpolated the minimum values of each block to calculate the down envelope. Finally, we averaged the upper and low envelope to approximate the low frequency drift.

Results

Figure 1 shows the original curve with Fourier series fit results using the ordinary least square method. In Fig. 2, we calculate the up envelope and down envelope of the curve, and averaged these two curves to calculate the low frequency drift (Fig. 3).

Discussion and Conclusion

Because of the inherently low signal to noise ratio (SNR) of fMRI data, removal of low frequency signal intensity drift is an important preprocessing step, particularly in those brain regions that weakly activate. The advantage of this method is that it is adaptive and easy to apply. In short,we presented an effective method for reducing the effect of low frequency drift in fMRI.

References

[1] Tenabe et al. Neuroimage 2002 15:902-907; [2] Skudlarski et al. Neuroimage 1999 9:311-329; [3] Smith et al. Neuroimage 1999 9:526-533.

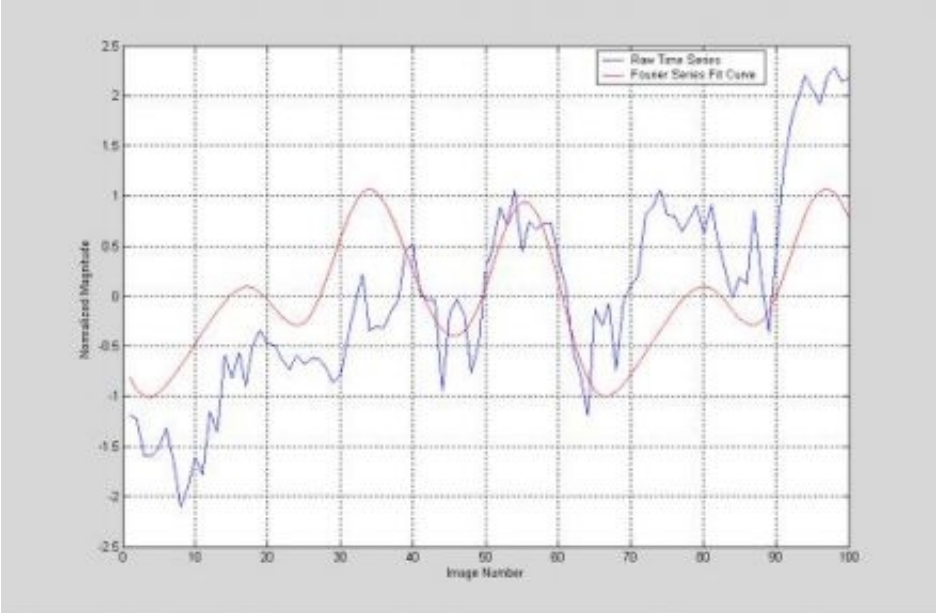

Figure 1. One example of raw time series and its fit result using Fourier series.

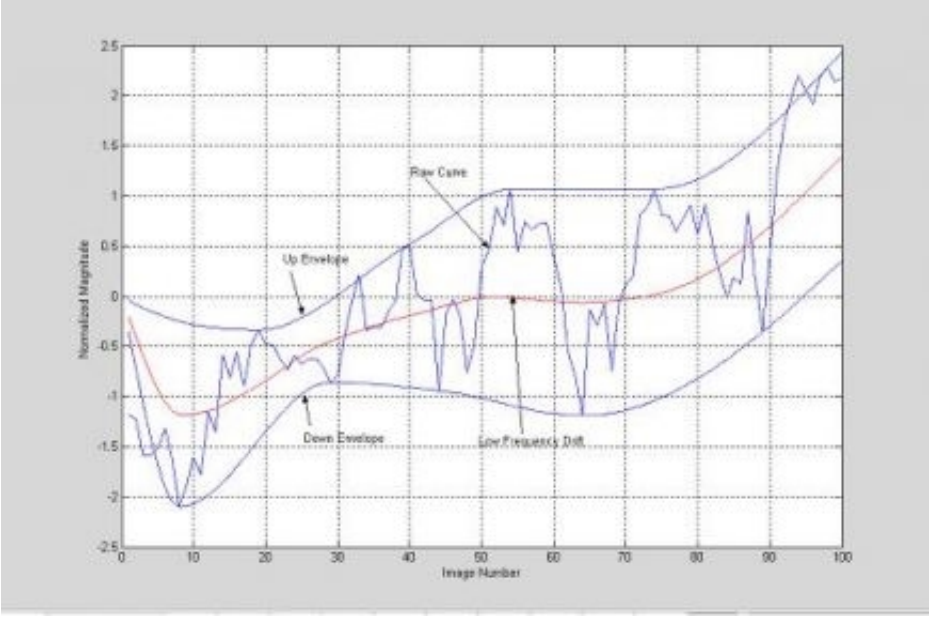

Figure 2. Procedure of calculating the low frequency drift.

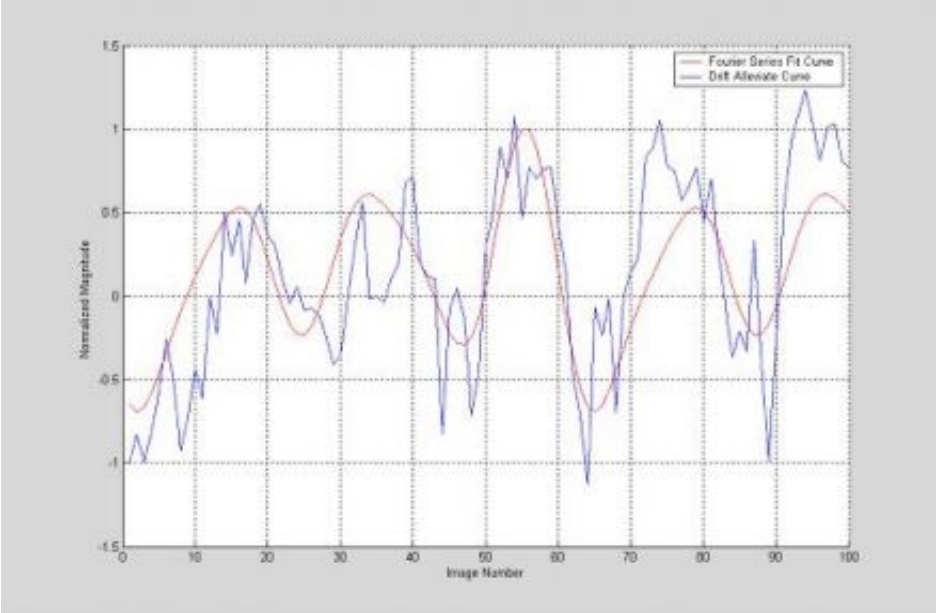

Figure 3. After removing the low frequency drift, the curve was fitted to a Fourier series.

WE 225
Outlier Detection in fMRI Time Series

Xingfeng Li[1], Jie Tian[1], Xiaoxiang Wang[1], Jianping Dai[2], Lin Ai[2]
[1]Medical Image Processing Group, Institute of Automation, Chinese Academy of Sciences, [2]Department of Radiology, Tiantan Hospital, Chinese Capital University of Medical Sciences

Modeling & Analysis

Abstract

Introduction

The fMRI time series obtained from activated regions contain both system noise and physiological noise. These noise components may be unrelated to the experimental design or reflect variations about evoked responses that are inadequately models in the design matrix. To model the time series, ordinary least square method is often utilized to fit the certain function. The method is sensitive to outlier in the time series. We developed an approach to eliminate the outlier for robust modeling the fMRI time series.

Materials and Methods

The following methods for image acquisition were employed in the hand flexing and extending experiment. Imaging was performed on a 3.0-T GE Signa system (General Electric, Milwaukee WI, USA) with a standard head coil. T2*-weighted time series images depicting BOLD contrast were acquired using a gradient-echo EPI sequence. The imaging parameters were as follows: TR = 3000 ms, TE = 30ms, flip angle = 90 degree, 24x24cm, matrix size = 64x64, voxel dimensions = 3.75x3.75x3.75mm, and 24 slices. We collected 36 axial, contiguous slices covering the whole brain. In addition, high-resolution (matrix size = 512x512) anatomical scans were performed as well. The algorithm is as follows:

Computing

MAD = median(|X1-M|,|X2-M|,,|Xn-M|)

X1,X2,,Xn is the intensity at the time point; M is the median value of the time series; MAD is the median absolute deviation statistic. We can modify out rule for detecting outlier in a simple manner: Declare the value X an outlier if

|X-M|>2*MAD/0.6754

We discard the outlier when we model the time series.

Results

Ten healthy subjects (7 men, mean age 35 years, standard deviation 15.6 years) participated in a hand flexing and extending experiment. A typical block design was employed with alternating control condition, subjects relaxed and stayed still. During the experimental condition, subjects performed a hand flexing and extending task, in which they flexed and extended their hands repeated. Subjects were required to flex and extend their hands as rapidly as possible. The whole scan took 5 min 12 seconds. The control and experimental conditions were alternated every 30 s (10 scans) and repeated so that each condition would occur 5 times. Each hand flexing and extending data set comprised 100 volumes. Figure 1 shows the original curve with Fourier series fit results using the ordinary least square (OLS) method without eliminating the outlier. In Fig. 2, we determined the activation regions after eliminating the outlier.

Discussion and Conclusion

OLS method that have practical value when there is not outlier, but the method are unsatisfactory when the outliers exist. We developed a simple but robust method for outlier detection.Our method is effective and can be used to eliminate the outlier before using OLS method to model the time series.

References

[1] Atkinson et al.1998. Robust diagnostic regression analysis. Springer; [2] Wilcox Introduction to robust estimation and hypothesis testing. 1997; [3] Friston et al. To smooth or not to smooth? Neuroimage 2000 12:196-208.

Figure 1. Without outlier elimination.

Figure 2. With outlier elimination.

WE 226

Assessment and improvement on the spatial accuracy in MEG source localization by depth weighting corrected minimum-norm estimate

Fa-Hsuan Lin , Thomas Witzel , Seppo P. Ahlfors , Steven M. Stufflebeam , John W. Belliveau , Matti S. Hamalainen
MGH-MIT-HMS Athinoula A. Martinos Center for Biomedical Imaging

INTRODUCTION

A popular method to locate sources of neuromagnetic signals is to employ the L2-minimum-norm solution (1). This minimum-norm estimate (MNE) framework was subsequently extended to incorporate cortical location and orientation constraints (2). Furthermore, noise normalization has been employed to derive the statistical significance of neuronal activation (3). However, MNE has an inherent bias towards surperficial source locations. Here we show how one can alleviate this bias with depth weighting correction (DWC) and optimize the amount of correction by introducing source location shift metrics.. Our analysis shows that DWC order of 1.3 gives minimal depth shift and displacement shift in MNEs with free or fixed dipole orientation constraint while noise-normalized solutions are insensitive to DWC.

METHOD

A realistic anatomical brain surface was constructed from segmented high-resolution T1-weighted MRI data consisting 340,000 vertices (4, 5). The MEG source points were decimated to create 7,500 dipole sources on this surface. The MEG lead fields for a 306-channel MEG system were calculated using the Boundary Element Method (BEM) (6). Simulated MEG signals were computed using single current dipole located at distinct decimated dipole locations with orientation perpendicular to the localized gray matter on the neocotex. Distributed cortical sources were estimated using the MNE approach. Specifically,

$$\mathbf{x}=\mathbf{W}\mathbf{y}$$
$$\mathbf{W}_{\mathbf{mne}}=\mathbf{R}\mathbf{A}^{\mathbf{T}}(\mathbf{A}\mathbf{R}\mathbf{A}^{\mathbf{T}}+\lambda\mathbf{C})^{-1}$$
$$\mathbf{W}_{\mathbf{SPM}}=\mathbf{W}_{\mathbf{mne}}/\mathbf{sqrt}(\mathbf{diag}(\mathbf{W}_{\mathbf{mne}}\ \mathbf{C}\ \mathbf{W}_{\mathbf{mne}}^{\ \mathbf{T}}))$$

$\mathbf{y}$ denotes the simulated MEG data, and $\mathbf{W}$ denotes the inverse operator. $\mathbf{A}$ is the BEM lead fields, and $\mathbf{C}$ is the noise covariance matrix from pre-stimulus baseline. λ indicates the regularization parameter. The two inverse operators, $\mathbf{W}_{\mathbf{MNE}}$ and $\mathbf{W}_{\mathbf{SPM}}$ yield the MNE and the noise-normalized MNE, respectively. To reduce the bias toward superficial locations, we adjusted the source covariance matrix, $\mathbf{R}$, parametrically by creating a diagonal matrix.

$$\mathbf{R}=1/|\mathbf{diag}(\mathbf{A}^{\mathbf{T}}\mathbf{A})|^{\mathbf{p}}$$

where **diag** is the opeartor to extract the diagonal entries. The depth-weighting correction (DWC) parameter $\mathbf{p}$ was varied systematically from 0.0 to 2.0 in the simulations.

The spatial mis-localization was quantified by two shift metrics: Depth shift ($\mathbf{S}_{\mathbf{depth}}$) is the minimal distance between the source dipole to the inner skull. Displacement shift ($\mathbf{S}_{\mathbf{displace}}$) denotes the distance between the source dipole and the maximum of the estimated source distribution.

RESULTS

Figure 2 shows the depth shifts and displacement shifts. The depth shift in both free-orientation and contstrained-orientation MNE solutions is minimized with p = 1.3. DWC does not improve depth shift error significantly in noise-normalized (SPM) solutions.

CONCLUSIONS

The depth-weighting significantly reduces the source location bias in cortically constrained minimum-norm solutions. The same optimum value, p = 1.3, applies to both free-orientation and orientation-constrained solutions. The noise-normalized MNE estimate was found to be insensitive to DWC.

REFERENCES

1. Hamalainen, M. & Ilmoniemi, R. (1984) (Helsinki University of Technology, Helsinki, Finland).
2. Dale, A. & Sereno, M. (1993) J. Cog. Neurosci 5, 162-176.
3. Dale, A. M., Liu, A. K., Fischl, B. R., Buckner, R. L., Belliveau, J. W., Lewine, J. D. & Halgren, E. (2000) Neuron 26, 55-67.
4. Dale, A. M., Fischl, B. & Sereno, M. I. (1999) Neuroimage 9, 179-94.
5. Fischl, B., Sereno, M. I. & Dale, A. M. (1999) Neuroimage 9, 195-207.
6. Oostendorp, T. F. & van Oosterom, A. (1989) IEEE Trans Biomed Eng 36, 382-91.

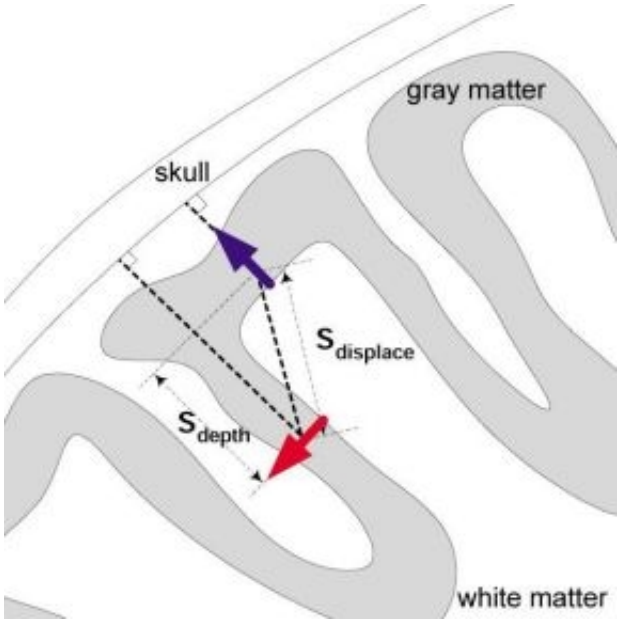

Location errors in source localization. The red arrow indicates the site of the actual source and the blue arrow denotes the location of the maximum of the source estimate. S_{depth} and $S_{displace}$ represent the errors in depth and spatial shifts during source localization respectively.

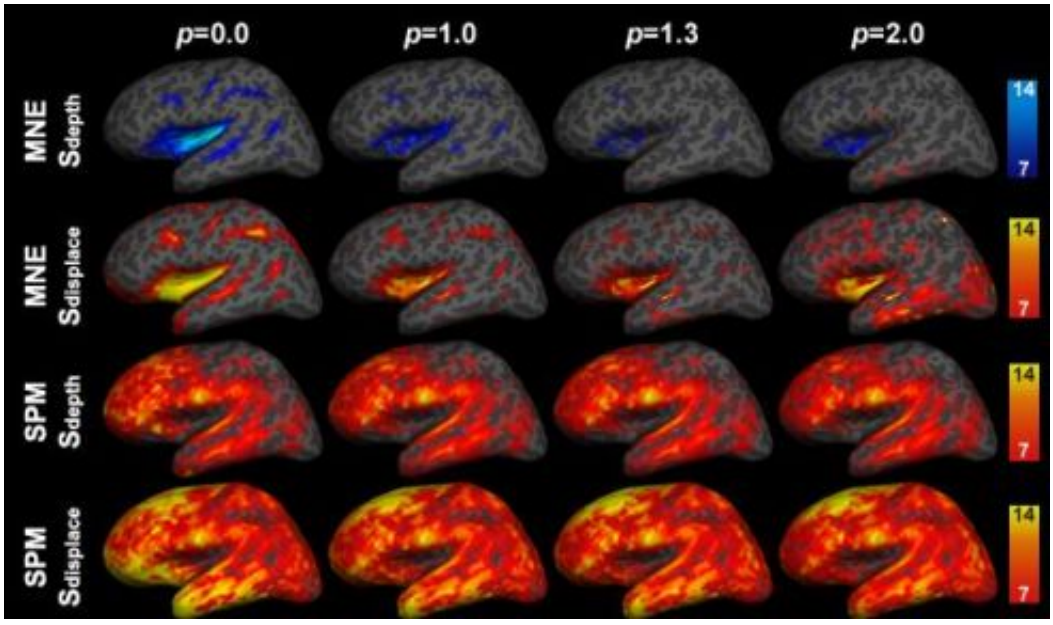

Depth and displacement shifts in MNE and SPM inverse solutions using DWC with p = 0.0, 1.0, 1.3, and 2.0. In S_{depth} plots, blue scale indicates shifts toward superficial cortical surfaces, yellow scale indicates shifts toward deep cortical surface. In $S_{displace}$ plots, the color indicates the absolute shifts. All values are given in mm.

WE 227
USER INDEPENDENCY, ACCURACY, AND STABILITY OF SIENAX TO MEASURE BRAIN VOLUMES BASED ON MR IMAGING

Enrico Locatelli[1], Roberta Riello[1], Cristina Testa[1], Francesca Sabattoli[1], Maria G Perrone[1], Roberta Rossi[1], Lorena Bresciani[1], Malgorzata Noiszewska[1], Samantha Galluzzi[1], Monica Ettori[1], Giuseppina Alaimo[1], Alberto Beltramello[2], Enrico Piovan[2], Matteo Bonetti[3], Andrea Falini[4], Giovanni B Frisoni[1]
[1]Laboratory of Epidemiology & Neuroimaging, IRCCS San Giovanni di Dio FBF, Brescia, Italy, [2]Service of Neuroradiology, Ospedale Maggiore, Verona, Italy, [3]Service of Neuroradiology, Istituto Clinico Città di Brescia, Brescia, Italy, [4]Service of Neuroradiology, Fondazione Centro S. Raffaele, Milano, Italy

Background
SIENAX, an adaptation of SIENA (Structural Image Evaluation, using Normalization, of Atrophy) has been proposed as a user independent cross-sectional method to measure total and grey and white matter (GM, WM) brain volumes based on T1 MR images. SIENAX has been designed to automatically strip non-brain tissue and perform CSF, GM, and WM segmentation. Although SIENAX is robust and accurate, user independency and accuracy have never been compared across different MR scanners.
Aim
The aim of the present work was to explore the user independency and accuracy of SIENAX across three different MR scanners.
Methods
The subjects of this study were 91 consecutive normal volunteers (age: 58±11) scanned for clinical reasons and no pathological MR findings at the Città di Brescia Hospital, Brescia (n=37), San Raffaele Hospital, Milan (n=18), and Ospedale Borgo Trento, Verona (n=35). MR imaging was performed on a 1.0T Philips Gyroscan (PG) in Brescia, 1.0T Siemens Impact (SI) in Verona and 1.5T Siemens Vision (SV) in Milano. T1 sequences were chosen by expert radiologists based on the optimal GM-WM contrast. The threshold parameter allowing the optimal tradeoff between "soft" and "hard" extraction (more or less extracted brain quantity) was chosen based on the visually assessed segmentation of the cortical layer from the subarachnoid CSF in the vault. The results were compared to those of the modulated protocol of voxel based morphometry based on SPM99, chosen as a measure of convergence validity for its recognized accuracy.
Results
Despite an optimal segmentation of the brain in most regions, for all patients of both SI and SV scanners, the eye-bulbs/optic nerves structures had to be manually removed. SIENAX required no amount of human intervention only for the PG scanner. Total intracranial volumes computed with SIENAX were similar to those of SPM for the PG (1367±126 vs 1374±134 cc, p=.30) and SV (1395±93 vs 1399±114, p=.62) scanner, and relatively close but significantly different for the SI scanner (1354±109 vs 1372±115, p=.003). The agreement between the two methods was very high, the intraclass correlation coefficient being .96 (95%C.I. .92-98) for the PG and SI, and .95 (95%C.I. .88-.98) for the SV scanner. The figure shows that although the association between SIENAX and SPM had a similar slope for all scanners, SIENAX systematically underestimated the grey matter and CSF (dots below the bisecting line) and overestimated the white matter. The GM underestimate was 107 cc (95%C.I. 100-113, p<.0005) for the PG, 89 (95%C.I. 83-95, p<.0005) for the SV, and 87 (95%C.I. 82-93, p<.0005) for the SI scanner. The WM overestimate was 114 (95%C.I. 108-121, p<.0005) for the PG, 128 (95%C.I. 120-135, p<.0005) for the SV, and 115 (95%C.I. 110-120, p<.0005) for the SI scanner. The CSF underestimate was 9±15 (95%C.I 3-13, p=.003) for the PG, 39 (95%C.I. 31-46, p<.0005) for the SV, and 28 (95%C.I. 22-33, p<.0005) for the SI scanner.
Conclusion
The user-independency of SIENAX is dependent on the MR scanner. Its performance to measure total intracranial volume is relatively invariant through scanners, while to measure GM, WM, and CSF volumes the differences are marked.

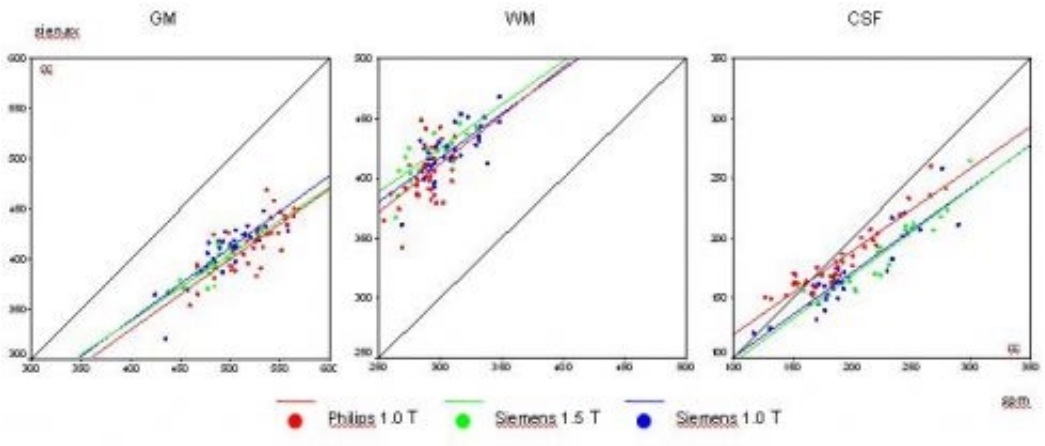

Figure 1. *Relationship between GM, WM, and CSF volumes measured with SIENAX and SPM for three different RM scanners.*

WE 228

A Novel Clustering Technique for Associating Brain Regions with Statistically Similar Low Frequency BOLD Fluctuations

Mark J Lowe[1], Sea Chen[2], Charles A Bouman[3]
[1]Division of Radiology, The Cleveland Clinic Foundation, [2]Indiana University School of Medicine,
[3]Department of Computer and Electrical Engineering, Purdue University

Introduction

BOLD MRI timeseries contain low-frequency fluctuations that are highly correlated between functionally connected brain regions(1, 2). Typically, connectivity is determined from cross-correlation of low-pass filtered timeseries from a seed region to other regions. We present a method of classifying pixels in resting state timeseries data that have similar temporal behavior. The method determines the intrinsic temporal degrees of freedom and the number of statistically distinct temporal signatures present in the data. It is shown that the resulting classifications group regions with known functional connectivity.

Methods

Our method consists of reducing the temporal degrees of freedom using signal subspace estimation (SSE), followed by clustered components analysis(CCA). The signal subspace estimation procedure has been previously described(3). The CCA method consists of two steps. First, the timecourses are estimated using the expectation minimization (EM) algorithm. Second, the estimated timecourses are grouped into clusters of similar signal shape using a distance criterion based on the statistical variance of the data. The distance factor is defined such that it will be large if the eigenvalue of the combined covariance of two clusters is small and the individual covariances are large (indicative of a lack of temporal coherence). The distance will be zero if the combined covariance is equal to the individual covariances. The clustering is done by starting with a large number of clusters and reducing the number to one single cluster. The optimal number (and grouping) of clusters is determined using a minimum description length (MDL). The MDL (4), is defined such that it is large if the data are well-described by the number of clusters. There is a penalty term included for the total number of clusters needed to describe the data, in order to balance the need for a good description with the need for as few clusters as possible.

Data Acquisition: MR imaging was performed with a 3 tesla Siemens Allegra Scanner. Five-5mm thick axial slices were chosen, from superior temporal gyrus through the primary motor cortex. 1024 BOLD-weighted gradient-echo echoplanar images were acquired.

Results and Conclusion

The CCA procedure identified 9 distinct temporal classes. Figure 1 shows the pixel locations for two of the detected classes.

We have introduced a method to group regions of the brain using low-frequency BOLD fluctuations. Application of this methodology to human data demonstrate that the classified brain regions correspond largely to regions with known functional connectivity. Our method differs from other component analysis techniques such a principal components analysis (PCA) and independent components analysis (ICA) in that the components are not required to be either orthogonal (as in PCA) or statistically independent (ICA). The data are analyzed for statistically distinct temporal behavior using a distance criterion determined from the data itself.

1. B. Biswal et al. Magn. Res. Med., 34, 537-41, (1995).
2. M. J. Lowe et al. Neuroimage, 7, 119-32, (1998).
3. M. J. Lowe et al. Proc. of ISMRM Eleventh Annual Meeting, S313 (2003).
4. S.Chen et al. IEEE Transactions in Medical Imaging, in press.

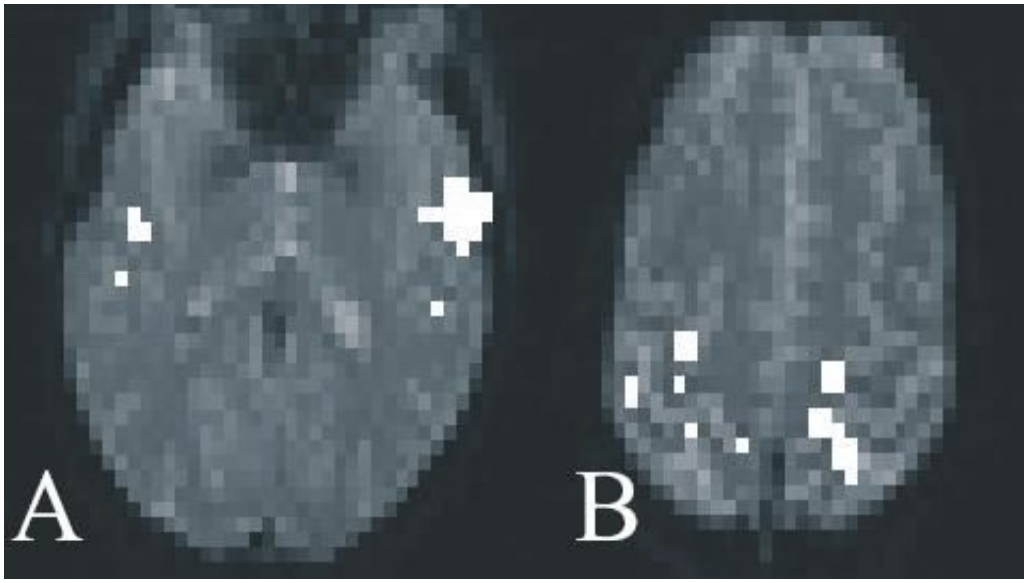

Figure 1: Results of CCA--A) Class 1-auditory cortex, B) Class 2-primary motor cortex

WE 229

Single-Trial Variable Model for Event-Related fMRI Data Analysis

Yingli Lu , Tianzi Jiang , Yufeng Zang
National Laboratory of Pattern Recognition, Institute of Automation, The Chinese Academy of Sciences, Beijing 100080, P. R. China

Introduction

Typical model-based methods for fMRI data analysis, for instance, the General Linear Model (GLM) and the deconvolution method, are based on basic assumption: the hemodynamic responses are same across trials, i.e., the trial-to-trial variability is considered as noise. When hemodynamic responses vary from trial to trail[1], an alternative approach is needed to include the trial-to-trial variability.

Theory and Methods

Step1: Estimation of iHRF for each voxel.

We assume that the hemodynamic system is a linear one, the measured time series z(t)for the stimulus f(t)should be

z(t)=f(t)Θh(t)+[script-phi] (1)

h(t)is the impulse response function, Θdenotes the convolution operation and [script-phi] is the noise. An approximate estimation of h(t) can be obtained from the measurements z(t) by utilizing deconvolution[2,3] method.

Step2: Estimatin of HRFs for each trial.

$\mathrm{Min}_{Hj}|Z\text{-}\mathrm{sum}_j H_j \Theta f_j|^2$ (2)

s.t. $H_j \in N(h,\varepsilon)$

Where decision vector H_j is the HRF for trial j, f_j is the single trial stimulus time series, N(h,ε) is the neighborhood of h, Z is the time series with no trend. Eq.2 is a basic framework. In practical application, some other constraints should be imposed. For instance, Richter et al[4]. claimed, in the mental rotation task, the full width of half maximum (FWHM) of the peak in the fMRI time series in the parietal lobe was equal to the reaction time (RT). This relation is

$FWHM(H_i):FWHM(H_j)=RT_i:RT_j$ (3)

$FWHM(H_i)$ is the FWHM of the HRF H_i, RT_i is the RT of the ith trial. By imposed the constraint of Eq.3 to the general framework in eq.2

$\mathrm{Min}_{Hj}|Z\text{-}\mathrm{sum}_j H_j \Theta f_j|^2$

s.t. $H_j \in N(h,\varepsilon)$

$FWHM(H_i):FWHM(H_j)=RT_i:RT_j$

Step3: Statistical hypothesis test.

The F statistic distribution under the null hypothesis are computed and larger value for F indicates that the corresponding voxel is activated.

Results and Discussion

This experiment is a study of phonetic decision of visual Chinese characters with fixed inter-stimulus intervals (ISI) event-related design. The EPI images with volume size 64 64 14. In order to show the effectiveness of the novel method, Deconvolution[3] method was utilized to compare with our method. Fig.1 indicates that the results of our methods and the deconvolution are in general agreement. However, the F-statistics of the proposed method and the deconvolution method are different. The difference map is presented in Fig. 6c. Since we have utilized the prior information of RT, we expect that the F-statistic based post-analysis of fMRI signal should be more reliable.

References

1. J. R. Duann, et al., NeuroImage,2002;15(4):823-835.
2. G. H. Glover, et al., NeuroImage, 1999; 9(4):416-429.
3. B. D. Ward, http:www.afni.nimh.gov /afni/edu, 2002.
4. W. Richter, et al., NeuroReport, 1997,8(17):3697-3702.

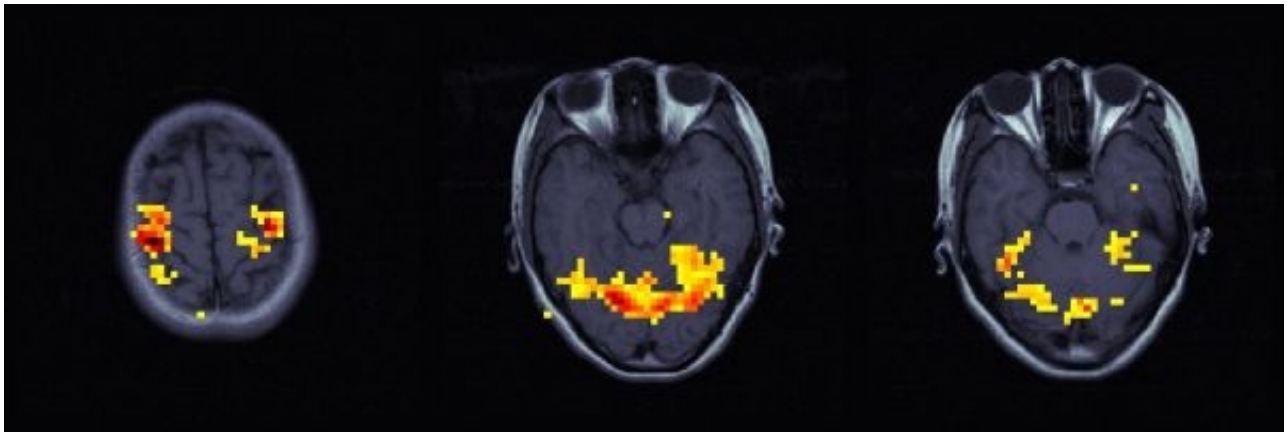

Fig. 1. Activation maps of the deconvolution

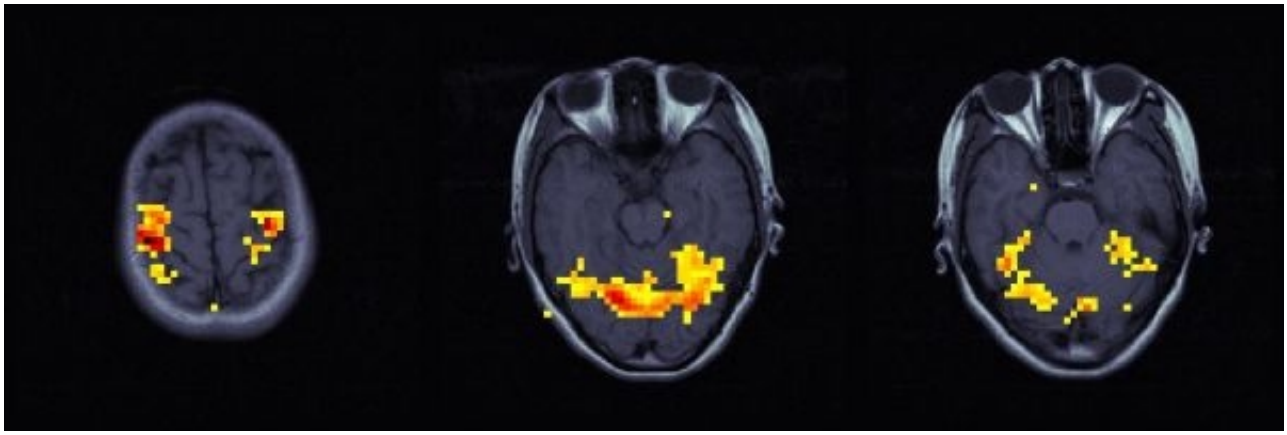

Fig. 2.Activation maps of our method

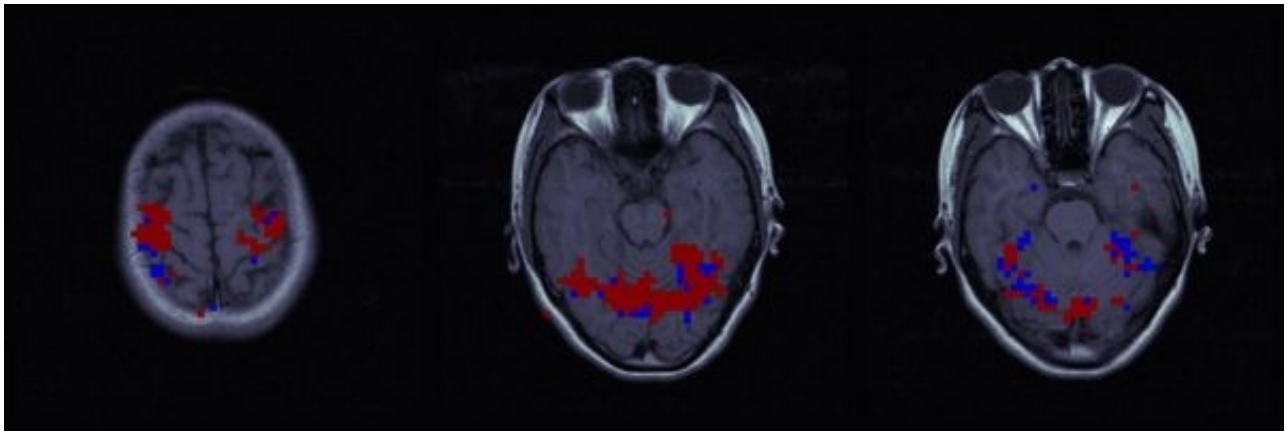

Fig. 3. The difference maps. Red areas denotes that the F-statistics of the deconvolution method greater than our method, and blue areas denotes that the F-statistics of our method greater than the deconvolution method.

WE 230
Gender Differences In Cortical Complexity

Eileen Luders[1], Katherine L Narr[1], Paul M Thompson[1], David E Rex[1], Lutz Jancke[2], Helmuth Steinmetz[3], Arthur W Toga[1]

[1]Laboratory of Neuro Imaging, Department of Neurology, Center of Brain Mapping, UCLA School of Medicine, Los Angeles, USA, [2]Department of Neuropsychology, University Zurich, Switzerland, [3]Department of Neurology, Johann-Wolfgang-Goethe University Frankfurt am Main, Germany

Introduction

Empirical examinations of individual differences in the frequency of gyrification/fissuration (cortical complexity) are rare, where previous studies were limited by 2D measures and/or post mortem data. Using MRI to resolve cortical anatomy at high-resolution in living subjects, we computed cortical complexity in a large and well-matched sample of young and healthy men and women (n = 60). We applied a sophisticated 3D parametric mesh-based approach to analyze the effects of gender and hemisphere on the cortical complexity of five functionally relevant cortical regions of interests (ROIs), including the frontal (superior and inferior), temporal, parietal, and occipital lobes.

Methods

Image volumes passed through a number of preprocessing steps using several manual and automated procedures (e.g. linear transformation into ICBM-305 space, cortical surface extraction, cortical pattern matching between subjects, dividing the cortical surface into ROIs). Cortical complexity was defined as the rate at which the surface area increases relative to increases in the spatial frequency (detail) in the surface. That is, a flat surface would not increase in area with more detail, but a really crumpled one would. The rate of area increase was computed by gridding the surface of the ROIs at many different resolutions. To obtain measures of cortical complexity for each ROI, the logarithmic (log) least squares regression of the surface area was plotted against the log of spatial frequency for surfaces belonging to each ROI. The slopes of these regression plots were derived and added to 2.00 resulting into complexity values between 2.00 (for a planar or flat surface) and 3.00 (for a surface with immense numbers of convolutions and extensive folding). To compare cortical complexity values between males and females and examine interactions between gender and hemisphere, we used repeated measures ANOVAs including hemisphere as a within subjects factor.

Results

Statistical comparisons of cortical complexity values showed significantly increased cortical complexity in women compared to men in the superior-frontal and parietal lobes bilaterally, and in the left inferior-frontal lobe. We did not detect any lobar region showing significantly increased cortical complexity in men compared to women. Interestingly, cortical complexity of parietal and occipital regions was higher in the right compared to the left hemisphere, while inferior-frontal cortices showed larger values for the left hemisphere.

Conclusion

Our findings of gender-specific cortical complexities may have important implications, given that cortical folding patterns are influenced by the underlying cytoarchitecture and reflect neural connectivity. Gender differences on folding complexities may thus contribute to gender-specific abilities and/or behavioral differences, where increased complexities in females may also compensate for their smaller brain volumes. Given the direction of asymmetries observed for cortical complexity, it is possible that increases in cortical surface area occur to compensate for the right frontal and left parieto-occipital petalias documented in the literature. That is, given that brain growth is restricted by the size of the intracranial cavity and the inner skull forms complementary asymmetries, increases in surface area, and thus more cortical folding may occur in the smaller hemispheric region.

WE 231
Modelling residual movement effects: The impact on intra- and intersession variability in fMRI

Torben E. Lund , Minna D. Nørgaad , Egill Rostrup , Olaf B. Rostrup
Danish Research Centre for MR, Copenhagen University Hospital, Hvidovre Denmark

Introduction
It is well known that fMRI possesses large intersession variability [1]. The purpose of this study was to investigate whether modelling residual movement artifacts reduces intersession and inters-subject variability in the observed fMRI activation.
Materials & Methods
Ten healthy volunteers (A,B,C,D,E,H,I,J,K,L) were examined with three different word generation tasks: Categorical, Alphabetical and Semantic. Two of the subjects (A&B) were examined 10 times. All three paradigms were presented in a boxcar design with active and baseline condition lasting 44s each (20 seconds for the semantic paradigm). Using a 1.5T Siemens Vision scanner and GE EPI, a set of 104 volumes (128x128x20), resolution: (xyz) 1.56mm5x1.56mmx55mm) was acquired in each of the three paradigms. Data was realigned and spatially normalized and spatially smoothed (FWHM 5mm) using SPM99. Residual movement effects were modelled by including a Volterra expansion of the 6 motion parameters as nuisance covariates in the design matrix of a GLM as implemented in SPM2 http://www.fil.ion.ucl.ac.uk/spm/spm2.html). The Volterra expanded motion parameters model linear and quadratic effects of the 6 movement parameters belonging to each volume, but also model spin-history effects [2] as linear and quadratic effects of motion parameters in the previous volume, giving a total of 24 regressors in addition to those describing the paradigm and baseline. Nine different sets of images (A-Categorical, A-Alphabetical, A-Semantic, B-Categorical, B-Alphabetical, Semantic, 10Subjects-Categorical, 10Subjects-Alphabetical and 10Subjects-Semantic) were analyzed with two models each. Both models were a fixed-effect analysis of the word generation paradigms, and both modelled serial correlations as an AR(1)-process and low frequency drifts as a discrete cosine set (128s cut-off). In the first model, only the paradigm regressor and session specific baseline were included in the design matrix (size1040x20). In the second model, the Volterra expanded motion parameters (24 regressors per session) were also included in the design matrix (size 1040x260). For each of the 12 analyses a t-contrast was used to test for the effect of the paradigm, and an F-contrast was used to test for the intersession or inter-subject variation. The F-test was constructed so that each of the 10 rows (SPM notation) in the F-contrast tested for the deviation of a specific session (or subject) from the mean of the other 9 sessions/subjects. For example, the third row in the F-contrast of a model without motion parameters reads [-1/9 1/9 1 1/9 1/9 1/9 1/9 1/9 1/9 1/9]. All statistic maps were thresholded at p=0.05 (FWE corrected).
Results & Discussion
In all 6 intra-subject analyses, inclusion of motion parameters reduced the intersession variation (see Figure 1) and cleaned up the activation map. In all three of the inter-subject analyses, inclusion of the motion parameters also reduced the intra-session variance significantly (see Figure 2), leaving only a few voxels located in areas found active in the activation map. This indicates that a large amount of the intersession variability in fMRI can be asigned to movement related effects not accounted for during normal realignment.
References
[1] McGonigle, DJ. et al. Neuroimage 11: 708-734, 2000
[2] Friston, K. et al. MRM 35: 346-355, 1996

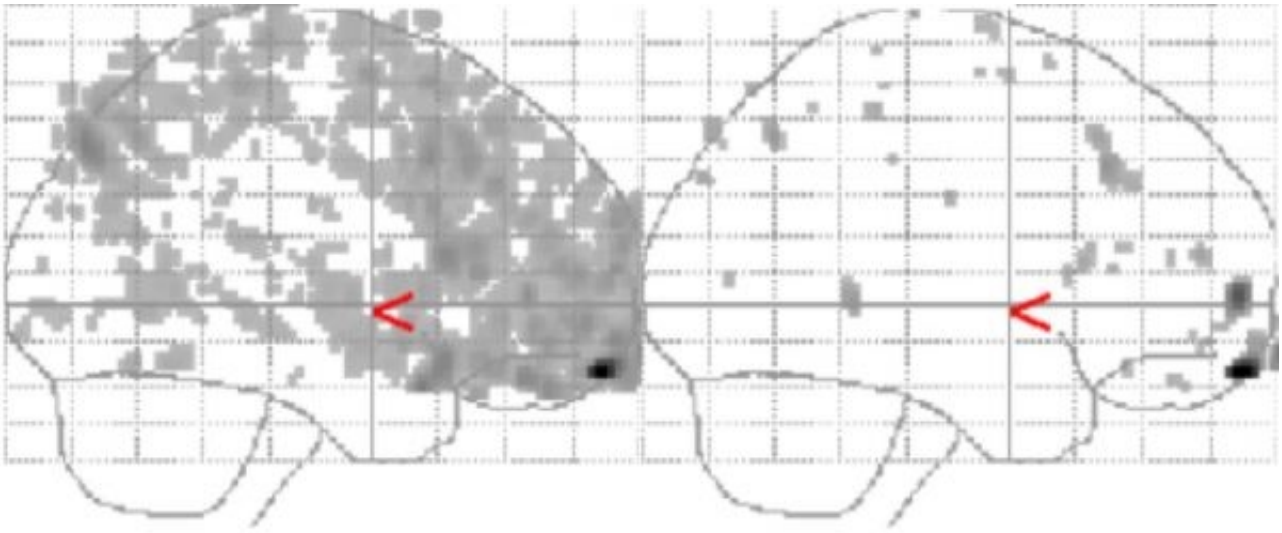

Figure 1: Categorical word generation. Intra-subject variation in activation with (right) and without (left) motion parameters included in the design matrix.

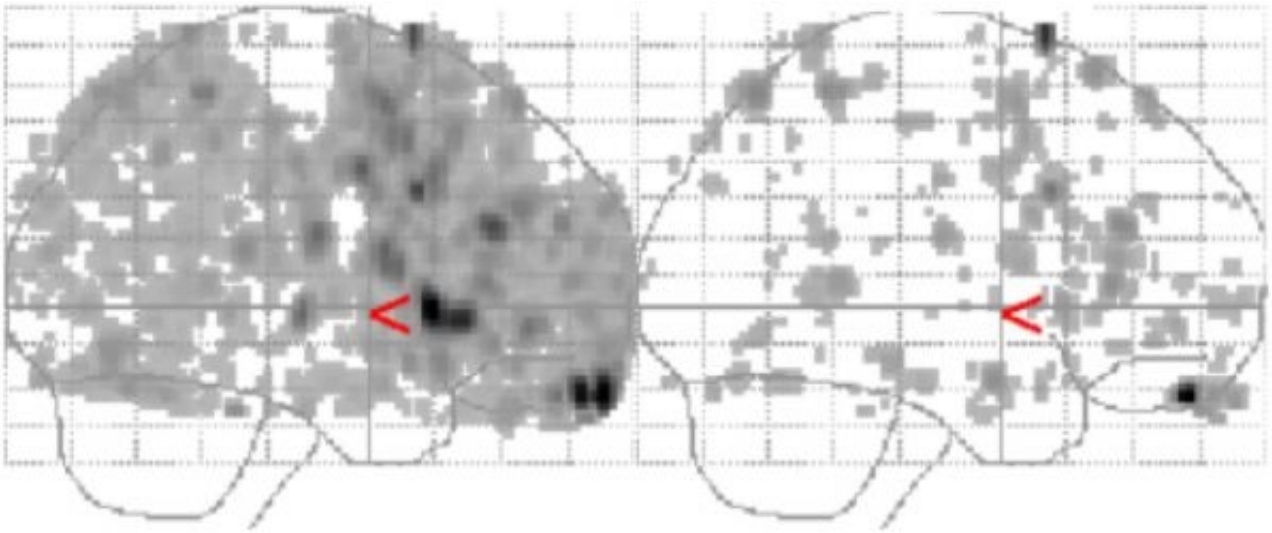

Figure 2: Alphabetical word generation. Inter-subject variation in activation with (right) and without (left) motion parameters included in the design matrix.

WE 232

Automated Region of Interest (ROI) Analysis for PET Studies

Yeming Ma[1,2], Nora D. Volkow[1,3], Wei Zhu[2], Manlong Rao[2], Kith Pradhan[2], Gene-Jack Wang[4,5]
[1]National Institue of Health, Bethesda, MD 20892-8115, [2]Department of Applied Mathematics & Statistics, Stony Brook University, NY 11790, [3]Department of Psychiatry, Stony Brook University, NY 11790, [4]Department of Radiology, Stony Brook University, NY 11790, [5]Medical Department, Brookhaven National Laboratory, Upton, NY 11973

Objective: Region of interest (ROI) analysis is an indispensable method complementary to the voxel-level analysis commonly done with SPM. Traditionally ROIs were hand-drawn for each image. It is subjective, time consuming and labor intensive. We have developed an algorithm to extract anatomically and functionally defined ROIs automatically. Software named autoROI with graphical user interface had been developed implementing the above algorithm. Several PET data sets were analyzed using both autoROI and SPM and the results compared.
Methods: The anatomically defined ROIs are based on the standard brain atlas (Talairach). There are five levels of partitions from major lobes to the Brodmann areas. The functionally defined ROIs are based on activation regions of SPM analysis. One can overlap the anatomically and functionally defined ROIs to obtain a cross-partitioned set of ROIs and statistical measures such as volume of activation. Each PET image is normalized to the Talairach space using SPM99. The ROIs are projected on normalized PET image to extract individual subjects ROI data in the Talairach space for ROI based analysis. ROI display, extraction and basic analysis can be done within the autoROI platform.
Results: Analysis of several PET data sets at BNL confirmed that the activation regions located by autoROI are in excellent agreement with the corresponding SPM results. Furthermore autoROI adds information to SPM by quantifying the activation/deactivation volume of each anatomical region, and by projecting the significantly changed regions to individual brain for inter-subject variability studies. Correlation between manually drawn ROI results on 35 PET images in four anatomical regions caudate, middle temporal lobe, post central lobe and striatum on both left and right hemisphere had been consistantly show within the range of 0.85-0.985 in Pearson correlation coefficient (Figure 1).
Conclusions: The widely adopted human brain imaging analysis methodolgy SPM had been testing on the voxel-level while anatomical level ROI analysis had been left at a stage relying on hand-drawing. So the software of autoROI not only will provide a convenient tool for ROI extraction and analysis, but also provides valuable information at quantitative anatomical level in a complete, automated and reproducible way in complement to SPM.

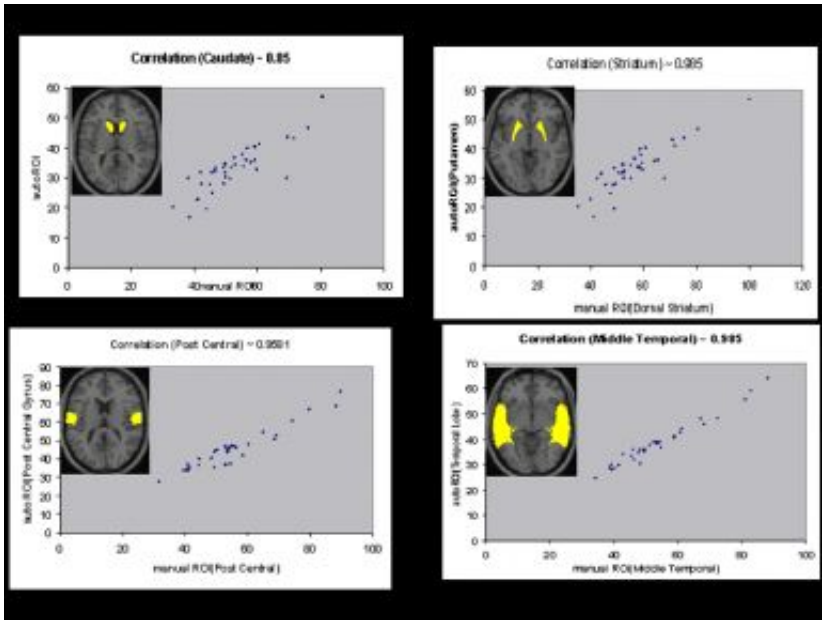

Pearson correlation analysis on manaully drwan ROI values and Talairach Atlas guided autoROI values from four anatomical regions: caudate, post central gyrus, striatum and middle temporal gyrus.

WE 233
BOLD latency: relationship to stimulus duration

Marta Maieron[1,2], Carlo A. Porro[2], Peter A. Bandettini[1]
[1]Laboratory of Brain and Cognition, NIMH, Bethesda, 20892-1148 Maryland, [2]Dip. Scienze e Tecnologie Biomediche, Università di Udine, I-33100 Udine

Temporal latency is a potentially important aspect of the BOLD functional MRI activation response. Researchers have shown that latency is correlated with task latency [1, 2, 3]. An issue is that, latency heterogeneity may be dominated by vascular structure. There is evidence of the encoding of the temporal ordering of neuronal firing within hemodynamic response to stimuli for spatially contiguous brain regions [3], but less so for disparate regions [4] or for different stimulus duration. It is well known that different duration in stimuli presentation induce a variation of spatial extension of activation (within a range, longer stimuli durations create a larger and therefore more extensive hemodynamic response), but the precise relationship between early activated regions and focus of neuronal firing is an area of active investigation. In this study, the spatial variability of the hemodynamic latency with task duration modulation is studied.
METHODS: Imaging was performed on a GE 3 Tesla using the BOLD-EPI (TR = 500ms, TE = 30ms, slice thickness = 7mm, matrix = 64X64, FOV = 24mm), 5 not contiguous oblique slices were positioned covering the visual, auditory and motor cortex. Four healthy subjects were studied. Subjects were presented simultaneously two different stimuli: one auditory stimulus and one visual stimulus, while the presentation they have to carry out a finger tapping movement (1Hz freq) with both hands. Stimuli were hardware synchronized with the scanner in each trial. The design of stimuli presentation was a block paradigm with a varied duration: 4sec - 26sec, 8sec - 22 sec, 10sec - 20sec (activity - rest), The duration was constant during each run, 3 runs was acquired for every duration. BOLD contrast latency was measured and mapped using a Hilbert Transform based estimator, (a 'plugin' in the AFNI software suite) which allowed to determine the phase shift between the reference time series and the stimulated fMRI response time series [5,6].
RESULTS and CONCLUSION: Number of activated pixels was assessed in different regions using cross correlation analysis (p = 0.001 uncorrected). In Figure 1 we can see that activated regions linearly increase its extension in correlation on the duration of stimuli presentation (red = visual, green = motor, blue = auditory). We don't find a significant increase of mean latency measurements related to different spatial extension of activation map (Figure 2). We evaluated the latency of overlapped pixels and we found that it remains unchanged. This implies, in agreement with Saad et al [6] that latency is not necessarily correlated with magnitude of activation, and in agreement with Saad et al [7], that the fringe areas of activation are not necessarily 'downstream' vasculature.

[1]Kim S et at. MRM(37): 631-636, 1997,
[2] Bellgowan PS et al. PNAS 100(3):1415-9 13:74-93, 2003,
[3] Menon RS et al. PNAS 95(18):10902-7, 1998,
[4] Calhoun VD et al. Proc. ISMRM Vol1. 983, 2000,
[5] Saad Z et al. HBM 13:74-93, 2000
[6] Saad Z et al. Neuroimage 18(2):494-504, 2003
[7] Saad Z et al. Neuroimage 19(1):132-44, 2003

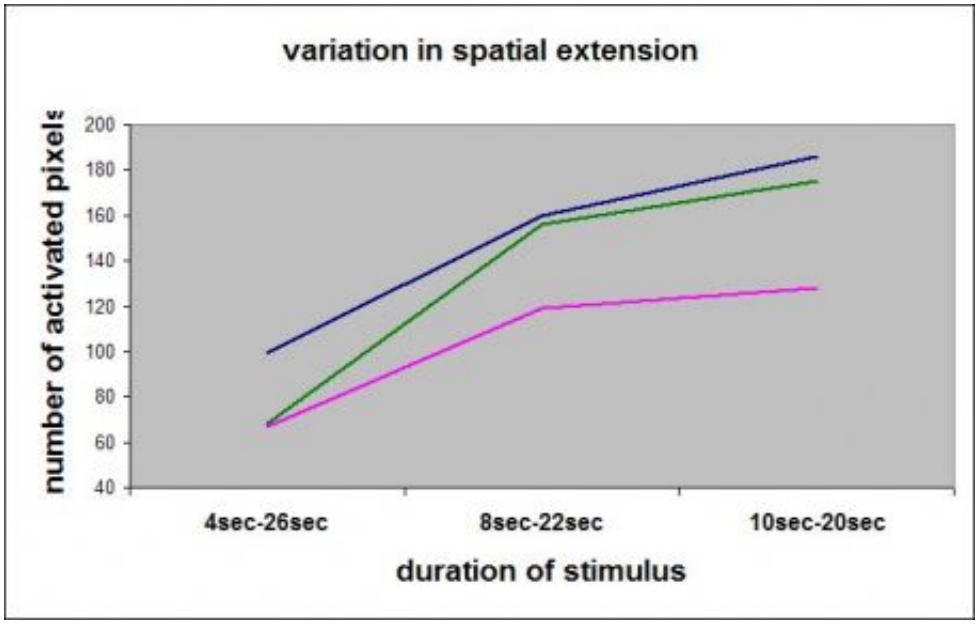

Variation of spatial extension of activarted region

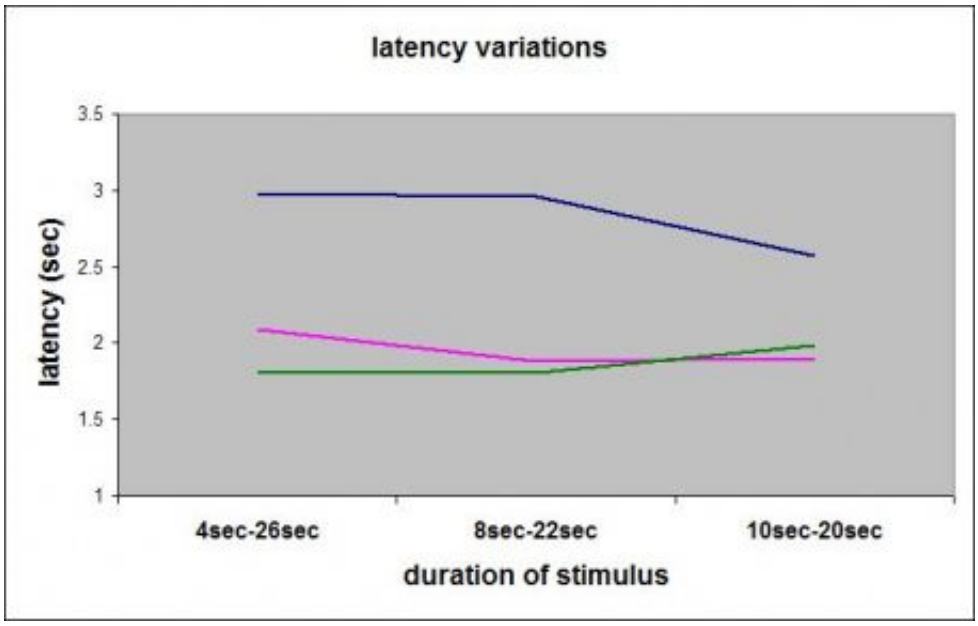

Latency values in different areas

WE 234
Matrices of Human Cerebral Cortical Connections

Nikos Makris[1], David N. Kennedy[1], Matthew D. Albaugh[1], Joseph J. Normandin[1], Verne S. Caviness[1], Edward H. Yeterian[2]
[1]Center for Morphometric Analysis, Massachusetts General Hospital, [2]Department of Psychology, Colby College

Introduction

We have previously formulated an MRI-based parcellation system of the white matter and the maps of cerebral connectivity of the human brain (Makris et al., 1999). This system of analysis considers the anatomic individuality of the brain under investigation as well as the topography of the different white matter fiber pathways within specific, volumetrically quantifiable parcellation units. Although this system is neocortex-centric concerning the afferent and efferent connections of the cortical areas, it does not provide explicit lists of each cortical region or parcellation unit (PU) in the form of the matrix of cortical and subcortical areas sharing connections with that PU. In this study we include such matrices. The matrix is a mathematical construct to embody the anatomical knowledge about connections.

Matrices defining the connectivity of each cortical PU are defined based on experimental animal and human data. Though substantial in its detail, it may be assumed to be at best only a partial list and approximately correct in many respects. This is inevitable given that the sources of data relating to fiber system organization are limited largely to inferences from crude dissections of anatomic specimens or extrapolations from primate experiments. This set of matrices, which embodies a systematic description of cerebral connectivity will be used in cognitive and clinical studies in neuroscience.

Methods

As in our previous approach (Makris et al., 1999) using the white matter as the focus for the mapping of cerebral connectivity, a meta-analysis of relevant literature was conducted.

Results

48 cortical PU matrices have been formulated. One example is shown in Table 1 for PU AG (angular gyrus).

Discussion

The cortical mantle orchestrates information processing in the brain via associational, commissural and projectional connections. Through these types of connections, each cortical area relates to other cortical and subcortical regions following a general scheme of connectivity, allowing for integrated functioning within the central nervous system. These connections are mediated by fiber bundles, which are topographically organized within the white matter of the brain. The neocortex is interconnected and organized as neural systems, functionally and structurally. Thus the knowledge of connections of each cortical region with other cortical regions is relevant for formulating hypotheses in cognitive and clinical neuroscience (Stephan et al., 2001).

References

Makris N, Meyer JW, Bates JF, Yeterian EH, Kennedy DN, Caviness VS. MRI-Based topographic parcellation of human cerebral white matter and nuclei II. Rationale and applications with systematics of cerebral connectivity. Neuroimage. 1999 Jan; 9(1): 18-45.

Stephan KE, Kamper L, Bozkurt A, Burns GA, Young MP, Kotter R. Advanced database methodology for the Collation of Connectivity data on the Macaque brain (CoCoMac). Philosophical Transactions of the Royal Society of London Series B: Biological Sciences. 2001 Aug 29; 356(1412): 1159-86.

Table 1: Connectivity Matrix for AG

PU: AG	Connectivity Summary
Cga	0
CO	3

F1	3
F2	3
F3t	3
F3o	3
FMC	0
FO	3
FOC	0
FP	3
PAC	0
PRG	0
SC	0
JPL	3
AG	1, 2, 3, 4
CGp	2
PCN	2, 3
PO	2, 3
POG	2
Sga	2, 3
SGp	1, 2, 3
SPL	1, 2, 3
H	0
INS	2, 3
Pha	3
PHp	3
PP	0
PT	3
T1a	3
T1p	3
T2a	3
T2p	3
T3a	3

T3p	3
Tfa	3
TFp	3
TO2	1, 3
TO3	3
TOF	3
TP	3
CALC	0
CN	0
LG	3
OF	3
Oli	1, 3
Ols	1, 3
OP	3
SCLC	0

1=short fibers, 2=medium fibers, 3=long fibers, 4=commissural

WE 235
A 3-D tracer kinetic model using the mass balance principle

Alexander Malyshev[1], Arvid Lundervold[2]
[1]Department of Informatics, [2]Department of Biomedicine, Neuroinformatics and Image Analysis Group, University of Bergen, Jonas Lies vei 91, N-5009 Bergen, Norway Email:Arvid.Lundervold@biomed.uib.no

Indicator dilution (or *tracer kinetic*) methods have been used for measurement of tissue parameters for many years in physiology, and there is a large body of experience and literature to draw upon [1,2,3]. To apply these methods, several assumptions should be imposed on a system under study, whether it is an organ or a sample of tissue. The main assumption is *stationarity* of the system with respect to the parameters of interest. For example, blood flow and other relevant parameters are assumed to be constant. Generally the system is also considered to be linear with respect to the indicator. Stationarity and *linearity* of indicator responses are needed for using the convolution principle, a most important concept in indicator methods.

The present work points to some weaknesses of the classical theory that is applied to perfusion MR imaging data, and introduces a new rigorous tracer kinetic theory from first principles. Like in the classical theory (e.g. [4]), we assume the injected contrast agent (e.g. Gd-DTPA) acts as a *non-diffusible indicator* substance, in the sense that all contrast agent molecules pass through the system and no fraction of the molecules is retained or metabolized inside the system. This assumption underlies the mass balance principle extensively used in our approach. We assume additionally that the non-diffusible indicator completely mixes through the volume of the system and behaves like, and moves at the same speed as, the rest of the flow. More specifically, we deal with a fluid (blood) flow that carries a dissolved substance (Gd-DTPA) through a porous medium (the brain) and consider variables such as porosity of the medium ([script-phi]) solute mass fraction (*c*) and concentration (*C*) of the solute. Using dynamic susceptibility contrast MR imaging, the concentration curves *C(t)* at each voxel are computed as $-log(S(t)/S_0)$, where *S(t)* is the measured signal intensity and S_0 is the baseline signal. For each voxel v_0 and its boundary face E_j $(j=1,...6)$, we define the flux F_j as the volume of fluid flowing into v_0 through E_j during one unit of time. Assuming conservation of mass, i.e. that the increment in the solute in v_0 equals the decrement in the solute, we derive a mass balance equation at voxel v_0 relating the fluxes F_j and the concentration curves at v_0 and those at the 6 neighboring voxels. By means of the linear least squares method with nonnegativity constraints [5]we numerically invert this equation and obtain voxel-wise estimates of the porosity (CBV), volume of blood flowing into v_0 in unit time (CBF) and mean transit time of solute, defined as MTT=CBV/CBF. The model and estimation procedure was tested on real MRI perfusion data from a healthy volunteer, using contiguous slices for the 3-D model to be applicable.

[1] Zierler, *Circ. Res.*, 1962;10:393-407. **[2]** Lassen & Perl, *Tracer Kinetic Models in Medical Physiology*, Raven Press, 1979. **[3]** Kiselev, *MRM*, 2001;46:1113-1122. **[4]** Østergaard et al. *MRM*, 1996;36:715-725. *[5]* Lawson & Hanson, *Solving Least Squares Problems*, SIAM, 1995.

WE 236
Systematic regularization of the MEG inverse problem using multiple constraints

Jeremie Mattout[1], Christophe Phillips[2], Michael D. Rugg[3], Karl J. Friston[1]
[1]Wellcome Deptartment of Imaging Neuroscience, Institute of Neurology, London, UK, [2]Cyclotron Research Centre, University of Liege, Belgium, [3]Center for Neurobiology of Learning and Memory, University of California, Irvine, USA

Introduction

Localizing the sources of MEG activity constitutes an ill-posed inverse problem that requires constraints from additional information [1]. The critical issue then lies in the balancing of the data fit and the constraints, using appropriate regularization or hyperparameters.

In the context of linear inverse operators, we describe and evaluate a general regularization framework based on the formulation of the MEG inverse problem in terms of hierarchical models [2,3]. This formalism enables one to compute both the Restricted Maximum Likelihood (ReML) estimate of each hyperparameter [2] and the Maximum a Posteriori inverse solution.

Method

Distributed source models rest on a general linear writing of the MEG forward relation, $M = GJ + E$ (1^{st} level). Under the assumption $E \sim N(0, C_e)$ about the noise, when C_j is the prior covariance matrix of the sources, the linear inverse operator is given by $T = C_j G^T (G C_j G^T + C_e)^{-1}$.

While Ce can be estimated empirically, C_j embodies an unknown mixture of constraints.

Classical weighted minimum norm (WMN):

Here, $C_j = \lambda (W^T W)^{-1}$. Only one prior weighting matrix W is considered in WMN solutions, since only one hyperparameter λ is required, which can be estimated by the commonly used L-curve approach [4].

Hierarchical linear model:

This model assumes $J \sim N(0, C_j)$ (2^{nd} level) and a linear decomposition for the prior covariance matrix, $C_j = \mu_1 C_1 + \mu_2 C_2 + \ldots$. Multiple independent constraints can thus be introduced.

By comparing the sample and predicted data covariance $C_m = G C_j G^T + C_e$, ReML estimates of the hyperparameters μ_i were obtained using an Expectation-Maximization algorithm.

Application

WMN and ReML approaches were evaluated on two hundred simulated noisy MEG data sets (SNR = 20dB), corresponding to the activation of two randomly chosen sources. The following constraints were considered:

- a LORETA-like spatial smoothness prior,
- an intrinsic functional constraint, a prior covariance matrix being estimated from the MEG data itself [5],
- an extrinsic functional prior that could be derived from fMRI data and which had either a valid or invalid location.

To evaluate the two inverse approaches and the different constraints, the Localization Errors were compared along with the areas under the related ROC curves [6].

Results

- When using only one constraint, the ReML solution proved significantly better than the WMN, whatever this constraint.
- When considering multiple constraints, ReML was able to properly discount the effect of invalid extrinsic functional priors, by reinforcing the weight of the other valid priors.

References

[1] Baillet et al. IEEE Sign. Proc. Mag. 18:14-30 (2001)
[2] Friston et al. NeuroImage 16:465-483 (2002)
[3] Phillips et al. NeuroImage 17:287-301 (2002)
[4] Gorodnitsky et al. Electroenceph. Clin. Neurophysiol. 95:231-251 (1995)
[5] Mattout et al. IPMI03 536-547 (2003)
[6] Metz et al. Med. Decis. Making 18:110-121 (1998)

WE 237
Fractional Gaussian noise parameters in resting fMRI data

Voichita Maxim[1], Jalal Fadili[2], John Suckling[1], Ed Bullmore[1]
[1]1) Brain Mapping Unit, Addenbrookes Hospital, University of Cambridge, UK, [2]GREYC-ISMRA, Caen, France

The statistical properties of fMRI noise remain an active focus for methodological investigation. Here we explore the model of fractional Gaussian noise (fGn) for fMRI null data acquired from subjects at rest. Fractional Gaussian noise is parameterised by its variance $\sigma 2$ and the Hurst exponent $0 < H < 1$, which is related to the spectral exponent γ by the simple relation $1 < \gamma = 2H-1 < 1$. In other words, fGn subsumes a range of noises from predominantly high frequency, short-range dependent or antipersistent processes with $\gamma < 0$ and $H < 0.5$; Gaussian white noise with $\gamma = 0$ and $H = 0.5$; and predominantly low frequency, 1/f-like, long memory or persistent processes with $\gamma > 0$ and $H > 0.5$. Maximum likelihood estimation of fGn parameters can be achieved by taking the discrete wavelet transform (DWT) of the time series. The DWT coefficients of fGn are theoretically decorrelated or whitened. Iterative estimation of the GLM parameter vector b can also be combined with ML estimation of fGn parameters. Here we apply and validate these methods to analysis of fGn parameters in resting datasets from 6 subjects scanned at 3.0T. We demonstrate consistent regional heterogeneity of H, indicating long memory or persistent noise concentrated in frontal and medial parietal cortices; white noise in the central white matter; and local antipersistent noise in the vicinity of the ventricles and sulcal CSF. We show that type 1 error control on multiple tests of the standardised GLM parameter vector is improved by modelling the GLM residuals as fGn compared to alternative estimators for β which assume an autoregressive process for the residuals.
We also describe the effects on fGn parameters of variation in sampling rate (TR), data pre-processing for movement correction, and level of consciousness. We conclude that fMRI noise shows considerable variability for which fractional Gaussian noise provides a parsimonious and statistically convenient model.
This work was supported by a Human Brain Project grant from the National Institutes of Health.

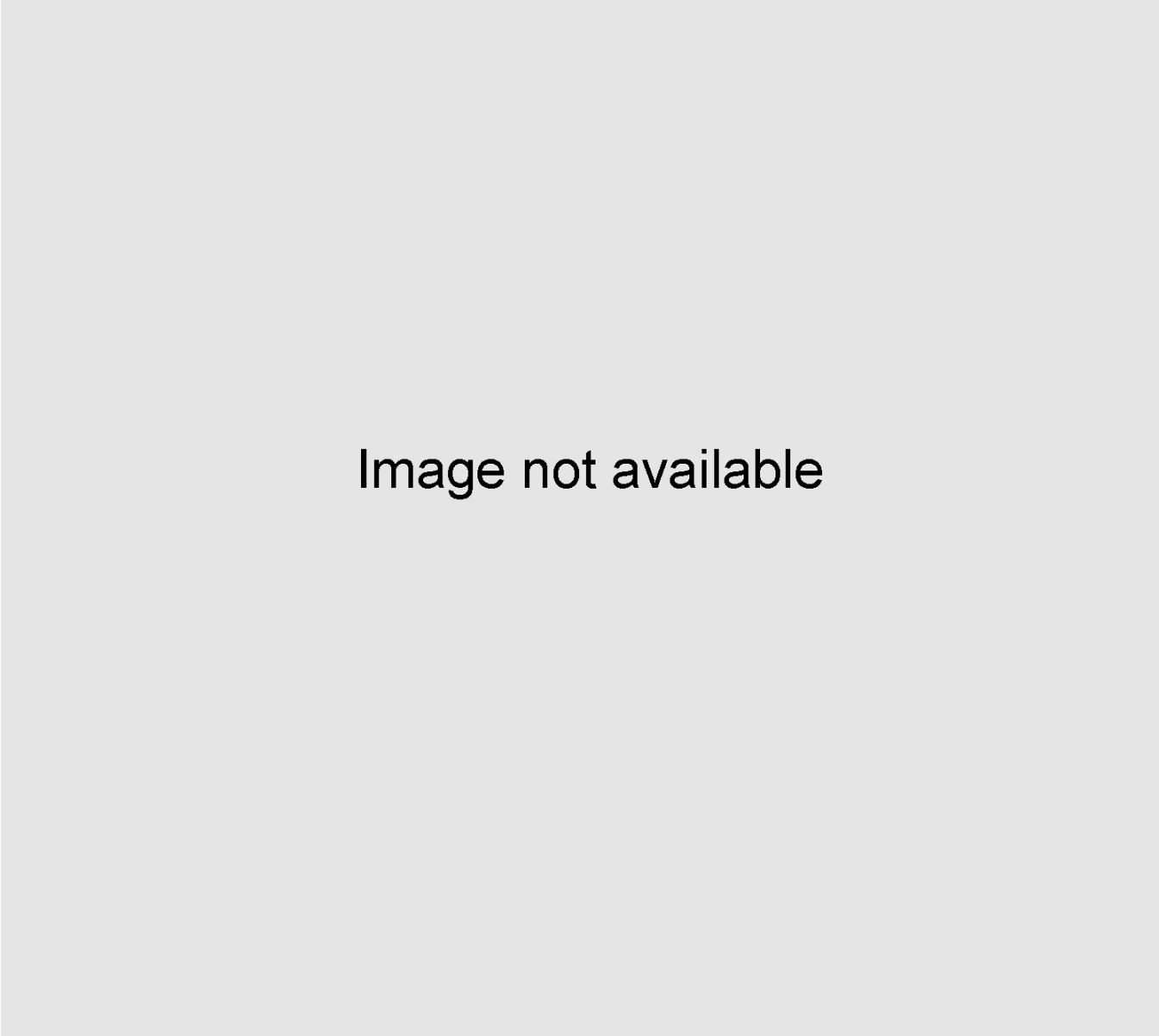

Map of the Hurst exponent H (median of 6 subjects)

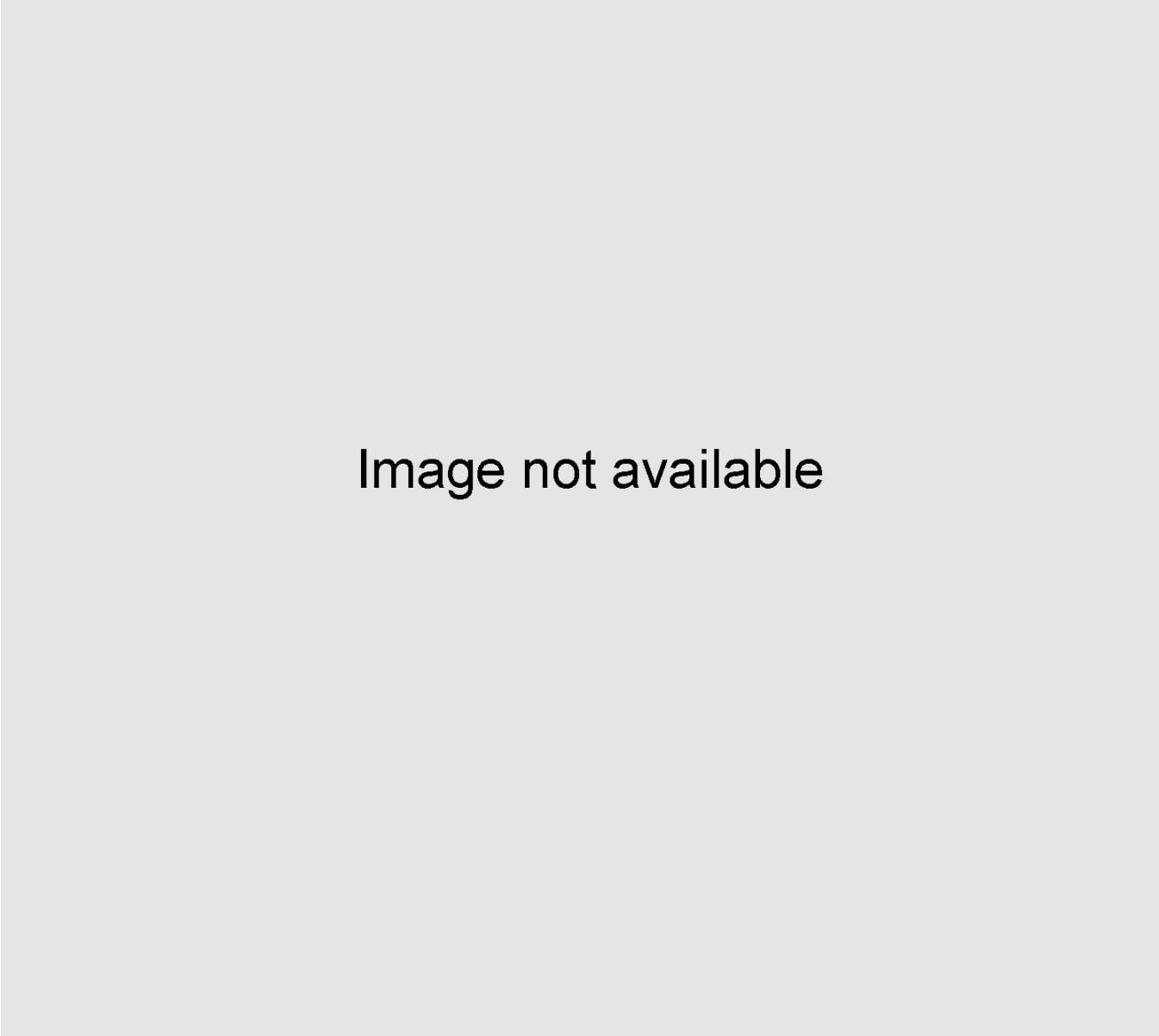

Map of the hurst exponent H (median of 6 subjects)

WE 238

Analysis of Flow Dispersion as a Meaningful Measurable Parameter in Arterial Spin Labeling

Yousef Mazaheri , Thomas T. Liu , Eric C. Wong , Miriam Scadeng , Richard B. Buxton
Center for Functional Magnetic Resonance Imaging, UCSD, San Diego, CA, U.S.A.

INTRODUCTION

Arterial spin labeling (ASL) techniques provide a direct noninvasive measure of local cerebral blood flow. The kinetics of signal enhancement of tagged arterial blood [1] requires knowledge of the velocity flow profile. Often a constant velocity flow profile (plug flow) is assumed. Here we investigate flow dispersion as a meaningful physiological parameter. Shown in Figure 1 are velocity flow distributions f(v) for (a) plug flow, (b) laminar flow, and (c) flow dispersion. For the idealized case of plug flow, the flow profile across the vessel is assumed constant, and the velocity distribution is a delta function (Fig. 1a). Pure laminar flow has a parabolic flow profile across the vessel. The velocity distribution, $f(v)=1/v_{max}$ (Fig. 1b). An intermediate case between plug and laminar flow occurs if: 1) there are several vessels within a voxel with different flow profiles, 2) there is mixing within the cylindrical shells of laminar flow, 3) flow is turbulent which often occurs at higher flow rates, 4) there is a distribution of path lengths for tagged blood traversing to the activation site. The width of the velocity flow distribution, w, measures the degree of flow dispersion (Fig. 1c). Modeling laminar flow requires fitting no additional parameters as compared to plug flow. For flow dispersion the width of the velocity distribution w, was also fitted to the model.

METHODS

Seven adults (ages 20-30, 3 female) were scanned on a 3T Varian System (Palo Alto, CA) after giving written informed consent. Perfusion images were obtained with the PICORE [2] sequence using a single-shot gradient-echo EPI readout. Imaging parameters were: FOV = 24.0x24.0 cm2, TR/TE = 2000/27.3 ms, 3 slices, slice thickness = 8.0 mm, and 160 time frames. The inversion delay times, TI were: 300, 600, 900, 1200, 1400, and 1600 ms. The task consisted of a block design visual paradigm, 4 cycles, with 40 s on/off colored radial checkerboard flashing at 8 Hz. Perfusion time-series were calculated and functional maps were generated. Laminar flow velocity distribution was approximated to range from $0.1v_{avg}$ to $1.9v_{avg}$. The flow profile due to each model is approximated as the sum of the contribution of 100 distinct flow velocities.

RESULTS AND DISCUSSION

Selected data were fitted to a theoretical ASL kinetic model [1], with plug, laminar, and flow dispersion flow profiles. Figure 2 is a histogram of the velocity flow distribution, w, during rest and activity. The distributions are similar in the two states. In most cases plug flow model provides the best fit to the data. The range of values of w indicates that the width of the velocity flow distribution can potentially be a physiologically meaningful parameter. In particular, in applications such as angiogenesis where the tumor vasculature is significantly different than normal tissue, measuring the distribution of path lengths blood traverses may provide insight into the brain microvasculature.

REFERENCES

[1] Buxton R. B., et al., MRM 40, 383-396, 1998.
[2] Wong E. C., et al., NMR in Biomed 10, 237-249, 1997.

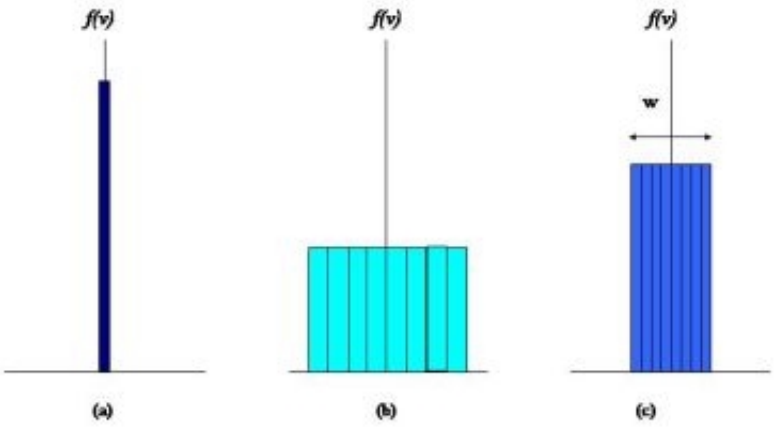

Figure 1: Flow velocity distribution for (a) plug flow, (b) laminar flow, and (c) flow dispersion.

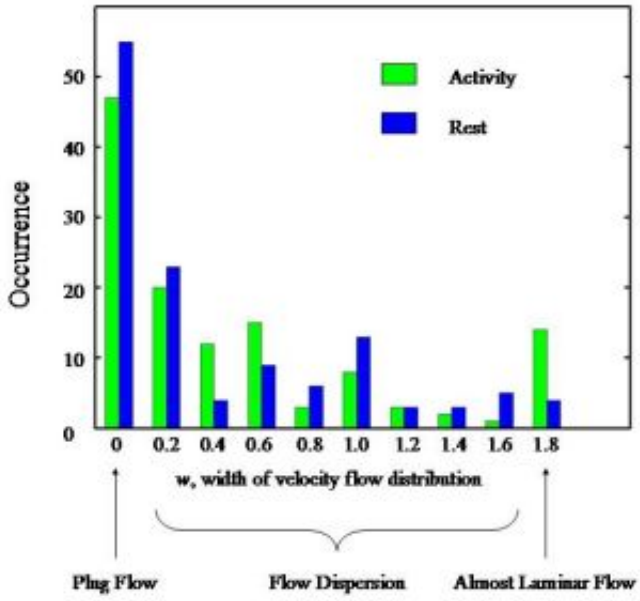

FIgure 2: Histogram of velocity flow distribution during rest and activity.

WE 239
Validation of Detecting Speech Boundaries in fMRI

Sonya Mehta[1], Kirrie J. Ballard[2], Jerald B. Moon[2], William W. Graves[1], Thomas J. Grabowski[1,3]
[1]Department of Neurology, University of Iowa, [2]Department of Speech Pathology and Audiology, University of Iowa, [3]Department of Radiology, University of Iowa

Introduction: Speech latencies are important dependent measures in studies of semantic and lexical processing, where effects < 50 ms may be significant. In such fMRI experiments, it is difficult to identify speech onsets, since gradient noise overlaps speech in both time and frequency domains. Filters that remove scanner noise may degrade the speech signal. We evaluated the performance of spectral subtraction, using a synthetic benchmark data set created by superimposing scanner noise on a speech recording obtained in a sound-proof booth. The effects of filtering and the accuracy of speech onsets and offsets were evaluated by comparison to the manual performance from two speech scientists.
Methods: An acoustic recording of a male subject reading a phonetically balanced list of 101 monosyllabic words (all phonemes occurred at onset and offset) was acquired at 44 kHz. The recording was manually segmented by independent experts using Cspeech software to display the time and frequency spectrogram and the speech waveform. Scanner noise from a typical fMRI experiment was added to this speech sample, with SNR typical for our overt speech experiments. The data were downsampled to 16 kHz and filtered using spectral subtraction (Nelles, et al, 2003, Boll et al, 1979) with modifications leveraging a time-aware data acquisition system (Smyser et al, 2001), such that spectra were constructed separately for each slice. For each slice, the method estimated the maximum magnitude difference at each frequency bin that occurred between successive image acquisitions when speech was not present. The magnitude spectrum of the previous speech-free segment, plus the maximum difference, was subtracted from each segment. The segments were then reverse-transformed using the original phase of the segment. Local variance thresholds were used to detect and bound speech. A naive investigator reviewed and corrected audible bounding errors. The filtered file was also manually delineated by an expert. Results were analyzed using two factor ANOVAs comparing segmentation methods, and initial or final phoneme.
Results and Discussion: The manually-segmented speech data was the gold standard, where inter-rater agreement was 0.6 ms (sd 31.6 ms) for onsets and 14.1 ms (sd 43.4 ms) for offsets. All speech events were successfully detected by the algorithm. The detected onsets were on average significantly earlier than the standard (-29.9 ms +/- 51ms) and offsets were not different than the standard (0.5 ms +/- 117.1 ms). Relative to the standard, the algorithm tended to truncate unvoiced fricatives and extend unvoiced plosives and vowels. Relative to the standard, expert segmentation of the filtered file was truncated at onset and offset [+20.3 (48.0) ms, -37.7 (75.2) ms]. Unvoiced fricatives and voiced plosives were truncated; unvoiced plosives were extended.
Conclusions: The algorithm detected speech events reliably. It showed a 30ms bias toward premature detection and was affected by initial phoneme. Onsets were more consistent with the standard than offsets, but the initial phoneme effect underscores the importance of balancing this factor in experimental designs. Manual performance on the filtered file was not better than the algorithm, and was characterized by truncation of speech. This validation quantifies these effects and provides a framework for future refinements.

WE 240
Identifying and modeling the time-course of speech-related signal variance in fMRI

Sonya Mehta[1], Thomas J. Grabowski[1, 2], Mehrdad Razavi[1], David Rudrauf[1], Jocelyn Cole[1], Lizann Bolinger[3]
[1]Department of Neurology, University of Iowa, [2]Department of Radiology, University of Iowa, [3]NRC Institute for Biodiagnostics, Winnipeg, MB

Introduction: Speech is associated with changes in signal in fMRI experiments, due to head motion, changes in magnetic susceptibility and possibly other effects. Even when designs minimize correlation of these effects with effects of interest, they increase the residual variance. Methods for combating them are often predicated on assumptions about their time-course (i.e. that they coincide with speech envelopes). We investigated the presence, magnitude, and timing of speech-related signal artifacts with an overt naming paradigm and a time-aware data acquisition system (Smyser et al, 2001), in which the timing of speech envelopes with respect to image acquisition was known precisely.
Methods: 9 right-handed subjects were scanned using EPI-BOLD fMRI (TE 40ms, FOV 24cm, matrix 64x64) on a GE LX CV/I scanner (1.5T). Six runs of 220 axial images (20 slices, TR=2s) oriented parallel to the intercommissual line were acquired. Time-stamped speech and respiratory data were also acquired. Subjects underwent three overt and three covert runs in which they performed visual confrontation naming using an event-related design. Speech data were filtered and segmented to identify speech boundaries using a modified spectral subtraction approach (Nelles et al, 2003; Mehta et al, this meeting). Speech boundaries were reviewed by the investigator. The speech boundary timing information was used to inform several regression analyses on the overt data. They were: 1) a base model (task regressors and global signal); 2) EXC, the base model with omission of images coinciding with the presence of a speech envelope; 3) ENV, the base model plus a box-car reference function to model the mean signal in the speech envelope; 4) BIN, ENV plus four additional regressors modeling the mean signal in time bins immediately before and after the speech envelope [-1000 ms to -500 ms, -500 to 0 ms, 0 to +500 ms, and +500 to +1000 ms]. Voxelwise analysis was performed within subject, and regressors were evaluated using t/F tests. Models were compared to the base model on the basis of adjusted R2 (Razavi et al, 2003).
Results and Discussion: 15.0% +/- 2.7% of the images were acquired during speech envelopes. The occurrence of these speech events produced systematic intensity artifacts. Excluding images coinciding with the speech envelope did not improve adjusted R2. On the other hand, models ENV and BIN produced significant improvements in adjusted R2, with the latter being superior. The effect varied spatially, and was most pronounced on inferior slices and in voxels corresponding to CSF spaces. Analysis of individual time bins showed significant effects from 500 ms to +1000 ms. Analysis of respiratory pressure belt data revealed significantly greater entropy in the overt condition than in the covert condition. The first derivative of these data revealed a consistent and pronounced pattern of exhalation preceding the onset of the speech event and inhalation with the offset of the speech event.
Conclusions: Signal artifacts associated with speech extend beyond speech boundaries. While these artifacts probably arise in part from motion, susceptibility and their interaction, the data presented here suggest an additional effect mediated by respiration, and its indirect effect on CSF flow.

WE 241
Anisotropy Characterization in Diffusion Weighted MRI via Reversible Jump MCMC

Lester Melie-García , Erick Canales-Rodríguez , Pedro Valdés-Hernández
Cuban Neuroscience Center, Havana, Cuba

This work presents a new method to characterize the anisotropy in one voxel in High Angular Resolution Diffusion Weighted Imaging (DWI). DWI is a Magnetic resonance technique that measures locally the water diffusion *in vivo* in animal and human brains. Several papers have given an anisotropy description from the analysis of this neuroimaging technique by different ways (Tuch et. al. 2002, Alexander et. al. 2002, Lawrence 2002). The anisotropy in one voxel could be described by some parameters such as: number of fibers, their spatial distribution, the diffusion coefficients and the fraction of volume associated with each fiber. This new method is based on the estimation of these parameters whereas the number of fibers is determined in the same estimation process by using a Bayesian Framework. The joint posterior probability of the parameters and the model (determined by the number of fibers) is given by the Bayes rule:
$P(\Theta,M|S) \propto P(S|\Theta,M)\, P(\Theta|M)\, P(M)$, where Θ are the model parameters, S is the data and M represents the model. The optimum values of Θ and M that maximize this posterior is achieved through Reversible Jump Markov Chain Monte Carlo (RJMCMC) algorithm (Green 1995).
The diffusion signal is modeled on the partial volume equation (Behrens et. al. 2003) that is a discrete mixture of Gaussian diffusion processes in slow exchange as shown in figure 1. In the figure, $\boldsymbol{R}_j$ is the matrix that rotates $\boldsymbol{A}$ to the direction defined by the angles (θ_j, ϕ_j), D is the diffusivity outside the fiber tract, b_i and the vector $\boldsymbol{r}_i$ are the b-value and the gradient direction associated with the *i-th* measurement respectively. The number of fibers is k and d_j , f_j and $\boldsymbol{R}^T{}_j \boldsymbol{A} \boldsymbol{R}_j$ are the diffusivity, the fraction of volume and the diffusion tensor along the *j-th* fiber direction on (θ_j, ϕ_j) respectively.
Synthetic and real data was used to described the capabilities of the method. The figure 2 (A and B) shows results for synthetic data coming from a mixture of 4 fibers with different orientations, volume fractions and diffusivity. In this case 42 gradient directions were used and $b = 3000\ s/mm^2$. The application in real data for some voxels with crossing fibers was performed obtaining very good signal reconstruction (figure 2, C, D and E). The number of iterations of the RJMCMC algorithm was the same (50 000) in both sets of data.

References:

1. Lawrence F.R. 2002. Characterization of Anisotropy in High Angular Resolution Diffusion-Weighted MRI. *Magnetic Resonance in Medicine* 47, 1083-1099.
2. Alexander D.C., et. al. 2002. Detection and Modeling of Non-Gaussian Apparent Diffusion Coefficient Profiles in Human Brain Data. *Magnetic Resonance in Medicine* 48, 331-340.
3. Tuch D., et. al. 2002. High Angular Resolution Diffusion Imaging Reveals Intravoxel White Matter Fiber Heterogeneity. *Magnetic Resonance in Medicine* 48, 577-582.
4. Behrens T., et. al. 2003. Non-invasive mapping of connections between human thalamus and cortex using diffusion imaging. *Nature Neuroscience* 6, 750-757.
5. Green P. 1995. Reversible Jump Markov chain Monte Carlo computation and Bayesian model determination. *Biometrika*, 82(4), 711-732.

$$\mu_i = S_0 \left\{ \left(1 - \sum_{j=1}^{k} f_j \right) \exp(-b_i D) + \sum_{j=1}^{k} f_j \exp(-b_i d_j \mathbf{r}_i^T \mathbf{R}_j^T A \mathbf{R}_j \mathbf{r}_i) \right\}.$$

$$\text{Where } A = \begin{pmatrix} 1 & 0 & 0 \\ 0 & 0 & 0 \\ 0 & 0 & 0 \end{pmatrix}$$

Figure 1

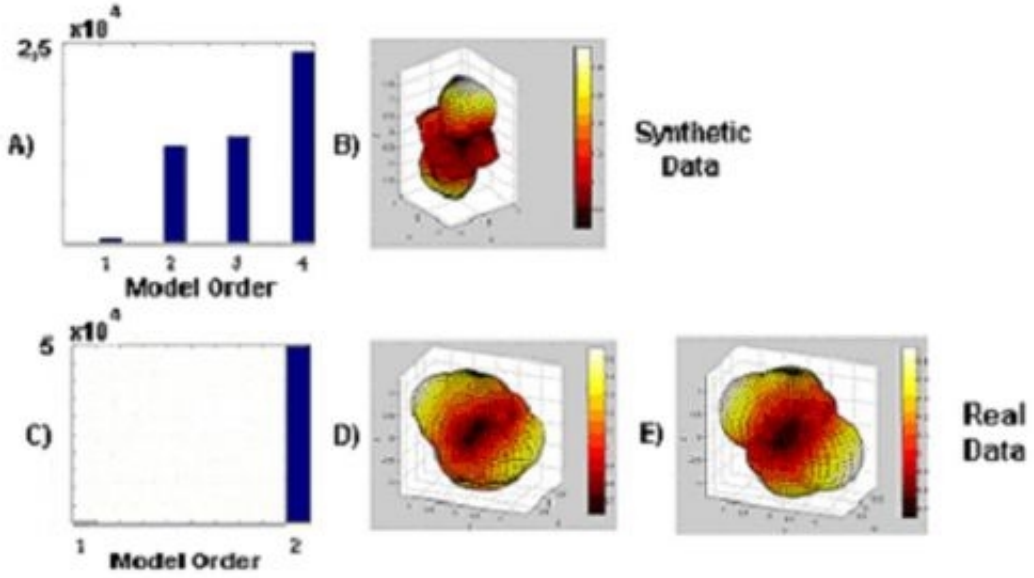

Figure 2: A) Histogram of visited models by the RJMCMC, the model of 4 fibers was the most visited B) 3D view of the reconstructed Apparent Diffusion Coeficient (ADC). C) Histogram of visited models by RJMCMC in Real Data case. D) ADC for real Data. E) Reconstructed Apparent Diffusion Coeficient.

WE 242

Anisotropy Characterization in Diffusion Weighted MRI via Reversible Jump MCMC

Lester Melie-García , Erick Canales-Rodríguez , Pedro A. Valdés-Hernández
Cuban Neuroscience Center, Havana, Cuba

This work presents a new method to characterize anisotropy in a voxel in High Angular Resolution Diffusion Weighted Imaging (HARDWI). HARDWI is a MRI technique that measures locally the water diffusion *in vivo* in animal and human brains. Several papers have proposed anisotropy descriptions based on this neuroimaging tecnique by different ways (Tuch et. al. 2002, Alexander et. al. 2002, Lawrence 2002). The anisotropy in a voxel can be described by some parameters such as: number of fibers, their spatial distribution, the diffusion coefficients and the fraction of volume associated with each fiber. This new method is based on the estimation of these parameters whereas the number of fibers is determined in the same estimation process by using a Bayesian Framework. The joint posterior probability of the parameters and the model (determined by the number of fibers) is given by the Bayes rule:

$P(\Theta,M|S) \propto P(S|\Theta,M)\, P(\Theta|M)\, P(M)$, where Θ are the model parameters, S is the data and M represents the model. The optimum values of Θ and M that maximize this posterior is achieved through Reversible Jump Markov Chain Monte Carlo (RJMCMC) algorithm (Green 1995).

The diffusion signal is modeled on the partial volume equation (Behrens et. al. 2003) that is a discrete mixture of Gaussian diffusion processes in slow exchange as shown in figure 1. In the figure, $\boldsymbol{R}_j$ is the matrix that rotates $\boldsymbol{A}$ to the direction defined by the angles (θ_j, ϕ_j), D is the diffusivity outside the fiber tract, b_i and the vector $\boldsymbol{r}_i$ are the b-value and the gradient direction associated with the *i-th* measurement respectively. The number of fibers is k and d_j , f_j and $\boldsymbol{R}^T{}_j \boldsymbol{A} \boldsymbol{R}_j$ are the diffusivity, the fraction of volume and the diffusion tensor along the *j-th* fiber direction on (θ_j, ϕ_j) respectively.

Synthetic and real data was used to described the capabilities of the method. The figure 2 (A and B) shows results for synthetic data coming from a mixture of 4 fibers with different orientations, volume fractions and diffusivity. In this case 42 gradient directions were used and $b = 3000\ s/mm^2$. The application in real data for some voxels with crossing fibers was performed obtaining very good signal reconstruction (figure 2, C, D and E). The number of iterations of the RJMCMC algorithm was the same (50 000) in both sets of data.

References:

1. Lawrence F.R. 2002. Characterization of Anisotropy in High Angular Resolution Diffusion-Weighted MRI. *Magnetic Resonance in Medicine* 47, 1083-1099.
2. Alexander D.C., et. al. 2002. Detection and Modeling of Non-Gaussian Apparent Diffusion Coefficient Profiles in Human Brain Data. *Magnetic Resonance in Medicine* 48, 331-340.
3. Tuch D., et. al. 2002. High Angular Resolution Diffusion Imaging Reveals Intravoxel White Matter Fiber Heterogeneity. *Magnetic Resonance in Medicine* 48, 577-582.
4. Behrens T., et. al. 2003. Non-invasive mapping of connections between human thalamus and cortex using diffusion imaging. *Nature Neuroscience* 6, 750-757.
5. Green P. 1995. Reversible Jump Markov chain Monte Carlo computation and Bayesian model determination. *Biometrika*, 82(4), 711-732.

$$\mu_i = S_0 \left\{ \left(1 - \sum_{j=1}^{k} f_j \right) \exp(-b_i D) + \sum_{j=1}^{k} f_j \exp(-b_i d_j \boldsymbol{r}_i^T \boldsymbol{R}_j^T \boldsymbol{A} \boldsymbol{R}_j \boldsymbol{r}_i) \right\}.$$

$$\text{Where } \boldsymbol{A} = \begin{pmatrix} 1 & 0 & 0 \\ 0 & 0 & 0 \\ 0 & 0 & 0 \end{pmatrix}$$

Figure 1

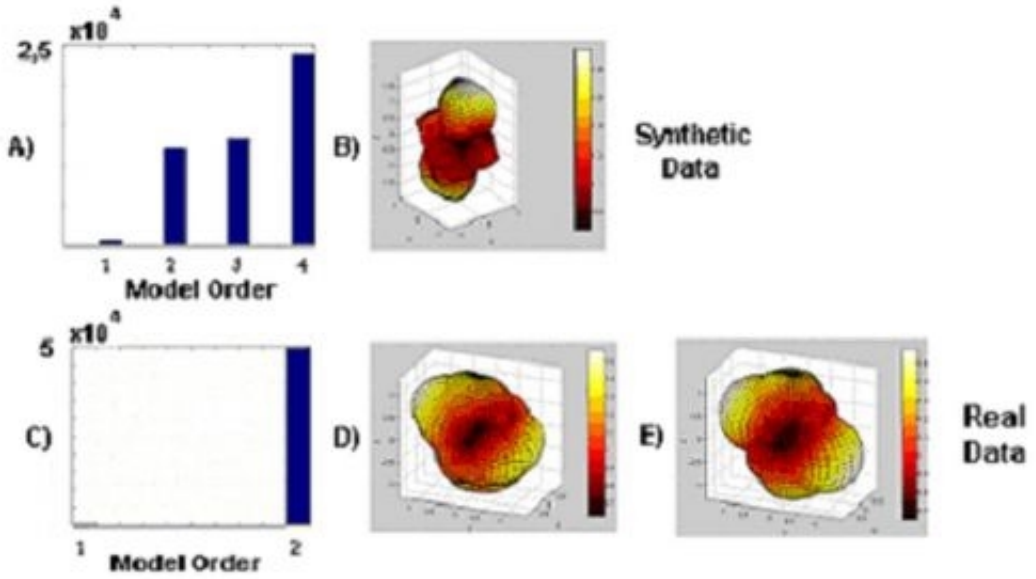

Figure 2: A) Histogram of visited models by the RJMCMC, the model of 4 fibers was the most visited B) 3D view of the reconstructed Apparent Diffusion Coeficient (ADC). C) Histogram of visited models by RJMCMC in Real Data case. D) ADC for real Data. E) Reconstructed Apparent Diffusion Coeficient.

WE 243
Bayesian Model Averaging in EEG/MEG imaging in Individual Brain Anatomy

Lester Melie-García[1], Nelson Trujillo-Barreto[1], Thomas Koenig[2], Eduardo Martínez-Montes[1]
[1]Cuban Neuroscience Center, Havana, Cuba, [2]University Hospital Bern, Switzerland

Recently, an original method (hereinafter BMA) has been developed (Trujillo et. al. 2003) based on a third inference level in the Bayesian formulation for the EEG and MEG inverse problem. The methodology used in that work consider different anatomical constraints taken from a segmentation in 69 compartments of the Average Brain Atlas of the Montreal Neurological Institute (MNI) (Evans et. al. 1994). The aim of this work is twofold: 1) to show the applicability of this new method in the individual brain anatomy, 2) to develop a methodology for the automatic computation of an Individual Atlas used for the source localization.
The methodology for the computation of the Individual Atlases consisted of the automatic classification of different structures (segmentation in 67 compartments) of each individual high resolution T1 weighted 3D MRI. Several steps were necessary: 1) Non-uniformity Correction of MRI 3D image, 2) Normalization: Spatial transformation to Standardized Space (Tailarach space), 3) Gray matter Segmentation and Identification of the Structures (from Atlas) in the standardized space, 4) Individual Atlas: Transformation of the MRI segmented and classified MRI back to the Individual space (see figure 1).
Once the Individual Atlases were constructed, the BMA method was applied to find the localization of sources involved in the processing of a specific visual stimulus. This stimulus consisted of a checkerboard (reversal frequency = 3 Hz; left and right hemifields separately, as well as full visual field stimulation) alternating with a fixation point, in a block design paradigm. The EEG and BOLD (Blood Oxygen Level Dependent) signals were recorded by using the EEG-fMRI simultaneous recording technique (Goldman et. al. 2000) in 5 subjects. The EEG recordings were properly cleaned, windowed and averaged over trials and source localization analysis via the BMA method was applied to the N1 component. In all cases well defined sources on the individual brain were obtained, matching the fMRI activation pattern. The BMA solution for one of the subject analyzed is depicted in Figure 2.

References:

1. Trujillo-Barreto N.J., Aubert-Vázquez E. and Valdés-Sosa P. 2003. Bayesian Model Averaging in EEG/MEG imaging. *Neuroimage (in press)*.
2. Evans A.C., Collins D.L., Mills S.R., Brown E.D., Kelly, R.L. and Peters T.M. 1993. 3D statistical neuroanatomical models from 305 MRI volumes. *Proc. IEEE-Nuclear Science Symposium and Medical Imaging Conference, London: M.T.P Press*, 95, 1813-1817.
3. Goldman R.I., Stern J.M., Engel J.Jr, Cohen M.S. 2000. Acquiring simultaneous EEG and functional MRI. *Clinical Neurophysiology*, 111(11):1974-80.

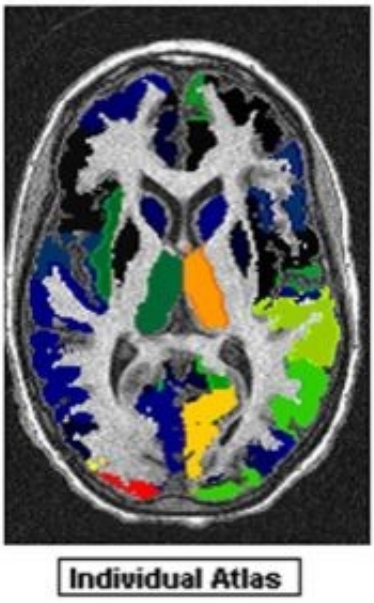

Figure 1: Individual Atlas of one subject. The classified structures (compartments) in the individual anatomy are highlighted in different colors.

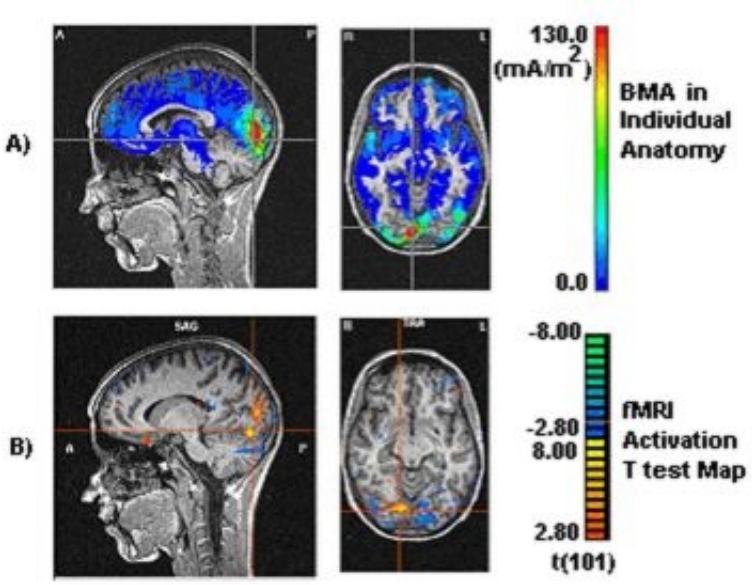

Figure 2: A) BMA solution for the N1 component of the evoked potential for Left Hemifield Stimulation. B) fMRI activation contrasting Left Hemifield Stimulation (in hot scale) versus Right Hemifield Stimulation (in winter scale).

WE 244
BAYESIAN MODEL AVERAGING IN EEG/MEG IMAGING IN INDIVIDUAL BRAIN ANATOMY

Lester Melie-García[1], Nelson Trujillo-Barreto[1], Thomas Koenig[2], Eduardo Martínez-Montes[1], Daniela Hubl[2]
[1]Cuban Neuroscience Center, Havana, Cuba, [2]University Hospital of Clinical Psychiatry, Bern, Switzerland

Recently, a new method, Bayesian Model Averaging in EEG/MEG imaging (BMA) has been developed (Trujillo et. al. 2004) based on a third inference level in the Bayesian formulation for the EEG and MEG inverse problem. The methodology used in that work considers different anatomical constraints taken from a segmentation into 69 compartments of the Average Brain Atlas of the Montreal Neurological Institute (MNI) (Evans et. al. 1994). The aim of this work is twofold: 1) to show the applicability of this new method using individual brain anatomy, 2) implementation of a methodology for obtaining Individual Atlases used for the sources localization.
The process to obtain an Individual Atlas consisted of the automatic segmentation and classification of different structures (67 compartments) of each individual high resolution T1 weighted 3D MRI. The procedure followed here was: 1) Non-uniformity Correction of MRI 3D image, 2) Normalization: spatial transformation to standardized space (Tailarach space), 3) Gray matter segmentation and identification of the Structures (from Average Atlas) in the standardized space, 4) Individual Atlas: transformation of the segmented and classified MRI back to the individual space (see figure 1). An analog procedure has been described previously (Collins et. al. 1995, Collins et. al. 1998), for estimating automatically the volume of gross cerebral structures.
Once the Individual Atlases were constructed, the BMA method was applied to find the localization of sources involved in the processing of a specific visual stimulus. This stimulus consisted of a checkerboard (reversal frequency = 3 Hz; left and right hemifields separately, as well as full visual field stimulation) alternating with a fixation point, in a block design paradigm. The EEG and BOLD signals were recorded using the EEG-fMRI simultaneous recording technique (Goldman et al. 2000) in 5 subjects. The EEG recordings were properly artifact-filtered, windowed and averaged over trials. The source localization analysis via BMA method was applied to the N1 component. In all cases well defined sources on the individual brain were obtained, matching with the fMRI activation pattern. The BMA solution for one of the subject analyzed is shown in Figure 2.

References:

1. Trujillo-Barreto N.J., Aubert-Vázquez E. and Valdés-Sosa P. 2004. Bayesian Model Averaging in EEG/MEG imaging. *Neuroimage* (in press).
2. Evans A.C., Collins D.L., Mills S.R., Brown E.D., Kelly R.L. and Peters T.M. 1993. 3D statistical neuroanatomical models from 305 MRI volumes. Proc. *IEEE-Nuclear Science Symposium and Medical Imaging Conference*, London: M.T.P Press; 95, 1813-1817.
3. Goldman R.I., Stern J.M., Engel J.Jr, Cohen M.S. 2000 Acquiring simultaneous EEG and functional MRI. *Clinical Neurophysiology*. 111(11):1974-80.
4. D.L. Collins, C.J. Holmes, et. al. Automatic 3D model-based neuroanatomical segmentation. *Human Brain Mapping* , 3(3) : 190-208, 1995
5. D. Collins, A. Zijdenbos, and A. Evans. Improved automatic gross cerebral structure segmentation. In A. Evans, editor, *4th International Conference on Functional Mapping of the Human Brain*, 1998.

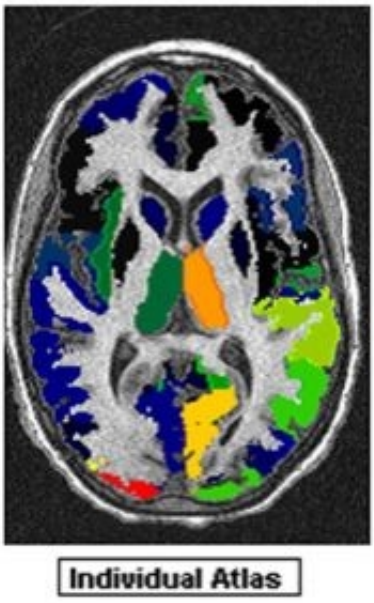

Figure 1: Individual Atlas of one subject. The segmented structures (compartments) in the individual anatomy are highlighted in different colors.

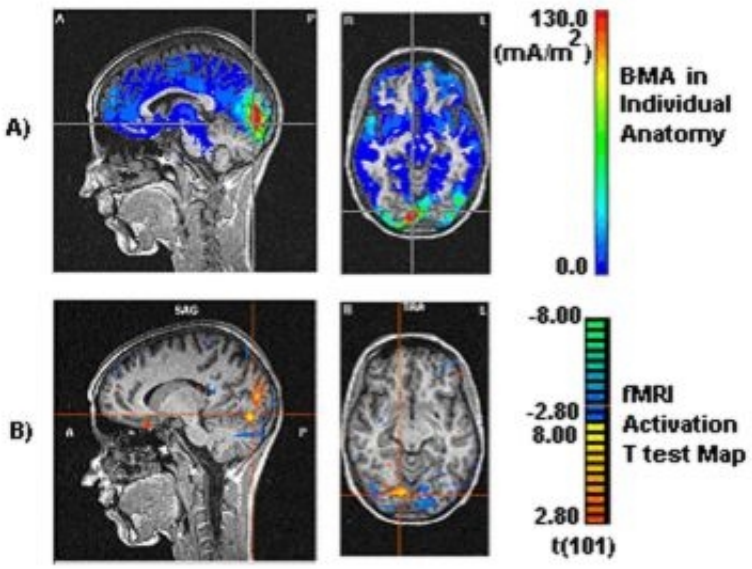

Figure 2: A) BMA solution for the N1 component of the evoked potential for Left Hemifield Stimulation. B) fMRI activation contrasting Left Hemifield Stimulation (in hot scale) versus Right Hemifield Stimulation (in winter scale).

WE 245
EEG imaging via BMA with fMRI pre-defined prior model probabilities

Lester Melie-García[1], Nelson Trujillo-Barreto[1], Eduardo Martínez-Montes[1], Thomas Koenig[2], Pedro A. Valdés-Sosa[1]

[1]Cuban Neuroscience Center, Havana, Cuba, [2]University Hospital of Clinical Psychiatry, Bern, Switzerland

In the present work, a modification of the EEG/MEG inverse solution method presented by Trujillo et. al. 2004 (known as Bayesian Model Averaging (BMA)), is introduced in order to include prior information provided by fMRI. This BMA approach basically finds a model-free Primary Current Density (PCD) inside the brain by dealing with the uncertainty of selecting a specific model to carry out inference upon it. The models differ in the anatomical constraint used to find the solution, which are defined by different combinations of brain areas taken from a segmentation of the brain into 69 compartments. As a result, the final solution is calculated through a linear combination of the estimators of the PCD for each model M_k, (E[j|v,M_k]), weighted by the posterior probability of the corresponding models given the data $p(M_k|\mathrm{v})$, that is: $E[\mathrm{j}|\mathrm{v}] = \Sigma^{K}{}_{k=0}\, E[\mathrm{j}|\mathrm{v},M_k]\, p(M_k|\mathrm{v})$, where the posterior probabilities for the models are defined as $p(M_k|\mathrm{v}) = \alpha_k B_{k0} \,/\, \Sigma^{K}{}_{r=0}\, \alpha_r B_{r0}$, $k = 0..K$, with $\alpha_k = p(M_k) \,/\, p(M_0)$ and B_{k0} are the so called Bayes Factors (Kass et al.,1994). In the previous approach, all the models are considered to have the same a priori probability ($\alpha_k = 1$) for all k. The main contribution of this paper consists in considering a different prior probability for each model, which are defined based on the probability associated with the significance of the t-test map (t-map) in each region obtained from a conjoint fMRI-EEG recording. The probability of each compartment (simplest models) is defined as: $p(M_r) = (1/N)\, \Sigma^{N}{}_{i=0}\, p(\mathrm{v}_i)$, where $p(\mathrm{v}_i)$ is the probability associated with the t-statistic for each voxel that belongs to *i-th* compartment and N is the total number of voxels in that compartment. The probability of each model consisting of either one (simplest model) or more regions (complex models) is then defined as: $p(M_k) = (1/R)\, \Sigma^{R}{}_{r=1}\, p(M_r)$, where R is the number of regions or compartments in the model M_k.

The capabilities of this new methodology were tested with synthetic and real data. The inverse solutions found by this method inherited the good properties of the previous BMA approach (finding deep activations with less ghost sources) described in Trujillo et. al. 2004. Particularly, the blurring (FWHM) of the reconstructed sources is further reduced when the information from the fMRI is taken into account.

References:

1. Trujillo-Barreto N.J., Aubert-Vázquez E. and Valdés-Sosa P. 2004. Bayesian Model Averaging in EEG/MEG imaging. *Neuroimage* (in press).

2. Kass R.E. and Raftery A.E. 1994. Bayes Factors. Technical Report no. 254. *Department of Statistics, University of Washington*.

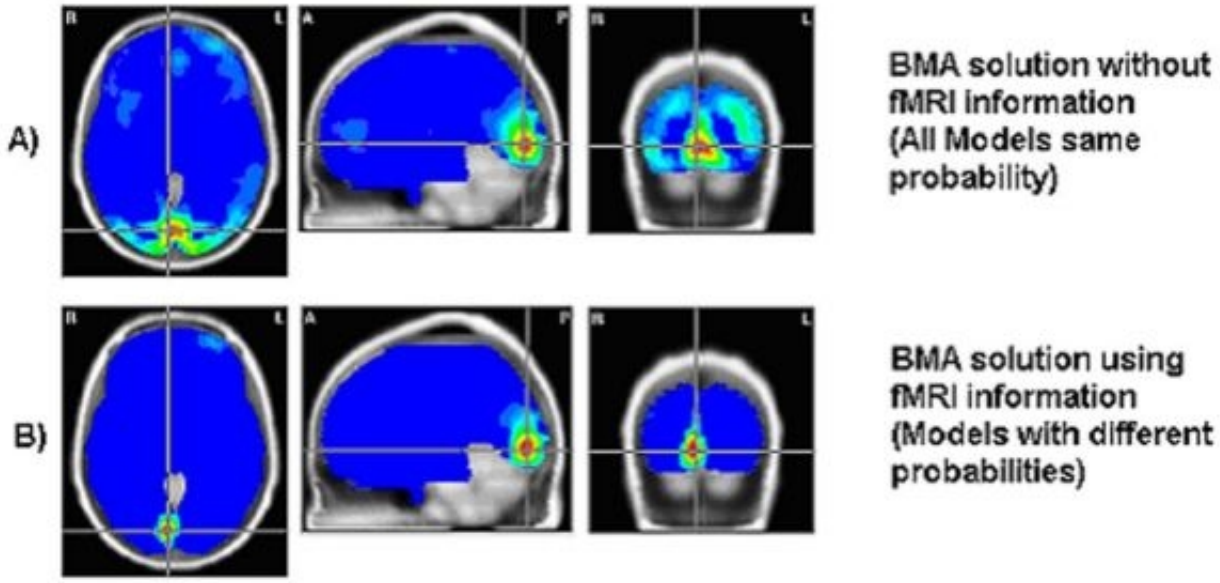

Figure 1: BMA solutions for negative N1 component of evoked potential obtained from visual stimulus presented in the Left visual Hemifield. EEG and fMRI were recorded simultaneously. A) Solution with all models having the same prior probability. B) Solution when is used fMRI to define prior probabilities for the models. The solution is less blurred and well lateralized.

WE 246
EEG imaging via BMA with fMRI pre-defined prior model probabilities

Lester Melie-García[1], Nelson Trujillo-Barreto[1], Eduardo Martínez-Montes[1], Thomas Koenig[2], Pedro A. Valdés-Sosa[1]

[1]Cuban Neuroscience Center, Havana, Cuba, [2]University Hospital of Clinical Psychiatry, Bern, Switzerland

In the present work, a modification of the EEG/MEG inverse solution method presented by Trujillo et. al. 2003 (known as Bayesian Model Averaging (BMA)), is introduced in order to include prior information coming from fMRI. This BMA approach basically finds a model-free Primary Current Density (PCD) inside the brain by dealing with the uncertainty of selecting a specific model to carry out inference upon it. The models differ in the anatomical constraint used to find the solution, which are defined by different combinations of brain areas taken from a segmentation of the brain in 69 compartments. As a result, the final solution is calculated through a linear combination of the estimators of the PCD for each model M_k, (E[j|v,M_k]), weighted by the posterior probability of the corresponding models given the data $p(M_k|\mathrm{v})$, that is: $E[\mathrm{j}|\mathrm{v}] = \Sigma^{\mathrm{K}}{}_{k=0}\, \mathrm{E}[\mathrm{j}|\mathrm{v},M_k]\, p(M_k|\mathrm{v})$, where the posterior probabilities for the models are defined as
$p(M_k|\mathrm{v}) = \alpha_k B_{k0} \,/\, \Sigma^{K}{}_{r=0}\, \alpha_r B_{r0}$, $k = 0...K$, with $\alpha_k = p(M_k) \,/\, p(M_0)$ and B_{k0} are the so called Bayes Factors (Kass et. al. 1994). In the previous approach, all the models are considered to have the same probability a priori ($\alpha_k = 1$) for all k. The main contribution of this paper consists in considering a different prior probability for each model, which are defined based on the probability associated with the significance of the T test map (Tmap) in each region obtained from a conjoint fMRI-EEG recording. The probability of each compartment (simplest models) is defined as: $p(M_r) = (1/N)\, \Sigma^{N}{}_{i=0}\, p(\mathrm{v}_i)$, where $p(\mathrm{v}_i)$ is the probability associated with Tmap for each voxel that belongs to compartment r and N is the total number of voxels in that compartment. The probability of each model that can be composed by one (simplest model) or more regions (complex models) is then defined as: $p(M_k) = (1/R)\, \Sigma^{R}{}_{r=1}\, p(M_r)$, where R is the number of regions or compartments in the model M_k.
The capabilities of this new methodology were tested with synthetic and real data. The inverse solutions found by this method inherited the good properties of the previous BMA approach (finding deep activations with less ghost sources) described in Trujillo et. al. 2003. Particularly, the blurring of the reconstructed sources is further reduced when the information from the fMRI is taken into account.

References:

1. Trujillo-Barreto N.J., Aubert-Vázquez E. and Valdés-Sosa P. 2003. Bayesian Model Averaging in EEG/MEG imaging. *Neuroimage (in press).*
2. Kass R.E. and Raftery A.E. 1994. Bayes Factors. *Technical Report no. 254.* Department of Statistics, University of Washington.

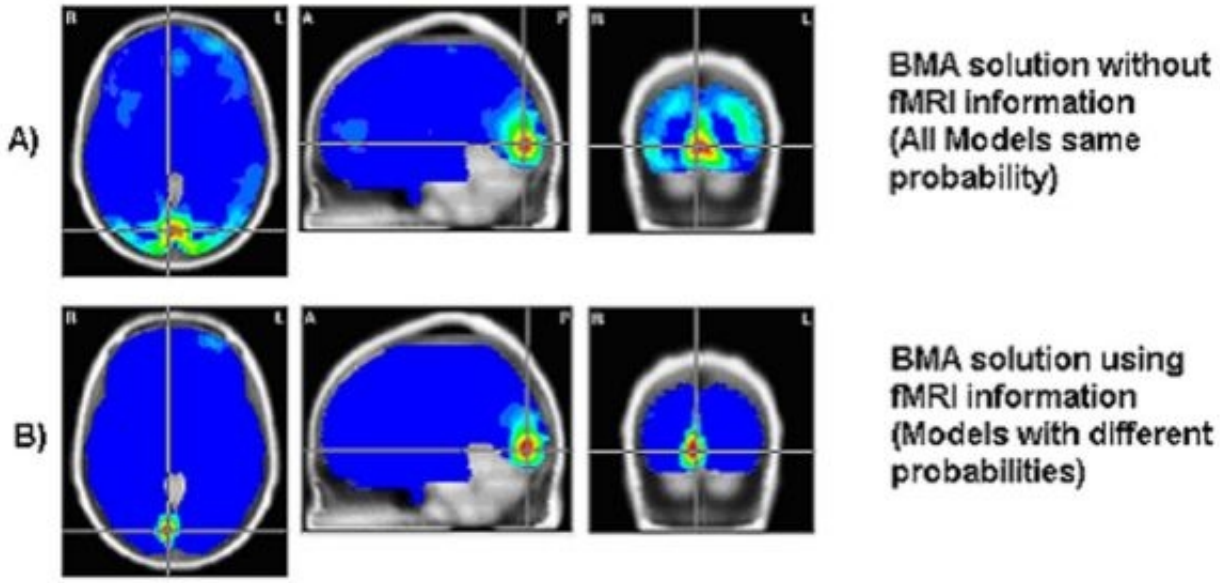

Figure 1: BMA solutions for negative N1 component of evoked potential obtained from visual stimulus presented in the Left visual Hemifield. EEG and fMRI were recorded simultaneously. A) Solution with all models having the same prior probability. B) Solution when is used fMRI to define prior probabilities for the models. The solution is less blurred and well lateralized.

WE 247
Dependence of hand motor centre localization on the number of measurements

Gregor Meller[1,2], Alexander Geissler[1,2], Rupert Lanzenberger[1,2], Amir Tahamtam[1,2], Denny Milakara[1,2], Andreas Gartus[1,2], Roland Beisteiner[1,2]
[1]Study Group Clinical fMRI at the Departments of Neurology and Radiology, [2]General Hospital and University of Vienna

Introduction: Classical fMRI-techniques process hemodynamic correlations of cortical volume-elements with repeated stimulations by calculating their mean. Since averaged data don't allow judgement of a voxel's reliability over repeated measurements, fMRI riskmaps have been introduced (1-3) to separate the evaluation of a voxel's reliability from that of it's correlation. Riskmaps hypothesize, that a voxel's lowest correlation with a reference function during repeated fMRI measurements provides a marker for the risk, that lesioning this cortical area will imply a task-specific functional deficit. Consequently, the voxel with the highest minimal correlation over all runs is identified with the physiologically most active, hence most specifically responding voxel according to the given paradigm. This voxel is called "riskmap centre" (here "motor centre"). The slice it belongs to is called the "most active slice". We studied, how the localization quality of the primary hand motor cortex through riskmaps depends on the amount of accessible data. We are interested in the smallest number of measurements enabling a valid localization given our subject population characteristics used. **Methods:** We performed repetitive measurements (runs) on right-handed healthy test-persons carrying out right-handed fist-clenching tasks during 5-10 runs with 3 stimulation- and 4 rest-phases and using a 128x128 Matrix with voxelsize 1.8x1.8x3 mm. For each voxel and each run we calculated the correlation coefficients from measured signal intensity time courses with a boxcar reference function using a delay of 2 TR-times. We recorded the motor centre and it's varying spatial positions while selecting (no recycling) all possible samples of a specific size (subsamples) from each voxel's set of correlation values. Each combination possesses an individual drawing probability mirroring it's representativeness (sampling error). In mean a subsample is less volatile than an individual voxel-correlation measurement, further it's lexicographic order must not be mixed within the slice, because the runspecific signal-to-noise ratio restricts the evaluation to voxels of the same run (table 1). Starting from subsamples of size 1, we increased them iteratively, until they were maximal, i.e. contained all runs of the corresponding voxel. We observed the averaged deviations of all equally-sized subsamples from the "true" motor-centre (= total sample motor center) and claimed congruence, if this mean was <= 1 voxelsize in both coordinates. **Results:** Table 2 shows the congruence results within the most active slice, table 3 shows the somewhat deviating behavior of the slices immediately above and below. The number of runs necessary to achieve congruence of the subsample motor center (mean over all subsamples with the same number of runs) with the "true" motor center is given in column 2. The rightmost column of tables 2 and 3 shows the percentage of individual subsample motor centers differing from the "true" motor-centre in at least one direction by more than one voxel. E.g. fulfilling the congruence criterion when calculating the mean center deviation over all subsamples still allows some outliers not fulfilling the congruence criterion. The percentage of outliers is calculated in relation to the total number of possible subsamples with the same run count. **Discussion:** We estimated the minimal dataset necessary to guarantee a valid hand motor localization. Given our run definition and young, healthy cooperative test persons, already 3 runs can produce good results, provided riskmaps are employed. A concise analysis of these and more problematic patient data may lead to an online-algorithm supplying a real-time termination criterion for measurements. **Acknowledgement:** We want to acknowledge support by the Ludwig Boltzmann Institute for Functional Brain Topography (head:Prof.Dr.L.Deecke) and by the Austrian Science Foundation (FWF P15102).We are grateful to Prof.Trattnig and Prof.Barth for organisatory and scientific support.
Literature: 1. Beisteiner,R.,et al. Neurosci.Lett.290(1):13-6(2000). **2.** Beisteiner,R.,et al. NeuroImage 13(6):1016-1026(2001) **3.** Beisteiner,R. Pädiatrische Praxis 64(2),2004.

Test-person	Sample-size	Measured runs/voxel	Averaged sub-samples	Most active slice	Fraction of deviating samples (%)
B	2	5	10	20/25	00.00
G	2	6	15	23/25	00.00
K	2	6	15	19/25	13.34
S	2	6	15	23/25	13.34
M	3	10	120	16/25	6.56
L	1	6	15	19/25	00.00

Table 2: most active slices as detected with the riskmap technique

Test-person	Sample-size	Measured runs/voxel	Averaged sub-samples	slice	fraction of deviating samples (%)
B	2	5	10	19/25	19.00
B	2	5	10	21/25	00.00
G	2	6	15	22/25	00.00
G	2	6	15	24/25	13.34
K	2	6	15	18/25	26.67
K	2	6	15	20/25	19.11
S	2	6	15	22/25	68.00
S	2	6	15	24/25	100.00
M	3	10	120	15/25	98.37
M	3	10	120	17/25	98.23
L	1	6	15	18/25	44.44
L	1	6	15	20/25	55.56

Table 3: neighbouring slices above and below the most active slice

voxel A	**-0.132**	**0.039**	**-0.105**	**-0.204**	**-0.093**
voxel B	**0.139**	**0.005**	**-0.134**	**0.012**	**-0.066**
A	-0.132	0.039	-0.105	-0.204	-0.093 missing
B	0.139	0.005	-0.134	0.012	-0.066 missing
A	-0.132	0.039	-0.105	-0.093	-0.204 missing
B	0.139	0.005	-0.134	-0.066	0.012 missing
A	-0.132	0.039	-0.204	-0.093	-0.105 missing
B	0.139	0.005	-0.012	-0.066	-0.134 missing
A	-0.132	-0.105	-0.204	-0.093	0.039 missing
B	0.139	-0.134	0.012	-0.066	0.005 missing
A	0.039	-0.105	-0.204	-0.093	-0.132 missing
B	0.005	-0.134	0.012	-0.066	0.139 missing

Table 1: Example for admissible voxel-combinations for sample size 4 in case of a total of 5 measured runs (as given in the first two lines). We considered all admissible combinations for all samplesizes within a slice.

WE 248

How frequently do we sample inhomogeneous group of subjects in fMRI studies ?

Sébastien Mériaux[1,2], Ferath Kherif[3], Alexis Roche[1,2], Matthew Brett[3], Line Garnero[2,4], Jean-Baptiste Poline[1,2]

[1]CEA/DSV/DRM, Service Hospitalier Frédéric Joliot, Orsay, France, [2]IFR 49, Institut d'Imagerie Neurofonctionnelle, Paris, France, [3]MRC Cognition and Brain Unit, Cambridge, United Kingdom, [4]LENA, Neurosciences cognitives et Imagerie cérébrale, Hôpital de la Salpêtrière, Paris, France

Introduction

Most functional brain imaging experiments consist in the acquisition and analysis of data collected from different subjects. Typically, random effects analyses are conducted to generalize the results to the population of interest. Although taking into account the inter-subject variability, this operation relies on the relevance of averaging individuals that is only sensible when the spatial or temporal mean is a good representation of the subjects group. However, the homogeneity assumption can be violated in several cases. The purpose of this work is to evaluate how often atypical data greatly influence group analysis results (ie change their interpretation significantly). We have therefore developed a new method to detect those situations and assess data homogeneity [1]. This method was tested on eleven fMRI datasets from several laboratories (see **Acknowledgments**).

Materials and Methods

The data homogeneity testing method is implemented as a SPM99 toolbox ("DISTANCE" toolbox freely available on *www.madic.org*). For a given contrast of interest, inter-subject distances are computed in space (anatomical) or in time (functional) domains. These distances allow to position each subject with respect to each other and these positions can be visualized using a Multi Dimensional Scaling (*MDS*) procedure. A specific test (*Cook test*) is used to detect atypical subjects.

The method was tested on 11 fMRI datasets, analyzed with SPM99 and corresponding to various cognitive paradigms. In all cases, we looked for outliers or specific clustering between subjects for one or several main contrasts of interest defined in the experiment. Whenever subjects could apriori be partitioned in several groups (2 datasets concerned), we also tested the ability of the method to retrieve this partition.

Results

For four datasets (one out of 3), we detected outliers in the original group of subjects for the contrast of interest. Further investigations revealed some factors which could explain these outliers : atypical behaviorial responses, high subject movement, one session with atypical temporal responses, and so forth.

We repeated the random effects analyses with "homogeneous" sub-groups of subjects (outlier removed) and found in all cases significant differences with the original analysis and in two cases much more sensitive results with the "homogeneous" sub-group. Moreover, for one of the datasets with a known partition of subjects, the method was able to retrieve the expected clustering.

Conclusion

The results show that the method is useful in detecting outlying subjects and its software implementation has been found to be fast and easy to use. This routine assessment may have important consequences on the interpretation of the group data results. It should provide important information while establishing a functional imaging database. Future works are directed towards the development of robust statistics able to cope with the subject inhomogeneity.

Acknowledgments

The authors gratefully acknowledge their colleagues who kindly provided datasets. Special thanks to Russel Poldrack at UCLA Psychology Department (Los Angeles, USA), Sylvain Takerkart and James Rilling at Princeton University (Princeton, USA), and members of SHFJ (Orsay, France).

Reference

[1] Kherif et al., submitted to Neuroimage (2003)

WE 249
MIDAS - A multi-site fMRI simulator consortium

The MIDAS Consortium , Fernando Boada[1], Louis Collins[2], Ivana Drobnjak[3], William Eddy[3], Alan Evans[2], Mark Griffin[2], Mark Jenkinson[3], Douglas Noll[1], Bruce Pike[2], Haiwen Shi[1], Deepa Shroff[1], V. Andrew Stenger[1], Keith Worsley[2]
[1]University of Pittsburgh, [2]Montreal Neurological Institute, McGill University, [3]FMRIB Centre, University of Oxford

Many techniques have been proposed for the acquisition and analysis of fMRI data. Significantly fewer attempts have been made to validate and characterize these tools. Computer simulations have become a widely accepted evaluation method, however there are difficulties associated with simulations, particularly where the signal and noise components of fMRI data have not been fully characterized.

A consortium has recently been formed from research groups at the Montreal Neurological Institute (MNI), the University of Oxford (FMRIB Centre) and the University of Pittsburgh with complementary expertise in fMRI modelling to create a comprehensive fMRI simulation environment named MIDAS (MR Imaging Data Acquisition Simulator, www.midas-online.org). The simulation will incorporate the major sources of variation present in an fMRI acquisition: acquisition type (e.g. EPI, spiral-EPI, anatomical spin-echo), susceptibility artifacts, RF inhomogeneities, physiological noise, random noise, motion, and activation. This simulator will be freely available to the fMRI community to aid researchers in validating data processing streams and to provide insight into MRI physics.

Previously, the University of Pittsburgh has been developing an open source C++ GUI-based fMRI Acquisition Informatics Tool (fAIT) for the simulation of fMRI data acquisitions (www.mrctr.upmc.edu/~andy/fAIT.html) (Stenger et al, HBM2003). The FMRIB Centre has a strong background in the development and validation of analysis tools through the FSL package (www.fmrib.ox.ac.uk/fsl) and its application in motion and B0-artifact correction (e.g. MCFLIRT and FUGUE). The MNI has a long-standing interest in the physiological origins of neuronal activation seen in MRI and PET, as well as previous experience in anatomical MRI simulation - BrainWeb (www.bic.mni.mcgill.ca/brainweb) (Kwan, IEEE Trans. Med. Imag., 1999) - which has been widely used for evaluating post-processing algorithms (approximately 20 groups and 39 publications).

Figure 1 shows, schematically, how the areas of expertise are combined within in the MIDAS simulation environment. This involves a coordinated effort between our three centers in signal generation using the Bloch equations, simulation of different pulse sequences, and image reconstruction. In addition, investigation of cardiac and respiratory sources of physiological noise (MNI - see Griffin et al, HBM2004), and quantitative simulation of B0-motion artifacts in EPI, (FMRIB - see Drobnjak and Jenkinson, HBM2004) have been undertaken.

Figure 2 shows an example of data simulated using MIDAS. A digital phantom and co-registered CT scan (MNI - Collins, IEEE Trans. Med. Imag., 1998) are processed using a perturbation-based B0 calculation module (FMRIB - see Jenkinson et al, ISMRM2002). The B0 data and digital phantom are then processed in a fast imaging module (Pittsburgh) which generates the EPI MR signal by numerically solving the Bloch equations (Stenger et al, HBM2003, poster 951). The result is a fully simulated EPI fMRI image, where the susceptibility artifact in the frontal region is clearly visible.

In summary, we present a unified fMRI simulation environment for fMRI research which integrates existing efforts and establishes a coherent simulation platform for the broader fMRI research community.

Project Funding
MNI - NIfTI (1 R01 MH067172-01)
Oxford - UK EPSRC (MIAS-IRC)
Pittsburgh - NIfTI (1 R01 MH067166-01)

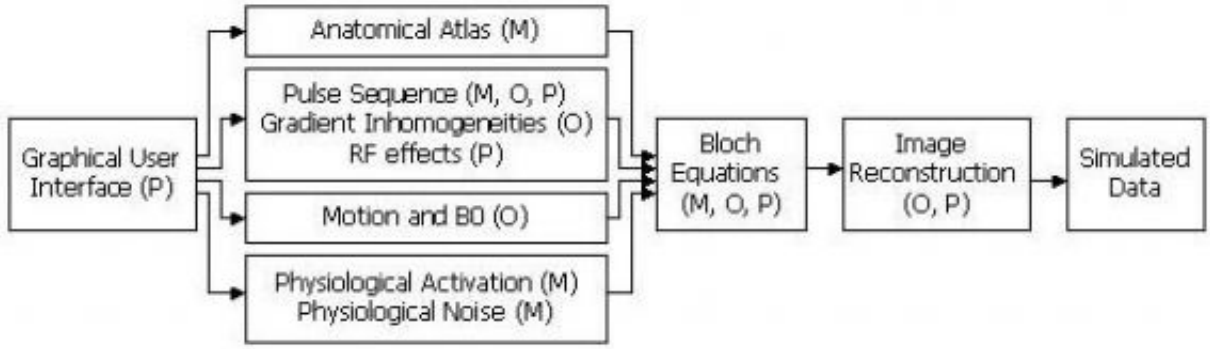

Figure 1. The major components of the MIDAS fMRI simulator as developed bythe Montreal Neurological Institute (M), the University of Oxford (O), andthe University of Pittsburgh (P)

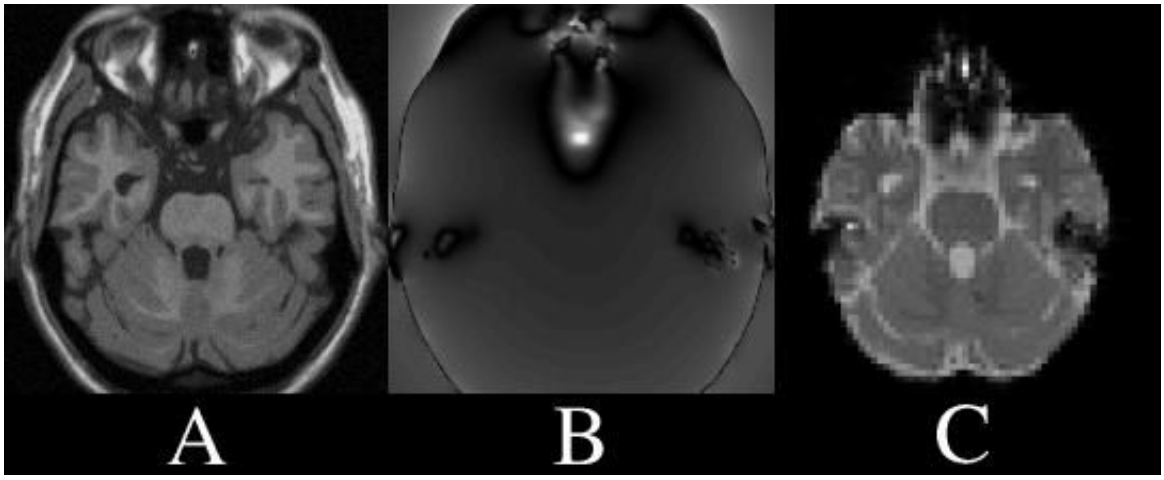

Figure 2. (a) A simulated T1-weighted image using the MNI's anatomical atlas, (b) theB0 field (generated by the University of Oxford), and (c) the resultingdistorted EPI image (simulated by the University of Pittsburgh).

WE 250
Estimation of hemodynamic response corresponding to spontaneous and successive changes in EEG rhythm

Masaya Misaki , Satoru Miyauchi , Yasuto Tanaka , Takahide Fukunaga , Shigeyuki Kan
Brain Information Group, Kansai Advanced Research Center, Communications Research Laboratory

In this study, we applied a new analysis method [1] to estimate the hemodynamic response corresponding to the spontaneous and successive changes of theta band EEG power. Recent studies use simultaneous EEG-correlated fMRI data for investigating spontaneous EEG phenomena such as the alpha rhythm, sleep spindles and slow waves during NREM sleep [2]. Although most studies use the canonical hemodynamic response function to regress the blood oxygen level dependent (BOLD) signal, this has not yet been validated, because the relationship between spontaneous and successive changes in EEG power and the BOLD signal is unknown. To estimate that relationship, we used a nonlinear regression analysis by a three-layered back-propagation neural network. This class of neural networks can fit any relations between input (EEG power) and output (BOLD) signals, so we can directly regress the BOLD signals with EEG power.
In the experiment, the subject slept for about one hour in an MRI scanner. We simultaneously recorded the BOLD signals (T2*, EPI, TR: 4 sec, TE: 55.24 ms, Matrix: 64 x 64 x 25, Voxel size: 4 x 4 x 5 mm, 999 scans; Siemens Vision, Erlangen, Germany) with the EEG signals using the BrainAmp MR (Brainproducts, Munich, Germany). Distortions caused by artifacts were removed from the EEG signals. The theta band power (3 - 7.9 Hz) in each TR was used as the regressor.
The analysis consisted of two stages: first, the regression analysis was done (one time point of the BOLD signal was regressed by 10 time points of theta power before the sample time of the BOLD signal (from 0 - -36 sec) using the neural network); next an estimation of the hemodynamic response was made at the voxels where the regression was highly significant ($F(10,979) > 60$). In this estimation, we used a neural network that was already fitted to the relation between theta power and BOLD signals. An input time-course representing the change in theta power was made, and part of this time-course was input to the network to get an output (Fig. 1). By moving the time window of the input sequence, we obtained an output sequence, which represented the hemodynamic response corresponding to the input sequence.
When we used the impulse time-course as the input, we found not only canonical shapes but also non-canonical shapes (delayed or negative) of the hemodynamic responses (Fig. 2). These results validated past studies that used the convolution of the canonical hemodynamic response and the time-course of EEG power. The finding of non-canonical hemodynamic responses, however, suggests that previous studies had overlooked some of the brain activations correlated with the EEG power in a non-canonical way.
It has been difficult estimating the hemodynamic response for the spontaneously and incessantly changing EEG signal. This analysis method enabled us to estimate such hemodynamic responses and will help us to understand the brain activations on which the spontaneous EEG rhythm is based.

1. Misaki and Miyauchi (2003), NeuroImage 19, S46.
2. Miyauchi et al. (2003), NeuroImage 19, S25.

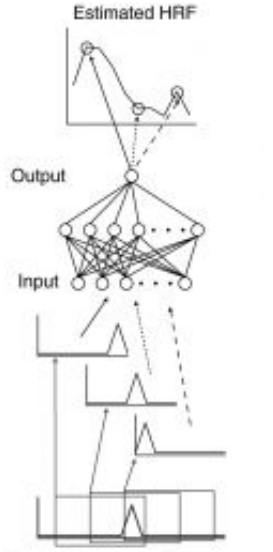
Estimated HRF
Output
Input
Input time-course of theta power

Fig. 1

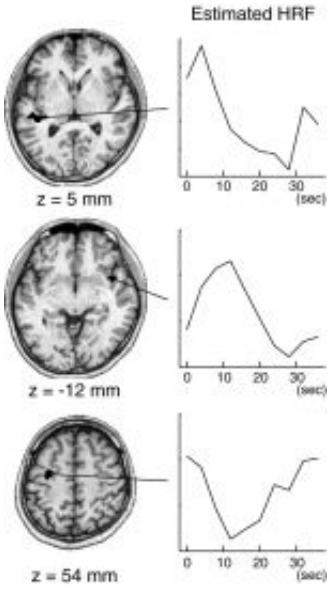
Estimated HRF
z = 5 mm
z = -12 mm
z = 54 mm
0
10
20
30
(sec)

Fig. 2

WE 251

How nonlinear is the hemodyanmic response?: analysis of EEG/fMRI with semiparametric autoregression

Fumikazu Miwakeichi[1], Pedro A. Valdes-Sosa[2], Hiroaki Mizuhara[1], Li-Qun Wang[3], Koichiro Kobayashi[4], Yoko Yamaguchi[1]

[1]RIKEN, Brain Science Institute, Japan, [2]Cuban Neuroscience Center, Cuba, [3]Tokyo Denki University, Japan, [4]Iwate University, Japan

Concurrent EEG/fRMI offers the potential for achieving information about brain function with simultaneous high spatial and temporal resolution. One approach takes advantage of the temporal fluctuations of the EEG frequency spectrum by using its envelope as a reference signal in order to identify that portion of the BOLD signal related to oscillatory networks (Goldman et al.(2002); Laufs et al.(2003)). We have recently shown that multi-linear statistical methods allow a fruitful exploration of these EEG/fMRI relations. Miwakeichi et al.(2003) showed that Parallel Factor Analysis (PARAFAC) can perform a time/frequency/spatial (T/F/S) atomic decomposition that identifies fundamental modes of oscillatory EEG activity. Two atoms were identified as very common over subjects, alpha and theta, each with corresponding T/F/S signatures. Martinez et al.(2003) then went on to relate these modes to spatial components of BOLD signal changes. A limitation of all these studies is the assumption of a linear relation of the EEG with a standard hemodynamic response function (HRF) modeled as a sum of gamma functions. This study will examine these assumptions.

The EEG of a subject was obtained for every 30 seconds during two conditions: resting and mental arithmetic task; and then transformed into a three dimensional T/F/S data set by a Morlet wavelet transform. The wavelet spectrum was averaged every 5 second to match to samples of the concurrently recorded fMRI. Alpha and theta atoms were in common with both rest/arithmetic (Fig.1(1)) showed the previously found respectively occipital and frontal spatial signatures (Fig.1(2)), temporal signatures being shown in Fig.1(3). At each voxel the BOLD signal at time t, B_t was modeled by means of a semi-parametric auto-regression (Speckman(1988); Härdle(1990)):

$$B_t = \beta_0 + \Sigma_{\{i;1,\ldots,M\}} \beta_i x_{t-i} + f(x_{t-1},\ldots,x_{t-N}) + e_t,$$

where, e_t is the prediction error, x_t is the temporal signature of each PARAFAC atom, $\Sigma_{\{i;1,\ldots,M\}} \beta_i x_{t-i}$ is a an autoregressive component, and $f(x_{t-1},\ldots,x_{t-N})$ is the nonparametric nonlinear autoregressive component. Model selection was preformed by means of the ordinary cross-validation criterion. It was found that in all cases the nonlinear model component increased model adequacy by at least 21%. Correlation maps obtained for the linear and nonlinear models showed strikingly different patterns (Fig.2), indicating the importance of adequately modeling the HRF in EEG/fMRI studies.

References

Goldman,R. et al.(2002), *Simultaneous EEG and fMRI of the alpha rhythm*, 13-18, PP2487-92, NeuroReport

Härdle,W.(1990), *Econometric Society Monographys 19; Applied nonparametric regression*, Cambridge University Press, New York

Laufs,H. et al.(2003), *EEG-correlated fMRI of human alpha activity*, 19,pp1463-76, NeuroImage

Martinez,E. et al.(2003), *Concurrent EEG/fMRI Analysis by Multi-way Partial Least Squares*,submitted to NeuroImage

Miwakeichi,F. et al.(2003), *Decomposing EEG data into Space-Time-Frequency Components using Parallel Factor Analysis*, submitted to NeuroImage

Speckman,P.(1988), *Kernel Smoothing in Partical Linear Models*, 50-3,pp 413-36, Journal of the Royal Statistical Society B

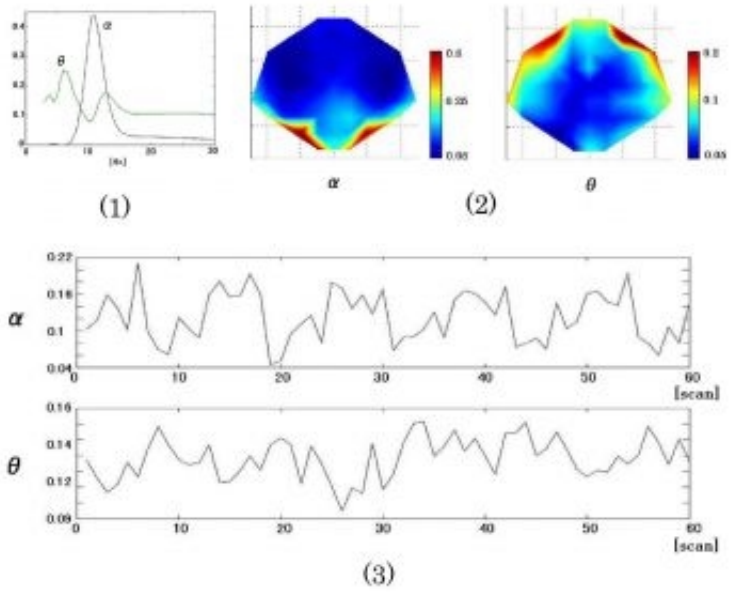

Figure 1, (1) Frequency, (2) spatial and (3) temporal signatures of alpha and theta atoms

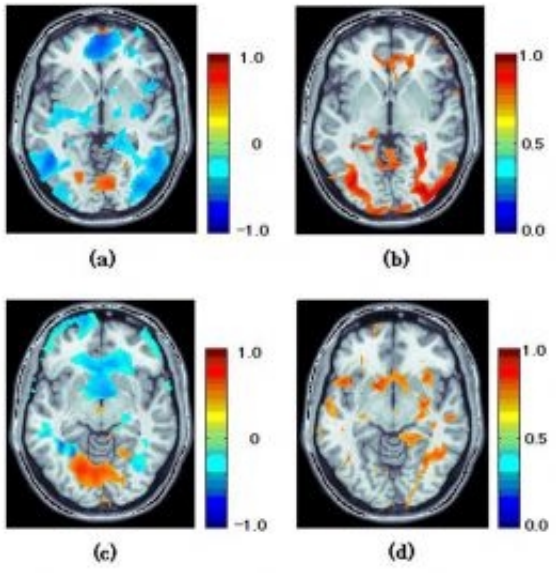

Figure 2, Linear (left) and non-linear (right) correlation maps of the to alpha(a,b), theta a (c,d) atoms.

WE 252
Training Classifiers to Detect Cognitive States

Janaina Mourao-Miranda[1], Arun LW Bokde[2], Harald Hampel[2], Martin Stetter[1]
[1]Neural Computation - Siemens Corporate Technology - Munich - Germany, [2]Department of Psychiatry - Ludwig Maximilians Universität - Munich - Germany

We used machine learning algorithms to train classifiers to detect differences in brain activity between two cognitive states. One previous work demonstrated the feasibility of training classifiers to distinguish a variety of cognitive states, based on fMRI observations (Mitchell et al., 2003). In this study regions of interest were chosen based in some feature abstraction method and afterwards the signals of these regions were used as input to a classifier. The novelty of the present work is to use the time sequences of whole brain volumes as a high dimensional input vector to a classifier. The brain regions at which the two cognitive states differ most result as an outcome from the classification.

We used fMRI data from 5 subjects with average age of 64.7 (6.2) years. The task was a face perception matching task and the control task was to press the response button when 2 abstract images appeared. It was a block design with 3 active blocks and 4 control blocks. The preprocessing stages applied were time shift correction, motion correction, and normalization to standard space (MNI template). A regression model was applied to the time series of each voxel to remove the base line and the low frequency components.

For creating a benchmark we used the Fisher Linear Discriminant (FLD) classifier. The FLD classifies by linearly projecting the training set on the axis that is defined by the difference between the center of mass for both classes (tasks). The procedure consists of first finding a difference between the mean feature vectors (input vector) for each class. The second step is to project individual volume scans onto the difference vector. The threshold value representing the limit between the classes is chosen according to $\mathbf{thr} = (\mathbf{m}_2 + \mathbf{m}_1 / 2)$ (where $\mathbf{m}_i$ is the mean feature vector for the class i), in order to evaluate a decision function. The results obtained are shown in the Table 1. Figure 1 shows the difference vector between the two classes.

We also used the Support Vector Machine (SVM) classifier. The advantage of this method is the selection of the examples that are most informative for the classification (the support vectors), and the weights that are put on the individual data in the decision function, this procedure decreases the influence of outlier examples. The results obtained are shown in Table 1.

The results summarized in Table 1 show that both classifiers (FLD and SVM) can find the cross-subjects regularities enabling them to distinguish between the face perception matching task and the control task.

Mitchell, T., Hutchinson, R., Niculescu, R., Pereira, F., Wang, X., Just, M. and Newman, S. "Learning to Decode Cognitive States from Brain Images", Machine Learning, 2003 (submitted).

Results for the leave-one-subject-out cross validation test

Classifier	Error rate	Sensitivity	Specificity
FLD	0.29	0.73	0.69
SVM	0.19	0.83	0.80

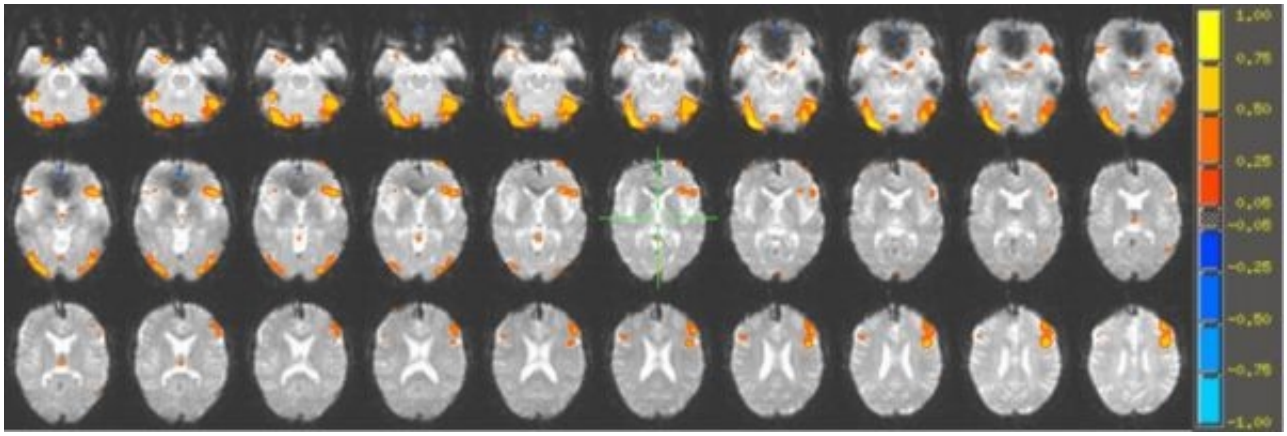

Difference vector between the mean feature vectors for each class (face perception matching task vs. control task).

WE 253

Robust and local nonsphericity modeling for second level PET and fMRI analysis

Jeanette Mumford , Wen-Lin Luo , Thomas E. Nichols
Department of Biostatistics, University of Michigan

Introduction

Second level analysis in functional neuroimaging is complicated by non-sphericity. Non-sphericity is caused by heterogeneous variance and correlated responses within subject. Friston et al. (2002) proposed an Empirical Bayesian approach, where a global correlation estimate is used to improve the efficiency of the voxel-level estimates. While this yields a stable estimate of the dependence between the experimental effects, it cannot account for spatial heterogeneity in this dependence.

We propose the use of Generalized Estimating Equation (GEE) methods for second level data in functional neuroimaging. This strategy allows for use of two different correlation matrices, one for estimation of β's, and one for computation of standard errors. The first only affects the efficiency of the β^*'s, while the second allows accurate estimation of covariance. Our method provides statistically consistent standard errors, where as Friston et al.'s inferences will be consistent only when dependence is homogeneous across the brain. We demonstrate the performance of our method with simulations and a real-data analysis.

Methods

At each voxel we fit a general linear model for each subject's contrast images; for subject i, $Y_i = X\beta + \varepsilon_i$, where Y_i is the observed response, X is the design matrix, and β are the fixed parameters to be estimated. The error ε_i is assumed to be N(0,V) distributed, where V is the true covariance matrix. The key to our approach is the use of a generalized least-squares estimator of β, defined as $\beta^* = (X'WX)^{-1}X'WY$, in conjunction with sandwich estimator of variance matrix, $Var(\beta^*) = \{(X'WX)^{-1}X'W\}V^*\{WX(X'WX)^{-1}\}$ where W^{-1} is the working correlation matrix abd V^* is a consistent estimator for V.

We choose an unstructured correlation for W^{-1}, which is pooled over either all voxels or only activated voxels, those with F P-value < 0.001. We estimate an unstructured V^* at each voxel. This guarantees that our estimated standard errors are consistent regardless of the true covariance structure V at each voxel.

Results

We simulated a second level analysis with 3 conditions, 14 subjects and 10,000 voxels. We considered two types of nonsphericity among the 3 conditions, compound symmetric (homogeneous variance, equicorrelation) and heteroscadastic (heterogeneous variance, independence). The true covariance parameters varied randomly over space. Table 1 shows the results, showing our method has same efficiency of SPM (not shown), but has comparable or reduced bias in the estimated variance.

We analyzed a second level fMRI dataset consisting of three types of response inhibition: stimulus response compatibility (SRC), a go-no-go (GNG) task and a flanker task (Flank). Figure 1 shows the results for the contrast comparing SRC to Flanker; it shows that contrast variance varies appreciably between areas.

Discussion

We have proposed the use of GEE methods for second level fMRI analysis. Our method provides statistically consistent standard errors even when dependence among conditions is spatially heterogeneous. With simulation and real data, we have shown that it is more accurate than assuming a globally pooled dependence structure. These results suggest that local *co*variance estimation is essential as local variance estimation.

Table 1. Simulation results: Spatially heterogeneous compound symmetric and heteroscadastic nonsphericity

	GEE		SPM2		OLS
Method	Global	Activated	Global	Activated	
Compound Symmetric Variance					
Estimated Variance	0.0493	0.0493	0.0544	0.0549	0.1068
Bias of Variance (%)	-7.17	-7.17	10.51	11.82	131.76
Emp. Variance of Variance	0.0007	0.0007	0.0002	0.0002	0.0009
Heteroscadastic Variance					
Estimated Variance	0.0846	0.0846	0.0836	0.0804	0.0538
Bias of Variance (%)	-7.10	-7.10	-5.11	-8.88	-40.38
Emp. Variance of Variance	0.0015	0.0015	0.0005	0.0005	0.0004

Global: estimation of correlation is pooled over the whole brain.
Activated: estimation of correlation is pooled over activated voxels only.

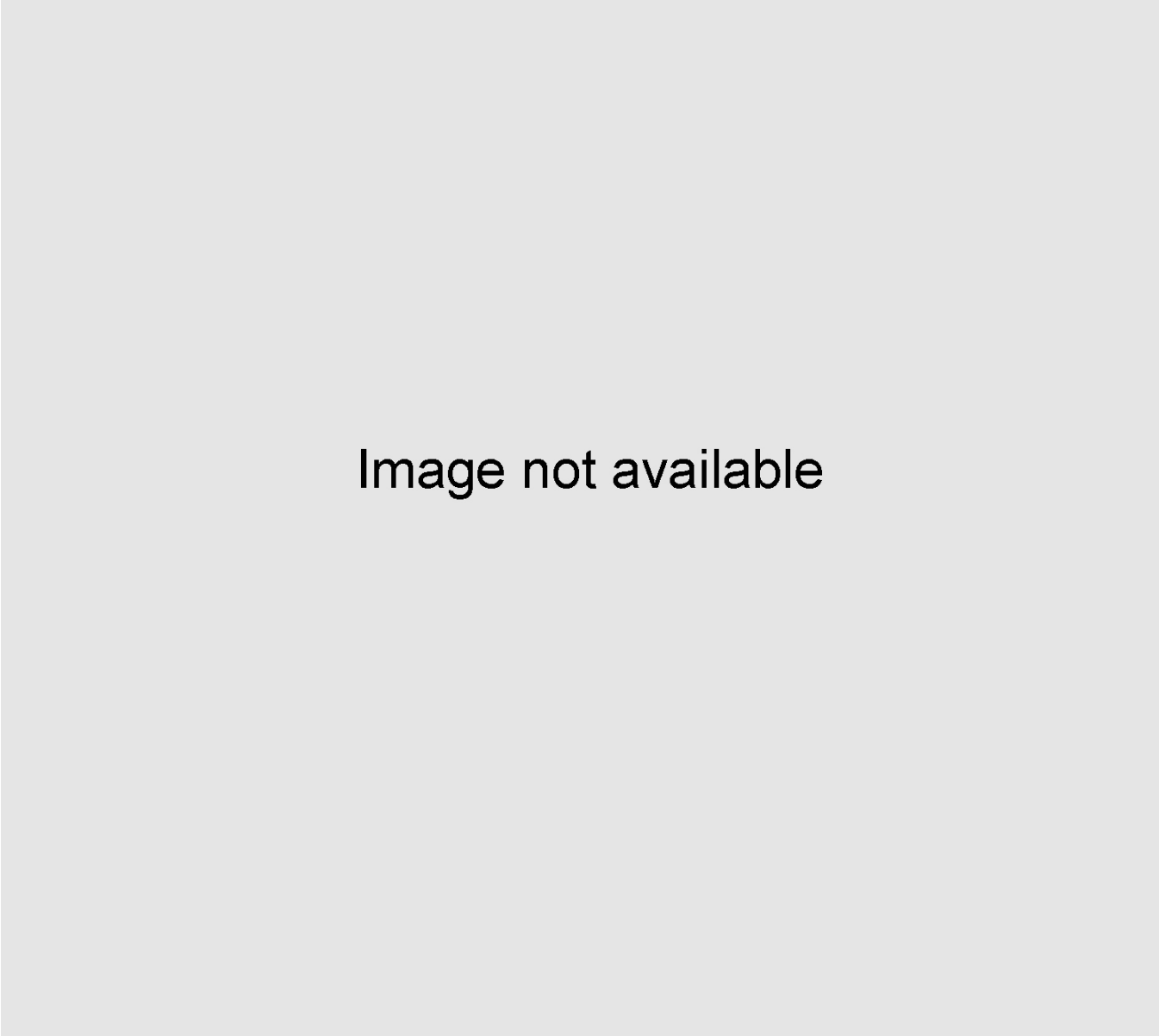
Image not available

WE 254
Exploratory Analysis of fMRI Data Reveals Modulation of Auditory Perception During a Visuo-Motor Task

R. Mutihac[1,2], J.G.B. Schafer[3], J.S. Gillen[1,2], S.H. Mostofsky[3], A.C. Boyce[3], M. Goldberg[3], M.B. Denckla[3], S.M. Courtney[1,4], M. Kraut[2], V.D. Calhoun[5,6], T. Adali[7], J.J. Pekar[1,2]

[1]F.M. Kirby Research Center, Kennedy Krieger Institute, [2]Department of Radiology, Johns Hopkins University, [3]Department of Developmental Cognitive Neurology, Kennedy Krieger Institute, [4]Department of Psychological and Brain Sciences, Johns Hopkins University, [5]Institute of Living, Hartford Hospital, [6]Department of Psychiatry, Yale University, [7]Department of EECS, University of Maryland, Baltimore County

INTRODUCTION: Exploratory analysis approaches fMRI data without specific prior hypotheses, and aims to discover features reporting upon the organization of brain activity. Here we use an exploratory approach to reveal that fMRI data from a visuo-motor Go/No-Go task report on attentional modulation of auditory perception. Recently we used novel Go/No-Go tasks to study response inhibition using fMRI (1). In the simplest task, participants saw a spaceship every 1.5 seconds; most (84%) are green, which elicit a response (button-press to rescue the spaceship). Participants were told not to so respond to the infrequent red spaceships (which contain only garbage); inhibition of the pre-potent response is required. Each 450 mission includes four brief rest periods. Analysis using the General Linear Model (GLM), modeling successful responses as well as errors, revealed activity in contralateral sensorimotor cortex, bilateral cerebellum, and supplementary motor area (SMA) for Go, and in pre-SMA for No-Go (1)

METHODS: Data from 10 subjects (total of 12 "missions") were selected at random for exploratory analysis. Data from each "mission" were entered into a spatial Independent Component Analysis (ICA) estimation, which uses higher-order statistics to express the fMRI data as a sum of temporally-modulated spatially-independent sources (2). Following reduction to 24 principle components, 24 independent components were estimated and then ranked by temporal correlation with the Go regressor. In this communication, we discuss only one component.

RESULTS: In 9 of 10 subjects (10 of 12 "missions"), spatial ICA yielded a component primarily localized in auditory cortex, with a time course displaying transient deactivation upon initiation of the paradigm, and transient activation during each rest period.

DISCUSSION: This component is consistent with attentional modulation of auditory perception (3), namely a subjective experience that the scanners acoustic noise seems louder when the participant is not concentrating on task performance. This is an example of a brain activation which, because it did not fit an *a priori* hypothesis about changes in activity during the task paradigm, was therefore omitted from standard (univariate inferential) analysis. This components time course is obviously related to the timing of paradigm events, and therefore is, *post hoc*, recognizable as being related to the paradigm.

This finding demonstrates that exploratory approaches (such as ICA) can reveal interesting features reporting on brain activations not anticipated by the investigator. These previously unanticipated activations can then be incorporated into improved temporal models for inferential analysis.

REFERENCES

1. Mostofsky, et al., Cogn. Brain Res. 17:419 (2003).
2. McKeown, et al., Proc. Natl. Acad. Sci. USA 95:803 (1998); Calhoun, et al., Hum. Brain Mapp. 13:43 (2001).
3. Woodruff, et al., NeuroReport 7:1909 (1996).

WE 255
Removing ballistocardiogram artifact from EEG data recorded simultaneously with fMRI data by independent component analysis

Wakako Nakamura[1], Kimitaka Anami[2], Takeyuki Mori[2], Osamu Saitoh[2], Andrzej Cichocki[1], Shun-ichi Amari[3]

[1]Lab. for Advanced Brain Signal Processing, Brain Science Institute, RIKEN, [2]National Center Hospital for Mental, Nervous, and Muscular Disorders, NCNP, [3]Lab. for Mathematical Neuroscience, Brain Science Institute, RIKEN

Introduction:
EEG data recorded simultaneously with fMRI data suffer from two specific artifacts and one of them is called Ballistocardiogram(BCG). Average subtraction has been used for removing it[1]. However, we suppose that this method is not appropriate to data with short or irregular intervals of cardiac pulses. In this study, we apply independent component analysis(ICA) to removing BCG. ICA is a statistical method to separate multi-dimensional data into statistically independent components.
Methods:
We recorded EEG data from 9 scalp electrodes, F3, F4, C3, C4, Pz, O1, O2, A1, A2, referenced to Cz. After the removal of BCG, Cz reference was modified to linked mastoid (A1 + A2). We recorded EEG data in the MR scanner, with and without MR imaging. We also recorded EEG data of the same subject under the same condition but outside the MR scanner for comparison. To the data recorded with MR imaging, we applied the SSS method[2] for removing imaging artifacts. We tested four algorithms of ICA, using or not using time structures of data, extracting components one by one or separating data into several components at once. We used distributed softwares for two algorithms [3,4].
Typically, three of components obtained by ICA include BCG. A simple way to retrieve EEG is removing these three components and projecting other components back to the data space. However, often these three components were mixtures of BCG and EEG. Therefore, as a post-processing, we applied high-pass filter to these three components and removed only lower frequency part. Because BCG is mainly caused by physical movements, it does not include high frequency signals.
We proposed two indices for evaluating removal of artifacts. One is the difference of power spectrum between retrieved EEG data and that of EEG data recorded outside the MR scanner. The other index is the value of the auto correlation function of retrieved EEG around the interval of cardiac pulses.
Results:
With the post-processing of high-pass-filtering that we proposed, ICA could remove BCG as good as conventional average subtraction. The post-processing always improved the indices. Difference among abilities of algorithms measured by proposed indices was small.
Discussion:
We showed that with appropriate post-processing, ICA could remove BCG as good as average subtraction. We suppose that the proposed method works better when intervals between cardiac pulses are short or irregular. We also formulated how head movements cause BCG and showed why ICA is effective.
References
[1] Allen, P. J., et al. (1998) Neuroimage, 8, 229-239.
[2] Anami, K., et al. (2003) Neuroimage, 19, 281-295.
[3] www.sccn.ucsd.edu/eeglab/index.html
[4] www.bsp.brain.riken.jp/ICALAB/

WE 256
Solving the multiple comparison problem in fMRI using a method based on bootstrapping the Order Statistics of the resting state data

Rajesh R Nandy , Dietmar Cordes
University of Washington, Department of Radiology

Introduction

The multiple comparison problem is relevant when we have a family of hypotheses $\{H_\omega : \omega \in \Omega\}$ at voxel ω. In fMRI, Ω stands for the collection of all intracerebral voxels. The omnibus null hypothesis H_Ω is the hypothesis of no activation anywhere in the brain. If we test every individual H_ω at the same level, the omnibus hypothesis is really tested at a higher value than originally assigned. This implies that the p-value for each individual test needs to be adjusted to test the omnibus hypothesis. Here we propose a versatile method based on bootstrap techniques applied to the order statistics of the resting state data to generate resamples of the order statistics and then calculate the distribution of the maximum statistic to account for multiple comparison.

Methods

For any threshold u for the test statistic Y_ω at voxel ω, we want to calculate the probability of incorrectly rejecting the omnibus hypothesis H_Ω (rather than the individual hypotheses H_ω). It can be shown that

$$P[H_\Omega \text{ is rejected incorrectly}] = P[\max Y_\omega > u].$$

Let $\{Y^1,..,Y^k\}$ denote the k largest order statistics. It is preferable to make a transformation of the test statistic, if the parametric distribution of the test statistic is known. We calculate the negative logarithm of the p-value corresponding to the test statistic to obtain our transformed variable. We can assume that Y is already transformed. Define $\{d_i = i(Y^i - Y^{i+1}), i=1,..,k\}$ as normalized sample spacings for the k largest order statistics. If the observed samples at the voxels are i.i.d., then so are the normalized sample spacings. In the present context, the samples are not independent, but we make that assumption anyway. This method can be refined to address the dependence issue, but will not be discussed here. The k largest order statistics can be expressed as follows.

$$Y^j = Y^{k+1} + \Sigma^k{}_{i=j}\ i^{-1}\ d_i,\ j=1,..,k.$$

We can use bootstrap to obtain resamples of normalized spacings $\{d^*{}_i, i=1,..,k\}$ which can be used to generate resamples $\{Y^{*1},..,Y^{*k}\}$ of the k largest order statistics from which the distribution of $\{\max Y_\omega\}$ can be obtained empirically.

Results

We consider the activation map obtained from a periodic phoneme matching task using a convolved boxcar function. In Figure 1, we have plotted the estimated density function for $\{\max Y_\omega\}$. In Figure 2, we have plotted activation maps corresponding to an adjusted p-value of 0.05 using Bonferroni correction (left) and the proposed method (right), respectively, for one slice. The chosen value for k is 30 for the bootstrap. The numbers of total voxels detected to be active in the whole brain (14000 voxels) are 297 and 434, respectively. This indicates that the proposed method is a significant improvement over Bonferroni correction. It is also known that Gaussian random field approach is not a vast improvement over Bonferroni due to the various assumptions made on the smoothness of the data. Hence, this method may prove to be an improvement over all existing methods to address the multiple comparison problem.

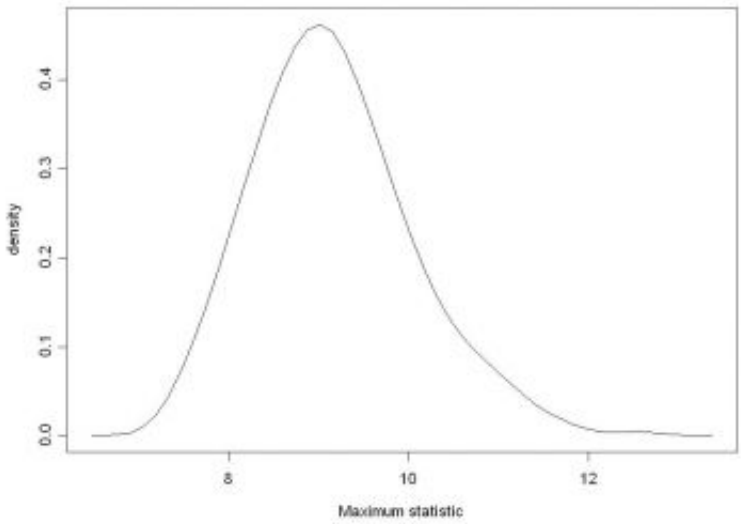

Figure 1. Distribution of the maximum statistic.

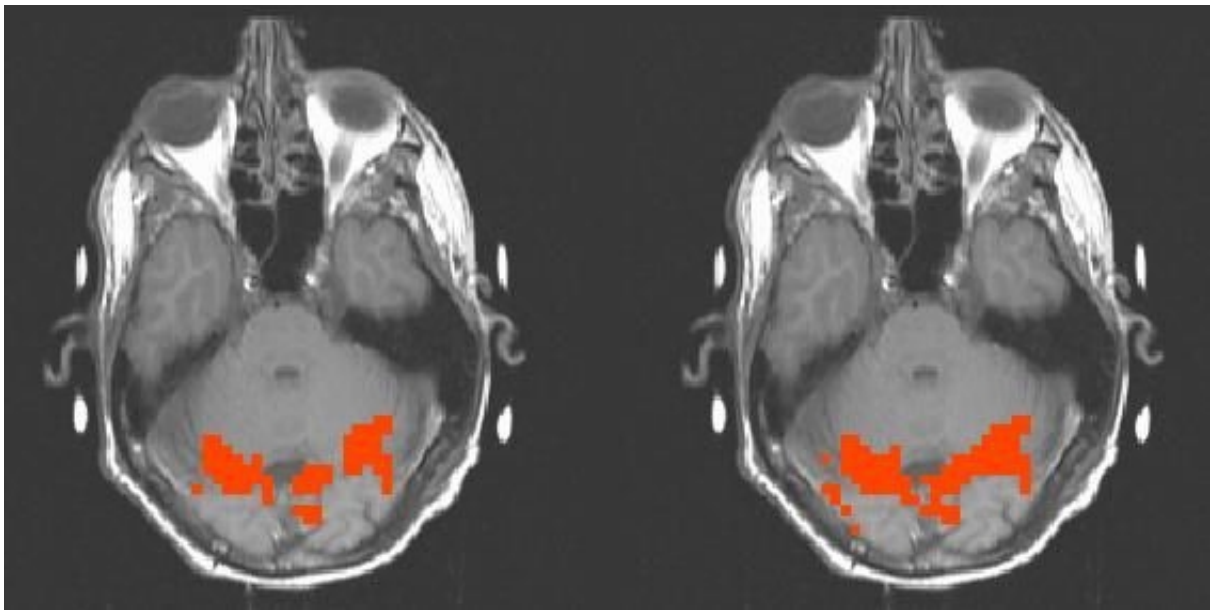

Figure 2. Adjusted activation maps using Bonferroni correction (left) and the maximum statistic (right).

WE 257

Analysis of the spatial specificity of canonical correlation analysis in fMRI

Rajesh R Nandy , Dietmar Cordes
University of Washington, Department of Radiology

Introduction

A popular multivariate method in fMRI is canonical correlation analysis (CCA), where the joint timecourses of a group of neighboring voxels are investigated. It is customary to assign the measure of activation to the center voxel. But this is prone to false activations as activations tend to bleed to the neighboring voxels. To rectify this deficiency an adaptive method has been proposed recently [1]. Here, we apply the conventional CCA and the adaptive method to pseudo-real and real datasets with certain features which are expected to be detrimental to the conventional assignment scheme and compare the two methods.

Methods

Suppose $X^{(1)}$ and $X^{(2)}$ (known as canonical variates) are two random vectors with n_1 and n_2 components respectively. In CCA, we look for the linear combinations $Y=\alpha^T X^{(1)}$ and $Z=\beta^T X^{(2)}$ so that their correlation coefficient (ρ) is maximum. In an fMRI setup, the vector $X^{(1)}$ stands for the observed signals at neighboring voxels and $X^{(2)}$ stands for the basis functions of a finite dimensional signal subspace for the paradigm. A conventional choice is to assign the activation measure to the center voxel, which is not appropriate. These considerations lead to a recently proposed adaptive scheme, where p-values are assigned as measures of activation dynamically to the voxels so that the values get updated periodically [2].

Here we use pseudo-real data to investigate the effectiveness of this new assignment scheme. We first identify a highly active 9×6 region in a slice of the brain, while the subject performs a periodic phoneme-matching task. We then choose significantly smaller subsets of this region with different shapes. For each voxel in such a subset, we replace the active state timecourse with the corresponding resting state timecourse acquired during a resting state scan. In the results section, we will observe if CCA indeed incorrectly detects these voxels as active and also if the adaptive scheme can successfully rectify the problem.

Results

In Figure 1, we have provided a map of relative CNR for the chosen 9×6 region with high activation (left) and the cross-shaped subset (right), where we replace the active state timecourses with the corresponding resting state timecourses. In Figure 2, we provide the activation map for the modified data using conventional CCA (left) and the adaptive scheme (right). In the figures, brighter voxels correspond to higher values. As suspected, with conventional CCA, the activation values are incorrectly depicted to be high also on the voxels of the cross which is observed to be rectified using the adaptive scheme. Finally, in Figure 3, we present the activation maps at a p-value threshold of 10^{-8} (unadjusted) for the entire slice of interest using conventional CCA (left) and adaptive CCA (right) without modifying the data. As expected, the map using the adaptive scheme exhibits no obvious bleeding artifact and has an increased specificity. It in fact picks up a voxel missed by conventional CCA (see arrow).

References

1. Nandy R., Cordes D. Proceedings ISMRM, 489 (2003).

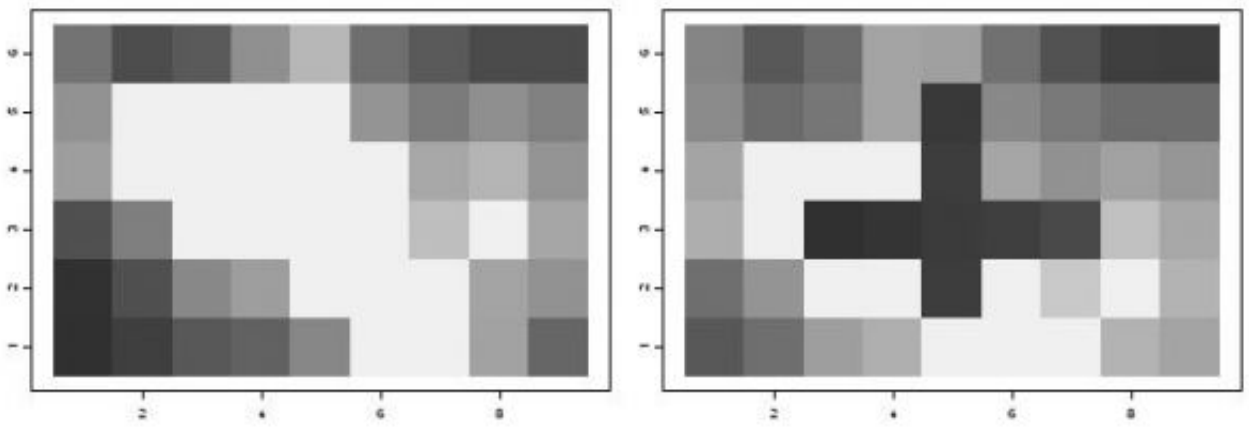

Figure 1. Map of relative CNR for the chosen 9×6 region with high activation (left) and a cross-shaped subset (right)

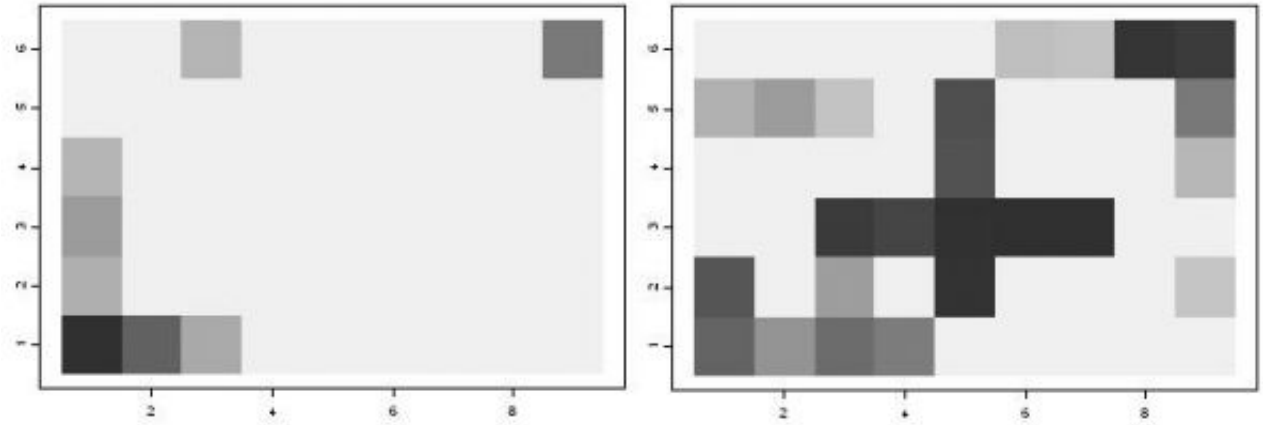

Figure 2. Activation map for the modified data using conventional CCA (left) and the adaptive scheme (right)

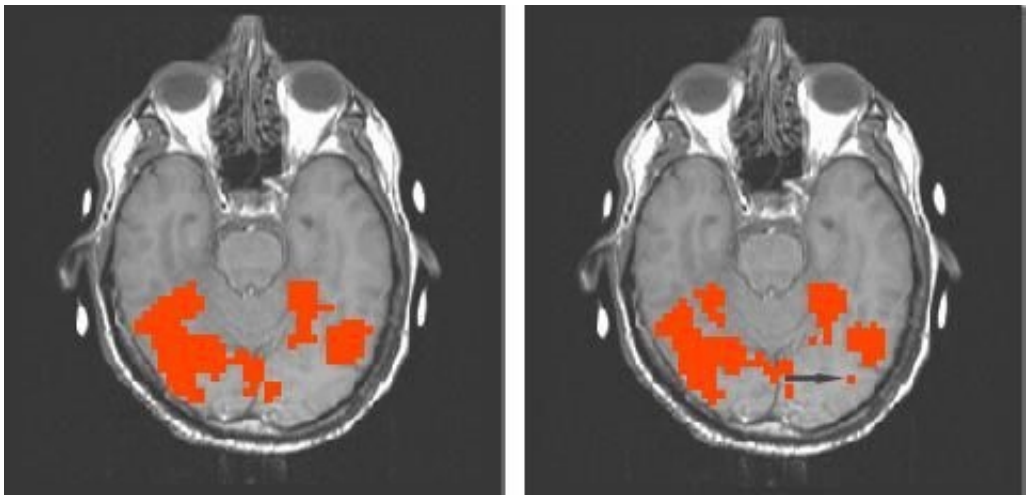

Figure 3. Activation maps for the entire slice of interest using conventional CCA (left) and adaptive CCA (right)

WE 258

Modeling of the spatial covariance structure of the brain using variograms with a non-Euclidean metric

Rajesh R Nandy , Dietmar Cordes
University of Washington, Department of Radiology

Introduction

A popular statistical technique to analyze spatial data is based on variograms, which analyzes the effect of spatial separation on the observed quantities. If the spatial process is stationary, then the spatial covariance function only depends on the spatial distance and parametric model fitting is possible. However, the assumption of stationarity is not valid for the spatial image of the inhomogeneous brain. However, stationarity may be satisfied if the brain is segmented into gray matter, white matter and CSF. This however creates additional problems as there may be holes inside the individual segments. Hence we propose the use of a non-Euclidean distance function for the variogram analysis.

Methods

Let $X(\mathbf{u})$ be the observed value of a voxel with coordinates **u**, which may be considered as a spatial random process with a covariance structure Ω. Due to segmentation, we may assume that for each individual segment, the process is stationary. From the stationarity assumption, the covariance only depends on the distance between the two points and can be obtained from the semi-variogram

$$V(\mathbf{u},\mathbf{v})=0.5E[X(\mathbf{u})-X(\mathbf{v})]^2.$$

The semi-variogram can be estimated directly from the data and it is possible to perform a parametric model fitting to the semi-variogram as a function of distance (from stationarity). A popular choice for the parametric fit to the semi-variogram is the exponential function

$$V(\mathbf{u},\mathbf{v})= \rho+\sigma^2(1-e^{-d/r}),$$

where σ^2 (sill), r(range) and ρ(nugget) are the parameters to be estimated to fit the curve. The quantity d is the distance between voxels with locations **u** and **v**.

We now describe how we measure the distance function with a non-Euclidean metric. We make use of the fact that we have a finite number of voxels which may be considered as a subset of a finite rectangular graph with nodes at voxel locations. We can now make it a connected graph by joining adjacent vertical and horizontal nodes. Each single edge is assigned a length of one voxel unit. We can then compute the shortest distance between any two points in this graph along the edges.

Results

For computational simplicity, we only consider a 256×256 segmented gray matter slice in the sagittal plane. In Figure 1, we plot the semi-variogram for the data. For very large values of distance, the semi-variogram appears to be unstable. There are two reasons behind that. Large distance in general corresponds to voxels which are far apart from one another and predictive ability is expected to be low in such a case. More importantly, since we are only considering a single slice, there may be points with large non-Euclidean distances among them which would be significantly reduced if the paths are considered in 3D. Nevertheless, we observe a nice exponential behavior if we restrict ourselves to distances less than 80 voxel units (Figure 2). In Figure 3, we plotted the semi-variogram using Euclidean distance which appears to be scattered without a definite structure.

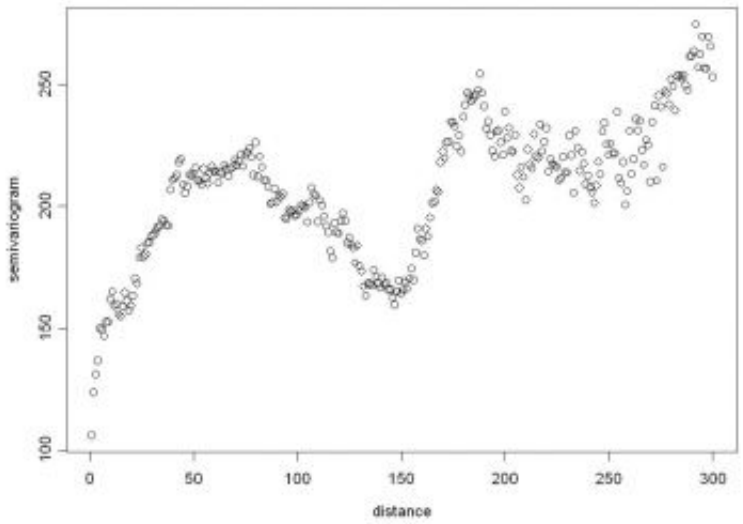

Figure 1. Semi-variogram using non-Euclidean metric

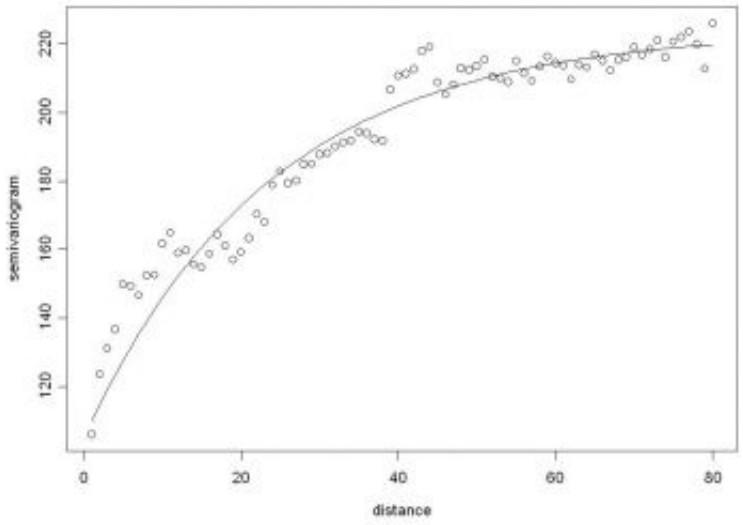

Figure 2. Fitted exponential for distances upto 80

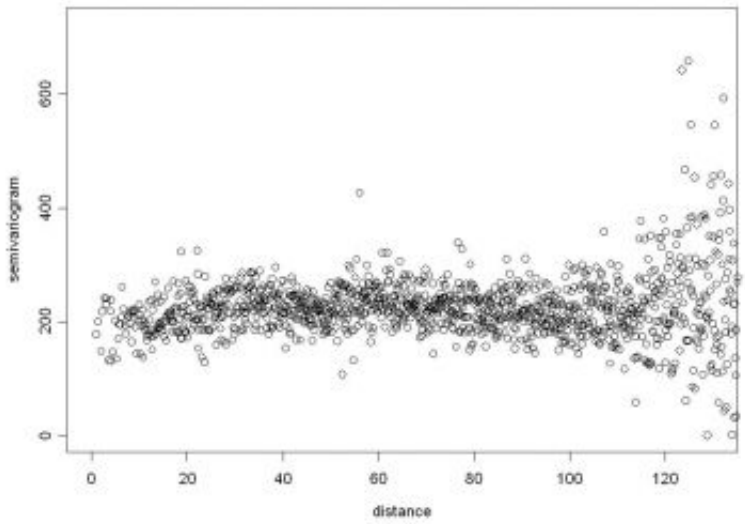

Figure 3. Semi-variogram using Euclidean metric

WE 259

ROC methods in fMRI with real data using repeated trials: Limitations and Improvements

Rajesh R Nandy , Dietmar Cordes
University of Washington, Department of Radiology

Introduction

The most popular and useful tools to assess the efficiency of different fMRI post-processing algorithms are methods based on receiver operating characteristic (ROC). The method is based on simulation and is limited in scope primarily due to difficulties in incorporating the spatial dependence among neighboring voxels in the simulation. A modified method has been suggested previously using real fMRI data by Le & Hu [1]. We propose an improvement of Le & Hus method using some mathematical relationships and also demonstrate how to reconstruct the conventional ROC curves from the modified curves.

Theory and methods

The ROC curve is a plot of True Positive Fractions (TPF) against False Positive Fractions (FPF) for detected voxels in an fMRI post processing algorithm. In Le & Hus method, the subject is presented with a standard periodic ON/OFF paradigm repeated for several periods. True positives are then estimated using a t-test with a very high degree of confidence. A second set of data is collected with a similar paradigm and ROC curves are plotted using the postulated true positives from the first dataset. However, under certain regularity conditions, it can be mathematically shown that Le & Hus ROC curve lies above the true ROC curve. To correct that, we suggest using a threshold such that the proportion of voxels detected to be active in the first dataset is equal to the expected proportion of truly active voxels, which is estimated using p-values [2]. With our choice of threshold there is no obvious bias in the modified ROC curve. It is also possible to reconstruct the true ROC curve.

Results

To compare the ROC curves, we have used simulated data. To construct the simulated data, resting state data is used as noise which is added to simulated activation. The post-processing method for the second dataset to generate the ROC curve has been the standard univariate regression analysis with Fourier basis functions. A p-value threshold of 10^{-6} is used with the first dataset to identify the active voxels according to Le & Hus method. In Figure 1, we plot Le & Hus curve, the true ROC curve as well as the curve proposed by us using a modified threshold. In Figure 2, we plot the estimated ROC curve using our reconstruction method with the same data. For real data, we have used a standard on-off motor paradigm (six periods, each period being 40 sec. long) which has been repeated in identical environment. In Figure 3, ROC curves for a standard univariate regression analysis (with Fourier basis functions of same periodicity as regressors) are plotted from the second dataset for different choices of thresholds for the t-test applied to the first dataset. We have labeled the proportion of voxels initially selected to be true positives for the corresponding threshold as p (not p-value). As expected, the ROC curve is pushed up with a conservative threshold as opposed to a more relaxed one.

References

1. Le T. H, Hu X., NMR Biomed 1997; 10: 160-164.
2. Nandy R. R, Cordes D. Magn Reson Med 2003; 49: 11521162.

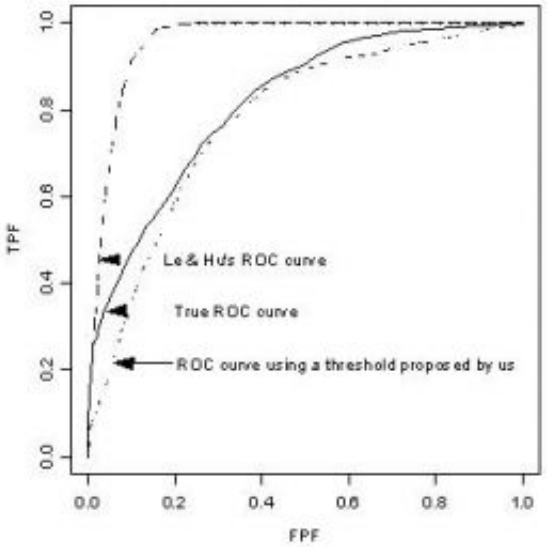

Figure 1. ROC curves from simulated data

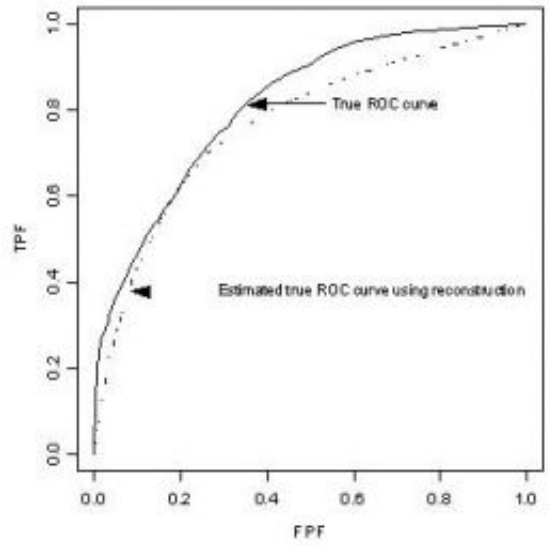

Figure 2. Comparison of true and reconstructed ROC curves

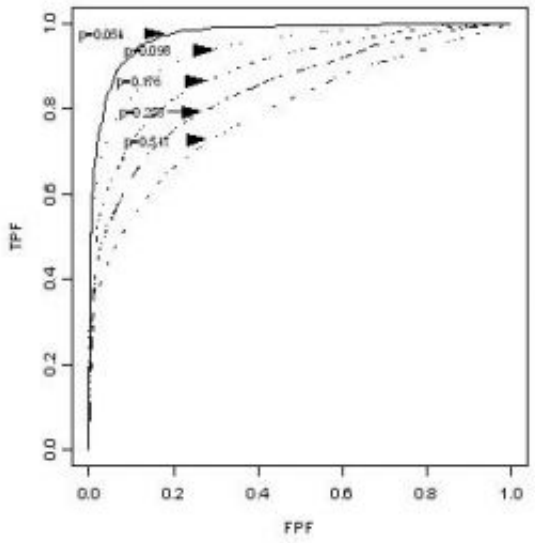

Figure 3. Le & Hus curves for different thresholds

WE 260
Conjunction Inference Using the Bayesian Interpretation of the Positive False Discovery Rate (pFDR)

Thomas E. Nichols[1], Tor D. Wager[2]
[1]Department of Biostatistics, University Michigan, Ann Arbor, MI 48109, [2]Department of Psychology, Columbia University, New York, NY 10027

Introduction

Functional neuroimaging often requires a test for the conjunction of several effects. For example, task A and B may each involve working memory but use different modalities; it is of interest to find brain regions where both task A and B are significantly activated.

In separate work (see poster by Brett etal), we show that conjunction inference based on the minimum statistic test (Worsley & Friston, 2000; SPM99; SPM2) does not control the relevant false positive rate. That is, a significant P-value for a minimum statistic only means that one or more of the effects are significant, *not* that all effects are significant.

In this work we propose an approach to conjunction inference which overcomes this fundamental limitations of the minimum statistic test. We use the Bayesian interpretation of the Positive False Discovery Rate (pFDR) (Storey, 2002).

A pFDR "q-value" is also the posterior probability of the (random) null hypothesis given the extremity of the data. It is precisely the Bayesian complement of the P-value (a P-value is the probability of the extremity of the data given the null hypothesis). Using posterior probabilities, it is easy to control the relevant conjunction false positive rate, the probability of "not all effects true".

We introduce pFDR, describe our method, and apply it to a real dataset.

Gentle Methods

1. Create images of pFDR q-values. 2. Sum the q-value images to be conjoined. 3. Reject the conjunction null where sum image is less than 0.05.

Statistical Methods:

pFDR. For one statistic image and a given threshold *u*, the FDR is the expected proportion of false positives among suprathreshold voxels. The pFDR is same *except* that it conditions on there being at least one suprathreshold voxel. pFDR has been described as "the rate at which discoveries are false".

Bayes & pFDR. Let T_i be the statistic value at voxel *i* and let H_i be the null hypothesis; $H_i = 0$ if the null is true or 1 otherwise. Let H_i be *random*. Then for a threshold *u*, pFDR(*u*) = $P(H_i = 0 \mid T_i \geq u)$ (Storey 2002). This is the posterior probability of the null given that voxel *i* is as or more extreme than *u*.

Conjunction. Now consider conjoining *K* statistic images. The conjunction null is $\cup_k \{H_i{}^k = 0\}$, the state of one or more nulls being true. We control the posterior conjunction null probability:

$P(\cup_k \{H_i{}^k = 0\} \mid \cap_k \{T_i{}^k > t_i\}) < B] \Sigma_k P(H_i{}^k = 0 \mid \cap_k \{T_i{}^k > t_i\})$

$= \Sigma_k P(H_i{}^k = 0 \mid T_i{}^k > t_i)$

The inequality uses Bonferroni and the equality uses independence over the *K* statistics at each voxel (not spatial independence). The last summation is just a summation of pFDR q-values.

Results

We applied this method to a study of response inhibition. We considered *K*=2 tasks, a go-no-go task and a flanker task. See Figure.

Conclusion

Using pFDR we have proposed a new method for conjunction inference. Our method is easy to apply, yet controls the appropriate conjunction false positive rate.

References

Storey JD. (2003) The positive false discovery rate: A Bayesian interpretation and the q-value. Annals of Statistics, 31: 2013-2035

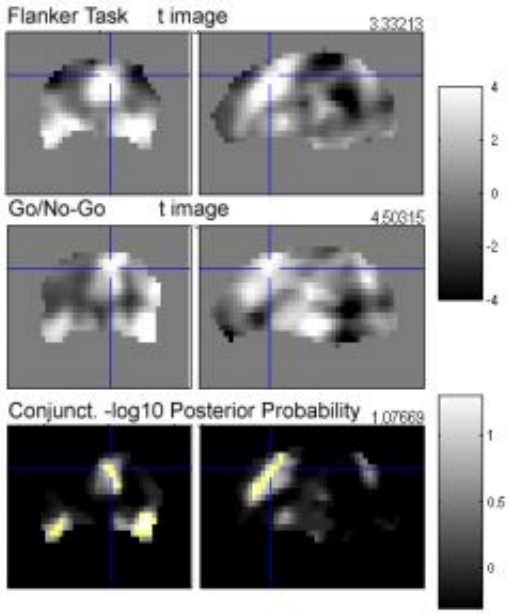

Conjunction of two tasks involving response inhibition. Top two panels show t statistic images. Bottom shows -log10 posterior probability of either or both effects being null. Yellow regions correspond to posterior probability less than 0.1; 3 voxels are less than 0.05.

WE 261
Mining Posterior Cingulate

Finn Årup Nielsen[1], Daniela Balslev[2], Lars Kai Hansen[1]
[1]Informatics and Mathematical Modelling, Technical University of Denmark, Denmark, [2]Neurobiology Research Unit and Hvidovre Hospital, Denmark

Introduction
One of the goals in human brain mapping is to relate brain areas to psychological functions. Meta-analyses can confirm presumed links and further suggest new directions for hypothesis-testing research [1]. The mounting functional imaging literature calls for new innovative computer assisted meta-analysis schemes. Here we describe a semi-automated data mining method combining text analysis of PubMed abstracts and analysis of the spatial distribution of Talairach activation foci. The method is applied to extract main functions associated with the posterior cingulate and describe their spatial distribution within this area.

Method
We queried PubMed for articles about posterior cingulate including the retrosplenial area and further restricting the query to functional neuroimaging. The articles retrieved by the query were downloaded and converted to a vectorial bag-of-words representation by counting the number of occurrences of each word in each article. An extensive stop word list was applied to focus on words pertaining to brain function. The set of abstracts were represented in an abstract-times-words matrix and this matrix was subjected to non-negative matrix factorization (NMF) [2]. The number of components in the NMF was varied between K=1-12. Talairach coordinates were extracted from articles that had a high load on the NMF components and grouped according to their component. Multivariate statistical tests were performed to investigate whether the centroids of the sets of Talairach coordinates overlapped.

Results
The text analysis with NMF showed that the most dominating theme related to the posterior cingulate was memory: "memory", "retrieval", and "episodic" were the words that had the highest load on the component and, e.g., an article with the title *Remembering the past: two facets of episodic memory explored with positron emission tomography* was found to be a prototypical article for this component. "Alzheimer" (’s disease) was found as another prominent theme (figure 1). As the number of NMF components increased these two themes would typically be modeled with several components. Pain and emotion were also found as major themes. Spatial analysis of extracted Talairach coordinates revealed that memory and pain showed a difference in focus (Figure 2; Hotelling’s T^2 test: P=0.0022; permutation test: P=0.002) where the memory coordinates showed an affinity toward the caudal aspect of posterior cingulate while pain was mostly confined to the rostral part.

Discussion
The finding that episodic memory retrieval and Alzheimer’s disease were highly associated with posterior cingulate is in accordance with "manual" reviews [1, 3]. The involvement of the posterior cingulate cortex in pain was unexpected (e.g.[4]). Our analysis of the spatial distribution of Talairach coordinates showed functional heterogeneity along the rostrocaudal axis. This is "orthogonal" to the ventrodorsal cytoarchictonic division [5].

References
[1] Cabeza R, Nyberg L, J. Cogn. Neurosci., 2000, 12:1-47
[2] Lee DD, Seung HS, Nature, 1999, 401:788-791.
[3] Matsuda H, Ann. Nucl. Med., 2001, 15:85-92.
[4] Peyron R, Laurent B, Garcia-Larrea L, Neurophysiol. Clin., 2000, 5:263-288.
[5] Vogt BA, Vogt LJ., Perl DP, J. Comp. Neurol., 2001, 438:353-376.

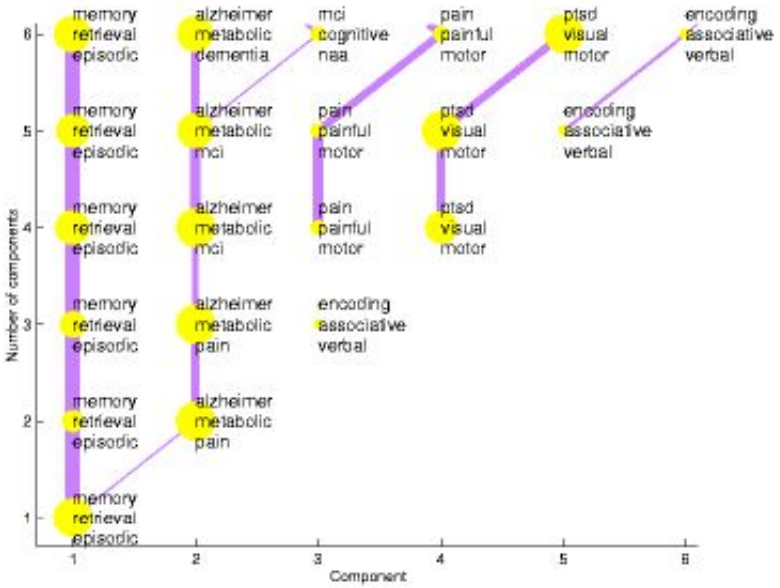

Overview of the NMF components. The *y*-axis represents the number of components *K*=1-6 in the NMF while the *x*-axis is the individual components. The words on each component are those with the highest load on the component.

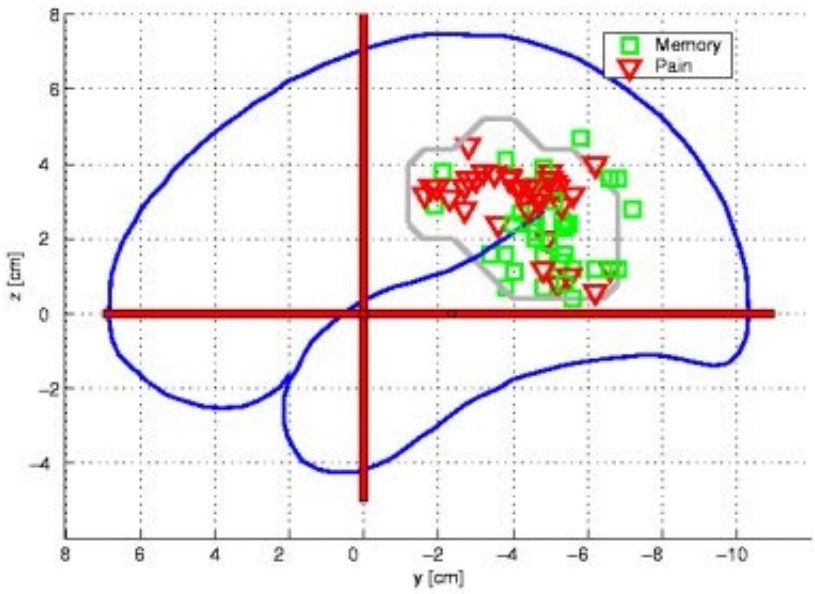

Sagittal view of memory and pain Talairach locations in posterior cingulate.

WE 262
Assessing the reproducibility in sets of Talairach coordinates

Finn Årup Nielsen , Lars Kai Hansen
Informatics and Mathematical Modelling, Technical University of Denmark, Lyngby, Denmark

Introduction
Statements like "this study demonstrates highly consistent findings" or "our results reveal a striking degree of overlap" appear commonly in the literature. Such statements are typically based on informal comparison between activation maps. Computerized methods for comparing activation maps in the form of images exist, e.g., see [1]. Here we propose methods for comparing activation maps when they exist in the form of sets of stereotaxic coordinates. We extented the method developed in connection with information retrieval where a metric was provided for assessing the similarity between the coordinate sets [2]. Our aim is to develop quantitative supports for phrases like "striking degree of overlap" and "highly consistent", i.e., a statistical test for replication, reproducibility or consistency.

Methods
We describe two methods. The first method uses a database of "experiments" (sets of Talairach coordinates) to generate a null-distribution for a similarity measure: A distribution is computed for the similarity between all pairs of experiments in the database. When two new experiments are to be assessed for reproducibility their similarity is compared against the distribution of the database. A *P*-value is generated based on the rank of the similarity. We use the Brede database [3] and a similarity based on voxelization and the cross-correlation coefficient [2]. Our second method tests whether two coordinates from two different experiments are statistically the same, and the statistic is based on the minimum distance between all pairs of coordinates $(\mathbf{x}_n, \mathbf{x}_m)$ in two experiments: $d = \min_{n,m} \mathrm{sqrt}[(\mathbf{x}_n - \mathbf{x}_m)'(\mathbf{x}_n - \mathbf{x}_m)]$. To form a *P*-value a new distance is compared against the distribution found from all pairs of experiments in the database.

Results
The Brede database presently contains 368 experiments from 118 different papers. Figure 1 shows the sorted similarities from all pairs in the database, excluding those pairs that are from the same paper. A threshold for *P*=0.05 appears at a similarity of 0.35. A histogram of the minimum distance *d* is shown in figure 2 and the associated *d*-value for a *P*-value of 0.05 is *d*=6.9mm.

Discussion
The distribution of the minimum distance tells us that if we would like to say that two coordinates from two different experiments are the same they should be closer than approximately 7 millimeters, and the similarity distribution indicates that the similarity should be larger than 0.35 before we can accept that an experiment is reproduced. The statistics do not model the number of coordinates in each experiment nor their distribution in the brain. One would expect the minimum distance to be smaller if the experiments have many coordinates. Furthermore, the distribution of the similarity measure changes depending on the type of voxelization and type of similarity measure. Nevertheless, our method provides a first step for a quantitative reproducibility measure for sets of coordinates.

References
1. Lange, N., et al., NeuroImage, September 1999, 10(3):282-303.
2. Nielsen, F. Å., Hansen, L. K., Artificial Intelligence in Medicine, 2003, In print.
3. Nielsen, F. Å., NeuroImage, 2003, 19(2), Presented at the 9th International Conference on Functional Mapping of the Human Brain.

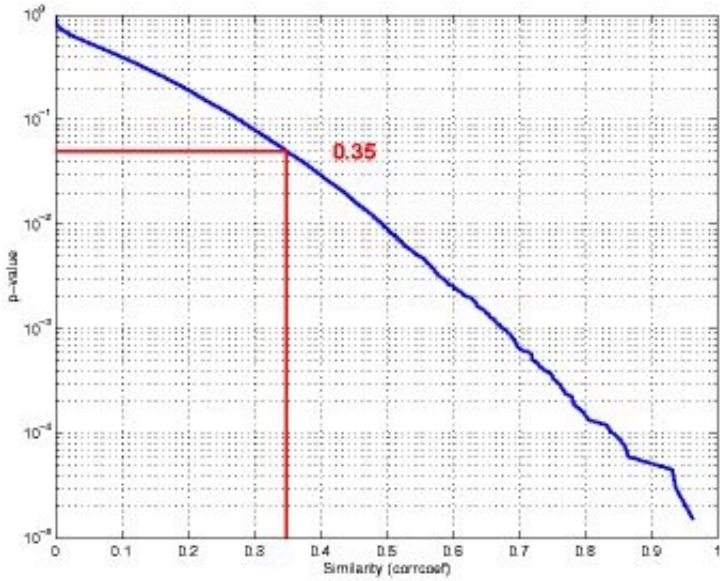

Plot of *P*-values as a function of similarity.

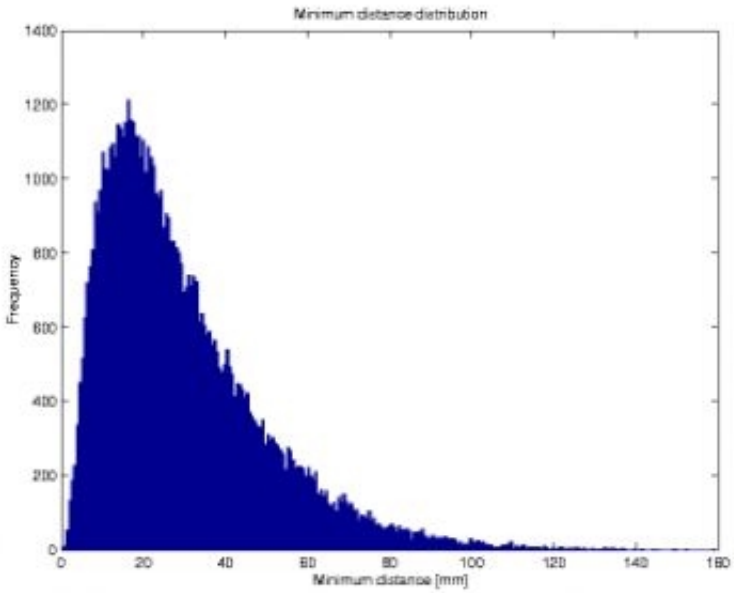

Histogram of the minimum distance statistics.

WE 263
Probabilistic Partial Least Squares: How many factors?

Frederik Brink Nielsen[1], Lars Kai Hansen[1], Stephen C. Strother[2]
[1]Technical University of Denmark, Denmark, [2]University of Minnesota, Minneapolis, USA

Background
Partial least squares (PLS) is a popular multivariate approach to neuroimage analysis (see e.g. Lin, et al. 2003). The PLS model establishes a relation between a typically high-dimensional functional data set (dimension Dx) and a relatively high-dimensional design matrix (dimension D), though a narrow linear bottleneck of dimension K<< D,Dx. The conventional application of this technique is based on a constructive SVD-like algorithm. Here we are interested in pursuing a probabilistic model, similar to Factor Analysis, which can provide an estimate of the noise level and (using cross-validation on a validation set) an unbiased estimate of the appropriate factor space dimension K.
Methods
We analysed a visual stimulus fMRI BOLD contrast data set acquired by Dr. Egill Rostrup, Hvidovre Hospital, (TR=333ms, see Hansen et al., 1999 for more details of this data set), An epoch of 30 pre-stimulus scans, 31 activated scans, and 60 post-stimulus scans was repeated 10 times. The design matrix was set up representing the so-called agnostic label scheme (Strother et al., 2003) with D = 30+31+60 = 121 effects. The scheme is uncommitted in the sense that each scan is treated as a potential separate effect and no information on the stimulus is provided. From the original BOLD image set Dx =1000 pixels were extracted using a simple omnibus F-test (Goutte et al. 2000). The Dx-dimensional pixel vector and the D-dimensional design vector were concatenated and subject to Factor analysis at variable number of factors K=1-20. For each model (i.e. dimension K) all model parameters were estimated and the likelihood computed for the training set (5 epochs). Then the parameters were applied to a test set (another 5 epochs) and the likelihood computed. The test set likelihood is an unbiased performance measure, which can be used to select the optimal model for the given training set size (see Hansen et al., 1999 for this method applied to principal component analysis).
Results
In Figure 1 we show the log-likelihood evaluated on training and test sets. The test set likelihood is maximal for a Factor model with K=11 factors. To visualize the model we show in Figure 2s four panels: a) The spatial representation of the component with maximal variance; b) the associated time course (hidden state variable) for the training set; c) the design vector representation of the maximum variance component, i.e., the actual effect which can be understood as the prototype activation response; d) the power spectrum of the time course: there is mainly power at low frequencies and relatively little energy at the frequencies corresponding to the cardiac cycle.
Conclusion
A partial least squares-like analysis can be cast as a Factor Analysis of the concatenated set of image and design matrices. Within the probabilistic framework it is possible to estimate noise variances (data not shown) as well as estimating the number of model dimensions that best generalize to fresh test data.
Acknowledgement
This work is supported by NIH Human Brain Project Grant P20 MN57180 and by the Danish Research Councils.

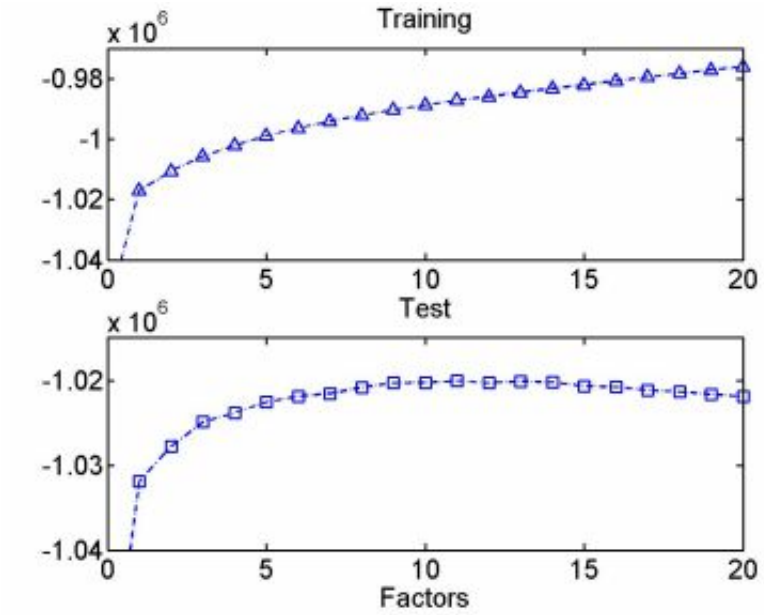

Average log-likelihoods on training and test sets as function of the number of factors

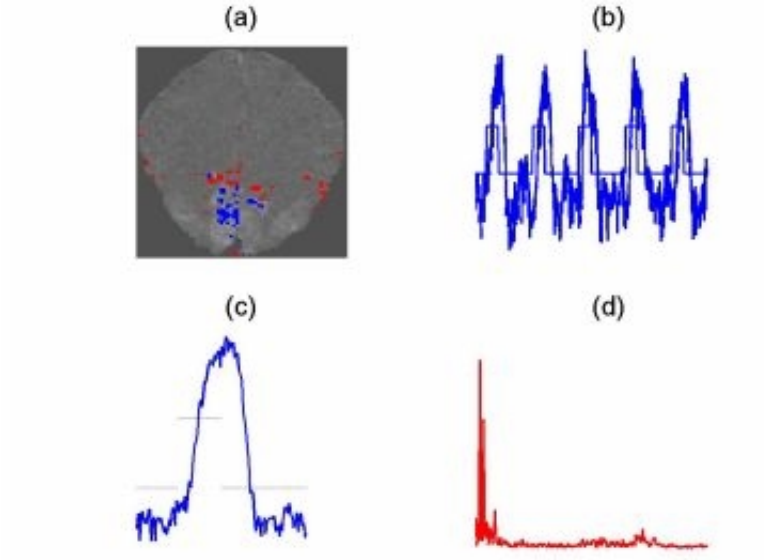

The maximum variance factor: a) spatial representation b) training set time course c) design vector d) power spectrum of training set time course

WE 265
A Hierarchical Bayesian Approach in Distributed MEG Source Modelling

Aapo Nummenmaa[1], Toni Auranen[1], Matti S. Hämäläinen[2], Iiro P. Jääskeläinen[1,2], Jouko Lampinen[1], Mikko Sams[1], Aki Vehtari[1]

[1]Laboratory of Computational Engineering, Helsinki University of Technology, Espoo, Finland, [2]Massachusetts General Hospital - Massachusetts Institute of Technology - Harvard Medical School, Athinoula A. Martinos Center for Biomedical Imaging, Charlestown, MA, USA

Introduction

The most traditional approach to distributed source model estimation based on MEG/EEG data is the regularized pseudoinverse method, also known as the minimum-norm estimate (MNE) [1, 2]. With a Bayesian interpretation, the MNE amounts to assuming a zero-mean Gaussian prior to the distributed neural currents with a linear observation model and Gaussian noise for the measurements. Furthermore, the same Gaussian prior distribution is assumed for all source current locations. While being computationally very efficient, as the maximum *a posteriori* probability (MAP) estimate is unique and can be computed in a closed form, MNE is known to produce rather diffuse estimates even in case of focal sources. Here, we implemented a hierarchical generalization of the Gaussian prior: each of the source currents has a Gaussian prior with zero mean and an individual variance. The source variances are then assumed to have a common inverse chi-square hyperprior distribution entailing a hierarchical nature to the model [3]. From posterior inference point of view, the prior variances are not of interest, but are considered as nuisance parameters and integrated out from the posterior distribution using Markov chain Monte Carlo (MCMC) methods. The limiting effect of such an integration is that it imposes a Student t-distribution prior on the source currents [3].

Methods

The possible locations and orientations of the source currents were constrained by the individual cortical geometry [2]. A single-compartment boundary-element model comprising the inner skull surface was used as the MEG forward model. Simulated data were generated by adding Gaussian noise to the magnetic fields computed from simulated sources. Fast Gibbs sampling was used to obtain numerical samples from the posterior distribution.

Results and Discussion

An interesting consequence of the hierarchical treatment is that the posterior distribution of the distributed currents becomes multimodal. This is illustrated in Figure 1, which shows the simulated source consisting of two cortical patches and a couple of posterior modes obtained from the MCMC simulations. These modes now correspond to different solutions of the MEG inverse problem. As the posterior distribution is multimodal, the MAP-estimate or the posterior expectation value is insufficient for characterizing the whole range of acceptable solutions to the distributed source reconstruction problem. Rather, an automatic clustering algorithm could be employed to locate as many modes as possible. In principle, it would be also possible to compute the relative amount of probability mass concentrated in the vicinity of the different modes, which would give information about their importance. It seems that the hierarchical prior favours solutions for which only few currents are significantly nonzero; as such the method would be especially suitable for reconstructing focal sources.

References

[1] Hämäläinen, M. S., and Ilmoniemi, R. J., *HUT Report TKK-F-A559*, 1984.

[2] Dale, A. M., and Sereno, M. I. *Journal of Cognitive Neuroscience*, Vol 5, 2:162176, 1993.

[3] Gelman, A. *et al.*, *Bayesian Data Analysis*, 2nd ed., Chapman & Hall, 2003.

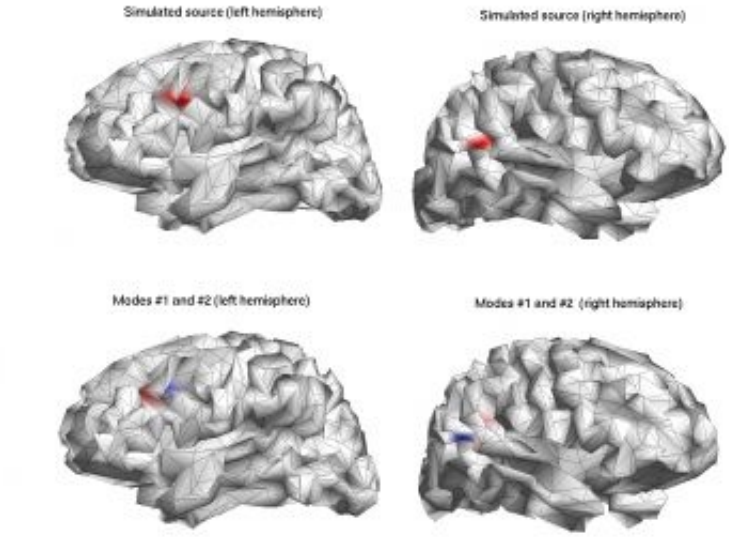

Figure 1. Top row shows the simulated source viewed from both sides. Bottom row displays two modes of the posterior distribution in different colours .

WE 266
Detection of Finger Movements from Magnetoencephalography Recordings Using Particle Filters

Tommi Nykopp , Jukka Heikkonen , Mikko Sams
Laboratory of Computational Engineering, Helsinki University of Technology, Finland

Brain activity can be used to communicate directly without using any peripheral information channels such as nerves or muscles. To do this, brain activity related to different real or imagined tasks, such as lifting a finger, has to be classified. The classified activity is then used, e.g., to select a key from a virtual keyboard. The systems enabling such communication are called Brain-Computer Interfaces (BCIs).
Various approaches have been used for the classification task [1]. However, one of these approaches takes into account that brain activity is highly non-stationary, even though the used statistical models require the signal source to be stationary. Usually classifiers are batch trained before a measurement. In batch training a classifier is trained using a set of previously collected samples. Due to the non-stationarity of the brain activity, the statistical properties change in the measured signal over time. This causes the measured samples to have different statistical properties than the samples used to train the classifier. This is a potential source for poor classification.
We have applied sequential classification, in which the classifier is updated after every processed sample. In this way the sequential classifier is able to follow the changes in the signal's statistical properties. Classification was done by using a radial basis function (RBF) network. For the sequential classifier update particle filter was used [2]. Particle filters are sequential Monte Carlo algorithms for solving on-line Bayesian inference problems. Particle filter was used to sequentially update the weighing of Gaussian kernels of RBF network.
The goal of the classification task was to separate brain activity related to left and right index finger movements. Analysis was done off-line from MEG signals. The classification was mainly based on the post-movement "rebounds" of the 20-Hz activity at the contralateral sensorimotor cortex [3]. The corresponding feature space was formed by combining the 20-Hz band power from several measurement sensors. The used data set consist of two 10-12 min session from 5 subjects (2 females).
Sequential classification were tested in two approaches. In the first approach the subjects chosed freely between left and right finger movements. Batch classifier, could differentiate them with an average classification accuracy of 83%. The use of sequential classification increased the average classification accuracy to 88%. In the second approach the subjects concentrated to perform same task consecutive times. This approach simulated an application where subject moves a cursor across a computer screen to a predefined target area. In this approach the improvement was 12% on average. An example results of the second approach for a high and a low performing subject are presented in figures 1 and 2, correspondingly.
Our results indicate that the sequential classification using particle filters is a potent method for BCIs and other brain state monitoring applications.

[1] J. Wolpaw, T. Vaughan. *Brain-Computer Interface Technology: A Review.* IEEE Transactions on Rehabilitation Engineering, 2000
[2] A. Doucet el al. *Sequential Monte Carlo Methods in Practise*, 2001
[3] R. Salmelin, R. Hari. *Spatiotemporal characteristics of Sensorimotor Neuromagnetic Rhythms Related to Thumb Movement.* Neuroscience, 1994

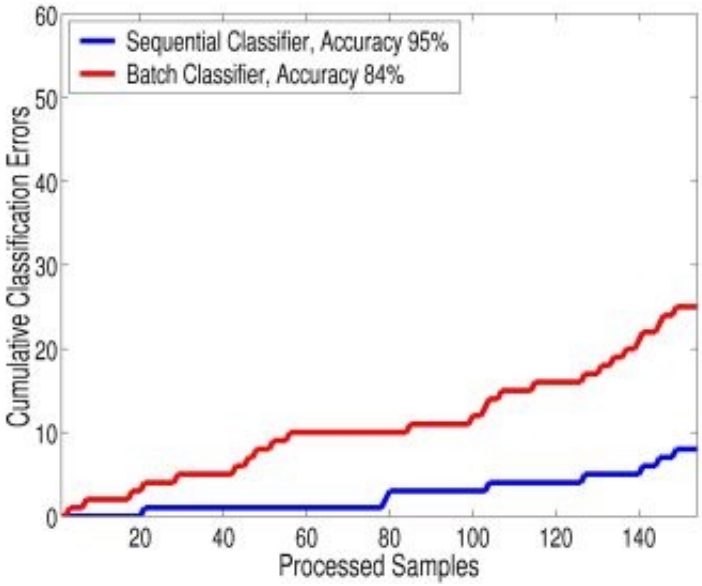

Figure 1: Performance difference between batch classifier and sequential classifier on high performing subject

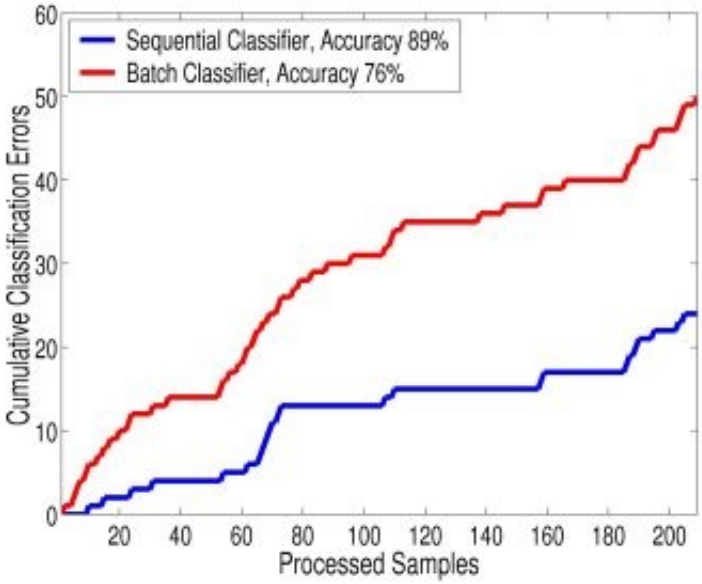

Figure 2: Performance difference between batch classifier and sequential classifier on low performing subject

WE 267
Comparison of fMRI Motion Corrections Using Realistic Synthetic Data

Terrence R Oakes[1], Kathleen S Ores[1], I. Thomas Johnstone[1], Andrew L Alexander[1, 2], Andrew S Fox[1], Lawrence L Greischar[3], Richard J Davidson[1,3,4]
[1]W.M.Keck Lab for Functional Brain Imaging, [2]Medical Physics Dept., [3]Psychology Dept., [4]Psychiatry Dept., University of Wisconsin-Madison

Introduction: The effect of motion correction for several popular fMRI analysis tools was examined using a synthesized fMRI time sequence with a variety of activations added.
Methods: To construct a family of synthetic fMRI data series (phantoms), a time series from a human BOLD-sequence was used to obtain typical motion parameters using AIR[1]. A single image from the sequence was used as the basis for a series of activation images. Eight Gaussian-shaped 3D activations of various sizes were added to the image. Activation sizes yielded detection difficulties ranging from background to obvious. The relative magnitudes of the activations from one image to the next were defined by either an alternating block-function or a well-spaced event-related function. Both activation functions were convolved with a hemodynamic response function. Phantoms were created using either a moderate or high amount of random noise (maximal noise of 12% or 20% of image values) scaled to each voxels value. Realistic motion with an interleaved slice acquisition order was modeled by randomly selecting a slice within each volume when the motion for that frame occurred.
Popular fMRI analysis packages (AFNI[2], FSL[3], SPM[4]) were used to motion-correct the data, realigning each frame to the first frame in the series. The motion parameters from each package were compared to the known motions used to create the series. Activations were detected using a General Linear Model (GLM) analysis *via* the fmristat[5] software package. The magnitudes of the central voxel for each activation in the t-statistic images were compared between packages.
Results: Each of the packages discovered movement in the phantoms for the appropriate times and magnitudes compared to the original motions, although none of the packages recovered the full amount of motion. However, the differences in the GLM activation results between each package were generally small, indicating comparable performance. The ratio between software tools of max/min t-values averaged over all activations within each phantom ranged from 1.03 to 1.14. The larger differences were found for unsmoothed t-maps, higher noise, and the event-related design. When the t-statistic maps for the block design were smoothed, FSL produced the highest t-statistics, while AFNI yielded the lowest. For the unsmoothed block design, AFNI yielded 7 of the 14 highest values, while FSL had 7 of the lowest values. However, for the unsmoothed event-related design, SPM performed slightly better, with 6 of the 13 highest t-values. Results for other parameter combinations showed no differences between the packages. Interestingly, for several of the small activations, motion correction degraded the detection ability.
Conclusion: Overall differences in motion-correction between these packages upon the final GLM t-statistic results are negligible. FSLs motion correction performs slightly better for larger, more obvious activations, and when the t-statistic maps are smoothed. AFNI performs slightly better for unsmoothed maps from the block design, while SPMs motion-corrected data yielded the largest number of maximal t-values for the unsmoothed event design, which were the most difficult activations to detect.
References:
[1]Woods,1998.
[2]Cox,1997.
[3Jenkinson,2001
[4]Friston,1994.
[5]Worseley,2002

WE 268
Minimum norm estimates as the basis for statistical parametric mapping of EEG/MEG data

Hauk Olaf
MRC, Cognition and Brain Sciences Unit, Cambridge

An analysis strategy for EEG/MEG data in the absence of reliable a priori information about the generating sources is suggested. The problem to be solved is given by the simple linear equation **d**=**Ls**, where the lead field **L** incorporates information on head geometry, sensor and source locations; and **d** and **s** are vectors of measurements and source strengths, respectively.
Four approaches to tackle this problem are compared theoretically:
1) Null-space approach, which requires of the estimated solution that it does not contain any "non-visible" sources
2) Minimum norm approach, where a weighted norm of the solution shall be minimized.
3) Maximum likelihood approach, where the most likely solution shall be found according to assumed probability distributions
4) Backus-Gilbert approach, where the resolution matrix shall be as close to the identity matrix as possible (the basis of beam-forming approaches).
All these approaches can make use of the same kind of a priori information if available. In particular, they all yield the minimum norm pseudo-inverse (MNP) in the complete absence of such information [1].
This indicates that the limitations of the MNP are not specific to this method, but are fundamental properties of the recording modalities. The minimum norm solution provides the amount of information that is actually present in the data themselves, and is therefore optimally suited to investigate the general resolution and accuracy limits of EEG and MEG measurement configurations. Furthermore, the classical minimum norm solution is a valuable method when complex cognitive tasks are employed or when very noisy data (e.g. single trial data) are analyzed. For that purpose, an efficient and practical implementation of this method will be suggested and illustrated with simulations using a realistic head geometry (fig. 1/2).
It will be demonstrated that the solutions obtained by the MNP can be subjected to group statistical analysis using Statistical Parametric Mapping (SPM) (fig. 3). The problem of multiple comparisons can be approached in a similar fashion as in fMRI analysis, for example using the False Discovery Rate (FDR) technique [2]. This method controls the rate of false positives among the sources significantly activated. If this rate is chosen to be 5%, for example, the resulting distribution of significantly activated sources will contain on average 5% false positives. This accomplishes a compromise between not correcting at all (such that 5% of all voxels may be false positive), and Bonferroni-correction which intends to avoid any false positives (5% of experiments will generate a single false positive voxel).
[1] Hauk O (2004). Keep it simple: A case for using classical minimum norm estimates in the analysis of EEG and MEG data. Neuroimage, in press.
[2] Genovese CR, Lazar NA, Nichols T (2002). Thresholding of statistical maps in functional neuroimaging using the false discovery rate. Neuroimage 15(4), 870-8.

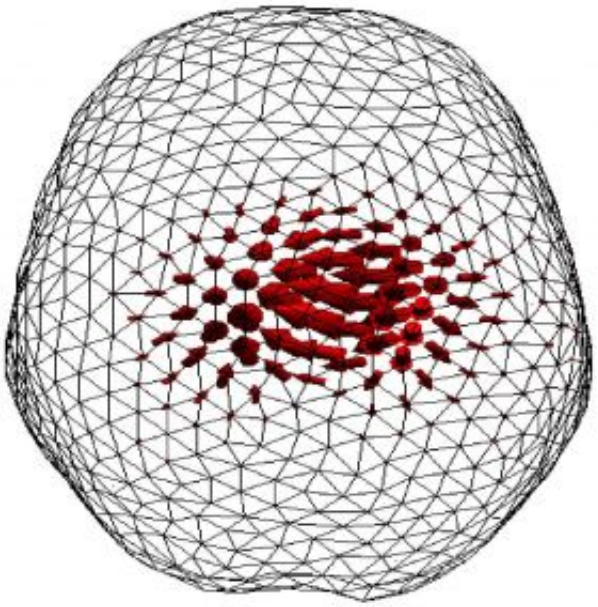

Fig. 1: Example of a minimum estimate for a tangential dipole source below the vertex. The arrows indicate the strength as well as the orientation of each dipole source.

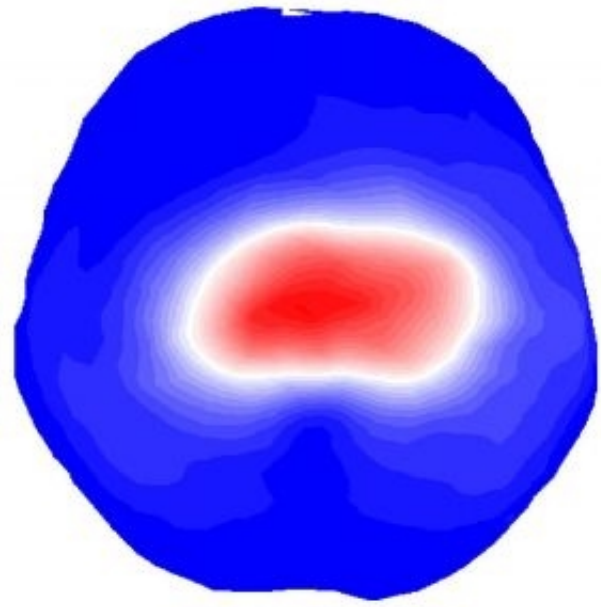

Fig. 2: As in figure 1, but the intensities for each source were computed and interpolated. The peaks of these distributions reflect the true source positions, and no ghost sources are present.

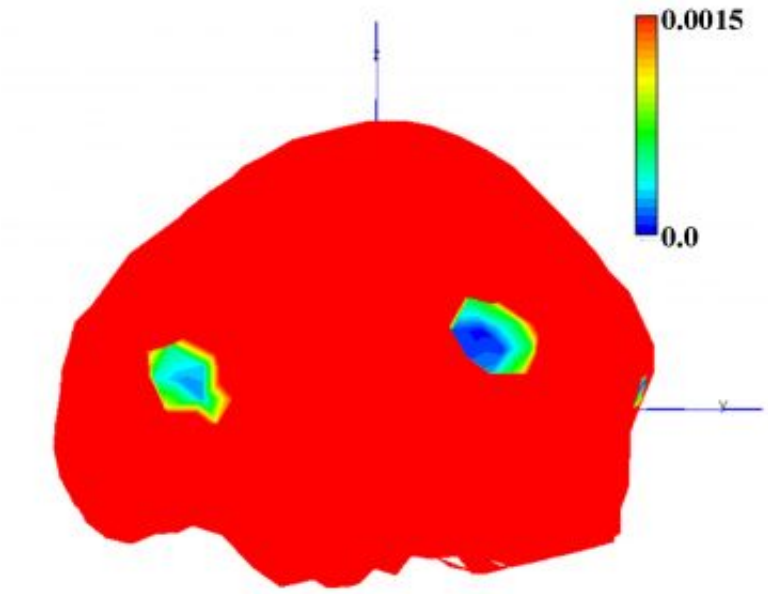

Fig. 3: Example of a statistical map based on source estimates. Data were obtained from an experiment on word evoked ERP activity. Conditions of high and low word form frequencies were contrasted. The image showing the significance distribution at 212ms reveals two activity foci in left posterior and anterior brain areas, respectively. The threshold of significance was FDR adjusted.

WE 269
Using Eclipse to develop a modular image processing pipeline and GUI for functional MRI data analysis

Cinly Ooi , John Suckling , Ed Bullmore
Brain Mapping Unit, University of Cambridge, Addenbrookes Hospital, Cambridge UK

Different research groups have developed different software tools for analysis of fMRI data and often disseminate them as complete packages. This practice arguably conceals major generic similarities between data processing pipelines originating from different labs and tends to inhibit users from building custom pipelines that incorporate modules originating in different packages. The development of explicitly modular graphical user interfaces (GUIs) has been advocated by several groups (LONI Pipeline (*www.loni.ucla.edu/NCRR/Software/Pipeline.html*), FisWidget (*neurocog.lrdc.pitt.edu/fiswidgets*), BrainVisa (*brainvisa.free.fr*) , SCIrun (*neurocog.lrdc.pitt.edu/fiswidgets/*)) as one way of overcoming some of these issues and making it considerably easier for users to cross-validate and compare component algorithms from different labs. Here we describe work (*www-staff.psychiatry.cam.ac.uk/~co224/EPLlab/*) using a similar strategic approach but benefiting in some important ways by the adoption of the Java-based Eclipse platform. Eclipse provides both a development framework for C, Java and other programmers and a rich GUI library for intuitively accessible customization and control of data analysis pipelines. Some key advantages for programmers are i) the easy incorporation of modules written in C/C++, Matlab, R or other languages, with no requirement for re-writing and minimal requirements for wrappers; ii) source code version control and automated update via the internet; iii) excellent documentation; iv) support for parallel or mixed parallel/serial processing; and v) platform independence. Some key advantages for end users are i) the ability to load, store and share standard and customized pipelines; ii) to do batch and interactive processing; iii) one click installation and integrated help functions; and iv) immediate visual overview of the algorithmic structure of the data analytic process. Our work to date has involved creating a framework in Eclipse Platform that acknowledges modular contributions from different sources, provides the logic that governs the construction of the pipeline and its execution in both interactive and batch/queue mode, and ensures the optimum use of computing resources. Algorithm contributions are accepted as modules or pipelines. Different ways of module incorporation in pipelines, including automatic recognition by the GUI and use of step-by-step installation wizards have been developed. Pipelines for fMRI time series analysis, spatial normalization, second level group and factorial analysis, and web-based visualization of results, have been successfully conceived and developed in a prototype version. We plan to provide the software as a free and open source product.
This project is supported by a Human Brain Project grant from the National Institutes of Health (*www.nimh.nih.gov/neuroinformatics/bullmore.cfm*) and by an IBM Eclipse Innovation Grant 2004 (*ibm.com/university/eig*)

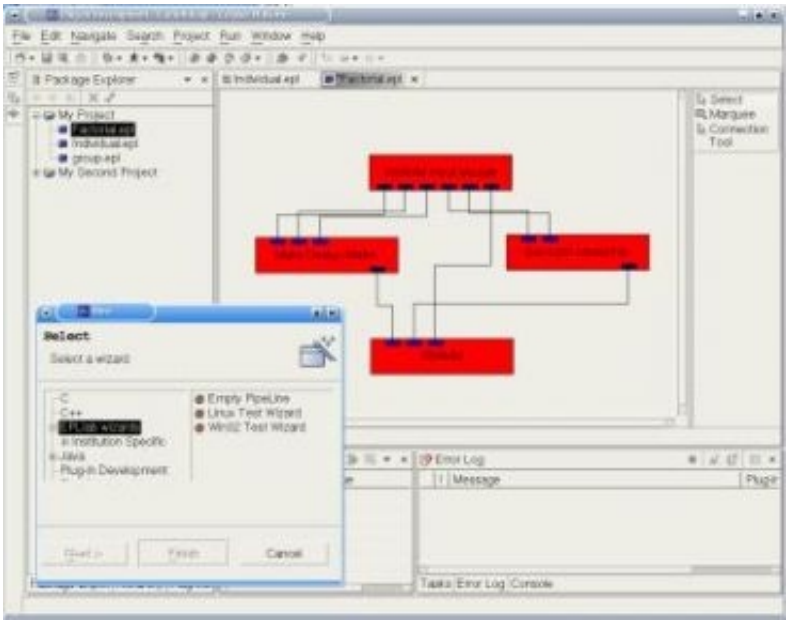

Prototype GUI

WE 270
Comparison of EEG and MEG Beamformer Source Localization Performance

Robert Oostenveld[1,2], Andrew CN Chen[1], Lars Arendt-Nielsen[1]
[1]Center for Sensory-Motor Interaction, University Aalborg, Denmark, [2]F.C. Donders Centre, University Nijmegen, The Netherlands

Background

An inverse source analysis technique that recently gained a lot of interest is spatially adaptive filtering, or beamforming. Using beamforming, it is possible to localize multiple areas of activity in the brain without a priori assumptions about the number or location of those areas. Although it does not offer a high spatial resolution compared to other localization techniques, it is especially valuable as a tool to study the temporal dynamics of brain function for which EEG and MEG are touted. Recent beamformer advances make it possible to characterize induced activity in specific frequency bands, connectivity and directionality in cortical networks [1,2]. Beamforming was initially described for EEG [3], but has almost exclusively been applied to MEG. Given its the potential value and the widespread availability of high-density EEG, it is desirable to have it available as a tool for EEG, and to compare its performance between EEG and MEG.

Methods

We implemented several beamformer techniques for EEG and MEG. We evaluated the localization accuracy using simulated data, based on a multiple sphere volume conductor and an identical sensor configuration for EEG and MEG (138 sensors that were equally distributed over upper half of a sphere). The data was constructed by with a single dipole at a specified location and with a sinusoidal timecourse. Uncorrelated noise was added to the dipole signal, with an equal signal to noise ratio of 0.7 in the raw EEG and MEG data. Repeating this for 10 trials resulted in a S/N ratio of 2.2 in the average.

Results & Discussion

Figure 1 demonstrates the source power distribution trough the head for a tangential source at 67% eccentricity. Both the EEG and MEG beamformer localize the source at the correct location, but the EEG source reconstruction is clearly more blurred. The power distribution for the MEG shows its insensitivity for deep sources, resulting in a noise bias toward the center of the sphere. This bias can be corrected by projecting noise through the spatial filter and computing the neural activity index (ratio between projected signal and noise). More elaborate simulations will show the spatial distribution of beamformer performance, and will quantify the differences between EEG and MEG.

References

1) Gross et al. (2001) Dynamic imaging of coherent sources: studying neural interactions in the human brain. PNAS 16:694-9.
2) Gross et al. (2002) The neural basis of intermittent motor control in humans. PNAS 19:2299-302.
3) Van Veen et al. (1997) Localization of brain electrical activity via linearly constrained minimum variance spatial filtering. IEEE-BME 44:867-80.

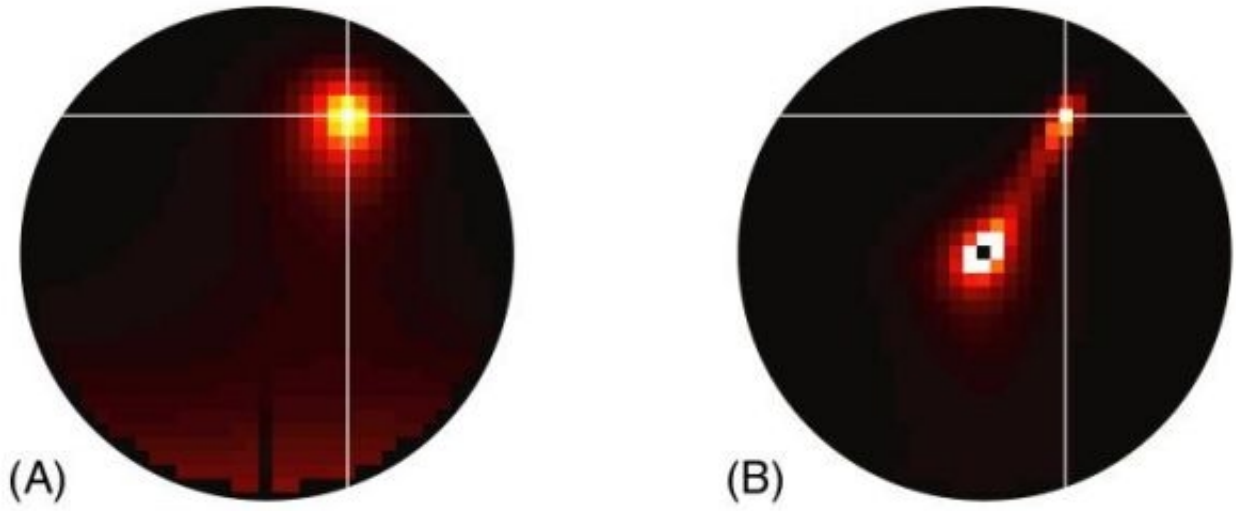

Figure 1; Localization accuracy of (A) EEG and (B) MEG beamformer.

WE 271
Comparison of Motion Correction Tools for fMRI ER Data.

Kathleen S Ores[1], Terrence R Oakes[1], I Thomas Johnstone[1], Andrew L Alexander[1,2], Andrew S Fox[1], Larry Greishar[3], Richard J Davidson[1, 3, 4]
[1]W.M.Keck Lab for Functional Brain Imaging, University of Wisconsin-Madison, [2]Medical Physics Department, University of Wisconsin-Madison, [3]Psychology Department, University of Wisconsin-Madison, [4]Psychiatry Department, University of Wisconsin-Madison

Introduction: A crucial step in analyzing fMRI data is correcting the time series for any movement that occurs during the scanning session. This study compares the motion correction tools of commonly used fMRI analysis software in detecting and correcting for subject movement during an fMRI imaging session and its effects on the resulting statistical images. Packages compared are: SPM2, AFNI(2.52) and FSL(3.1).
Methods: Functional images from 40 subjects were collected on a 3T GE SIGNA MR scanner. They were presented with 2 runs of a go/no-go task (random iti between 1.5 and 3.5 sec). The time-series image data were reconstructed using in-house software, slice time corrected using AFNI and converted to the formats needed for each package. The default motion correction parameters were used for the corresponding tools. Movement parameters were graphed and visually compared for similarity. The corrected and non-motion corrected time series were then analyzed in fmristat [1] to obtain T-statistical images using a GLM (General Linear Model). Subjects were not coregistered to a template in order to preserve the original data. However, the statistical images were smoothed with a 8mm isotropic Gaussian kernel. Clusters were extracted across all 40 subjects for similar functional activations for each of the three packages and for non-motion corrected images. The motion parameters per subject and the maximal T values per cluster per package were evaluated.
Results: Maximal T values for each cluster across packages were normalized by the non-motion corrected maximal T value of the same cluster. The ratios ranged from 0% to 27% over individual clusters. Within each package, AFNI and FSL had a range from 0% and 25%, while SPM ranged from 0% and 27%. Of the 8 activated regions extracted across all subjects, 100 clusters survived a threshold of 2.0. Of these, FSL had greatest amount of clusters with maximal change from the non-motion corrected image. (Table 1).
Each subject was given a score of movement (high, medium and low) based on inspection of the motion parameters. (Table 2). Using this grouping, FSL again has the greatest number of clusters with maximal change(~7%) from the non-motion corrected images in the medium and low movement categories. SPM has the highest ratio to the non-motion corrected value (13%) in the high movement category. Over all averages among motion groupings however, did not demonstrate any significant differences between algorithms in the post correction performance.
Ratios to the non-motion corrected data are also compared over 5 different functional regions. In region M1 (mean max t value 4.19, mean extent = 7) SPM has an extremely low percent change (0.2%) compared with FSL and AFNI.
After inspection of the motion parameters, although some packages placed more emphasis on translations versus rotations, all discovered motion of similar magnitude at the same time points.
Conclusions: In general, no substantial differences were found in the GLM results. All packages improved the maximal T values from the non-motion corrected data. FSL seemed to have the most maximal improvements, however, no major differences were seen.
Reference:
[1] Worsley, 2002

Table1: Mean Ratio of Max Cluster T Values; **Table 2**: Mean Max Ratio per Motion Group

Table 1:		n
SPM	1.0913	32
FSL	1.0738	50
AFNI	1.0572	18

Table2:	SPM	n	FSL	n	AFNI	n
High	1.1309	5	1.1216	3	1.0765	1
Med	1.0776	11	1.0689	15	1.0743	5
Low	1.0884	16	1.0717	32	1.0485	12

WE 272
An Orthogonal Infomax Algorithm for Spatial ICA of fMRI Data

Lili Pan[1,2], Zhenwei Shi[1,2], Zhenhua Wu[1,2], Huanwen Tang[1], Yijun Liu[5], Yiyuan Tang[2,3,4]
[1]Institute of Computational Biology and Bioinformatics, Dalian University of Technology, Dalian 116023, P.R. China, [2]Institute of Neuroinformatics, Dalian University of Technology, Dalian 116023, P.R. China, [3]Laboratory of Visual Information Processing, The Chinese Academy of Sciences, Beijing 100101, P.R. China, [4]Key Lab for Mental Health, The Chinese Academy of Sciences, Beijing 100101, P.R. China, [5]Departments of Psychiatry & Neuroscience, McKnight Brain Institute, University of Florida, USA

Introduction
ICA has been successfully employed to decompose fMRI time-series into sets of activation maps and associated time-courses. Two spatial ICA (sICA) algorithms have been developed so far: Infomax algorithm (Bell and Sejnowski, 1995) and Fixed-Point algorithm (Hyvärinen, 1999). Esposito et al. compared the two algorithms used for sICA of fMRI time-series (Esposito et al., 2002) and the results showed that each of them has its own advantages. Here we present a new algorithm, termed Orthogonal-Infomax algorithm, to combine the features from both the Infomax and Fixed-Point algorithms.
Methods
Our Orthogonal-Infomax algorithm searches for the optimal solution in an orthogonal space with the approach of Infomax algorithm. We applied our algorithm to fMRI data to test if it is efficient for detecting reliable brain activations. The data was acquired on three Chinese college students, who participated in an fMRI experiment performing a grapheme-identifying task. The subjects were scanned on a 1.5T GE Sigma MRI system by using an EPIBOLD sequence (TR=2000ms, TE=40ms, field of view (FOV) =240x240, matrix=64x64, flip angle=30 degree, slice thickness=7mm, slice gap=1mm, number of slices=18).
Results and Discussion
We compared the activation results (will be reported separately) using these three algorithms (Fixed-Point, Infomax and Orth-Infomax) in the following three aspects: (1) Linear correlation analysis and (2) receiver operating characteristics (ROC) analysis were used to assess the algorithms' accuracy of estimating the temporal dynamics and spatial layout of activations; (3) likelihood analysis was used to evaluate the goodness-of-fit (GOF) to the decomposition of the fMRI data using these algorithms. Our results show that all three algorithms worked properly on our data, but as far as the temporal dynamics of the fMRI data is concerned, Orthogonal Infomax algorithm gives the best results. As for spatial accuracy of the consistently task-related (CTR) component maps, the new algorithm outperforms Infomax algorithm, while in terms of GOF to the decomposition of the fMRI data, our new algorithm is superior to the Fixed-Point algorithm. We conclude that the Orthogonal Infomax algorithm is an efficient algorithm for sICA of fMRI data.
References
1. Bell A, Sejnowski T. Neural Computation 1995;7(6):1129-1159.
2. Hyvärinen A. IEEE Transactions on Neural Networks 1999;10(3):626-634.
3. Esposito F, Formisano E, et al. Human Brain Mapping 2002;16:146-157.
Acknowledgments
This work is supported by the MOST (2100CCA00700) and MOST International Program, NSFC (30170321) and MOE (KP0302).

WE 273
Inverse EEG Problem: A Contrained Finite Volume Element Method.

Theodore Papadopoulo , Frederic Demoors , Maureen Clerc , Olivier Faugeras , Renaud Keriven
Projet Odyssee, ENPC, ENS Ulm, INRIA Sophia-Antipolis.

This work contributes to the problem of the mathematical reconstruction of the brain electric activity from electrical EEG measurements. This aims at recovering the location of the activity in terms of dipole sources that are located in the cortex. In our approach, we look for a "continuous" primary current distribution (as in [1] or [2] for example) given some anatomical constraints, such as:
- The dipoles currents are exclusively located in the cortex.
- They are potentially oriented along the direction of the hyper-columns (which is approximated to be the direction orthogonal to the surfaces delimiting the cortex).
- The solution can furthermore be restrained to be located on a few set of patches of the cortex (if this prior knowledge is available, e.g. from functional MRI).

To do so, the head is represented as a tetrahedral mesh generated from anatomical MRI and the inverse problem is solved using a finite volume element approach where the relevant head quantities are modeled by locally affine function on each tetrahedron. Compared to finite boundary elements, this formulation allows to deal with the head tissues anisotropy (e.g. non isotropic conductivities in the skull or the white matter), and the method is usually faster even if slightly less accurate. It also has the nice property of being linear which allows for efficient numerical solutions using optimal steps and the adjoint state method. As for other methods based on "continuous" current distributions the solution is, however, not unique because the number of measurements is very low compared to the number of tetrahedrons required to model the head. Thus, a second set of constraints must be added to regularize the solution. These constraints are in effect assumptions on the smoothness of the dipole distribution and their sole role is to select a particularly simple solution among all the solution set. We study various regularization schemes (e.g. minimum norm solution, minimum gradient norm solution) using Lagrange multipliers to enforce the fact that the solution must predict accurately the measurement values. The results are compared on some simple data sets. It is also important to note that this constrained formulation implies that the energy that is minimized is no longer convex, so the optimization scheme must be rethought as a succession of minimizations-maximizations, that is experimentally shown to converge toward the searched optimum.

[1] R.D. Pascual Marqui et al. "Low resolution electromagnetic tomography: A new method for localizing electrical activity of the brain", International Journal of Psychophysiology, 18:49-65, 1994.
[2] S. Baillet and Line Garnero. "A bayesian approach to introducing anatomo-functional priors in the EEG/MEG inverse problem". IEEE Transactions on Biomedical Engineering, 44(5):374-385, May 1997.

WE 274
Direct Observation of Neuronal Activities by MRI: A Snail Ganglia Study

Tae S. Park , Sang-Yeon Lee , Ho K. Kim , Soo Y. Lee , Ji-Ho Park
Graduate School of East-West Medical Science, Kyung Hee University, Korea

FMRI has been widely used in functional brain studies owing to its superb spatial resolution compared with other brain mapping modalities. However, poor temporal resolution of fMRI is still a big barrier to dynamic functional brain studies. Recently, direct observation of neuronal activities in the brain has been tried with MRI. Based on the fact that the magnetic fields produced by the neuronal currents have effects on the MRI signal, Xiong et al proposed magnetic source MRI (msMRI) to observe the neuronal activities in a direct way other than the BOLD effect. The feasibility of msMRI is still controversial due to the lack of fundamental studies.
In this study, we have tried direct observation of the neuronal activity in the ganglia of an Achatina fulica, an African agate snail, which can sustain neuronal activities in saline without additional oxygen supply for a time period as long as one hour. Snails weighing 30-40g were anesthetized by injection (50% of the body weight) of isotonic MgCl2 (337mM). The whole ganglia were dissected out. The connective tissues surrounding the ganglia were carefully removed to prevent possible tissue contractions during the MRI studies. Cleared ganglia were pinned using ~5mm length copper wire on an elastic sylgard covered dish that had a volume of ~5 ml of saline (composition [in mM]: 53.7 NaCl, 3.4 KCl, 12.9 MgCl2·6H2O, 10.7 CaCl2·2H2O, 4.4 Na2SO4, 3.3 NaHCO3 and pH = 7.6). Figure 1 shows a photographic image of the dissected snail ganglia. To increase the neuronal activity in the ganglia, we applied carbachol containing saline for the final bath concentration (5mM). It was reported that carbachol could induce a feeding motor rhythm in Aplysia. Figure 2(a) and (b) show the action potential signals measured with extracellular electrodes on the ganglia before and after the application of the carbachol, respectively. The neuronal activities were significantly increased by the carbachol. We have obtained T2-weighted MR images every 3 minutes with the gradient echo sequence. The TE and TR were 50 ms and 300 ms, respectively. Figure 3 shows an image of the dissected ganglia. Figure 4(a) shows the action potential signal amplitudes after the application of the carbachol. After the initial increase of activity by the carbachol, the neuronal activities decreased slowly. Figure 4(b) shows the MRI signals changes at the cerebral ganglia region (marked as a in Figure 3) after the application of the carbachol. To compensate the system instability, we have corrected the signal intensity with the average signal at the background saline region (marked as b in Figure 3). The MRI signal intensity increases as much as 20% as the neuronal activities in the ganglia decreases. This implies that the magnetic fields produced by the neuronal activity have measurable effects on the MRI signal intensity.
We think further works including the physiological modeling and corresponding MRI experiments are still necessary for applications of the direct observations to the functional brain studies.

Fig.1

A photographic image of the dissected snail ganglia

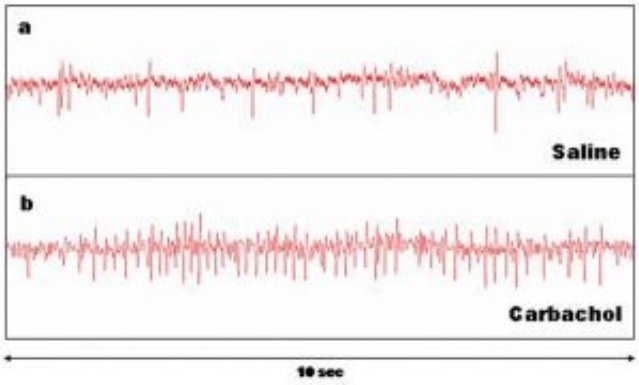

Fig.2

Action potential signals of the ganglia (a) before and (b) after the application of the carbachol

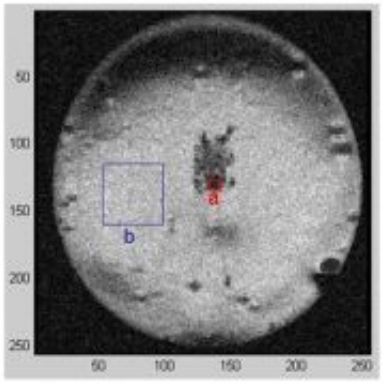

Fig.3

An MRI image of the dissected snail ganglia

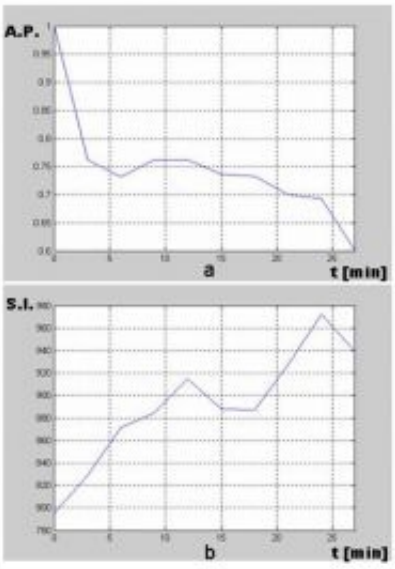

Fig.4

(a) The action potentials signal amplitudes and (b) the MRI signal intensities at the cerebral ganglia

WE 275
The BOLD correlate of the post-movement beta rebound

Laura M Parkes , Marcel CM Bastiaansen
F.C. Donders Centre for Cognitive Neuroimaging, University of Nijmegen, Adelbertusplein 1, 6525 EK Nijmegen, The Netherlands.

Introduction
Recent work [1,2] has shown that spontaneous changes in alpha and beta power show associated changes in BOLD activity. This suggests that there should also be a BOLD change accompanying event-related oscillations, such as the strong increase in power in the beta range following movement offset. By parametrically varying the strength of this post-movement beta rebound, it was possible to use it as a regressor in the fMRI analysis and so identify its locus.

Methods
Six volunteers participated in the study. The task was to perform right index finger extensions at three different rates, cued by a flashing cross on a screen (Figure 1). A button fixed above the finger recorded movement onsets and offsets. EEG measurements from 225 trials were collected both outside and inside the MRI scanner.
EEG was acquired with 29 EEG channels, and 1 EOG channel (Brainproducts, Munich, Germany), sampled at 500Hz. MRI measurements were performed using a 3T Trio scanner (Siemens, Erlangen, Germany). Images were acquired using an EPI sequence (TR 2s including 56ms dead time, TE 36ms, 27slices, voxels 3.5mm3) covering the whole brain.

Analysis
The EEG data were segmented with respect to movement offset (from 1s before to 3.5s after), baseline-corrected, and segments contaminated with artefacts were rejected. For a time-frequency analysis, we used a multi-taper approach [3]. Standard MRI pre-processing was done using BrainVoyager including motion correction, scan time correction, spatial and temporal smoothing and transformation into Talairach space. Four regressors were used in a general linear model: three motor regressors corresponding to the three extension rates (onsets and offsets determined from the button presses), and a beta regressor (constructed from the averaged EEG beta rebound waveforms at electrode C3). The beta regressor was scaled according to the strength of each subject's beta rebound. The regressors were convolved with a Gaussian HRF [4].

Results
Typical EEG rebound data is shown in Figure 2. Figure 3 shows the results of the group analysis, highlighting regions where the beta regressor accounted for a significant degree of variance in the fMRI data. A region of positive correlation can be seen in the left motor cortex, which we identify as the source of the beta rebound. Figure 4 shows a correlation of the strength of the MRI data within this region with the strength of the beta rebound as measured with EEG over 5 subjects (there was one out-lier) and all conditions. The baseline chosen for the EEG analysis is during movement, when beta power is known to be suppressed, which could explain the non-zero intercept.

Conclusion
The BOLD signal is shown to be positively correlated with the post-movement increase in beta power. The locus of the beta rebound is found to be in primary motor cortex, lateral to the region most significantly activated by the finger movements.

References
1. Goldman R.I. et. al. NeuroReport 13:2487-2492(2002).
2. Laufs H. et. al. PNAS 100:11053-11058(2003).
3. Mitra P.P. et. al. J. Biophys 76:691-708(1999).
4. Rajapakse J.C. et. al. HBM 6:283-300(1998).

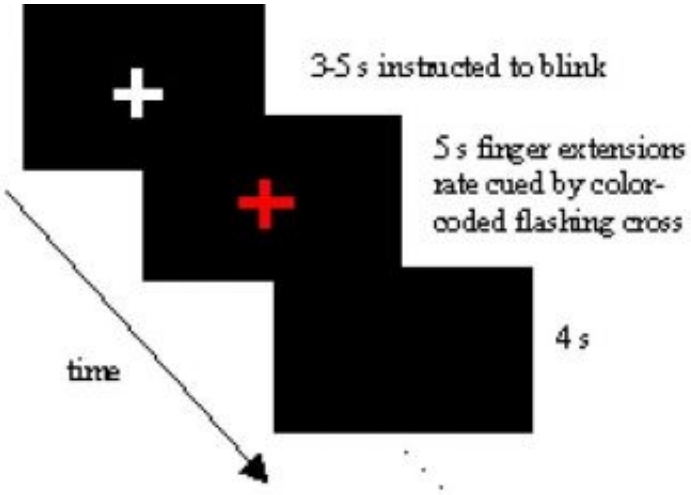

Figure 1. The task

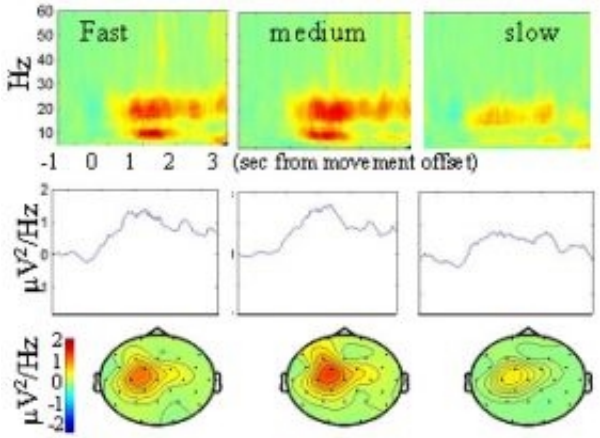

Figure 2. Beta rebound from a typical subject for the three different movement rates, electrode C3. The second row shows the beta waveforms that are used in the fMRI beta regressor. The third row shows the topography of the rebound for each condition.

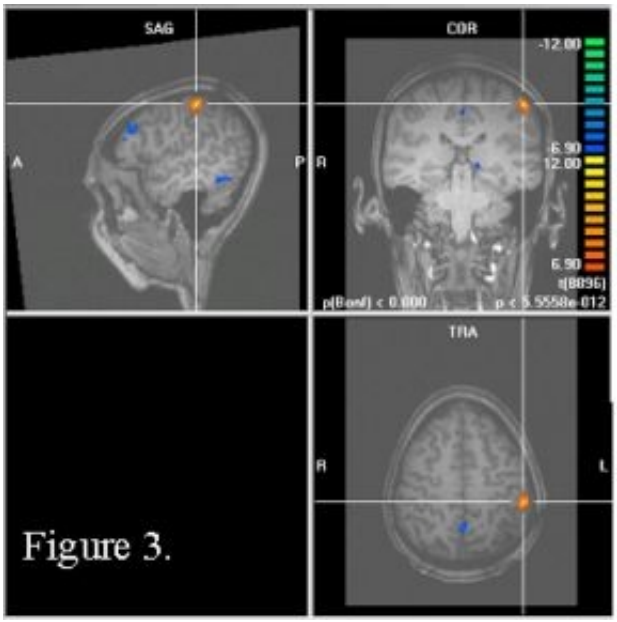

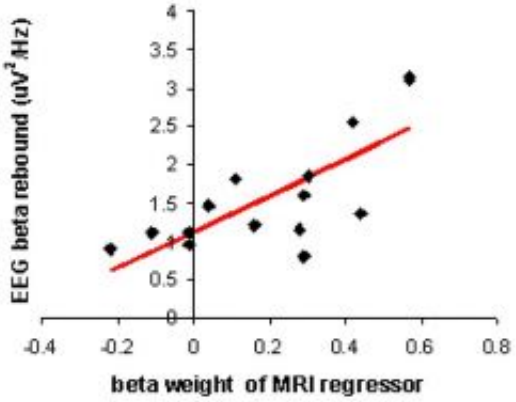

Figure 4. Positive correlation ($p<0.005$) of EEG and MRI data from each movement condition of 5 subjects. MRI beta weights are calculated using a general linear model with a uniform beta regressor for all conditions.

WE 276
Comparing Dynamic Causal Models

William D. Penny , Klaas E. Stephan , Andrea Mechelli , Karl J. Friston
Wellcome Department of Imaging Neuroscience, UCL, UK

Dynamic Causal Models (DCMs) [1] are used to make inferences about effective connectivity from functional Magnetic Resonance Imaging (fMRI) data. These inferences, however, are contingent upon assumptions about the connectivity pattern between the regions included in the model. Specifying this connectivity is often difficult due to the current lack of detailed knowledge of anatomical connectivity in the human brain. In addition, many plausible scientific hypotheses may exist about which connections could be changed by experimental manipulation. A formal procedure for comparing different connectivities is therefore highly desirable.

In DCMs fMRI activity is modelled as arising from neuronal activity, z, via the Balloon model [1]. Neuronal activity is modelled by the differential equation $dz/dt=(A+ \Sigma u_i B_i)z + Cu$ where u is a vector of experimental inputs and the matrices A, B and C contain 'intrinsic', 'modulatory' and 'input' connections. The connectivity assumptions in a DCM are defined by the structure of the A, B and C matrics (see eg. Figures, where connections in A and C have solid lines and connections in B have dotted lines).

Given a data set D we wish to compare a number of different models which we can index by j. We can then compute the evidence for model j, p(D|j). The Bayes factor for comparing model i to model j is defined as $B_{ij} = p(D|i)/p(D|j)$. To compute the evidence, however, we must evaluate the integral $p(D|j)= \int p(D|\theta,j)\, p(\theta|j)\, d\theta$, where θ are DCM parameters. In practice we approximate this integral using the Bayesian Information Criterion (BIC) and Akaike's Information Criterion (AIC). Information theoretic considerations lead to the definition of a criterion of 'consistent evidence' in favour of model i if $B_{ij} > 2.718$ for both AIC and BIC.

We applied the method to data from an 'attention to visual motion' experiment [1] in which subjects viewed a computer screen which displayed either a fixation point, stationary dots or dots moving radially outward. The 'photic' variable indicates the dots were on the screen, the 'motion' variable that the dots were moving and the 'attention' variable that the subject was attending to possible velocity changes. We then set up four different DCMs to model activity in the regions V1, V5 and Superior Parietal Cortex (SPC). All models were driven by photic stimulation, the intrinsic connections were assumed to be hierarchical and the connection from V1 to V5 was modulated by motion. In models 1 to 3 regions were reciprocally connected whereas in model 4 there were no backward connections. Models 1 to 3 differ as to which connections were modulated by attention. The Bayes factors in the table provide consistent evidence in favour of model 1. This example shows that Bayes factors, DCM and fMRI can be used to evaluate competing scientific theories about the large scale architecture of neural networks that mediate perception and cognition in the human brain.

References

[1] K. Friston, L. Harrison and W. Penny (2003) Dynamic causal modelling . Neuroimage, 19(4), pages 1273-1302.

	B_{12}	B_{13}	B_{14}
AIC	3.6	2.8	$>10^{20}$
BIC	3.6	19.6	$>10^{19}$

Bayes factors provide consistent evidence in favour of the hypothesis embodied in model 1 that attention modulates (solely) the forward connection from V1 to V5, in a reciprocally connected network.

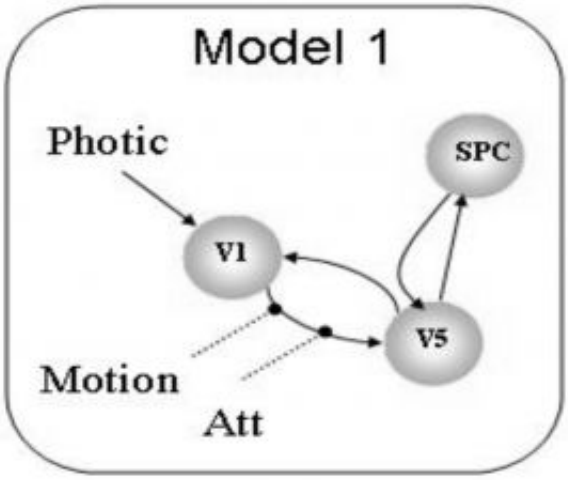
Model 1
Photic
SPC
V1
V5
Motion
Att

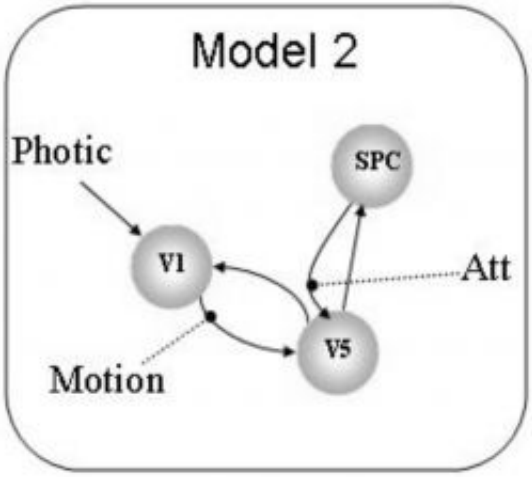
Model 2
Photic
SPC
V1
Att
V5
Motion

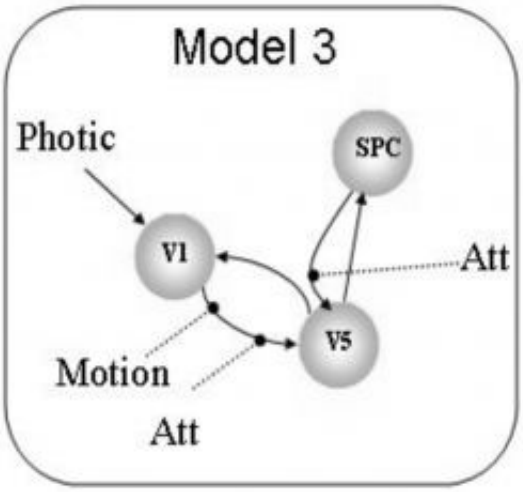
Model 3
Photic
SPC
V1
Att
V5
Motion
Att

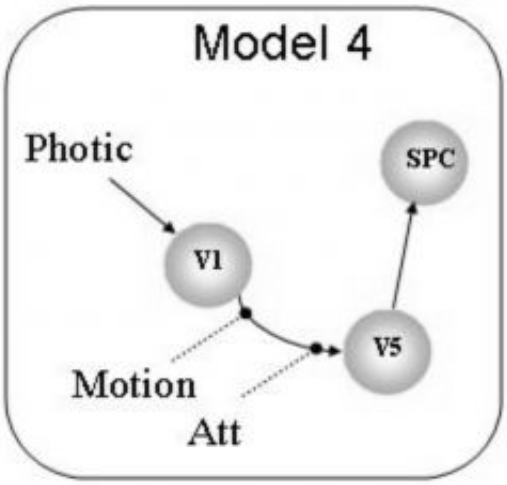
Model 4
Photic
SPC
V1
V5
Motion
Att

WE 277
Selection of spatially independent components to reduce physiological noise in fMRI data

Vincent Perlbarg [1,5], Pierre Bellec [1,5], Guillaume Marrelec [1,4,5], Saâd Jbabdi [1,5], Mélanie Pélégrini-Issac [2,5], Stéphane Lehéricy [3,5], Julien Doyon [1,4,5], Habib Benali [1,5]
[1] INSERM U494, Paris, France, [2] INSERM U483, Paris, France, [3] Service de Neuroradiologie CHU Pitié-Salpêtrière, Paris, France, [4] Université de Montréal, Montréal, Canada, [5] IFR49, Orsay, France

Introduction
FMRI is a non invasive technique using BOLD (Blood Oxygen Level Dependent) effect to explore neural activity. BOLD signal depends on neural heamodynamics and is corrupted by physiological activity (breathing and heartbeat). A recent technique based on Independent Component Analysis (ICA) has proved its efficiency to reduce physiological noise [1]. However, this method needs cardio-respiratory monitoring to identify physiological components to remove. Such information is usually unavailable in general fMRI settings. Nevertheless, spatial distribution of physiological noise is well known [2-3]. We therefore propose a new exploratory method which makes use of spatial information to identify physiology-related components of ICA.

Methods
On the one hand, decomposition of fMRI data was performed using the spatial ICA Infomax algorithm [4]. On the other hand, regions of interest with known preponderant physiological noise contribution (i.e. ventricles) were roughly manually delineated. We selected physiology-related components with a matching pursuit among the independent components calculated by ICA. The components were selected one by one in order to optimize the reconstruction of fMRI signals in the regions of interest at each step. Our method selected automatically the components whose contribution to the measured signals was statistically significant.

Results on real data
EPI functional data were acquired on two right-handed healthy volunteers performing motor tasks (finger tapping of both hands) alternated with rest (1.5T scanner, TR = 2000 ms, 73 T2*-weighted volumes of size 64*64*14, paradigm frequency = 0.03 Hz). Preliminary results on both subjects show that only three components were selected by our method (fig.1-3 showing results for one subject). The spatial distribution of components #4 and #5 was localized near blood vessels and their frequency contribution was preponderant around 0.16 Hz, which corresponds to the aliased cardiac frequency and suggests these components were related to cardiac effects. The spatial distribution of component #12 was localized around ventricles and its frequency contribution was preponderant around 0.09 Hz (in the admitted respiratory frequency-band), which suggests that this component was related to respiratory effects. Finally, we calculated the power spectrum of the signal of a single voxel randomly selected in the ventricles, before and after removing the three physiological components (fig.4), and verified that the cardiac and respiratory peaks were indeed removed.

Conclusion
We developed an exploratory method based on spatial information for identifying physiological components in a set of independent components, without any external monitoring of breathing and heartbeat. This new method automatically selects physiology-related ICA components with only priors on spatial distribution. This information is directly reachable and more reliable than time-frequency information. This original approach proved its efficiency on real data and yielded results consistent with a priori knowledge of frequency distribution of physiological activity. A more accurate study should be led to estimate the efficiency of the noise reduction in fMRI data with this method.

References
[1] Thomas et al. 2002 NeuroImage 17:1521-1537; [2] Dagli et al. 1999 NeuroImage 9:407-415; [3] Windischberger et al. 2002 MRI 20:575-582 ; [4] Bell et al. 1995 Neur. Comp. 7 :1129-1159.

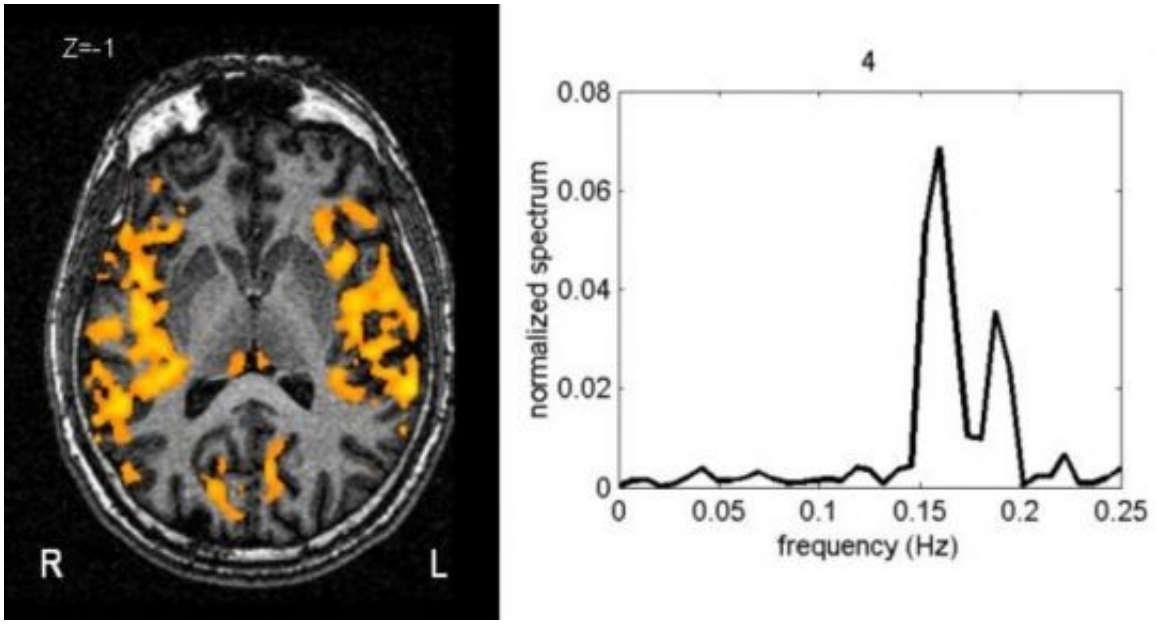

One slice of spatial component #4 superimposed to the corresponding anatomical T1-image and power spectrum of the corresponding time course.

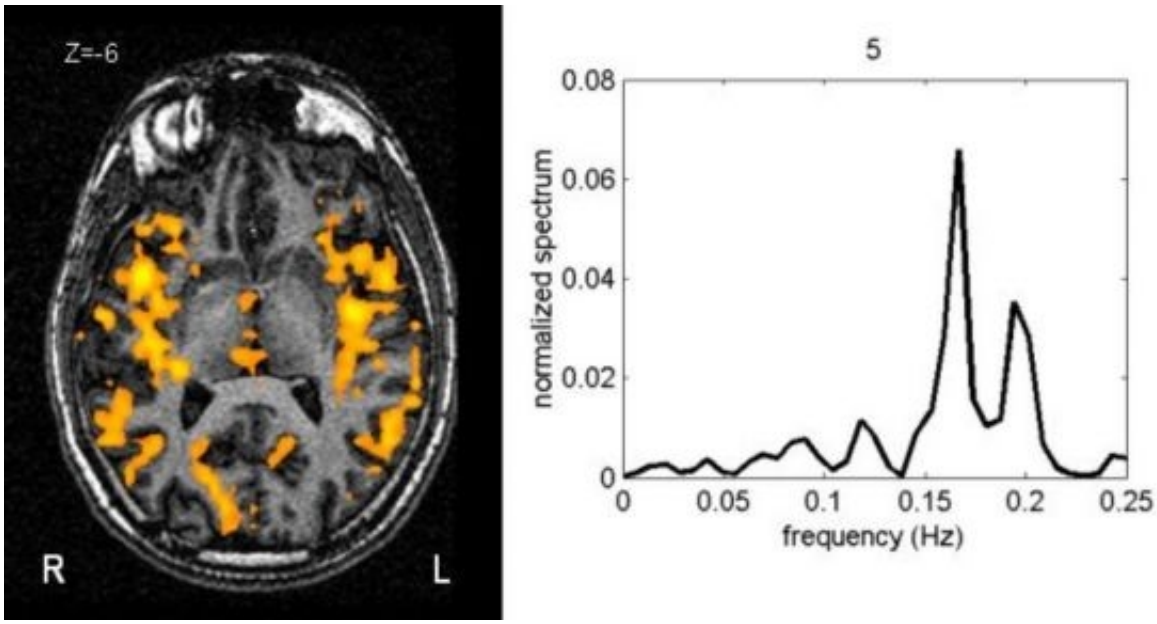

One slice of spatial component #5 superimposed to the corresponding anatomical T1-image and power spectrum of the corresponding time course.

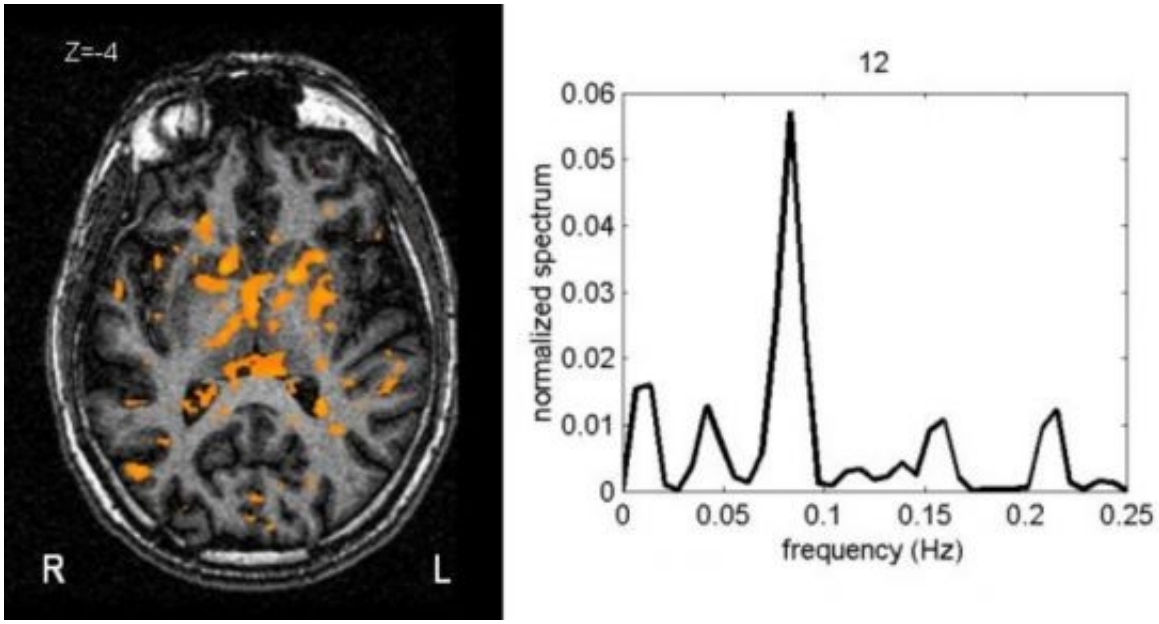

One slice of spatial component #12 superimposed to the corresponding anatomical T1-image and power spectrum of the corresponding time course.

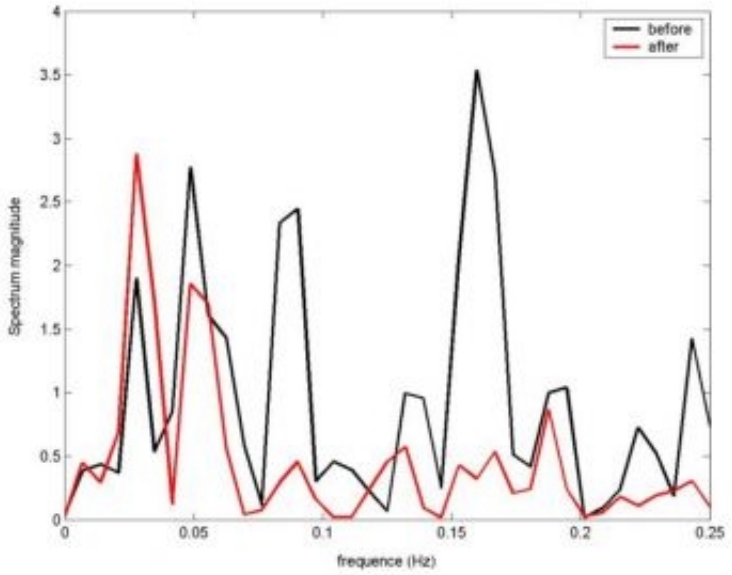

Power spectrum of a single voxel in ventricles before (black) and after (red) correction of physiological noise

WE 278

Effective Connectivity Differences in Mathematically Gifted Adolescents compared to Controls Performing Mental Rotation: An fMRI study

James Pescott[1,2], Maria Gavrilescu[1,2], Ross Cunnington[1], Michael O'Boyle[3], Gary Egan[1,2]
[1]Howard Florey Institute, University of Melbourne, Victoria 3010, Australia, [2]Centre for Neuroscience , University of Melbourne, Victoria 3010, Australia, [3]Department of Psychology, University of Melbourne, Victoria 3010, Australia

Introduction

We investigated two cohorts of male adolescents performing a 3D mental rotation task: a mathematically gifted group and an average mathematical ability group. The result of standard univariate (SPM99) analysis identified a more extensive brain network in the mathematically gifted group when compared to controls (1). Previous studies have concluded that mathematical intuition may arise from the interplay between anterior and posterior cortical systems (2) and that frontal lobe and anterior cingulate activation correlates with fluid intelligence (3). We aimed to further investigate these findings by studying the differences in the effective connectivity of a model of cortical activation in these two groups when performing mental rotation.

Method

Eight healthy controls (4RH; mean age 14.2 years, range 12-16; numerical IQ 111, SD 3) and eight gifted subjects (4RH; age 14.3, range 13-15; numerical IQ 133, SD 2) participated in the study. Subjects were presented 18 individual rotation trials, consisting of a single target stimulus and four test stimuli presented at 10sec intervals (1sec ISI). Subjects selected the test stimulus that matched the target by pressing one of four fibre-optic buttons. The control task required a similar response with the stimulus being the Fourier transform of the rotation stimulus and therefore had no identifiable shape. EPI scans were acquired on a GE 3T MR scanner (TR=3000ms, TE=40ms, FA=60^{o}, 128x128 matrix, voxel=1.875x1.875mm^2, slice thickness=4.5mm, inter-slice gap=0.5mm) with 132 volumes acquired per scanning session.

The data sets were motion corrected using Flirt (www.fmrib.ox.ac.uk/fsl/flirt) and an ICA decomposition (www.fmrib.ox.ac.uk/fsl/melodic) was performed to remove obvious artifacts(residual motion, slice dropout). The images were normalised to the SPM2 EPI template and smoothed (8mm FWHM). A fixed effects group analysis was performed for each cohort and ROI time courses extracted for a 8mm radius sphere centered on the the voxel with the largest Z score within each anatomically defined non-overlapping region, resulting in one time course per region. A network model (Fig 1) for each group included 9 regions: dorsolateral prefrontal, premotor, inferior and superior parietal regions bilaterally and a mid-line anterior cingulate region. The models were fitted using structural equation modeling (SEM) applied within condition and across subjects (AMOS 4.0, www.smallwaters.com.).

Results and Discussion

Good model fits were achieved for the gifted group (χ^2=16.89, df=14, p=0.262) and the control group (χ^2=18.95, df=17, p=0.330). Significant differences between the two groups were assessed with the nested (stacked) models approach (4) resulting in an overall significance difference (χ^2_{diff} = 108.7, df=40, p<< 0.05). When the connections between the anterior and posterior regions (red arrows in fig 1) were grouped and tested as coefficients of interest a fronto-parietal significant difference (χ^2_{diff} = 38.1, df=16, p= 0.0004) was observed with the average of the path coefficients for these connections in the control group being 74% of those for the gifted group. This difference was maximal in the right hemisphere where the average path coefficients for the control group were 45% of the gifted group compared to 95% in the left hemisphere. When the frontal connections (green arrows in fig 1) were tested the path coefficients for the control group were significantly different (χ^2_{diff} = 45.1, df=16, p= 0.00005) being 77% of the gifted group coefficients.

These results demonstrate that the model path coefficients intrahemispherically between the anterior and posterior cortical regions and between the frontal regions were significantly higher in the math gifted group than in the control group. Furthermore the right hemisphere fronto-parietal coefficients were further enhanced in the gifted group when performing mental rotation.

References

(1) O'Boyle et al submitted
(2) Dehaene et al (2002). Science, 284, 970-974
(3) Duncan, J. (2003) Nature Neuroscience, 6, 207-208
(4) McIntosh, AR and Gonzales-Lima, F (1994) Human Brain Mapping 2:2-22

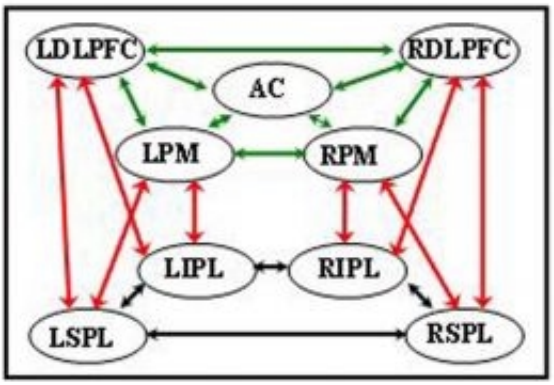

Figure 1: Proposed anatomical model for mental rotation.

WE 279
Statistical assessment of linear and nonlinear causal interactions

Mark E Pflieger
Source Signal Imaging, Inc.

A major task of large-scale neurocomputational theory is to explain how space-time interactions inside the brain participate in (and somehow signify) relationships outside the brain that engage the central nervous system as a whole. One facet of this task is to develop a framework for inferring space-time *causal* interactions via whole-brain modalities such as M/EEG and fMRI. An information theoretic framework for treating linear and general nonlinear time-lagged interactions (between brain regions, mediated by white matter) was introduced at last years meeting [1]. The present report focuses on *statistical assessment* of causal information.

Brain region A causally influences region B at lag s if A's state at time t, A(t), predicts (to some degree) B's subsequent state, B(t+s), *discounting* contributions from noncausal conditions such as B(t), A(t+s), or states of another region C that mediate apparent interactions. *Predictive information* is the simple mutual information quantity I(A(t),B(t+s)), whereas *causal information* is the *conditional* mutual information quantity I(A(t),B(t+s)|A(t+s),B(t),C(t),C(t+s),). These are computed via multivariate differential entropies, which are relative to the state vector coordinate systems. *Linear* entropy relative to original state coordinates equals the entropy change after a sphering transformation has removed all Gaussian content from the joint state distribution. *Nonlinear* entropy is computed relative to the sphered states, and thus depends on residual non-Gaussian properties.

Four measures of inter-regional brain interactions in this framework are: linear predictive (LP), nonlinear predictive (NP), linear causal (LC), and nonlinear causal (NC). Because LP and NP are based on simple mutual information, a correspondingly simple statistical test for these may be constructed by operating directly on the state data to destroy all joint timing relationships between A(t) and B(t+s). By contrast, special surrogate data generation is required to construct randomization tests for LC and NC, because it is required to selectively destroy only those relationships between A(t) and B(t+s) that are unmediated by the noncausal conditions (i.e., mediated relationships must be preserved). Because LC is concerned only with Gaussianity, its surrogate data generation process may utilize covariance matrices of a particular form. NC must use a different method that can handle general probability distributions.

To illustrate detection of causal interactions between brain regions of interest, these methods are applied to ongoing EEG data, using regional source estimation (REGAE) and singular spectrum analysis (SSA) to estimate regional brain states.

[1] Pflieger ME (2003): Time-lagged causal information: a new metric for effective connectivity analysis. HBM 2003 poster, online at www.sourcesignal.com/papers.html.

WE 280
Dynamic ReML solution for the EEG source reconstruction problem

Christophe L. Phillips[1], Jérémie Mattout[2], Pierre Maquet[1], Karl J. Friston[2]
[1]Cyclotron Research Centre, University of Liège, Belgium., [2]Welcome Department of Imaging Neuroscience, University College, UK.

Distributed linear solutions of the EEG source localization problem are used routinely. In contrast to discrete dipole equivalent models, distributed linear solutions embody no assumptions about the number of active sources and lead to a discretized fully 3D representation of electrical activity in the brain. However the problem is under-determined and, to ensure the uniqueness of the solution, constraints are required. In a Bayesian framework, the conditional expectation of the source distribution, given the data, is attained by carefully balancing the minimization of the residuals induced by noise and the improbability of the estimates as determined by their priors [1]. This balance is specified by hyper-parameters that control the relative importance of fitting and conforming to various constraints. In [2] the conventional "weighted minimum norm" (WMN) solution was formulated in terms of hierarchical linear models. An "Expectation-Maximization" (EM) algorithm was used to obtain a "Restricted Maximum Likelihood" (ReML) estimate of the hyper-parameters, before estimating the Maximum a Posteriori solution itself.
Usually hyper-parameters are estimated as time invariant constants (stationarity assumption) for the ERP time series (or some extended time window). Here we introduce a dynamic or non-stationary ReML solution, by allowing the hyper-parameters to change smoothly over time. A sliding window is used to estimate an instantaneous sample covariance matrix, from which the time-varying hyper-parameters are estimated.
The approach was tested on a simplified 2D source model: 1716 oriented dipoles spread on a horizontal plane within a sphere. The leadfield for each source was calculated for a set of 29 electrodes spread uniformly on the upper hemisphere of the sphere. Spatial basis functions were extracted to reduce the solution space a priori [3]. 200 pairs of source sets were generated at random locations. With each source set, time extended data sets were obtained, see figure 1, and scaled white noise was added to emulate an ERP, with early and late components, see figure 2,. For each data set, the stationary and non-stationary ReML solutions were calculated with different source (co-)variance constraints: with accurate and/or inaccurate location priors. The non-stationary ReML approach proved useful, in comparison to the stationary one, as: (i) The time course of the sources was recovered more accurately and showed less spurious activity, with the non-stationary solution. (ii) When accurate location priors were used, their constraint weights were appropriately modulated over time and localization error was negligible. (iii) When accurate and inaccurate location priors were used simultaneously, the solution was not influenced by the inaccurate priors.
1. Phillips C., Rugg M.D., Friston K.J., Systematic noise regularization of linear inverse solutions of the EEG source localisation problem, 2002, NeuroImage, 17, 287-301.
2. Phillips C., Mattout J., Rugg M.D., Maquet P., Friston K.J., Classical Parametric empirical Bayes solution of the source reconstruction problem in EEG, Submitted.
3. Phillips C., Rugg M.D., Friston K.J., Anatomically informed basis functions.for EEG source localization: Combining functional and anatomical constraints, 2002, NeuroImage, 16, 678-695.
Supported by FNRS, Belgium

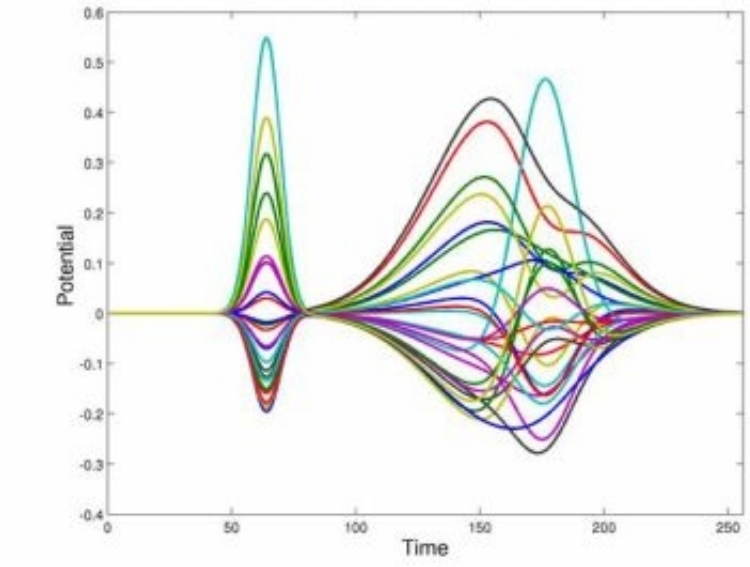

Noise free data.

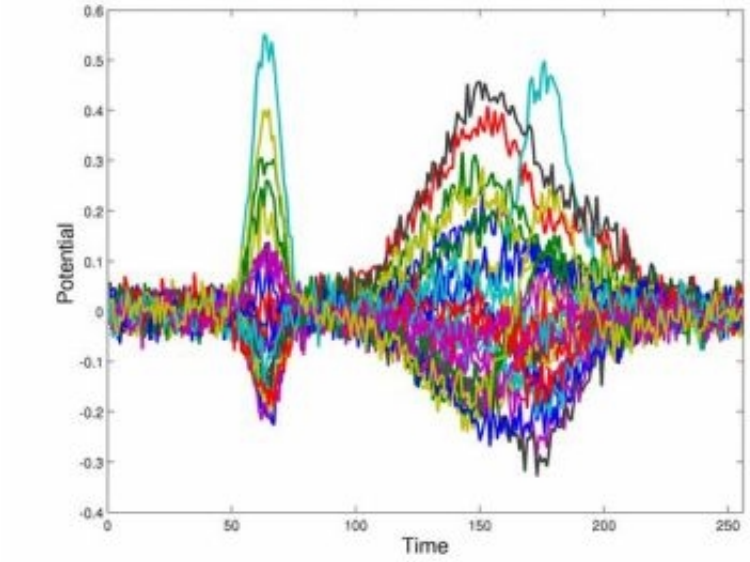

Data with added white noise

WE 281
Modeling Shape in a Self-Adoptive Segmentation Algorithm

Kilian M Pohl[1], Samson Timoner[2], Ron Kikinis[2], W. Eric L. Grimson[1]
[1] Artificial Intelligence Laboratory, Massachusetts Institute of Technology, Cambridge, MA, USA., {kpohl,samson,welg}@ai.mit.edu, [2] Surgical Planning Laboratory, Harvard Medical School and Brigham and Womens Hospital, 75 Francis St., Boston, MA, USA, kikinis@bwh.harvard.edu

1. Introduction
For many age and disease related brain studies, large quantities of MRI Images have to be segmented into anatomical regions. Completing this task manually is very time consuming, therefore researchers often rely on automatic methods. Many regions have barely visible boundaries like the thalamus making it quite challenging for automatic methods to achieve high quality segmentation. We address this problem by introducing an intensity-based segmentation method that includes prior information on shape and location.

2. Method
Our method is based on an Expectation Maximization algorithm (EM) incorporating shape constraints and spatial distributions of anatomical structures. The method is characterized by the Segmentation Step (S-Step) and Deformable Model Step (D-Step) (see Figure 1). The S-Step, which captures image intensity, is defined by the EM method which estimates the bias field and tissue likelihood (see [1]). The D-Step captures the shape of anatomical structures through a deformable model [2]. It first analyzes the results of the S-Step for errors. Then it deforms the shape model based on the error corrected results, thereby adding shape information. The results of the deformable model are returned to the S-Step by updating the anatomical structure's spatial distribution. These two steps are repeated until convergence is reached.

3. Results
To validate our method we segmented 39 MRI images with and without shape priors. The images were parcellated into background, cerebrospinal fluid, gray matter, white matter, and right and left thalamus. We compared these results to manual segmentations of the thalamus using the Dice measure. In fifteen cases the initial non-rigid alignment of the spatial distribution failed so that the Dice measure of the two automatic method was below 75%. In the remaining twenty-four cases, the method with shape outperformed the one without shape for the left thalamus by an average of 3.3%, which is due to the smoother results (see Figure 2). For the right thalamus, the method with shape constraints only achieved better results in fifteen of the twenty-four cases when compared to the method without shape constraints. By tailoring the D-Step closer to the segmentation scenario, this can be easily fixed.

4. Summary and Conclusions
We presented a new approach that allows high quality segmentation of anatomical structures with barely visible boundaries. While the shape constraints generally increased the quality of the EM segmenter, it did not achieve the reliability wanted. We believe that an integration of the shape model, as hidden data or parameters in the EM framework, will solve this problem.

Acknowledgments
This research was supported by the Brain Morphometry Biomedical Informatics Research Network (BIRN, www.nbirn.net), which is funded by the National Center for Research Resources at the National Institutes of Health.

References
1. K.M. Pohl, W.M. Wells, A. Guimond, K. Kasai, M.E. Shenton, R. Kikinis, W.E.L. Grimson, S.K. Warfield, Incorporating Non-Rigid Registration into Expectation Maximization Algorithm to Segment MR Images, in MICCAI, pp. 564 572, 2002.
2. S.J. Timoner, W.E.L. Grimson, R. Kikinis and W.M. Wells, Fast Linear Elastic Matching without Landmarks, in MICCAI, 2001.

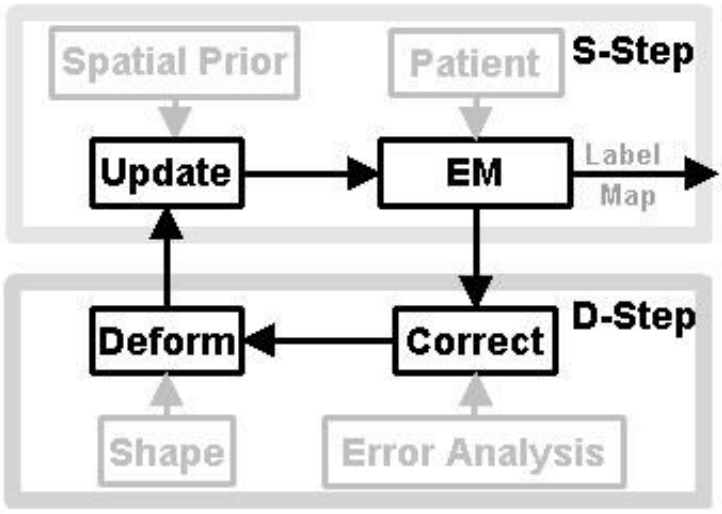

Figure 1: ***The Algorithm consists of two steps. In the Segmentation Step (S-Step) the bias field and tissue likelihood are estimated. The Deformable Model Step (D-Step) captures shape of anatomical structures.***

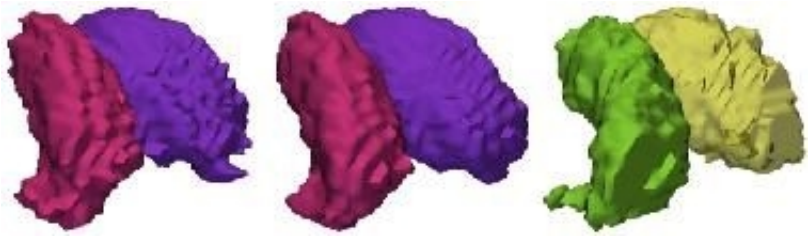

Figure 2: ***3D models of the right (maroon) and left (violet) thalamus generated by the segmentation algorithm without shape prior (left), the new algorithm with shape priors (middle), and a manual segmentation (right). Note that the thalami produced by the new algorithm (middle) are significantly smoother than the other thalami, which have protrusion and sharp edges.***

WE 282
Using neural network algorithms to investigate distributed patterns of brain activity in fMRI.

Sean M Polyn , Leigh E Nystrom , Kenneth A Norman , James V Haxby , M Ida Gobbini , Jonathan D Cohen
Center for the Study of Brain, Mind and Behavior; Dept. of Psychology, Princeton University, Princeton NJ, USA

Introduction. We describe a method for using error-driven neural network algorithms to classify and investigate distributed patterns of activity drawn from a number of fMRI experiments. There are currently several techniques available for classifying these distributed patterns (Haxby et. al, 2001; Cox & Savoy, 2003; Carlson et. al, 2003), however, the use of neural networks has several advantages, including increased classification performance and the ability to use smaller temporal slices of data. Existing methods have focused on using these techniques to investigate the brain representations of perceptual categories, but the technique has broader applicability, as we will show in our investigation of frontal control of task performance. We compare the neural networks to other analysis techniques (including support vector machines and linear discriminant analysis).
Preprocessing of data. Raw signal from the scanner is motion corrected. Individual voxel timecourses are detrended and transformed to z-scores. We average the signal over some number of TRs; the size of the averaging window is explored. An ANOVA is performed on each voxel to determine if it significantly varies over the conditions of interest. The resulting set of significantly varying voxels are used to create input patterns for a neural network.
Neural network algorithms. Two types of error-driven neural network architectures are investigated, a set of backpropagation algorithms and Leabra (OReilly, 1998), which uses a mixture of error-driven and Hebbian learning (network diagram shown in fig. 1). During the iterative training process, the networks become sensitive to regularities in the data that allow them to categorize the patterns. Once trained, the networks are tested for generalization on a set of never-before-seen input patterns.
Results and discussion. The networks were used to reanalyze data from Haxby et. al (2001), in which subjects viewed visual stimuli from 8 categories (examples: faces, houses and cats). The networks were also applied to unpublished data on similar, but more subtle categories (including male versus female faces). In many cases, the networks perform near ceiling. Furthermore, the networks were applied to data from the frontal lobe of these subjects, with similar performance. Finally, we apply the networks to task-switching data, in an attempt to classify frontal patterns associated with task performance.
This nonlinear, multivariate technique is broadly applicable to neuroimaging data analysis; we begin here to explore the promise of the technique. By exploring the weight structure of the trained network we attempt to identify the voxels of interest: Those voxels that were the most important for the network to make its categorization. This set of voxels are then used to create subject-specific masks for each category, for use in standard event-related analysis techniques. Finally, we present a first attempt at correlating network-based measures (such as classification performance and hidden state analysis) with behavior of the subject.
References.
Carlson et. al, 2003. Journal of Cognitive Neuroscience 15: 704-717.
Cox & Savoy, 2003. NeuroImage 19: 261-270.
Haxby et. al, 2001. Science 293: 2425-2430.
OReilly, 1998. Trends in Cognitive Sciences 2: 455-462.

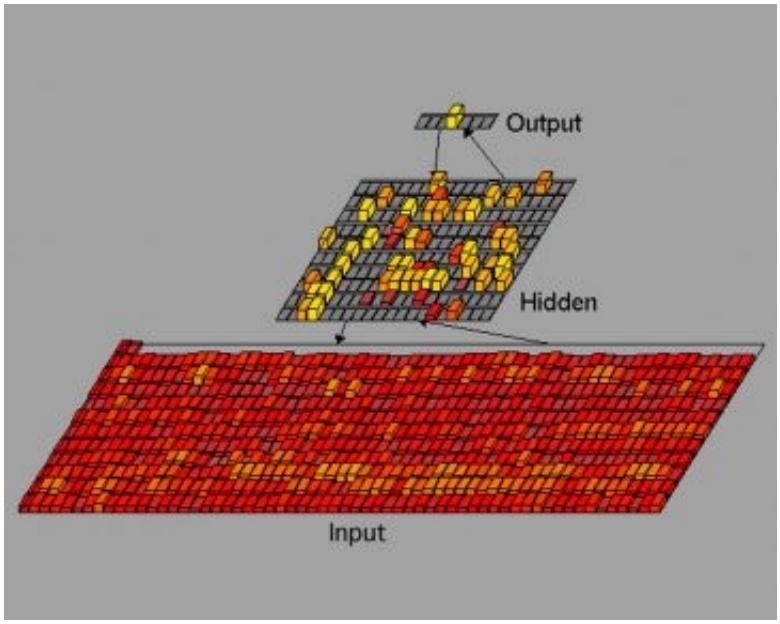

Figure 1: ***A screenshot of the Leabra network used to classify imaging data.***

WE 283
A Parametric Statistical Model for Measuring Cortical Thickness

Anqi Qiu[1], Patrick Barta[2], Michael Miller[3]
[1]Dept. of Electrical Computer and Engineering, Johns Hopkins University, Baltimore, MD 21218, [2]Dept. of Psychiatry, Johns Hopkins University School of Medicine, MD 21205, [3]Center of Image Science, Johns Hopkins University, Baltimore, MD 21218

Recent anatomical MRI studies on the human brain have been focused on the cerebral cortex, which is a highly folded sheet of gray matter. The cortical thickness varies between 1.3mm and 4.5 mm in the various parts of the brain, with an overall average of about 2.7mm[1]. Cortical thickness becomes interesting in a wide variety of studies on neurodegenerative and psychiatric disorders, such as aging, Alzheimer's disease and other dementias, Huntington's disease, sclerosis and schizophrenia. Recent measurements of cortical thickness are based on segmentation information from MRI volumes. Thickness has been measured as the distance between exterior and interior surfaces (the boundary between the gray matter and cerebrospinal fluid (CSF) and the boundary between the white and gray matter)[2,3,4]. However, accurate extraction of the outer surface remains a major problem, especially when two gyri in reality separated by CSF appear fused in MRI images due to the resolution of MRI images and highly folded structure of the cortex. Unlike other methods, we provide an innovative parametric statistical model, which nowhere needs the reconstruction of the exterior surface. The goal of this model is to give more accurate measurement of the cortical thickness for not only unburied cortex but also buried cortex.
Our approach is built on the construction of local normal coordinate system, for which we introduce an orthogonal frame consisting of two axes spanning the tangent plane to the interior surface and the third normal axis measuring the relative normal distance from the interior surface to the center of individual voxels[5]. Our basic insight is that the cortical thickness is directly evidenced by the change in tissue type as a function of the normal distance. For example, the white matter has a negative normal distance and the gray matter as well as CSF has a positive normal distance. However, CSF has a greater distance than the gray matter does. Therefore, instead of the conventional intensity histogram, we generate the Intensity-Distance Histogram (IDH) which is a two-dimensional data structure counting the number of voxels of some image intensity at a particular distance interval. The amount of voxels at various distances is modeled as a Poisson arrival process; the distribution of intensity at a particular distance is modeled as a Gaussian random field conditioned by the normal distances. Based on these two assumptions, the log-likelihood function of IDH is parameterized by the cortical structural parameters that can be measured by Maximum Likelihood Estimation over the statistical law.
The advantage of this model is that it can be applied in estimating the thickness for small cortical regions of interest. In addition, it also measures the variation of the interior surface location and the effect of the partial volume.

Refereces:

[1] von Economo, C., Oxford Univ. Press, London, 1929.
[2] Fischl B. and Dale A. M. PNAS, 97:11050-11055, 2000.
[3] Zeng X. et. al. IEEE TMI, 18:100-111, 1999.
[4] MacDonald D. et. al. NeuroImage, 12:340-356, 2000.
[5] Miller M. I. et. al., PNAS, 100:15172-15177, 2003.

Research supported by NIH R01 MH60590-05.

WE 285

Assessment of False Alarm and Missed Detection in fMRI Phase-Encode Mapping

Ashish A Rao[1], Thomas M Talavage[1,2,3]

[1]School of Electrical and Computer Engineering, Purdue University, [2]Department of Biomedical Engineering, Purdue University, [3]Department of Radiology, Indiana University School of Medicine

Introduction

Spatial variation of response properties of visual [1] and auditory [2] cortex has been imaged in fMRI using phase-encode techniques. Such techniques produce one-to-one mappings of stimulus properties to experiment time. For each cortical location, the averaged response to multiple presentations of the time-varying stimulus is computed and maps of Fourier phase (proportional to latency) are generated. Phase-encode maps rely on response latency being invariant across cortex. However, latency of fMRI response has been found to exhibit spatial and temporal non-stationarity of ~3s [3]. In this work we examine, via simulation, impact of latency variance on phase-encode mapping. Our findings indicate that error rates remain acceptable, particularly for multi-subject analyses.

Methods

Data Synthesis: Simulated data were used to evaluate rates of missed detection (P_M) and false alarm (P_{FA}) for three levels of latency variance, assuming a 64s stimulus. Latencies as a function of position were generated for a matrix of size 7x[3*(K-1)+1], where K (=4-7 voxels), was chosen to be representative of the linear size (in 3mm voxels) of sensory cortical areas. For rows 1,4 and 7, end-points (shortest and longest latencies) were generated to fall within the first and last thirds of the [0,1) response cycle. Every 3rd data point was generated to be (P_M) uniformly spaced-assuming stimulus variation maps linearly onto cortex-between end-points, or (P_{FA}) random, with uniform distribution between end-points. Two uniformly distributed random noises, jitter ([-J,J], J=0.0125, 0.025 cycles) and latency ([0,N], N=0.05, 0.1, 0.15 cycles) were added to each point. Corresponding latency variances are consistent with results of [3], assuming neuronal activity will persist for ~15 of 64 s. Remaining elements were generated through bilinear interpolation, modeling high-resolution tessellation in flat mapping. A 3x3 kernel was applied three times to obtain nearest-neighbor weighted averages, consistent with analysis procedures in [1] and [2]. *Data Analysis:* Deviations from monotonicity were identified using a window (0.05 cycle half-size) progressed along each row, centered at 0.05, 0.15,..., 0.95 and then 0.0, 0.1, ..., 1.0. The spatially first and last active voxels (defined by the temporal window) were examined for retrograde motion. Monotonicity detection required non-decreasing advancement of spatially first and last active voxels in both checks, for 4 adjacent rows.

Discussion

P_M was ≤5.6%, occurring for worse-than-expected maximal latency of 0.15 cycles . P_{FA} was notably larger (>7%) for short maps (<5 voxels), but was acceptable (<3%) for maps ≥6 voxels (16mm) in linear size. If observation in 3 of 5 subjects is required, the worst-case group P_{FA} is <5%. Therefore, we conclude that the dominant error in phase-encode mapping is not due to latency variation, but produced by interaction of imaging volume with size of, and non-linear representation of properties in cortical areas.

References

[1] Sereno et al., Sci, 268:889-893, 1995
[2] Talavage et al., J Neurophys, Mar 2004
[3] Saad et al., HBM, 13:74-93, 2001

Empirical Type I and Type II Error Rates (10^6 trials)

Map Length (K; #voxels)	Max Latency (N; cycles)	P_M J=0.0125 cycles	P_{FA} J=0.0125 cycles	P_M J=0.0250 cycles	P_{FA} J=0.0250 cycles
4	0.05	$<10^{-6}$	0.120	$<10^{-6}$	0.122
	0.10	$<10^{-6}$	0.130	$<10^{-6}$	0.132
	0.15	$<10^{-6}$	0.143	$3.0x10^{-6}$	0.144
5	0.05	$<10^{-6}$	0.076	$<10^{-6}$	0.076
	0.10	$<10^{-6}$	0.077	$<10^{-6}$	0.077
	0.15	$2.6x10^{-4}$	0.077	$9.3x10^{-4}$	0.077
6	0.05	$<10^{-6}$	0.023	$<10^{-6}$	0.022
	0.10	$5.0x10^{-6}$	0.022	$1.0x10^{-4}$	0.023
	0.15	0.009	0.021	0.015	0.022
7	0.05	$<10^{-6}$	0.004	$<10^{-6}$	0.004
	0.10	$3.2x10^{-4}$	0.004	0.002	0.004
	0.15	0.042	0.004	0.056	0.004

WE 286
PVElab: Software for correction of functional images for partial volume errors

Thomas Rask[1], Tim Dyrby[1,2], Marco Comerci[3], Mario Quarantelli[3], Bruno Alfano[3], Karim Berkouk[4], Jean-Claude Baron[4,5], Alan Colchester[6], S. Ali Hojjat[6], Gitte M. Knudsen[1], Olaf B. Paulson[1,2], Claus Svarer[1]
[1]Neurobiology Research Unit, Rigshospitalet, Copenhagen, Denmark, [2]Danish Research Centre for Magnetic Resonance, Hvidovre Hospital, Denmark, [3]Biostructure and Bioimaging Institute, National Council for Research, Naples, Italy, [4]INSERM E0218, Cyceron, Caen, France, [5]Dept. of Neurology, University of Cambridge, UK, [6]Kent Institute of Medicine & Health Sciences, University of Kent at Canterbury, UK

Introduction: A major problem using functional SPECT and PET images is the relatively low resolution in the images the so-called partial volume effect. In this abstract a common software framework for controlling the process of correcting the functional images using structural information derived from structural MR images, is presented. The software is implemented in Matlab (Mathworks Inc.) and includes tools for controlling the process, logging the results, presenting the results, and it is easily extensible to include own methods for each step in the process.

Methods: The interface to the PVElab software tool is illustrated in Fig. 1. The partial volume correction process includes interfaces to standard software that can handle the following steps in a partial volume correction process:

· Loads and converts functional and structural information images into the software (Dicom or Analyze format).
· Identifies alignment parameters between functional and structural images (interface to public domain software SPM2[1] and AIR[10] and NRU software for manual alignment[9]).
· Segments structural images into gray and white matter classes (interface to SPM2, Naples[5] and Canterbury routines).
· Reslices structural images to match functional images (BrainWarp[2], AIR, and trilinear interpolation).
· Applies template atlases on the functional images (ROIs/VOIs) (Naples strict Talairach approach[6] and NRU[8] methods).
· Conducts partial volume correction (Naples[5] implementation of published available methods[3;4;7]).

Further, the toolbox also includes software for visualization of the outcome from any steps and the toolbox allows for very easy incorporation of external methods at any stage along the process.

Conclusion: PVElab is available as a research tool for correction of functional SPECT and PET images. It can be downloaded from http:/ /nru.dk/publications/downloads/PVElab.tar.gz for free. The software facilitates an automatic partial volume correction of functional images and new or in-house methods can easily be incorporated in the toolbox at any stage in the process.

Acknowledgment: EU fifth framework program QLG3-CT2000-00594 PVEOut has funded the project.

References:

1. J. Ashburner and K. Friston, Neuroimage 6, 209-17 (1997).
2. Kjems, U. et al., IEEE Trans Med Imaging 18(4), 306-19. 99.
3. Meltzer, C. C. et al., J Comput Assist Tomogr 14(4), 561-70. 90.
4. Muller Gartner, H. W., et al., J Cereb Blood Flow Metab 12(4), 571-83. 92.
5. M. Quarantelli et al., J Nucl Med (2004).
6. M. Quarantelli et al., Neuroimage 17, 373-84 (2002).
7. Rousset, O. G et al., J Nucl Med 39(5), 904-11. 98.
8. Svarer, C et al., Society of Nuclear Medicine. 50. 2003. Reston, VA, USA ,
9. Willendrup, P. et al., NeuroImage., 16(3), S85. 2002.
10. Woods, R. P. et al.,J Comput Assist Tomogr 17(4), 536-46. 93.

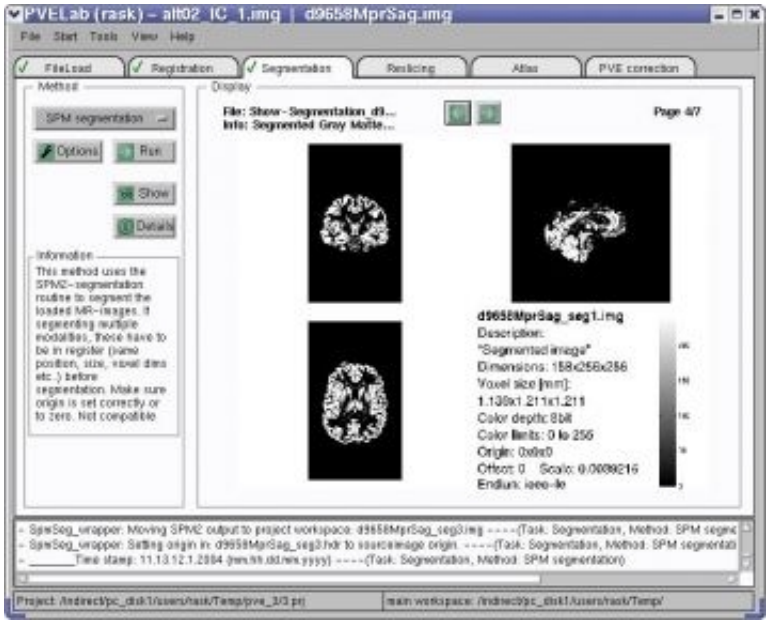

Figure 1: PVElab user interface, segmentation step completed.

WE 287
ParcelMan and Pigment: interactive tools for parcellation of cortical grey matter

Kelly Rehm[1], Lili Ju[2], Josh Stern[3], Kirt Schaper[3], David Rottenberg[3]
[1]Department of Radiology, University of Minnesota, Minneapolis, USA, [2]Institute for Mathematics and its Applications, University of Minnesota, Minneapolis, USA, [3]Department of Neurology, University of Minnesota, Minneapolis, USA

Labelling an MRI brain volume is a demanding task -- tracking sulci and gyri through a 3D volume is non-trivial. Volume labelling is voxel-based and typically performed using orthogonal slices through the volume. When a cortical surface is extracted from an MRI volume it acquires its labels from the voxel labelling and, ideally, the surface labels are reconciled with the volume labels. In practice, flaws in a volume labelling can become apparent when they are transferred to an extracted cortical surface (Figure 1, left).

Although much of the cortical surface is buried, examination of the cortex is useful for tracking gyri and defining anatomical landmarks. A surface represented by a triangulated mesh with the appropriate topology can be remapped to a sphere or "inflated" brain to reveal buried cortex [1,2,3].

ParcelMan permits a user to paint labels on linked representations of the cortical surface -- one folded ("wrinkled") and one conformally mapped to a sphere (Figure 1, right). This permits the user to view buried cortex and define contiguous patches.

Embedding a surface labelling into an MRI volume can guide creation or correction of a voxel-based labelling but leaves the majority of cortical voxels unlabelled. To address this problem we have developed a tool (Pigment) for allowing surface paint to "seep" into cortical grey matter. The seepage is governed by directionality and tissue-weighting rules, and a contiguous patch of surface is expected to contribute to subjacent cortex.

In a pilot experiment the cortical surface of a left hemisphere was extracted from a T1 MRI volume; anatomical labels for that volume were provided by N. Kabani, University of Toronto. Gyral labels for the volume were grouped into lobe labels (Figure 2; left) and used to provide labels for the cortical surface. Grey-white tissue segmentation [4] of the MRI volume identified the voxels where seepage was permitted. Surface labels were corrected to form contiguous patches (Figure 2; center) and allowed to seep into the cortex (Figure 2; right). Although not every sulcus was accurately represented in our surface mesh, the labels that were propagated into the MRI volume from the mesh reproduced the expert labels in 88% of grey-matter voxels. Of the mismatched labels, some resulted from problems in the expert labelling -- as evidenced by isolated white voxels (Figure 2; left).

We hypothesize that using a labelled cortical surface to initialize volume labelling can significantly reduce the effort of manual parcellation, and that a combination of surface- and volume-based tools will permit volume and surface labels to be reconciled in a principled manner.

1. Hurdal M, et al.(1999). *Lec. Notes in Comp. Sci.* Springer-Verlag, Berlin. Vol 1679; 279-286.
2. Fischl B, et al.(1999). *NeuroImage* 9(2):195-207.
3. Ju L, et al. (2004). *NeuroImage* 19:S864.
4. Collins D,et al. (1995). *Human Brain Mapping*, 3(3):190-208.

This work was supported in part by NIH grant EB02013.

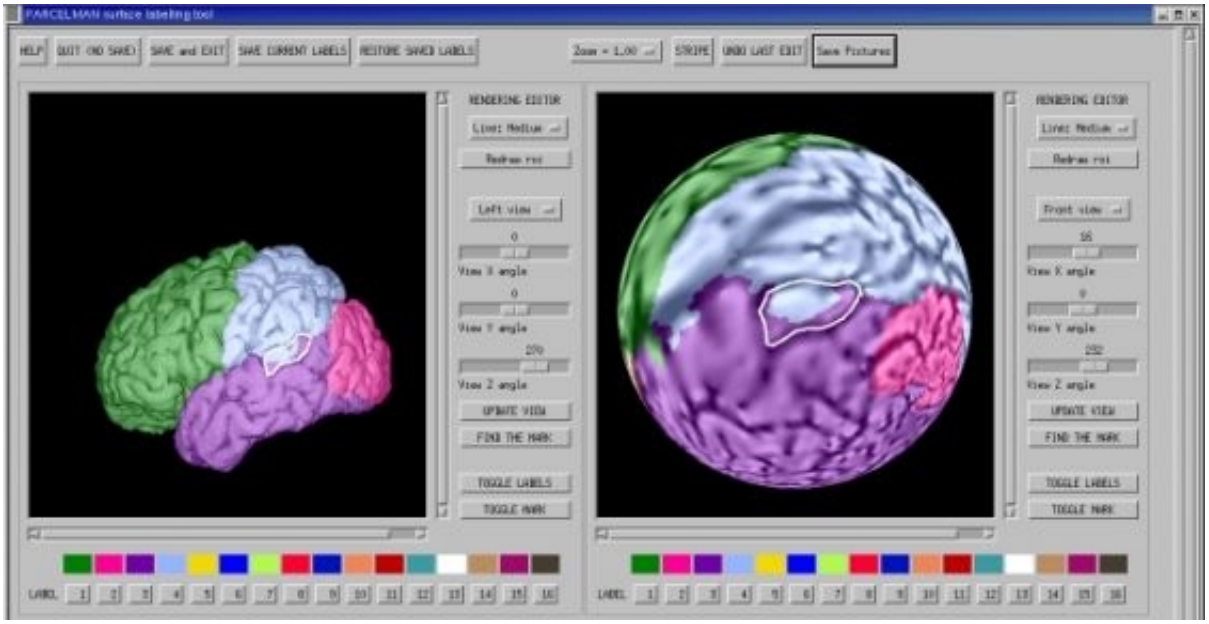

Figure 1. Cerebral surfaces displayed within ParcelMan (Left: folded surface; Right: surface conformally mapped to a sphere). The white outline indicates a portion of mislabelled cortex.

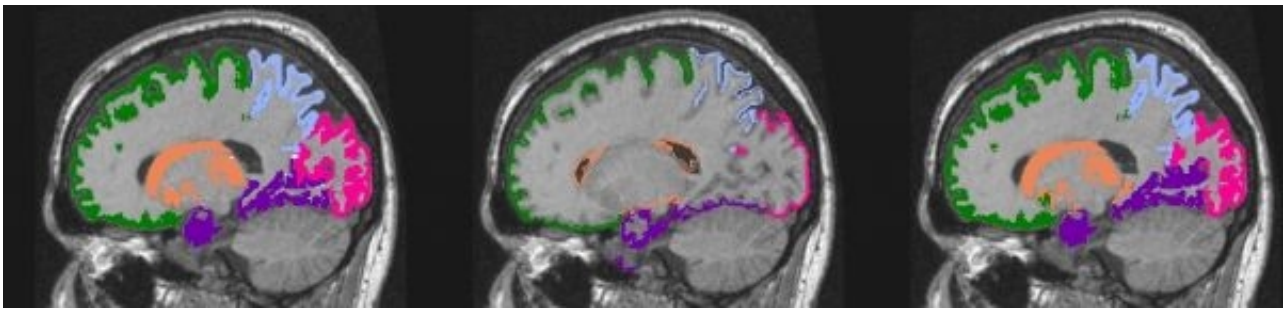

Figure 2. Surface-based labelling. Left: expert volume labelling; Center: surface labels derived from expert labels; Right: volume labels automatically derived from surface labels.

WE 288
Multi-variate analysis: a tool for examining influences of mask and polynomial order on non-linear registration of T1-MRI volumes

Kelly Rehm[1], Stephen C Strother[1], Jon R Anderson[2], Roger P Woods[3], David A Rottenberg[2]
[1]Department of Radiology, University of Minnesota, Minneapolis, USA, [2]Department of Neurology, University of Minnesota, Minneapolis, USA, [3]Department of Neurology, University of California, Los Angeles, USA

Spatial normalization of a structural MRI volume to a standard coordinate system is an essential preprocessing stage in inter-subject voxel-based analysis of functional neuroimaging data. Automated Image Registration (AIR5, [1]) is a widely used non-linear "warping" algorithm that achieves spatial normalization by employing high-order polynomials to co-register an MRI volume to a reference volume in the desired coordinate space. It is recommended that MRI volumes be spatially masked before registration by AIR; the design of the algorithm is such that variation in a spatial mask will affect the ultimate registration of volumes (to an unknown degree). Because registration problems are assumed to influence subsequent analysis it is desirable to examine the effects of polynomial warp order and mask quality on the process. Liow, et al [2] used Canonical Variable Analysis (CVA) to evaluate the effects of PET reconstruction algorithms on [^{15}Owater] task activation. In this work we use CVA to evaluate the effects of polynomial warp order and mask quality on inter-subject registration.

We acquired T1-weighted MRI volumes from 16 normal subjects. Spatial masks for the volumes were computed automatically and later manually corrected; the Dice similarity metric [3] for the two sets of masks ranged from 0.96 to 0.98. AIR5 was used to register volumes to a masked reference volume. For each volume we created spatially-normalized volumes using polynomials of order 1 through 8 and the uncorrected mask; the process was repeated with the manually-corrected mask.

The 256 volumes (16 subjects x 8 polynomial orders x 2 masks) were submitted to a CVA analysis with 16 groups (8 orders x 2 masks). The results of the CVA are summarized in Figure 1. The first canonical variate accounted for 92.8% of the variance and demonstrates a strong influence of warp orders 1-5 on group registration with a small mask effect (greatest for polynomial order 3). Overall, using the corrected mask reduced the variance by 1.8% compared to using the uncorrected mask. For the second canonical variate use of the corrected mask resulted in similar group means but slightly tighter between-subject clustering when polynomials of orders 6-8 were used. For the third canonical variate there was a clear difference in polynomial warps due to mask choice when polynomials of order 5-8 were used.

Figure 2 depicts slices through the eigenvolumes associated with the first three canonical variates. The majority of highly-weighted voxels in the first and second eigenvolumes appear at ventricles and other high-contrast edges. In the third eigenvolume the most influential voxels occur toward the periphery. Note that although the differences in spatial masks were restricted to the outer later of the volumes, their influences propagate well into the cortical mantle.

Multi-variate analysis of registration results for these 16 subjects clearly reveals that 1) the order of the polynomial warp was the dominant effect, 2) polynomial orders greater than 5 produced virtually the same result, and 3) mask choice had a negligible effect except for higher-order warps.

1. Woods RP, et al (1988). *JCAT* 22:153-165.
2. Liow J-S, Anderson JR, Strother SC (2000). *IEEE Trans. Nuc. Sci.* 47(3): 1136-1142.
3. Zijdenbos AP, et al (1994). *IEEE Trans. Med. Img.* 13(4):716-724.

This work was supported in part by NIH grant EB02013.

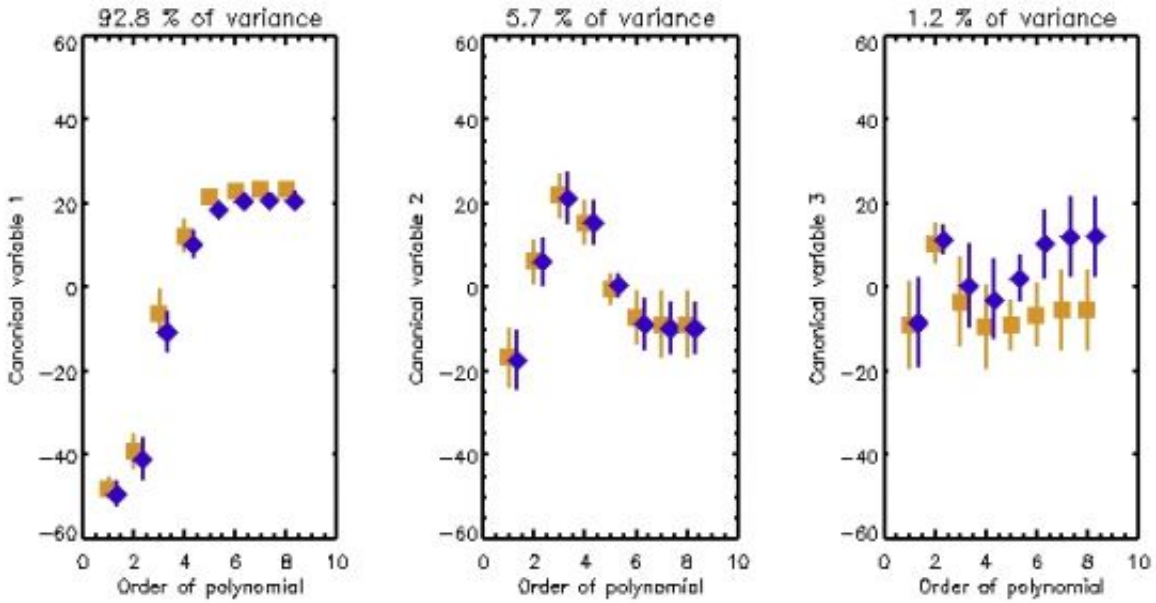

Figure 1. Canonical variates plotted as a function of polynomial order. Gold symbols (squares) represent the mean and one standard deviation of the canonical variate for 16 subjects co-registered using the uncorrected mask; blue symbols (diamonds) represent results from co-registrations using the corrected mask.

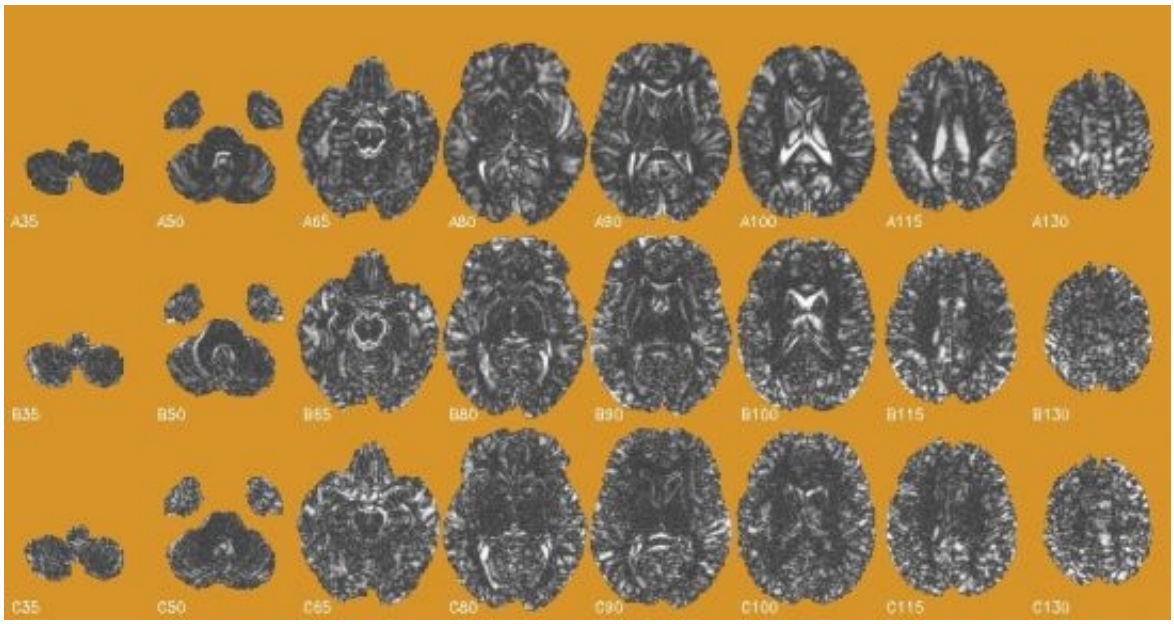

Figure 2. Canonical eigenvolumes. Axial slices through the eigenvolumes of canonical variates 1, 2, and 3 are presented, respectively, in the top, center and bottom rows. White voxels are those with the greatest positive and negative weights.

WE 289
PET SORTEO: Validation and Application of a Monte Carlo-based PET simulator

Anthonin Reilhac [1,2], Alan C. Evans [1,2]
[1] McConnell Brain Imaging Centre, Montreal Neurological Institute, [2] McGill University

Background:
We have designed a new Monte Carlo-based PET simulator to address the increasing need of simulated PET studies for validation purposes. The program is able to generate realistic 2D and 3D emission and transmission projections in accordance with both the numerical phantom description as well as with the scanner geometry and its physical characteristics. The simulation model accounts for most of the phenomena encountered during PET acquisitions including scatter counts, randoms and system dead-time. While a series of tests were performed to compare simulated and measured projections [1], we still had to validate the complete processing line involved with full PET acquisition / data correction and reconstructions.

Methods:
protocol: cylinder filled with Ge-68 scanned by the Ecat Exact HR+ operating in 3D mode.
Fig 1 represents the different steps involved in the generation of simulated PET volumes. The simulation program PET SORTEO generates simulated projections for emission and transmission scans from the numerical phantom description associated with the ideal time activity curves.

Random correction:
Random coincidences are measured from an off-time window and subtracted from the projections.

Normalization:
Emission data are normalized using a method similar to the standard one for Ecat scanners, where individual coincidence detector channel efficiency is modeled as the combination of geometric components and individual detector efficiencies. However, instead of using a high statistic blank scan as suggested, we computed the different components using projections from cylindrical phantoms so as to account for the difference in detector efficiency between scattered and unscattered events.

Dead-time:
Dead-time correction factors (dt_k) are calculated at each block k as a function of the detected single photons (s): $dt\_k = 1+A*s+B*s^2$.
The two parameters A, B, were computed for each block from a decaying F-18 filled cylinder.

Scatter correction:
The scatter distribution is modeled then removed from the projections.

Attenuation compensation:
The 2D correction factors are generated from the ratio of the 2D transmission and blank scans. The attenuation map is then reconstructed and forward projected to obtain the oblique correction factors.

Reconstruction: 3D-FBP or OS-EM.

Results:
Fig 2, compares the scatter distribution estimate given by the correction program with the true scatter distribution generated by the simulation model.
Fig 3, compares the attenuation factors derived from the simulated transmission and blank scans with theoretical values.
Fig 4, shows an axial slice of the reconstructed cylinder. The horizontal profile is also displayed.

Conclusion:
All the procedures are well tuned for correcting the simulated data.
The reconstructed volumes are calibrated and therefore quantifiable.

Applications:
Generation of a database of simulated studies.
Simulated volumes are being used for the validation of dedicated algorithms (partial volume effects correction, volume registration algorithms, denoising / image contrast restoration methods, surface extraction etc...).
Furthermore, PET-SORTEO is used for design studies of new tomographs.

[1] Reilhac et al, IEEE TNS Feb. 2004.

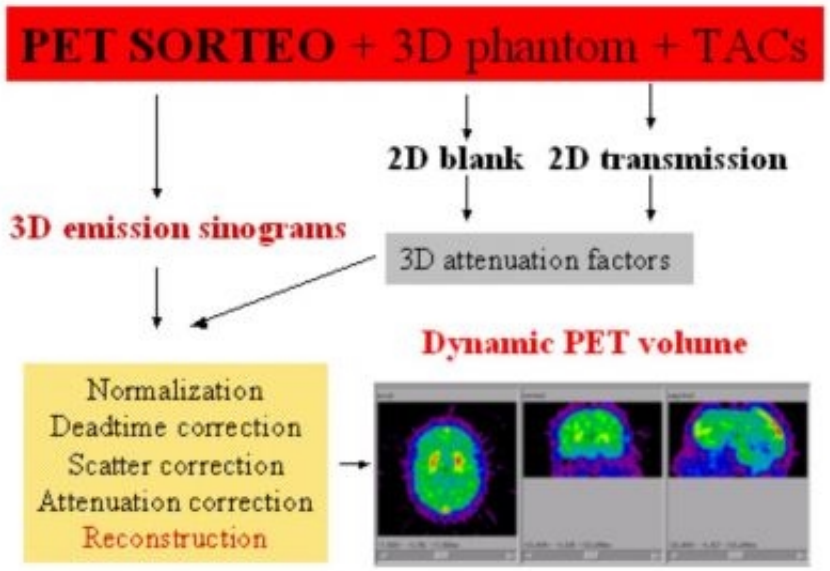

Steps involved for the correction and reconstruction of PET volumes

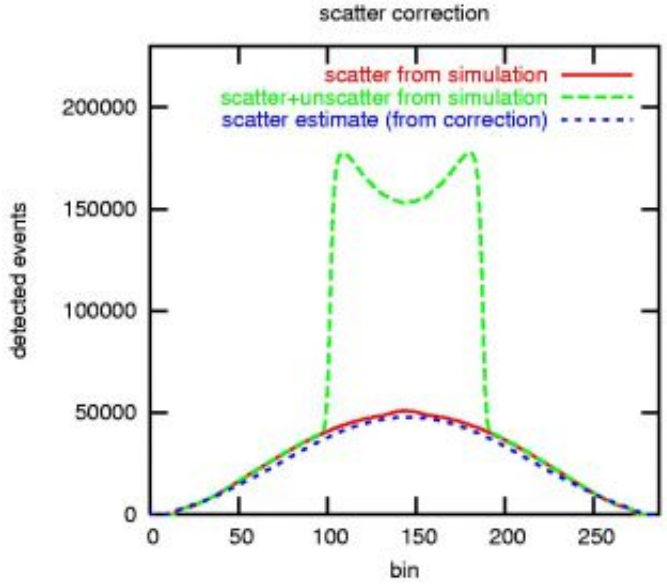

scatter correction

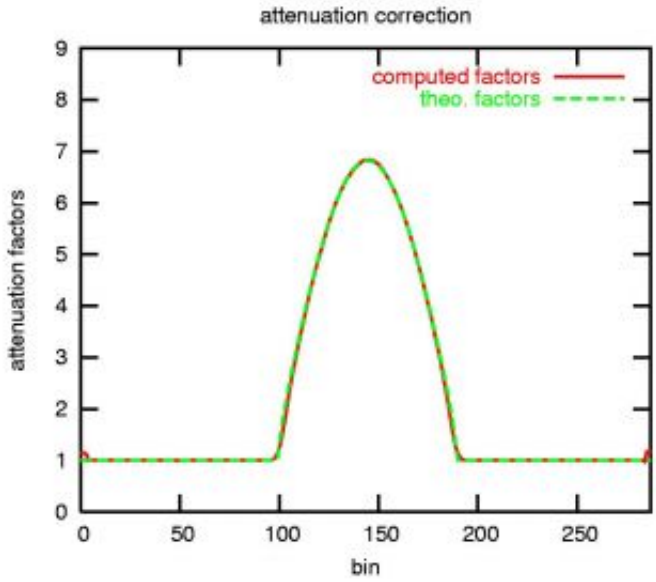

attenuation correction

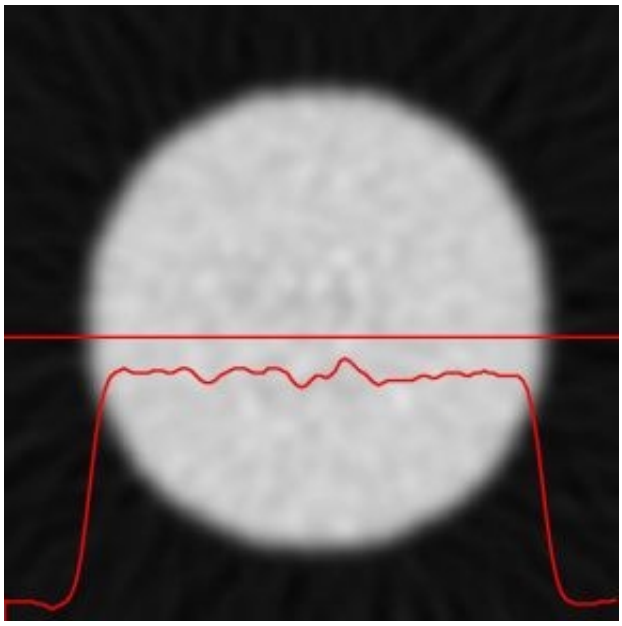

axial slice from the reconstructed cylinder

WE 290
A bottom-up approach for fMRI and NIRs fusion. I- Theory

J Riera[1], K Iwata[1], JC Jimenez[2], T Ozaki[3], R Kawashima[1]
[1]Advanced Science and Technology of Materials, NICHe, Tohoku University, Japan, [2]Instituto de Cibernetica, Matematica y Fisica, Havana, Cuba, [3]The Institute of Statistical Mathematics, Tokyo, Japan

The use of fMRI and NIRs imaging has permitted obtaining significant progresses in the study of brain functions. In spite of data obtained by these techniques indirectly reflect neuronal activations after low-pass filtering by the brain vasculature (i.e. hence, sharing a similar etiology), they summarize different aspects of the neuronal activity. Recently, Kato and Yamamoto (2002) have reported that there is an opposite balance for the contributions of capillary bed and venous compartments to the BOLD and optical signals. Additionally, the physical foundations that relate those measurements to some non-observable state-space variables "x" have been proposed in the literature, in what the authors henceforward denominate as the bottom-up approach. In the last few years, the simultaneous recording of BOLD and optical signals has emerged as a potential technique, endowing to neuroscientists with remarkable possibilities. Notwithstanding, in pioneer works the attention has been paid to determine how/when/where optical signals correlate to fMRI data. To the present date, the results have not been conclusive and it remains unclear whether the optical and BOLD signals provide complementary or redundant information about the hemodynamics of the brain. In our opinion, the interrelationship between neuronal processes and vascular control mechanisms, specifically the biophysical principles that establish a bridge between x and the observations, must be carefully included while evaluating signals correlations.

In the present study, a new bottom-up model is proposed for the case of steady-state stimulation condition; even so a generalization to transient events can be easily obtained from the original assumptions. The model makes a distinction between the contributions of capillaries and venous compartments to both BOLD and optical signals at the observation level, through a parameter κ that control the effective transparency of capillary bed to the incident light. The methodology proposed in Riera et al (2004) was generalized to include: non-linear observation equation and multi-modal data with heterogeneous missing values and diferent instrumental error sources.

A non-linear and non-autonomous state-space model (1), with additive noise, represents the hemodynamics approach. The table below differentiates each component of the dynamics and its respective literature. Buxton et al. (1998) deduced a direct relationship between the BOLD signals and some intrinsic variables of the state vector. A new observation equation $\boldsymbol{h}(x)$ for the optical signals that scales the contributions of capillary bed and venous compartment is proposed. It is possible to linearize the observation equation in (1) by simple increasing the order of the state equation and additionally introducing a multiplicative noise (2). The local linearization filter proposed by Riera et al. (2004) is extended in the present work to include data with different sampling rates and instrumental errors. It represents an iterative filter that uses a maximum likelihood principle. Table on the right summarizes the equations of the filter.

The filter proposed represents the first viable method to perform a fusion of fMRI and NIRs data in humans from a bottom-up approach. The factor κ will permit us to evaluate the contribution to NIRs of both capillary bed and venous compartments.

$$\left.\begin{array}{ll} dx = f(x,t)dt + gd\omega & \textbf{States Equation} \\ y_t = h(x(t_t)) + \epsilon_t & \textbf{Observation Equation} \end{array}\right\} \quad (1)$$

Flow Inducing	$f_1(x,u) = \varepsilon u - a_1 x_1 - a_2(x_2 - 1)$	Friston et al. (2000)
CBF	$f_2(x,u) = x_1$	
CBV	$f_3(x,u) = \left(x_2 - x_3^{1/a_4}\right)/a_2$	Mandeville et al. (1999)
De-oxy hemoglobin	$f_4(x,u) = \frac{1}{a_3}\left(\frac{x_2}{a_2}\left[1-(1-a_2)^{1/x_2}\right] - x_4 x_3^{(1-a_4)/a_4}\right)$	Buxton and Frank (1998)
Oxy hemoglobin	$f_5(x,u) = \frac{1}{a_3}\left(\frac{x_2}{(1-a_2)}(1-a_2)^{1/x_2} - x_5 x_3^{(1-a_4)/a_4}\right)$	New equation

fMRI & NIRs data

$$y_t = (y_1, y_2)'$$

$$h(x) = (h(x), \boldsymbol{h}(x))'$$

$$\begin{cases} h(x) = V_0\left[k_1(1-x_4) + k_2\left(1-\frac{x_4}{x_3}\right) + k_3(1-x_3)\right] \\ \boldsymbol{h}(x) = \rho\begin{pmatrix} (x_4 - x_0(4)) + \frac{\kappa}{\log(1-a_5)}\left[\left(1-(1-a_5)^{1/x_2}\right)x_2 - a_5\right] \\ (x_5 - x_0(5)) + \frac{\kappa}{\log(1-a_5)}\left[a_5 - \left(1-(1-a_5)^{1/x_2}\right)x_2\right] \end{pmatrix} \end{cases}$$

$$\left.\begin{array}{ll} dx' = f'(x',t)dt + g'(x')d\omega & \textbf{States Equation} \\ y_t = Cx'(t_t) + \epsilon_t & \textbf{Observation Equation} \end{array}\right\} \quad (2)$$

Local Linearization Filter

$$\hat{x}'_{t+\Delta t} = \hat{x}'_{t/t} + r_0\left(J^{x'}_{f'}(\hat{x}'_{t/t},t),\Delta\right)f'(\hat{x}'_{t/t},t) + \\ + \left(\Delta r_0\left(J^{x'}_{f'}(\hat{x}'_{t/t},t),\Delta\right) - r_1\left(J^{x'}_{f'}(\hat{x}'_{t/t},t),\Delta\right)\right)J^{x'}_{f'}(\hat{x}'_{t/t},t)$$

$$\mathrm{vec}\left(P'_{t+\Delta t/t}\right) = e^{\mathcal{A}\Delta}\left(\mathrm{vec}\left(P'_{t/t}\right) + \sum_{j=1}^{\xi}\int_0^{\Delta} e^{-\mathcal{A}s}\mathcal{B}_j e^{\mathcal{A}_j s}\mathcal{C}_j e_j(s)\,ds\right)$$

	fMRI data available	**NIRs data available**
The zero mean innovation	***Scalar*** $v_t = y_t - C\hat{x}'_{t_t/t_t-\Delta}$	***Vector*** $\boldsymbol{v}_t = y_t - C\hat{x}'_{t_t/t_t-\Delta}$
Observation Matrix	$C = (0_{1\times 3}, 1, 0_{1\times 2})$	$C = (0_{2\times 3}, I_{2\times 2})$
Variance Covariance	$\sigma_t = CP'_{t_t/t_t-\Delta}C' + \sigma^2$	$\Sigma_t = CP'_{t_t/t_t-\Delta}C' + \Sigma$
Equations for differences	$\hat{x}'_{t_t/t_t} = \hat{x}'_{t_t/t_t-\Delta} + k_t v_t$ $P'_{t_t/t_t} = P'_{t_t/t_t-\Delta} - k_t CP'_{t_t/t_t-\Delta}$	$\hat{x}'_{t_t/t_t} = \hat{x}'_{t_t/t_t-\Delta} + K_t \boldsymbol{v}_t$ $P'_{t_t/t_t} = P'_{t_t/t_t-\Delta} - K_t CP'_{t_t/t_t-\Delta}$
The LL filter gain	$k_t = P'_{t_t/t_t-\Delta}C'/\sigma_t^2$	$K_t = P'_{t_t/t_t-\Delta}C'\Sigma_t^{-1}$

WE 291
Analysis of Functional Magnetic Resonance Images Using a Linear Time Invariant Model - Multiple Input Evoked Response on Single Subject

Daniel E. Rio[1], Robert R. Rawlings[1], Jasmin B. Salloum[1], Lawrence A. Wottz[2], Daniel W. Hommer[1]
[1] Section of Brain Electrophysiology and Imaging, Laboratory of Clinical Studies,National Institute on Alcohol Abuse and Alcoholism, National Institutes of Health,Bethesda, MD 20892., [2] Synergy Research Inc., 12051 Greystone Drive, Monrovia, MD 21770

Two Poisson distributed simultaneous non-overlapping visual stimuli consisting of erotic and negative images were presented to the subjects. 900 T_2*-weighted echo-planer MR volumes (TR 400 msec, 64 x 64 x 10 slices sampled at 3.75 x 3.75 x 5 mm) on a GE Signa 1.5 Tesla scanner were collected during the presentation.
A linear time invariant model was then used to analyze this data. The model assumes the signal is determined by a constant plus a linear filter (hemodynamic response function) of several fixed deterministic inputs with a zero mean stationary error term. That is
$s(\mathbf{x},t) = \mu(\mathbf{x}) + \Sigma\, a(\mathbf{x},t-u)r(u) + \varepsilon(\mathbf{x},t)$, $\mathbf{x} = (x,y,z)$, t - time
where $s(\mathbf{x},t)$ is the fMRI signal, r(t) is the Poisson input (2 input x 1 matrix, 900 time points long), $a(\mathbf{x},t)$ is the filter, $\mu(\mathbf{x})$ is a constant and $\varepsilon(\mathbf{x},t)$ is the error term whose spectrum is $f_{\varepsilon\varepsilon}(\mathbf{x},\lambda)$ (a measure of the extent to which the output signal is determined from the input) where λ is a given frequency in the Fourier domain.
Rigorous F-tests were then constructed in the Fourier domain to test for response of the output signal, $s(\mathbf{x},t)$ to the input, r(t) or to either the erotic or negative stimuli parts of r(t) and also to test the differential response of $s(\mathbf{x},t)$ to the stimuli. F-tests take on the following form
$F(\mathbf{x},\lambda)_{2;2(2m+1)} = (2m+1)A(\mathbf{x},\lambda)B[B^T[f_{rr}(\lambda)]^{-1}B]^{-1}B^T A(\mathbf{x},\lambda)^{*T}/g_{\varepsilon\varepsilon}(\mathbf{x},\lambda)$
where $f_{rr}(\lambda)$ is the cross covariance functions of the Fourier transformed input. The transfer function (filter in the Fourier domain), $A(\mathbf{x},\lambda)$ is estimated from the cross covariance functions of both the input and output signal. $g_{\varepsilon\varepsilon}(\mathbf{x},\lambda)$ estimates the error spectrum and B is a contrast matrix. Statistical power is enhanced by summing over frequencies (2m+1 wide bands) and preprocessing $s(\mathbf{x},t)$ with Gaussian filters in the spatial domain and band-pass frequency filtering in the temporal domain to eliminate noise and/or unwanted signal produced by other physiological processes that may interfere with the evoked response.
Data in this experiment was analyzed with the following parameter choices: spatial filter - Gaussian (4 mm FWHM), temporal filter - cut off above .9 Hz, band size 13 - producing 34 bands. Then at each band and spatial position at the center frequency λ an F-statistical image was constructed and tested ($\alpha = .001/34$) to see whether each input elicited a response in the output signal. Masks were produced at each spatial position and frequency at which activation was determined. Sample mask can be seen for the occipital area in the figure.
In conclusion, Poisson distributed multiple input stimuli are presented in a fMRI experiment (TR 400 msec) enabling the construction of a short duration experiment that reduces subject movement artifacts and allows for filtering of unwanted physiological processes. No assumptions are made about the hemodynamic transfer function. Problems with temporal correlation are avoided by performing the statistics in the Fourier domain using a rigorous statistical model for which numerous F-tests can be constructed.

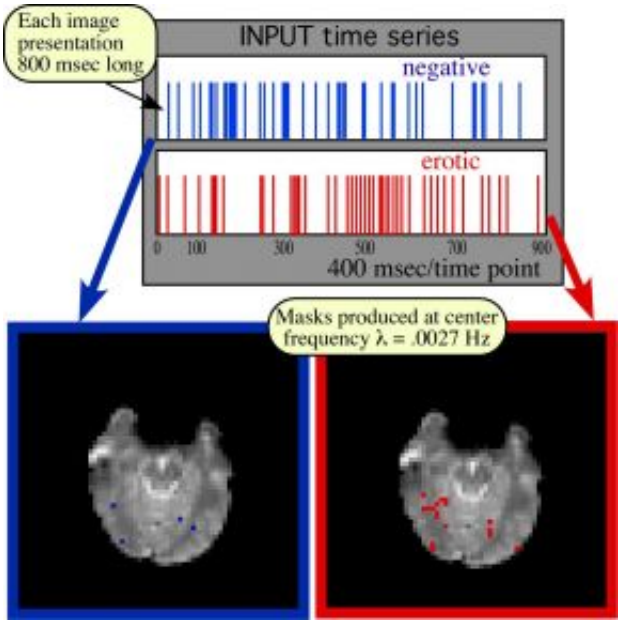
Each image presentation 800 msec long
INPUT time series
negative
erotic
0
100
300
500
700
900
400 msec/time point
Masks produced at center frequency λ = .0027 Hz

WE 292
Localization Volume, a New Measure for Capturing Neuroanatomical Variability

Steven M Robbins[1,2], Sue Whitesides[1], Alan C Evans[2]
[1] School of Computer Science, McGill University, [2] Montreal Neurological Institute

Quantifying spatial variability of a structure across a population is an important part of brain mapping. Among other reasons, the variability of an anatomical structure is useful to gauge the efficacy of a spatial normalization method. As the goal of spatial normalization in brain imaging is to reduce anatomical variability in a population by warping each individual's anatomy into a standardized space, anatomical variability is a natural measure of performance of a spatial normalization algorithm [3]. The spatial variability of a functional region is also of interest: the linkage between structure and function can be examined by measuring the spatial variability of a functionally-defined region after spatial normalization using anatomy. We propose a new measure of spatial variability that is applicable to extended (i.e. non-point) structures (structural or functional) that does not require point-to-point correspondence between individuals.

One common method for assessing variability employs homologous landmark points in each brain, computing the dispersion of each set of landmarks [1]. An extended structure (e.g. a curve or 2D surface patch) is typically discretized as a polygonal curve or polyhedral surface patch and the corresponding nodes are assumed to be homologous, thus reducing the problem to one of homologous landmarks. An alternative approach employs a segmentation of the input images into discrete classes, measuring label agreement at each voxel [3,4].

The measure obtained with the first approach is interpretable as a dispersion of the points about a central point. For extended structures, however, we must produce a point-to-point homology between the structures. The second method does not require the homology, but the resulting variability measure is based on entropy and isn't interpretable in terms of Euclidean distance. We propose Localization Volume, a new measure which improves on both by providing an intuitive measure while not requiring a point-to-point matching. The figure illustrates our procedure, which comprises three steps. The four gray shapes are the input structures. The first step is to obtain a suitable "average structure" (shown in red) from the inputs, analogous to computing the centroid of a set of points [2]. The second step uses the Hausdorff distance to measure the distance between the average structure and each input structure. The average of these distances, denoted by r, is a dispersion measure analogous to the mean distance to the centroid in the case of point structures. The third step is to dilate the mean structure by distance r, obtaining the region shown in yellow. The volume (for 3D images) of this region is our localization measure.

References

[1] I. Grachev, et al., NeuroImage, 9:250-268, 1999.
[2] T. Lewis, et al., Pattern Recognition, 32(9):331-339, 1999.
[3] S. Robbins et al., MICCAI pages 910-917, 2003.
[4] S. Warfield et al., MICCAI pages 266-274, 2001.

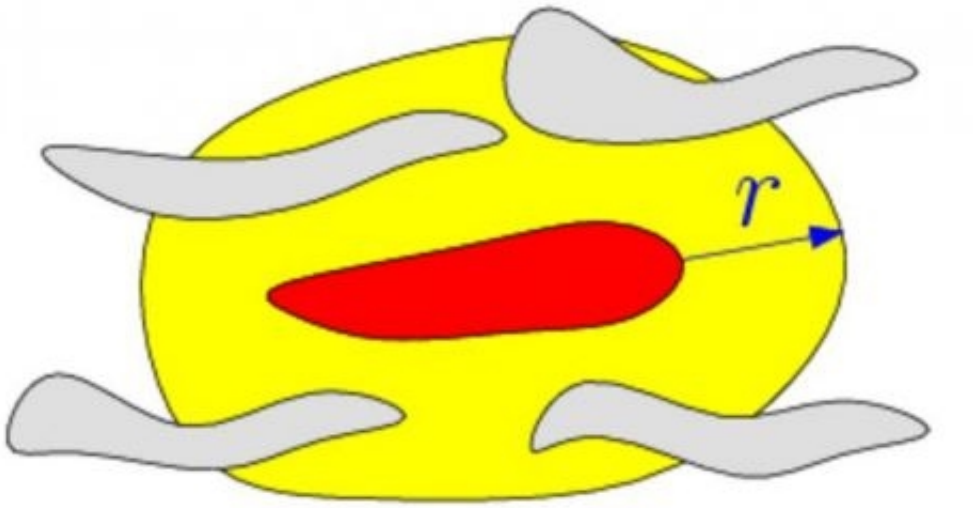

Input structures (gray) give rise to a mean structure (red) which is dilated to form the localization region (yellow).

WE 293
Localization Comparison of High-Dimensional Spatial Normalization: 2D versus 3D

Steven M. Robbins[1,2], Sue Whitesides[1], Alan C. Evans[2]
[1] School of Computer Science, McGill University, [2] Montreal Neurological Institute

Spatial normalization is a key process in cross-sectional studies of brain structure and function. Although normalization methods in widespread use today employ low-dimensional 3D warping functions, a high-dimensional warping might remove more of the natural anatomical variability. For studies involving only the cortical surface, another approach proposed in recent years [5] normalizes only the cortex using a 2D spatial mapping from the cortex to a standardized 2D space (typically the plane or the sphere). This abstract reports on our experiments to compare the quality of spatial normalization in 2D versus normalization in 3D for cortical structures.

Since the goal of spatial normalization is to reduce the normal anatomical variability, we choose a measure of variability to gauge the performance of a spatial normalization method. Specifically, we use the localization volume [4] computed for selected cortical sulci. Briefly, this measure reflects the size of the region in standardized space that contains the set of sulci (one from each input brain), after normalization. We work in a 2D standardized space, so the localization "volume" computed is actually a measure of area.

Figure 1 illustrates two paths for a sulcus, delineated on a subject's 3D image, to be mapped to a 2D standardized space associated with a template. The red arrow is the 3D path: the sulcus is transferred via a 3D mapping to the template image, then it is projected onto the cortical surface of the template, and finally on to a spherical standardized surface. The blue arrow is the 2D path: the sulcus is first projected on to the subject's cortical surface, then into the 2D space, and finally after a 2D spatial normalization arrives in the standardized space. See [4] for the details of each step.

We perform both mappings for 40 normal subjects and then compute localization volume measures for the 3D path and for the 2D path for 4 sulci in each hemisphere. In all 8 cases, the localization after 2D normalization is better than the localization after 3D normalization. The main reason for the superiority of 2D normalization is that the population sulci tend to be mapped onto the corresponding template sulcus. In contrast, the 3D normalization results show a large number of subjects being mapped to regions outside the template sulcus. This is illustrated by the probability functions displayed in Figure 2.

Previous studies [2,3] compared a high-dimensional 2D normalization with low-dimensional 3D warping. In contrast, we have used a high-dimensional 3D warping [1] with a new high-dimensional 2D warping [4]. Our comparison is thus much more stringent.

References

[1] D.L. Collins et al., HBM 3:190-208, 1995
[2] H.A. Drury et al., Chapter 19 in *Brain Warping*, 1999.
[3] B. Fischl et al., HBM 8(4):272-284, 1999.
[4] S. Robbins, PhD Thesis, 2003.
[5] D.C. Van Essen, PNAS 95:788-795, 1998.

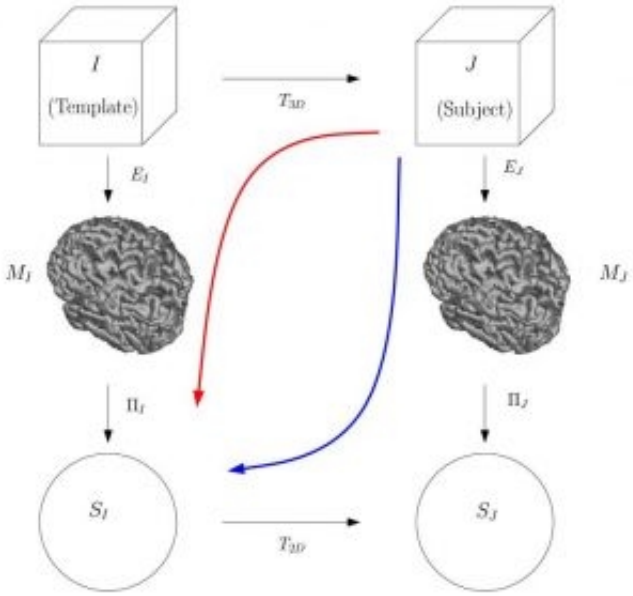

Mapping strategies: 3D path in red, 2D path in blue.

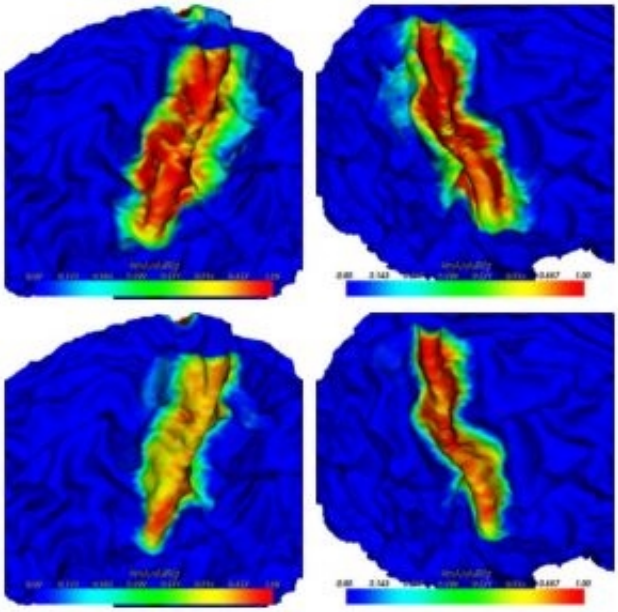

Probability maps for the central sulcus after 3D spatial normalization (top) or 2D spatial normalization (bottom).

WE 294
Positive Results in Amygdala fMRI: Emotion or Head Motion?

Simon D Robinson[1], Ewald Moser[1,2,3]
[1]MR Centre of Excellence, Vienna Medical University, Vienna, Austria, [2]Department of Radiognostics, University and General Hospital, Vienna, Austria, [3]Department of Psychiatry, University of Pennsylvania Medical Center, Philadelphia, USA

Introduction
In an fMRI study of emotional discrimination in schizophrenics and controls we observed stimulus-correlated head motion as has been reported elsewhere (Hajnal et al. 1994) in response to the presentation of images of faces in both groups. Here, healthy subjects were imaged without stimuli but reproducing the head motion observed in the initial study both voluntarily by subjects themselves and by moving the patient couch.

Materials and methods
Four subjects were studied with single-shot EPI with parameters that have typically been applied in amygdala fMRI to date (64x64 matrix, 4mm slices with 6mm interslice interval, TE=34ms) and 17 slices in TR=2s, NR=100 with a 3T Bruker Medspec whole-body scanner. Subjects were instructed to generate a small z-axis displacement of the head when a small circle at the centre of the crosshair changed from green to red before returning to the rest position when it changed back to green (a common head motion during a blocked design study). In a second run the patient table was shifted with a range of displacements below 1mm with the same timing as in the first run.

Analysis
In accordance with current common practice, data were analysed using SPM99, including image normalisation to a standard template, spatial smoothing with a 9mm Gaussian kernel, and were evaluated both with and without motion correction ("Realignment"). Regressors in the model were periods of displacement.

Results
Motion was identified to be less than 0.8mm in all cases. There was no sign of peripheral correlations, commonly taken to be a hallmark of substantial motion. High and focal correlation values were seen in the amygdalae region in all subjects, however (Figure 1), and in the anterior cingulate gyrus in some (Figure 2). In most cases correlation values were extremely high ($t>20$ in Figure 1), and were not reduced when data were motion-corrected.

Discussion and conclusion
Highly significant focal correlations arise from submillimetre head movements although no stimulus is present. These arise from boundaries of high signal and non-linear geometric distortions in regions of high magnetic susceptibility gradients and are not easily distinguishable from the correlations seen in emotion discrimination experiments in which the same degree of head motion is to be observed. Even contrasts employing differences in responses in different periods, all involving apparently similar levels of motion, as are commonly used in cognitive subtraction experiments have been shown to give rise to highly significant and focal correlations from the motion alone. Given that the subject motion examined here would generally be regarded as innocuous and would be treated with standard motion correction algorithms, such correlations may explain some or all of the observed correlations in limbic region fMRI experiments to date. There is clearly a need for techniques to avoid or separate such artifacts from genuine activation.

Reference Hajnal JV, et al (1994). Magn Reson Med. 31(3):283-91.

Acknowledgement S.R. gratefully acknowledges receipt of a Human Frontiers Science Program short-term fellowship award. E.M. acknowledges a grant by the Austrian Science Foundation (P-16669)

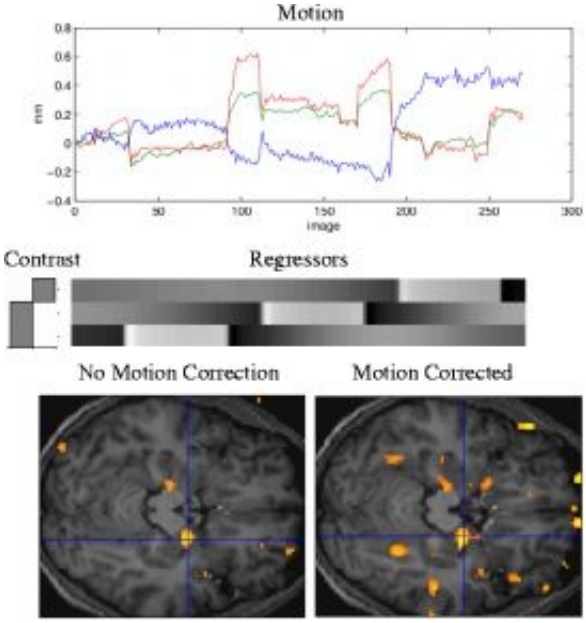

Figure 1. Identified translational motion (top) and regressors (middle) for periods of self-generated head motion. SPMs evaluated both without motion correction (bottom left) and with motion correction (bottom right) show highly significant (corrected p<0.0001) for the contrast indicated (middle left). SPMs are overlayed on T1-weighted images of the subject.

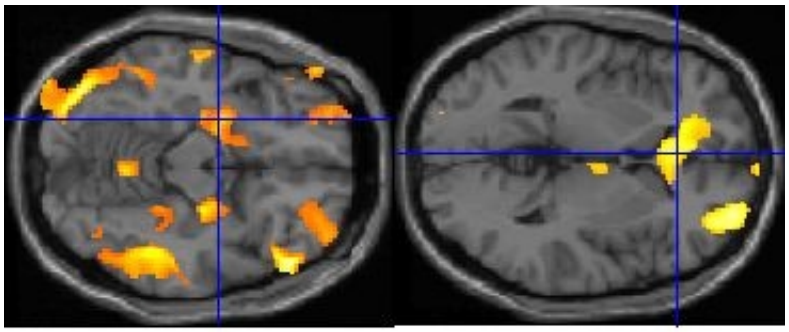

Figure 2. Motion-corrected SPMs from data generated by periodic shifts of the patient table show correlations in both the amygdala (left) and anterior cingulate gyrus (right) (indicated by the position of crosshairs), overlayed on the SPM99 single subject T1 template.

WE 295
Kalman Filtering for Real-Time fMRI Analysis

Alexis Roche[1,2], Jean-Baptiste Poline[1,2]
[1] Service Hospitalier Frédéric Joliot, CEA, Orsay, France, [2] IFR49, Institut d'Imagerie Neurofonctionnelle, Paris, France

One of the current challenges in functional magnetic resonance imaging (fMRI) is to display reconstructed volumes and map brain activations in real time during an ongoing scan. This will make it possible to interact with fMRI experiments in a much more efficient way, either by monitoring acquisition parameters online depending on subject's performance, or by designing paradigms that incorporate neurophysiological feedback. To date, the feasibility of real-time fMRI processing has been limited by the computational cost of both the three-dimensional reconstruction of MR data sets and their statistical analysis. We focus here on the latter item.

We developed a new detection algorithm that uses an extended Kalman filter (EKF) to fit a general linear model on fMRI time courses. Because the EKF is designed to be an incremental algorithm, it enables us to update activation maps on each scan time, and this at constant, moderate computational cost and memory load. Typically, for fMRI volumes of dimension 64 x 64 x 20, our C language implementation runs in several tenth of second per scan on a standard PC (1.80GHz processor). Notice that, unlike previous real-time detection approaches [1,2], the EKF handles the situation where the errors are modeled as an autoregressive noise with unknown temporal autocorrelation.

The method was tested *offline* on several fMRI datasets acquired on the SHFJ site (Orsay, France) from both GE Signa 1.5T and Bruker 3T whole-body scanners, always providing results consistent with SPM'99. In figure 1, the frames (a), (b) and (c) show the evolution of the activation map obtained for a run involving a mental calculation task [3]. The protocol consisted of three successive blocks, each block including one activation epoch and one control epoch (26 seconds each), for a total of 93 scans (TR = 2 sec). As expected for a mental calculation task, activations are found in both the right and left parietal lobes, especially on the right in this case. Interestingly, they start appearing shortly after the second block presentation and are remarkably stable afterwards. We also observe an activation in the right fronto-lateral lobe, known to be involved in attentional tasks, that clearly spreads out with time. Conversely, an activation in the right frontal lobe can be noticed to vanish progressively, suggesting an adaptation effect in this region.

Our preliminary offline evaluation suggests that the method has the potential to provide sensible activation maps across time. Beside the actual real-time implementation, we plan to develop a more general Kalman filter that uses a time-varying state model in order to account for adaptation or attention effects.

[1] R. Cox, A. Jesmanowicz, and J. Hyde, "Real-Time Functional Magnetic Resonance Imaging", *Magnetic Resonance in Medicine*, vol. 33, pp. 230-236, 1995.

[2] D. Gembris, J. Taylor, S. Schor, W. Frings, D. Suter, and S. Posse, "Functional Magnetic Resonance Imaging in Real Time (FIRE): Sliding-Window Correlation Analysis and Reference-Vector Optimization", *Magnetic Resonance in Medicine*, vol. 43, pp. 259-268, 2000.

[3] O. Simon, J.-F. Mangin, L. Cohen, D.L. Bihan, and S. Dehaene, "Topographical layout of hand, eye, calculation, and language-related areas in human parietal lobe", *Neuron*, vol. 33, pp. 475-487, 2002.

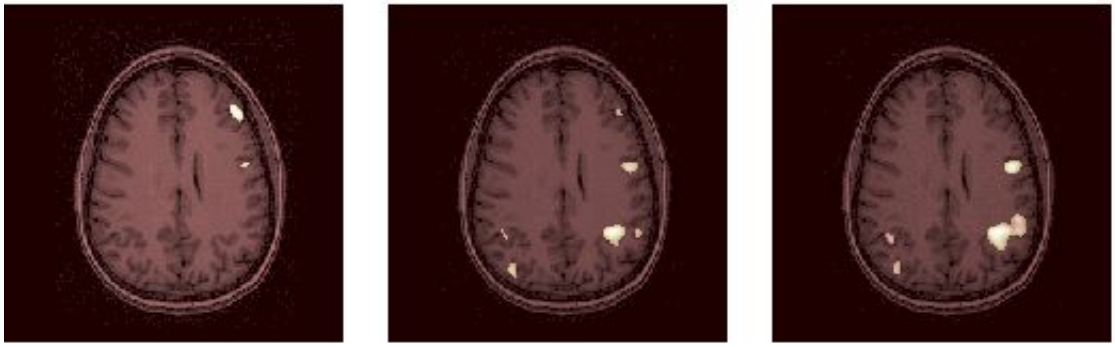

(a) After one block (62") (b) After two blocks (2'04") (c) After three blocks (3'08")

Incremental activation maps computed in a mental calculation block-paradigm

WE 296
Using large scale neural models to understand fMRI Granger causality analysis

A. Roebroeck[1], B. Horwitz[2], B. Warner[2], J. Fitzer[2], R. Goebel[1]
[1]Cognitive Neuroscience Section, Dept. Psychology , University of Maastricht, the Netherlands, [2]Brain Imaging & Modeling Section, NIDCD, NIH, Bethesda, MD USA

Introduction
Determining how anatomically distinct neural populations interact in the brain to process information and generate action is pivotal to our understanding of cognitive function. The investigation of neural interactions at the level of fMRI data has primarily consisted of two complementary classes of modeling attempts: systems-level modeling and large-scale neural modeling[1]. Systems-level modeling, characterized by its inference about effective connectivity (the influence exerted by one population on another), focuses mainly on estimating (and performing inference on) models from measured imaging data[2,3]. Large-scale neural modeling aims at constructing neurobiologically realistic computational models capable of performing a certain cognitive or perceptual task. The function of every population and the flow of information between them are, therefore, known. We applied Granger causality analysis as an effective connectivity measure[4,5] to the simulated output of large-scale neural models to investigate whether insights can be gained into the neurobiological substrates of effective connectivity models. Activity in a brain region X granger causes activity in a region Y if past activity of X can help predict the current activity of Y.

Methods
We used a large-scale neurobiologically realistic model[6], constructed to perform visual match-to-sample tasks, consisting of multiple interconnected brain regions: primary and secondary visual cortex, inferotemporal cortex and prefrontal cortex. The models basic unit is an excitatory-inhibitory pair representing a cortical column. The simulated electrical activities of these units resemble recordings made at the neuron level in monkeys. The synaptic activity of the units spatially and temporally integrated over a region is similar to measurements of local field potentials (LFPs). To simulate an fMRI measurement these simulated LFPs were convolved with a canonical hemodynamic response function (HRF) and temporally sampled at an interval corresponding to a volume repetition time (TR). A number of parameters in the stimulus sequence, the interconnections between areas, the shape of the HRF, and the scanner sampling were varied. Granger causality, calculated from fitted autoregressive models, was then evaluated between regions of the model both at the level of simulated LFPs and fMRI data.

Results and Conclusion
The primary flow of information, from primary visual regions via inferotemporal regions to prefrontal cortex could be discerned by Granger causality analysis at the LFP level. At the level of the simulated fMRI signal, after hemodynamic convolution and simulated scanner data acquisition, the ability to detect directed influence from one region to another decreased, mostly affected by the value of the TR parameter. At relatively fast TRs (400-1000ms) the coarse sequence of processing over areas could still be detected, but at larger TRs that ability declined. These results confirm the important role of temporally optimized scanning in applying Granger causality to fMRI data and suggest that large-scale neural models can help reveal the interpretation, at a neural population level, of effective connectivity inferences.

References
1. Horwitz et al.,2000,*Neural Networks*
2. McIntosh&Gonzalez-Lima,1994,*Human Brain Mapping*
3. Friston,1994,*Human Brain Mapping*
4. Goebel et al.,2003,*Magnetic Resonance Imaging*
5. Goebel et al.,2004,in *Attention & Performance XX*
6. Tagamets&Horwitz,1998,*Cerebral Cortex*

WE 297
An Automated Method for the Extraction of Regional Data from PET Images

Pablo M. Rusjan[1], Doug Hussey[1], David C. Mamo[1,2], Nathalie Ginovart[1,2], Shitij Kapur[1,2]
[1] PET Centre. Centre for Addiction and Mental Health. Toronto.ON. Canada, [2] University of Toronto, ON, Canada

The region based analysis of a Positron Emission Tomography (PET) image aims to extract the radioactivity concentration from an anatomical structure this approach is termed the ROI approach. Manual techniques for drawing ROIs on PET images require high trained personnel and are susceptible to subjectivity and lack of reproducibility.

PET images offer imprecise anatomical information because they have limited spatial resolution and because the tracer distribution does not adequately reflect underlying anatomical variations. Therefore, a preferred way to determine ROIs requires transforming and registering a high-resolution anatomical magnetic resonance image (MRI). The typical procedure consists (1) to transform a standard atlas or template of ROI to fit an individual high-resolution image (MRI), (2) to register the individual MRI image with the PET image, (3) to transfer the individual transformed ROI to the PET image space.

In an effort to automate this process, Yasumo *et al.* (Neuroimage 2002 (16) 577-86) have developed software that is able to undertake steps 1-3 with minimal user interaction, and adds an additional step of individualizing the template-derived ROIs based on the probabilities of gray matter of the individual MRI image. However, this method worked well only for cortical regions, was based on manual identification of cut-offs for regional intensities, and was expressed in a non-standard space. To overcome these limitations we have further developed this concept by:

(i) Adding a new step in the refinement of subcortical regions such as the caudate, putamen, and thalamus which can be accurately estimated,

(ii) We have developed the template in the MNI space and a set of parameters for this template with a rigorous and reliable system, and

(iii) We have improved the definition of intensity cut-offs regions reliably localizing the maximum of intensities in a histogram.

To validate the new software we determined the binding potential (BP) from time activities curves (TAC) in subjects and across a wide range of BPs. The radiotracers employed were [^{11}C]-raclopride, [^{11}C]-FLB 457 and *Carbonyl*-[^{11}C]-WAY 100635. For each ROI one or more tracers were used depending on the affinity of the receptor and the signal-to-noise ratio. Results of our automatic method were compared with the ones obtained by trained raters.

The results showed that the automatized BPs are within the range of the interoperator variability values. Furthermore, our new step (i) showed accurate results for subcortical regions. The criterions for intensities cut-off (iii) regions showed adequate reliability.

The developed software will be available, since middle of 2004 at http:/www.camhpet.ca/software

WE 298
Modeling the Hemodynamic Response in fMRI by Laguerre Polynomials

Supratim Saha[1], Christopher Long[2], Emery Brown[1], Elissa Aminoff[2], Moshe Bar[2], Victor Solo[2,3]
[1]Neuroscience & Statistics Research Lab, MGH, Boston,Massachusetts,USA, [2]MGH-NMR Center, Charlestown, Massachusetts, USA, [3]School of Electrical Engineering, University of Michigan, Ann Arbor, USA.

Method:
The true shape of hemodynamic response (HR) is only known empirically as a localized hump shaped *causal* function. The HR to the underlying neuronal activity and noise will cause the HR to be a blurred, delayed and noisy version of the stimulus. The accuracy of of any method proposed to detect activation will depend on the model chosen chosen and how well the model parameters have been estimated.
In the past Poison shaped impulses, Gamma functions etc. have been used in parametrically modeling the HR. Even finite impulse response (FIR) models have been used, even though a high FIR order is required. It has been demonstrated in control literature that discrete Laguerre polynomials have been quite effective in reducing the model order and provide a useful low order approximation to time delay systems if some apriori knowledge of time constants is available. In particular their superiority over FIR modeling of time delay systems in control problems have been verified. Owing to the similarity of shape of discrete Laguerre polynomials with the assessed HR shape which would possibly result in estimation of *fewer* parameters and thus a *reduction* in *bias* and *variance* , we propose the use of these polynomials in modeling the HR. Figure 1 shows a plot of Laguerre polynomials of orders 1 to 6 for a given typical time constant. The basis functions are highly localized, causal and have shape similar to the empirically assumed HR. It is thus expected that a few basis functions will be able to characterize the HR resulting in better estimation and a low noise representation.
Results:
A visual blocked design experiment was carried out in which a subject was presented with a readily recognizable stimulus present on a screen for 1700 ms. Each condition included forty different pictures that were presented three times. Blocks of experimental images were separated by 20 second interval of rest during which a fixation dot was presented. Each block consisted of ten consecutive presentations of different pictures within a specific experimental condition appearing in a random order. The total block duration was 20 seconds. We carried out the modeling of HR at each pixel by Laguerre polynomials of order 2 and time constant of 0.66 obtained from blood flow parameters. Figure 2 shows the relative activation levels at each pixel of a slice. The activation is computed as the ratio of the square of the estimated signal energy to the sum of squares of whitened residuals. Strong activations have been observed in the visual cortex as expected. Figure 3 shows the estimated signal in the time domain overlaid over the observed waveform at an activated pixel of a given slice. It can be observed from figure 3 that the response appears physiological.

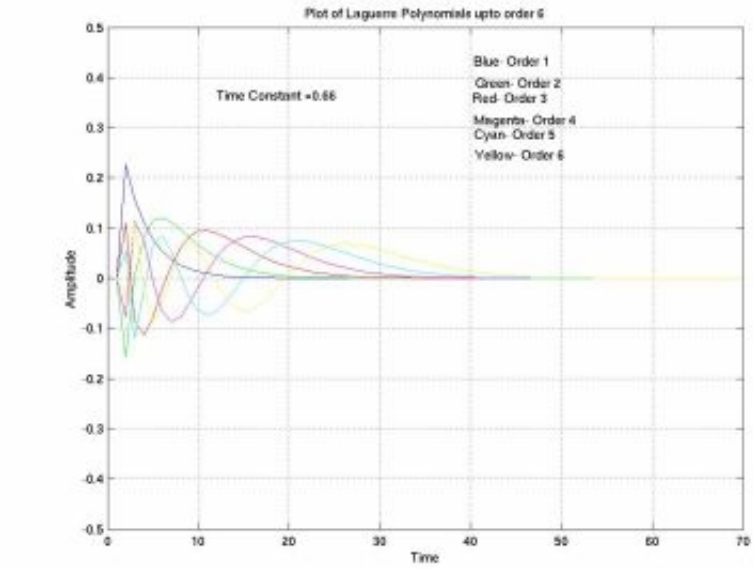

Basis Functions in Time Domain

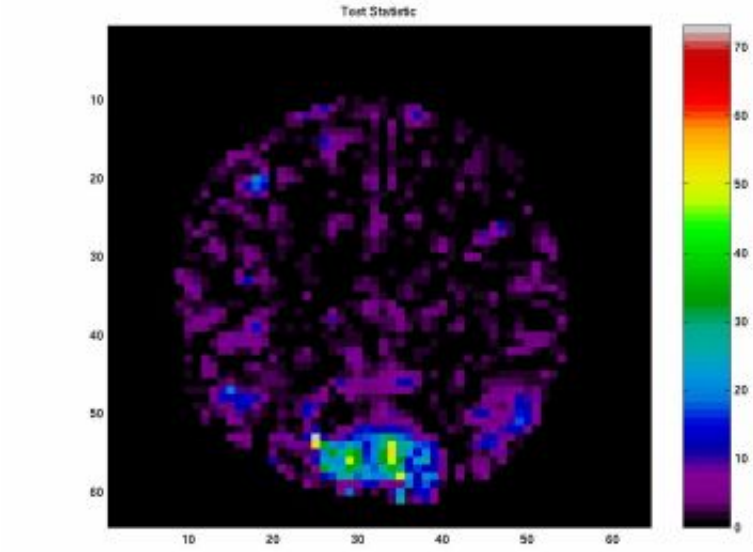

Activation Map for a slice

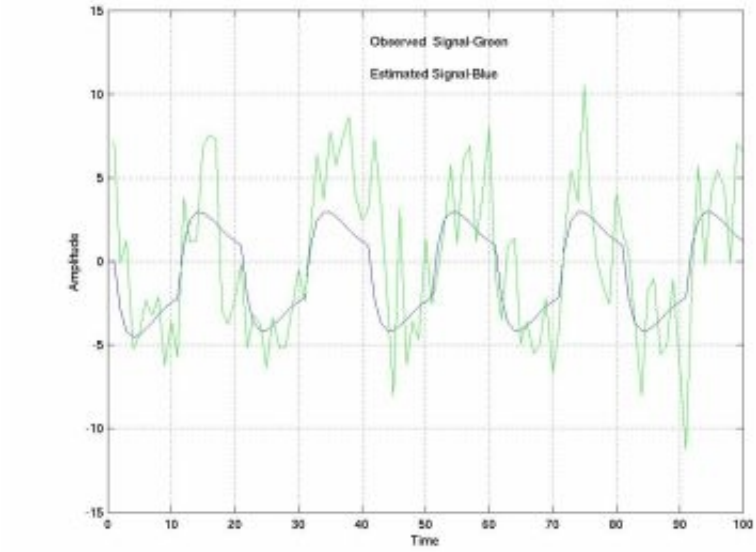

Time Domain Waveforms at Activated Pixel

WE 299
Quantitative Evaluation of MRI Brain Tissue Segmentation Algorithms

Kirt A Schaper[1], Timothy R Jarvis[1], Kristi Boesen[1], Kelly Rehm[2], Joseph Gati[3], Ravi Menon[3], David A Rottenberg[1,2]

[1]Department of Neurology, University of Minnesota, MPLS, USA, [2]Department of Radiology, University of Minnesota, MPLS, USA, [3]Robarts Research Institute, London, Canada

Segmentation of MRI brain volumes to determine the tissue composition at each voxel location is a critical step in many medical imaging applications. Numerous algorithms have been developed to perform this task, employing a variety of strategies, requiring different data inputs, and producing different types of tissue segmentations -- "hard", "soft" and "semi-soft". The performance of three popular segmentation algorithms which operate on T1-weighted MRI brain volumes -- FAST [1], SPM [2] and PVS [3] -- was assessed in terms of both accuracy and precision. Accuracy was assessed by comparing the segmentation output to manual segmentations produced by three expert raters and precision by segmenting repeat MRI brain volumes of the same subject. Additionally, we assessed the impact of varying the SNR and voxel size of the MRI volume on algorithmic performance.

Methods

Four MRI brain volumes of the same normal volunteer subject were acquired: one at 1.5 mm isotropic resolution and three repeat scans at 1 mm isotropic resolution. All volumes were corrected for intensity non-uniformity using N3 [4] and a brain mask produced by McStrip [5]. The stripped intensity-corrected volumes were then input to the three segmentation algorithms. Manual segmentation was performed by three expert raters using a global dual-threshold approach (CSF/Grey and Grey/White) on the intensity-corrected volumes. All raters underwent an initial training period on a brain volume acquired from a different subject. Raters adjusted the brightness/contrast of the display and then interactively adjusted the two thresholds to create a CSF-GM-WM (black-gray-white) cartoon that most closely corresponded to the input volume. The average fractional intensity in every algorithmically-segmented volume was computed for the labels (CSF, GM, WM) obtained from each rater-segmented volume and averaged across raters (Table 1). Additionally, we reconstructed the input volume to the segmentation algorithms from the fractional content volumes using pure tissue estimates based on the average of voxels containing at least 98% of the given tissue type (i.e., $v' = g*G + w*W + c*C$, where v' is the reconstructed voxel intensity, g, w and c are the percent GM, WM and CSF at that voxel location and G, W, and C are the corresponding pure-tissue estimates). These reconstructed volumes were correlated with the non-uniformity corrected volume to assess algorithmic consistency (Table 1, right column).

Results/Discussion

The average percentage for the "correct" tissue label was minimally affected by partial voluming (1.5 mm vs. 1 mm voxel size). [We were unable to generate an SPM result for the 1.5 mm volume for technical reasons.] Whereas FAST performed better overall with respect to GM and WM content, PVS was aided most by increased SNR with an average increase of 0.30 in GM and WM percentages in the corresponding reference label. With regard to internal consistency, SPM performed least well of the three algorithms evaluated (Table 1, right column).

This work was supported in part by NIH grant P20 EB02013.

References

1. Zhang Y, et al. IEEE TMI 20(1):45-57, 2001.
2. Ashburner J, Friston C. NeuroImage 11: 805-821, 2000.
3. Shattuck DW, et al. NeuroImage 13(5):856-876, 2001.
4. Sled JG, et al., IEEE TMI 17:87-97,1998.
5. Rehm K, et al. NeuroImage (submitted), 2004.

Table 1. Average fractional content and correlation.

method	**volume**	**CSF**	**GM**	**WM**	**r***
PVS	1.5 mm	0.838	0.626	0.534	0.9680
	1 mm	0.755	0.531	0.558	0.9510
	3 NEX	0.685	0.838	0.883	0.9785
FAST	1.5 mm	0.618	0.744	0.767	0.9364
	1 mm	0.559	0.710	0.840	0.9215
	3 NEX	0.549	0.767	0.817	0.9375
SPM	1 mm	0.312	0.730	0.636	0.6875
	3 NEX	0.348	0.817	0.666	0.8045

*Correlations are between the reconstructed and input volumes.

WE 300

Comparison of DTI principal diffusion directions using directional statistics

Armin Schwartzman[1], Robert F Dougherty[2], Jonathan E Taylor[1]
[1]Statistics Department, Stanford University, [2]Psychology Department, Stanford University

Abstract

Diffusion Tensor Imaging data differ fundamentally from most functional brain imaging data in that values at each voxel are not scalars but 3x3 positive definite matrices (also called diffusion tensors). Frequently, investigators simplify the data analysis by summarizing the tensor as a single scalar, such as fractional anisotropy (FA), and then applying standard methods such as t-maps and random field corrections to the resulting images [1]. Such scalar summaries do not capture all the information available in the data. In particular, tensors might be oriented differently and have the same set of eigenvalues and thus the same FA (Figure 1). Here we introduce a statistical method that captures a different aspect of the tensor information, namely the tensor orientation. This is defined as the direction of the principal eigenvector (the eigenvector that corresponds to the largest eigenvalue). This direction is important since it is generally assumed to be parallel to the fiber direction at that point [2].

As an initial approach, we propose a statistical model for the principal eigenvector based on the bipolar Watson distribution. We chose this distribution because it is one of the simplest that possesses the property of being antipodally symmetric, giving to each direction and its negative the same probability. This is crucial because the diffusion tensor is invariant under sign changes of the principal eigenvector. Specifically, if $\mathbf{x}$ is a random unit vector in R^3 and μ its mean (also a unit vector), then the density of the observed direction $\pm\mathbf{x}$ is given by [3]:

$f(\pm\mathbf{x}; \mu, \kappa) = C \exp\{\kappa (\mu^T \mathbf{x})^2\}$

where κ is a positive constant that controls the concentration of the density around the mean (Figure 2) and C is an appropriate normalization factor chosen so that the density integrates to one.

We describe the maximum likelihood estimates of the mean direction and concentration parameters in a sample of principal diffusion directions (e.g. a set of contiguous voxels). We also present a test of whether two samples (e.g. same voxel across two groups of subjects) have the same mean direction by constructing a scalar statistic (analogous to a t-statistic) and comparing it to a large sample approximation of its distribution under the null hypothesis. We illustrate these methods in an artificial data set as well as in the data set used in [1].

References

[1] Deutch et al. (in press), Correlations Between White Matter Microstructure and Reading Performance in Children, *Cortex*

[2] Le Bihan et al. (2001), Diffusion Tensor Imaging: Concepts and Applications, *J Mag Res Imaging* 13:534-546

[3] Mardia & Jupp (2000), Directional Statistics, John Wiley & Sons Ltd, pp 180, 239.

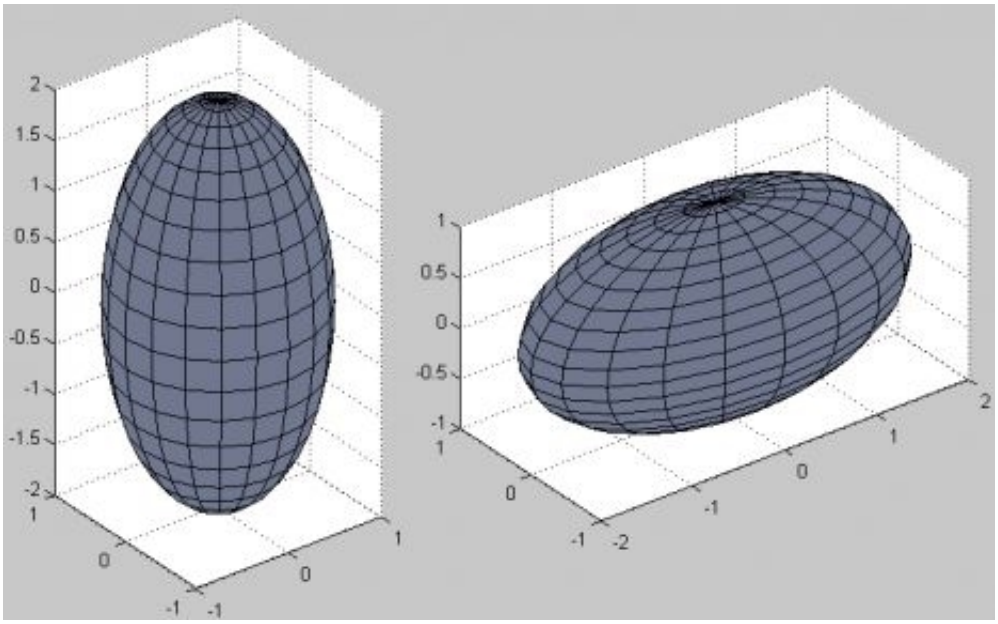

Figure 1: Ellipsoids with same eigenvalues and FA = 0.7, different orientations

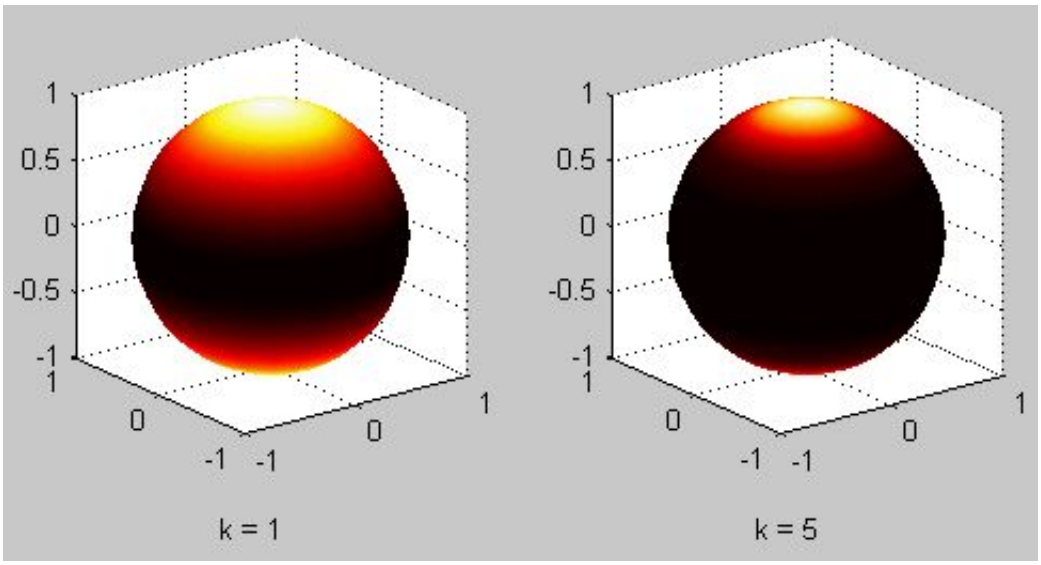

Figure 2: Bipolar Watson density function on the sphere (bright areas indicate high probability)

WE 301
Inter-trial variability of BOLD signal temporal characteristics using slow event-related fMRI

Mohamed L SEGHIER , Michel KOCHER , François LAZEYRAS
Dpt. Radiology and Medical Computing, University Hospitals of Geneva. Switzerland.

Introduction. The ER-fMRI approach allows flexible paradigm designs, with random stimuli presentation [1] at fast rates (as short as 1s [2]), or at fixed inter-stimuli interval without [3] or with [4] responses overlapping. When using rapid ER-fMRI, activated regions are generally localized by assuming linear BOLD responses with same temporal characteristics across trials, missing thus relevant temporal informations about the dynamic of the BOLD signal. For example, onset differences of 6sec between cortical regions may exist when performing same tasks [5]. Here we show the inter-trial variability of BOLD temporal characteristics and their dependence with the number of averaged trials.

Methods. All experiments were performed on a 1.5T Philips system. Functional data were acquired with EPI GRE sequence (TR/TE/Flip=1s/40ms/80°, 7 contiguous 5mm slices). Task consisted of a simple finger tapping initiated by the presentation of a 1.5sec 4Hz visual flash. The inter-stimuli-interval was 20sec and the number of trials was 30.

Data processing was done by averaging trials and using a four-parameter gamma variate function to fit the averaging response (nonlinear data fit). The gamma function, fitted to the average response of each voxel, was characterized by the time-to-onset t0, the time-to-peak ttp, the amplitude A, the width factor w, and the polynomial power α.

$h(t)=0,\ t \leq t0$

$h(t)=A*(t-t0/\alpha*w)^{\alpha}*\exp(\alpha-(t-t0)/w),\ t>t0$

$dh(ttp)/dt=0,\ h(ttp)=A,\ ttp=\alpha*w+t0.$

To assess the influence of the number of trials on the estimation of these parameters, N trials (N varied from 1 to 30) were averaged and fitted to the gamma model. To determine the inter-trial variability, a set of 10 trials, shifted across events, was averaged and the temporal parameters of the gamma fit were calculated for each set.

Results and Discussion. Different regions were implicated, including the visual area V1, and the motor areas M1 and SMA. Table1 presents the variability of the parameters across voxels within each area. Temporal parameters (first visual then motor responses) agree well with tasks presentation [6]. Figure1 shows that 10 to 12 averaged trials are sufficient to obtain a good approximation of the parameters of the gamma fit. Moreover, the parameters of the BOLD response differ across trial sets (10 successive events), indicating possible long term fluctuations of the BOLD signal. This might be due to effect of habituation and attention which can vary over time.

We show that such variability can be quantified and should be taken into account in ER-fMRI experiment, in particular when high level cognitive tasks are employed. Furthermore, this type of analysis may provide new informations about changes in cognitive strategies by correlating this parameters variability with task performances such as difficulty, accuracy and speed.

References. [1]Clark *J. Neurophysiol.* 1998. [2]Dale *Hum. Brain Mapp.* 1999. [3]Bandettini *Magn. Res. Med.* 2000. [4]Glover, *NeuroImage* 1999. [5]Schacter *NeuroImage* 1997. [6]Miezin *NeuroImage* 2000.

Mean ± std of the gamma fit parameters of activated areas.

Area	A (%)	t0 (sec)	ttp (sec)	w (a.u.)
V1	3.53 ± 1.5	1.80 ± 0.7	7.10 ± 0.3	1.20 ± 0.3
M1	1.47 ± 0.4	3.68 ± 1.1	7.61 ± 0.3	1.08 ± 0.3
SMA	2.72 ± 1.5	3.77 ± 0.9	7.75 ± 0.3	1.12 ± 0.3

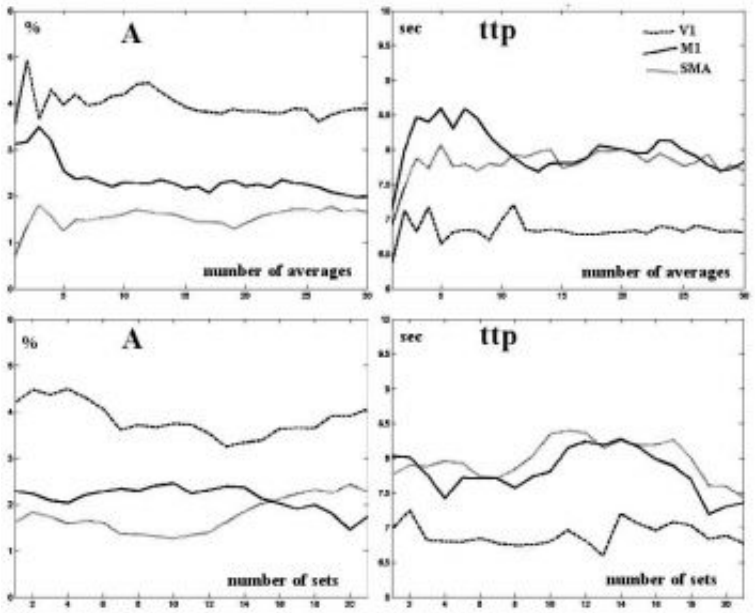

TOP: A(%) and ttp(sec) dependence with the number of averaged trials. DOWN: A(%) and ttp(sec) inter-trial variability (across sets of 10 averaged trials).

WE 303
Paramagnetic artifacts in functional MRI for the human brain mapping.

Akitoshi Seiyama[1,2], Junji Seki[3], Mari Iwamoto[4], Toshio Yanagida[1,2]
[1]Brain Information Group, KARC, CRL, [2]Division of Physiology and Biosignaling, Osaka University Graduate School of Medicine, [3]Department of Biomedical Engineering, National Cardiovascular Center Research Institute, [4]Department of Obstetrics and Gynecology, Ehime University, School of Medicine

Once the functional magnetic resonance imaging technique (fMRI) has been developed in 1980Ÿs, it has promptly prevailed as a vital tool for investigation of the human brain function as well as for clinical diagnosis. Although it is 1.5 T in currently prevailing MRI system, the strength of magnetic filed is planning to be elevated up to 7T in order to achieve a higher spatiotemporal resolution and a higher signal to noise ratio of MR images. However, biological effects of the intense magnetic filed are still unclear, and the guide line currently applied for MRI as a safety criteria in the world is based on the experimental results accumulated before dozen years. The following factors should be reconsidered as the biological effect of magnetic field: (1) strength of magnetic field, (2) area and duration exposed to the magnetic field, and (3) dynamic property of the magnetic field. In the previous study, we have shown changes in the distribution of flowing erythrocytes in a model branched vessels under an inhomogeneous magnetic field as follows [1]: 1) The attraction of paramagnetic erythrocytes induced by a gradient magnetic field was demonstrated by an increase in the concentration (hematocrit) of erythrocytes, 2) the degree of attraction was proportional to the šmagnetic susceptibilityŠ of the erythrocytes and also proportional to š(magnetic flux density) x (magnetic field gradient)Š as long as it was up to 10 T^2/m. In the present study, we discuss effects of gradient magnetic fields on the in vivo observation with the blood oxygenation level-dependent (BOLD)-fMRI and the flow sensitive alternating inversion recovery (FAIR)-fMRI from the viewpoint of imaging artifacts and safety criteria on human brain mapping.

[1] Seiyama, A., et al., Eur Biophys J 1996, 25:1-7

WE 304
Wavelet-Based Preprocessing for fMRI

Levent Sendur , Ed Bullmore
Brain Mapping Unit, University of Cambridge

Here we explore the use of wavelet-based denoising methods as a pre-processing step for fMRI data analysis. In other applications, denoising algorithms based on the discrete wavelet transform (DWT) have demonstrated improved performance compared, for example, to linear low pass filtering, because wavelet-based methods are inherently multiresolutional and adaptive to transients and other nonstationary components of noise. The classic wavelet denoising methods consist of three basic steps:
1. Calculate the discrete wavelet transform of the noisy signal,
2. Modify the noisy wavelet coefficients according to some rule, eg the soft thresholding rule developed by Donoho & Johnstone [Donoho95],
3. Compute the inverse transform using the modified coefficients.
More recent research has addressed the development of statistical models for natural images and their transform coefficients. In [Sendur], a new non-Gaussian bivariate pdf is proposed in order to explore the interscale dependencies of wavelet coefficients and a bivariate shrinkage function has been derived using Bayesian estimation theory. Both soft thresholding and bivariate shrinkage rules are threshold dependent nonlinear functions, and the threshold value selection is a very important part of the denoising algorithms. We have explored the relative performance of 1D, 2D and 3D wavelet denoising algorithms, using both classical soft thresholding and bivariate shrinkage rules, in simulated datasets with blocked and event-related experimental designs of variable SNR embedded in physiological noise.
One of the objective of this work is to investigate the performance of different image denoising algorithms using soft thresholding and bivariate shrinkage functions on fMRI imaging. We also explore the different threshold estimation techniques. However, it is well-known that the orthogonal wavelet transform has some disadvantages, i.e. it is not shift invariant and the basis functions in higher dimensions do not provide efficient representations for real world signals. In order to overcome these issues, the overcomplete wavelet transforms have been proposed such as the dual-tree complex wavelet transform (DT-DWT)[Kingsbury] We have therefore also explored the application and performance of these enhanced transforms in fMRI data analysis. We show that wavelet denoising algorithms can powerfully enhance SNR in noisy fMRI datasets; that algorithmic details can be refined by analysis of appropriate simulations;
and that there are real-life benefits in statistical detection of experimentally generated signals.
This work was supported by a Human Brain Project grant from the National Institutes of Health.
[SENDUR] L.Sendur, I.W. Selesnick, "Bivariate shrinkage functions for wavelet-based denoising exploiting interscale dependency Signal Processing", IEEE Transactions on,
Volume: 50 Issue: 11 , Nov. 2002 Page(s): 2744 -2756
[DONOHO95]D.L. Donoho, "Denoising by soft thresholding," IEEE Trans. on Inform. Theory, Vol. 41, pp. 613-627, 1995.
[Kingsbury]N.G. Kingsbury, "Complex Wavelets for shift invariant analysis and filtering of signals. Applied and Comp. Harmonic Analysis, 234-253, May 2001.

WE 305
CBV-based fMRI has improved temporal resolution compared to BOLD fMRI

Afonso C Silva , Alan P Koretsky , Peter Kellman , Jeff Duyn
1LFMI, NINDS, National Institutes of Health, 2LCE,NHLBI, National Institutes of Health

Introduction: BOLD fMRI contrast results from several processes with different timescales. These include vascular dilation, a flow response, and the transit hemoglobin through the cerebral vasculature. Together, these processes add up to an impulse response (IR) with a 3-6 s full width at half maximum amplitude (FWHM) in humans. The purpose of this work was to investigate 1) if the reduced vascular transit times in rat result in improved temporal resolution, and 2) to what extent is the resolution limited by hemoglobin transit.
Materials and Methods: Experiments were performed on adult male Sprague-Dawley rats (n=7) under a-chloralose anesthesia [1] on an 11.7 T/31 cm Bruker scanner. BOLD (n=7) and CBV (n=5, subset) fMRI was performed using a gradient-recalled echo EPI sequence with the following parameters: resolution 0.3x0.3x1.0 mm3, TE = 16-20 ms (BOLD) or 9.1-20 ms (CBV), TR = 500 ms or 1000 ms. To allow estimation of the fMRI IR width, bilateral electrical forepaw stimulation (0.333 ms pulses, 2 mA amplitude) was performed using an m-sequence paradigm with a 500 ms or 1000 ms baseperiod and 255 bin length, and inverse repeat [2]. Two runs were performed each for BOLD and CBV fMRI. For CBV fMRI, a dose of 20 mg/kg of iron oxide was injected intravenously 5 minutes before commencing the CBV studies. The IR was calculated from correlation analysis [2]. In activated pixels, FWHM and time-to-peak of the IR were estimated after 5-10 fold temporal interpolation.
Results and Discussion: All BOLD and 3 of the CBV fMRI studies showed substantial activation (2 CBV studies were technical failures). An example is given in the figures. Regions of activation were significantly larger in BOLD (Fig. 1, left column), than in CBV (Fig. 1, right column), attributed to BOLD effects in large draining veins. A substantial spread in BOLD FWHM (Fig. 1, middle row) and TTP (Fig. 1, bottom row) over the activated area was observed, with the responses showing a longer delay in large pial veins. This effect was much reduced in the CBV data, presumed to have less contamination from larger veins [3]. In all rats, the CBV IR was narrower and peaked earlier than the BOLD IR (Figs. 1,2). Interestingly, the CBV IR did not return to baseline for many seconds (Fig. 2), consistent with other CBV-based fMRI studies in rats [4]. Averaged BOLD fMRI FWHM and TTP were 2.30?.6 s and 2.7?0.6 s (n=8), respectively. These values are significantly reduced compared to human values, suggesting a substantial contribution of flow response and hemoglobin transit to the human IR. Furthermore, CBV FWHM (1.6?0.2 s,n=3) and TTP (1.9?0.3 s,n=3) were even shorter than their BOLD counterparts, suggesting a substantial hemoglobin transit effect to the BOLD IR in rats. We conclude that CBV fMRI allows for improved temporal resolution, and that the temporal resolution of neurovascular control mechanisms is below 1.6 s FWHM.
References: [1] Silva, PNAS 2002; [2] Kellman, Neuroimage 2003; [3] Mandeville, MRM 1999; [4] Mandeville, JCBF 1999.

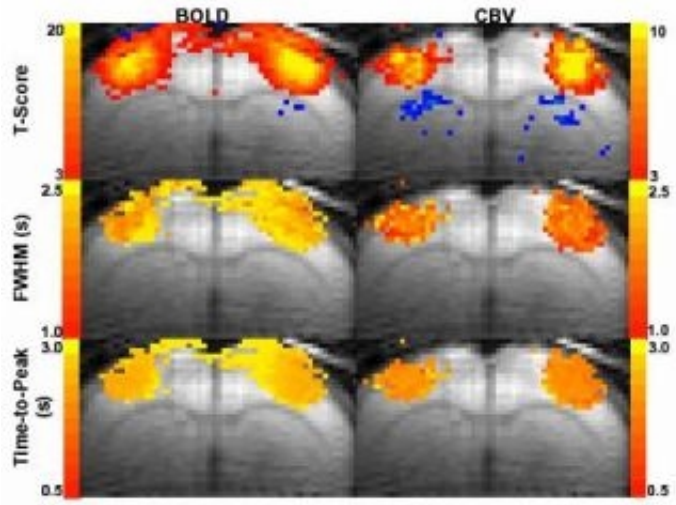

Figure 1: BOLD (left) and CBV (right) activation maps to bilateral stimulation of the rat forelimb. Top row: T-score maps; Middle row: Full-Width-at-Half-Maximum maps of the Impulse Response; Bottom row: Time-to-Peak maps.

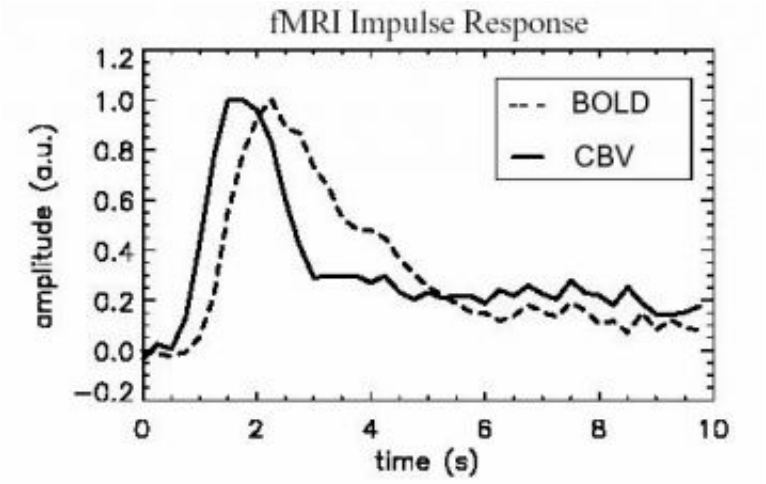

Figure 2: BOLD (red) and CBV (blue) impulse responses derived from the activation maps shown in Fig. 1. The BOLD IR is significantly broader, and peaks significantly later than the CBV IR.

WE 306
Measuring Consistency of Brain Tissue Classification Methods

Vivek Singh , Jason Lerch , Najmeh Khalili , Alan C. Evans
McConnell Brain Imaging Centre, Montreal Neurological Institute, Montreal, Canada

An important metric in the validation of a classification technique is the assessment of consistency. Unlike the difficulty inherent in measuring classification accuracy, which can only be determined if a gold standard is available (e.g., through manual classification, simulation of the imaging process, etc.), a method does exist for the direct measurement of consistency, though it is rarely employed for the validation of brain tissue classification techniques in the literature. This method consists in performing repeated scans of a single healthy individual within a time period during which one would not reasonably expect major anatomical changes to take place and then evaluating the classification similarity among the images. The objective of our study was therefore to use this procedure to assess the consistency of several different classification methods.

Methods

18 T1-weighted MRI images were obtained of a single individual over a short time period as part of the colin27 dataset [1]. The images were registered into standardized MNI-talairach space using an affine transformation [2] and simultaneously corrected for non-uniformity artifacts [3]. The images were then classified into white matter, grey matter and cerbro-spinal fluid with several classification techniques commonly used at our research institution. Three fully-automated classification techniques were assessed, including artificial neural network (ANN) [4], kohonen nearest neighbour (KNN) [5] and statistical partial volume classifiers (PVE) [6]. The effect of two automated techniques for pruning the input training points to the supervised ANN and KNN classifiers were also examined, including pruning based on an initial minimum distance classification (MD) [4] and a minimum spanning tree (MST) pruner [5]. The partial volume labels produced by the PVE classifier were discretized by setting the label at each voxel to the discrete tissue class label with the highest fraction of tissue measured to be present in a particular voxel. Consistency was determined by measuring the co-efficient of variance (std/mean) across the white matter volumes obtained from the 18 classified images. The white matter volume was determined with a mask applied to non-cortical structures.

Results

As accompanying figure shows, the classification technique that produced the most consistent white matter volume estimate was the partial volume classifier. Another notable result was the fact that the MD pruner produced more consistent results relative to the MST pruner using the ANN classifier, while the opposite was found using the KNN classifier.

Conclusion

The results suggest an advantage in the use of partial volume estimation techniques even if a discretely classified volume is all that is desired. An assessment of accuracy in conjunction with this consistency measure is necessary to make these measurements truly robust. The results also illustrates the utility of using repeated scans of a single individual to assess the validity of medical image processing techniques.

[1] C. J. Holmes et. al. JCAT, 22:324-33, 1998.
[2] D. L. Collins et. al. JCAT, 18:192-205, 1994.
[3] J. G. Sled, A. P. Zijdenbos, A. C. Evans. IEEE TMI, 17:87-97, 1998.
[4] A. P. Zijdenbos, R. Forghani, A. C. Evans. MICCAI 1:439-448, 1998.
[5] C. A. Cocosco, A. P. Zijdenbos, A. C. Evans. MIA 7:513-528, 1993.
[6] J. Tohka, A. Zijdenbos, A. C. Evans (Submitted for publication).

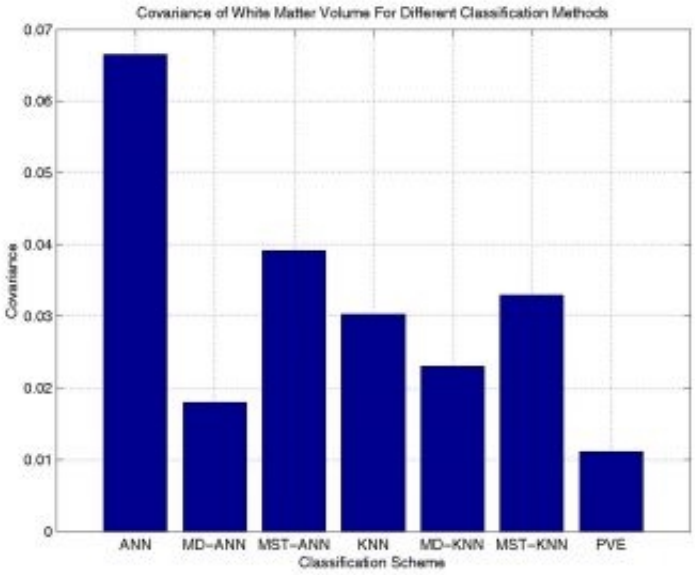
Covariance of White Matter Volume For Different Classification Methods
Covariance
0.07
0.06
0.05
0.04
0.03
0.02
0.01
0
ANN
MD−ANN
MST−ANN
KNN
MD−KNN
MST−KNN
PVE
Classification Scheme

WE 307
Investigation of binding processes with BOLD signal coherence analysis

Jeremy L. Smith[1], Alessandra M. Passarotti[2], Jie Huang[3]
[1]Program in Neuroscience, Michigan State University, [2]Program in Cognitive Science, Michigan State University, [3]Department of Radiology, Michigan State University

Introduction. Although there has been increasing interest in the involvement of dynamic interregional interactions in cognition, the invasiveness of present electrophysiological methods prevents their application in healthy subjects. Therefore, the present study uses principal components and coherence analysis to investigate these "binding processes" using FMRI.

Methods. Similar to Passarotti et al. (2003), we administered a block-design face matching task to nine adults (4 female). During the task blocks, subjects were presented with two neutral, monochrome male faces, followed by a 5 second delay (blank screen) and a target face. The subjects were instructed to respond by pressing one button if the target face matched either of the previous two faces, and a different button if the target face did not match the previous two faces. Control blocks consisted of a simple motor response to scrambled faces.

Imaging. BOLD-signal functional image acquisition was performed on a 3T GE system using a single shot gradient-echo sequence (TR=2 sec, TE=40, FOV=220 mm, FA=80; 25 5.5 mm axial slices, 64 x 64 matrix, voxel size=3.4 x 3.4 x 5.5 mm), which were superimposed on a T1-weighted anatomical acquired as 116 sagittal fast-SPGR images (FOV=256, 1.5 mm slices, 1.5 x 1.5 x 1.5 mm voxels).

FMRI image processing. Each dataset was motion-corrected using the NIMH AFNI software suite (Cox, 1997). A smoothed-boxcar waveform, representing the estimated HRF, was duplicated 19 times, with each duplicate ("index") offset by 200 msec. This allowed us to generate a phase map representing the mean activation time for each region. Individual datasets were then Talairached and combined to create a merged anatomical/functional dataset for level II region-to-region coherence analysis.

Level II analysis. To minimize processing time during coherence analysis, we obtained a covariance matrix for regions of interest (ROIs) to determine which regions were significantly coactivated. We then subjected the indicated areas to intraregional principal components analysis (PCA), similar to Bullmore et al. (1996). PCA yielded, on average, one to five clusters within each ROI that were significantly ($x \geq 0.33$) contributing to the total regional variance. Based on the statistical "weight" of each voxel we computed the center of mass for each cluster, which was then used as the representative coordinate for time series extraction.

Results and Discussion. a) The pilot data from our analyses have allowed us to disentangle truly interacting areas from those that are simply covariant due to a common input. b) Our results also suggest that different subregions within the hippocampus and amygdala are activated depending on laterality. In particular, the left and right amygdalae have predominately negative and positive effects on regional variance, respectively. This laterality effect may reflect phase-delayed (left amygdala) and phase-advanced (right amygdala) interactions with other regions. These preliminary findings suggest that, using PCA and coherence analysis, FMRI can be used sas a viable alternative to invasive methods for investigation of binding effects.

WE 308
Quantification of F-18-Diprenorphine Kinetics

Mary E. Spilker[1], Till Sprenger[2], Michael Valet[2], Gjermund Henriksen[1], Hans-J. Wester[1], Thomas R. Toelle[2], Henning Boecker[1]
[1]Nuklearmedizinische Klinik, TU München, [2]Neurologische Klinik, TU München

Introduction:
F-18-Diprenorphine (F-18-DPN) is a relatively new opioid radioligand whose kinetic behavior in the human brain has yet to be characterized. This radioligand has similar pharmacologic properties as its C-11 counterpart, but the longer half-life of F-18 makes this compound applicable to a variety of experimental and clinical protocols. Therefore, we have undertaken an analysis of F-18-DPN to evaluate the performance of invasive and noninvasive modeling methods for quantification of distribution volumes (DV) and binding potentials (BP).

Methods:
After giving informed written consent, six subjects (mean age: 42 ± 12 years; 2 females, 4 males) underwent a 120 minute F-18-DPN PET study with arterial blood sampling. An MRI scan was also acquired for each subject and the MRI and PET data sets were realigned and coregistered using SPM99. The MRI data was used to select individualized Volumes of Interest (VOIs) for each subject for the following regions: occipital cortex; cerebellum; frontal cortex; cingulate cortex; putamen/caudate; and thalamus. Three invasive models (the two- and one- tissue compartmental models and the Logan model) and three noninvasive models (the simplified reference tissue model, the noninvasive Logan model, and the tissue ratio method) were applied to the data. Model performance and derived DV and BP values were compared.

Results:
The two-tissue (2T) compartmental model was found to best characterize the data. The estimated DV and BP values were consistent between the various models (Table 1). The DV values estimated from the invasive Logan model and the one-tissue (1T) compartmental model were both highly correlated ($R^2 > 0.993$) with those from the 2T model; although compared with the 2T model, the invasive Logan model showed more bias in DV values (<12%) than the 1T model (<5%). The BP values determined from the invasive and noninvasive methods were slightly more variable, but also correlated well with BP values determined from the 2T model ($R^2 > 0.937$). While the BP results showed more bias than that observed with the DV values, all models resulted in similar regional distributions. The tissue ratio method showed the most bias in BP, but resulted in regional distributions consistent with the other models. The other noninvasive models performed similar to that of the invasvie models yet consistently resulted in lower BP values.

Conclusions:
DV and BP values for F-18-DPN are robustly estimated by a variety of invasive and noninvasive modeling approaches. While DV appears to be the more stable outcome parameter, BP values estimated from the noninvasive methods may be of use in a clinical setting when arterial sampling is not a feasible option.

Table 1. Mean Regional Distribution Volume and Binding Potential Values

	Distribution Volume			Binding Potential					
Region	2T	1T	Invasive Logan	2T*	1T	Invasive Logan	SRTM	Noninvasive Logan	TRM
Thalamus	19.12	18.87	16.63	1.99	2.12	1.87	1.76	1.76	2.85
Putamen/Caudate	16.10	15.82	14.61	1.54	1.69	1.56	1.46	1.47	2.40
Cingulate	14.40	14.29	12.60	1.30	1.43	1.23	1.15	1.15	1.99
Frontal	12.15	11.86	10.99	0.93	1.02	0.93	0.88	0.89	1.49
Cerebellum	9.15	8.86	8.10	0.43	0.46	0.40	0.40	0.40	0.52
Occipital	6.34	5.93	5.68	--	--	--	--	--	--

2T: two-tissue compartmental model; 1T: one-tissue compartmental model; SRTM: simplified reference tissue model; TRM: tissue ratio method. *BP was calculated as (DV_{VOI} / DV_{REF}) - 1 rather than k3/k4.

WE 309
Spin-spin Relaxometry of Blood at 1.5 T

Bojana Stefanovic , G. Bruce Pike
McConnell Brain Imaging Centre, Montreal Neurological Institute, Montreal, Quebec, Canada

Despite numerous blood spin-spin relaxometry studies, a complete understanding of the dHb-induced $R_{2,blood}$ enhancement mechanism is still lacking. Various models having been proposed, including fast chemical exchange of water protons between the plasmatic and the erythrocytic compartments, diffusion in the intra- and/or extracellular gradients, or a combination of all of these [2,4]. We tested the performance of a recently proposed diffusion model [3] against the exchange model on a large set of T_2 blood estimates spanning the fMRI relevant range of blood oxygenations (Y) and an extensive set of refocusing intervals (τ_{180}) to determine the superior model for prediction of intravascular SE BOLD effect.

Blood was drawn from the superficial veins of the non-dominant forearm of 4 healthy adults before, during and after alternating elbow flexion and extension, spanning 4 minutes of forearm occlusion, to allow for in vivo modification of Y. Gated rotation of the vacutainers about their long axes (at 20 rpm) prevented the settling of erythrocytes. A T_2 prepared segmented EPI sequence [1] (2.3x2.3x5 mm^3, EPI factor of 3, TR of 3 s) was used for T_2 relaxometry, with τ_{180} varying from 2 to 40 ms. The order of acquisitions with different refocusing intervals was randomized and 6 effective echo times probed for each τ_{180}. The imaging slice was 5 mm thick and positioned axially at the centre of the vacutainer. Following the MRI, blood gas and cooximetry analyses were performed. The T_2 estimates were fitted to Luz and Meiboom s model of fast chemical exchange [5] and Jensen and Chandra s model of spin-spin relaxation in the presence of diffusion of significant magnitude relative to the length scale of the weak microscopic field inhomogeneities [3]. Two model orders were investigated within each model structure: a constrained model, in which the intrinsic spin-spin relaxation ($T_{2,0}$) was fixed and an unconstrained one, in which the $T_{2,0}$ was allowed to vary with Y.

The estimated blood T_2 values at different Y as well as the fits of the unconstrained exchange and constrained diffusion models are shown in Figure 1. The corresponding parameter estimates are summarized in Table 1. The comparison of the sum of squared residuals (SSR) of the fits to the models led to the selection of the diffusion model ($SSR_{diffusion}$~1.85 ms^2 vs. $SSR_{exchange}$~2.49 ms^2). Allowing for variation of the intrinsic T_2 of blood with Y produced a better fit (at α=0.01) in the exchange but not in the diffusion modeling, as established by the F-test of the reduction in SSR.

The present study lends support to the application of the recently reported model of diffusion in weak microscopic field inhomogeneities in describing the spin-spin relaxation rate enhancement in human blood at 1.5 T. The model may be employed for calculation of the intravascular SE BOLD effect under normal physiological conditions.

[1] Brittain, MRM, 33:689 696, 1995.
[2] Gasparovic, MRM, 26:274 299, 1992.
[3] Jensen, MRM, 44:144 156, 2000.
[4] Matwiyoff, MRM, 20:144 150, 1991.
[5] Luz and Meiboom, JCP, 39:366 370, 1963.

Y [%]	$T_{2_{0,exchange}}$ [ms]	K_0 [10^{-14} T^2]	G_0 [10^{-14} T^2]
93	198±5	0.53±0.14	0.8±0.1
87	197±5	1.36±0.21	1.9±0.2
72	200±6	2.87±0.36	3.7±0.4
66	183±7	3.67±0.48	5.5±0.6
62	184±7	4.65±0.60	6.6±0.8
48	179±9	7.31±0.98	10.1±1.2
43	169±10	9.31±1.31	13.2±1.7
42	166±10	9.38±1.33	13.6±1.8

Table 1: Exchange and diffusion model parameter estimates. The exchange time (τ_{ex}) estimate was 3.0±0.2ms, with the intrinsic spin-spin relaxation time ($T_{2,0,exchange}$) and the curvature term (K_0) shown in columns 2 and 3 below. For the diffusion model, the characteristic length scale of spatial variations of field inhomogeneities (r_c) was 4.3±0.2μm; and the intrinsic spin-spin relaxation time ($T_{2,0,diffusion}$), 203±3ms, with the curvature term ($G_{0)}$ listed in column 4.

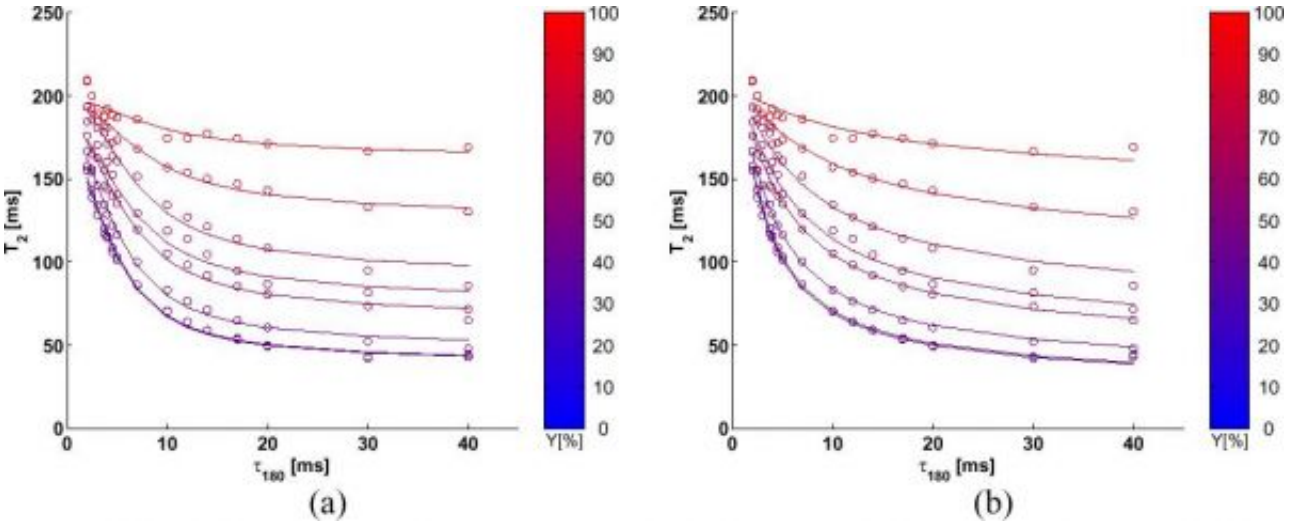

Figure 1: The $T_{2,blood}$ estimates and the fits of the unconstrained exchange (a) and constrained diffusion (b) models. The hematocrit of the blood samples used was 51.2±0.4% (mean±standard error).

WE 310
Quantifying the Intravascular SE BOLD Effect at 1.5 T

Bojana Stefanovic , G. Bruce Pike
McConnell Brain Imaging Centre, Montreal Neurological Institute, Montreal, Quebec, Canada

Despite a very small cerebral blood volume fraction (2-5%), the decrease in the T_2 blood with deoxygenation is so much greater than that of tissue that almost all of SE BOLD [4] at 1.5 T originates in the intravasculature. This IV BOLD phenomenon has been exploited for tissue oximetry [5]. Recently, we have proposed a non-invasive method for blood volume quantification that isolates the blood signal by relying on the dependency of T_2 blood on the refocusing interval (τ_{180}). In this study, we obtained the parameterization of the diffusion model of T_2 blood relaxation. To characterize the blood signal completely, the dependence of T_1 blood on Y was also quantified, over the fMRI-relevant range.

Blood was drawn from the superficial veins in the course of an exercise paradigm, allowing in vivo Y modification. A T_2 prepared segmented EPI sequence [1] was used for T_2 relaxometry, with τ_{180} varying from 2 to 40 ms. The T_1 of blood was quantified using a single-slice Look-Locker sequence with a segmented EPI readout. The imaging slice was 5 mm thick and positioned axially at the centre of the vacutainer. Following the completion of the MR relaxometry measurements, the blood gas and cooximetry analyses were performed. The T_2 estimates were fitted to the Jensen and Chandra's model of spin-spin relaxation in the presence of diffusion of significant magnitude relative to the length scale of the weak microscopic field inhomogeneities [2]: $R_{2,blood} = R_{2,0} + G_0 (\gamma r_c^2/2D) F(2D\tau_{180}/r_c^2)$,

where G_0 is the mean square magnitude of the field inhomogeneities; r_c is the characteristic length scale for the spatial variations of the field inhomogeneities; D is the diffusion constant and F is defined in [2]. The dependency of intrinsic spin-spin lattice relaxation time ($T_{2,0}$) on Y was investigated, by contrasting a constrained model, in which $T_{2,0}$ was fixed across Y and an unconstrained one, with $T_{2,0}$ varying with Y.

The constrained diffusion model fit to the T_2 estimates is shown in Figure 1. Allowing for variation of $T_{2,0}$ with Y did not produce a better fit (at α=0.01), as established by the F-test of the reduction in the sum of squared residuals (SSR). Fitting the G_0 as a quadratic function of Y (cf. Figure 2) and combining the results, the dependence of $T_{2,blood}$ on Y and τ_{180}, at 1.5 T, for the physiologically relevant hematocrit, is well modeled by the Eqn. (1) above with $T_{2,0}$ of 203±3 ms, $r_c^2/2D$ of 4.60±0.42 ms and G_0 given by: $G_0=(4.50\pm0.51)10^{-13}[T^2](1-Y/100)^2$. The dependence of the resulting T_1 estimates on Y was obtained by linear fitting of the $R_{1,blood}$ (cf. Figure 3). Two-way ANOVA reported a statistically
significant effect of hematocrit on the T_1 estimates when controlling for Y ($p<10^{-9}$).

The presented parameterization of the diffusion model of spin-spin relaxation rate enhancement in human blood for the hematocrit levels pertinent to studies of functional activation allows quantification of intravascular spin-echo BOLD. The empirical linear model of $R_{1,blood}$ decrease with Y, in agreement with a recent report~[3], is also required for accurate characterization of the blood signal in spin-echo fMRI experiments at 1.5 T.

[1] Brittain, MRM, 33:689 696, 1995.
[2] Jensen, MRM, 44:144 156, 2000.
[3] Silvennoinen, MRM, 49:568 571, 2003.
[4] VanZijl, NM, 4:159 167, 1998.
[5] Wright, MRM, 16:126 140, 1991.

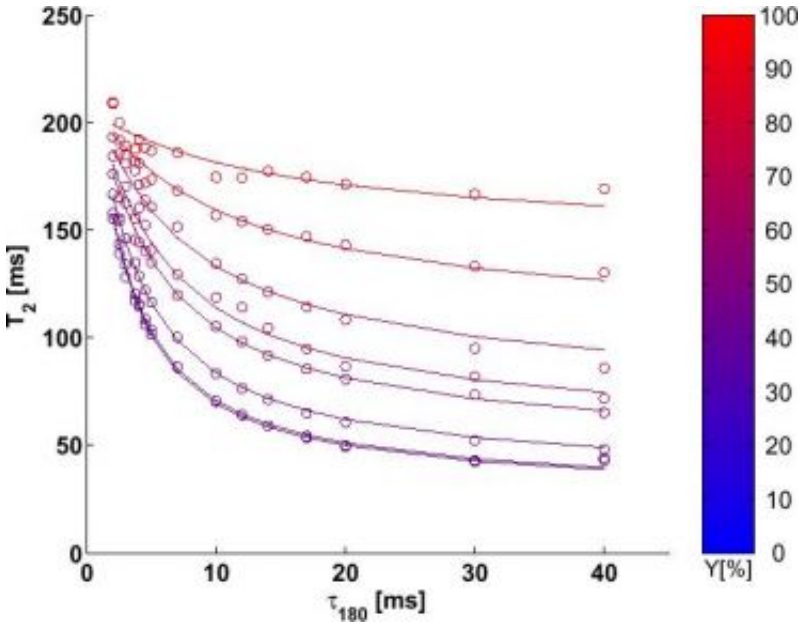

Figure1: The T_2 estimates and the fit of the constrained diffusion model The blood samples used had a hematocrit of 51.2±0.4$ (mean±standard error).

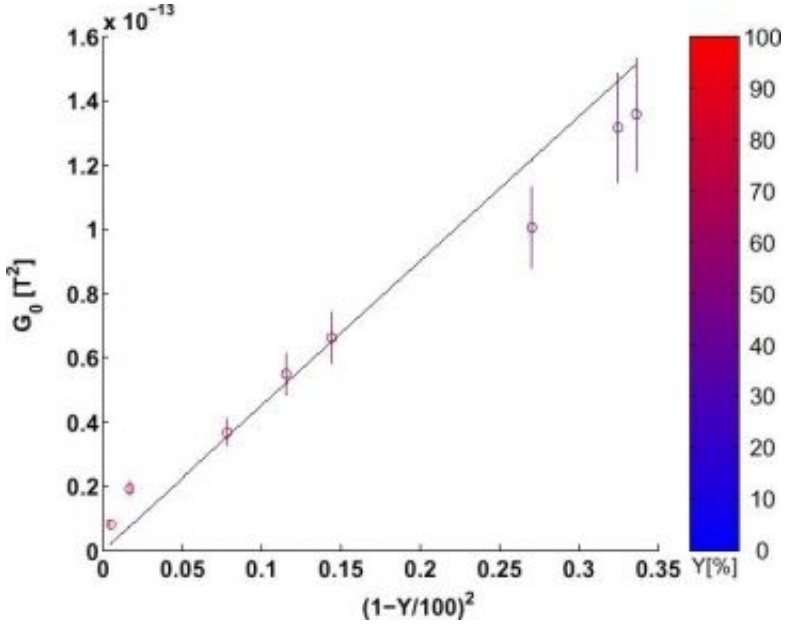

The G_0 estimates from the diffusion model fitted as a quadratic function of the oxygen saturation level.

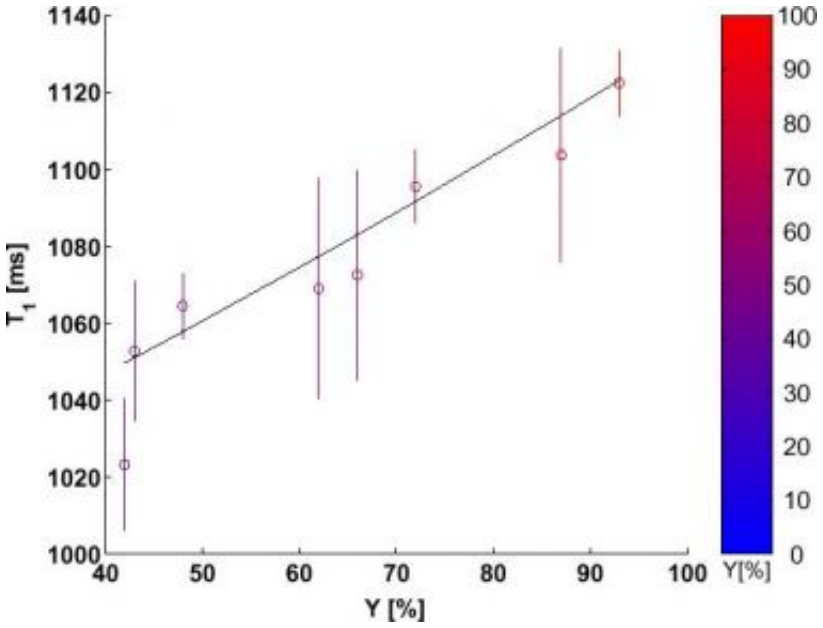

The spin-lattice relaxation time of blood fitted against oxygen saturation. The intercept estimate was 996±36 ms and dR_1/dY, -1.22±0.54 μs/%.

WE 311
Differentiating between Primary and Secondary Olfactory Cortex using the Kalman Filter in an fMRI Experiment

Jason R Steffener[1], Matthias H Tabert[2,3], Haiying Tang[4], Truman R Brown[4], Davangere P Devanand[2,3], Stanley Reisman[1]

[1]Department of Biomedical Engineering, New Jersey Institute of Technology, Newark, NJ, [2]Department of Biological Psychiatry, New York State Psychiatric Institute, New York, NY, [3]Department of Psychiatry, Columbia University, College of Physicians and Surgeons, New York, NY, [4]Department of Radiology, Columbia University, College of Physicians and Surgeons, New York, NY

Background
Previous olfactory fMRI studies have demonstrated that primary and secondary olfactory- brain areas show differential odor-induced signal responses (1,2). These responses include a transient response to odors in primary olfactory areas and sustained levels of signal change throughout odor presentation in secondary olfactory cortex. In the current study we used the Kalman filter to extract the temporal response to odorants with the goal of differentiating brain areas that show a tranisient versus a sustained odor-induced signal change. This technique uses stimulus presentation times to extract the temporal response at every voxel across the brain. Classification of the extracted information as either sustained, transient, or no response allowed for differentiation between the primary and secondary cortices.

Methods
This experiment tests the hypothesis that primary and secondary olfactory cortices can be differentiated with the Kalman filter based on their extracted fMRI temporal response patterns. The experiment involved 4 separate fMRI scans, 3 min, 45 sec each in duration. During each scan, 4 odors (phenyl ethyl alcohol [having a rose like smell], mint, banana, and vanilla) were presented at suprathreshold concentrations in a pseudorandom order (15 sec ON and 30 sec OFF) via an olfactometer (3). A rest period of at least 5 minutes (no odor present) between each scan allowed for recovery from adaptation and habituation. A Phillips Medical Systems Intera 1.5 Tesla MRI research machine, equipped with echo planar capabilities acquired all images. The functional image acquisitions used a standard EPI gradient echo sequence (TR=3000, TE=50, flip=90, slice thickness 5 mm with no gap, 20 slices from frontal pole to the posterior end of the temporal lobe, 20x20 cm FOV, 64x64 matrix). Fast spin echo T2 images were acquired for subsequent co-registration of the fMRI data, allowing for better anatomical localization.

Results
We will present results from six healthy young individuals. Data from one individual was analyzed using the Kalman filter after spatial preprocessing using the FMRIB Software Library (4). As predicted, results showed differential temporal responses throughout olfactory-related brain areas. The piriform cortex, part of the primary olfactory cortex, showed transient responses to each 15-second odor presentation. In contrast, the orbitofrontal regions, part of the secondary olfactory cortex, showed a more sustained response, lasting for the duration of the 15-second odor presentation period.

Conclusions
The presented method makes no prediction of the temporal shape of a response in a particular brain location. This makes it more flexible and sensitive to waveforms with different temporal characteristics that may occur in different parts of a brain network in response to a given stimulus. Finally, This technique may also hold promise for further elucidating the neural basis of olfactory dysfunctions in clinical populations.

References
1. Poellinger et al. (2001). Neuroimage, 13, 547-60
2. Sobel et al. (2000). Neurophysiol, 83, 537-51
3. Lorig et al (1999). Behav Res Methods Instrum Comput, 31, 370-5
4. Jenkinson and Smith (2001). Medical Image Analysis, 5(2):143-156.

WE 312
Reproducibility Analysis in Bold-based Event-Related Functional MRI Experiments

Hong-Ren Su , Chien-Chih Huang , Michelle Liou , Juin-Der Lee , Philip E. Cheng
Institute of Statistical Science, Academia Sinica, Taipei 115, Taiwan

The bold-based event-related functional MRI experiments have been widely used to research into human brain functions. We have recently proposed a methodology for assessing reproducibility evidence in fMRI studies using an on-andoff paradigm without conducting separate experiments(Liou et al. , 2003); we also suggested interpreting SPMs in conjunction with reproducibility evidence in fMRI studies. In this study, we generalized the method to analyzing fMRI data collected from event-related experiments. In the empirical example, we applied the method to analyzing data from the study by Arrington et al. (2000). The
original experiments involved 12 human subjects and investigated brain function during cued discrimination tasks. The experimental tasks required subjects to orient attention either to a region bounded by an object (object-based spatial attention) or to an unbounded region of space (location-based spatial attention) in anticipation of an upcoming target. The experiment additionally compared the difference between validly and invalidly cued trials. Through reproducibility analysis, we clearly discriminated between stimulus-related and task-related
activation components in subjects performing the experimental tasks while responding to stimuli. We have not found any reproducible component that particularly associated with
object-based attention. Furthermore invalidly cued trials did not consistently result in greater activation.
References:
Arrington, C.M., Carr, T.H., Mayer, A.R. & Rao, S.M. (2000). Neural mechanisms of visual attention : objectbased selection of a region in space. Journal of Cognitive Neuroscience 12. Supp. 2, 116-117.
Liou, M., Su, H.R., Lee, J.D., Cheng, P.E.,Huang, C.C. & Tsai, C.H. (2003). Bridging functional MR images and Scientific inference: reproducibility maps.Journal of Cognitive
Neuroscience, 15 (7), 935-945.

WE 313
A Structured Secant Method for fMRI Time Series Registration

Shaoyan Sun[1,2], Huanwen Tang[1], Wenyu Liu[2,3], Yijun Liu[4], Yiyuan Tang[2]
[1]Institute of Computational Biology and Bioinformatics, Dalian University of Technology,Dalian 116023, [2]Institute of Neuroinformatics, Dalian University of Technology, Dalian 116023, [3]School of Foreign Languages, Dalian University of Technology, Dalian 116023, [4]Departments of Psychiatry & Neuroscience, McKnight Brain Institute, University of Florida, USA

Introduction

In functional MRI (fMRI) studies, it is a necessary but time consuming step to register time series images cross scanning sessions as well as cross subjects. Nonlinear least squares approximation,

$f(x)=0.5R(x)^T R(x)=0.5\Sigma_{i=1}^{m*n} r_i^2(x)$,

has been an attractive method for registering the time series images, where $r_i^2(x)$ is defined as the distance of the corresponding voxel intensities between the two images. Thus, the registration procedure can be reduced to solving a mathematical problem, i.e., optimizing f(x), and there is only one registration parameter remaining, the variable x. The conventional algorithm for the optimization is through the Gauss-Newton method, which simply deletes the second-order information of the Hessian of f(x) when approximating the Hessian. Making fully use of the second-order information instead of ignoring it needs accurate approximation to the Hessian.

Methods

Recently, a completely-structured secant method has been proposed to solve the nonlinear least squares problem, which combines a novel quasi-Newton equation with a "product structure" and accurately approximates the Hessian by secant update (Zhang et al., 2003). At the same time, the update matrix is always kept symmetrical and positive, which makes the process reversible, so that a descent direction can be established in each approximating step. Following is a particular algorithm for the completely-structured secant method.

Given a start point and a start matrix $A=A_0$.

Step 1: Let $B=J(x)_T+\theta A$, where J(x) is the Jacobian of R(x). Find the solution d to the equation $Bd=-\Delta f(x)$.

Step 2: If $||\Delta f(x)||<\delta_1$ or $||d||<\delta_2$, then stop; otherwise go to step 3.

Step 3: Let $\alpha=1$. If

$f(x+\alpha d) < f(x) + \eta\alpha\Delta f(x)^T d$ (4.1)

go to step 4; otherwise set $\alpha=0.5\alpha$, and repeat until (4.1) is satisfied.

Step 4: Set $s=\alpha d$, $x_+=x+s$, and $A_+=A-Ass^T A/s^T As+y^{\#}(y^{\#})^T/(y^{\#})^T s$, where

$y^{\#}=y^{\#*}+3R(x^+)^T/||R(x)||||s||^2[(J(x_+)+J(x))s-2(R(x_+)-R(x))]s$,

$(y^{\#})^*=(J(x_+)^T R(x_+)-J(x)R(x_+))/||R(x)||$.

Step 5: Set $x=x_+$, $A=A_+$ and go to step 1.

Results and Conclusion

Using the above algorithm we can obtain an accurate approximation to the Hessian of f(x). The results based on simulated registration show that we can resolve the registration parameters in much shorter time but with high precision when combining the above criteria and new algorithm. The images used here are from 100x100 fMRI scans. The results are shown in Table 1. Our study suggests that the completely-structured secant method may be an effective tool for the registration of fMRI time series images.

Reference

J. Z. Zhang, et al (2003). BIT Numerical Mathematics 43: 217-229

Acknowledgements

This work is supported by the MOST (2100CCA00700) and MOST International Program, NSFC (30170321) and MOE (KP0302).

WE 314
A new wavelet-based method to detect and characterize spatially distributed patterns of activation in fMRI datasets

Sylvain Takerkart[1, 2], Maria I Gobbini[1, 3], James V Haxby[1,3], Ingrid C Daubechies[1,4]
[1]Princeton University, Center for the Study of Brain, Mind and Behavior, [2]University of Maastricht, Department of Cognitive Neuroscience, [3]Princeton University, Pyschology Department, [4]Princeton University, Program in Applied and Computational Mathematics

Recent fMRI studies (for instance, Haxby et al. 2001) have demonstrated that the spatial distribution of the magnitude of activation, within a region of interest, contains relevant brain mapping information: for each experimental condition, the pattern was reproducible, and distinguishable for different conditions. The analysis of such spatially distributed patterns of response is composed of three sub-problems: 1) Detection - how can the voxels that contribute to a distributed pattern of response be identified ; 2) Estimation - how is the information in these patterns best represented ; and 3) Discrimination - what tools are best suited to comparing different patterns. Despite the intrinsic multivariate character of the information contained in distributed patterns (in the sense that it resides in several voxels), the detection and estimation methods proposed in previously published studies are univariate (GLM applied independently at each voxel).

We here propose a new method that aims at benefiting from the multivariate aspect of the information by efficiently encoding the shape of the neighboring signal at every location. We apply a translation-invariant three-dimensional wavelet transform on the images, which allows description of the neighboring spatial pattern around each voxel. In the subsequent statistical model, the observation is a vector of wavelet coefficients (in all spatial directions, at several spatial scales), instead of only the scalar intensity at this voxel. Voxels that show a differential neighboring spatial pattern across categories, as detected by a MANOVA, are labeled as being part of a distributed pattern. The wavelet coefficients at these voxels can then be used with any classifier (SVM, as in Cox & Savoy, 2003, linear discriminant analysis, as in Carlson et al., 2003, or neural network, as in Polyn et al., 2004) to identify the category corresponding to an unknown pattern.

From a computational standpoint, the linearity of the spatial wavelet transform and temporal model allows a fast implementation. Indeed, rather than applying the translation-invariant wavelet decomposition on all the original images, then running the MANOVA, it is equivalent and much more computationally efficient to estimate a univariate temporal linear model at the first level (with one predictor per condition), apply the spatial wavelet transform on the beta maps and run the MANOVA at the second level of analysis.

Initial results are very promising. In a new experiment similar to the one in Haxby et al. 2001, but with categories chosen to be more subtly different (male vs. female faces for instance), the proposed method combined with a linear SVM classifier, achieved an accurate identification of the category in more than 80% of the cases, as compared with a chance level of 14.3% (since there were 7 categories of stimuli).

Carlson et al., 2003. Journal of Cognitive Neuroscience 15: 704-717.
Cox & Savoy, 2003. NeuroImage 19: 261-270.
Haxby et al., 2001. Science 293: 2425-2430.
Polyn et al., 2004. OHBM 2004, submitted.

WE 315

Predicting Single-trial Performance in a Target Detection Task from High Density EEG

Akaysha C. Tang [1,2,3], K.C. Chang [4], Matthew T. Sutherland [1], Christopher J. McKinney [1]
[1] Department of Psychology, University of New Mexico, Albuquerque, NM, USA, [2] Neurosciences Department, University of New Mexico, Albuquerque, NM, USA, [3] Department of Computer Science, University of New Mexico, Albuquerque, NM, USA, [4] George Mason University, Washington, DC. USA

The goal of the present study was to predict subject responses in a simple target detection task from the EEG. Combining a blind source separation algorithm (BSS) with conventional classification methods we sought to determine whether a subject made a correct or incorrect response on a given trial using single-trial EEG. The detection task required a subject to respond with a right hand button press if the middle line in a 5x5 array of lines was tilted (see Fig 1.) The tilt of the line located at the center of the array varied between 0-45¢ª from vertical, by 5 ¢ª increments to create a range of difficulty (less tilt more difficult to detect). Half of the trials were ¡°catch trials¡± (no tilt) and the other half were equally distributed between 5-45¢ª of tilt. Thus, correct responses consist of making button presses when a tilted line is present and withholding button presses when a tilted line is absent. Similarly incorrect responses also include both the making and withholding motor responses. We collected continuous 128-channel EEG throughout the task performance and subsequently decomposed the scalp EEG signals into 128 putative underlying sources (components) by applying a BSS algorithm. Previously using Second-order blind identification (SOBI), a BSS algorithm, we were able to detect neuronal source activation that was otherwise difficult to detect and to measure single trial response onset times in a greater number of trials in comparison to measurements obtained directly from scalp EEG/ERP from the best sensors (Tang et al, 2002, Neural Computation; Neuroimage). In the present study, we found that without SOBI pre-processing, a combination of conventional classification methods can correctly predict single-trial correct vs. incorrect responses in ~77% of trials. In contrast, when scalp EEG data were first processed by SOBI to generate a set of SOBI components, which in turn were used as inputs to the conventional classification methods, single-trial behavioral responses can be correctly predicted in ~91% of the trials (Fig. 2). When these overall prediction results were assessed across multiple levels of difficulty, the predicted responses derived from SOBI components (Predicted) closely matched the actual observed responses made by the subjects (Observed) across the full range of task difficulty (Fig. 3, N=5 subjects). These results demonstrated that correct vs. incorrect behavioral responses in a target detection task can be determined at each single trial from EEG signals corresponding to that trial. Furthermore, SOBI pre-processing can significantly increase the overall success rate of prediction from below 80% to over 90%.

Figure 1.

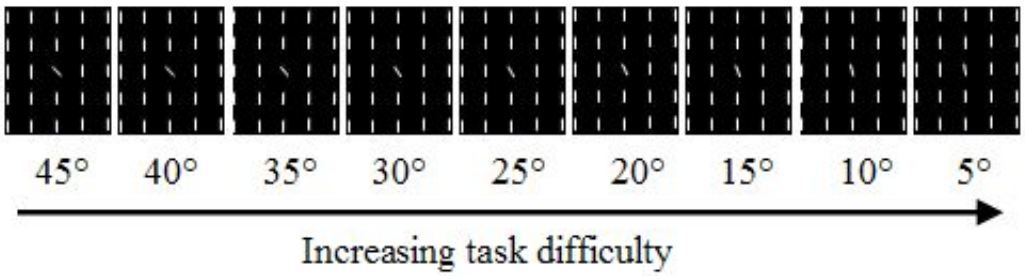

Figure 2.

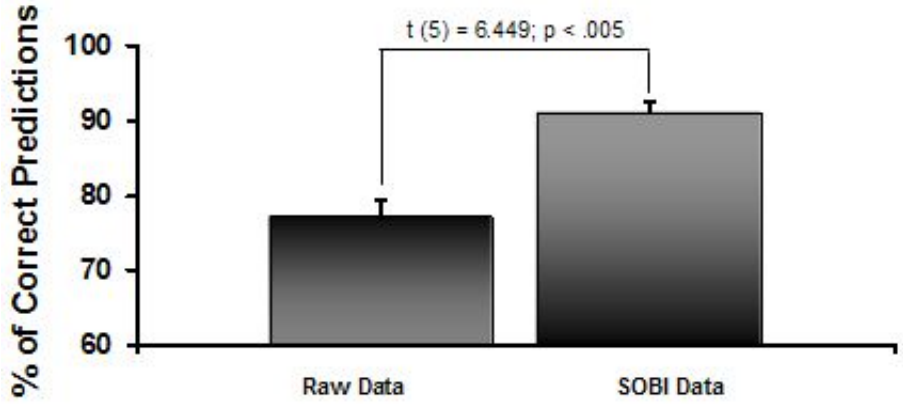

Figure 3.

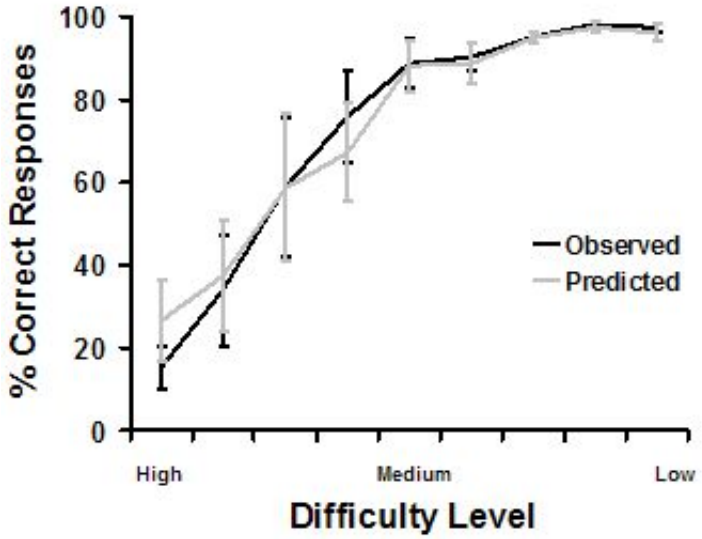

WE 316
A New Non-rigid Medical Image Registration

Songyuan Tang , Tianzi Jiang
National Laboratory of Pattern Recognition, Institute of Automation, Chinese Academy of Sciences, Beijing 100080, P. R. China

1. Introduction

We proposed a non-rigid medical image registration approach based on the physical laws. The presented method is novel on two aspects. First, we model the template image as a viscoelastic matter. The rationale behind this is that the mechanical behaviors of brain have been shown to be viscoelastic. The local shape variations are assumed to have the property of Maxwell model of viscoelasticity. Second, an adaptive force is introduced to decrease the computation cost. We applied the proposed algorithm to 2D simulated datasets and 3D real datasets of different subjects. Experimental results showed that the performance of proposed method were satisfactory in accuracy, speed and robustness.

2. Methods

In the method, we use Maxwell model [1] to model the deformation. The model is made of a spring and dashpot in series (Fig. 1). The total displacement is the sum of the displacements of two parts and the stresses of the two parts are equal. We extend the Maxwell model to the three-dimensional situation. All the above-mentioned properties can be kept. The spring part becomes an elastic solid, and the dashpot part becomes a viscous fluid. The displacements are constrained by elastic and fluid equations respectively.

We adopted the gradient of the SSD metrics as the forces. To prevent very small displacement, an adaptive force is introduced. Some parameters are introduced that adjust force automatically according to the maximum displacements to prevent the maximum displacements from very small.

3. Results

The proposed approach is applied to the 2D brain MRI. The template is shown in Fig.2 (a), and the target in Fig.2. (b). The proposed costs 88 seconds while the viscous fluid method costs 450 seconds. The proposed can match the images well. The result is shown in Fig.2(c) and the difference image of target with the result in Fig.2 (d). We also applied the proposed method to the real 3D datasets got by our group. The mean time of the proposed is about 1hour 35 minutes, while the fluid method about 4 hours 3 minutes. The proposed approach matches all data correctly, while only 40% couples are matched right by fluid method. An example is shown in Fig. 3. Fig.3 (a)-(d) correspond to the template, target result of proposed and the result of fluid. From visual inspection, the result of proposed (Fig. 3(c)) is very similar to the target (Fig.3 (b), while the result of fluid (Fig.3 (d)) is distortion severely.

4. Conclusion

The proposed method is more fast, accurate and robust than the custom fluid method.

Reference

[1] Roderic S. Lakes, Viscoelastic solids. Boca Raton : CRC Press, 1999

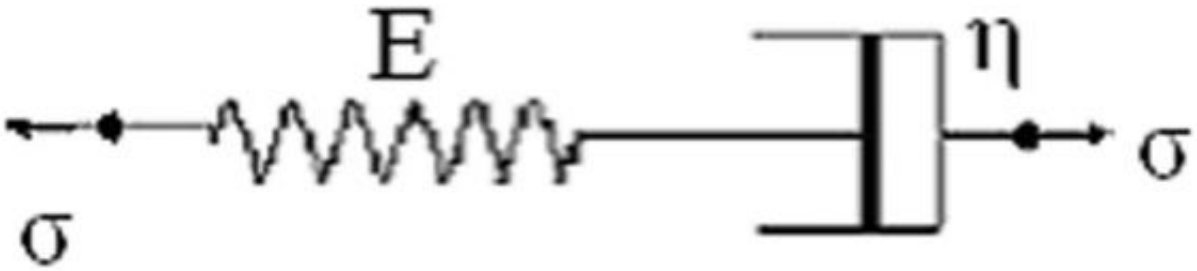

Fig. 1. Maxwell Model

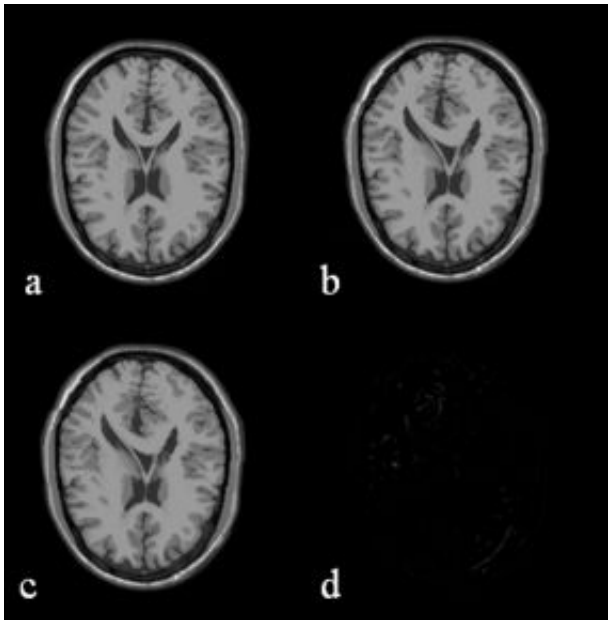

Fig. 2. (a) template, (b) target, (c) result (d) difference image of target with the result of proposed method.

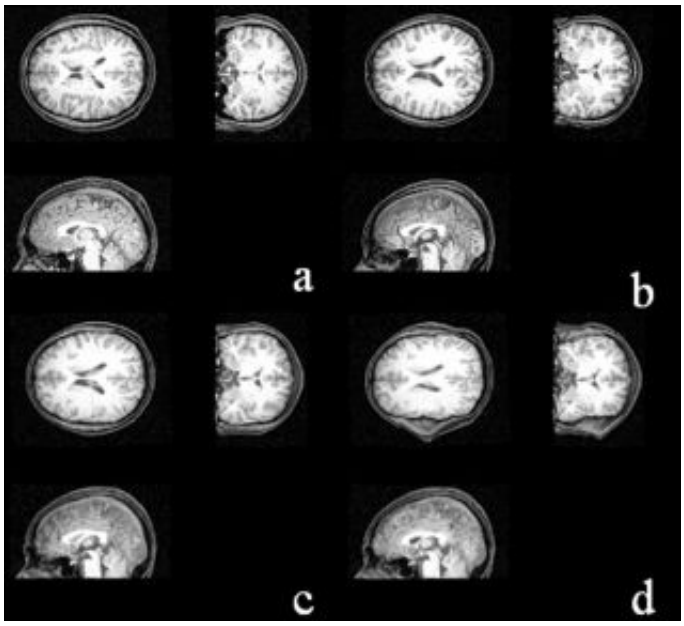

Fig. 3. (a) template (b) target (c) result by propose method (d) misregistration by the fluid method

WE 317

District-related frequency specificity in hand cortical representation: dynamics of regional activation and intra-regional functional connectivity

Franca Tecchio[1,2], Marzia De Lucia[3], Carlo Salustri[1], Filippo Zappasodi[1,2], Claudio Babiloni[4,5], Vittorio Pizzella[6,7], Maurizio Bottaccio[3], Marco Montuori[3], Luciano Pietronero[3], Paolo M Rossini[2,5,8]
[1]ISTC-CNR, Roma, Italy, [2]AFaR-Dip Neuroscienze, Osp. Fatebenefratelli, Roma, Italy, [3]Dip. Fisica ed INFM, Univ. La Sapienza, Roma, Italy, [4]Dip. Fisiologia Umana e Farmacologia - University, [5]IRCCS Centro S. Giovanni di Dio FBF, Brescia, Italy, [6]Institute for Advanced Biomedical Technologies - University of Chieti, Italy, [7]INFM - GC Chieti, Italy, [8]Clinical Neurology - University Campus Biomedico, Rome, Italy

We have used a *dynamic synchronization index*, obtained via the Hilbert transform of recorded magnetoencephalographic data, to study the degree of synchronization generated within the portion of the somatosensory cortex devoted to hand control by stimulation of the thumb or the little finger. It is widely accepted that the cerebral processes underlying sensory discrimination of different body districts involve the activation of neuronal pools located in different areas, theory referred to as somatotopic coding. Our results indicate that the hand representation in humans primary cortex follows also a frequency coding, in addition to the somatotopic one. This appears to be a property of the functional coupling between networks of neuronal pools distributed along the central sulcus and quite distant from each other. We found that in the gamma band the strength of this coupling is higher for thumb than for little finger stimulation, suggesting that the strength of gamma synchronization works as a code for functional supremacy (higher functional importance -> higher gamma synchronization strength).

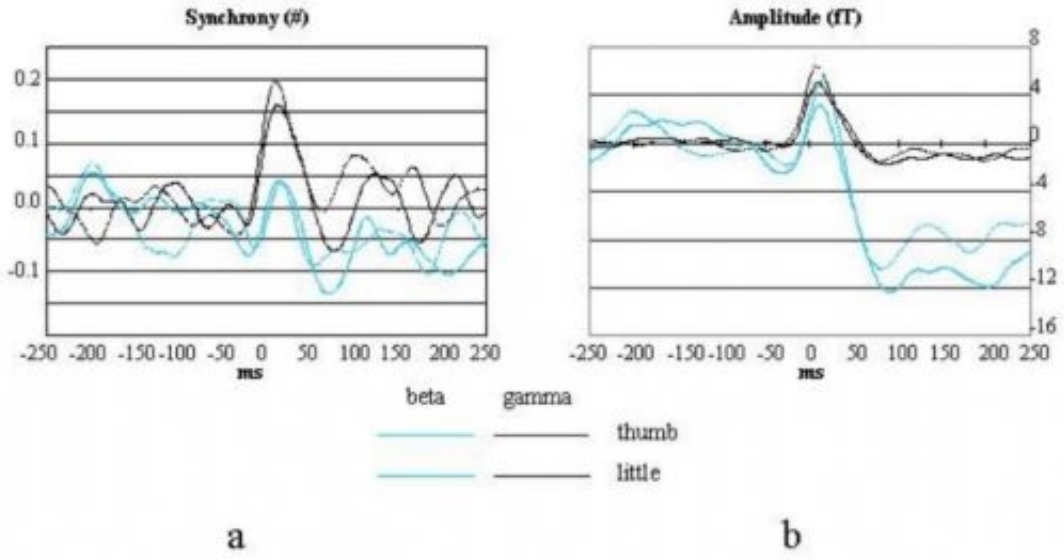

Temporal evolution of synchronization index (a) and signal amplitude (b) in beta (light blue) and gamma (black) bands, following thumb (bold) and little finger stimulation (thin). All values are referred to the mean of the 250 points preceding the stimuli. These mean values were in the range (0.4-0.6) for synchronization , (80-150) fT in beta and (45-80) fT in gamma band for amplitude.

WE 318
Study of effect variability in fMRI data: a high-level clustering approach

Bertrand Thirion [1], Philippe Pinel [2], Jean-Baptiste Poline [1]
[1] CEA SHFJ, Orsay, France, [2] INSERM U562, Orsay, France

Statistical inference based on fMRI data builds on the observation that activation maps related to a given stimulus are reproducible across subjects and sessions. However, reproducibility holds only partially, and the variability of the measured responses is essential in the assessment of the neuroimaging results [2]. This variability can be decomposed into inter- and intra-subject variability.
Intra-subject variability [3] may consist in fluctuations of the size of the effects (i.e. the beta images related to a given effect within the SPM framework) or of the confounds (i.e. of the magnitude of the residuals within the General Linear Model framework). We first study the effect of both of these sources of variability.
At a second level, besides inter-session variability and anatomical differences, inter-subject variability raises interesting questions: 1) whether generalizable inference can be drawn from a population of subjects 2) whether empirical differences can be significant in the neurophysiological domain.
Using a protocol whose experimental paradigm involves high (understanding of sentences, computation) and low level (visual stimulation, click, audition) conditions, we collect datasets from multiple sessions and subjects. A preliminary analysis is performed with the standard SPM99 procedure.
A summary of the different activation patterns that result from this analysis is constructed, using a functional parcellation technique (see e.g. [1]). We use here the algorithm presented in
[4], which clusters the effects of each experimental condition, blindly to the spatial location. This procedure shows in a compelling way that some effects are reproducible from session to session while others are not (see joint figure).
Based on this clustering, a second investigation can be performed concerning the origin of the differences of the cluster maps. In particular, we study the relative impact of effects and residuals variability.
Some preliminary results on intra-subject experiments allow us to conclude that
- Some of the activation patterns are quite reproducible across
sessions/subjects, e.g. visual-auditive contrasts, while other contrasts are less evidently reproducible, e.g. computation-understanding.
- There are session-related variations of the overall signal to noise ratio; this could interpreted as a prominent effect of the residuals (unmodeled effects) in the map variability.
- However, the observation of regions of interest indicates that the effect variability is at probably greater than the estimated noise variability.
Our analysis opens a way to account for the size of the effects, and not only the SNR (t or F statistics) within the data.

[1]. G. Flandin, F. Kherif, X. Pennec, G. Malandain, N. Ayache, and J-B. Poline. Improved detection sensitivity of functional MRI data using a brain parcellation technique. In 5th MICCAI, LNCS 2488 (Part I), pages 467-474, September 2002.
[2]. M. Liou, H-R. Su, J-D. Lee, P. E. Cheng, Huang C-C., and C-H. Tsai. Bridging functional MR images and scientific inference : Reproducibility maps. Journal of Cognitive Neuroscience, 15(7) :935-945, 2003.
[3]. D.J. McGonigle, A.M. Howseman, et al. Variability in fMRI : an examination of intersession differences. NeuroImage, 11 :708-734, 2000.
[4]. B. Thirion and O. Faugeras. Feature detection in fMRI data : The information bottleneck approach. In 6th MICCAI, pages 83-91, November 2003.

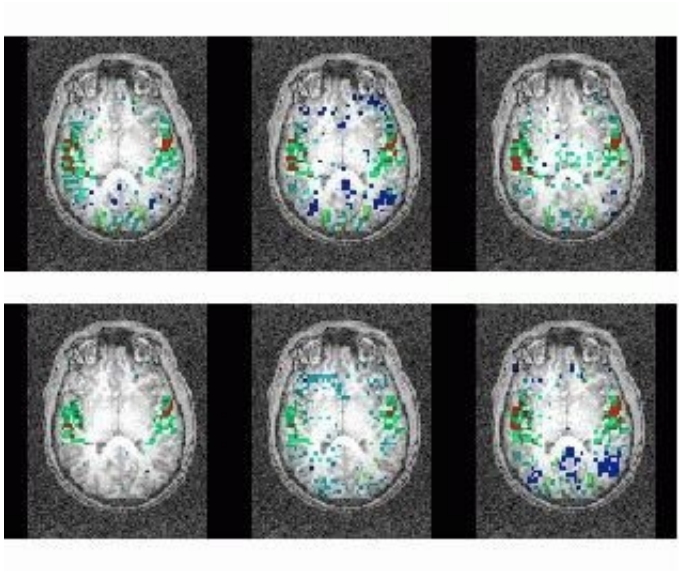

Example of inter-session clustering: The red and green cluster are reproducible auditive activations, while the dark blue cluster (deactivation during understanding and computation) shows a more variable pattern across sessions.

WE 319
Variability of morphometric findings: An inter- scanner comparison.

Marc Tittgemeyer[1], Stefan Zysset[1], Toralf Mildner[1], Christoph Preul[1,2], Margret Hund-Georgiadis[1], D. Yves von Cramon[1,2]

[1]Max Planck Institute for Human Cognitive and Brain Science, Leipzig, Germany, [2]Day-Clinic of Cognitive Neurology, University of Leipzig, Leipzig, Germany

In neurobiological applications, morphometry aims on a description of brain structure from imaging modalities in terms of size, shape, and texture. Such measures may be evaluated by automated statistical techniques and analysed together with other clinical and experimental parameters. Therewith, morphometry offers promising approaches for an in-vivo characterisation of many neurological or psychiatric pathologies. A survey of recent publications only allusively reflects this attractiveness. Published findings are heterogeneous, partly contradictory and not always plausible in terms of known neuropathological correlates. Hence, it is to question the sensitivity of the applied methods.

Variations in morphometric measurements can reflect differences in image acquisition and analysis techniques, alterations in neuronal and non-neuronal tissue compartments, physiological alterations in brain tissue, and changes in other chemical constituents that make up the living brain. With this contribution we review the sources of variation that can rapidly produce changes in MR- based morphometric measurements, some of greater magnitude than those reported for a specific neuropathology. In particular, we focus on the error in morphometric measurements determined by the MR- scanner.

Alongside with starting up a new MR- scanner at our lab we addressed the within- scanner and between- scanner reliability of volumetric measurements on two 3T MR- devices. Three young healthy volunteers were scanned on three separate days using the two different systems. One 3D T1- weighted scan was acquired with a Bruker system, and four 3D T1- weighted scans were acquired consecutively on four different occasions on a Siemens TRIO system. Sequence parameters (FoV, TR, TE, etc.) were identical on both systems, while the standard T1 sequence for the respective system was applied (MDEFT on the Bruker, and MPRAGE on the Siemens scanner). The resulting datasets were analysed by the same protocol with the identical image processing tools: To avoid bias in the matching procedure by extracranial tissue, the intracranial compartment was extracted first. Following signal normalisation and rigid body matching, image volumes were subtracted. The resulting difference image can be overlaid in colour to display the changes visually, while the actual difference in volume can be calculated as the integral of shift in the boundaries. The procedure revealed an average apparent volume loss of 2.5 % for the supratentorial brain at between- scanner comparison (figure) whereas the within- scanner reliability was excellent for all three subjects. Further, we carried out standard (voxel- based and deformation- based) computational techniques that revealed local morphologic changes being an artefact of different scanner protocols. To account for this effect any interference of anatomical scans from different systems should be avoided in any structural brain study. This result has significant implications on the analysis of multi- centre data.

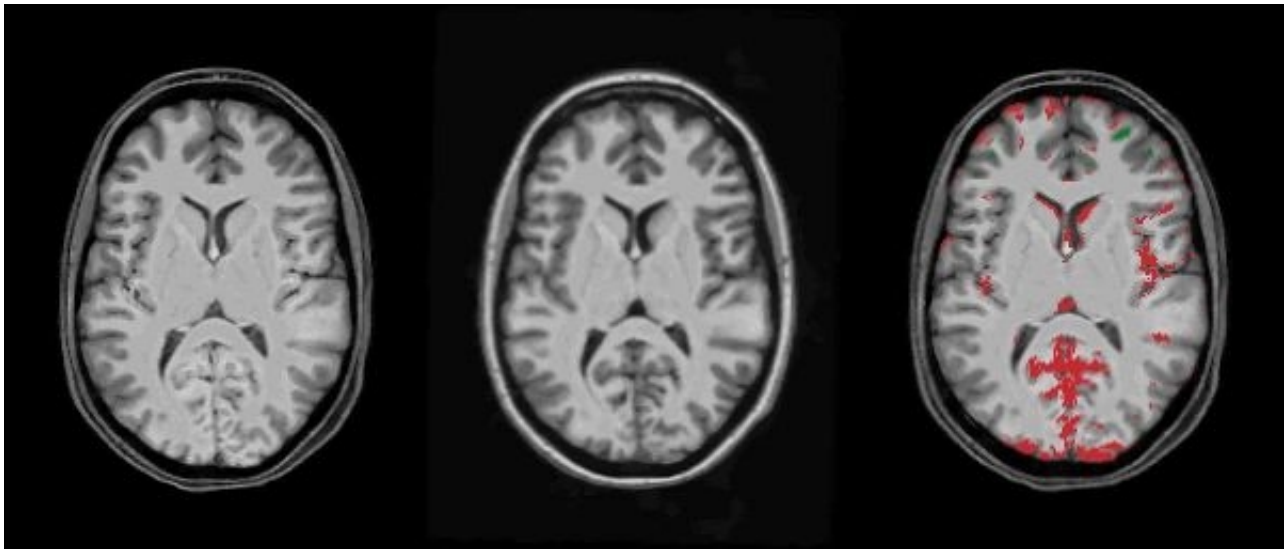

Registration of scans taken at different scanners (Bruker, left, and TRIO, middle). From the morphometric analysis an apparent tissue loss would be inferred (red colour, right panel).

WE 320

Quantitative definition of primary, secondary and tertiary convolutions

Roberto Toro , Yves Burnod
Institut des Sciences Cognitives, Bron-France

Background. Convolutions are classified into primary, secondary and tertiary depending on their developmental time. Primary convolutions in the adult brain are rather invariant in their position and relation to cytoarchitecture, they are also the deepest convolutions. Secondary and tertiary convolutions are progressively more variable, superficial and numerous. The analysis of neuroimaging data is frequently based on convolutional anatomy to identify functional regions, as a direct assessment of cytoarchitecture is impossible at present. Considering the hierarchy of convolutions is an important step in the analysis of neuroimaging data, however, there is no quantitative method to distinguish among different convolutions.
Purpose. To provide a quantitative definition of primary, secondary and tertiary convolutions
Methods. Reconstructions of the cortical surface are obtained from MRI data. Sulci and gyri are defined by mapping the mean curvature. The surfaces are progressively smoothed and convolutions are classified depending on their depth and persistence.
Results. The quantitative classification of convolutions obtained is in agreement with the traditional classification of many important sulci, and provides a standard method for the hierarchical analysis of convolutional anatomy.

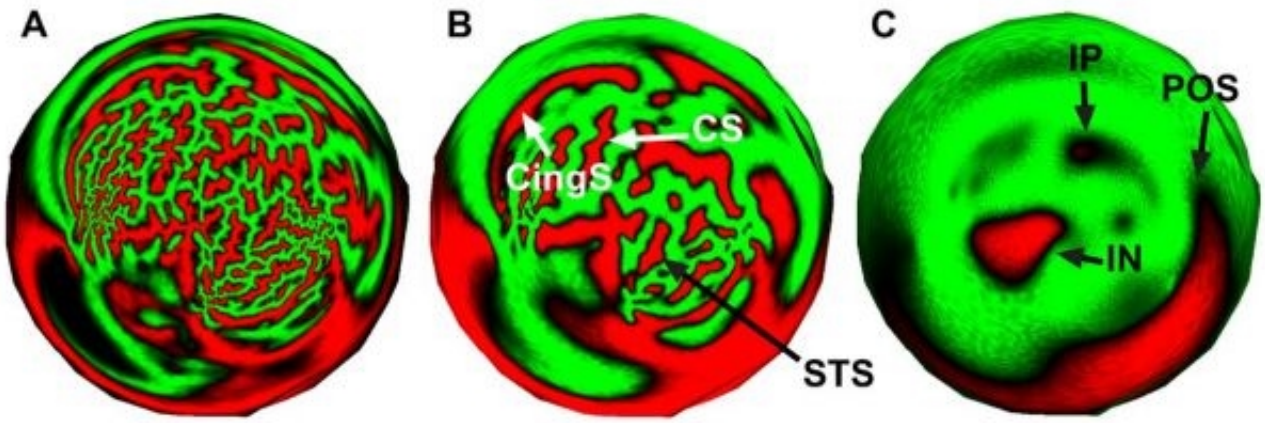

Polar stereographic representations of the whole cortex at three different stages. A. Five iteration steps: primary, secondary and tertiary sulci are represented. B. Fifty iteration steps: Only primary and secondary sulci. C. Five hundred iteration steps: only earlier primary sulci.

WE 321
EEG Cortical Source Imaging Using Spatiotemporal Independent Component Analysis

Arthur C. Tsai [1], Michelle Liou [1], Tzyy-Ping Jung [2,3], Philip E. Cheng [1], Chien-Chih Huang [1], Scott Makeig [2,3]
[1] Institute of Statistical Science Academia Sinica, Taiwan, [2] Computational Neurobiology Laboratory, and,
[3] Institute for Neural Computation, University of California, San Diego, CA 92093, USA

The excellent temporal resolution as well as direct association with the underlying neuronal activities of EEG gives us a unique non-invasive window on the dynamics of human brain functions. By incorporating techniques of forward head modeling and information about cortical geometry from MRI (Dale et al., 1993), EEG may achieve resolutions similar to those of fMRI and PET. However, electrophysiological data is often corrupted by isolated artifacts that include line noise, eye blinks, electrical muscle activity, and cardiac noise. To make EEG a reliable functional imaging modality, source localization method would separate the various components of brains electrical responses as well as artifacts.

Recently, much progress has been made in parallel over the last decade to understand and attain the segregation of EEG signals using independent component analysis (ICA). Zhukov et al. (2000) took an advantage of ICA preprocessing step to reduce the complexity of localizing multiple neural sources which reconstructs spatial surface topographies for individual sources separately. They employ a downhill simplex search method to independently localize separated sources for spatial surface topographies of particular components contribution. However, since assumptions about the number of equivalent dipole sources have to be made, this technique may be not suited to situations with many overlapping sources of cortical activity.

Here, we propose a new approach by incorporating the leadfield matrix in spatiotemporal ICA is proposed for inverse problem. The corresponding learning algorithm for estimating the cortical activation topography is build. The sparse priors are imposed in the cortical activation topography and spatiotemporal independence are imposed in Bayesian framework to permit a trade-off between the mutual independence of spatial cortical activation topology and the mutual independence of their corresponding time courses. The method is illustrated through an application to empirical EEG data from a modified Sternberg memory task. The proposed spatiotemporal ICA applied to the single-trial data identified several classes of contributing components and their corresponding cortical activation topography, including multiple alpha, right mu, and frontal right theta rhythms.

WE 322
Exploratory Analysis of Large Scale Network Interactions in Functional Neuroimaging Experiments

And U. Turken , Sue L. Gabrieli , John D. Gabrieli
Psychology Dept, Stanford University

Advanced methods for investigating network interactions in neuroimaging studies typically require highly specific hypotheses to constrain the range of possible network interactions, by limiting the number of regions and the particular connections in the modeled networks based on prior knowledge on functional neuroanatomy. When this knowledge is lacking, especially in the context of studies that explore high-level cognitive phenomena, investigation of potentially interesting interregional interactions might remain limited in scope. On the other hand, performing exploratory analysis of all possible functional network architectures by considering all possible interactions among multiple brain voxels in a typical fMRI dataset from an experiment with multiple factors would be both computationally prohibitive and pose significant problems for setting appropriate criteria for statistical tests.

We focused on finding a strategy to explore a wide range of possible network interactions that might emerge in an fMRI study, while maintaining control over the scope of the analysis in order to remain centered on network patterns that can have meaningful interpretations in the context of the experiment. Our approach is to first use the general linear model (GLM) to identify a set of brain regions responding to any of the experimental manipulations in an fMRI study through voxel-wise tests. The MR signal time series from each of the regions are then extracted and deconvolved using SPM2. Time series representing the physiological interactions across the regions are also derived using SPM2. Following the methods for analyzing psychophysiological interactions (PPI) described by Friston et al. (Neuroimage, 1997), the direct and modulatory contributions to each brain area by the remaining regions, and their relation to experimental manipulations are modeled using GLM separately for each region of interest. In order to accommodate delayed interactions, the model might also include time-lagged versions of the regressors representing contributions from different regions in the network.

For each target brain area, multiple PPI models for influences coming from other regions are fitted. After each model fit, the regressors for those regions and interactions that do not contribute to the overall fit of the model to the data from the target region area eliminated, until there remains no significant reduction in fitness. At the end of this process, for each brain region of interest, a group of other areas that have direct or modulatory influences on its task-related activation profile are determined, which, when linked together, sketch a distributed network of interacting regions, and as the case might be, multiple networks that operate in parallel. The estimated connectivity patterns and path coefficients can serve to develop hypotheses and priors on parameter values for subsequent analyses with hypothesis driven and statistically rigorous methods

WE 323
MINC 2.0: A modality independent format for multidimensional medical images

Robert D. Vincent[1], Andrew Janke[1], John G. Sled[2], Leila Baghdadi[2], Peter Neelin[1], Alan C. Evans[1]
[1]McConnell Brain Imaging Centre, Montreal Neurological Institute, Montreal, Canada, [2]Mouse Imaging Centre, Hospital for Sick Children, Toronto, Canada

Introduction:
The MINC (Medical Imaging NetCDF) file format, libraries, and tools provide a framework for manipulating medical images independent of modality. MINC 1.0 was created in 1993 to meet the needs of the brain imaging research community. The format is extremely flexible, providing a range of voxel data types, arbitrary dimensions, and a rich set of supporting data. New functionality and data fields can be added to the specification without requiring the modification of existing files or software. MINC 1.0 files define both a voxel coordinate system and a transformation to a world or stereotaxic coordinate system. Voxel data may include an optional range conversion from an integer storage format to a floating-point memory format.
MINC 2.0 is a major revision of the software and file format, drawing upon ten years of experience with MINC 1.0. The increasing complexity of functional imaging experiments, continuing improvements in the resolution of medical imaging scanners, and the proliferation of micro-imaging devices for preclinical and ex-vivo work has pushed data volumes beyond what current file formats can efficiently address. MINC 2.0 adds new data types, improved processing of huge files, and enhanced flexibility for future expansion. By altering the internal layout of the image data, MINC 2.0 enables existing computing resources to process these large datasets.
Methods:
MINC 2.0 is a specialization of the HDF5 (Hierarchical Data Format 5) format [1], but also provides backward compatibility for MINC 1.0 files built upon the NetCDF format [2]. A C language library provides a well-documented and straightforward interface to the new MINC 2.0 features and options, making them more accessible than MINC 1.0.
Building MINC 2.0 using HDF5 allows for improved data compression, non-scalar voxel data, and a hierarchical file structure. This file hierarchy permits storage of voxel data at several resolutions. MINC 2.0 also provides 64-bit addressing as needed for huge data files such as 3D mouse imaging or macrocryotome data, and block addressing for rapid extraction of sub-blocks of data.
The MINC 1.0 library and tools have been extended to interoperate with files using either version of the format.
Results and Conclusion:
The MINC file format has been established as a basis for a medical image analysis research environment, acting as the glue that holds a range of software together. The format combines generality, flexibility and extensibility with a conceptual and organizational framework that ensures inter-operability between programs. Scientists at the Montreal Neurological Institute and over 20 other institutions worldwide incorporate many modalities and methodologies in a single analysis environment built around the MINC format. MINC 2.0 forms the basis for further enhancement and extension of this software environment. Future work will allow the manipulation of MINC files within scripting languages such as Perl and Python. An active development community contributes to the expansion of MINC capabilities; a recent MINC workshop held in advance of the MINC 2.0 release had 180 attendees.
MINC software is available at **www.bic.mni.mcgill.ca/software/**
References:
[1] Folk et al., 2003 (**hdf.ncsa.uiuc.edu/HDF5/**).
[2] Rew et al., 1997 (**www.unidata.ucar.edu/packages/netcdf/guidec/**).

WE 324

Statistics of Statistics vs. Statistics of Signal Change at Group Level fMRI Analysis

Peizhi Wang , Yufeng Zang , Tianzi Jiang , Yong He , Lixia Tian , Meng Liang
National Laboratory of Pattern Recognition, Institute of Automation, Chinese Academy of Sciences

In fMRI study, the individual data analysis is usually called first-stage analysis and the analysis at group level is called second-stage analysis. Such second-stage analysis is to extend inference to population. Biostatisticians often prefer individual physiological meaningful measurements, e.g., signal change, to individual statistical measurements for the second-stage statistical analysis. But a few researchers do have used statistical measurements in their studies (e.g., Doyon et al., PNAS, 2002; Hampson et al., Hum Brain Mapp, 2002). Though it seems to be a very simple question, we failed to find any reports on comparing the results by using the two kinds of measurements. In the current study, we applied simple left and right finger movements to compare the physiologically meaningful measurement with statistical measurement at the second-stage statistical analysis. Deconvolution and multiple linear regression (in AFNI software package) was used to generate individual activation (F statistical) maps and to estimate the impulse response function (IRF). Individual F maps were converted into Z maps and the area under the curve (AUC) was calculated from IRF. At the second-stage analysis, paired t-test (n = 6 subjects) was done based on either the Z maps or the AUC to compare the activation by left with by right finger movements. Results show that both Z maps and AUC could effectively detect the difference between left and right finger movements in bilateral primary motor cortex (M1). But in right M1, mass center for results based on Z maps is located in central sulcus, whereas the mass center based on AUC located posterior to the central sulcus (Fig. 1). In posterior supplementary motor area (SMA proper), difference between left and right finger movements was found in bilateral SMA proper based on Z maps, whereas found in only left SMA proper based on AUC. In some other areas, e.g., right anterior cingulate cortex (ACC) and left superior frontal gyrus (SFG), difference was found only by AUC. We conclude that both statistical and physiologically meaningful measurements could be used in the second-stage statistical analysis: the former may be more suitable to detect lower function areas like M1 and SMA proper, while the latter may be more sensitive for detecting higher function areas (e.g., ACC and SFG).

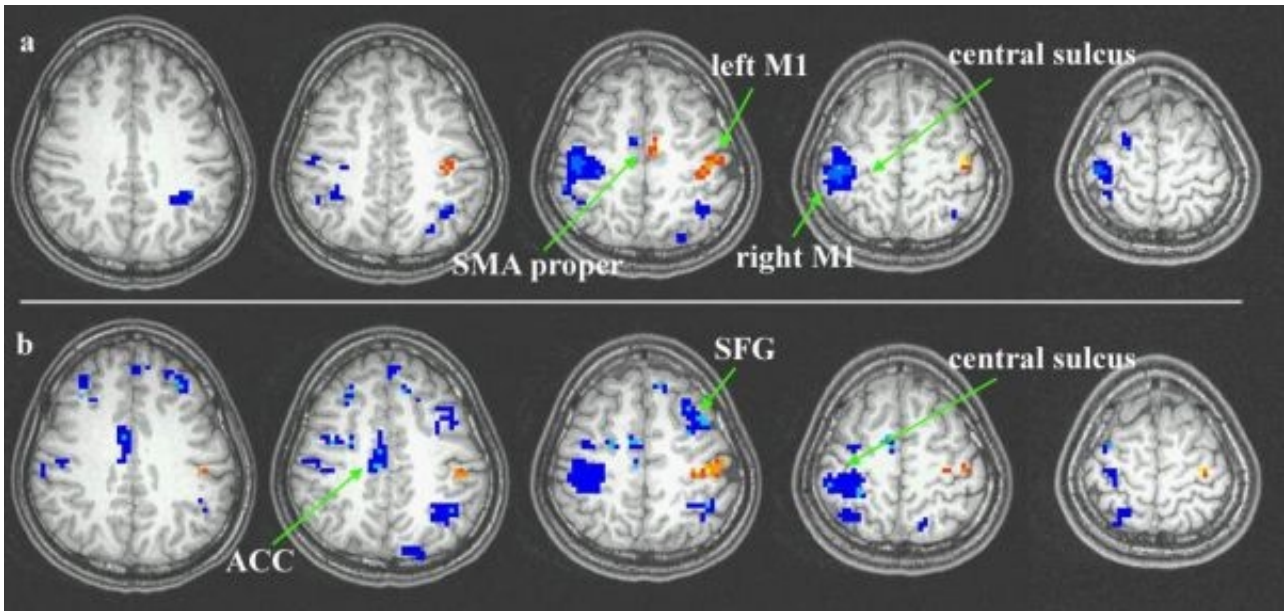

Fig. 1. Results of paired t-test on Z maps (a) and AUC (b). Bright color: right hand > left hand. Blue color: left hand > right hand. Significance thresholds: $|t| > 2.571$, $p < 0.05$, cluster size > 270 mm^3.

WE 325
Volumetric Harmonic Brain Mapping using a Variational Method

Yalin Wang[1], Xianfeng Gu[2], Tony F. Chan[1], Paul M. Thompson[3], Shing-Tung Yau[4]
[1]Mathematics Department, UCLA, Los Angeles, CA, USA, [2]CISE, Univ. of Florida, Gainesville, FL, USA,
[3]Lab. of Neuro Imaging and Brain Research Institute, UCLA Medical School, Los Angeles, CA, USA,
[4]Department of Mathematics, Harvard University, Boston, MA, USA

Brain surface conformal mapping research has been successful and this motivates our more general investigation of 3D volumetric brain harmonic mapping. By transforming the full 3D brain volume to a solid sphere, our goal is to investigate how features map into this canonical 3D coordinate system in the same way as 2D conformal flattening has helped in analyzing cortical surface geometry. Nonlinear mapping of two brain volumes to a sphere may also assist with the subsequent nonlinear registration of one brain volume to another. We suggest that 3D harmonic mapping of brain volumes to a solid sphere can provide a canonical coordinate system for feature identification and segmentation, as well as anatomical normalization.

We developed two different techniques to tackle the volume mapping problem. The first finds a 3D harmonic map from a volumetric brain image to a 3D solid sphere and the second uses a sphere carving algorithm to compute a simplicial decomposition of the volume which is adapted to the surfaces.

We derived the harmonic energy computation equation. We construct a harmonic map in R^3 with a heat flow method. First we conformally map the boundary of the 3D volume to a sphere. During this step, we can easily include other biological constraints (e.g. mappings of superficial sulci). Our method then minimizes the volumetric harmonic energy while keeping the surface fixed. This mapping is determined by the geometric structure and also the boundary conditions.

Once we fixed the mapping of the brain surfaces, the surface mapping is conformal in our case, the interior harmonic map consistently maps similar brain structures to canonical locations.

Methods to tetrahedralize the brain for FEM analysis are somewhat rare in the literature, although they are used occasionally for surgical simulation, or mapping intraoperative brain change. In our current experiments, we apply the sphere carving algorithm to build a brain-based tetrahedral mesh. The algorithm initially constructs a large sphere that contains all the brain data. Then it keeps removing exterior tetrahedra while maintaining the surface genus number.

In our experiments, we tested our algorithm on both synthetic and brain volume data. Our synthetic data was a cube consisting of many tetrahedra. For the brain data, the input image to this algorithm is a binary 3D volumetric brain image which results from applying a Gaussian mixture tissue classifier to an MRI, in order to classify each pixel as white matter (in this case, for illustration purposes) and non-white matter. The sphere carving algorithm then builds a finite element mesh by removing tetrahedra exterior to the binary brain volume. Our experiments show that the resulting embedding can be used to induce a canonical spherical coordinate system for the brain interior. Some experimental results are shown in the Figure below.

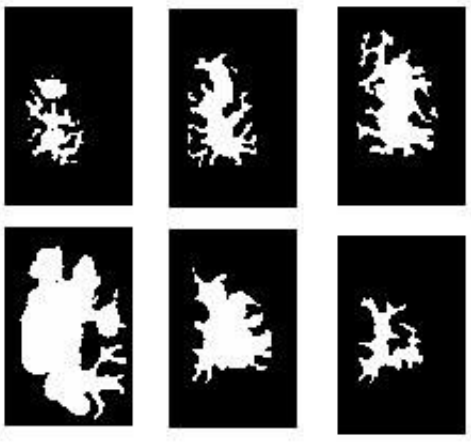

Shows some binary brain images, with white pixels are brain's white matter.

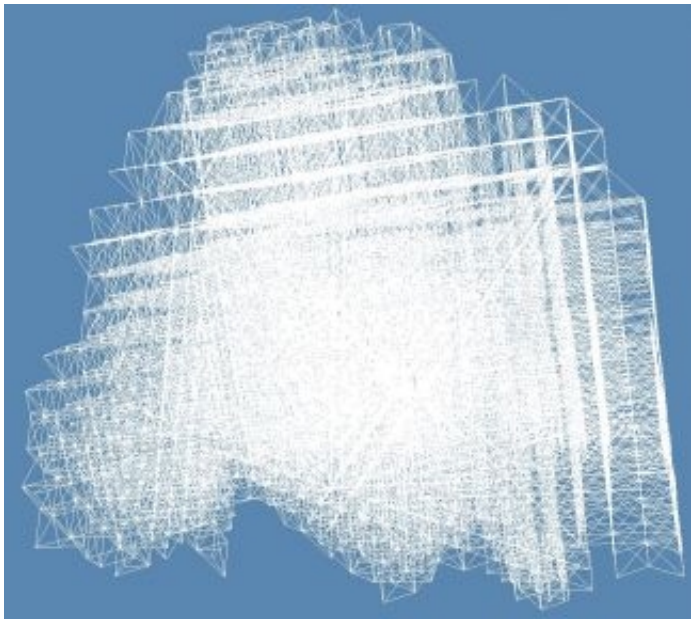

Shows a constructed brain volume shown in wireframe. We compute a harmonic map of the brain onto a solid sphere.

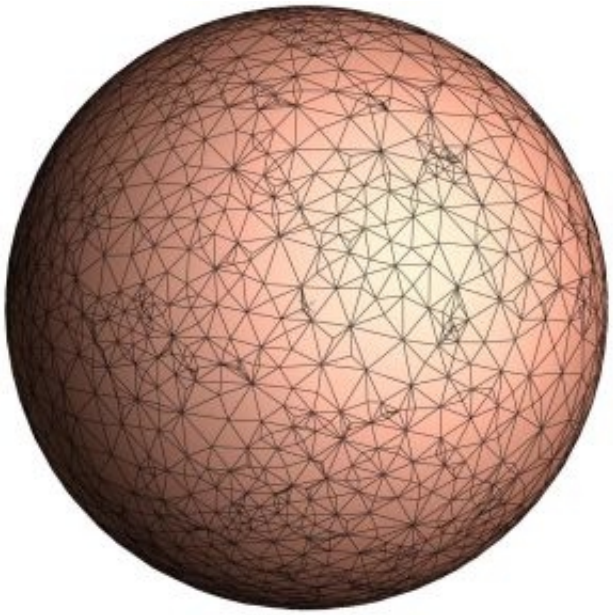

The surface of the solid sphere onto which there is a conformal mapping from the boundary of the brain volume.

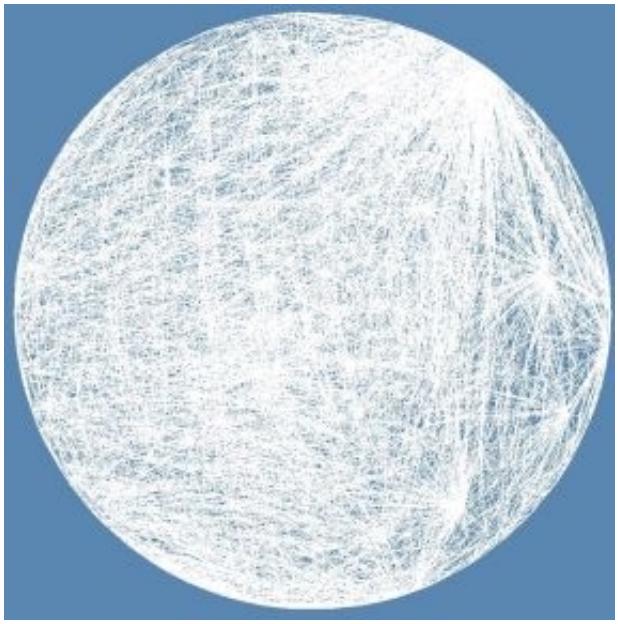

The solid sphere onto which the brain volume harmonically maps in wireframe mode.

WE 326
Mapping of white matter hyperintensities on brain MRI in healthy middle-aged individuals

Wei Wen [1,2], Perminder Sachdev [1,2]
[1] Neuropsychiatric Institute, Prince of Wales Hospital, Randwick, NSW, Australia, [2] School of Psychiatry, University of NSW, Sydney, Australia

Across the developed countries, the population is ageing, with a significant projected increase in the number of people aged over 60. Foci of high signal intensity on T2-weighted magnetic resonance imaging (MRI) in the white matter are a common finding in the brains of asymptomatic elderly individuals as well as in disease-specific brains, with reported prevalence in the healthy elderly varying from 10% up to 100% in different studies [1]. The etiology of white matter hyperintensities (WMHs), sometimes referred to as leuokoaraiosis, is not specific and may relate to ischemia, demyelinating disorders, hydrocephalus, trauma, inflammatory disease, radiation injury, amyloidosis and other causes. Their pathology is similarly varied, with reports of normal findings to complete infarction [2]. The volume and number of WMHs have been found to be associated with brain atrophy, reduced cerebral blood flow and focal neurologic signs [3]. WMHs have been noted to be associated with cognitive impairment, with a suggestion that a certain threshold of their extent must be reached before this becomes clinically apparent. WMHs have also been linked to neuropsychiatric disorders such as Major Depression, Bipolar disorder and Schizophrenia.

We report topography of brain white matter hyperintensities (WMHs) on T2-weighted FLAIR magnetic resonance imaging in 477 healthy middle-aged subjects (60-64 years) selected randomly from the community. We found that all subjects had periventricular WMHs, and 96.6% subjects also had deep WMHs.

We first constructed a WMH probability map from these 477 subjects WMH volumes that were detected and delineated in the standard space (MNI-space). We then took ROI approach in quantifying the number and volumes of WMH clusters in both lobar and arterial territory partitions. WMHs were delineated by using a computer algorithm. The mean volume of WMHs was 4.9 ml, comprising 0.83% of the white matter, of which 1.2 ml was severe in intensity. The deep WMHs were distributed throughout the cerebral hemispheres, with the occipital and frontal white matter bearing the greatest burden. The territory of the lenticulostriate arteries had the greatest WMHs. A white matter region of 4 mm adjacent to the cortex was not affected by hyperintensities. The mean (SD) number of discrete WMHs was 19.6 (7.1) per subject, of which 6.1 (4.4) were severe in intensity. Nearly half (48.6%) of the subjects had at least one large WMH (>12 mm diameter) and one eighth (12.5%) of the subjects had at least one large WMH that appeared to be severe in MRI. This study provides the first detailed topographic analysis of WMHs in a large representative middle-aged sample, emphasizes their high prevalence in mid-adult life, and raises issues about their etiology and significance.

References:

1. De Leeuw, et al., 2000. White matter changes. Frequency and risk factors, in: Pantoni L, (Eds.), The Matter of White Matter. Academic Pharmaceutical Productions, Utrecht, p.19.
2. Fazekas F., et al., 1993. Pathologic correlates of incidental MRI white matter signal hyperintensities. Neurology 43, 1683-1689.
3. DeCarli, C., et. al., 1995. The effect of white matter hyperintensity volume on brain structure, cognitive performance, and cerebral metabolism of glucose in 51 healthy adults. Neurology 45, 20772084.

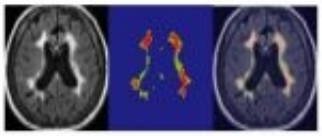

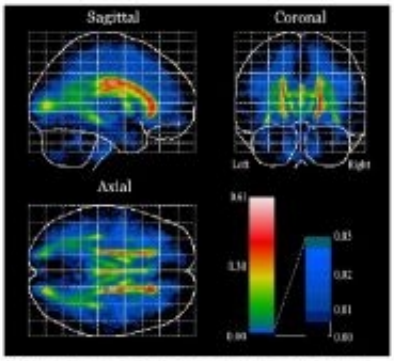
Sagittal
Coronal
Left
Right
Axial

WE 327
Brain Activity Movies: A Novel Approach to Examining Spatio-Temporal Activation Characteristics

Christian Windischberger[1], Ross Cunnington[2], Simon Robinson[1], Lüder Deecke[3], Ewald Moser[1,4,5]
[1]MR Center of Excellence, Medical University and General Hospital, Vienna, Austria, [2]Howard Florey Institute, University of Melbourne, Melbourne, Australia, [3]Department of Clinical Neurology, Medical University and General Hospital, Vienna, Austria, [4]Department of Radiodiagnostics, Medical University and General Hospital, Vienna, Austria, [5]Department of Psychiatry, University of Pennsylvania, Philadelphia, USA

Introduction:
Functional MRI offers the great advantage of high spatial resolution and deeper penetration compared to electrophysiological methods. This benefit, however, is associated with long repetition times between subsequent time instances, typically in the order of seconds. In conjunction with blocked design paradigms this has lead to the general view that fMRI is limited to the assessment of stationary activation states. Even studies that use event-related stimulus paradigms rarely assess the temporal features of brain activation. Here we present an elegant approach to analyzing event-related fMRI data sets, yielding activation maps for each time instance within the inter-stimulus interval.

Methods:
Six subjects participated in this study. In each of the twelve trials they listened to an auditory countdown and were asked to perform a brief button pressing task as soon as they heard 0. All measurements were performed on a 3 Tesla Medspec (Bruker Biospin, Germany) acquiring gradient-recalled EPI (TE=40ms) positioned over the motor cortex (MA=64x64 pixels). A very short TR of 300ms (4 axial slices) was used to ensure adequate coverage of the haemodynamic response function. Before analysis functional data sets were realigned in 2D and spatially smoothed with a Gaussian kernel of 9mm FWHM. Twelve trials of 110 time points each were measured with an inter-stimulus interval of 33s. For analysis a set of 110 regressors of a general linear model (GLM) was constructed in a FIR approach. The first regressor is zero except for the first time instance in each trial. The other regressors are generated by simple shifting of the first regressor such that each regressor represents a single time instance within one trial. The GLM was estimated in SPM99 and contrast images for each of the 110 regressors were calculated. Activation maps were thresholded at p [less] 0.05 (corrected), overlaid on non-saturated EPIs and brain activity movies (BAM) were generated from the 110 activation maps for each subject.

Results:
The figure shows four out of 110 activation maps of a single subject at different times after trial onset. In (a) map #26, 4.8s after auditory onset and 5.2s before movement, activity in SMA is already visible. This activation pattern is rather constant for 7.5s as seen in map #51, 2.3s after movement (b). First activity in M1 occurs 3.5s after movement, shown in map #55 (c), increasing to a maximum 6.2s after movement execution (map #64, (d)).

Discussion:
Provided that TR is sufficiently short, the BAM analysis approach enables the creation of movies that visualize the temporal evolution of brain activity in real-time for the whole data sets, i.e. without restriction to ROIs. Such spatio-temporal characteristics of brain activity can be assessed more easily, allowing the study of the temporal sequence in which different areas are activated. The generation of BAMs requires no assumptions about the individual haemodynamic response function other than reproducibility between trials. This represents an important analysis technique situated between strictly model-based method and exploratory analysis approaches.

Acknowledgements:
This study was supported by the Austrian Science Foundation (P-16669) and the HSJS (1472/2002).

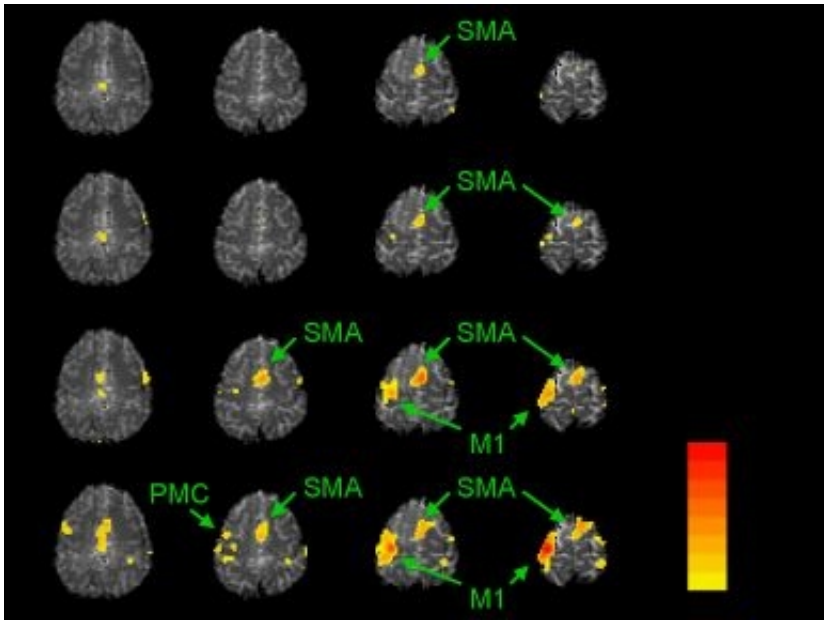
SMA
SMA
SMA
SMA
M1
PMC
SMA
SMA
M1

WE 328
Constrained Linear Basis Sets for HRF Modelling Using Variational Bayes

Mark W. Woolrich[1,2], Timothy E.J. Behrens[1,2], Stephen M. Smith[1]
[1]Oxford Centre for Functional Magnetic Resonance Imaging of the Brain (FMRIB), University of Oxford, UK,
[2]Department of Engineering Science, University of Oxford, UK

Introduction

FMRI modelling requires flexible HRF modelling, with the HRF being allowed to vary spatially and between subjects. To achieve this flexibility, voxel-wise parameterised HRFs have been proposed, however inference on such models is very slow (Woolrich et al., 2004). An alternative approach is to use basis functions allowing inference to proceed in the more manageable General Linear Model (GLM) framework (Josephs et al., 1997). However, a large amount of the subspace spanned by the basis functions produces nonsensical HRF shapes. In this work we propose a means to constrain the subspace spanned by the basis set to only include sensible HRF shapes, resulting in an increase in sensitivity.

Basis functions

For FMRI data, y, the GLM is:

$y_{it} = \Sigma_{eb} x_{ebt} \beta_{ieb} + e_{it}$

where β_{ieb} is the regression parameters, e indexes basis function, b indexes underlying condition, and x_{ebt} is the convolution of the corresponding basis and stimulus functions. We generate a basis set using a singular value decomposition (SVD) on HRF samples from a half-cosine HRF parameterisation in figure 1, using sensible priors on the half-cosine parameters. Figure 1 shows the resulting four eigenHRFs we use as our basis set.

Constraining Basis functions

Firstly, we reparameterise the vector β_{ie}:

$\beta_{ie} = \rho_{ie} D_{ie} / |D_{ie}|$

where D_{ie} is a vector of parameters describing the HRF shape, and ρ_{ie} is the scalar value representing the scaling of that HRF. It is via a multivariate normal prior, with mean m and and covariance matrix C, on D_{ie} that we can constrain the possible linear combinations of basis functions to represent the HRF. To provide m and C we regress the HRF samples we used in the SVD back onto the basis set. Figure 2 shows example HRF shapes randomly drawn from the basis set with and without constraints.

Inference

It is not possible to solve for the distributions of interest analytically. Hence we use the Variational Bayes framework, in which we assume a factorised form to the joint posterior (Penny et al., 2003). We could look to use the posterior probability of the normalised power explained by the f-contrast. Instead, the approach we take here is to convert them to z-statistics and perform spatial mixture modelling.

Results and Conclusions

Here we use a single-event pain dataset and a visual boxcar dataset. Figure 3 shows the histogram of pseudo-z-statistics obtained with and without HRF constraints. We can see how the right hand tail, i.e. those voxels which are strongly activating, is relatively unaffected. Whereas, the main body of the histogram, i.e. the background non-activating voxels, is shifted to the left. Figure 4 shows the difference in voxel classification between the constrained HRF model and the unconstrained HRF model using the spatial mixture modelling. This difference highlights the increased sensitivity. With the constrained HRF model, smaller strength activating voxels have increased probability of being in the activation class.

Josephs et al., 1997. Human Brain Mapping.
Penny et al., 2003. NeuroImage.
Woolrich et al., 2004. IEEE TMI.

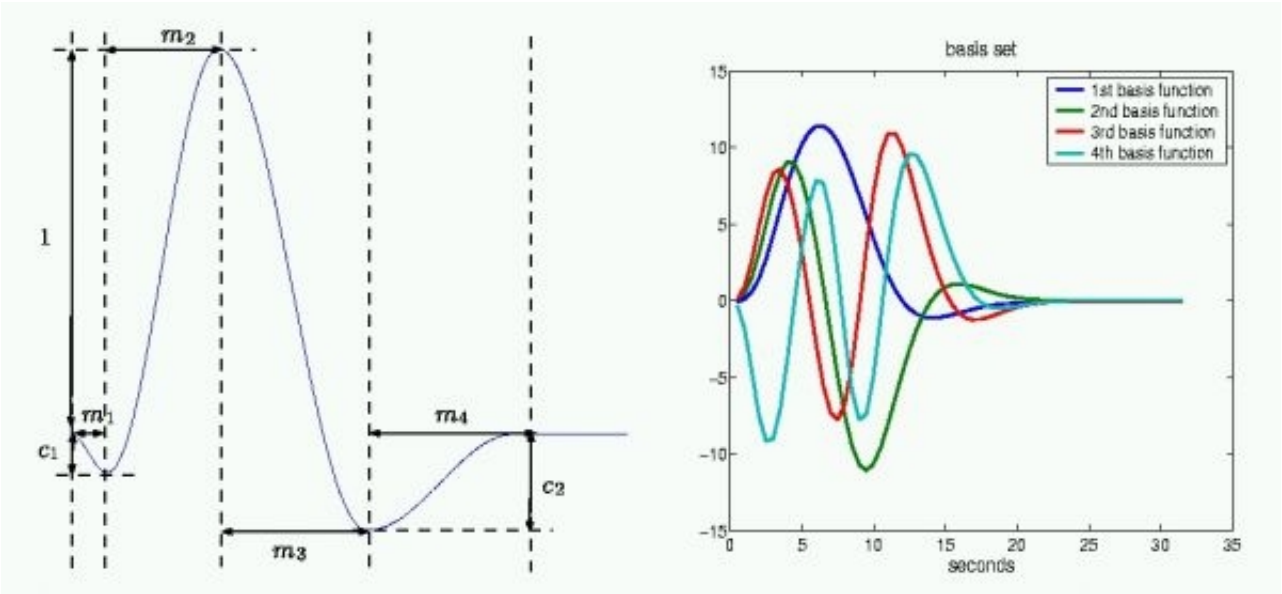

Figure 1: Parameterisation of the HRF into four half-period cosines and the top four eigenHRFs.

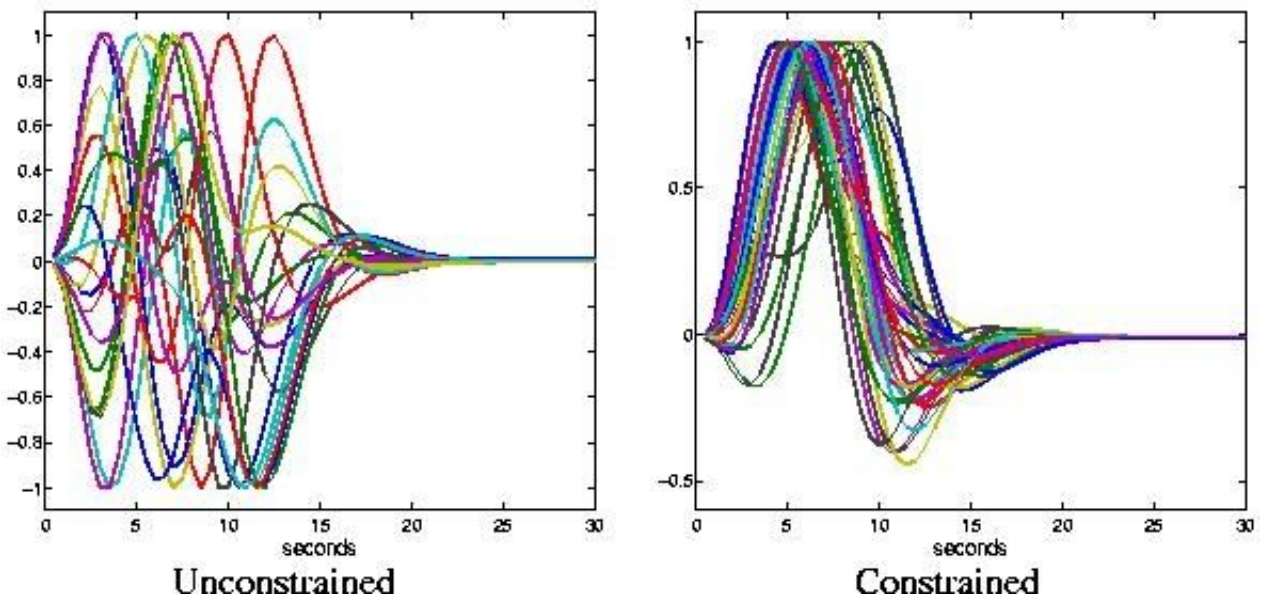

Figure 2: Samples from the basis set with and without HRF constraints.

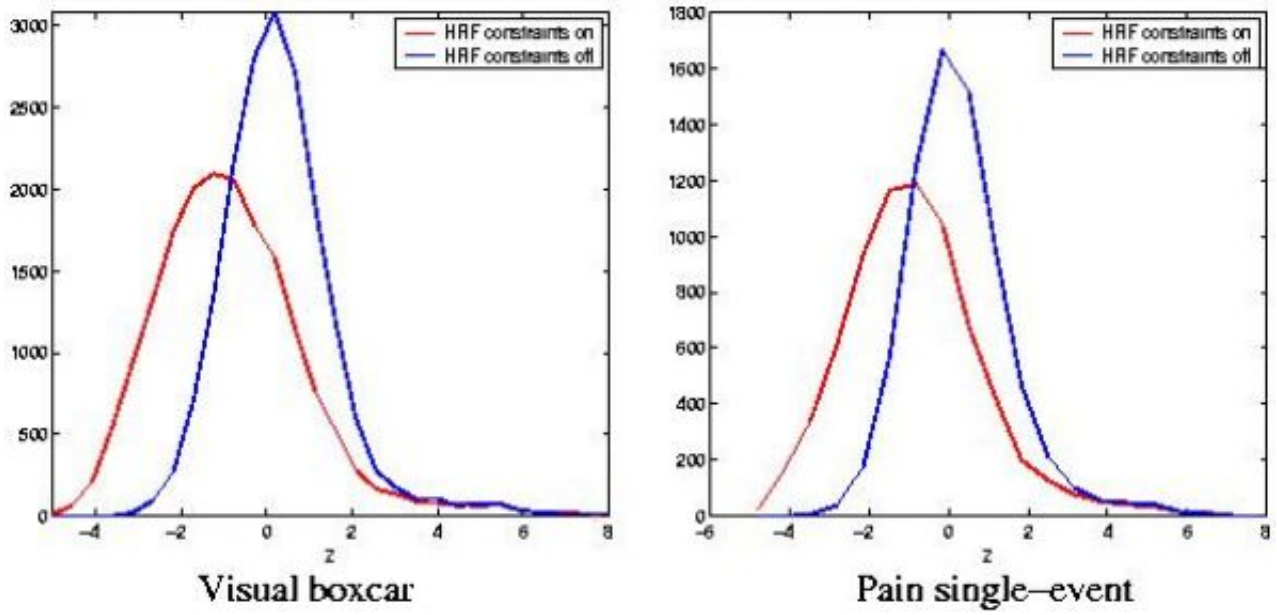

Figure 3: Histogram of pseudo-z-statistics with and without HRF constraints.

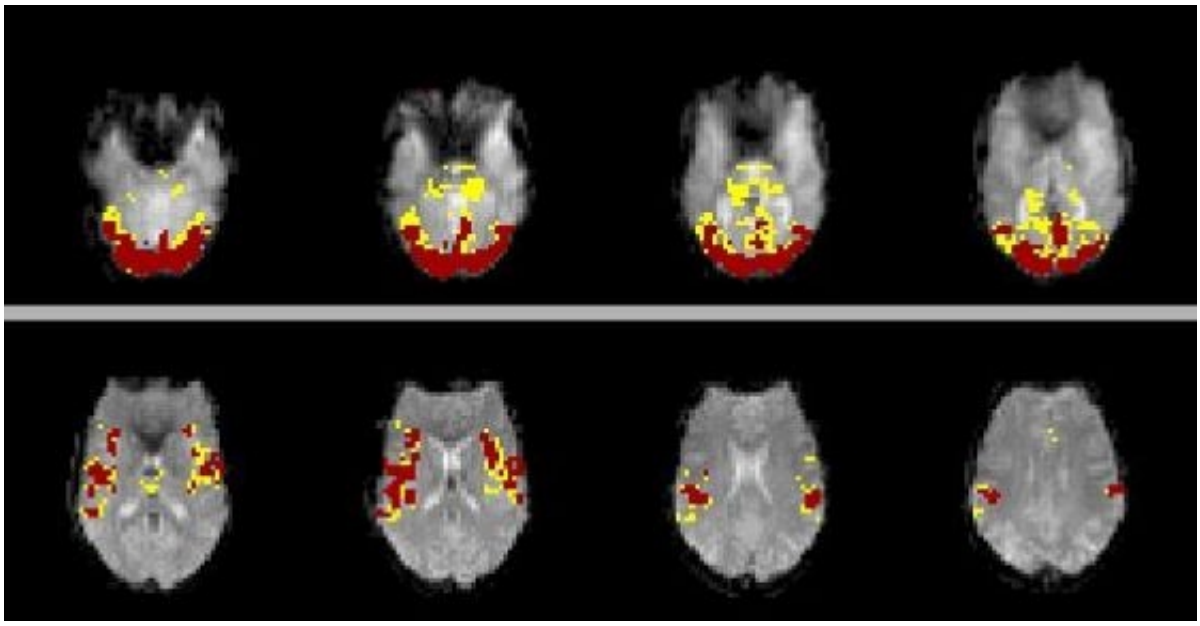

Figure 4: Difference in voxel classification with and without HRF constraints. [top] Visual boxcar dataset [Bottom] Pain single-event dataset. Active voxels with no constraints in blue, with constraints in yellow, and with either in red.

WE 329
fMRI data smoothing constrained to the cortical surface: a comparison of the level-set and mesh-based approaches

Nicolas Wotawa , Jean-Philippe Pons , Lucero Lopez-Perez , Rachid Deriche , Olivier Faugeras
Odyssee Lab., INRIA Sophia Antipolis, FRANCE

Introduction:
It is well known that fMRI data have low SNR. In order to increase the signal of interest, a spatial smoothing procedure is commonly used. The smoothness of the data is also assumed in Gaussian Random Field theory used in the SPM analysis. However, this smoothing is usually 3D-isotropic, thus mixing voxels from different anatomical tissues (e.g. gray matter, white matter and CSF). This leads to undesirable averaging of signals at neighboring voxels, potentially affecting the analysis sensitivity. Furthermore, due to the highly convoluted geometry of the cortex, the "tissue-blindness" of this smoothing yields a mixing of signals across sulci at voxels close to each other in the volume but distant on the cortical surface, reducing further the spatial discrimination power [1]. Taking into account the cortical geometry in the smoothing process seems to be a natural way to avoid these drawbacks.

Methods:
We implemented and compared two algorithms for surface-based smoothing, one based on an explicit mesh scheme and the other on a level-set framework. Both aim at minimizing the variations of the values defined along the cortical surface, leading to a partial differential equation (PDE) involving the Laplace-Beltrami operator, as shown respectively in [2] and [3]. The equivalent gaussian kernel FWHM is easily linked to the equation running time. Our cortical surface meshes are obtained with masks extracted with the Brainvisa software [4] and a segmentation algorithm based on the level-set evolution framework.
The mesh-based approach starts with a projection of the cortical functional voxels on the cortical surface and, after smoothing, performs a "back projection" into the original volume. This enables the direct use of the classical functional data analysis tools, but restricts the projection technique to the nearest neighbor method.
The level-set approach relies on the computation of a distance function, a 3D volume of the Euclidian distance from the cortical surface mesh. The PDE is then solved in a band around the cortical sheet directly in the functional volumes.
Finally, a formula is derived to adapt the threshold value for a T-test, taking into account the cortical surface area. This allows us to compare the results of both methods with the standard volumetric SPM-smoothing at equivalent p-value, on synthetic and real fMRI datasets related to visual perception experiments.

Results:
Surface-based smoothing provides better sensitivity in activation detection, leading to higher statistical values. It furthermore enhances their spatial localization and discrimination. According to our algorithms, the level set approach seems more straightforward and more easily adaptable to any functional data analysis framework.

References:
[1] Andrade, A., Kherif, F., et al., HBM, 2001.
[2] Chung, M.K., Taylor, J., et al., IEEE Transactions on Medical Imaging (submitted), 2000.
[3] Bertalmio, M., Memoli, F., et al., IEEE Workshop on Variational and Level Set Methods, 2001.
[4] Cointepas, Y., Poupon, C., et al., HBM, 2003.

WE 330
Influence of Spatial Normalization on Diffusion Tensor

Yukari Yamamoto[1, 2], Atsushi Maki[1, 2], Kuniyoshi Sakai[2, 3]
[1]Advanced Research Laboratory, Hitachi, Ltd., Hatoyama-cho, Japan, [2]CREST, Japan Science and Technology Agency, Kawaguchi-shi, Japan, [3]Dept. of Cognitive & Behavioral Science, Univ. of Tokyo, Komaba, Tokyo, Japan

Introduction

Examining the connectivity between functional areas in the brain is important for further understanding of brain functions. Methods of fiber tractography using diffusion tensor imaging (DTI) have been recently developed [1-3], and they have enabled us to obtain connectivity data non-invasively. It thus became possible to obtain connectivity data and functional data from the same subject. For direct comparison of the functional image and the fiber image, co-registration of these images is required. One straightforward method of co-registration is to normalize both images to a template image by using a spatial-normalization algorithm such as SPM (statistical parametric mapping). In the present study, fiber tracking after spatial normalization was, however, found to be difficult. We therefore examined the influence of image transformation on the diffusion tensor.

Methods and Results

In spatial-normalization algorithms such as SPM, optimum parameters of linear and non-linear transformations are calculated by evaluating the difference between the source image and the template [4]. We first applied SPM normalization to diffusion-weighted images (DWIs) before calculating the diffusion tensor. In the eigenvector map obtained without spatial normalization, regularities consistent with the brain structure appeared (Fig. 1(a)). The regularities were removed by applying spatial normalization, however, as shown in Fig. 1(b). It was thus found that the spatial normalization induces a disarrangement of eigenvectors. A similar disarrangement was seen in the case that only linear transformation was employed (Fig. 1(c)).

To discriminate the contributions by each term of the linear transformation to the disarrangement, eigenvector maps calculated after "zoom", "shear", and "rotation" transformations were compared. The test for "translation" was abbreviated because it has no apparent effect on the disarrangement. In the following arguments, X, Y, and Z denote horizontal, vertical, and depth directions, respectively. Figures 2(a) and (b) show the eigenvector maps with "zoom" transformation (0.8 times in the Y-direction) and "shear" transformation (Y=0.1*X-10). It is clear that the disarrangement is due to neither "zoom" nor "shear". The regularities of eigenvectors were obviously spoiled when "rotations" were employed, however, as shown in Figs. 2(c)-(d). The disarrangements were seen in either cases that the axis of rotation was set to X or Z.

Discussion

Since functional images are usually normalized to the template image, fiber images should also be normalized, though "rotation" transformation of DWIs prevents fiber tracking. To minimize the influence to the diffusion tensor, imaging positions of fiber images should be chosen carefully so as to avoid "rotation" transformation in the spatial normalization.

References

1)S. Mori et al., Ann. Neurol., 45, 265-269 (1999)
2)C. Poupon et al., NeuroImage, 12, 184-195 (2000)
3)P. J. Basser et al., Magn. Reson. Med., 44, 625-632 (2000)
4)K. J. Friston et al., Hum. Brain Map., 2, 165-189 (1995)

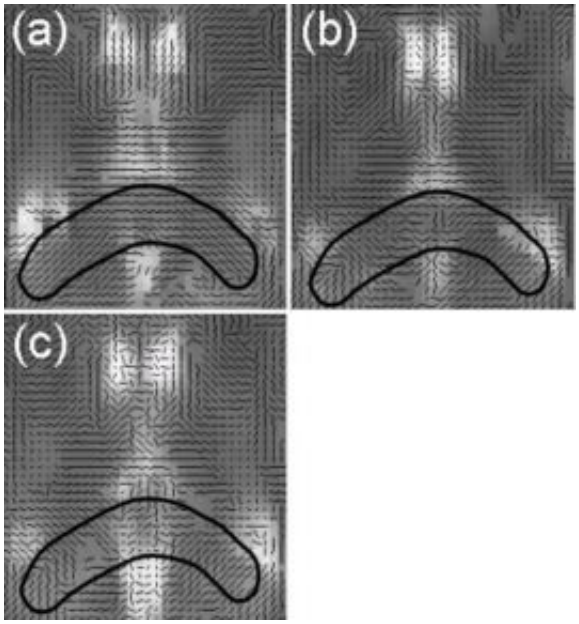

Fig. 1: Eigenvector maps obtained with or without spatial normalization:(a) without normalization; (b) with linear and non-linear normalizations; (c) with linear normalization.

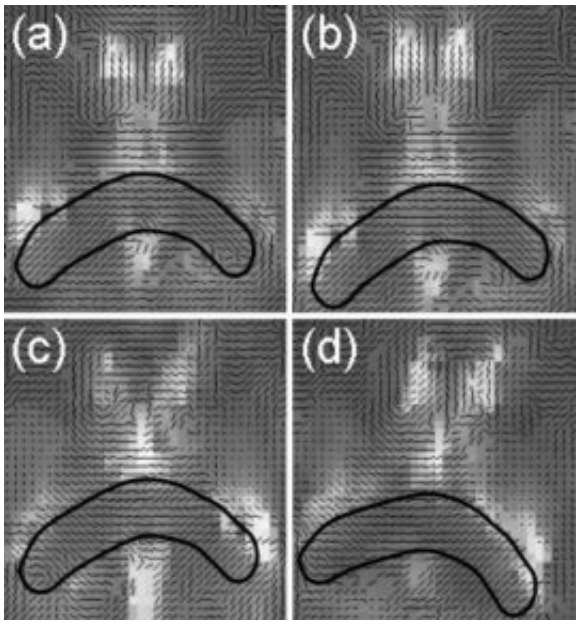

Fig. 2: Eigenvector maps calculated after linear transformations: (a) zoom in Y direction (0.8 times); (b) shear (Y=0.1*X-10); (c) rotation around X-axis; (d) rotation around Z-axis.

WE 331
Evaluating effective connectivity via relative power contribution ratios

Okito Yamashita [1], Norihiro Sadato [2], Tohru Ozaki [1,3]
[1] Department of Statistical Science, The Graduate University for Advanced Studies, Japan, [2] National Institute for Physiological Science (NIPS), Japan, [3] The Institute of Statistical Mathematics (ISM), Japan

Introduction
In this presentation we propose the statistical method of fMRI data to evaluate effective connectivity defined as "the influence that one neural system exerts over another" according to K. Friston(1995).
So far the structure equation model (SEM) has been commonly employed for the evaluation of effective connectivity (McIntosh1994) although they can work only in a highly constrained way, typically exploring the connections between a network of brain areas whose anatomy is explicitly defined by a model (i.e. the direction of connections needs to be prespecified).
As an alternative to overcome this disadvantage, we propose an approach based on multivariate time series analysis, especially causal analysis. The multivariate AR model and relative power contribution ratios (RPRC) proposed by Akaike (1968) are key tools for the evaluation of both the direction and the magnitude of connections. This work can be considered as an extension of the pioneering work based on causal analysis as proposed by Harrison et.al. (2003), where the direction of connections is examined via multivariate AR model and Granger causality.

Method
We model the system constituted by several regions of interest using the multivariate AR model and quantify effective connectivity using the relative power contribution ratios (RPCR). The RPCR characterizes the interrelations among elements of a feedback system in frequency domain.

Result
The method was applied to the visual experimental data (random dot). The first session consists in 3 periods of the 30sec. task state and the 30sec. control state. The second session consists in the continuous control state of duration 270sec.
The RPCR between V1, V5 and PP resulting from the time series of the first session is compared with that resulting from the time series of the second session (Fig.1).

Conclusion
Since the RPCR can quantify connectivity for each frequency component, the RPCR from the first session in the frequency corresponding to the task-control period is interpreted as a measure of task-related effective connectivity, whereas the RPCR from the second session of the same frequency is interpreted as a measure of no-task-related effective connectivity. By comparison of these two values, we can observe that the magnitude of bottom-up connectivity (V1->V5, V1->PP) increases.

Reference
H. Akaike (1968), *Annals of the Institute of Statistical Mathematics*, 20, 425-439
K. Friston et.al. (1995), *Human Brain Mapping*, 2, 211-224
L. Harrison et.al. (2003), *NeuroImage*, 19, 1477-1491
A. R. McIntosh and F. Gonzalez-Lima (1994), *Human Brain Mapping*, 2, 2-22

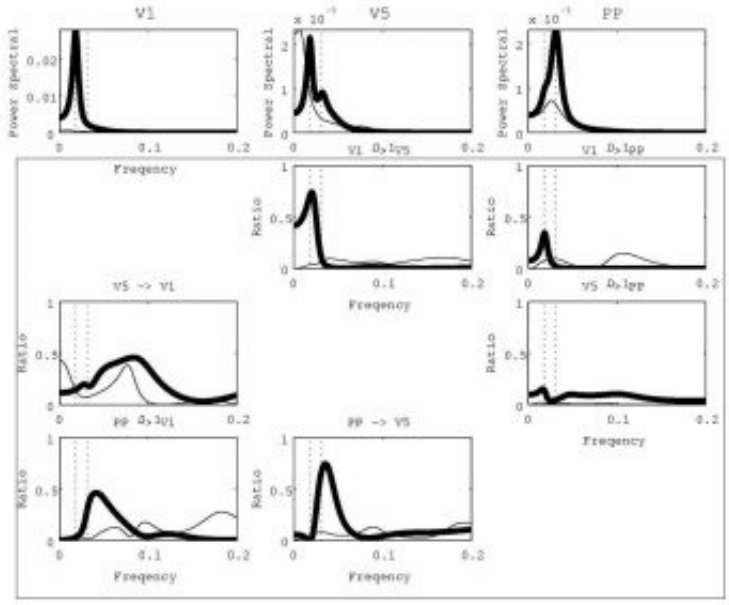

The power spectrum and the RPCR versus frequency (Hz). Thick line represents the results from the time series of the first session and thin line represents the results from the time series of the second session.

WE 332

Spatial and Temporal Dispersion of Hemodynamic Response in fMRI Data: a Sequential Approach

Lirong Yan , Zongtan Zhou , Dewen Hu , Yadong Liu
Department of Automatic Control, National University of Defence Technology, Changsha, Hunan 410073, P.R.China

As the foundation of BOLD signal measurement and analysis, evaluating hemodynamic response (HDR) attracts much interest and most work is based on optical imaging and event-related fMRI. However, block schema is widely used in experimental design, and we believe there is much information underlying in these block-mannered datasets.

This paper suggests a new schema for activation detection and HDR evaluation in a sequential manner: the first frame in each block after the onset of the stimuli (i.e. the task block) was included in the analysis and activation areas were detected, then the next frame (totally 2 frames now) is added in and activation areas were detected again, then first three frames were analysed and so on, until all the frames in task blocks were included. In this way, a sequence of activation data corresponding to different number of frames was obtained. Spatially, with the increase of number of frames, newly arisen activated areas were distinguished; then temporally, the timeseries of areas are extracted. To model the HDR, two gamma functions with unknown parameters is utilized. The parameterised HDR function is convolved with the stimulus function, generating a predicated response to the given stimuli, which is fit to the actual timeseries using the nonlinear least-squares procedure.

The method is applied to 8 datasets of right hand movement experiment where stimuli occurred in a periodic design consisting of 5 blocks. Each block consists 10 baseline scans followed by 10 scans during stimulation. The whole experiment lasted 300s.

Results from all subjects are similar and consistent. Mean numbers of activated areas are shown in Fig.1. There is a steady increase until the first seven or eight frames are analyzed, though a slight decrease when the first nine or all frames are included. More intuitively, the first 4 groups of areas are overlapped in one map (Fig.2). And the spatial dispersion of HDR is quite obvious. Next to evaluate the temporal characteristic of HDR in each region of interest, timeseries of up to 100 voxels are extracted and fitted to the HDR function. Result of BA1/2/3 and cerebellum are shown in Fig.3. To distinguish the timing difference of activated areas in different frames, temporal characteristic of HDR function are compared: Let denote time to peak when the first i frames are analyzed then the null hypothesis: where is tested using Students t distribution. The resultant statistics, are shown in Table 1. It can be seen that if the activated voxels occurred at least two frames apart, the timing difference is always significant (See , , in Table 1), and different regions have different characteristics in the sequent frames, e.g., for cerebellum, difference in the whole time domain is significant, but for BA 1/2/3, BA 4 and BA 6, and are not significantly different, while for BA 5/7, and are not significantly different.

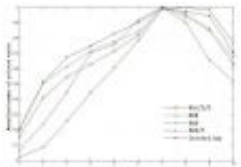

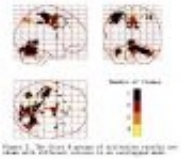

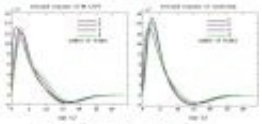

WE 333
Cortical Power Mapping of Alpha Activities by Charge-Layer Modelling

Dezhong Yao[1,2], Li Wang[1], Robert Oostenveld[1], Kim D Nielsen[1], Lars Arendt-Nelsen[1], Andrew C N Chen
[1]Human Brain Mapping and Cortical Imaging Laboratory, Aalborg University, Denmark, [2]School of Life Science and Technology, University of Electronic Science and Technology of China, China

[Background] Spontaneous EEG phenomena are of interest both scientifically and clinically. The alpha rhythm, which oscillates in the 8-12Hz frequencies, is the dominant rhythm in the human scalp EEG of relaxed, alert adults when the eyes are closed. Alpha activity is now also known in relation to diverse brain functions comprising sensory, motor, and memory processes. The generators of Alpha are not yet conclusively identified, several candidate sites include the parieto-occipital area, calcarine fissure, basal portions of the occipital lobe. This study aimed to explore the cortical power mapping of alpha activities by a new developed distributed Charge Layer approach (CL) (Yao, Phys Med and Biol, 48:1997, 2003).
[Methods] The EEG was recorded from 128 surface electrodes mounted on the scalp using a standard EEG-cap (A.N.T, Enschede, The Netherlands) from 11 healthy volunteers. The recording length is 2 minutes, the sample rate is 512, and the on-line reference is the left Mastoid (M). The subjects were required to relax and site at a comfort chair in a quiet and soft light room with eyes close. For the CL inversion, four concentric sphere layer is used as the head model, the radii for the cortical surface and scalp surface are 7.9 and 8.8 cm, and CL was set on an inner sphere with radius 7.5cm. The scalp potential V are segmented to epochs with length of 1 seconds, and epochs free of muscle, EOG and movement artifacts are selected on off-line editing. The CL inversion is done by solving the linear equation V=GX where V is the selected epochs of the scalp potential recordings, G is the transfer matrix from the CL to the scalp electrode array, and X is CL. Both the inverted CL and scalp V are analyzed for FFTF power mapping. For each subject, an individual Alpha peak frequency (IAPF) in the power curves are identified and the frequency band with IAPF ± 2Hz is used to plot the power maps for the scalp and cortex mapping, separately.
[Results] Fig.1 shows results of two subjects. IAPF of the scalp potential are 10 and 9 Hz, and IAPF of the cortical CL are 12 and 10Hz. There are at least two generators located at the occipital regions, and in case sources along the midline are also clearly visibly discriminated. A parietal alpha, in addition to the occipital site is also shown in the Ss-2. Similar results have been identified in all 11 subjects studied.
[Conclusion] The charge layer is shown to provide a much higher spatial resolution map of alpha activities than those of scalp potential in high-resolution EEG. The results show the main activities are located in the left and right occipital regions.
Acknowledgement: The work was supported by the Danish Technological Council, Aalborg University visiting Scientist Awards and NSFC (No.90208003), the China 973 Project (No. 2003CB716106) (D Yao).

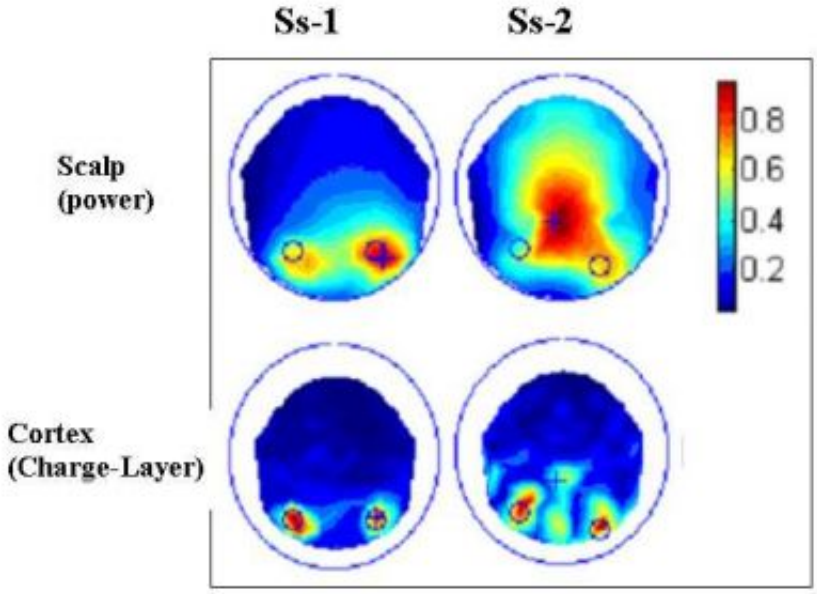

Figure 1. Normalized Power map of scalp potentials and cortical charge layer. The + shows the position of maximum on the scalp map, and o shows the left and right maximum powers of the cortical charge-layer.

WE 334

Systematic Effect of Reference on Power Mapping of EEG: The Use of Infinity Reference

Dezhong Yao[1,2], Li Wang[1], Robert Oostenveld[1], Kim D Nielsen[1], Lars Arendt-Nelsen[1], Andrew C N Chen[1]
[1]Human Brain Mapping and Cortical Imaging Laboratory, Aalborg University, Denmark, [2] School of Life Science and Technology, University of Electronic Science and Technology of China, China(dyao@uestc.edu.cn)

[Background] It is well known that only the difference between two potentials can be measured, so it is indispensable to set a physical reference in human scalp recordings. A popular practice is to record EEG with a reference at one of the Mastoids (M), and then re-reference to Linked mastoids (L) or Average (A) through an off-line processing. A new technique (REST)(Yao, Physiol. Meas., 22(4), 693, 2001) approximately re-references EEG to a point at Infinity (I). The effects of different references on power mappings in quantitative EEG are evaluated by a comparison study between the four references (M, L, A and I) techniques with measured EEG data.

[Methods] The EEG is recorded from 128 surface electrodes mounted on the scalp using a standard EEG-cap (A.N.T., Enschede, The Netherlands) from 11 healthy volunteers. The recording length is 2 minutes, sample rate is 512, and the on-line reference is the left Mastoid (M). The subjects were required to relax and site at a comfort chair in a quiet and soft light room with eyes open. The data are re-referenced to references L, A and I (REST). Data is segmented in 2-second epochs. Epochs free of muscle, EOG and movement artifacts are selected for FFTF power mapping. The powers are divided into 7 frequency bands: Delta (0.53.5 Hz), Theta (4.07.0 Hz), Alpha1 (7.59.5 Hz), alpha2 (10.0-12.0Hz) and Beta 1 (1323 Hz), Beta 2 (24--34-Hz) and Gamma (35-45Hz). The head is modeled with a sphere with radius 10cm, and a Cartesian coordinate system is defined with the center of the sphere as the origin, the x-axis towards the right ear, the y-axis towards the nasion and the z-axis towards the vertex. Based on the coordinates of the electrodes and the power values at each electrode, the Amplitude Weight Centers (AWC) of each band are calculated.

[Results] Fig.1 were the average map results of Alpha 2 over the 11 subjects. Compared AWCs of M , L and A with that of the new reference I, the original reference M (left mastoid) showed significant ($p<0.001$) right (+x), frontal(+y) and superficial(+z) shifts (x: 0.5±0.2; y: 0.8±0.2; z: 0.26±0.07 (cm)). The linked bilateral reference L (linked mastoids) showed a well balance between left and right, but a significant ($p<0.001$) frontal and superficial shifts (x: 0.03±0.09; y: 0.8±0.2; z: 0.28±0.07). In contrast, the averaged reference A resulted in a reduction of power and a significant ($p<0.001$) shift to the bottom (x: 0.0±0.2; y: 0.5±0.5; z: -0.3±0.1).

[Conclusion] This study results clearly demonstrate that different references induce systematic changes of AWC in EEG power map. In order to minimize effect of such systematic shifts for proper explanation of EEG power maps, a common reference is necessary. Since the I-reference is theoretically far from all the electrodes thus being a neutral reference, we recommend it for common practice.

Acknowledgement: The work was supported by the Danish Technological Council,Aalborg University visiting Scientist Awards and NSFC(No.90208003), the China 973 Project (No. 2003CB716106) (D Yao).

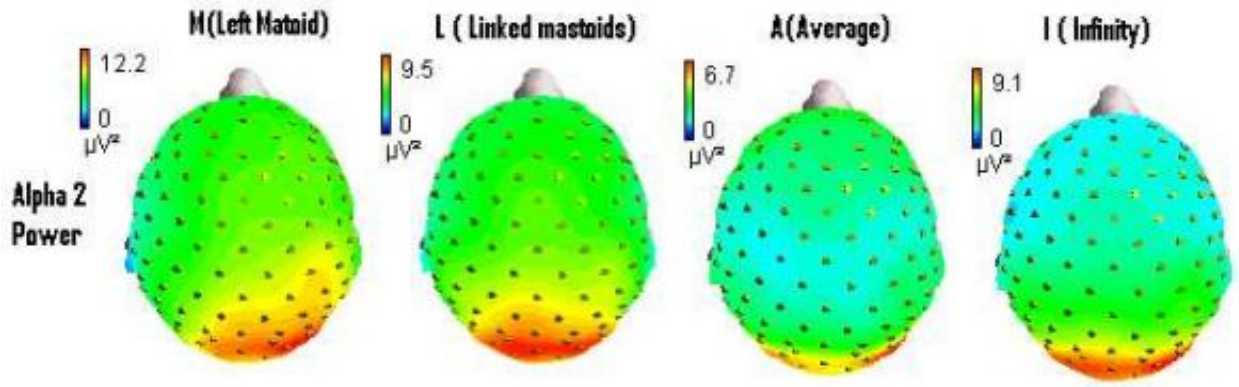

Fig.1 Power mapping of EEG with different references. The frequency band is Alpha 2 (10.012.0 Hz).

WE 335
Improved Statistical Sensitivity of FMRI by Removing Resting Rhythms Using Independent Component Analysis

Tzu-Chen Yeh[1,2], Jeng-Ren Duann[3], Wen-Jui Kuo[1,4,6], Yu-Te Wu[1,5], Yung-Yang Lin[1,2], Jen-Chuen Hsieh[1,2,6]

[1]Integrated Brain Research Unit, Department of Medical Research and Education, Taipei Veterans General Hospital, Taipei, Taiwan, [2]Faculty of Medicine, School of Medicine, National Yang-Ming University, Taipei, Taiwan, [3]Institute for Neural Computation, University of California San Diego, La Jolla CA, USA, [4]Cognitive Neuropsychology Laboratory, National Yang-Ming University, Taipei, Taiwan, [5]Institute of Radiological Sciences, National Yang-Ming University, Taipei, Taiwan, [6]Institute of Neuroscience, School of Life Science, National Yang-Ming University, Taipei, Taiwan

Specific Aim

By utilizing independent component analysis (ICA) of functional MRI data, task-irrelevant brain activities recognized as resting rhythms co-existing with task-relevant response during a Chinese covert naming task. Spatial extension of the consistent task-irrelevant resting rhythm, named as a tripod component, mainly involves bilateral occipital, precuneus, posterior cingulate, inferior parietal lobule and prefrontal cortices. In this study, the effect of the tripod component on fMRI analysis was evaluated by signal correlation to designed paradigm convolved with assumed hemodynamic response and task-related response derived from ICA. By removing the task-irrelevant resting rhythms from fMRI data, the statistical significance of task-relevant activation was dramatically improved.

Material and Methods

Seven healthy volunteers (age: 22~29, male/female: 4/3) received fMRI studies of two blocked conditions, reading and control tasks. In the reading task (R), subjects read the displayed two-character Chinese words covertly. In the control task (F), a cross-hair was presented for eye fixation. By utilizing a 1.5T MRI (TR/TE/NR/flip angle = 2s/0.05s/204/90), each condition persisted for 24 seconds with the paradigm of FRFRFRFRFRFRFRF.

An off-line analysis, modified from AFNI (Analysis of Functional NeuroImages, NIMH, Bethesda, USA), of the head motion ensured the quality of fMRI study with head translation < 1 mm and head rotation < 0.5 degree within each session. No motion correction was applied before ICA. Data preprocessing of a slice time-alignment process to minimize image intensity inhomogeneity arising from differences in slice image acquisition timing of 2000 ms in multi-slice studies. The time-realigned fMRI images were extracted for within-brain voxels by thresholding intensity histograms of the EPI images for data reduction in a fraction of more than 20%. Data were analyzed using spatial informax ICA for identifying components with statistically independent spatial distributions. One-hundred spatial independent components with corresponding fMRI BOLD time course were derived by ICA with initial values of learning rate and data points chosen as 0.0001 and 100, respectively. Task-irrelevant resting rhythms of functional MRI data were recognized by correlation to paradigm and removed from original data by ICA. Statistical significance was evaluated by the penetration maps with correlation to designed paradigm convolved with assumed hemodynamic response and task-relevant response derived from ICA.

Results

After removal of tripod component from the mixing matrix of ICA, the activation regions of the Chinese covert naming task showed the expansion of activation region with correlations to paradigm and task-relevant response in factors of 9.7±4.7 (mean±one standard deviation, n = 7) and 4.3±2.0 folds, respectively. Statistical significance (the maximal correlation coefficient within activation regions, mean±one standard deviation, n = 7) was enhanced from 0.63±0.10 to 0.72±0.11 (correlation to paradigm) and from 0.75±0.03 to 0.84±0.03 (correlation to task-relevant response). Penetration maps of seven subjects demonstrated statistical improvement with the correlation coefficient of 0.4.(Figure 1)

Conclusion

Task-irrelevant resting rhythms contribute to functional noise during cognitive task, e.g. Chinese covert naming task.

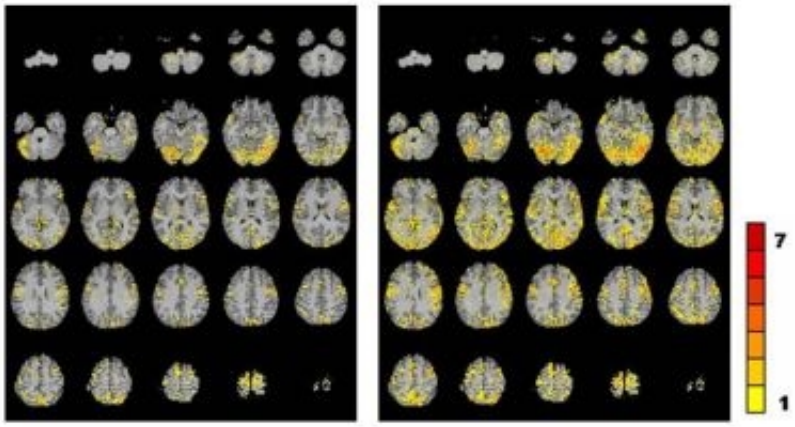

Figure 1: Penetration maps of seven subjects (scaling from 1 to 7) were obtained by correlation to paradigm utilizing original data (left) and data after removing tripod component by ICA (right).

WE 336
Exploring the Optimization of fMRI Processing Pipelines within the NPAIRS Framework

Jane Zhang[1], Sujit Pulapura[2], John Anderson[1], Stephen Strother[1,3]
[1]Neurology Department, University of Minnesota, [2]Electrical Engineering, University of Minnesota, [3]Radiology Department, University of Minnesota

Introduction: fMRI processing pipeline options have a big impact on the final fMRI analysis results due to the low SNR of fMRI data. Therefore, it is important to evaluate different processing options and to optimize fMRI pipelines[1,2]. The standard evaluation method--simulations and ROC curves has the advantage of accuracy due to known ground truth, but it has serious limitations due to the unknown match between a simulation and any real data set[1,2,3].
Methods: The 16 subjects' static force dataset described by LaConte et al. was utilized ([2]). Optimization was based on two criteria: prediction accuracy and activation pattern reproducibility, generated by NPAIRS through cross-validation[4]. Four main preprocessing options were considered generating 10 processing pipelines: (1) motion correction (black lines); (2) spatial smoothing at 0,1.5,6 pixels with 2D Gaussian filter, plotted as filled circles, triangles and squares, respectively; (3) temporal filtering at 0,1,3 cosine cycles with cosine basis function in GLM, plotted as ; fourth, denoising through PCA/CVA dimension reduction with subspace selection 10,25,50,75 components. Data analysis was performed by PCA/CVA model within NPAIRS framework. According to the experiment design and research interest, different CVA models were employed. 11 class CVA model was grouped by 11 brain states (including 5 force levels and 6 baselines) in a single trial/run. In addition, 2 class CVA (grouped by baselines and activations) was performed as a comparison with the 11 class CVA. NPAIRS was integrated into Fiswidgets environment[4]. This allows us to exchange resources with other fMRI packages and to better control the execution of fMRI processing pipelines on the Fiswidgets platform.
Results: 10 processing pipelines were formed. The results of 11 class CVA analysis are summarized in Fig.1 and Fig.2 which give the average prediction accuracy and reproducibility across all 16 subjects for baselines (Fig. 1) and for activations (Fig.2). Although there is considerable variance in the analysis results among subjects, the mean prediction vs. reproducibility plots illustrate the trend in 11 class CVA case. First, detrending flattens the baselines (at 3 cosine cycle (Fig.1)), but it also seriously lowers the prediction accuracy for activations and causes the model badly predict the data (below randomly guessing probability). Second, spatial smoothing helps increase prediction accuracy and reproducibility only when the data is not highly detrended and the dimension reduction (denoising) is properly performed. Fig. 3 and Fig. 4 provide 2 class CVA results which were obtained by the same pipeline options. We observed that detrending increases the prediction accuracy for !
baselines in this case while there is a reverse trend at 1 cosine and 3 cosine for force levels. Again, close relationship between spatial smoothing, temporal filtering and denoising was observed here. Further, 2 class CVA model reveals that motion correction plays a significant role in terms of increasing prediction accuracy and reproducibility as shown in Fig 3 and 4.

References

1.Shaw ME et al, Neuroimage 19:988-1001, 2003.
2.LaConte S et al, NeuroImage 18:10-27, 2003
3.Strother SC et al, Neuroimage. Apr; 15(4): 747-71 2002
4.Fissell K et al, Neuroinformatics 1:1 111-160, 2003

Acknowledgments: This work is supported by NIH grand MH57180.

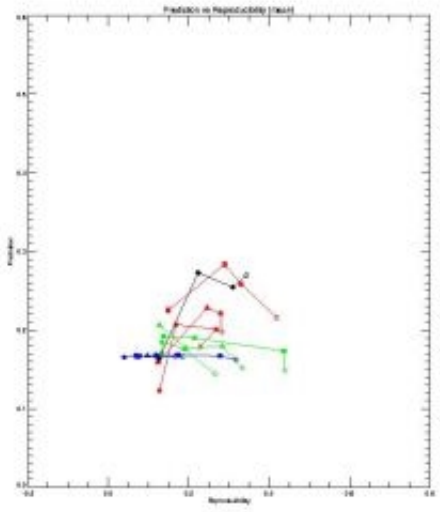

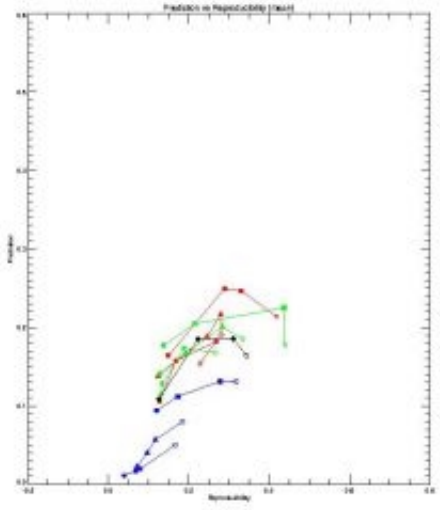

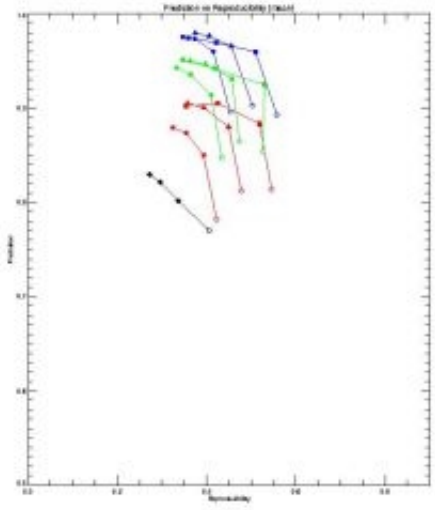

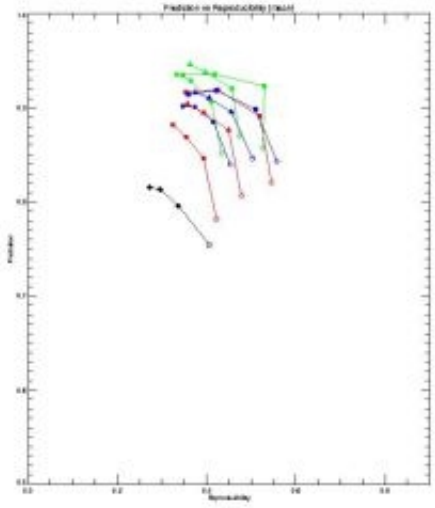

WE 337
Propagable region-growing for 3D segmentation of white matter fascicules with diffusion tensor MRI data

Chaozhe Zhu , Gaolong Gong , Tianzi Jiang
National Laboratory of Pattern Recognition, Institute of Automation, Chinese Academy of Sciences, Beijing 100080, P. R. China

In conventional structural MR images, white matter (WM) can only be distinguished as a whole tissue class from other ones, while the isolation of anatomically distinct WM fascicules from surrounding WM is never achievable. This, however, has greatly hindered the studies of neurological and psychiatric diseases since the involved pathology or degeneration may emerge not only at gray matter (GM) but also along the pathways connecting different function areas, e.g., cingulum bundle in the brain of schizophrenia patients [1].
DT-MRI is a new MRI technique with which significant progresses have been made in the studies of brain development, brain function connectivity and brain diseases [1,2,3]. DT-MRI provides information about the random displacement of water molecules. Using this information combined with mathematical tools we can further explore WM micro-architectures. This affords an unprecedented possibility to delineate anatomically distinct WM fascicules in the brain. To address this issue, we proposed a propagable region-growing (PRG) method to segment anatomically distinct white matter fascicules with diffusion tensor MRI data. It can be summarizes as follows: (1) firstly, a seed point is planted in the initial slice of the primary diffusion direction (PDD) map from which the 2D cross-section of the WM fascicules in the plane can be isolated by region growing. (2) Then the seed point can be propagated automatically to the neighboring slice under spatial and directional constraints. Such seed propagation and region growing will go on until the whole fascicules have been isolated. (3) At last, quantitative measurements and analysis can be performed on the separated volume of the white mater fascicules.
For validation, we tested our method to segment the central portion of the cingulum bundle, major white matter fascicules in the brain. All DT-MRI data were acquired with a GE 1.5 T MR scanner from 26 normal right-handed subjects. The imaging parameters were set as follows: TR, 4s; TE, 85ms; matrix, 128x128; FOV, 24x24cm; NEX, 3; slice thickness 3mm without gap. 25 non-collinear diffusion directions with b value=1000 s/mm^2 . The coronal FA map passing the AC point was set as the initial slice. The areas of each corresponding propagation step were averaged among the 26 subjects and the results shown in the following figure suggested a right < left tendency in area of cingulum bundles.

Reference:

[1] F. Wang, et al, Anterior cingulum abnormalities in male schizophrenia with diffusion tensor imaging, Am. J. Psychiatry, 2003. (In press)
[2] P. Fillard, J. Gilmore, J. Piven, W.L. Lin, G. Gerig, "Quantitative Analysis of White Matter Fiber Properties along Geodesic Paths," MICCAI, 2003.
[3] M. Kubicki, C. Westin, et al, Diffusion Tensor Imaging and Its Application to Neuropsychiatric Disorders, Harvard Rev Psychiatry November/December, 324-336 2002.

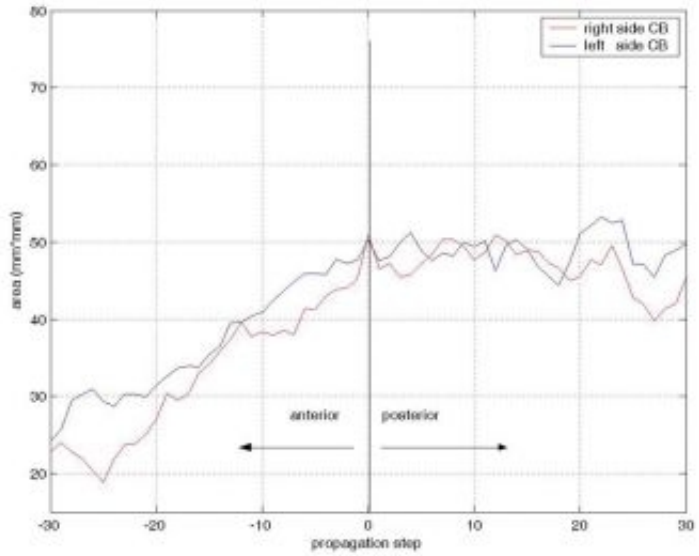
right side CB
left side CB
area (mm*mm)
anterior
posterior
propagation step
80
70
60
50
40
30
20
-30
-20
-10
0
10
20
30

Fig. 1

WE 338

Segmentation of Thalamic Nuclei from DTI using Spectral Clustering

Ulas Ziyan[1,2], David S. Tuch[1]

[1]Athinoula A. Martinos Center for Biomedical Imaging, Massachusetts General Hospital, Charlestown, Massachusetts, USA, [2]Massachusetts Institute of Technology, Department of Electrical Engineering and Computer Science, Cambridge, Massachusetts, USA

Introduction

Magnetic resonance diffusion tensor imaging (DTI) can resolve thalamic nuclei based on the distinct orientation of the thalamocortical/corticothalamic striations within each nucleus (1). However, a segmentation procedure is required to extract the nuclei geometries from the DTI. While the k-means algorithm (1) can extract the gross structure of the clusters, the algorithm has a number of weaknesses including susceptibility to local minima and geometric bias towards ellipsoidal clusters. Here, we describe a spectral clustering algorithm (2) which resolves the limitations of the k-means approach.

Algorithm

The spectral clustering algorithm identifies clusters based on the eigenspectrum of the voxel affinity graph (2). The affinity matrix W contains the pair-wise distances between voxels. The distance metric was chosen to be the exponential of the scaled angular distance between the first eigenvectors for neighboring voxels. The affinity matrix is then normalized by calculating $M=D^{-1/2}WD^{-1/2}$, where D is a diagonal matrix of the row sums of W (2). To assign voxels to clusters, k-means is applied on the rows of the matrix formed from the k largest eigenvectors of the normalized affinity matrix.

Methods

Data Acquisition

Whole-head, single-shot EPI DTI was acquired on a healthy subject on a 3.0T Siemens Trio MRI using an 8-channel phased array coil. The imaging parameters were TR/TE=8400/82 ms, b=700 s/mm^2, 70 directions, 1 average, 2 mm isotropic resolution. Whole-head, high-resolution MPRAGE structural data were also acquired in order to generate masks for the thalamic hemispheres (3).

Segmentation

The thalamic nuclei were clustered separately for each hemisphere using the spectral clustering algorithm. The number of nuclei, k, was set a priori to 16 per hemisphere based on preliminary visual inspection.

Results

Fig. 1 shows the DTI cuboid field with the segmentation results indicated by the contours. Fig. 2 shows the underlying voxel affinity graph. The segmentation was computed in three dimensions even though the segmentations are only shown in two dimensions.

Discussion

We have described a method for segmenting thalamic nuclei from DTI using spectral clustering. The spectral clustering algorithm has no local minima and requires no representation of the cluster geometry and therefore represents a significant advance over k-means.

Acknowledgments

This work was supported in part by Glaxo Smith Kline, NINDS NS046532, NCRR RR14075, and the MIND Institute.

References

1. Wiegell MR, et al. Neuroimage. 19:391-401, 2003.
2. Chung FRK. Spectral Graph Theory. American Mathematical Society, 1997.
3. Fischl B, et al. Neuron. 33:341-355, 2002.

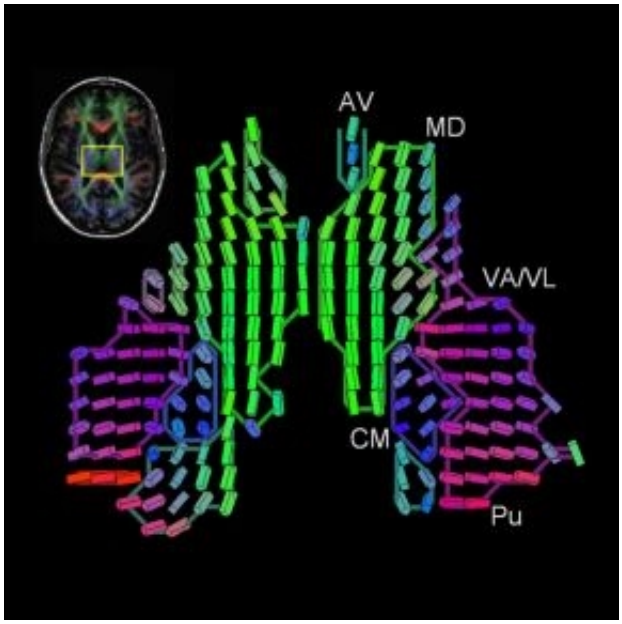

Fig. 1. DTI cuboid field of the thalamus taken from ROI shown at top left. The top-left image shows the MPRAGE-registered DTI superimposed as a semi-transparent RGB overlay on the MPRAGE. The hand-labeled nucleus assignments are shown at right.

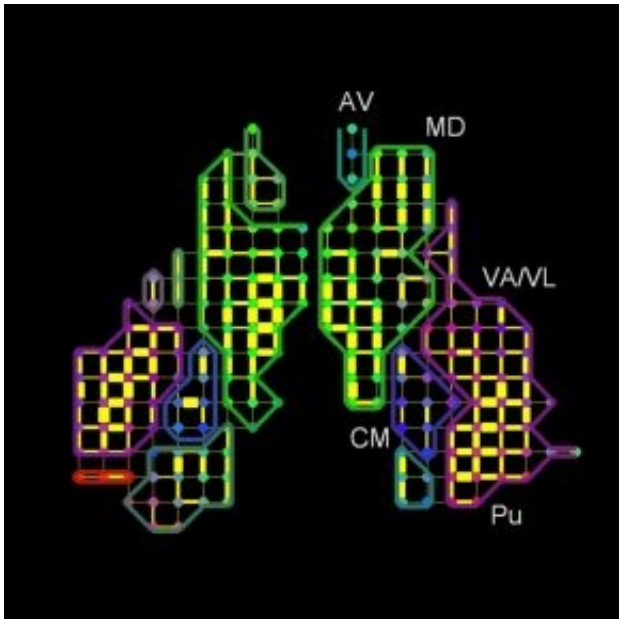

Fig. 2. Tensor-based voxel affinity graph. Only the in-plane connections are shown. The voxel-voxel affinity is indicated by the width of the yellow line segment connecting the nodes. Note how the segmentation contours tend to cut through low affinity connections.

WE 339
Multi-modal Medical Image Registration in a Unified Framework

Lilla Zollei[1], John W. Fisher[1], William M. Wells III[1,2]
[1]Massachusetts Institute of Technology, Computer Science and Artificial Intelligence Laboratory, Cambridge, MA 02139, USA, [2]Department of Radiology, Harvard Medical School and Brigham and Women's Hospital, Boston, MA 02115, USA

Introduction
Registration of multiple medical scans is the problem of identifying a geometrical transformation that locates the coordinate system of one in that of the other. We have previously provided a unified information theoretic framework for comparing registration methods whose objective functions rely on sound statistical principles, including maximum likelihood (ML) techniques, Kullback-Leibler divergence (KL) methods and Mutual Information (MI) [1]. We illustrated the underlying assumptions distinguishing these techniques and clarified the assumed behavior of joint intensity statistics as a function of transformation parameters.
Motivation
In the present work, we extend that framework with two additional methods. We reformulate and analyze the correlation ratio (CR) [2] and the iterative generalized maximum likelihood (MLit) [3] measures both of which represent somewhat similar but distinct interpretations of the image alignment problem. Our motivation is two-fold: we wish to make the unified registration framework more complete, and also to clarify the implicit underlying assumptions inherent in these approaches.
Discussion
The classical ML approach provides a theoretical framework to the problem. It assumes access to the complete continuous joint density space parameterized by transformations. It compares that model to the current observations to identify the solution. The approximate ML (MLa) and KL methods make more practical modeling assumptions. They presume that, at correct alignment, the joint probability density of a corresponding modality pair is fixed and it can be constructed from previous examples. The goal is then to closely approach the model. The KL framework achieves this optimization more robustly than the MLa. The MI formulation makes the weakest assumption. It hypothesizes that the inputs are maximally dependent when correctly aligned, and that increasing amounts of mis-alignment destroy that dependence. Instead of constructing a model for the goal density to be attained, it guides away from the independence scenario.
We have found that these newly incorporated measures mostly resemble the MLa approach. They presume the existence of a model joint density function at correct alignment and they attempt to converge to it. However, instead of treating the model as static and a priori obtainable, they estimate it online, along with the aligning transformation. The CR method solves a dual optimization problem, in a parameterized framework. At each iteration, it first optimizes for the parameters describing the assumed density model, then for the best transformation. The MLit method applies a non-parametric approach to best estimate the goal joint density function. It successively locates a transformation that further maximizes the likelihood criterion. We can (experimentally) demonstrate the type of registration problems for which this framework guarantees convergence and also the fact that under certain criteria these methods are equivalent to entropy minimization.
[1] Zollei et al.: A Unified Statistical and Information Theoretic Framework for Multi-modal Image Registration, IPMI 2003, LNCS 2732:366-377.
[2] Roche et al.: Unifying Maximum Likelihood Approaches in Medical Image Registration, International Journal of Imaging Systems and Technology, 2000, 11(7180):71-80.
[3] Timoner: Compact Representations for Fast Non-rigid Registration of Medical Images, MIT Ph.D. Thesis, 2003.

WE 340

A Prospective Multi-Institutional Study of the Reproducibility of fMRI: A Preliminary Report from the Biomedical Informatics Research Network

Kelly H. Zou[1,3], Douglas N. Greve[2,3], Meng Wang[1,3], Steven D. Pieper[1,3], Simon K. Warfield[1,3], Nathan S. White[2,3], Mark G. Vangel[2,3], Ron Kikinis[1,3], William M. Wells, III[1,3], FIRST BIRN[3]
[1]Surgical Planning Laboratory, Department of Radiology, Brigham and Womens Hospital, Harvard Medical School, [2]Athinoula A. Martinos Center for Biomedical Imaging, Department of Radiology, Massachusetts General Hospital, Harvard Medical School, [3]Functional Imaging Research of Schizophrenia Testbed (FIRST), Biomedical Informatics Research Network (BIRN)

Purpose
To investigate the effects of factors such as study site, field strength, visit and run on the reproducibility of the performance of a sensory-motor (SM) task by 5 healthy subjects in a prospective multi-institutional study.
Background
Functional MRI (fMRI) has significantly contributed to studies of the human brain. [1,2] Unfortunately, there exists high variability in the magnitude, spatial distribution, and statistical significance of fMRI maps. The Biomedical Informatics Research Network (BIRN) compared the fMRI signal to determine whether combining fMRI maps from different sites is meaningful. We used an estimation-maximization algorithm, Simultaneous Truth and Performance Level Estimation (STAPLE), [3,4] to characterize the variability in a sensory-motor (SM) task.
Methods
Eleven sites participated in the Functional Imaging Research of Schizophrenia Testbed BIRN study. Data was analyzed from 8 (5 1.5T and 3 3.0T scanners) of these sites. Five healthy right-handed males were scanned at each site in 2 visits. The SM task was performed for 4 of 10 runs per visit. A block design was used with 15-second epochs of alternating baseline (fixation) and task for 85 (plus 2 discarded) acquisitions per run. Subjects performed bilateral finger tapping on a dummy and an actual button box with a 3Hz audio cue and a reversing checkerboard. The subjects pressed buttons 1 through 4 in consecutive order and then back again using both hands simultaneously and in sync. Imaging was acquired with block-design echo-planar or spiral gradient echo (oblique axial, 64x64 matrix, 1 shot, 35 slices, 4mm, 3 sec, TE varied with strength). A bite bar helped minimize head movement. Motion correction for each run was applied to middle time point using AFNI. Smoothing was based on FWHM 5mm. Registration was performed over runs. STAPLE optimally estimated a composite true 3D activation map over the runs per visit, visualized in Slicer. [5] Sensitivity and specificity were derived from voxel counts. [6] Significance of the factors was analyzed via summary statistics and linear models.
Results
Significant factors for sensitivity included field strength ($p=0.002$), subject ($p=0.003$), site ($p=0.02$) and manufacturer ($p=0.02$), and for specificity included subject ($p=0.04$) and run ($p=0.04$). At 3.0T, the mean sensitivity per subject ranged 0.57-0.76 (SD =0.17-0.26) while the mean specificity ranged 0.99-1.00 (SD=0.002-0.02). At 1.5T, the mean sensitivity only ranged 0.42 to 0.69 (SD=0.18-0.34) while the mean specificity ranged 0.95-1.00 (SD=0.004-0.22) (Figs 1-3).
Conclusions
Subject: Moderate to high reproducibility within subject was found. Site: The variability across sites appeared less than that across subjects. Field Strength: 3.0T generally yielded greater activation and higher sensitivity than 1.5T. Run: Variable patterns over runs were observed, with less activation but more robust patterns during latter visits. Thus, a calibration plan may be possible to minimize the variability introduced by different sites.
References
1. Brannen JH et al. AJNR 2001; 22: 1711-8.
2. Machielsen WCM et al. HBM 2000; 9: 156-164.
3. Warfield SK et al. LNCS 2002; 2488: 290-297.
4. Zou KH et al. Acad Radiol 2003; 10: 1359-1368.
5. Gering D et al. JMRI 2001; 13: 967-975.
6. Genovese CR et al. Neuroimage 2002; 15: 870-878.

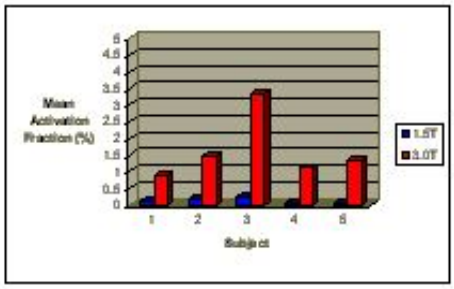

Fig 1. Mean activation percentage by subject and field strength

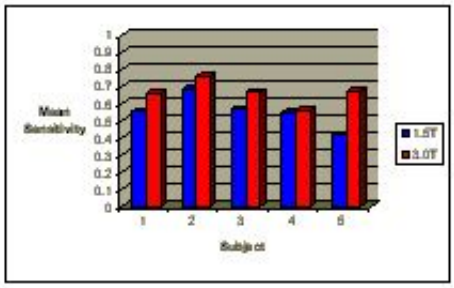

Fig 2. Mean sensitivity (true activation fraction) by subject and field strength

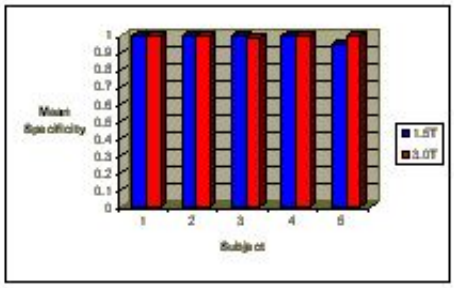

Fig 3. Mean specificity (true non-activation fraction) by subject and field strength

WE 341
Validation of manually fixed ROIs with an automatic Talairach space based method in dopamine transporter (^{99m}Tc-TRODAT) SPECT

Miklós Árgyelán[1], Attila Tanács[2], Balázs Kanyó[1], Zoltán Szabó[3], Zsuzsanna Kovács[3], Attila Kuba[2], Zoltán Janka[3], László Pávics[1]

[1]Department of Nuclear Medicine, University of Szeged, Hungary, [2]Department of Informatics, University of Szeged, Hungary, [3]Department of Psychiatry, University of Szeged, Hungary

In the last few decades a significant amount of new techniques have been developed in the field of image analysis. These techniques are common in trying to make observer independent evaluation of the images. One of the basic concept in these methods to register the images in Talairach space. Based on this concept an automatic technique was compiled by us. The purpose of these study was to compare the traditional manually fixed ROI method with our automatic method in dopamine transporter SPECT.

Six patients with major depression were investigated twice with ^{99m}Tc-TRODAT SPECT. Using the total 12 brain SPECT data sets striatum per occipital values (SOR) were calculated with the traditional manually fixed ROI method, and by an automatic analysis compiled by us. The automatic (observer-independent) image analysis was performed on a PC workstation, using MATLAB. First, the images were spatially normalized into the Talairach space with SPM2 using a brain blood flow SPECT template, and smoothing was used with 11 mm full-width of half-maximum (FWHM). 3D masks were generated by WFU Pickatlas 1.02 software (Fig. 1). These masks (also in Talairach space) were used as ROIs, and a MATLAB script calculated mean count densities for the striatum and occipital lobe (striatal size: 2815 voxels, occipital size: 21322 voxels, voxel size 2x2x2 mm). The SOR values in the automatic (average ± SD: 1.81 ± 0.24) and in the manual method (average ± SD: 1.82 ± 0.25) were nearly the same. The SOR data calculated by the automatic method correlated closely with the manually obtained data ($y = 0.9928x$, and Pearsons $r = 0.91$, $p < 0.001$, $n = 12$)(Fig. 2).

These results suggest that the results of manually and automatically fixed out ROI methods are comparable.

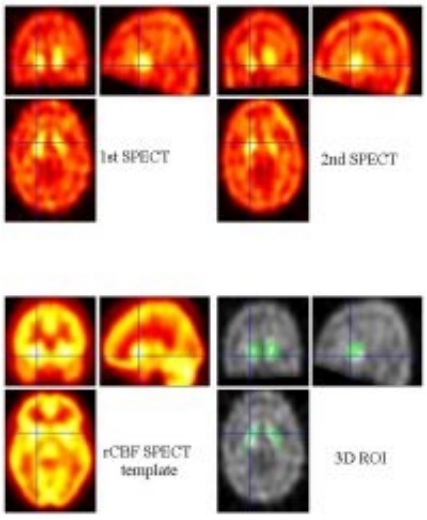

Automatic 3D ROI method in order to validate the manual method. The upper images represent the first and second SPECT of a 54-year-old female (before and after therapy) (the Striatum/occipital value is normal (2.20)).

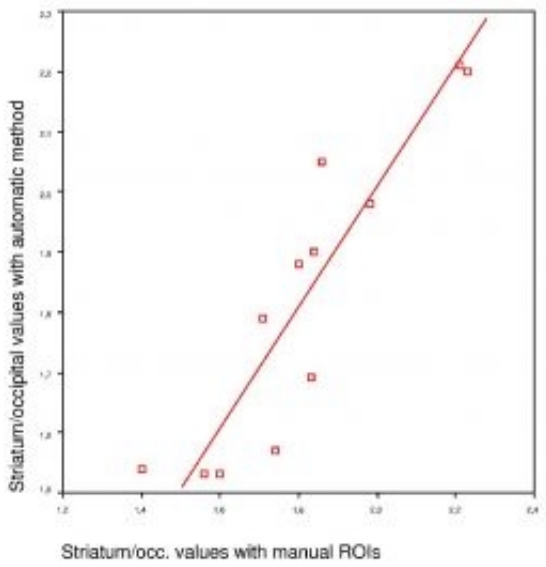
Striatum/occipital values with automatic method
Striatum/occ. values with manual ROIs

Results

WE 342

Increased brain atrophy in chronic back pain: Pain hurts the brain.

Apkar V. Apkarian[1], Yamaya Sosa[1], Sreepadma Sonty[2], Robert E. Levy[3], Robert N. Harden[4], Todd B. Parrish[5], Darren R. Gitelman[2, 5]

[1]Department of Physiology and Institute of Neuroscience, Northwestern University, Chicago, IL, 60611, USA., [2]Department of Neurology, Northwestern University, Chicago, IL, 60611, USA., [3]Department of Neurosurgery, Northwestern University, Chicago, IL, 60611, USA., [4]Rehabilitation Institute of Chicago, Chicago, IL, 60611, USA., [5]Department of Radiology, Northwestern University, Chicago, IL, 60611, USA.

Ten percent of adults suffer from severe chronic pain. A pathological state accompanied with reorganization of peripheral and spinal cord nociceptive coding. Although chronic pain greatly diminishes quality of life, and increases anxiety and depression, it is assumed that the cerebral cortex passively reflects spinal changes, and reverts to its normal, healthy state after cessation of chronic pain. Here we use whole brain and regional morphometric analyses of MRI brain scan data to examine the impact of chronic back pain (CBP) on brain atrophy. Patients with CBP had 5-8% (30 cm3) less cortical gray-matter volume than control subjects. The magnitude of this atrophy is equivalent to the gray matter volume lost in 10-15 years of normal aging. Whole-brain atrophy was strongly related to pain duration, and provided evidence for predisposition for brain atrophy. Regionally, gray-matter density was reduced in dorsolateral prefrontal cortex bilaterally and in the right thalamus, and was larger in patients where CBP included sciatic neuropathy. The regional specificity of the atrophy and its relationship to pain characteristics imply that CBP should be considered a neurodegenerative condition that continuously damages the brain.

WE 343

Extending SIENA for a Multi-Subject Statistical Analysis of Longitudinal Cerebral Edge Shifts: Substantiation of Early Brain Regeneration through Abstinence from Alcoholism

Andreas J. Bartsch[1], Martin Bendszus[1], Nicola DeStefano[2], Georg Homola[1], Stephen Smith[3]
[1]Division of Neuroradiology, University of Wuerzburg, [2]Dept. of Neurological & Behavioral Sciences, University of Siena, [3]FMRIB Center, University of Oxford

INTRODUCTION: Changes of global brain volume may reflect disease pro- or regression over time and are estimated by SIENA at high accuracy and robustness. However, the need to detect regional differences along the course of cerebral edges is obvious. Here, we extend SIENA's method for estimating longitudinal changes of global brain volume within individuals to a voxel-level statistical analysis of regional cerebral edge motion applicable to multi-subject analyses (SIENAR). Thereby, inference about significant regional edge flow exhibited by different brain areas becomes feasible without any stipulative restriction to predetermined ROIs. The method proposed is exemplified by assessing the morphometric as well as metabolic brain regeneration under short-term abstinence from alcoholism.
METHODS & MATERIAL: By means of flow images for cerebral edge motion, SIENA (part of FSL: www.fmrib.ox.ac.uk/fsl) derives a global estimate of percent brain volume change (PBVC) in intra-individual follow-ups. Here, the subject-specific edge flow images (which encode amount and direction of perpendicular local brain edge motion between successive scans) were processed with large spatial dilation, full affine transformation to a common standard space (by FLIRT, also part of FSL), masking with a standard-space-based edge image, smoothing by a Gaussian kernel (10mm FWHM) and re-masking. Thus, standardized cerebral edge flow images were obtained and fed into voxel-based, nonparametric statistical analysis (SnPM: www.fil.ion.ucl.ac.uk/spm/snpm/). To exemplify the SIENAR-approach, we studied the previously described early brain regeneration of 15 alcohol-dependent patients (DSM-IV & ICD-10 criteria; age 42±8 years, 10 males). They were examined immediately upon admission to inpatient treatment for detoxification and after about 6 weeks (38±3 days) of abstinence. MR-morphometry (1x1x1mm³ T1-w MP-RAGE), infra- and supratentorial MR-spectroscopy (1H-MRS: PRESS of 1 frontal & cerebellar voxel, TE=135ms, ± water suppression, 128/20 acquisitions, LCModel 6.0-1; 1.5T MagnetomVision) as well as neuropsychological tests (d2, AVLT) were performed.
RESULTS: Global brain volume increased significantly by 1.85±1.32% upon short-term abstinence. PBVC-values exhibited significant positive correlations with infra- and supratentorial cholin change ([%]) as well with d2-score gains ($p<0.05$). Cerebral water integrals, absolute creatin- as well as blood electrolyte and hematocrit values remained constant. Thus, simple rehydration cannot account for the entire total brain gain and apparent metabolic recovery through abstinence. Regeneration detected by SIENAR focussed on the superior vermis, cingular, perimesencephal and especially on periventicular edges (Figure 1). Given the recent demonstration of white-matter progenitor cells in the adult human brain, the latter is particularly intriguing.
DISCUSSION: The limits of low- vs. high-resolution standard edge images (e.g., based upon MNI152 vs. ICBM452- or customized templates) are discussed. The global and local morphometry of cerebral edge motion represents an alternative to SPM-driven VBM, provides further evidence for brain regeneration in alcoholics upon their short-term abstinence and may eventually be used to monitor therapeutic effects on cerebral (pseudo-)atrophic diseases. However, SIENAR's validity and reliability should be assessed in comparison with other methods (i.e. SPM's VBM, in particular) on larger data sets.

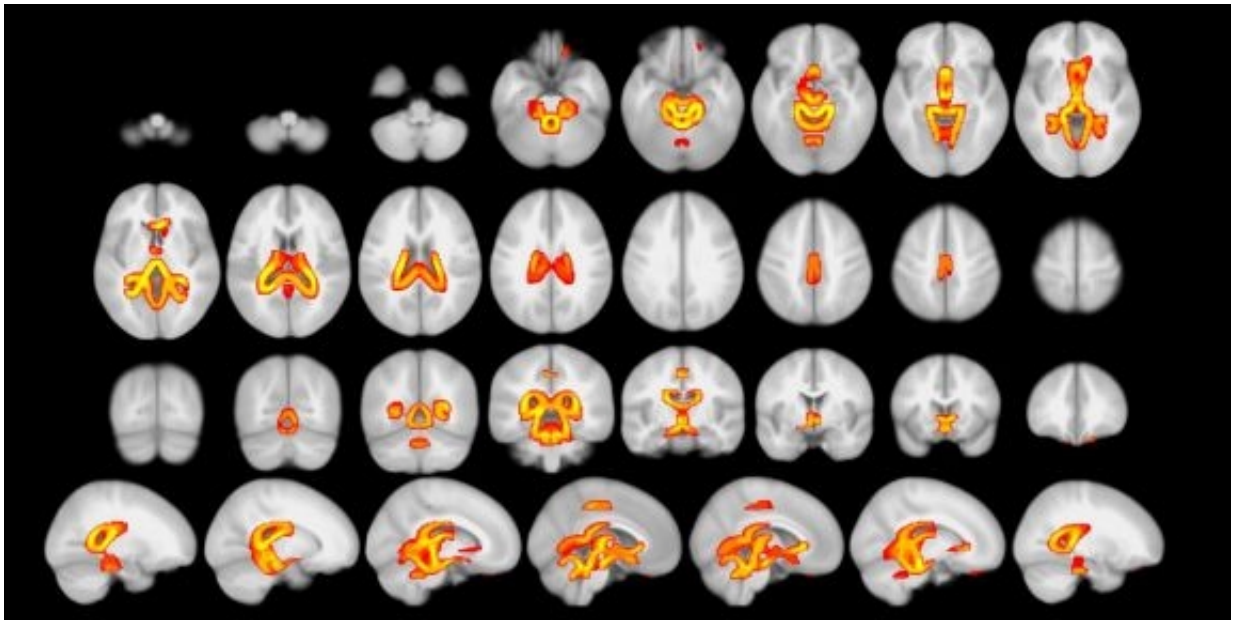

Figure 1: Regional Distribution of Early Brain Regeneration through Abstinence from Alcoholism (SIENAR: corrected p<0.05, u>4.33, 10^4 permutations, {Pseudo-t}-statistics computed with variance smoothing at 10mm FWHM by SnPM, df=14)

WE 344
Biomedical Informatics Research Network: Multi-Site Processing Pipeline for Shape Analysis of Brain Structures

M. Faisal Beg[1,2], Can Ceritoglu[2], Anthony E. Kolasny[2], Carey E. Priebe[2], J. Tilak Ratnanather[2], Rob Yashinski[2], Laurent Younes[2], Peng Yu[3,4], Jorge Jovicich[4], Randy L. Buckner[5], Steve Pieper[6], Bruce Fischl[3,4], Michael I. Miller[2]

[1]Simon Fraser University, Burnaby, BC, Canada, [2]Center for Imaging Science, Johns Hopkins University, Baltimore, MD, [3]Massachusetts Institute of Technology, Cambridge, MA, [4]Massachusetts General Hospital, Boston, MA, [5]Washington University, St Louis, MO, [6]Isomics, Cambridge, MA

Under the auspices of the Brain Morphometry Biomedical Informatics Research Network (mBIRN, www.nbirn.net), a processing pipeline is being developed to enable seamless application of brain morphometry and visualization tools independently developed at multiple sites of the BIRN consortium. As a testbed, the tools are being integrated to perform semi-automated shape analysis of hippocampus volumes in a study of Alzheimers Disease (see Fig. 1).

Brain structural MRI data from Washington University was made available to the MGH and JHU to drive the integration of the morphometric analysis tools that these sites are BIRN-enabling. The data consists of 18 subjects (6 controls, 6 Alzheimer's, 6 from a rare form of dementia, called semantic dementia) scanned using high resolution T1-weighted structural MRI at WashU. These scans were first anonymized and then segmented at MGHs Martinos Center using Freesurfer (Fischl et al., 2002) to automatically segment left and right hemisphere hippocampus data sets. These data sets were aligned and processed at JHUs Center for Imaging Science (CIS) using the Large Deformation Metric Mapping (LDMM) tool (Beg et al., 2004) and visualized with 3DSlicer (Gering et al., 2001) from the Surgical Planning Lab (SPL) at BWH. The resultant data was then uploaded into the Storage Resource Broker (SRB) for sharing among institutions and for further analysis. The extensibility of Freesurfer and LDMM to operate seamlessly on data that was acquired at neither the MGH nor the JHU BIRN sites is noteworthy.

Currently work continues on integrating the shape deformation analysis from LDMM for visualization with 3D Slicer. From LDMM, we obtain metric distances between segmented hippocampus in the group of infinite dimensional diffeomorphims (which is the generalization of the rotations, translation and scale group), the necessary group for studying shape. These distances give a precise mathematical description of what shapes are similar and different. We perform statistical analysis of these metric distances. In addition, we present a statistical analysis of vector fields characterizing the deformations generated by LDMM.

This research was supported by P41-RR015241 (JHU), P41-RR013218 (BWH) and P41-RR014075 (MGH) to the Brain Morphometry Biomedical Informatics Research Network (BIRN, www.nbirn.net), that is funded by the National Center for Research Resources (NCRR) at the National Institutes of Health (NIH).

Beg MF, Miller MI, Trouve A, Younes L (2004) Computing Metrics Via Geodesics on Flows of Diffeomorphisms. International Journal of Computer Vision.

Fischl B, Salat DH, Busa E, Albert M, Dieterich M, Haselgrove C, van der Kouwe A, Killiany R, Kennedy D, Klaveness S, Montillo A, Makris N, Rosen B, Dale AM (2002) Whole brain segmentation: automated labeling of neuroanatomical structures in the human brain. Neuron 33:341-355.

Gering D, Nabavi A, Kikinis R, Hata N, O'Donnell L, Grimson WEL, Jolesz F, Black P, III WW (2001) An Integrated Visualization System for Surgical planning and Guidance Using Image Fusion and an Open MR. J Magnetic Resonance Imaging 13:967-975.

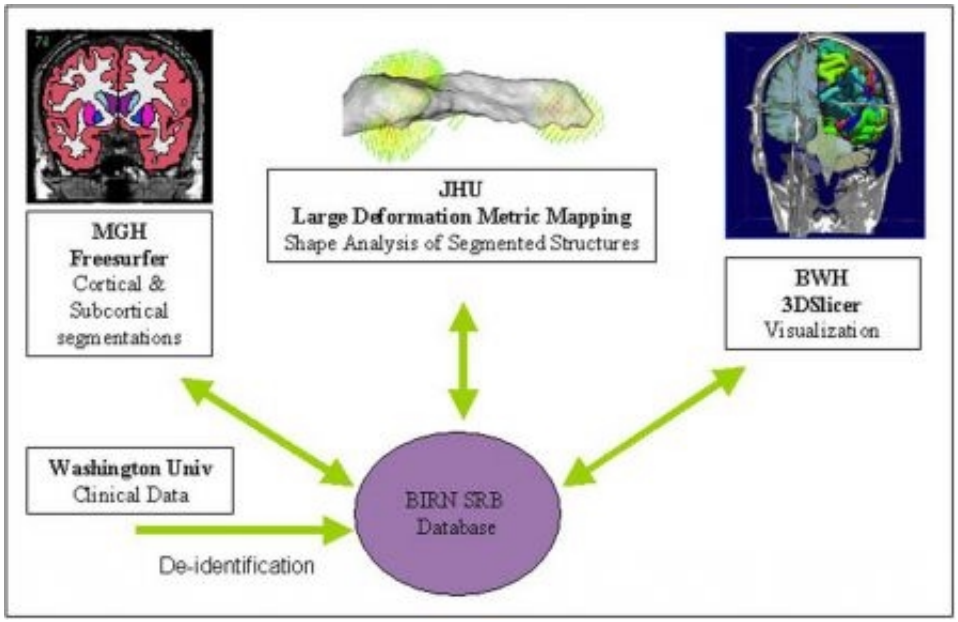

Integration of software tools. De-identified data uploaded to the image database is first automatically segmented at MGH using Freesurfer. Segmentation results from the Freesurfer analysis are uploaded to the database as derived data (surfaces, volumes, labels). Derived segmented data (e.g., the hippocampus surfaces) can be downloaded by the JHU site and used for shape analysis with their LDMM tool. Results are uploaded as derived data in the database. Combined morphometric results can be viewed from the database using 3D Slicer as the common visualization platform.

WE 345
Simultaneous EEG-fMRI of Epileptic Spikes: Comparison of fMRI and EEG Statistical Maps with Intracranial Recordings

Christian G. Benar , Andrew Bagshaw , Yahya Agha Khani , Colin Hawco , Francois Dubeau , Jean Gotman
Montreal Neurological Institute

Introduction

Our goal is to integrate the information (spatial and temporal) arising from EEG and fMRI for the localization of interictal epileptic spikes. With this in view, we propose to compare the results obtained from fMRI maps to that obtained with our recently proposed method for building EEG statistical maps [1]. These results are in turn compared to intracranial recordings performed for pre-surgical evaluation.

Methods

Patients: We selected three patients with partial epilepsy, who presented fMRI activation in response to scalp-recorded epileptic spikes and for whom intracerebral recordings were available.

Simultaneous EEG-FMRI: 1.5T MR scanner (Siemens), 21-channel EEG (EMR32, Schwarzer). We acquired 6 to 9 runs of 120 frames each (25 BOLD 64*64 slices, TR 50ms, voxel size 5x5x5mm, inter-frame 3s). Images were analyzed with fMRIStat, with the HRF modeled as single gamma functions peaking at 3, 5, 7 or 9 s; we retained the higher t stat at each voxel. The threshold on the t-stat maps (Bonferroni correction) was 4.7; we retained only the local maxima corresponding to clusters with more than three points.

EEG statistical maps: Based on a 43-channel recording (Stellate Harmonie) performed outside the scanner. We explored all combinations of three dipoles on a coarse grid, and computed for each combination a score based on an F test. For each point of the grid, we summed the scores of all combinations containing this point. This resulted in a map indicating the likelihood of the presence of a source. We selected the three local maxima of the map.

Results

We obtained 9 EEG maxima and 14 fMRI maxima; 3 (33.3%) EEG maxima were within 20mm of an fMRI maximum and 3 (21.4%) fMRI maxima were within 20mm of an EEG maximum. There were 8 EEG maxima in the vicinity of an intracranial electrode (<20mm for intracerebral, <30mm for epidural), 6 (75%) of which had been marked as active electrodes. There were 7 fMRI maxima in the vicinity of an intracranial electrode, 4 (57.1%) of which had been marked as active.

Discussion

The majority of EEG or fMRI findings that were in the vicinity of an intracranial electrode corresponded to interictal epileptic activity measured intracranially. A large proportion of EEG and fMRI findings were not in the vicinity of a finding by the other modality. This suggests that EEG and fMRI statistical maps are complementary non-invasive techniques for understanding epileptic activity.

[1] Bénar et al., HBM 2003

WE 346
A Technique for the Deidentification of Structural Brain MR Images

Amanda Bischoff-Grethe[1,2], Bruce Fischl[3,4], I. Burak Ozyurt[1], Shaunna Morris[1,2], Gregory G. Brown[1,2], Christine Fennema-Notestine[1,2], Camellia P. Clark[1,2], Mark W. Bondi[1,2], Terry L. Jernigan[1,2], Human Morphometry BIRN (www.birn.net)

[1]Department of Psychiatry, University of California, San Diego, La Jolla, CA, [2]Veterans Affairs San Diego Healthcare System, San Diego, CA, [3]Department of Radiology, Harvard Medical School, Charlestown, MA, [4]MIT Artificial Intelligence Laboratory, Massachusetts Institute of Technology, Cambridge, MA

To share human data in compliance with federal, state and local regulations, including the recently enacted Health Insurance Portability and Accountability Act of 1996 (HIPAA), it is crucial to have in place robust practices and procedures that protect the welfare of the individuals who participate in the research. These practices must include measures that ensure the privacy of the individual. This poses particular challenges for the archiving of brain structural MRI data in which surface reconstruction tools can easily render the facial features of a person from the file. Here we present the results of a novel face deidentification algorithm that removes facial features without disturbing the brain MRI data.

A program was developed that uses models of non-brain structures for removing potentially identifying facial features. The facial features of ten subjects were manually labeled, and an optimal linear transform was used to build an atlas of face membership. When a novel image is presented, the optimal linear transform is computed for the input volume (Fischl et al 2002). A brain mask is constructed by summing the prior probabilities at each image location of all brain tissue and then morphologically dilated to yield a mask indicating the presence of brain within *x* mm of each voxel. Finally, all voxels that are outside the mask and have a non-zero probability of being a facial feature are set to 0.

The algorithm was applied to 244 datasets that included two different T1-weighted pulse sequences and four different patient diagnoses (depressed, Alzheimers, and elderly and young control groups). Visual inspection of the defaced images showed none had brain tissue removed. In a preliminary analysis to quantify the effects of defacing on a volume, 22 of the above datasets were bias corrected with N3 (Sled et al 1998) and skull-stripped using a hybrid watershed algorithm (in FreeSurfer, Dale et al 1999); previous work suggested that this technique may be the most conservative skull stripping procedure for the pulse sequences and patient populations employed herein (Fennema-Notestine et al 2003). Within this subject population, the skull stripping tended to be conservative, with any remaining non-brain tissue predominately classified as cerebrospinal fluid. A set difference was calculated using the skull-stripped and defaced volumes to determine the percentage of voxels removed via defacing that were included in the stripped volume: $0.03 \pm 0.07\%$ of the voxels included in the skull-stripped image volume were removed by the defacing algorithm. The variability is most likely due to the hybrid watershed algorithm retaining non-brain tissue which the defacing algorithm removed. These results suggest that the automatic defacing algorithm is robust and efficiently removes non-brain tissue that would have similarly been removed via skull stripping. Further analyses are expected to support this algorithm as a viable method to allow data sharing within large-scale multi-site projects.

Support: Biomedical Informatics Research Network (www.nbirn.net), NCRR M01RR00827, BIRN002, and BIRN004; NIMH 5K08MH01642, R01MH42575, P41RR14075, and R01RR13609; NIA AG12674 and AG04085; P50AGO5131; MH45294; DVA Medical Research Service; and Mental Illness and Neuroscience Discovery Institute.

WE 347
Combined fMRI and dynamic perfusion MR in pre-surgical assessment of cerebral arteriovenous malformations

Atle Bjørnerud , Paulina Due-Tønnessen
Dept of Radiology. Rikshospitalet University Hospital. Oslo, Norway.

Introduction
Functional MRI has become a valuable tool for localisation of critical functional areas as part of the pre-surgical planning in patients with cerebral arteriovenous malformations (AVMs) (1). One major challenge using BOLD fMRI in the assessment of AVMs it the possible influence of the abnormal vascularisation on the BOLD response (2).
Purpose
The purpose of the current work was to combine dynamic perfusion MRI (DPMRI) with fMRI in patients with cerebral AVMs, in order to investigate the effect of abnormal flow on the BOLD signal response.
Methods
Imaging was performed at 1.5 Tesla in five patients with confirmed AVM. The AVMs were located in the vicinity of the motor cortex (n=3), visual cortex (n=1) and Brocas area (n=1). Image analysis was performed in SPM (www.fil.ion.ucl.ac.uk) and ICE (NordicNeuroLab AS, Norway)(3).
T1-weighted 3D images were acquired using an MP-RAGE sequence. Perfusion imaging was performed using an FID-EPI sequence and qualitative perfusion maps were generated from the first-pass T2* signal response following bolus injection of 0.2 mmol/kg of Gadovist (Schering AG, Germany).
Depending on lesion localisation, one of the following three paradigms was used: 1) Motor cortex: alternating left/right hand finger tapping. 2) Brocas area: think of words belonging to displayed category. 3) Visual cortex. Flicker board with flicker frequency of 8 Hz.
fMRI maps (FWE corrected, p=0.05) and perfusion maps were co-registered to the 3D images and the area of abnormal flow was identified from the perfusion maps as pixels with a relative perfusion index at least two times higher than the normal grey matter perfusion index. The area of the lesion and shortest distance from activation to lesion border was measured from the 3D images and the perfusion maps in the reformatted slice with closest lesion proximity to the BOLD activation.
Results
The AVM was well delineated on the 3D scans and a focal high flow region was identified on the perfusion maps in all five patients. The area of local perfusion increase was significantly (p=0.03, paired t-test) larger than the are of the AVM identified from the 3D scans. Figure 1 show fMRI (a) and combined fMRI and perfusion maps (b) overlaid on the 3D images in one patient. Reduced left motor activation is observed but there appears to be a clear margin between the lesion and the activated are based on the 3D scan alone. From the perfusion map, however, the area of disturbed flow can be seen to be significantly larger than the lesion in the 3D scan and may explain the absence of BOLD activation in closer proximity to the lesion.
Conclusion
Dynamic perfusion imaging may be used to determine areas of disturbed flow induced by cerebral AVMs as part of the pre-surgical fMRI protocol. The perfusion maps may be used to identify confidence regions in the activation maps and thereby increase the reliability of the fMRI examination.
References:
1. Maldjian et al. J Neurosurg. 1996;84:477-483
2. Thulborn et al. Topics in Magnetic Resonance Imaging. 1999;10:37-50.
3. Bjørnerud. Proc Human Brain Mapping 2003.

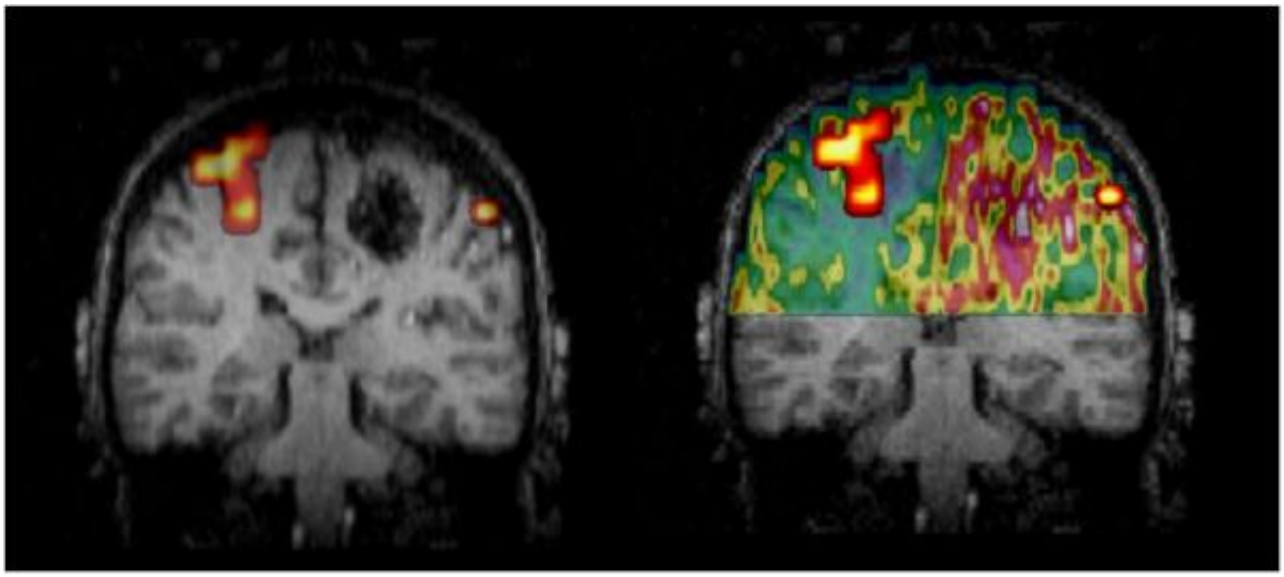

WE 348
Cortical Locations of International 10-20 System in Down Syndrome

Filippo Carducci[1], Giovanna Stefania Colafati[3], Lucia Majolini[2], Paolo Onorati[1,2], Giorgio Abertini[2]
[1]Dipartimento di Fisiologia Umana e Farmacologia, Università La Sapienza, Roma, Italy, [2]Dipartimento Pediatrico di Medicina Riabilitativa e Preventiva delle Disabilità dello Sviluppo, San Raffaele Pisana -Tosinvest Sanità, Roma, Italy, [3]Dipartimento di diagnostica per immagini, San Raffaele Pisana -Tosinvest Sanità, Roma, Italy

Down syndrome (DS) is a complex genetic disorder and the commonest identifiable cause of intellectual disability (incidence of approximately 1 in 660 live births). DS results from trisomy of human chromosome 21, producing dosage imbalance for several hundred genes, and resulting in a characteristic spectrum of developmental anomalies affecting many tissues (Epstein et al., 1991). Individuals with Trisomy 21 express different subsets of phenotypes that characterize the syndrome, but some DS traits occur in all DS individuals. One of these features is the characteristic DS heads, largely a product of the underlying craniofacial skeleton. Compared with euploid human, DS craniofacial phenotype presents: overall reduction in head dimensions, small midface, reduced facial height, orbital region reduced mediolaterally, reduced bizygomatic, short brachycephalic skull, reduction in most head dimensions but not in mediolateral dimensions producing a broad, and small mandible (Allanson et al., 1993; Fischer-Brandies, 1988; Pryor and Thelander, 1967; Farkas et al., 1985, 1991; Fink et al., 1975; Frostad et al., 1971; Joseph et al., 1970; Kolar and Salter, 1997; Thelander and Pryor, 1966 Kisling, 1966; ORiordan and Walker, 1978).

There are many specific medical issues related to DS and these include higher prevalences of visual and auditory deficits, and electroencephalography (EEG) abnormalities. Conventional EEG is the most clinically indicated exam to evaluated these deficits. The International 10-20 System (S.I. 10-20) is widely used for EEG electrode placement, and previous studies have reported an anatomically correlate for each electrode which is consistent from patient to patient (Jasper, 1958; Blume er al., 1974; Hellstrom et al., 1964). Unfortunately, these studies considering a very small subset of S.I. 10-20 electrodes and involving too few and only health subjects.

The characteristic DS craniofacial skeleton could affect the S.I. 10-20 anatomically correlate. In this study, cortical locations of S.I. 10-20 are evaluated in DS persons and in health subjects to give a reliable and complete evaluation of the anatomically correlate, by means of an automatic procedure (Echallier et al., 1992) operating on magnetic resonance images (MRI) of individual head.

WE 349
Cortical Atrophy in Multiple Sclerosis

Arnaud Charil , Jason Lerch , Alex P Zijdenbos , Alain Dagher , Alan C Evans
McConnell Brain Imaging Centre, Montreal Neurological Institute, Montreal, Canada

Introduction
Although diffuse atrophy in MS resulting from tissue reduction in both grey and white matter is well documented, little is known about cortical atrophy in MS and its relation to white matter lesions. The present study aims to investigate the relation between changes in cortical thickness and total lesion volume in relapsing-remitting MS.

Methods
Ninety nine patients (mean age: 36.6 yr (SD 6.4); 48 men, 51 women) with clinically definite relapsing-remitting MS were chosen from a cohort of patients investigated as part of a double-blind, placebo controlled, multi-center study of an oral formulation of bovine myelin in the treatment of early relapsing-remitting MS (MyloralTM, Autoimmune Inc., Lexington MA. [1]).
Lesions were automatically extracted using INSECT (Intensity Normalized Stereotaxic Environment for Classification of Tissue), an automatic image-processing pipeline [2]. The acquired images were first transformed into a standardized stereotaxic coordinate space based on the Talairach atlas using an automatic, multi-scale feature-matching algorithm [3]. Subsequently, a binary lesion mask was generated for each patient, using the T1, T2, and PD images, by means of an automatic tissue-classification algorithm [2] based on an artificial neural network classifier [4]. The total lesion load was measured for each patient using an automated voxel-counting program. The cortical thickness procedure was achieved by first extracting the inner and outer cortical surfaces using deformable models [5, 6]. Cortical thickness was measured at 40962 points across the cortex, and then blurred using a 20mm surface based kernel [7] to produce cortical thickness maps. Statistical analysis was performed across all 40962 vertices, with cortical thickness being regressed against lesion volume and multiple comparisons corrected for using random field theory [8]. According to this method a value of t =4.2 corresponds to P=0.05.

Results
Overall cortical thickness was inversely correlated to total lesion volume. The association was highly significant (t=-6.336, p=<7e-9), though only representing an average loss of 0.02 millimeters of cortical thickness per cm3 of white matter lesion and accounting for 28% of the variance (as measured by the adjusted R-square). Regions where cortical thinning correlated significantly with lesion load included the right anterior temporal pole (t= -8.1, fig.1,2), right orbito-frontal region (t= -7.6), bilateral cingulate cortex (right: t= -7.6, left: t=-6.9), and bilateral posterior parietal regions (right: t= -7, left: t= 6.3).

Conclusions
With increasing white matter lesion volume, the cortical grey matter tends to get thinner in specific areas including temporal, frontal, limbic and parietal regions. Still needing to be investigated is the relation between lesion location in the cerebral white matter and its influence on cortical thickness. Cortical thickness could also be regressed against other measures of the disease such as disability score, disease duration, depression, and number of attacks.
The approach presented here may provide valuable information about the integrity of the cerebral cortex in MS and help better understand the pathophysiology of the disease.

References
[1] Weiner HL. Annu. Rev. Med. 48:341-351, 1997.
[2] Zijdenbos AP, Forghani R, Evans AC. MICCAI 439-448, 1998.
[3] Collins DL, Neelin P, Peters TM, Evans AC. J. Comp. Assisited Tomography 18:192-205, 1994
[4] Ozkan M, Dawant BM and Maciunas RJ. IEEE Transactions on Medical Imaging 12:534-544, 1993.
[5] June Sic Kim et al. NeuroImage. Submitted on October.
[6] June Sic Kim et al. HBM2004. Submitted.
[7] Chung MK et al. Technical Report (U. Wisconsin) 1049, 2002.
[8] Worsley KJ et al. Human Brain Mapping 8:98-101, 1999.

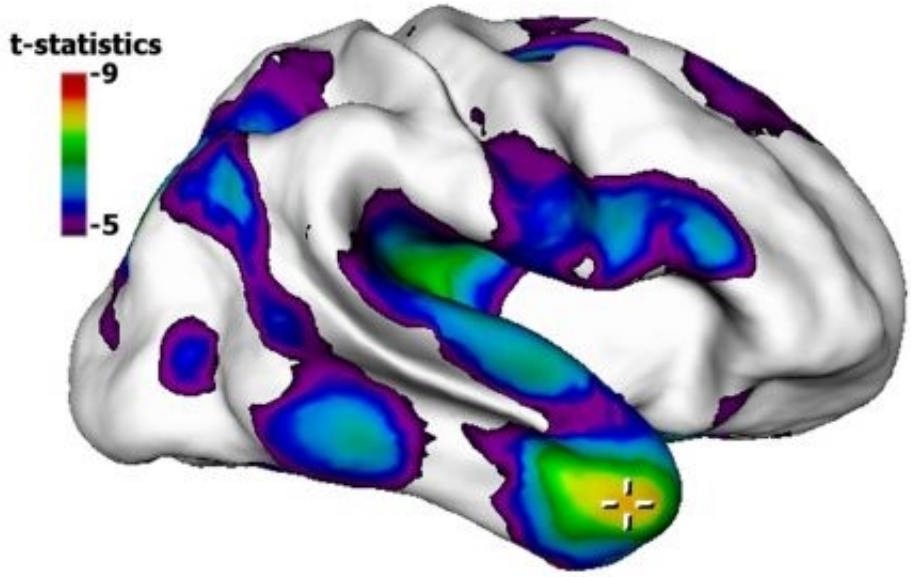
t-statistics
-9
-5

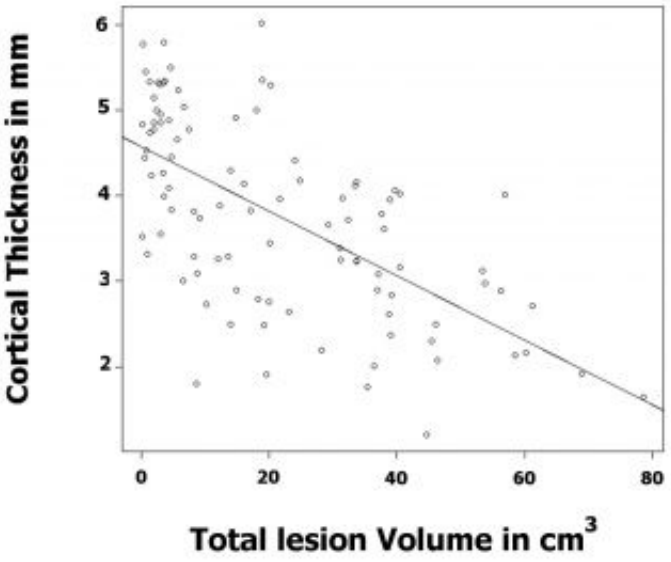
Cortical Thickness in mm
6
5
4
3
2
0
20
40
60
80
Total lesion Volume in cm3

WE 350
Nonparametric estimation of cortical thickness

Moo K. Chung [1,2,3], Shijie Tang [1]
[1] Department of Statistics, [2] Department of Biotatistics and Medical Informatics, [3] Keck Laboratory for Functional Brain Imaging and Behavior, University of Wisconsin-Madison

Abstract
The cerebral cortex has the topology of a 2D highly convoluted sheet. The cortical thickness that measures the distance between the outer and inner cortical surfaces has been used to characterize the brain shape [1]. There are many different techniques to measure the cortical thickness [1, 2, 3, 4]. Which method one uses, the thickness measurements are always contaminated with noise. The noise may come from a scanner or due to partial volume effect. To increase the signal-to-noise ratio and to increase Gausianess that is needed in the random fields theory, diffusion smoothing has been used so far [1]. We present a completely new smoothing technique that is simpler than diffusion smoothing.

Methods
T1 weighted MRIs are segmented and cortical thickness maps are computed based on deformable surface algorithm presented in [2] using FreeSurfer package. The triangular mesh generated in this way has about 300,000 triangle elements in average, which is the sufficient mesh resolution for 1mm resolution MRI obtained from 3T GE scanner. The cortical thickness measurement is assumed to follow the additive model of true signal plus noise. The true cortical thickness is assumed to be a continuous functional data that can be estimated via the Nadaraya-Waton (NW) smoother. The NW kernel smoothing is essentially a Gaussian kernel smoothing for sparse data. The amount of smoothing can be increased by iteratively applying NW kernel smoothing.

Results
Single iteration of Gaussian kernel smoothing takes about 1 min in Pentium M-processor machine which is compatible to the speed of diffusion smoothing. Figure 1 is the cortical thickness measurements obtained from FreeSurfer and Figure 2 is the NW kernel estimation of the thickness measure which shows huge reduction of noise. Figure 3 is the local comparison of the thickness maps before and after smoothing. The thickness maps are deformed onto a sphere to show hidden sulcal regions. Figure 4 is an application of the NW kernel estimation for smoothing out noisy brain surface. To show the effect of surface regularization, artificially large white noise has been added to the coordinates of the mesh.

Acknowledgments
This work was funded by WARF. The authors wish to thank Bruce Fischl and his research staff for valuable advice on segmentation.

[1] Chung, M.K., Worsley, K.J., Robbins, S., Paus, P., Taylor, J., Giedd, J.N., Rapoport, J.L., Evans, A.C. (2003) Deformation-Based Surface Morphometry with an Application to Gray Matter Deformation, NeuroImage. 18:198-213.
[2] Fischl, B. and Dale, A.M. (2000) Measuring the thickness of the human cerebral cortex from magnetic resonance images, PNAS 97:11050-11055.
[3] Jones, et al. (2000) Three-dimensional mapping of cortical thickness using Laplaces equation, Human Brain Mapping 11:12-32.
[4] Miller, M.I. et al. (2000) Bayesian construction of geometrically based cortical thickness metrics. NeuroImage. 12:676-687.

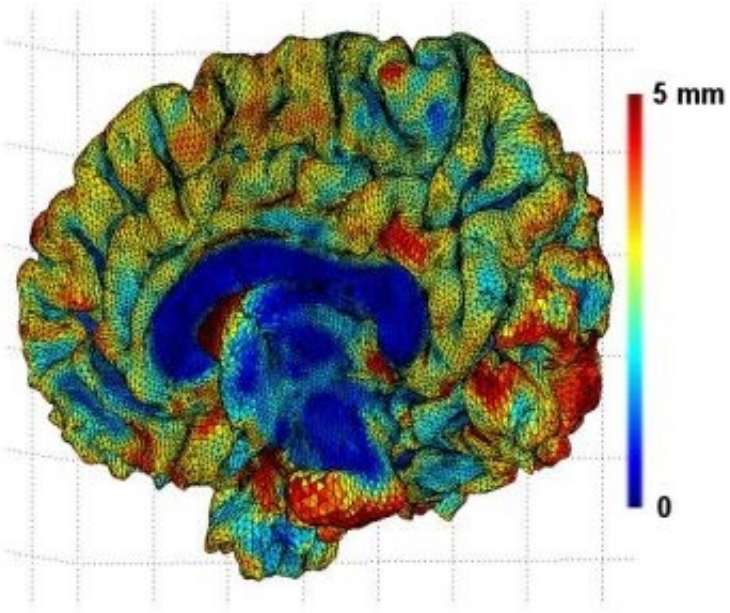

Figure 1. Cortical thickness measurement

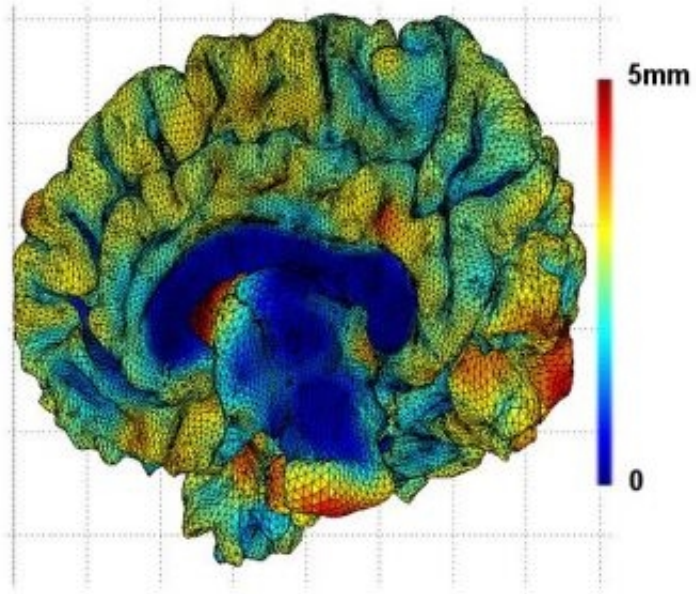

Figure 2. Cortical thickness estimation

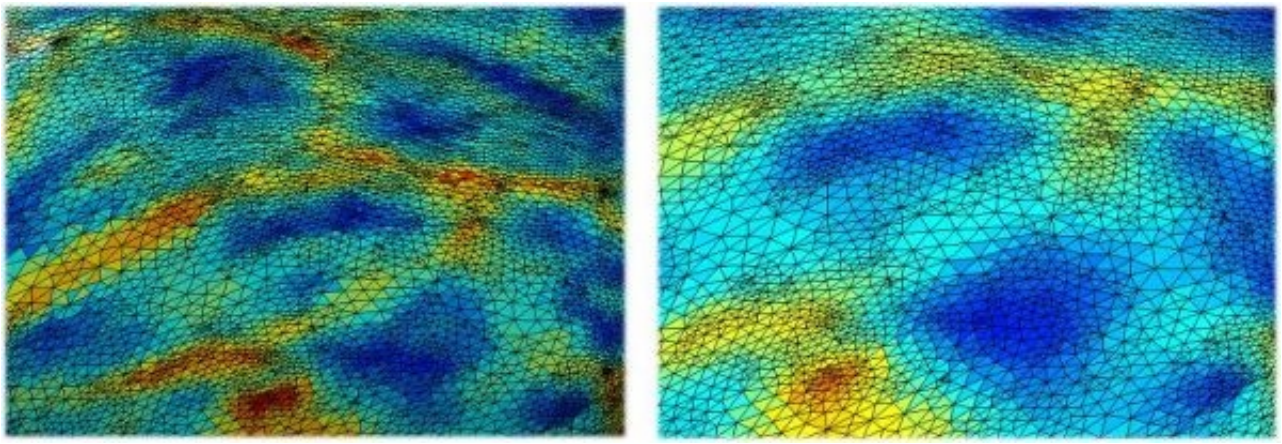

Figure 3. Comparision of before and after smoothing

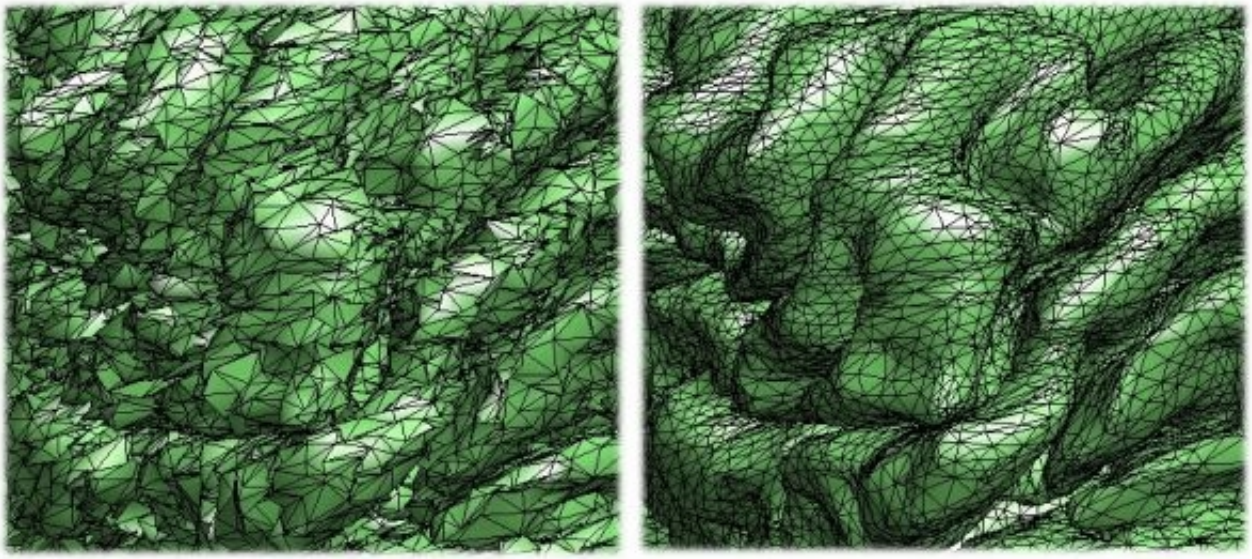

Figure 4. Nonparametric estimation of noise brain surface

WE 351
COMPETITIVE SEGMENTATION OF THE HIPPOCAMPUS AND THE AMYGDALA. VOLUMETRY IN ALZHEIMER'S DISEASE

Marie Chupin[1,3], Dominique Hasboun[1,3], Sylvain Baillet[1,3], Serge Kinkingnéhun[2,3], Bruno Dubois[2,3], Line Garnero[1,3]

[1]CNRS-UPR-640, Paris, France, [2]INSERM-EMI-007, Paris, France, [3]IFR-49, Neuroimagerie, Paris, France

Introduction

The hippocampus (H) and the amygdala (A), which both play essential roles in memory, learning and emotions, are involved in Alzheimers disease (AD) and epilepsy. Detecting early atrophies and shape variations could improve the diagnosis of these neurological disorders. In fact, their ill-defined boundaries make their time-consuming manual segmentation from routine MRI poorly repeatable, despite a rigorous protocol. A fast, reliable and robust automatic method would then improve time-load and repeatability for clinical routine.
Most reported segmentation algorithms extract H or the whole A-H complex, ignoring its internal boundaries. While some use statistical shape priors, maybe unsuitable with atrophies, others require an important manual initialization step. Quantitative and qualitative evaluations are seldom available. We propose a new region growing based algorithm, validated on healthy subjects, and apply it to A-H volumetry in AD.

Segmentation Method

Regions grow from two manually-placed seeds (one per structure), by alternate iterative topology preserving evolutions of their border fronts. The classification is achieved by minimizing a global energy composed of five terms (global and local data attachment, shape regularization, volume and surface priors), which influences are adjusted by various parameters.
A and H compete when they meet, with additional constraint brought by anatomical priors. These are built from automatically extracted points and anatomical relational knowledge around them.

Evaluation's Results

Eight young healthy controls were scanned on a 1.5 Tesla scanner, in the transverse plane (0.9375x0.9375x(1.3 or 1.5) mm3 voxels).
Evaluation then compares automatic and manual (reference) segmentations. Qualitative evaluation visually reveals consistent resulting structures. Quantitative evaluation use various indices, e.g. relative error on volume RV or overlap K. Its average results are comparable to the literature: K = 82% for H, compared to 75% in [2], and 89% in [3], and K = 80% for A, compared to 80% for H and 65% for A in [4], with similar RV around 10%. Furthermore, our method is fast (two minutes on a 800MHz computer with a 256MO RAM, using *The Anatomist* platform [5]) and adapted for healthy and pathological structures.

Volumetry in AD

Evaluations and volumetric analysis are undertaken for four early AD patients (ADP) (age 67, 70, 77, and 79), by comparing their A and H volumes with those of four age-matched controls (AMC) (age 70, 71, 77 and 79).
The automatic segmentation was run on ADPs and AMCs; the results were qualitatively consistent. The volume was computed for three groups: AMCs, ADP0s (first scan), and ADP3s (second scan: 2 years later). The average volume for right and left H was 2.4 cm3 (minimum: 2 cm3 - maximum: 2.8 cm3) for AMCs, 1.4 cm3 (1.2 cm3 - 1.7 cm3) for ADP0s, and 1.3 cm3 (0.9 cm3 - 1.5 cm3) for ADP3s. That is, automatically determined H volume seems a good criterion to discriminate between AMCs and ADPs. This volumetric analysis will be evaluated through the comparison with manual segmentations of AMCs and ADPs, in order to validate its reliability.
This part is supported by the France Alzheimer Association.

References

[1] A. Kelemen, et al., IEEE TMI, pp.828-839, 1999
[2] R.E. Hogan, et al., Radiology, pp.291-297, 2000
[3] D. Shen et al, Neuroimage, pp. 422-434, 2002
[4] B. Fischl, et al., Neuron, pp.341-355, 2002
[5] http:/ /anatomist.info

WE 352
Use of Voxel-Based Morphometry to Measure Striatal Atrophy in Huntington's Disease

Gwenaelle Douaud[1], Maria-Joao Ribeiro[1], Franck Lethimonnier[1], Renaud Maroy[1], Christophe Verny[2], Pierre Krystkowiak[3], Anne-Catherine Bachoud-Levi[4], Philippe Damier[5], Philippe Hantraye[1], Philippe Remy[1,4]
[1]SHFJ, CEA, Orsay, France, [2]CHRU Larrey, Angers, France, [3]CHRU Roger Salengro, Lille, France, [4]CHU Henri Mondor, Creteil, France, [5]CHRU Guillaume et Rene Laennec, Nantes, France

Background
Huntington's disease (HD) is an inherited neurodegenerative disease that targets first and foremost the striatum, a part of basal ganglia. Striatal atrophy begins before symptoms onset and progresses along disease course. Quantifying this atrophy would allow to monitor the disease progression and to measure the effect of experimental treatments of HD, such as neuronal grafts. Automatic analysis of MR images in HD patients is however difficult considering the major deformation of central brain regions induced by the striatal atrophy. Here, we test the ability of optimized Voxel-Based Morphometry (VBM, Ashburner, 2000), a 3D automatic tool, to quantify striatal atrophy in patients with mild to moderate HD.

Methods
Thirteen HD patients (aged 41.7 ± 8.2 years) were selected and compared to 12 healthy controls matched for age, sex and handedness. All subjects were examined with a 1.5T Signa imager using a 3D, T1-weighted sequence, with enhanced contrast-to-noise ratio.
Two analyses were performed. First, the striatum was segmented manually on axial planes in each MRI scan, creating 3D volumes, for the following sub-regions: the head and body of the caudate nucleus, the anterior and posterior putamen and the ventral striatum. The resulting volumes in each group were compared using an ANOVA.
Second, the VBM optimized protocol (Goode, 2001) was followed up in SPM2 using a template of grey matter (GM) built up by mixing patients and controls GM images, which were obtained by segmenting spatially normalized native scans to the MNI template (152 averaged MRIs).
The native MRIs were normalized using the matrix obtained by registering the automatically segmented GM of the initial scans to the adapted GM template. These normalized images according to GM were then segmented into GM, WM and CSF. Only the GM images were retained for subsequent processing. Eventually, a modulation was applied to compensate for elastic deformations in each voxel, and modulated images were smoothed using a 8x8x8 mm^3 gaussian kernel.
Regional differences in GM intensity were compared between controls and patients using a two-tailed unpaired t-test with a statistical threshold set at $p < 0.005$ corrected with FDR (false discovery rate).

Results
Both manual and automatic methods evidenced a highly significant (respectively, $p < 10^{-11}$, FDR-corrected $p < 0.005$, **Fig.1**) striatal atrophy in the HD patients compared to controls, although VBM was used with no a priori on location for atrophy.
Both methods also demonstrated a significant dorso-ventral gradient of atrophy, which is maximal in the body of the caudate nucleus (loss of 57% of normal volume), less marked in the head of the caudate and putamen (-53%) and spares relatively the ventral striatum (-46%) (VBM in **Fig.2**). Interestingly, even in the putamen itself, VBM revealed this uneven pattern of atrophy.

Conclusion
Atrophy is more severe in dorsal than in ventral parts of the striatum in mild HD patients. Optimized VBM is able to demonstrate striatal atrophy in HD patients without particular preprocessing of the MR images. Therefore, this method can likely be applied to look for the atrophy of subcortical structures in other brain diseases.

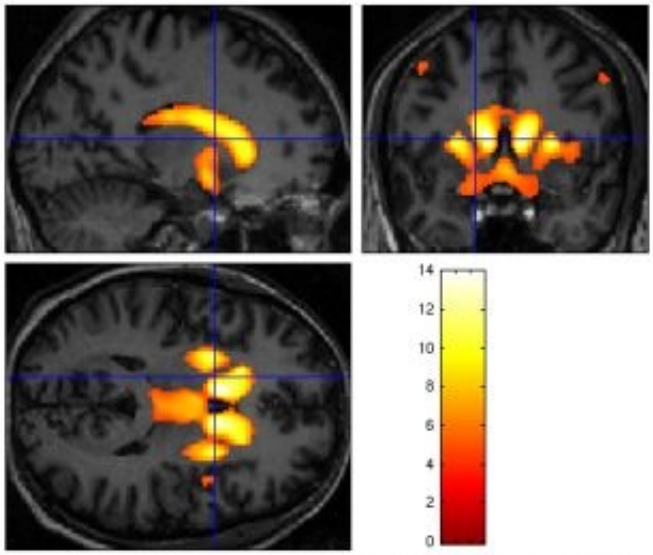

Fig. 1 Significant Reduction of GM Intensity in Patients Found with VBM

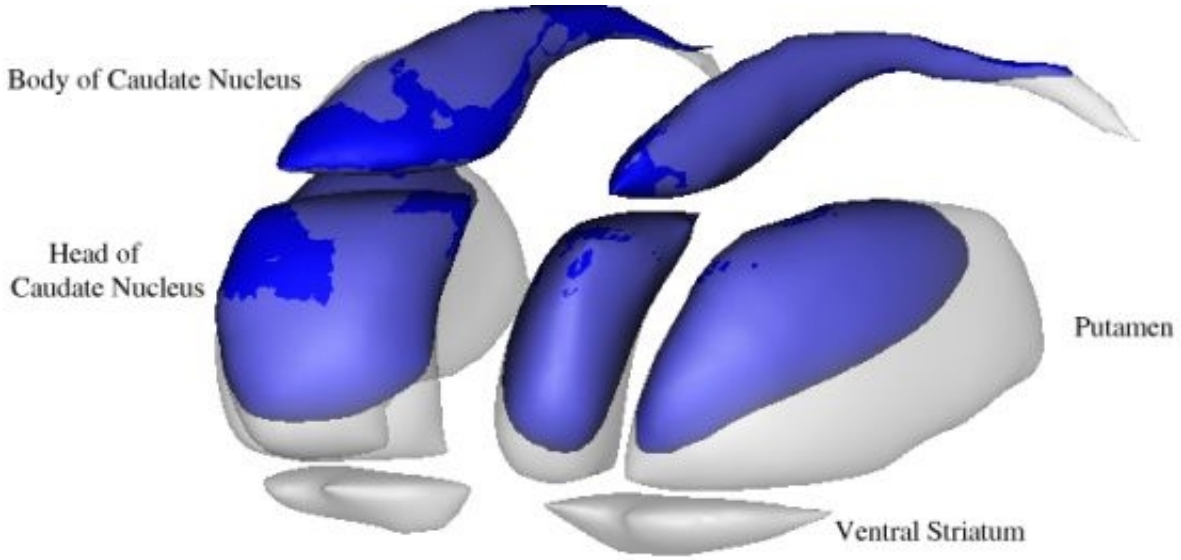

Fig. 2 Superposition of the Significant Atrophy Found in VBM (blue) onto a Normal Striatum (grey)

WE 353
A 3D Probabilistic Glioblastoma Multiforme Location Atlas

Andrew J Frew[1], Paul M Thompson[2], Timothy F Cloughesy[2], Pengju B Tseng[1], Arthur W Toga[2], Jeffry R Alger[1]

[1]Department of Radiology, University of California, Los Angeles, [2]Department of Neurology, University of California, Los Angeles

Abstract: A 3D probabilistic glioblastoma multiforme (GBM) location atlas was developed from a population of 136 de-novo GBM patient cases. The atlas displays an asymmetric - and nonuniform tumor distribution between brain lobes.

Methods: Anonymized MRI data from brain tumor patients presenting with initial diagnosis of GBM were selected from UCLAs Neuro-Oncology Database in March 2003. One hundred thirty six (136) patients were identified based on the availability of good quality, double-echo MR scans obtained at an early stagein the treatment. All studies used the same echo and repetition times to assure consistent computation of parametric T2 values using the mono-exponential approximation. Parametric T2 and apparent Proton Density (PD) maps were calculated from the PD- and T2-weighted multislice images and registered using a 12-affine algorithm to a target brain volume developed from a normal brain atlas.

Parametric T2 maps were used to identify volumes of tumor and necrotic tissue from normal and edematous tissues. In cases where a resection cavity was present, it was assumed that the cavity was originally composed entirely of tumor tissue. Thresholding of the parametric T2 images was use to map tumor/necrosis tissue and CSF into one category, and then CSF located outside of the resection cavities was manually removed from the maps on a case-by-case basis. The resulting tumor volume maps from each case were then used to create a tumor location atlasshown in Figure 1.

Results: Figure 1 demonstrates a spatially nonuniform pattern of GBM distribution. There is a greater incidence of tumor growth in the right temporal and left frontal lobes compared to other brain areas. This may be the result some yet to be understood fundamental aspect of GBM developmental biology. There is also the possibility of selection bias. Many of the cases included in the atlas were imaged after being referred to our center for neurosurgical consultation. Therefore the atlas may have a bias for tumor locations that can be safely resected.

Conclusions: The study has demonstrated that a large scale probabilistic GBM location atlas can be developed from clinically acquired parametric T2 MRI data. The results suggest that GBMs do not develop uniformly throughout the brain. To our knowledge this nonuniformity in GBM development has not been demonstrated previously. Atlases of GBM location may provide insight into the fundamental biology of the glioma development provided that selection bias can be eliminated.

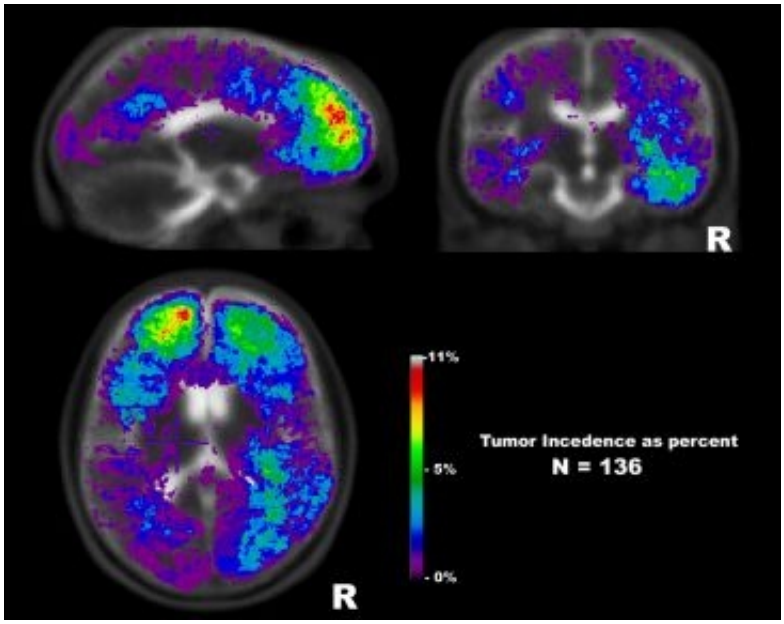

GBM tumor atlas: incedence as percentage.

WE 354
Statistical Power Maps for SPM Analysis of PET Scans

Juan D. Gispert[1], Santiago Reig[1], Javier Pascau[1], Monica Penedo[1], Juan J. Vaquero[1], Vicente Molina[2], Manuel Desco[1]

[1]Medicina y Cirugía Experimental. Hospital General Universitario Gregorio Marañón. Madrid, Spain., [2]Dept. of Psychiatry. Hospital Clínico Universitario. Salamanca, Spain.

INTRODUCTION

The statistical analysis of brain functional neuroimages (PET and fMRI) may result negative even though a true difference exists if the statistical test does not reach an adequate statistical power. When a negative result occurs, information about the statistical power achieved by the test is seldom provided. To a certain extent, this fact may explain the abundance of contradictory conclusions in the literature. A usual strategy to address this problem in other areas consists in reporting the results with confidence intervals (CI), which supply an estimation of the effect size while preserving the statistical significance information. However, there are no standardized procedures for displaying confidence intervals of statistic parametric maps. A solution may consist in reporting the statistical power of the test whenever a negative result is obtained. This approach has been previously proposed by Van Horn, et al. (1998) who developed a method for estimating the power of statistical parametric maps showing the probability of detecting as significant the effect size actually found.

This work presents an alternative method for reporting negative results in statistical parametric maps, consisting in estimating the maximum effect size that the test would not detect as significant with a certain probability.

MATERIAL AND METHODS

This maximum non-significant effect size is calculated as shown in Figure 1, in which t^{-1} denotes the inverse of Student's T cumulative distribution function, α the significance threshold of the statistical test, β the required statistical power, N_1 and N_2 the sample size of the two groups respectively and $_{s1}$ and $_{s2}$ its variances. We have applied this procedure to a statistical parametric map of a two-group comparison: ^{18}F-FDG PET images of 17 schizophrenic patients on classical neuroleptics were compared to those acquired six moths after switching their treatment to olanzapine.

RESULTS

The statistical parametric map revealed no significant differences ($\alpha = 0.001$) between the pre- and post-olanzapine groups. Figure 2 shows the estimation of the maximum non-significant effect size ($\alpha = 0.001$, $\beta = 0.80$) overlaid on a reference MR image.

CONCLUSIONS

If no statistical power analysis is performed when obtaining a negative result, the only correct inference that can be made is that the p-values are non-significant and the experiment is not conclusive. In these cases, concluding that there is no between-group difference is clearly erroneous, yet a common mistake. Our approach to assess statistical power differs from the previously reported method of Van Horn et al. who proposed to use the probability that the between-group differences would had been detected by the test. We believe that our method provides a more useful way to report statistical power since effect sizes can be directly compared between different studies thus facilitating the performance of meta-analyses.

$$d_{max\,N.S.} = t_{\alpha} \cdot s_{pooled}$$

where

$$t_{\alpha} = t^{-1}(1-\alpha/2, N_1+N_2-2) + t^{-1}(1-\beta/2, N_1+N_2-2)$$

and

$$s_{pooled} = \sqrt{\frac{[(N_1-1)\cdot s_1 + (N_2-1)\cdot s_2] + \left[\frac{1}{N_1}+\frac{1}{N_2}\right]}{N_1+N_2}}$$

Figure 1.

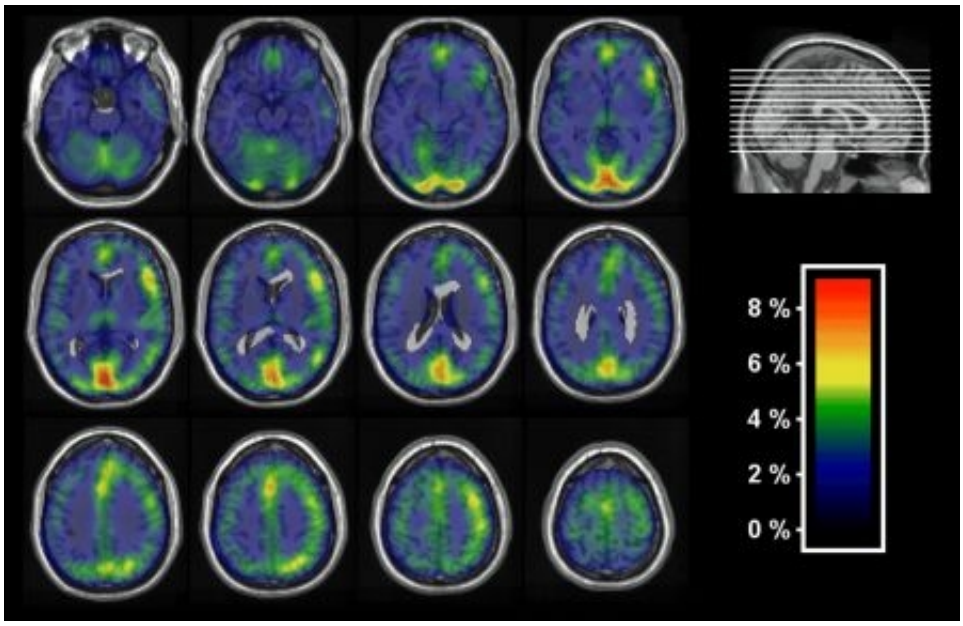

Figure 2: Maximum effect size not reaching statistical significance (α = 0.001; β = 0.80). The statistical power map is overlaid on a MR image for a better localization of the brain regions. This image allows us to discard (with a 80% probability) that changes above 9% of the global metabolism would occur anywhere between the two groups. Brain regions with lower statistical power are shown in red (visual cortex, anterior cingulated and left insula). In the rest of the cerebral cortex, between-group differences above 2% of the global metabolism could be discarded (blue regions).

WE 355

Analyses of Diffusion Tensor Images (DTI) by a morphometrical analysis of iterative normalized DTIs: An optimised procedure approved in a group of children with Tourette Syndrome

Renate Grüner[1,2], Karsten Specht[1,3], Kerstin von Plessen[1], Jochen Hirsch[4], Arvid Lundervold[1], Kenneth Hugdahl[1,2]

[1]University of Bergen, Norway, [2]Haukeland University Hospital, Bergen, Norway, [3]Research Center Jülich, Germany & University Hospital Aachen, Germany, [4]University Hospitals of Basel, Switzerland

Introduction

Several different methods have been proposed in recent years for the analysis of morphometrical data on a voxel-by-voxel basis [1]-[6]. We propose an optimised procedure for voxel-based analysis of anisotropy maps, obtained from Diffusion Tensor Imaging (DTI) data. The method is evaluated on a sample of children with Tourette Syndrome (TS) and an age-matched healthy control group. Both groups underwent scanning with an extensive MR protocol including a DTI protocol. Children with TS have previously been shown to have a reduced corpus callosum (CC) area, thus, we specifically looked at changes in white matter density in this region of the brain [7]. The corpus callosum is pronounced in anisotropy images due to its highly organized and dense fibre structure.

Methods

Acquisition

MR acquisitions were performed on a 1.5 T Symphony (Siemens) MR scanner with vendor-installed DTI capabilities. Acquisition parameters were chosen using a standard DTI protocol. For each of the19 slices, 6 non-collinear diffusion sensitive directions were acquired ($b = 1000 s/mm^2$ and $b0 = 0 s/mm^2$, slice thickness 4mm, 8 averages). The subsequent DTI evaluation supplied the isotropic diffusion weighted images and relative anisotropy index maps (RAI) to be used in the group evaluations.

Normalization

For voxelwise group comparison, all images were normalized to the same reference image. To avoid misregistration due to different levels of distortions, we created a new template. First, we normalized the isotropic diffusion weighted images to a standard EPI template and applied this transformation to the RAI image. Thereafter a RAI template was created in an iterative manner by averaging the normalized RAI images and using the averaged images to create a new, more accurate, template, which again was used to normalize the original RAI images. The resulting template shows sharp structures of large white matter fibre bundles (Fig.1).

Statistics

Based on these optimally normalized images, an ANCOVA-model for group comparison was calculated (implemented in SPM2) comparing the TS and control group (both n=14). A voxel threshold of p=0.01 and p=0.05 (corrected for multiple comparisons) was selected for the given cluster size.

Results

There was only one brain area that survived the significance criteria (voxel-level: p=0.01 (uncorrected), cluster-level p=0.05 (corrected) 330 voxels). This was in the middle part of the CC, and it showed a significantly higher RAI in the TS group compared with the control group (Fig. 2)

Discussion

The proposed analysis procedure demonstrated that statistical voxel-based analysis may successfully be applied to scalar maps, like relative anisotropy index (RAI) DTI maps,. Furthermore, the results nicely confirmed our hypotheses of a significant change within the CC in TS-children, indicating that the higher RAI could be thought of as an equivalent to a higher grade of axonal myelinisation [8].

References

[1]Ashburner, Neuroimage(11):805-821(2000)
[2]Ashburner, Neuroimage(14):1238-1243(2001)
[3]Good, Neuroimage(14):21-36(2001)
[4]Salmond, Neuroimage(17):1027-1030(2002)
[5]Sommer, Lancet(360):380-383(2002)
[6]Specht, Arch Neurol(60):1431-1435(2003)

[7]Peterson, Adv.Neurol(85):79-96(2001)
[8]Neil, NMRBiomed(15):543-52(2002)

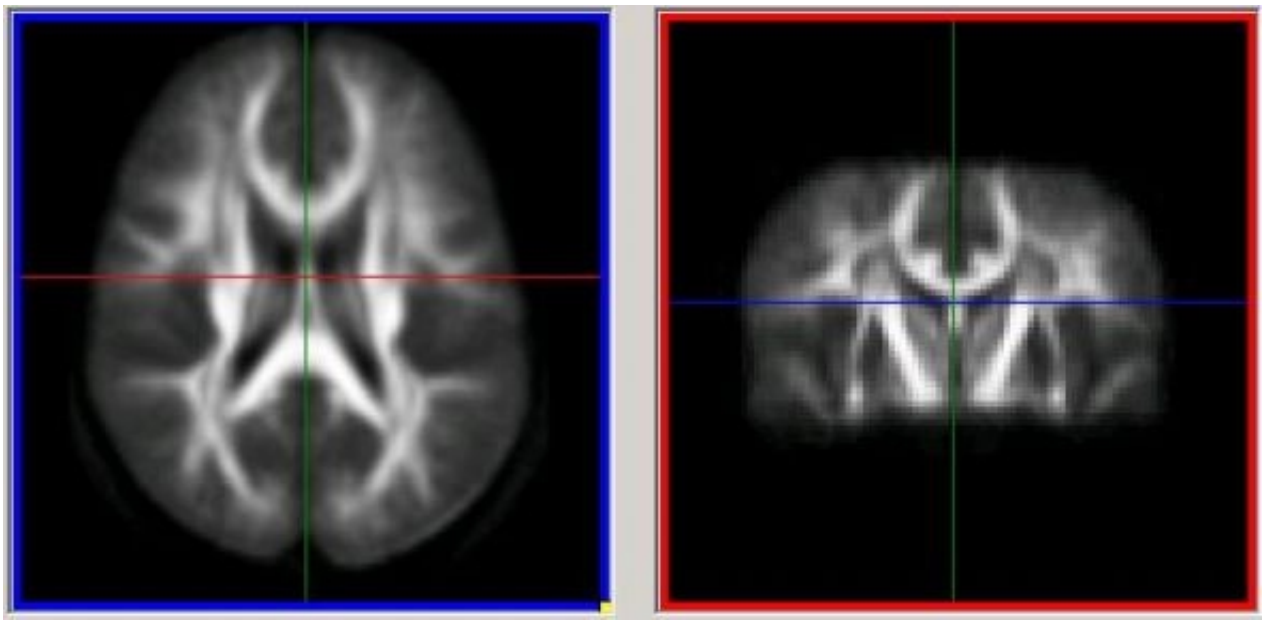

Figure 1: Template for normalizing RAI images

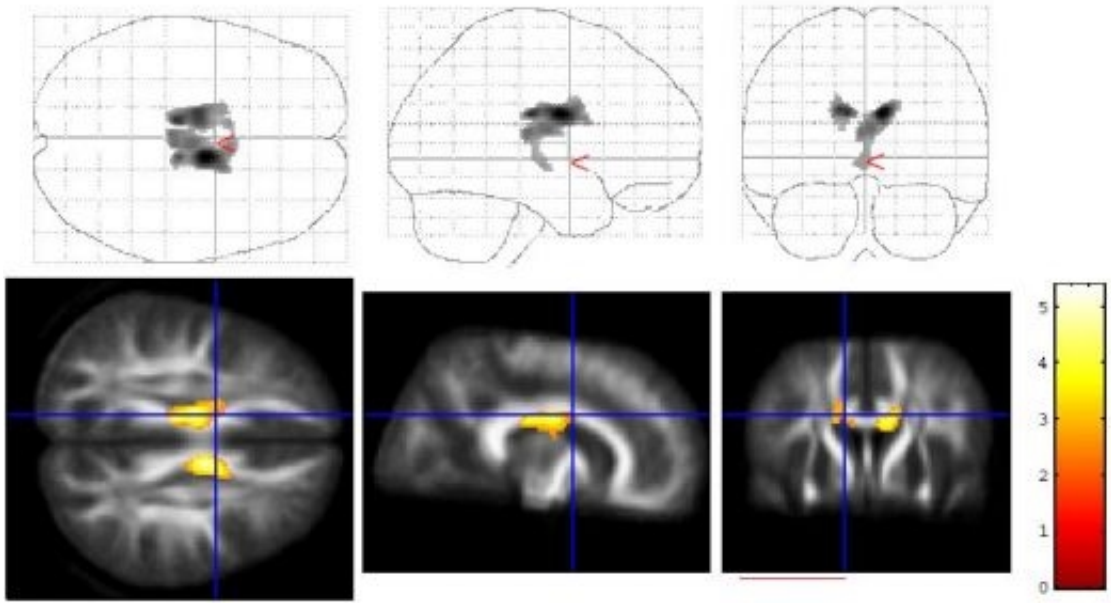

Figure 2: Significant difference in RAI values between TS children and controls. The colorbar indicates t-value scores.

WE 356

Evaluation of temporal clustering analysis in patients with epilepsy using simultaneous EEG/fMRI.

Khalid Hamandi[1,2], Afraim Salek-Haddadi[1,2], Adam Liston[1,2], John S Duncan[1,2], David R Fish[12,], Louis Lemieux[1,2]

[1] Department of Clinical and Experimantal Epilepsy, Institute of Neurology, University College, London, UK,
[2] National Society for Epilepsy, Chalfont St Peter, Bucks, UK

Introduction

Simultaneous EEG/fMRI allows the study of BOLD correlates of interictal discharges (IEDs) in patients with epilepsy. IEDs identified on the scalp EEG are used to construct models of the BOLD response. An intrinsic limitation of scalp EEG is the fact that a significant proportion of interictal epileptiform activity (particularly from deep structures) is not captured on surface recording. fMRI data driven techniques may help address this limitation. It has recently been proposed that temporal clustering analysis (TCA)(Gao et al 2003) can be used to study epileptic activity with fMRI (Morgan et al 2003). We sought to evaluate this approach with simultaneously acquired EEG/fMRI data.

Methods

Patient selection: Five patient datasets were selected on the basis of robust electro-clinically concordant activations, detected by simultaneous EEG/fMRI (Salek-Haddadi 2003). Data acquisition consisted BOLD EPI (TE/TR 40/3000, 21x5 interleaved slices, 64x64matrix) 700 volumes over 35 minutes at 1.5T (GE Horizon). 10 channels of scalp EEG plus ECG were recorded using an MR compatible system.

Data analysis: TCA analyses were performed on a Sun Ultra 5 workstation using programme written in C implementing the algorithm proposed by Morgan et al. Briefly, a time histogram of the number of voxels reaching their maximum signal intensity over the whole time-course (but within 102% to 110% of the initial value) was calculated. Temporal clusters (TCs) were taken as time points were the number of voxels reaching their maxima exceeded 2 standard deviations above the mean of the histogram. TCs were visually correlated with a plot of realignment parameters (RPs) and IEDs from the simultaneously recorded EEG. A 6 minute block of least motion, containing IEDs, were identified for each case. TCA was applied to this block. The peaks identified (minus 5 seconds to account for the delay imposed by HRF convolution) were modelled as individual events, convolved with the canonical HRF using SPM2, and used to create statistical maps for each subject. This was compared with electro-clinical data and statistical maps from EEG modeling.

Results

TCs from the the 35 minute session generally corresponded to to RPs but not EEG-IEDs. Further TCs for each 6 minute block failed to correspond with EEG-IEDs. SPM analyses of these 6 minute blocks using TCs as regressors found no activation in 3 and non concordant changes in 2 (periventricular deactivation in 1 and widespread posterior activation in another). Analyses using EEG-IEDs as regressors failed to reveal activations in the 6 minute block despite previous concordant activations using the whole 35 minute session. (all SPMs corrected FWE 0.05).

Discussion and Conclusion

We failed to detect interictal activity on fMRI using TCA in experiments that revealed robust electrclinically concordant BOLD activations based on IEDs from simultaneously recorded EEG. TCs did not correlate with EEG-IEDs, but were closely correlated with motion. Although data-driven fMRI analysis techniques provide an attractive approach to reveal BOLD correlates of epileptiform activity we emphasize the need for robust statistical methods, rigorous motion correction, whole brain analyses and initial validation with simultaneous EEG.

Ref

1) Gao et al.Mag.Reson.Imaging.21,51-53,2002
2) Morgan et al.Epilepsia 44 Suppl.9:169,2003
3) Salek-Haddadi et al.Epilepsia 44 Suppl. 9:87(Abst. 1.245), 2003

WE 357
Subpixel curvature estimation of the corpus callosum via splines and its application to autism

Thomas J. Hoffmann[1], Moo K. Chung[1,2,3], Kim M. Dalton[3], Andrew L. Alexander[3,4,5], Grace Wahba[1,2], Richard J. Davidson[3,4,6]

[1]Department of Statistics, [2]Department of Biotatistics and Medical Informatics, [3]Keck Laboratory for Functional Brain Imaging and Behavior, [4]Department of Psychiatry, [5]Department of Medical Physics, [6]Department of Psychology, University of Wisconsin-Madison

Abstract

Autism is a neurodevelopmental disorder with abnormal corpus callosum (CC) size [1]. Most previous studies used the area of predefined Witelson partition [5] as a morphometric measure but other shape metrics have not been considered. We present a novel computational technique for curvature estimation via piecewise quintic splines and use it in both CC nonlinear dynamic time warping algorithm [4] and detecting the regions of curvature difference.

Methods

A group of 2D mid sagittal cross section images of the corpus callosum was taken from males of similar age, 15 autistic, and 12 normal controls. The level set method [2] was used to extract the outline of the corpus callosum automatically. Thus the pixelated CC-contour was reconstructed into a rough closed curve (Figure 1. red). Smoothing of this zigzag contour was necessary to account for the partial volume effect (Figure 1. blue). Two different methods were used to smooth and estimate the curvature function. The first method uses Taubin's smoothing [3], a Gaussian filtering without shrinkage, followed by the least-squares estimation. The second method uses a series of quintic splines to estimate the first and second derivatives to compute the curvature. Afterwards a curve from the control group was chosen as a template and all other curves are registered to the template. First an affine registration was used to normalize the global CC-size differences. Second a fast nonlinear dynamic-time warping algorithm was used [4]. The algorithm penalized against large deformation and curvature difference, thereby matching the extrema of curvature while maintaining a smooth and stable deformation. After registering the curves, a local estimation of curvature could be compared across subjects, using Welch's t-test to correct for the unequal variance (Figure 3).

Results

Both methods provided effective estimates of curvature for the entire CC-contours. The smoothing splines performed better in terms of ease of fit and more stable results. The results of the comparison of curvatures between the autistic and control subjects are as shown in Figure 2 where the sample mean curvature functions are plotted (blue: autistic, red: control). Figure 4 is the P-value map where the blue areas indicate more significant curvature difference. Most significant curvature difference is detected at the posterior midbody (R1).

Acknowledgements

The original level set and dynamic time warping code were obtained from Fan Ding and Yuefeng Lu and have been modified extensively. This work was funded by WARF, NIMH U54 MH066398-1A1, NSF Grant DMS0072292 and by a NARSAD Distinguished Investigator Award to RJD.

References

[1] Harden, A.Y. *et al*. Neurology, 55:1033-1036, 2000.
[2] Malladi, R. and Sethian, J.A. Applied Mathematics 18:9389-9392, 1996.
[3] Taubin, G. Computer Graphics, 29:351-358, 1995.
[4] Wang, K. and Wang, Y. Annals of Statistics, 25:1251-1276, 1997.
[5] Witelson, S.F. Brain 112:799-835. 1989.

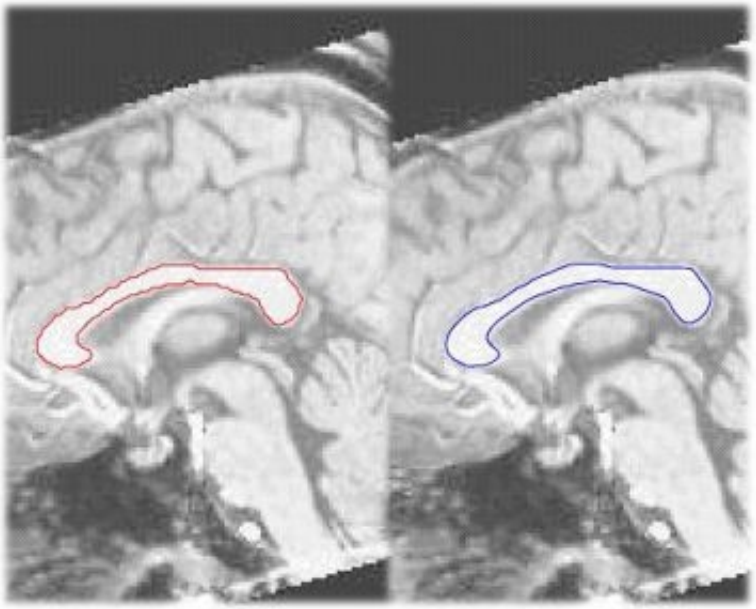

Figure 1. Leveset segmentation and smoothing

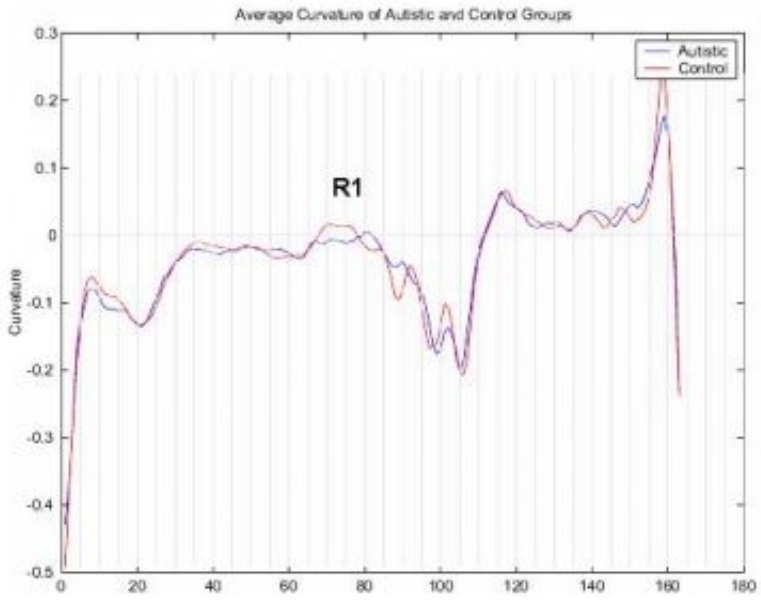

Figure 2. Mean curvatures for autism and control

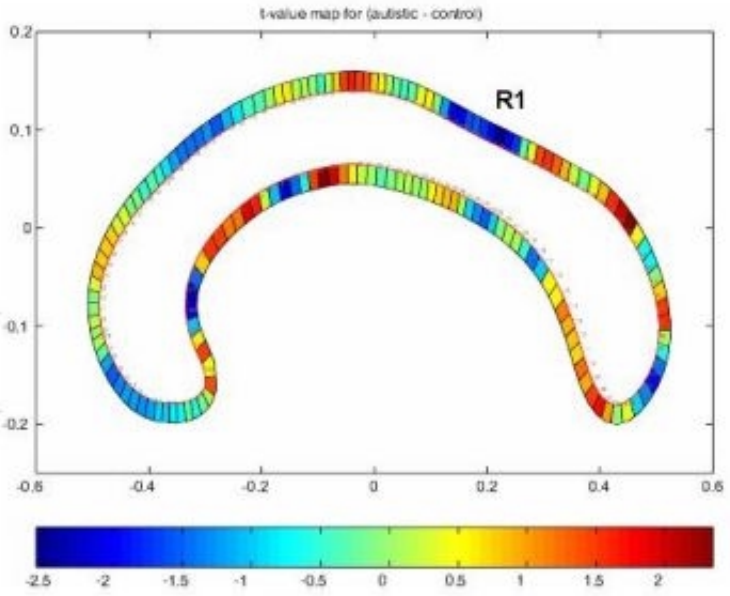

Figure 3. t-map of curvature difference between autism and control

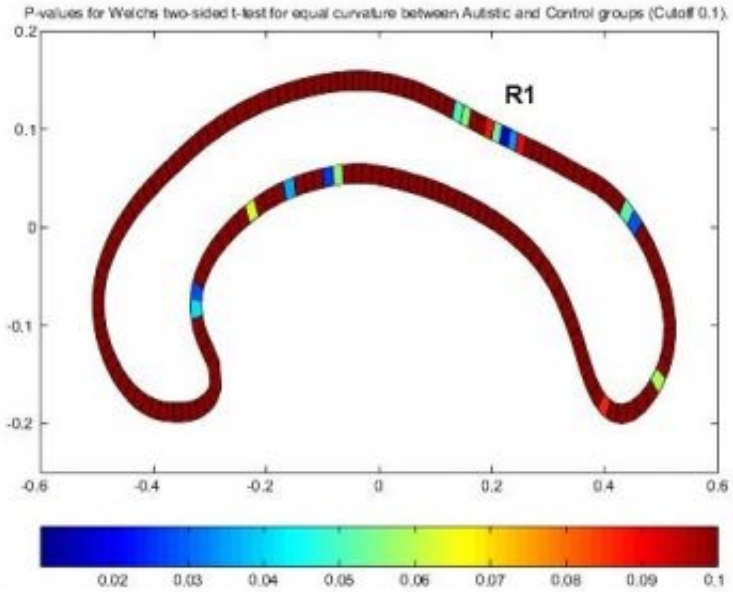

Figure 4. p-map of curvature difference

WE 358
Adjustments for global radiation counts: Different techniques, different results

J. Richard Jennings[1], Mark Gamalo[2], Carolyn Meltzer[3]
[1]Department of Psychiatry, University of Pittsburgh School of Medicine, [2]Department of Statistics, University of Pittsburgh, [3]Department of Radiology, University of Pittsburgh School of Medicine

Variation in the amount of radiation sensed during positron emission tomography scans is routinely treated as a nuisance variable. As such its effect is minimized by proportional scaling or analysis of covariance, e.g. within Statistical Parametric Mapping (SPM) 99. The influence of these adjustments on the interpretation of results becomes a significant issue when groups or conditions in a study show consistent differences in these global radiation counts. We performed an [15O] water positron emission tomography study comparing 37 hypertensive and 59 normotensive individuals using both a quantitative, region of interest (ROI)-based approach and the relative, voxel-based approach of SPM. Increases in regional cerebral blood flow (rCBF) were observed when comparing a control task to tasks with different working memory requirements. These increases were smaller among hypertensives relative to normotensives in our quantitative analysis, but SPM analyses either detected no differences in the relevant areas or relatively greater change in hypertensives. An examination of global counts showed that hypertensives had relatively greater counts during the control task relative to the memory tasks; while the hypertensives had the opposite pattern.

We investigated the influence of these differences and various correction approaches by selecting three subsamples: 24 normotensive individuals with clearly increasing global counts between tasks, 20 hypertensives with decreasing global counts between tasks, and 9 hypertensives with increasing global counts between tasks. The normotensives were compared separately to the two hypertensive groups. We present the results of omitting correction, analysis of covariance applied at the individual (random effects) and group (fixed effects) levels on these results as well as the effect of proportional scaling. Omission of any correction eliminates all significant differences. Correction by proportional scaling induces spurious activation over most of the brain for the comparison of groups. Both fixed and random effects applications of analysis of covariance yielded reasonable patterns of activation for this contrast that appeared stronger when groups showed concordant regression beta weights (total vs pixel counts). None of the corrections, however, yielded results similar to the quantitative results, i.e. greater task-induced rCBF in normotensives relative to hypertensives. This differences appears to be due to reduction of sensitivity of the SPM analysis due to co-linearity of task and total cerebral blood flow responses in addition to the differences between groups in degree of covariance adjustments.

These results suggest that global count values should be checked for trends and that the application of proportional scaling when trends are apparent may induce distortion in the results. It also remains possible that the trends that we observed are specific to the cerebrovascular adjustments to hypertension.

Global Adjustments on Hypertensive and Normotensive groups with divergent global changes across conditions

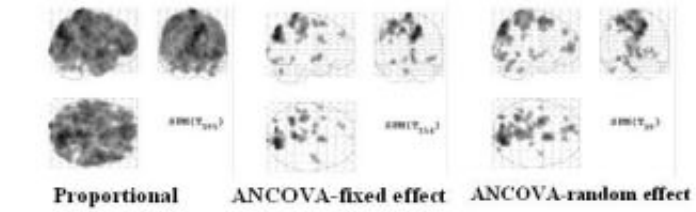

Images depict difference in increase in rCBF due to spatial working memory between groups at $p<.01$ threshold

WE 359
Smoothing Kernels in Voxel Based Morphometry of DT-MRI Data: Does Size Matter?

Derek K Jones[1, 2], Mark Symms[3], Mara Cercignani[3], Sukhwinder S Shergill[1], Robert J Howard[1]
[1]Institute of Psychiatry, London, UK, [2]National Institutes of Health, Bethesda, Maryland, USA, [3]Institute of Neurology, UCL, London, UK

INTRODUCTION:

Voxel-based morphometry (VBM) has been used to analyze diffusion tensor MRI (DT-MRI) data in schizophrenia, and other conditions, with inconsistent results. In VBM, following spatial normalization, data are smoothed to improve the validity of statistical inferences[1,2]. However, in the DT-MRI literature the smoothing kernel size is non-standard (Table 1) or unreported[3-5]. It was recently suggested that 4 mm smoothing may be the minimum to ensure statistical validity in VBM[6]. Here we report multi-scale VBM examinations of DT-MRI data in schizophrenia, highlighting the importance of kernel size when reporting findings.

METHOD:

Whole brain DT-MRI data (2.5 mm isotropic resolution)[7] were acquired from 14 schizophrenics and 14 age, handedness and gender-matched controls and T_2-weighted intensity, fractional anisotropy[8] (*FA*) and mean diffusivity (*MD*) images computed. Data were analyzed using SPM99. Initially, each subjects T_2-weighted image (*T2WI*) was affine co-registered with SPM99s EPI template. The 28 co-registered *T2WIs* were averaged and Gaussian-smoothed (8 mm kernel) to create a group template. Each subjects *T2WI* was co-registered to this template (affine followed by 7×8×7 non-linear basis functions) and the same transformations applied to the *MD* and *FA* images. These images were smoothed with kernel sizes ranging from 4 to 16 mm (in 1 mm increments). For each kernel size, two contrasts: (Patients>Controls) and (Controls>Patients), were used. Differences at the voxel level were considered significant at $p<0.05$ after multiple comparison correction.

RESULTS:

There were no significant differences in *MD* or with the (Patients>Controls) contrast in *FA*. The (Controls>Patients) contrast (in *FA*), revealed no significant differences with 4, 5 or 6 mm smoothing kernels. At 7 and 8 mm, a single region centered at MNI co-ordinate [54,50,22] was present. At 9 mm, a second significant region appeared at [-28,44,18]. As the smoothing window size was increased further, this latter region increased in size, while the former diminished to the point where (at 15 mm), it disappeared. Figure 1 shows results obtained at 8, 10, 12 and 14 mm.

DISCUSSION:

In VBM, while it is intuitive that the size of the smoothing window influences results, no standard exists in the DT-MRI literature (Table 1). *FA* data are considerably more heterogeneous than BOLD or PET data, increasing the sensitivity of VBM results to the choice of scale. Using the range of smoothing scales reported in the literature (4-12 mm) and beyond, we obtained vastly different results. With 4 and 6 mm kernels, no patient-control differences are detected. Above 6 mm, depending on the kernel size chosen, either the left cerebellum or right superior temporal gyrus can emerge as the site of significant schizophrenic-control *FA* differences.

CONCLUSION:

Strictly, the scale of any expected group difference should be specified *a priori* and only a smoothing kernel of this size used in investigations. Otherwise, one should correct for the multiple comparisons that have been performed. Choosing one length-scale, however, only reveals part of the picture. For exploratory analyses, one may consider examining the data at multiple length-scales but this requires extension of the Gaussian random field approach to multi-scale analyses to address the multiple-comparison issue. Finally, to interpret and replicate VBM studies of DT-MRI data it is **imperative** that groups report the size of the smoothing window used.

Table 1 - Literature citations for smoothing windows used in voxel based morphometry of DT-MRI data

REFERENCE	VOXEL DIMENSIONS	SIZE OF SMOOTHING WINDOW
Barnea-Goraly N *et al. Am J Psych.* **160:**1863-1869 (2003).	1.9 × 1.9 × 5 mm (1 mm slice gap)	4 mm
Sach M *et al. Brain* (in press, DOI: 101.1093/brain/awh041)	3 × 3 × 3 mm (no slice gap)	6 mm
Eriksson SH *et al. Brain* **124:**617-626 (2001)	2.5 × 2.5 × 2.5 mm (no slice gap)	8 mm
Eriksson SH *et al. Brain* **124:**617-626 (2001)	2.5 × 2.5 × 2.5 mm (no slice gap)	10 mm
Burns J *et al. Br J Psych.* **182:**439-443 (2003)	1.9 × 1.9 × 5 mm (no slice gap)	12 mm

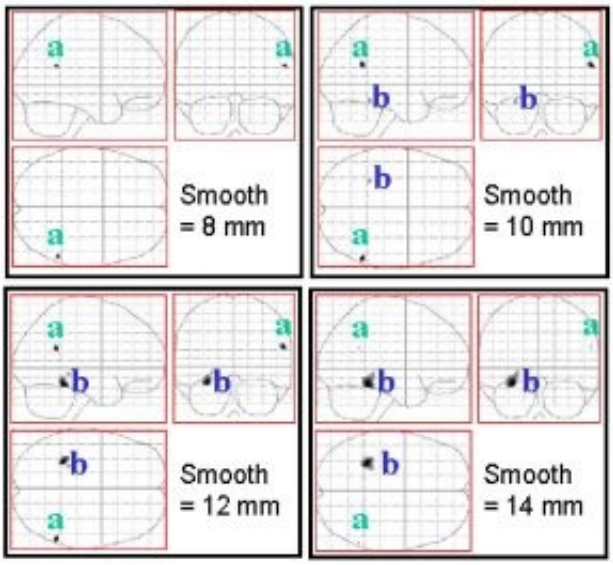

Figure 1 - Maximum Intensity Projections (MIPs) of voxels showing significantly reduced fractional anisotropy in schizophrenic patients compared with controls ($p < 0.05$ after correction for multiple comparisons)
Region a is centered at MNI co-ordinate [56 -50 22] - the superior temporal gyrus.
Region b is centered at [-28 -44 18] - the left cerebellum.

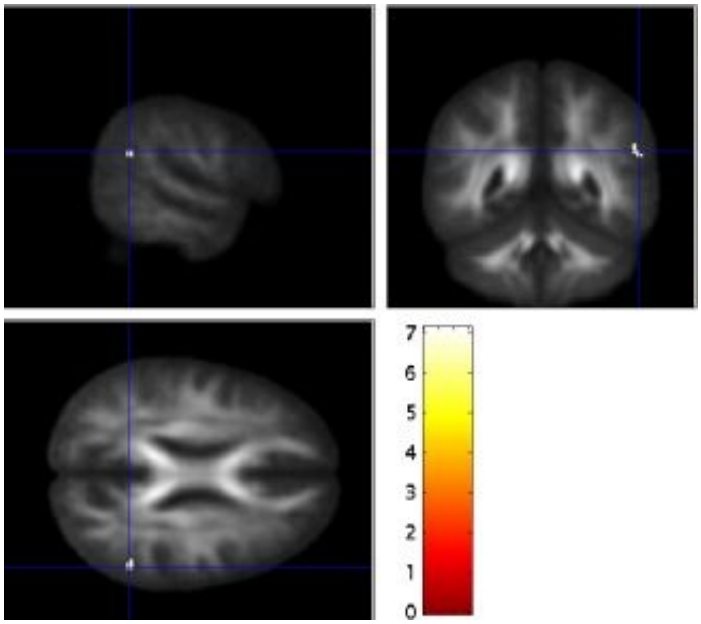

Figure 2 - Overlay of significant difference (Controls>Patients) in fractional anisotropy obtained with Gaussian smoothing kernel of 8mm. Location of most significant voxel = [56 -50 22]. The grayscale picture shows the mean of the 28 non-linearly co-registered *FA* images.

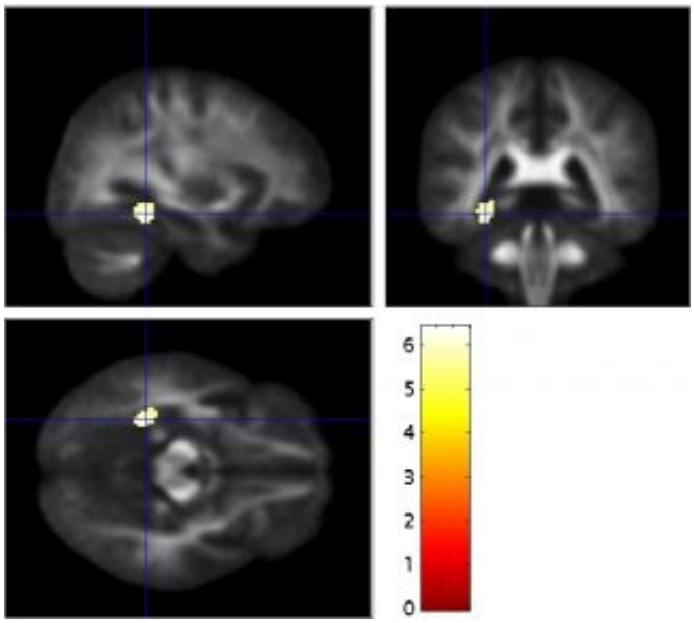

Figure 3 - Overlay of significant difference (Controls>Patients) in fractional anisotropy obtained with Gaussian smoothing kernel of 14mm. Location of most significant voxel = [-28 -44 -18]. The grayscale picture shows the mean of the 28 non-linearly co-registered *FA* images.

WE 360
The Capsula Interna in Families with Schizophrenia

Thomas Kamer , Anand Roy , Thomas Schneider-Axmann , Peter Falkai
Institute of Psychiatry, Saarland University Hospital, Homburg/Saar, Germany

Recent studies strengthen the notion of schizophrenia as a disease with connectivity disturbance. It has been shown that the volume of the capsula interna might be reduced. In order to verify this result, we examined the capsula interna in a priorly obtained MR database. 51 schizophrenic patients, 53 unrelated controls, 57 healthy relatives and 29 relatives with other psychiatric diseases were included. Relatives were included to identify morphological differences which might indicate genetic predisposition.
The MR images were obtained at 1.5 Tesla with high resolution. All images were manually edited in transversal orientation. Due to a lower signal-to-noise-ratio posterior only the frontal limb could be properly identified. Also for technical reasons only the inferior part has been extracted. Volume, length and maximum cross section were calculated from the extracted structure. Gray and white matter volumes were derived by segmentation into substanceclasses with SPM.
Statistical analysis detected significantly reduced volumes of the inferior frontal capsula interna for relatives ($p=0.03$ on the left side and $p=0.05$ on the right side) but not for schizophrenic patients. Generally the differences were slightly more pronounced on the left side. Analysis of length and cross section indicated the capsula interna being longer in schizophrenic patients and shorter in relatives without schizophrenia.

WE 361
Regional GM Loss in RR and SP Multiple Sclerosis

Irina Kezele[1], Andrew L. Janke[1], Patricia LeNezet[1], Sylvain Prima[3], Douglas L. Arnold[2], D. Louis Collins[1]
[1]McConnell Brain Imaging Centre, Montreal Neurological Institute, Quebec, Canda, [2]MRS Unit, Montreal Neurological Institute, Quebec, Canada, [3]IRISA/INRIA Rennes, France

Introduction

Brain atrophy occurs in MS even at its early stages [1,2] and can progress irrespective of the lesion load [3,4]. In spite of being recognized as measures of disease destructiveness, neither the time course nor the pathological basis of atrophy are well understood [5]. Our two main goals were: 1) to determine if the nature of grey matter (GM) loss in MS is homogeneous across the cerebrum and 2) if the loss is heterogeneous, to characterize the spatial patterns of GM atrophy. In the present study, we measured normalized GM volumes in MS patients and normal controls in cerebral lobes (frontal, temporal, parietal, and occipital), for each hemisphere. We tested whether the tissue loss was significantly different in the cerebrum or the particular lobe(s) and explored its correlation to MS subtype.

Methods

We studied 73 patients with clinically definite MS (mean age 40.0, 53 RR, 12 SP, 8 PP) and 44 normal controls (mean age 34.5). Whole brain MRI was performed on a 1.5T scanner (Philips Gyroscan ACS II). Three axial volumes with fifty 3mm thick slices were acquired for each subject with a 250mm FOV that included a T1-weighted 3D gradient-echo sequence (TR/TE=35/10.2ms) and a dual turbo spin-echo sequence yielding T2- and PD-weighted data (TR/TE=2075/30,90ms). The images were morphologically pre-processed to extract the intracranial volume (ICV), corrected for RF inhomogeneity by minimizing the image histogram entropy [6], linearly registered [7] into common stereotaxic space (optimizing 9 free parameters by maximizing the cross-correlation coefficient) and classified into 4 classes: WM, GM, CSF, and LESion using an EM algorithm [8]. The GM tissue class was masked with a model lobe segmentation to identify the amount of GM in each lobe. The GM volume was normalized by dividing the GM volume by the lobar volume, then analyzed using ANOVA and Tukey's HSD for post hoc testing in JMP 5.0.1 (SAS Institute).

Results

A significant difference in GM ($t=4.4$, $p<.0001$) was found when comparing NC vs patients. A difference in GM exists between all four groups ($F=12.3$, $p<0.0001$) and post hoc testing shows NC=PP; RR=PP; NC>RR;PP=SP;NC>SP. A significant difference in regional GM volumes was found for the frontal, parietal, and temporal lobes (cf. Table). Post hoc analysis (max $p<0.01$) showed that SP < RR < NC in frontal lobes, and SP < NC in temporal and parietal lobes. The generalized linear model analysis did not show a significant effect of age.

Discussion

These results support a heterogeneous pattern of GM atrophy in MS and suggest its progression. Our findings are concordant with previously reported regional GM cortical thinning [9], showing overlap of the affected regions. While the present results do not explain the origin of the selective GM loss, they confirm its considerable involvement in MS pathology.

[1] Fisher E, Neurology, 2000, 59(9):1412-20.
[2] Trapp BD, et al., New Engl J Med, 1998, 338:278-85.
[3] Losseff NA, et al. Brain, 1996, 6:2009-19.
[4] Narayanan S, et al., Ann Neurol., 1997, 41(3):385-91.
[5] Hardmeier M, et al., Arch Neurol, 2003, 60(12):1736-9.
[6] Sled JG, et al. IEEE Trans Med Imaging, 1998, 17(1):87-97.
[7] Collins DL, et al., J. Comput. Assist. Tomogr. 1994, 18:192205.
[8] Van Leemput K, IEEE Trans Med Imaging, 2003, 22(1): 105-19.
[9] Editorial, Brain, 2003, 126: 1719-21.

Normalized lobar GM differences

	Frontal Lobe	Temporal Lobe	Parietal Lobe
Left	F=21.5,p<.0001	F=6.8,p=.0003	F=9.9,p<.0001
Right	F=16.2,p<.0001	F=8.2,p<.0001	F=8.5,p<.0001

WE 362
Hippocampal asymmetry analysis in schizophrenia using deformable model with surface registration

Hyun-Pil Kim , Sun-Hyung Kim , Jong-Min Lee , In-Young Kim , Sun-Il Kim
Department of Biomedical Engineering, Hanyang University, Seoul, Korea

Introduction: The changes of hippocampal structure have been reported as one of the most consistent structural abnormalities and to be related to deficits in learning and memory in schizophrenia (SZ) [Laakso et al., 2002]. Though many scientists have carried out researches on volumetric aspects, fewer have focused on shape-based methods. In this article, we adopted shape-based-deformable model and statistical process to detect local-structural changes in the following two ways: How deformity is developed between two different groups of patients and how left/right-hippocampal asymmetry distributes in each group.
Subjects: The subjects were scanned using 1.5T GE SIGNA System with the following parameters: 3D-SPGR T1 weighted pulses, 1.5mm sagittal slices, TE/TR=5.5/14.4ms, matrix=256x256, and FOV=21x21cm. Each group is consisted of 22 subjects, who are matched for age, sex and handedness (mean age 26.2±6.1 years). The regions of interests were manually drawn by a trained expert.
Methods: Anatomic segmentation using proximities algorithm (ASP) [MacDonald et al., 2000] was used for the modeling process. We have utilized a coarse alignment method by finding out a principle axis of hippocampus, which is needed for fully automated alignment. After the coarse matching, models were aligned again using fine alignment which implements Powells optimization algorithm [Sun-Hyung Kim et al., 2003].
To detect inter-group deformity, all of the left hippocampus of schizophrenia and control group were aligned to the left of standard subject which belongs to the control group. The right hippocampi were processed in the same way. A slightly different method was used to find L/R hippocampal asymmetry. The right hippocampi of both groups were aligned to the left of standard subject, and then the left of SZ and control group were aligned to its own right. Mirroring process of left hippocampus was introduced before ASP modeling.
Corresponding points were defined by proximity between two points, and distance fields were constructed by calculating root-squares between two points. Finally, statistical analysis was carried out on the fields.
Results & Discussion:
We observed that there exist several distinct asymmetries. Right hippocampus of the control group has shown outward asymmetry around posterior CA1 and subiculum. Inward asymmetry was observed from the head along with gyrus dentatus and CA4. Right hippocampus of the schizophrenia group shows overall inward asymmetry on its superior side and slightly weaker outward asymmetry on its inferior side.
We have successfully detected the inter- and intra-group asymmetry with coarse alignment and surface registration. Interpreting neuro-anatomical meaning of the results remains for the future work. In addition, the statistical process could be refined by adding smoothing process. Furthermore, not only the p-value distribution but also the magnitude of asymmetry between groups could be compared between two groups.

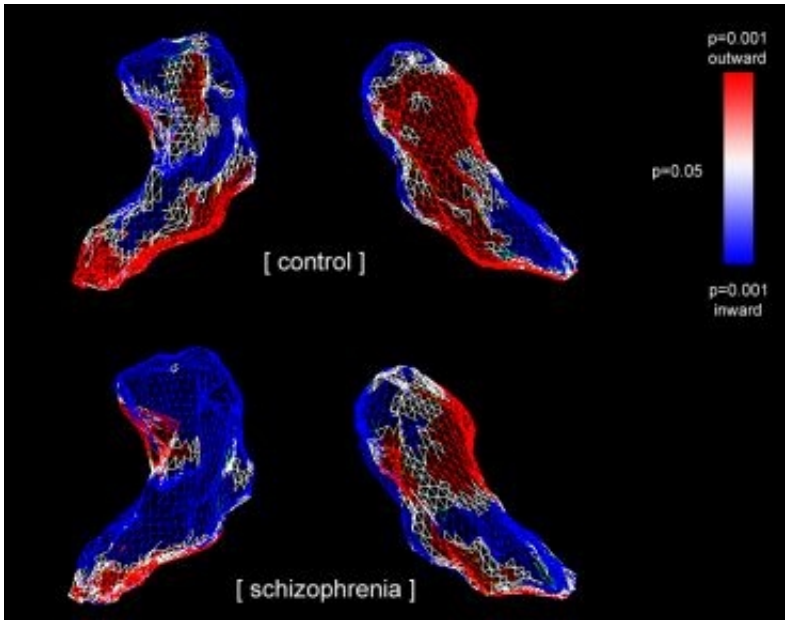

Fig. 1: ***The p-value distribution is displayed on the right hippocampus model of standard subject, which is consisted of 2,562 points. It is notable that the asymmetry pattern differs over groups.***

WE 363
Segmentation-dependent brain volume estimation using simulated MRI data

Frederick Klauschen , Arvid Lundervold
Department of Biomedicine, Neuroinformatics and Image Analysis Group, University of Bergen, Jonas Lies vei 91, N-5009 Bergen, Norway; Email:Arvid.Lundervold@biomed.uib.no

Brain volumetry from MRI acquisitions has become increasingly important in the study of brain development, neurodegeneration and dementia, neurological disease and psychiatric illness. Several approaches to tissue segmentation and brain volume estimation have been reported during the years [1,2,3].
Previously, we have investigated the effect of pulse sequence selection on multispectral brain tissue segmentation [4]. In this work we compare three brain volumetry methods and evaluate their performance using simulated MR-brain-datasets of different image quality, i.e. the MNI *BrainWeb* simulated MRI data
[5] that enables different levels of Gaussian noise and superimposed bias-fields to be selected, and comes with a "gold standard" tissue classification mask of gray- (GM), and white matter (WM) and CSF. To our knowledge a direct comparison of two of the most widely used brain segmenters, *SPM99/SPM2* and *FreeSurfer*, applied to the same set of MRI data, has not previously been reported. For multispectral data we also tested the *LVQ* algorithm [6], which is algorithmically simpler and faster than both *SPM* and *FreeSurfer*.
Results. We found *LVQ* was similar to the two other methods regarding GM- and total parenchyma (GM+WM)-volumes when applied to data of relatively good image quality. The results for WM-volume obtained with *LVQ* were approximately four times more accurate compared to *SPM99* and *FreeSurfer*. However, *LVQ* was less robust against decrease in image quality. With GM-/WM-volume deviations from "gold standard" values of more than 9% for *SPM* and >6% for *FreeSurfer*, even using data of relatively good quality, and over 30% on average for *SPM2*-derived CSF-volumes, the accuracy of these methods must be considered as relatively low. The comparison of results for WM calculated by *SPM* with those produced by *FreeSurfer* yielded discrepancies of nearly 20%. A still more important finding was that even with the same method relatively small differences in image quality (e.g. occurrence of some slightly more noisy acquisitions in a collection of 3D datasets) can have an impact on the deviations of the volumetry results from the "real" volumes that do not follow any regular pattern. This finding was particularly prominent for CSF using *SPM99* and *SPM2*, where the volumes of two different image qualities differed up to 15%, or for the GM-volumes (discrepancies of more than 5%), and was present nearly throughout the volumetry results. In this context *FreeSurfer* seemed more robust, where the deviations across different image qualities did not exceed 1.3% for the GM+WM-volume.
Impact on brain volumetry. Since the discrepancies between brain volumetry results using data of different image quality can reach the same order of magnitude as the volume changes that are relevant in pathologies, these segmenter-dependent effects should be taken into account carefully during the selection and analysis of data for studies of brain volumes.
[1] Bezdek et al. *Medical Physics*, 1993;20:1033-1048. **[2]** Pham et al. *Ann. Rev. Biomed. Eng.*, 2000;2:315-337. **[3]** Toga & Thompson, *Ann. Rev. Biomed. Eng.*, 2003;5:119-145. **[4]** Lundervold et al. *Med. Imag. Anal.*, 2000;4:123-136. **[5]** Collins et al. *IEEE Trans. Med. Imag.*, 1998;17:463-468. **[6]** Kohonen et al. *LVQ PAK: The learning vector quantization program package*, Helsinki University of Technology, 1996.

WE 364
Cortical Source Imaging of the EEG Manifestations of Schizophrenia and Depression in a Realistic Head Model

Zoltan J Koles[1], Aisha Yahya[1], John C Lind[2], Pierre Flor-Henry[2]
[1]Electrical and Computer Engineering, University of Alberta, [2]Clinical Diagnostics and Research Center, Alberta Hospital, Edmonton CANADA

We have recently completed a study of some 50 male schizophrenics and 25 male depressives with a view to eliciting the EEG signatures of these disorders with respect to a group of 65 matched controls. 43 electrodes were used to record the EEG during both passive and active cognitive conditions. The active conditions consisted of verbal and spatial challenges and the investigations focused on the delta, alpha and beta frequency bands. Source images were obtained for each subject from his cross-spectral matrix in each of these frequency bands. The images were obtained according to the relation $q_i = \mathrm{diag}(T\ Z\ \Sigma_i\ Z'\ T')$ where q_i is the source-current density in the ith subject, Σ_i is his cross-spectral matrix in one of the frequency bands, Z is a two-stage spatial filter designed to increase the signal to noise ratio in the cross-spectral matrix and T is the LORETA transformation matrix. In this work, the source-current vector qi consisted of 2394 voxels at 7 mm spatial resolution in the 3D space of the cortical gray matter and hippocampus parts of the head model. The head model consisted of the 3 concentric-shell sphere registered to the Talairach Human Brain Atlas available as digitized MRI from the Brain Imaging Centre, Montreal Neurological Institute. The results obtained were most intense in the beta band for both patient groups and during the verbal cognitive challenge in schizophrenia and during the spatial cognitive challenge in depression. Regions of significantly greater source-current density in schizophrenia were left fronto-temporal while in depression they were right precentral-frontal.

In the attempt to improve both the accuracy and the presentation of the results of this study, we have reanalyzed our data using an anatomically realistic head model also available from the Brain Imaging Centre. This head model was derived from the volumetic MRI of a normal subject's head and consists of 1mm3 elements. It has been segmented into scalp, skull, gray matter, white matter and CSF at the voxel level and contains of over 4 million elements. We created a source solution space 1mm inside the cortical surface of the model in the form of a convoluted 2D sheet. The lead-field matrix for the model was calculated using the method of finite elements from some 36,200 locations on the sheet. A transformation matrix T was calculated using the minimum-norm algorithm and included attenuation weightings. Significant differences ($p < 0.05$) between the patient and control groups were determined at the voxel level using randomized t-tests.

The figures show the cortical regions where the patient groups showed higher source-current activity than the control group. Due to shrinkage caused by the cognitive challenges 35 schizophrenics and 42 controls could be compared and 12 depressives and 48 controls. Both figures show the beta band during the verbal challenge for the schizophrenics and the spatial challenge for the depressives. The involvement of the language and verbal association areas are clearly implicated in schizophrenia and of the right prefrontal and somatic motor association areas in depression.

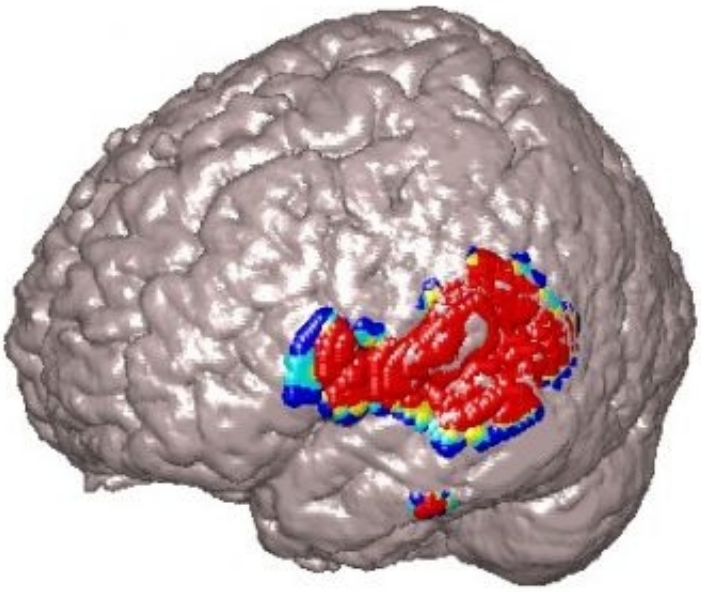

Fig. 1. Schizophrenics vs Controls

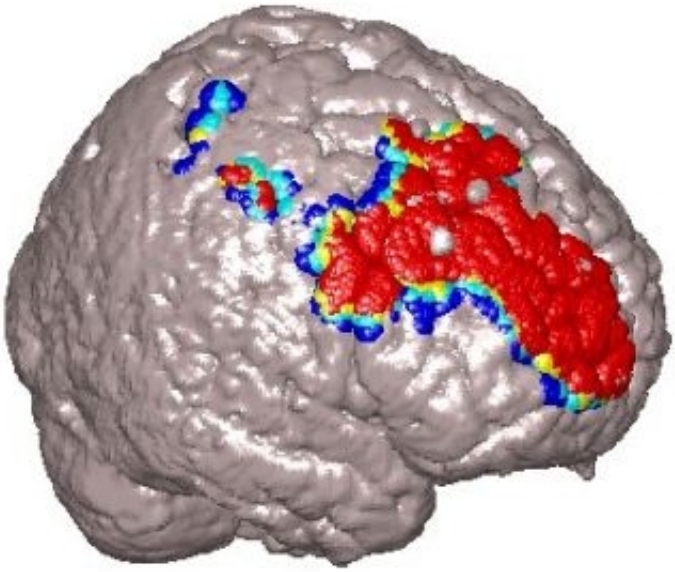

Fig. 2. Depressives vs Controls

WE 365
Quantitative Comparison of Function MRI and Direct Electro-Cortical Stimulation for Functional Mapping

Sara E Larsen[1], Alexandra Golby[2], Ion-Florin Talos[3], Ron Kikinis[3], William M Wells, III[1,3,4]
[1]Massachusetts Institute of Technology, Computer Science and Artificial Intelligence Laboratory, [2]Department of Neurosurgery, Brigham and Womens and Childrens Hospitals, [3]Surgical Planning Laboratory, Department of Radiology, Brigham and Womens Hospital, [4]Harvard Center for Neurodegeneration and Repair, Harvard Medical School

Purpose
To introduce a method for quantitative comparison of functional MRI (fMRI) and direct electro-cortical stimulation (DECS) using a patient-specific anisotropic conductivity model of the brain.
Background
Mapping functional areas of the brain is of vital importance for planning tumor resection. With the recent increase in the use of fMRI for such pre-surgical planning, there is a need to validate that fMRI activation mapping is consistent with the mapping obtained during surgery with the standard technique, DECS.
Methods
Comparison of DECS and fMRI mapping techniques was performed retrospectively on data collected from a neurosurgical case. The patients tumor was a large diffuse astrocytoma involving the frontal and temporal lobes in the left hemisphere.
Surgery was performed in the open magnet MRI scanner at the Brigham and Women's Hospital. During surgery functional mapping of the language areas by way of DECS was performed. The exposed cortex of the patient was stimulated at seven sites while the patient performed language tasks. The stimulation sites were marked, annotated, and then recorded using a sterotactic navigation probe.
The DECS stimulation map was generated using a patient-specific anisotropic conductivity model of the brain. The brain geometry was described using tetrahedral mesh elements [2] which contain corresponding conductivity tensors. Tuch et al. showed a linear relationship between the eigenvalues of the conductivity and diffusion tensors [3].
Using the finite element method, the current density throughout the brain was found. The magnitude of this current density is the DECS stimulation map, and was computed using SCI/BioPSE software [1].
Whole head fMRI image volumes were obtained. The language areas were mapped using a processing task that tested the patient's level of semantic versus perceptual judgment.
SPM99 was used for reconstruction and motion correction of the data. SPM99 was also used to calculate voxel by voxel paired T-statistic scores for each voxel. Thresholded scores were then used to generate a binary fMRI activation map
Results
The 3D fMRI activation and DECS stimulation maps can now be compared to determine the level of agreement between the volumes. This comparison is quantified using the maximal Dice similarity coefficient over current thresholds, which provides a quantitative measure of the degree of association between the two volumes [1]. The DSC is defined as the number of intersecting voxels divided by the average number of voxels in each volume and ranges between 0.0 and 1.0.
Conclusions
Our results show initial agreement between intra-operative DECS mapping results and fMRI activation results. Moreover, we have provided a method to quantitatively validate the utility of fMRI for pre-surgical planning. A more accurate localization of functional areas could lead to less injury of eloquent brain matter during surgery and a more ambitious approach to tumor removal.
This research was supported by NIH grants P41 RR13218 and R21 CA89449 and the Harvard Center for Neurodegeneration and Repair.
References
1. SCI:BioPSE. Scientific Computing and Imaging Institute 2002.
2. Timoner SJ. MIT 2003; PhD Thesis.

3. Tuch D et al. Proc Nat Acad Sci 2001; 98: 11697-11701

Maximal DSC values and patient response for all stimulation sites.

Stimulation Site	Patient Response	Maximal DSC
1	N	0.0533
2	N	0.0157
3	Y	0.1747
4	N	0
5	N	0
6	N	0
7	N	0

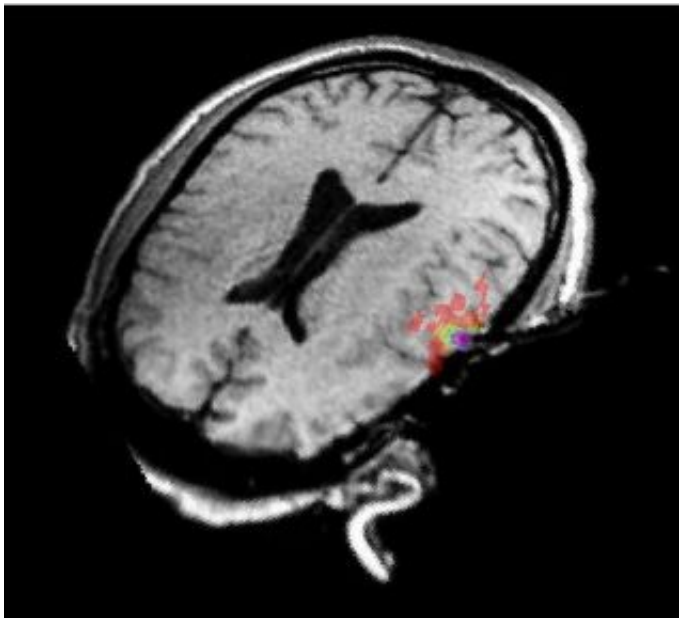

Figure 1: Current magnitude solution on an axial slice showing craniotomy

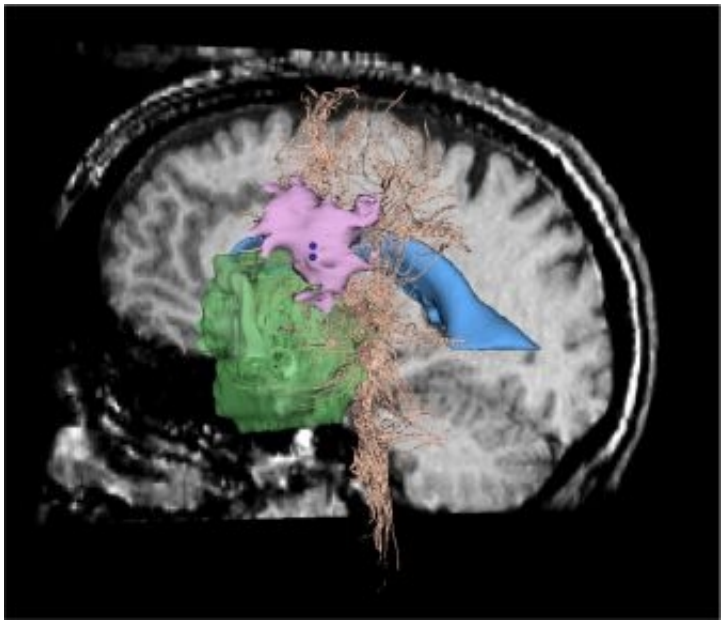

Figure 2: Comparison of current density solution (pink), and fMRI activation (orange). Sagittal pre-operative slice, tumor (green), ventricles (blue) and white fiber tracts (yellow) are also shown.

WE 366
Fast MR signal changes associated with 3Hz spike-and-wave discharges in generalised epilepsy

Adam Liston[1,2], Afraim Salek-Haddadi[1,2], Stefan Kiebel[3], Robert Turner[3], Khalid Hamandi[1,2], Louis Lemieux[1,2]

[1]Dept Clinical and Experimental Epilepsy, Institute of Neurology, UCL, London UK, [2]National Society for Epilepsy, Chalfont St Peter, [3]Wellcome Dept of Imaging Neuroscience, Institute of Neurology, UCL, London

Introduction

Recent investigations have demonstrated the possibility of MRI detection of magnetic field perturbations caused by neuronal depolarisation currents [1, 2]. If proven reliable, this novel contrast mechanism would reflect brain activity more directly than the BOLD effect. Neuroelectric activity might be revealed by MR acquisition sequences similar to those used for conventional BOLD imaging, although timing requirements are much more stringent. Previously, we presented activations observed in a patient with idiopathic, generalised epilepsy using EEG-correlated fMRI [3]. Four runs of 3Hz generalised spike-wave discharge (GSWD) occurred during 35 minutes of data acquisition and time-locked, bilateral, thalamic BOLD increases were reported to be accompanied by widespread, symmetric, cortical deactivation with a frontal maximum. We have reanalysed this data in an attempt to reveal a fast, 'neuroelectric' MR signal.

Methods

During a T2*-weighted gradient-echo EPI sequence (TE/TR 40/3000, 21x5mm interleaved slices, 64x64matrix) at 1.5T (GE Horizon), 700 BOLD sensitive scans were acquired continuously, realigned and then smoothed (8mm FWHM, isotropic Gaussian kernel). Six masked, voxel-based statistical analyses were carried out, using SPM2 (http://www.fil.ion.ucl.ac.uk/spm/spm2.html), on six individual slices covering the thalamus and main regions of cortical deactivation. For each, a vector of onsets was defined, containing the spike timing, in each 3Hz GSWD complex, relative to the acquisition time for that slice, during the first scan. Two different hypotheses were then tested using a single SPM model: 1) for seizure related BOLD changes, onsets were convolved with a canonical hemodynamic response function and its temporal derivative; 2) for fast MR signal changes during the 300ms after each spike, ten finite impulse responses (FIR) were proposed, occurring each in consecutive 30ms bins following each onset. Thus, we tested for a fast response, of unspecified shape, while taking into account the slow BOLD response. Two F-statistics were formed to test for the BOLD response and for fast changes represented by all 10 FIR regressors. Corrected SPM{F} maps were thresholded at $P<0.05$ and uncorrected maps at $P<0.001$.

Results

Significant BOLD activation was revealed as previously reported. Activity was seen also in association with the 10 FIRs for each slice analysed, and clusters of activation survived correction in 2 out of 6. A map is shown of one of these in Figure 1.

Discussion & Conclusions

We modelled the MRI response as the sum of a fast, neuroelectric signal and a slower, BOLD-related signal. Due to the slow sampling rate, experimental efficiency was limited with each FIR bin sampled a maximum of 5 times. The resulting, shown distribution of fast activity corresponds roughly to regions of BOLD activation, although the maxima do not coincide exactly. Interpretation of the findings is limited in part by the uncertain nature of the electrical generator(s) that underlie this type of activity.

In conclusion, we have demonstrated significant MRI activity at a time scale of the order of 30ms associated with generalised spike-wave discharges but further work is necessary before firm conclusions may be drawn.

References

[1] Bodurka,J. & Bandettini,P.A. Magn-Res-Med 47(6), 1052-1058. 2002.

[2] Xiong,J., Fox,P.T. & Gao,J.H. Hum Brain Mapp 20, 41-49 (2003).

[3] Salek-Haddadi A., Lemieux L., Merschhemke M., Friston, K.J., Duncan J.S., Fish D.R. Ann. Neurol,53: 663-667, 2003.

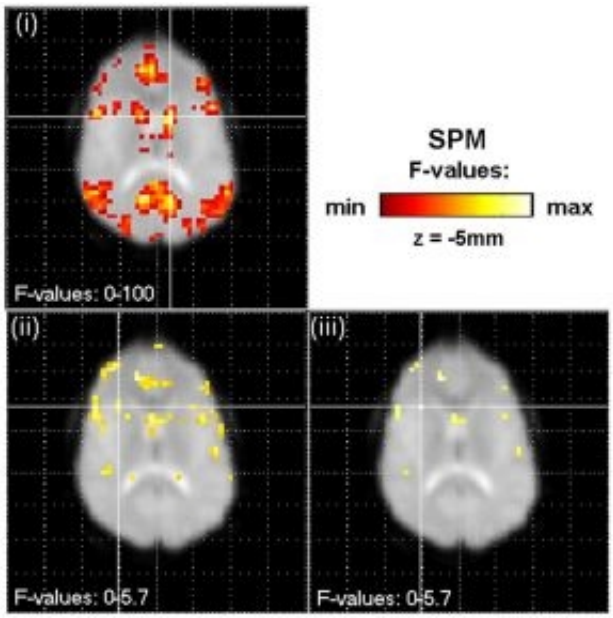

Figure 1. SPM{F} maps of activations in a single slice associated with (i) BOLD (P<0.05, corrected) and with immediate, fast changes (<300ms) (ii) P<0.001, uncorrected (iii) P<0.05, corrected. Maxima are indicated by the crosshairs.

WE 367
A region-based method for the estimation of the neural impulse response in event-related fMRI

Salima Makni[1], Philippe Ciuciu[1], Jérôme Idier[2], Jean-Baptiste Poline[1]
[1]CEA/SHFJ, [2]IRCCyN/CNRS

Recently, we developed an unsupervised robust non-parametric method [1, 2] to estimate the Hemodynamic Response Function (HRF) in event-related functional Magnetic Resonance Imaging (fMRI) data. Further to these works, we observed that the shape of the response tends to be spatially homogeneous for nearby voxels. This property of shape similarity also holds between HRFs elicited by different stimuli.
Here, we propose an extension that takes these features into account in a given region-of-interest (ROI). Our purpose is to estimate jointly a single HRF shape for a given ROI but magnitude coefficient for each voxel and stimulus type. This coefficient may better represent the neural response level and can be seen as a deconvolution of the BOLD response. The problem can be formulated as a semi-blind deconvolution inverse problem since the arrival times of stimuli are known.
Method
The HRF is modeled in a Bayesian approach as a smooth function of time. The stimulus-dependent neural magnitudes are assumed to be statistically independent across voxels and between stimulus types. The hyperparameters that govern Gaussian prior distributions as well as the noise variances (one per voxel) are estimated. Estimation is achieved through the well-known Gibbs sampler algorithm drawing random samples iteratively from the posterior distribution, that is obtained by marginalizing with respect to the "Physiological" artefacts that corrupt real fMRI data. Finally, posterior mean estimates of all unknown parameters are computed. The method was tested on both synthetic and real fMRI data.
Results
First, simulations demonstrate that the proposed model provides a robust estimation of the parameters of interest. Second, clusters of voxels detected with SPM on a visual paradigm were selected to define several ROIs. The corresponding fMRI data were extracted using MARSBAR toolbox. For each ROI, a single HRF shape and maps of the neural response levels for each stimulus are presented.
Figures bellow illustrate the estimation results for two visual conditions (h and v) used to detect transient activity in the primary visual cortex. We used raw fMRI data defined for a contrast h-v. The ROI-based HRF estimate is plotted in Figure 1 and the estimated neural magnitudes for each condition are represented in Figures 2-3. We observe that within a given condition, there is a spatial correlation between estimated magnitudes specially for neighbors voxels in the same slice.
This approach provides spatial activation maps in a given ROI with no assumptions on the exact shape of the HRF. The algorithm has proved to be robust for different conditions, ROIs and data sets.
Further work will investigate the spatial characteristics of the HRF magnitudes and the link with the underlying anatomical structure.
References
[1] G. Marrelec, and al., Bayesian estimation of the hemodynamic response function in functional MRI, in Bayesian Inference and Maximum Entropy Methods, R. Fry, Ed. Baltimore, MD: MaxEnt Workshops, August 2001.
[2] P. Ciuciu, and al., Unsupervised robust non-parametric estimation of the hemodynamic response function for any fMRI experiment, IEEE Trans. Medical Imaging, vol. 22, no. 10, pp. 1235 1251, Oct. 2003.

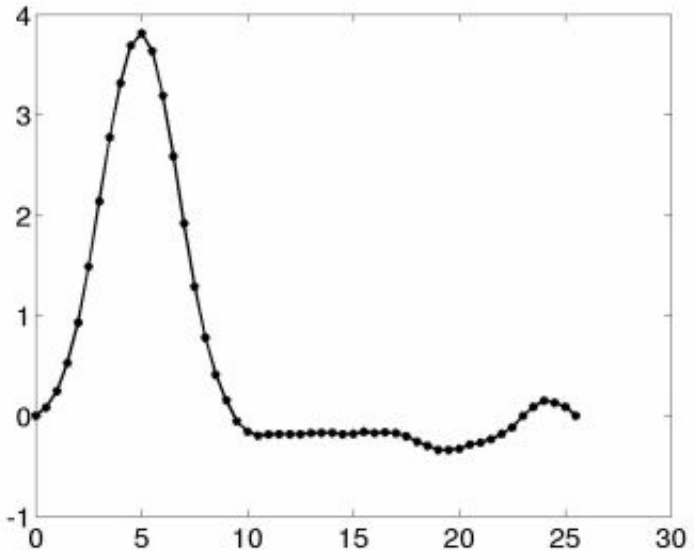

Figure 1 : ROI-based HRF estimate

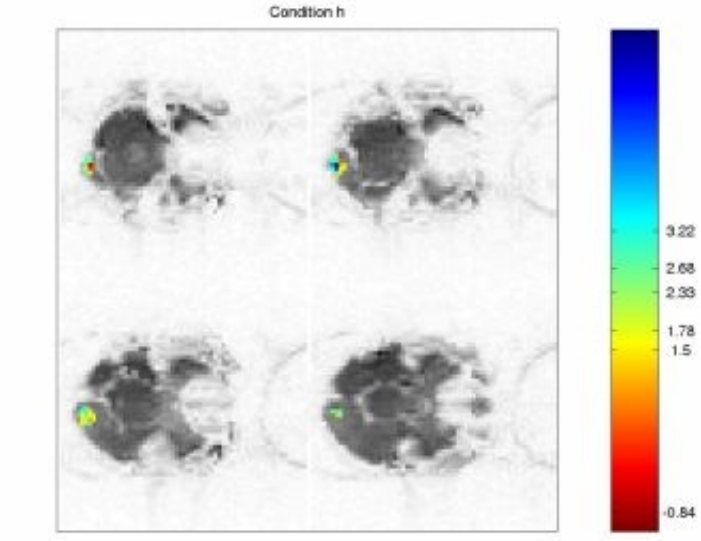

Figure 2 : Estimates of neural response levels for condition h

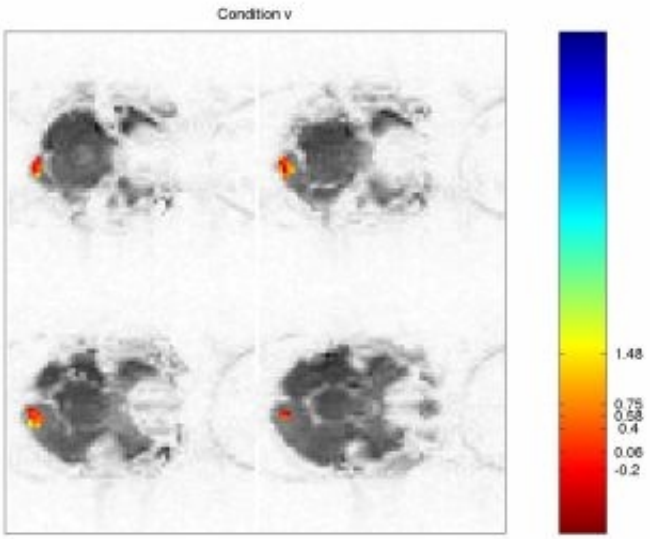

Figure 3 : Estimates of neural response levels for condition v

WE 368

Striatum Parameterisation : a new Basis for the Study of Neuro-Degenerative Processes in Huntingtons Disease

Renaud Maroy , Gwenaelle Douaud , Julien Dauguet , Jean F Mangin , Philippe Hantraye
Service Hospitalier Frédéric Joliot, CEA, Orsay, France.

If Huntington's disease causes are well know, the striatum degeneration it induces is not quite understood yet. Histology or T1 MRI modalities are mainly used to study the degeneration of striatum, heavily affected by Huntington's disease. T1 MRI modality suffers from a lack of resolution, but allows patients' follow-up, which is essential to model the degeneration process. T1 MRI studies use ROI volume measurement, (unable to catch local degeneration) or Voxel Based Morphometry with elastic transformation [1].
We introduce an absolute parametrization of the striatum that allows a cross-section to cross-section comparisons between subjects. Striatum has a long thin shape, thicker in putamen, thinner in caudate and folded up at ventral striatum. It can be modeled by an inner curve joining caudate and putamen extremities with cross-sections associated with each curvilinear abscissa.
Striatum inner curve is modeled in four automatic steps : (i) patients are co-registered using Talairach transform (with only 3 scaling factors) to correct for brain size inter-individual variability, (ii) extraction of putamen and caudate extremities, (iii) active contour model maximizing distance to striatum contour [2], (iv) extraction of the mass center of the cross-section of minimal size that goes through each active contour point. Curvilinear abscissa on inner curve point must be computed from a characteristic point existing even in strongly degenerated striata : we chose the inner curve point equally distant from putamen and caudate, obtained using a Voronoď diagram.
10 healthy subjects and 19 patients were manually segmented into putamen, caudate and ventral striatum. Inner curve and curvilinear abscissa were automatically extracted for each striatum. Inner curve based registration was compared to bloc-matching [3] applied on segmented striata images.
This absolute parametrization allows striata local thickness analysis and inner curve comparison by simple matching of curvilinear abscissa. This tool allows : (i) analysis of inner curve non linear deformation of the inner curve due to degeneration, (ii) registration using best least square affine transformation between matched inner curve points and (iii) measurement of the gradient of degeneration speed along inner curve due respectively to age and Huntington's disease.
[1] M. J. Thieben and al., "The distribution of structural neuropathology in pre-clinical Huntington's disease", Brain, 2002.
[2] L. Cohen, R. Kimmel, "Global Minimum for Active Contour Model : A Minimal Path Approach", Internal Journal of Computer Vision, 1997.
[3] S. Ourselin and al, "Reconstructing a 3D Structure from Serial Histological Sections", Image and Vision Computing, 19(1-2):25-31, January 2001.

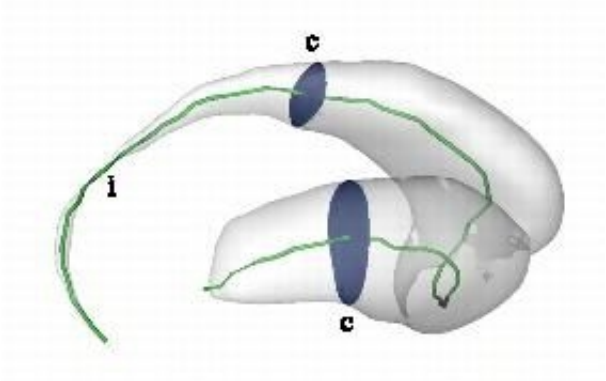

Striatum inner curve (i), and cross-section(c)

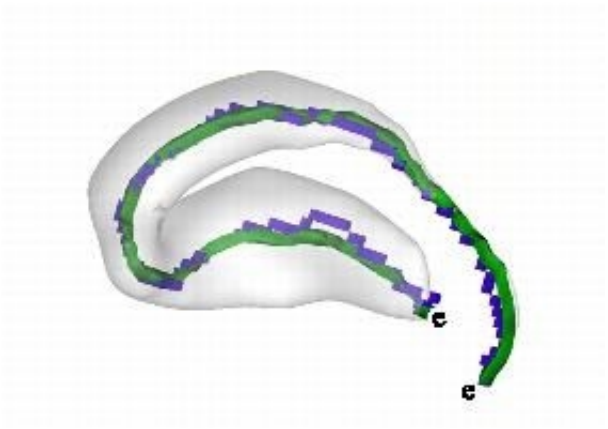

Extraction of : caudate and putamen extremities (e), active contour (blue), inner curve (green)

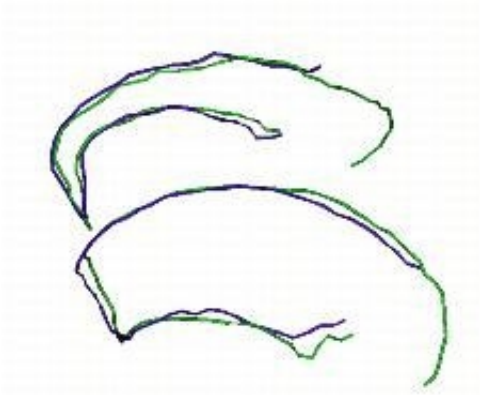

Healthy subject (green) and patient (blue) registration

WE 369
Analysis of Brain Image Data using Sequence Analysis Techniques

Vasileios Megalooikonomou[1,2], Qiang Wang[1,2], Despina Kontos[1,2], Guo Li[1,2], James Ford[3], Andrew Saykin[4,5]

[1]Department of Computer and Information Sciences, Temple University, Philadelphia, PA, USA, [2]Center for Information Science and Technology, Temple University, Philadelphia, PA, USA, [3]Department of Computer Science, Dartmouth College, Hanover, NH, USA, [4]Brain Imaging Laboratory, Departments of Psychiatry & Radiology, Dartmouth Medical School, Lebanon, NH, USA, [5]New Hampshire Hospital, Concord, NH, USA

Purpose:
To analyze the spatial patterns extracted from MRI and fMRI and facilitate searches for similar patterns in brain images based on their information content we propose the use of space filling curves and time series techniques.
Methods:
We developed a methodology for analyzing regions of interest in MRI (e.g., lesions, tumors) and fMRI (areas of brain activity). We first linearize a 3-D brain image by traversing the 3-D space using the Hilbert space-filling curve. This curve has been proved optimal in preserving the locality and clustering properties of data after the domain transformation. We then discover discriminative patterns by analyzing the spatial sequences in the transformed domain. In previous work by Kontos et al. [1], after the use of space filling curves, statistical tests of significance are applied to groups of points (that correspond to voxels) in the transformed domain to detect discriminative patterns. Here, in addition to the use of statistical tests and due to the similarity of the sequences with time series we propose the use of time series similarity techniques for further analysis of the spatial patterns. These techniques include Euclidean distance and dimensionality reduction techniques such as Discrete Fourier Transform, Discrete Wavelet Transform, Singular Value Decomposition, and Piecewise Aggregate Approximation.
Based on the distance (dissimilarity) calculated with these different methods, we performed experiments on clustering and similarity retrieval of brain images. For the experiments we used an fMRI contrast data set obtained from a study that was designed to systematically explore neuroanatomical correlates of semantic processing in Alzheimer's disease by contrasting patterns of activation in patients with those of controls during a series of semantic decision tasks. Each class of this dataset consisted of 9 subjects and the experimental results were evaluated using 9-fold cross validation.
Results:
The majority of the significant regions determined by this technique were within the medial temporal lobe. Experimental results using the time series analysis techniques when applied on the linearized brain image data showed that the discovered spatial patterns have strong discriminative power among different classes and the overall accuracy for clustering and similarity retrieval was above 90% and as high as 100% for certain experimental settings. These results are very encouraging showing that the methods are very robust and can deal with small and noisy datasets.
Conclusions:
By mapping the 3D space to 1D and applying statistical tests of significance in the linear domain, we detected discriminative patterns, which can be represented as time series. Preliminary experiments with an fMRI data set demonstrated that the employment of time series analysis methods to examine similarities among 3D images is very promising since it is very efficient and accurate.
Acknowledgements:
This work was supported, in part, by NSF (IIS0237921, IIS0083423), NIH (R01-MH068066-01), Alzheimer's Association and NIA AG19771.
References:
[1] D. Kontos, V. Megalooikonomou, N. Ghubade, C. Faloutsos, "Detecting discriminative functional MRI activation patterns using space filling curves", in Proceedings of the 25th Annual International Conference of the IEEE Engineering in Medicine and Biology Society, Cancun, Mexico, pp. 963-967, Sep. 2003.

WE 370

Comparison of various methods for detecting activation using PET

Catalina T. Mesina[1,2], Geurt Jongbloed[2], Ronald Boellaard[1], Aad W. van der Vaart[2], Adriaan A. Lammertsma[1]

[1] PET Center, VU University Medical Center, Amsterdam, The Netherlands, [2] Department of Mathematics, Vrije Universiteit, Amsterdam, The Netherlands

Introduction: The results of a PET activation study usually are expressed as a Statistical Parametric Map (SPM) [2]. This method is dependent on the reconstruction method used [3]. The raw data in the sinograms, however, can provide sufficient information about changes in activity distribution due to a specific task. Nevertheless only few PET activation studies follow a Sinogram Based Method (SBM) analysis as presented by Votaw and Li [5] and Cherry et al. [1]. In the present study an alternative SBM is presented based on the Poisson likelihood ratio statistic framework [4]. In addition, a method is developed for realignment of scans that is not based on reconstructed images. Further, the output of this new method, Sinogram Testing Mapping (STM), is compared with the other SBM methods and SPM.

Methods: First, a cylindrical phantom, containing 2 inserts with diameters of 2.5 and 3 cm, was used. This was filled with an aqueous solution of 18F, which is similar to the concentration seen in the human brain during $H_2{}^{15}O$ activation studies. The spheres were filled with an activity concentration equal to the background to simulate the baseline condition, and 20% higher activity concentration than background to simulate a cognitive task. Four scans were acquired for both conditions. Scans were performed using an ECAT EXACT HR+ (Siemens/CTI) PET scanner.

Secondly, computer simulations were used to generate sinogram data corresponding to an elliptical phantom (15x20 cm) filled with a homogeneous background activity. To simulate regions with increased CBF, spherical inserts with diameters of 1.5 or 3 cm were included in the phantom. The concentration within these inserts was 20% higher than background. Sinograms were generated containing 500000 counts, similar to the average number of counts for a 3D PET scan per plane. Data were simulated with attenuation and randoms. Five baseline and five activated sinograms were simulated and combined to form STM, Votaw and Cherry maps, to test for differences between both conditions. In addition, all sinograms were reconstructed using OSEM4x16. For the reconstructed images, SPM maps were created. The comparison was based on difference maps of the thresholded statistical maps and the true activation map.

Results and conclusions: Phantom and simulated data indicate that SBMs are good alternative for SPM in single subject PET activation studies. The minimal distance between activation map and template image was 2-4 times smaller for the SBMs than for SPM. No large differences between the SBMs were observed for low sphere to background contrast ratio. STM, however, performed better for higher (>4) contrast. An advantage of the SBM methods is that they do not require reconstruction of individual images. In addition, here it is shown that realignment of scans can be performed before reconstruction, using a recipe that applies to all SBM methods.

References:

[1] Cherry SR, Woods RP *et al.* in *Quantif. of Brain Funct.*:331-337 (1993)

[2] Friston KJ, Holmes AP *et al.*; *Hum. Brain Mapp* **2**: 189-210 (1995)

[3] Mesina CT , Boellaard R *et al. NeuroImage* **20**: 898-908 (2003)

[4] Mesina CT , Jongbloed G *et al. Journal Cereb. Blood Flow Metab.* **23**: 609 (2003)

[5] Votaw JR and Li HH. *Journal Cereb. Blood Flow Metab.* **15**: 492-504 (1995)

WE 371

Comparison of Parametric and Nonparametric Statistical Methods in a Voxel-Based Morphometry Study of Co-morbid Learning Disability with Schizophrenia

T. William J. Moorhead , Dominic E. Job , Heather C. Whalley , Eve C. Johnstone , Stephen M. Lawrie
Division of Psychiatry, Edinburgh University

Introduction

Voxel-based morphometry employing parametric analysis is an established means of testing for localised neuroanatomical difference between patient groups (1). The parametric analysis assumes the data to have a normal distribution and correction for multiple comparisons is based upon a measure of the spatial smoothness for whole brain statistics. Nichols & Holmes (2) have developed a nonparametric method that is not reliant upon an assumption of data normality or on smoothness estimates for correction. This permutation method requires significantly more processing resources than an equivalent parametric analysis. We demonstrate agreement of parametric and nonparametric results and illustrate the use of the nonparametric method for the validation of group labelling.

Methods

We implemented grey matter structural brain analyses on a four-group cohort. This age and sex matched cohort includes groups of normal controls, learning disabled, schizophrenia and co-morbid learning disability with schizophrenia. Grey matter pre-processing of MRI T1 scans was performed using SPM99 (1). A grey matter optimised methodology (3) allowed the structurally diverse brains in this cohort to be normalised into a common stereotactic space. ANCOVA was implemented on the cohort using SPM99 and parametric contrast analyses performed. Equivalent nonparametric contrast analyses were performed using SnPM (2).

Results

A height threshold of $t>3.18$ is used in the parametric contrasts; above this threshold the statistical analysis reports local maxima P-corrected < 0.05 with voxel separation > 4mm. The nonparametric analysis assesses significance based on the ranking of the observed maximal t-statistic within a distribution of maximal t-statistics recovered from 1000 random permutations of the contrast labels. Table 1 tabulates the nonparametric maximum t-statistic rankings of all possible contrasts in our cohort and gives the location of grey matter reductions in the corresponding parametric contrast analyses.

Discussion

In Table 1 where the nonparametric statistical analyses indicate a rejection of the null hypothesis we find the parametric analyses return focal point grey matter reductions that confirm the hypothesis rejection. Where there are no focal grey matter reductions in the parametric analyses the nonparametric results give a ranked p-value > 0.05. It is noted that the co-morbid and schizophrenia groups have similar grey matter distributions in normalised space (4). This similarity between the schizophrenia and co-morbid groups and their difference to the normal control and learning disability groups was previously found in an ROI study of this cohort (5). Our results demonstrate that nonparametric maximum t-statistics provide a means for the validation of contrast labelling used in parametric analyses.

References

[1] Ashburner & Friston, Neuroimage 6: 209-17, 2000
[2] Nichols & Holmes, Hum. Brain Mapping 15: 1-25, 2001
[3] Good et al., Neuroimage 14: 21-36, 2001
[4] Moorhead et al., Neuroimage (accepted for publication Dec 2003)
[5] Sanderson et al., Lancet 354:1867-1871, 1999

Acknowledgment

This study was funded by the Welcome Trust: T.M. is funded by a programme grant from the Medical Research Council of Great Britain

Table 1				
Contrast	p-value 1000 permutations	Parametric p-value	Parametric Maxima location	Side
Normal Controls > Schizophrenia	0.012	0.041	Superior Frontal Gyrus	R
		0.045	Superior Temporal Gyrus	R
		0.011	Superior Temporal Gyrus	L
		0.036	Cuneus	R
		0.047	Cuneus	L
Schizophrenia > Normal Controls	0.909	No maxima with p-value < 0.05		
Normal Controls > Co-morbid	0.002	0.006, 0.039	Inferior Frontal Gyrus	R
		0.001	Inferior Frontal Gyrus	L
		0.007, 0.008	Superior Temporal Gyrus	R
		0.049	Fusiform Gyrus	R
Co-morbid >Normal Controls	0.92	No maxima with p-value < 0.05		
Normal Controls > Learning Disabled	0.001	0.011	Superior Temporal Gyrus	L
		0.026	Caudate Nucleus	L
Learning Disabled > Normal Controls	0.010	0.002	Postcentral Gyrus	R
Co-morbids > Schizophrenia	0.083	No maxima with p-value < 0.05		
Schizophrenia > Co-morbids	0.750	No maxima with p-value < 0.05		
Learning Disabled > Schizophrenia	0.049	0.015	Postcentral Gyrus	R
Schizophrenia > Learning Disabled	0.141	No maxima with p-value < 0.05		
Learning Disabled > Co-morbids	0.021	0.009	Postcentral Gyrus	R
Co-morbids > Learning Disabled	0.614	No maxima with p-value < 0.05		

WE 372
Mapping cortical thickness and gray matter density in first episode schizophrenia

Katherine L Narr[1], Robert M Bilder[2,3], Roger P Woods[3], David E Rex[1], Philip Szeszko[4], Delbert Robinson[4], YungPing Wang[1], Heather DeLuca[1], Dina Asuncion[1], Arthur W Toga[1,3], Paul M Thompson[1]
[1]Laboratory of NeuroImaging, Department of Neurology, Geffen School of Medicine at UCLA, Los Angeles, CA, [2]Departments of Psychology and Psychiatry and Biobehavioral Sciences, Geffen School of Medicine at UCLA, Los Angeles, CA, [3]Ahmanson-Lovelace Brain Mapping Center, Department of Neurology, Geffen School of Medicine at UCLA, Los Angeles, CA, [4]Department of Psychiatry Research, The Zucker Hillside Hospital, North Shore - Long Island Jewish Health Systems, Glen Oaks, NY

Introduction: Advanced image analysis tools may be necessary to isolate subtle and regionally-specific cortical gray matter abnormalities in schizophrenia not detectable in volumetric studies. We used novel brain mapping methods to identify and map regional reductions in cortical thickness and gray matter density in first episode schizophrenia. Cortical thickness and gray matter density mapping results were compared.
Methods: High-resolution (256x256x124; 1.5 mm slice separation) T1-weighted MR images were obtained from 72 (51m/21f) first episode patients (mean age = 25.1±4.7 SD) and 78 (33m/44f) healthy comparison subjects (mean age = 27.3±6.6). Scans were corrected for RF inhomogeneities, resliced into a standard orientation using a six-parameter rigid-body transformation and classified into tissue types after editing extra-cortical tissue from the data. Computational cortical pattern matching methods were used to spatially relate homologous cortical regions between subjects. Cortical thickness, defined as the distance from the cortical white-gray matter boundary to the cortical surface, was estimated at sub-voxel resolution from tissue-classified images at thousands of homologous cortical locations in each subject. Gray matter density was also measured at homologous cortical surface points by computing the proportion of gray matter voxels relative to other tissue types within a sphere with a fixed radius. Principal Components Analyses (PCA) were employed to reduce gray matter thickness and density values obtained across the cortex for use as dependent variables in statistical analyses. Diagnosis was included as a predictor variable and sex, brain volume and age as covariates. To reveal regional changes in gray matter thickness and density in first episode schizophrenia, statistical differences were compared at thousands of spatially homologous cortical locations and mapped in 3D.
Results: For global tissue volumes, only CSF showed significant diagnostic group effects (patients larger). Males possessed larger overall brain tissue volumes than females. For cortical thickness, the first principal component accounted for 33 percent of the total variance and revealed main effects of diagnosis ($p<.01$); sex ($p<.001$); and age ($p<.001$). Similar results were observed for gray matter density factor scores, where the first component accounted for 28 percent of the variance and showed significant effects of diagnosis ($p<.0001$), sex ($p<.04$) and age ($p<.02$). For both analyses, diagnosis and age effects remained after brain size correction. Additional principal components accounting for >5 percent of the variance showed only main effects of sex and/or age. No interactions between diagnosis and sex or hemisphere were observed for any of the components examined. Factor scores for cortical thickness and gray matter density were highly correlated. Cortical thickness statistical maps showed significant regional gray matter thinning in temporal, parietal and prefrontal regions bilaterally in first episode patients. Local reductions in gray matter density were observed in similar regions but were more pronounced in the superior temporal lobe.
Conclusion: Local reductions in cortical thickness and gray matter density are present at disease onset in brain regions linked with functional disturbances in schizophrenia. Cortical thickness and gray matter density mapping produce similar results, although the density metric may be influenced by diagnostic differences in extra-cortical CSF and surface curvature/complexity.

WE 373
Non-invasive characterisation of white-matter integrity in stroke

Jennifer M Newton[1], Geoffrey JM Parker[2], Ralf Deichmann[1], Daniel C Alexander[3], Nick S Ward[1], Robert Turner[1], Karl J Friston[1], Richard SJ Frackowiak[1]
[1]Wellcome Department of Imaging Neuroscience, University College London, UK., [2]Imaging Science and Biomedical Engineering, University of Manchester, UK., [3]Department of Computer Science, University College London, UK.

Introduction:
Probabilistic tractography techniques have been applied successfully to diffusion tensor imaging data to identify specific white-matter connections in the brain. [1] However, these techniques also have the potential to characterise disruption of fibre bundles by lesions.
In the case of lacunar stroke, the highly directional diffusion, observed in normal white matter tracts, is disrupted by lesions [2]. Hence, it should be possible to use these pathology-related changes, within a tractography framework, to disclose abnormal streamline topography. Here we use a tractography technique that utilises whole-brain crossing fibre information to map the probabilistic topography of cerebral connections from the cerebral peduncles in a patient with a small lesion of the corona radiata.
Methods:
A patient with a small chronic infarct of the corona radiata was studied. (Fig-1) Using a 3-T Allegra MRI system (Siemens), whole brain DTI data were acquired with 64 diffusion-weighted images, acquired in non-collinear directions ($b=1000\ smm^{-2}$). The total acquisition time was ~23 minutes. A structural T1-weighted image was also acquired.
A spherical harmonic model was used to classify the diffusion occurring at each voxel as order 0 (isotropic diffusion), order 2 (single-tensor diffusion) or order 4 (multi-tensor diffusion). [3] In order 4 voxels, a mixture of two Gaussian densities was fitted, with the principal diffusion directions of the two tensors affording estimates of the orientations of probable crossing fibres. [4]
The cross-sections of each of the cerebral peduncles were used as seed points for the probabilistic tracking of the descending fibres, in each hemisphere, using the Probabilistic Index of Connectivity (PICo) framework. This allowed maps of connection probability from the cerebral peduncle to be generated. [1] Tracking was terminated if a non-parenchymal or lesioned voxel was reached.
Results:
Maps of connection probability for each peduncle were overlaid on the co-registered T1-weighted image as shown in Fig-2. A break in the topography of connection probabilities, marked by a magenta arrow, can be seen in the affected hemisphere directly above the lesion (Fig-2A) and in subsequent superior slices (2B-C), whereas the topography is continuous in the corona radiata of the healthy hemisphere. The discontinuity in the lesioned hemisphere is adjacent to the anterior bank of the precentral sulcus, suggesting that the lateral premotor cortex is the probable cortical origin of the descending fibres interrupted by the subcortical lesion. (Fig-2C, central sulcus marked in red)
Conclusion:
We successfully used a probabilistic tractography technique to map a discontinuity in the topography of connection probabilities between the cerebral peduncle and cortical grey matter. This technique has the potential to provide quantitative and topographic measures of tract integrity that may have an important role in predicting recovery and reorganisation following white matter lesions.
References:
[1] Parker et al (2003) JMRI 18:242-254.
[2] Werring et al (2000) JNNP 69:269-272.
[3] Alexander et al (2002) MRM 48:331-340.
[4] Parker & Alexander (2003) LNCS 2732:684-695.
This work was supported by Action Medical Research and the Rosetrees Trust.

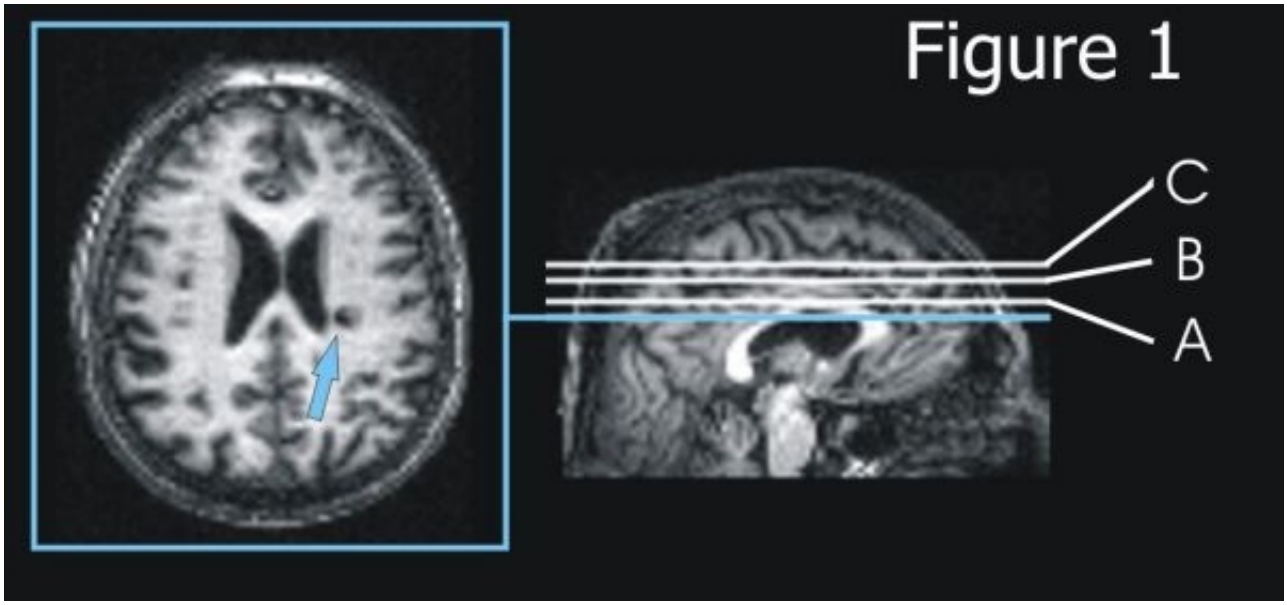
Figure 1
C
B
A

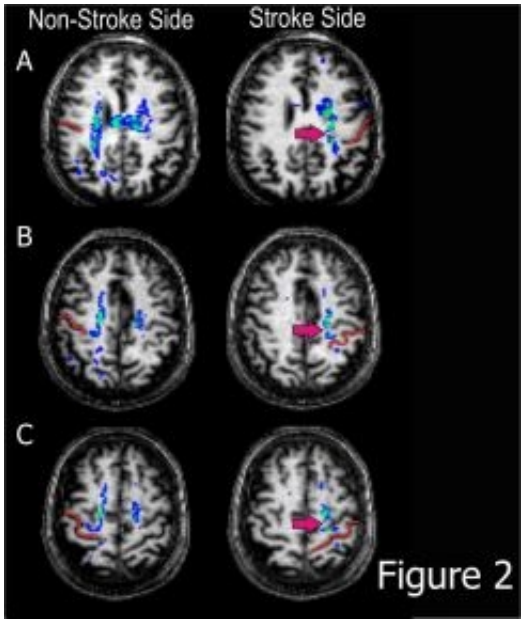
Non-Stroke Side
Stroke Side
A
B
C
Figure 2

WE 374
Voxel Based Morphometry in Bipolar Disorder

Allison C Nugent[1], Michael P Milham[2], Earle E Bain[1], Dara M Cannon[1], Linda Mah[1], Carlos Zarate[1], Daniel Pine[1], Dennis Charney[1], Wayne C Drevets[1]
[1]Mood and Anxiety Disorders Program, NIMH, Bethesda, MD, [2]The Beckman Institute, University of Illinois at Urbana-Champaign

Background: Neuromorphometric abnormalities are known to occur in bipolar disorder (BD). Post mortem studies have shown reduced cortical volumes in the prefrontal cortex of bipolar subjects a result confirmed by imaging studies utilizing hand segmentation of MRI images subjects (Ongur et. al., 1998). The current study utilized voxel based morphometry (VBM) to detect volumetric abnormalities in BD without hand segmentation.
Methods: Medically healthy subjects ages 19 to 60 who had no psychiatric history (n=37; 28 female; age 38.05±11.97), or had BD type II and had been off neurotrophic medications for at least 4 months (n=9; 7 female; age 37.11±8.16) or who were currently or recently on neurotrophic medications (n=11; 9 female; age 45.45±8.96) were imaged using a GE 3T MRI scanner, running an MP-RAGE pulse sequence optimized for tissue contrast. Images resolution was 0.9x0.9x1.2mm. Images were first skull stripped, using the FSL tool BET (FMRIB, Oxford, UK) and manual editing, then segmented into gray matter (GM), white matter (WM), and CSF using the FSL tool FAST. Images were then spatially normalized to a skull stripped template using SPM99 (Wellcome Department of Cognitive Neurology, Institute of Neurology, London). Both and affine and non-linear transformation were calculated, using 8x8x8 nonlinear discrete cosine transformation basis functions, and 16 iterations of the nonlinear optimization algorithm (Ashburner, et. al.). Regularization was used to prevent large non-linear warps. The regularization parameter was varied, with heavy regularization resulting in less distortion of the cortical surface and light regularization resulting in more accurate normalization of internal regions. In order to examine absolute volume, images were modulated by the Jacobian determinant of the transformation matrix, so that intensity at each voxel reflected the absolute amount of GM or WM. Images were then smoothed using a 12mm FWHM Gaussian smoothing kernel. GM and WM images were compared using an AnCova, with age and gender modeled as nuisance variables. For the affine transformation, statistics were calculated with and without the total GM or WM as a covariate, to examine relative and absolute volumes. Images shown are thresholded at $p<0.001$ uncorrected, with an extent threshold of 25 voxels. Reported p-values were corrected for multiple comparisons across the entire volume.
Results: The most consistent result observed was a decrease of WM and a corresponding apparent increase of GM in the precuneus/cuneus/posterior cingulate cortex in medicated BD subjects with respect to both healthy controls and unmedicated subjects. This effect was most significant in images normalized using an affine transformation only, although there were significant voxels with all routines. For WM, affine normalization with total WM covariate, medicated BD < normal control gave $p = 0.062$; while medicated BD < unmedicated BD gave $p = 0.011$. In GM, affine normalization, BD > normal control gave $p = 0.016$, while medicated BD > unmedicated BD gave $p = 0.003$.
Discussion: Voxel based morphometry offers an alternative to hand segmentation, as it examines the gray matter and white matter content at each voxel. The decrease in WM combined with the perplexing increase in GM could be an actual effect, or the result of group based shape differences, or a misclassification of WM voxels as GM. The decrease in white matter in the cuneus/posterior cingulate is potentially consistent with a reduction in oligodendroglia and reduction in the splenial portion of the corpus callosum observed in mood disorders. (reviewed in Drevets, et. al. 2003). The region found to be abnormal in this study is known to function as visual association cortex, and may be related to the processing of the affective valence of stimuli.
References:
Ashburner et. al., Hum Brain Mapp. 1999; 7(4):254-66.
Drevets et. al., Neurobiology of Mental Illness, ed. Charney, D. et. al., Oxford University Press, 2003.
Ongur, et. al., Proc Natl Acad Sci. 1998; 95(22):13290-5.

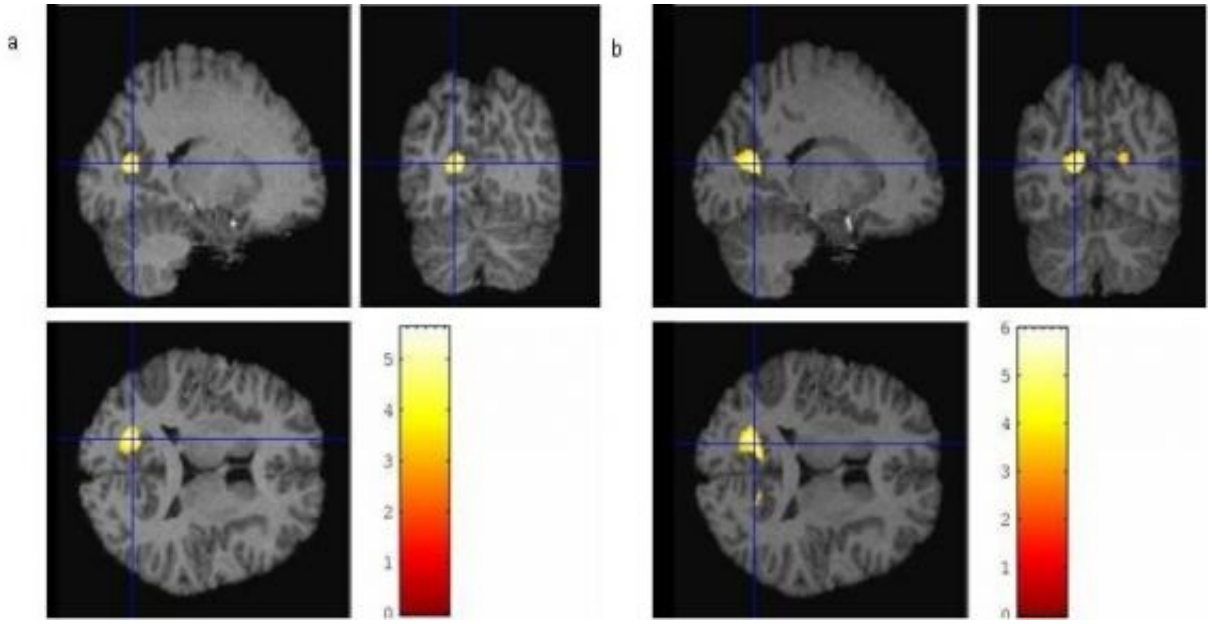

T-map of WM volumetric decreases in medicated BD subjects as compared to a) healthy controls; Tmax = 5.08, and b) unmedicated BD subjects; Tmax = 5.66

WE 375
Combined Electrical Source Imaging and Independent Components Analysis in Seizure Localization

Nora O'Neill[1,2], Donald Gross[3], Zoltan Koles[1]
[1]Department of Electrical and Computer Engineering, [2]Department of Biomedical Engineering, University of Alberta, [3]Division of Neurology, University of Alberta Hospital

Localization of the seizure focus is essential for the effective treatment of focal epilepsy. Due to the blurring effect of the skull, the scalp EEG provides poor localizing information about the origins of epileptic events inside the brain. Also, epileptic events are usually obscured in the EEG by background activity and by artifacts such as might arise from the EKG. To reduce the blurring effects, Electrical Source Imaging (ESI) has been shown to be effective while decomposition methods such as principal (PCA) and independent components analysis (ICA) have been shown to be effective for extracting the epileptic events. We have combined ESI with ICA to produce an effective method for localizing the seizure focus in focal epilepsy.

Our method is based on the spatial-temporal model of the EEG, $\mathbf{P(t)=K\,J(t)}$, where **P(t)** represents a vector of scalp potentials at the electrode sites at each time slice, **K** is the lead-field matrix and **J(t)** is the cortical source-current activity at the same time slice. An estimate of the source-current activity $\mathbf{J_e(t)}$, called the ESI, is obtained using a pseudoinverse of K, $\mathbf{J_e(t)=K^*P(t)}$. We apply ICA to $\mathbf{J_e(t)}$ to obtain a spatio-temporal decomposition of the form $\mathbf{J_e(t)=WS(t)}$ where the separation criterion is the nongaussianity (kurtosis) of the temporal components in **S(t)**. In the decomposition, **S(t)** is interpreted as a matrix whose rows contain waveforms with maximally different levels of kurtosis and where the columns of **W** contain the intensities of each of these waveforms over the cortical surface. In PCA, the decomposition is based more simply on the rows of **S(t)** containing maximally different levels of variance.

Fig. 1 shows PCA and ICA applied to a 27-electrode EEG recorded from a patient with epilepsy. The recording was contaminated with EKG artifact. The top two waveforms in the figure show the first two components extracted from the cortical surface using PCA and the bottom two waveforms show the first two components extracted using ICA. The EKG artifact is clearly evident in the first component extracted with both methods, however the background level appears to be significantly less with ICA. The second components extracted with the methods are less similar although, once again, the spike complex is much more evident with ICA.

Figs. 2 and 3 show the intensities of the second components extracted with the two methods on the cortical surface of a three-concentric shell spherical model of the head. The intensity of the cortical activity underlying the components is most intense at the red elements, followed by the yellow, green and aqua elements. The figures indicate that the components extracted with PCA and ICA are both centered in the left temporal region, however the activity extracted with PCA is distributed quite strongly over the entire cortical surface. ICA, on the other hand, suggests a clear left-temporal focus with some left occipital involvement as well.

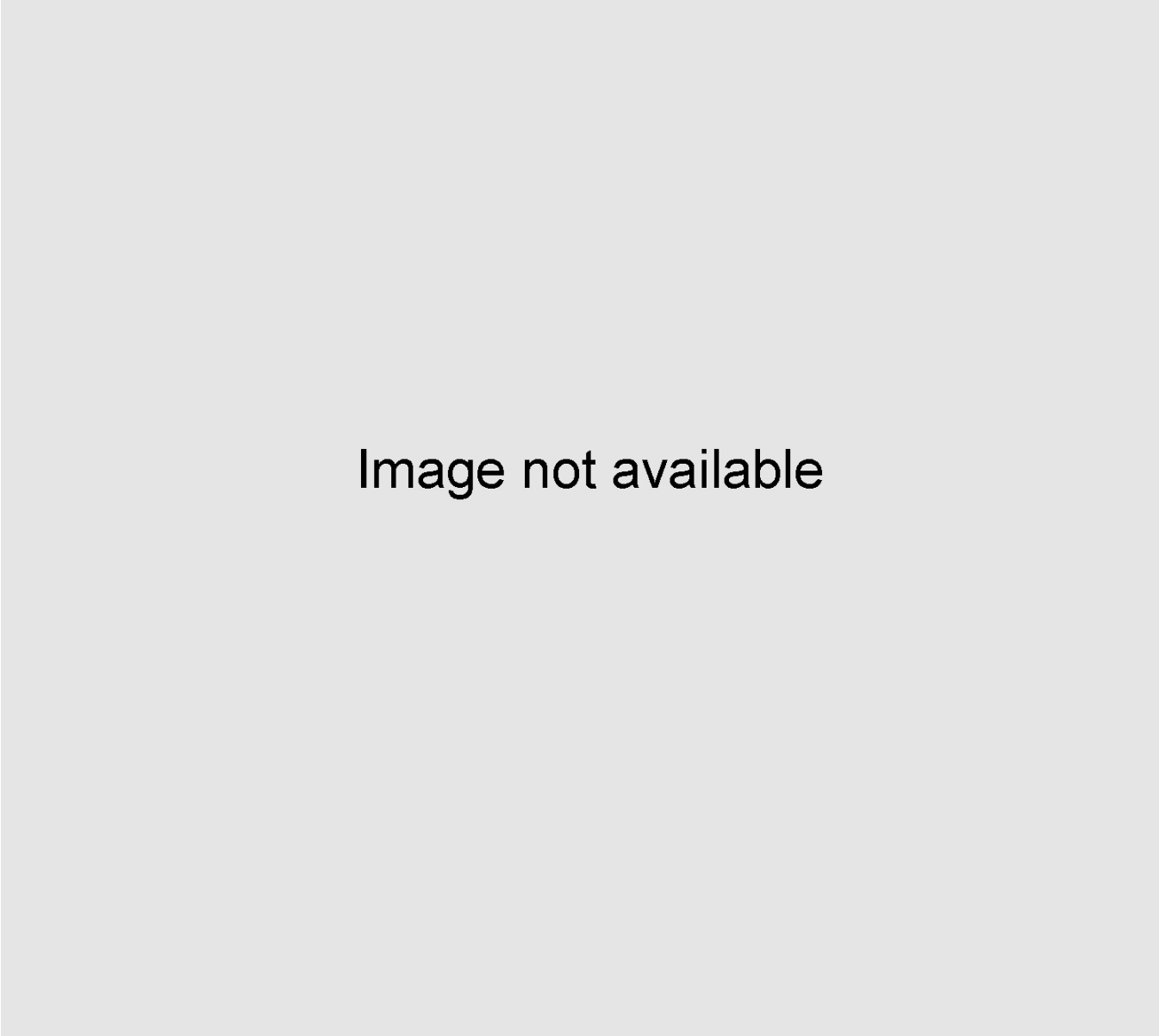

Fig. 1. The temporal components extracted with PCA and ICA

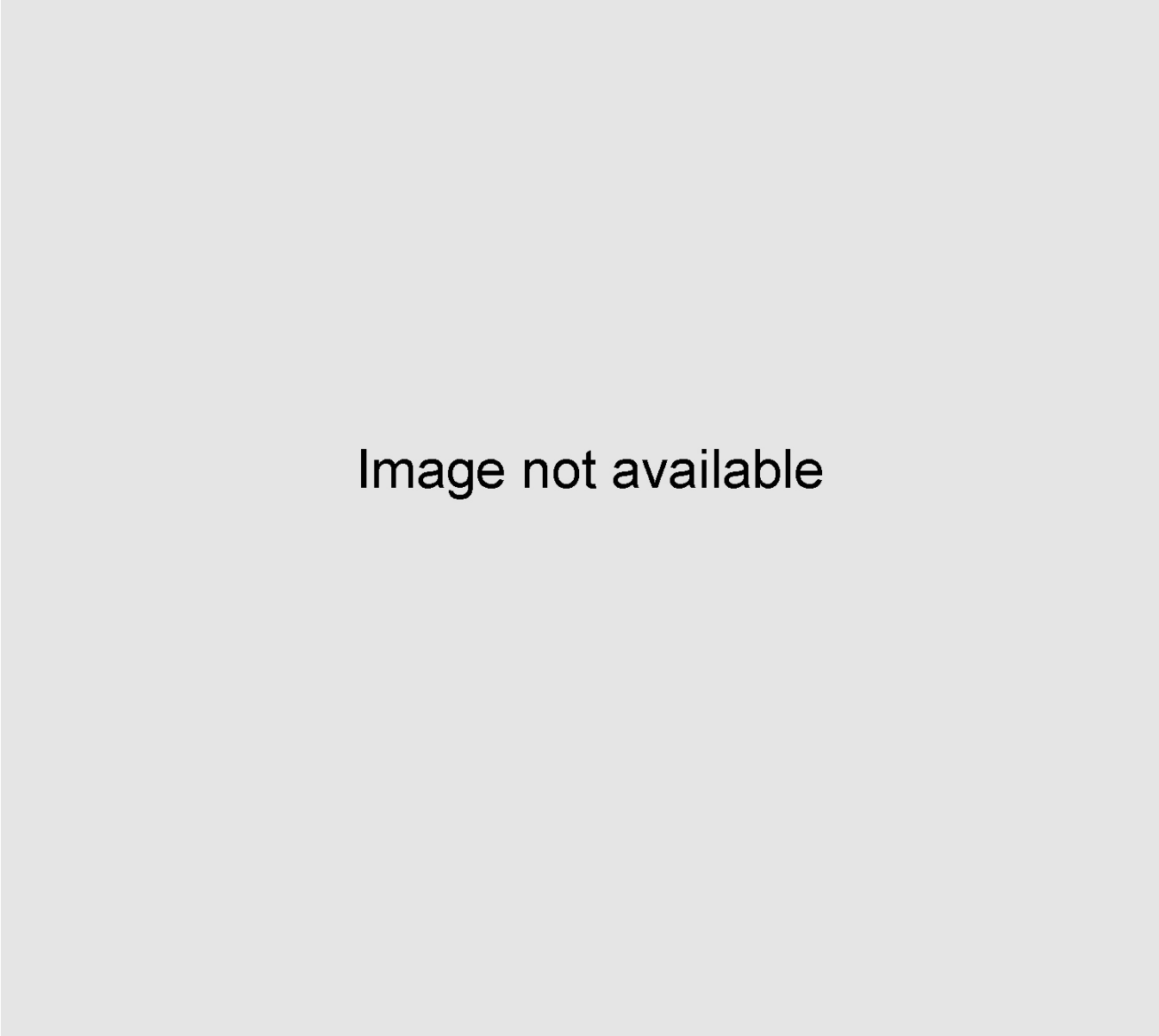

Fig. 2. The cortical distribution of the temporal component PCA-2

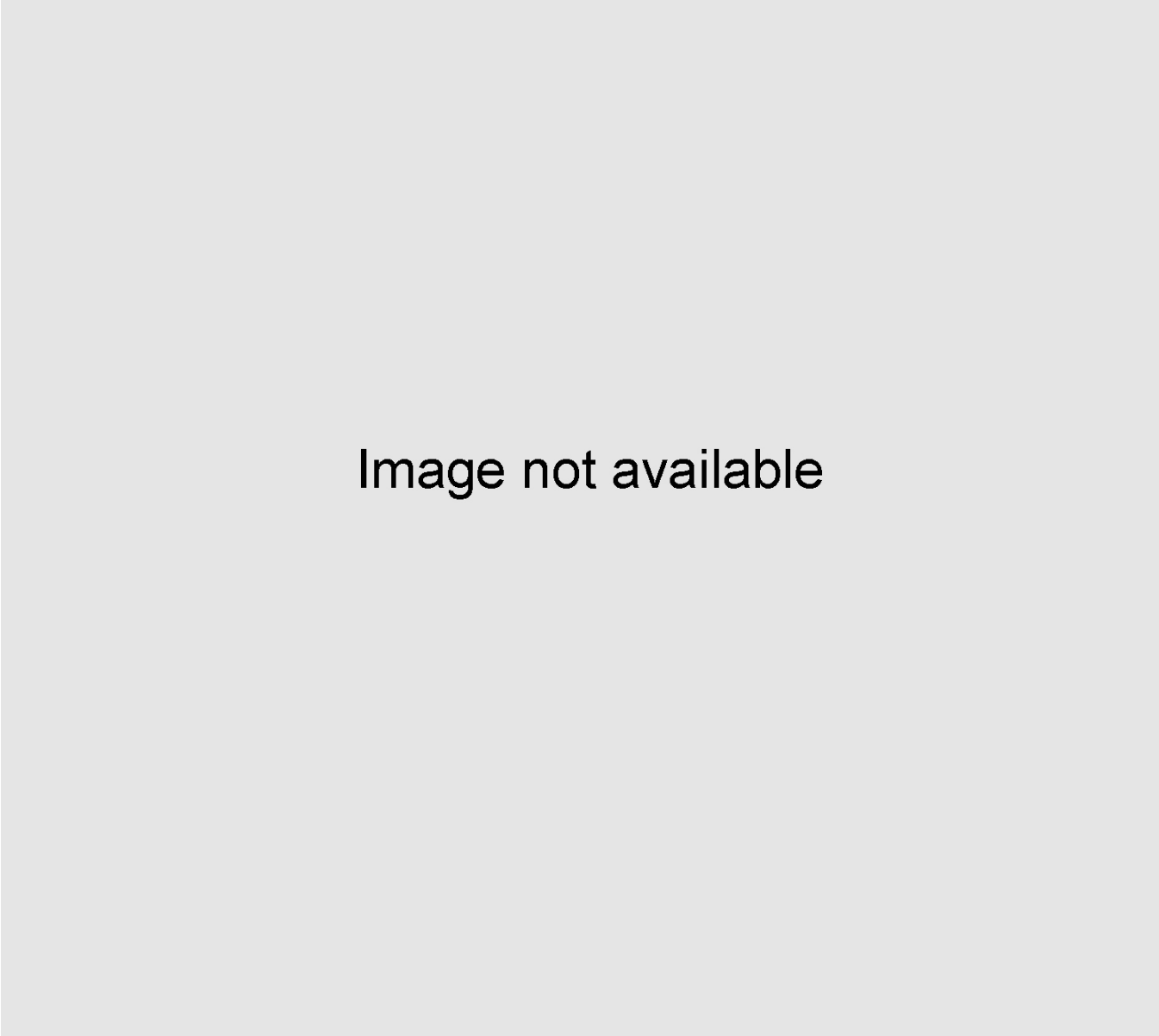

Fig. 3. The cortical distribution of the temporal component ICA-2

WE 376
A General and Extensible Database System for the Storage, Retrieval and Maintenance of Human Brain Imaging and Clinical Data

Burak I. Ozyurt[1], Dingying Wei[2], David B. Keator[2], Steven G. Potkin[2], Greg G. Brown[1], Jeffrey S. Grethe[1], Morphometry BIRN[3], FIRST BIRN[3]
[1]University of California, San Diego, La Jolla CA, [2]University of California, Irvine, Irvine CA, [3]Biomedical Informatics Research Network (http://www.nbirn.net)

To address the problems associated with managing the increasingly large and diverse datasets collected throughout the Biomedical Informatics Research Network (BIRN; www.nbirn.net) imaging communities, an extensible database management system has been developed and implemented as part of the Morphometry and Function BIRN test beds. This system is comprised of two core components:
1) The Human Imaging Database
2) A web based user interface (Figures 1,2 and 3)
The Human Imaging Database, a relational database currently implemented in Oracle, has been designed so that it can be extended to contain relevant information concerning the research subjects used in an experiment, subject assessments, the experimental data collected and their location, the experimental protocols used and any annotations or statistics (metadata) normally included with an experiment. Additionally, the database architecture uses row level fine-granular database security allowing data with different levels of security requirements to reside in a single database.
The user interface architecture is based on three tier Java 2 Enterprise Edition (J2EE) architecture and is illustrated in Figure 4. It consists of a thin client tier, a servlet/JSP based middle tier and a relational database based enterprise information source (EIS) tier. The client tier consists of a web browser. The EIS tier consists of the Human Imaging Database and a collection of stored procedures/packages for low level data access functions. The middle tier decouples presentation logic, the code preparing data to be presented to the user, and business logic, the code manipulating human brain imaging and/or clinical data, which allows flexibility in presentation layer selection and facilitates parallel multi-person/multi-site development. Each software layer communicates with neighbor layers via well defined interfaces, which remain stable while the actual implementation can change drastically over time facilitating software maintenance and robustness.
The complete system is used to maintain and query local human brain imaging databases for several Morphometry and FIRST BIRN sites. The current version provides an intuitive clinical and/or derived data complex query builder; query result export for statistical analysis tools; MRI image preview, conversion and download; subject visit and experiment management. A majority of the source code is generated from the database schema, allowing changes on the database schema to be reflected in the system easily. This has allowed BIRN sites to extend the database to reflect their site specific needs and data sets. The proposed architecture provides the extensibility, maintainability, security and parallel development features as demanded by the participating BIRN sites for building, accessing and maintaining their human brain imaging and related clinical data.
This research was supported by: BIRN Morphometric Project (BIRN002), BIRN FIRST Project (BIRN004), BIRN Coordinating Center (BIRN005) that are funded by the National Center for Research Resources (NCRR) at the National Institutes of Health (NIH).

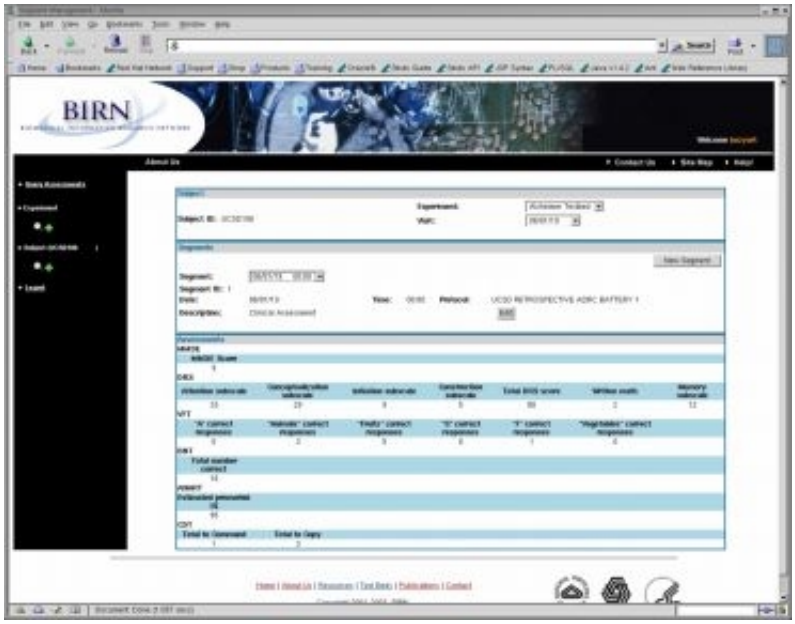

Visit detail and management interface for a subject that details visit and clinical information

Intuitive query builder allowing users to search on subject, clinical and statistical measures

Detailed MR scan information, from a subject returned by a query (figure 2), showing an anatomical preview with the option to download the data

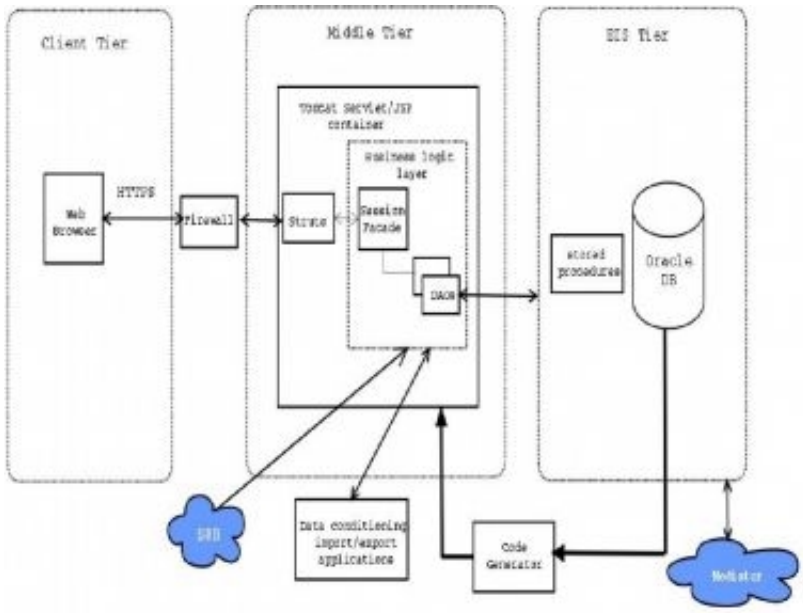

Tiered architecture of the Human Imaging Database system detailing the client, middle and enterprise information source tier

WE 377

Cortical GABA-A CBZR loss measured with ^{123}I-Iomazenil in Alzheimers disease: a SPECT study with Partial Volume Effect correction

Sabina Pappatà[1], Mario Quarantelli[1], Andrea Varrone[1], Andrea Ciarmiello[2], Valeria Sansone[3], Carmine Mollica[3], Alessandro Iavarone[4], Sergio Carlomagno[5], Alfredo Postiglione[6], Andrea Soricelli[7], Arturo Brunetti[3], Bruno Alfano[1]

[1]Biostructure and Bioimaging Institute, National Council for Research, Naples, Italy, [2]Nuclear Medicine, IRCCS Fondazione, [3]Department of Diagnostic Imaging, University Federico II , Naples, Italy, [4]Department of Neurological Sciences, University Federico II , Naples, Italy, [5]Departments of Clinical and Experimental Medicine, University Federico II , Naples, Italy, [6]Institute of Neurological Sciences, Second University of Naples, Italy, [7]Department of Diagnostic Imaging, University Partenope , Naples, Italy

Background: Cortical synaptic/neuronal loss has been reported in neuropathological studies of patients with Alzheimers disease and may contribute to GM density changes described recently in AD using VBM analysis of structural MRI images[1]. PET/SPECT markers of GABA-A central benzodiazepine receptors (cBZR) receptors have been proposed to detect in vivo early cortical synaptic/neuronal loss in AD. Only few studies have been reported with discordant results[2,3]. Moreover these results may be in part affected by errors due to partial volume effects (PVE), an issue particularly important when atrophy is associated to the disease, as in the case of AD.
Aim: The aim of this study was to investigate whether cortical synaptic/neuronal loss may be detected in vivo in AD patients using SPECT with ^{123}I-Iomazenil and to assess how the measurement of these receptor changes is affected by PVE. For this we used a ROI-based method for PVE-correction which takes into account both WM and CSF[4,5].
Materials and Methods: SPECT images were acquired during 20 minutes at 180 min after the intravenous injection of 111 MBq of ^{123}I-Iomazenil using a brain-dedicated camera (Ceraspect), providing 64 transaxial slices (voxel size 1.67x1.67x1.67 mm) reconstructed using a Butterworth filter and corrected for attenuation using the Changs algorithm (attenuation factor 0.120 cm-1)[6].
These 'late images' were assumed to reflect essentially receptor binding.
MRI protocol (1.5T Intera, Philips Medical Systems) included conventional spin-echo sequences providing T1w (600/15) and PD/T2w (2400/15-90) 3mm-thick axial images (25cm FOV, 256x256 acquisition matrix), sampling the entire brain at 32 levels.
MRI triplets were segmented into GM, WM, and CSF with a fully automated procedure[7].
8 AD patients (NINDS-ADRDA criteria; mean age 71 ± 10.5 yrs, MMSE: 19±4) 8 patients with Mild Cognitive Impairment (MCI, mean age 74±6.5 yrs, MMSE: 27±2) and only 3 healthy volunteers (HV, mean age 68±9, MMSE: 30) were studied.
GM, WM and CSF maps were co-registered to SPECT studies[8]. A set of regions of interest (ROI) including frontal, parietal, temporal and occipital lobes, hippocampus and posterior cingulate cortex for each side, and a single region for cerebellum, was defined in the MNI space and adapted to each co-registered segmented GM using the SPM99 affine normalization matrix. For each ROI, uncorrected and PVE-corrected mean tracer concentrations were calculated and normalized by corresponding cerebellum values.
Comparisons between MCI, AD and HC groups were performed by two tailed Student's T-test. Significance level was set to $P<0.05$. Although the number of HC is obviously too small for statistical inference, we report the results of AD and MCI comparison with HC because they are interesting for the general understanding of the results.
Results: Before PVE-correction, as compared to HC the AD revealed a significant ^{123}I-Iomazenil reduction bilaterally in the hippocampus (Right: $p<0.01$; Left:$p<0.05$) and in the parietal lobes (both $p<0.05$) while the MCI only showed a non significant trend for reduction in the Right hippocampus ($p=0.10$). These results were preserved after PVE-correction. The direct comparison of AD to MCI revealed a significant reduction of ^{123}I-Iomazenil in all cortical regions except the occipital lobes (p range: 0.05-0.003). After PVE-correction this decrease remained significant in the Right parietal lobe ($p<0.05$), the Right posterior cingulate ($p>0.001$) and in the left hippocampus ($p<0.02$).
Comments: These preliminary results provide two interesting observations: 1) In AD patients the

GABA-A-cBZD receptors are significantly reduced as compared to HC and MCI in the hippocampus, and other associative cortical areas. 2) This reduction survives the PVE-correction in some cortical areas particularly vulnerable in AD (hippocampus, parietal and posterior cingulate cortex).
Overall these findings suggest that GABA-A-cBZR alterations in AD exceed structural changes as measured by MRI segmentation. Further data are required to confirm these findings.
Acknowledgments: Support by the EC (QLK6-2000-00502 , QLG3-CT2000-594) and from the Italian Ministry of Health (Progetto Alzheimer, Attività di ricerca finalizzata D. Lgs. 502/92 e D. Lgs. 229/99, n. ICS150.1/RA00-47) is acknowledged.
References:
1) Baron JC, et al. Neuroimage 2001 ; 14:298-309
2) Meyer M et al, Arch neurol 1995; 52:314-317
3) Soricelli A, et al. Eur J Nucl Med 1996;23:1323-1328
4) Rousset OG, et al. J Nucl Med 1998;39:904-911
5) Quarantelli M, et al. 2003 HBM meeting 2003; Abs. 695
6) Chang, L. IEEE Trans Nucl Sci 1987;25: 638-643.
7) Alfano B, et al. Magn Reson Med 1997;37:84-93
8) Friston KJ, et al. Hum Brain Map 1995; 2:165189

WE 378

Brain Mapping of [^{15}O]-H_2O PET Scans Using Statistical Analysis in the Wavelet Domain

Monica Penedo , Juan D. Gispert , Santiago Reig , Juan J. Vaquero , Manuel Desco
Medicina y Cirugía Experimental. Hospital General Universitario Gregorio Marañón, Madrid, Spain

INTRODUCTION

In functional neuroimaging studies, wavelet analysis provides a multiresolution approach to the statistical analysis of brain activation regions. In this work, we present a wavelet-based statistical methodology for detecting activation regions. The method has been compared to the image-domain SPM approach, measuring sensitivity and specificity in a set of simulated [^{15}O]-H_2O PET studies.

METHODS

Simulated [^{15}O]-H_2O PET phantoms

Baseline [^{15}O]-H_2O PET scans were simulated (Fig.1): First, an MR image of a healthy subject was segmented into grey matter, white matter, and cerebral spinal fluid using a validated automatic method. Relative tracer concentrations were respectively set as 100:25:2. The PSF of the PET camera was simulated using a Gaussian filter (FWHM=8x8x6mm). This image was projected at 128 angles, 2:1 decimated, and its global count level set to $5x10^6$. Finally, Poisson noise was added before applying the inverse Radon transform.
Activated scans were similarly generated from the MR image by manually segmenting the thalamus and increasing its original intensity with factors of 2%, 5%, 10%, 15%, and 20% (Fig.1). For each activation factor, 3 baseline and 3 activation scans were obtained.

Wavelet-based statistical analysis

Figure 2 shows a flow-chart of the statistical wavelet-based analysis. For every simulated PET study, a 3D Discrete Wavelet Transform was applied to all scans (Symlets-4; fourth decomposition level). In the wavelet domain, mean images for each condition were subtracted to obtain a between-condition difference image. Student´s t-test was performed to detect wavelet coefficients showing significant between-conditions differences. An activation image in the spatial domain was reconstructed by applying the 3D Inverse DWT to the between-condition difference image with the statistically non-significant coefficients set to zero.
The activation image was thresholded to reduce the noise associated to the ringing artifacts produced by the reconstruction wavelet process. The threshold value chosen was the maximum difference that a Student´s t-test in the spatial domain would consider as non-activated with a statistical power of 80% (α= 0.01).

Evaluation

Evaluation of the wavelet approach was carried out comparing sensitivity at 99% and 95% of specificity for each PET study to that provided by image-domain SPM. The evaluation was also performed using pre-smoothed simulated scans (FWHM=5x5x5mm). Five experimental replications of the study were analyzed.

RESULTS

Sensitivity rates at 95% and 99% of specificity are shown in Figure 3. Figure 4 shows hyperactivity regions detected with the wavelet-based and SPM methods.

DISCUSSION

In PET studies, the wavelet transform allows performing the statistical analysis of activation differences between brain regions in a multiresolution scenario, compacting the relevant information associated to activated areas into a few coefficients. These features seem to yield higher statistical power than image-domain SPM, particularly in low activation and high noise situations. Previous studies presenting similar wavelet-based approaches claimed better results on the sole basis of an increment in sensitivity. Our assessment of the procedure, however, is based on sensitivity and specificity pairs.

CONCLUSIONS

Our statistical wavelet-based method outperform image-domain SPM in the detection of brain activity in simulated [^{15}O]-H_2O PET studies.

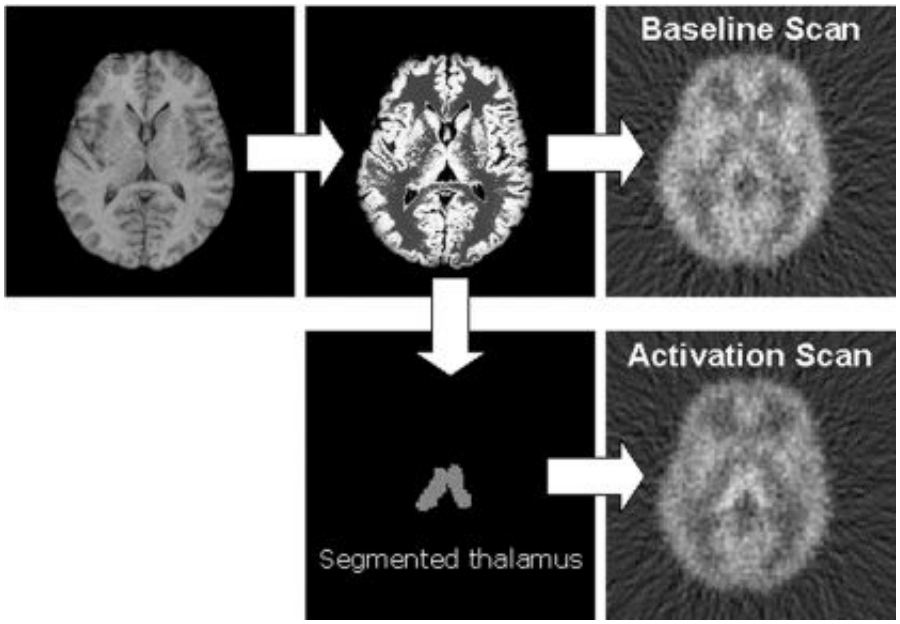

Figure 1. Simulation procedure of [^{15}O]-H_2O PET scans.

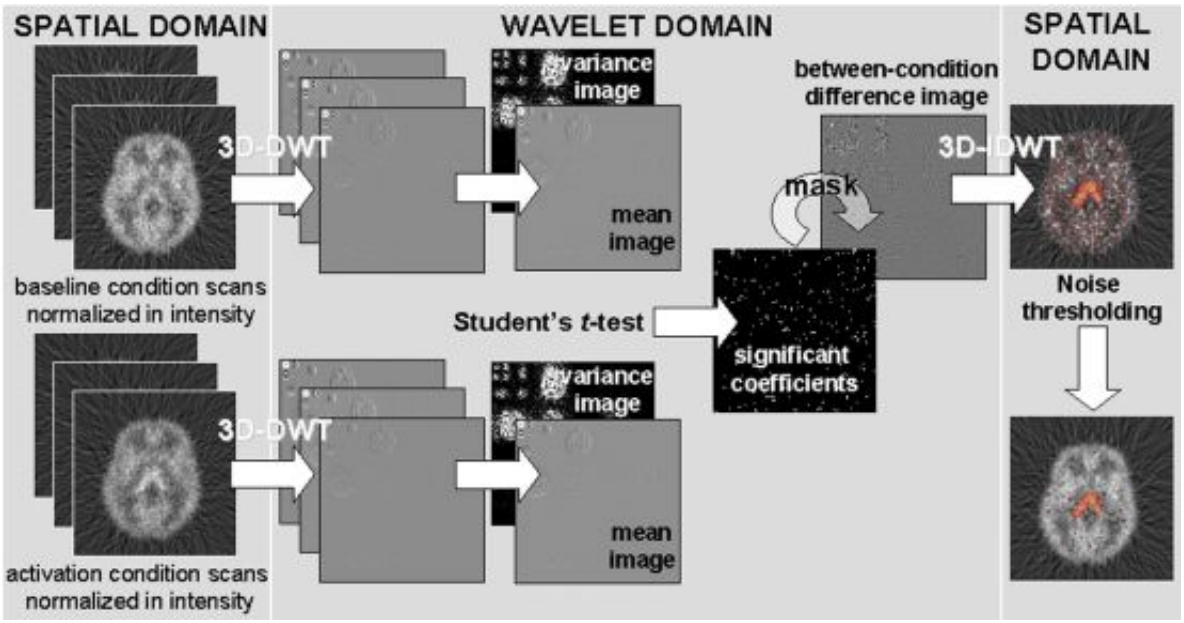

Figure 2. Statistical wavelet-based analysis for detecting brain activation regions.

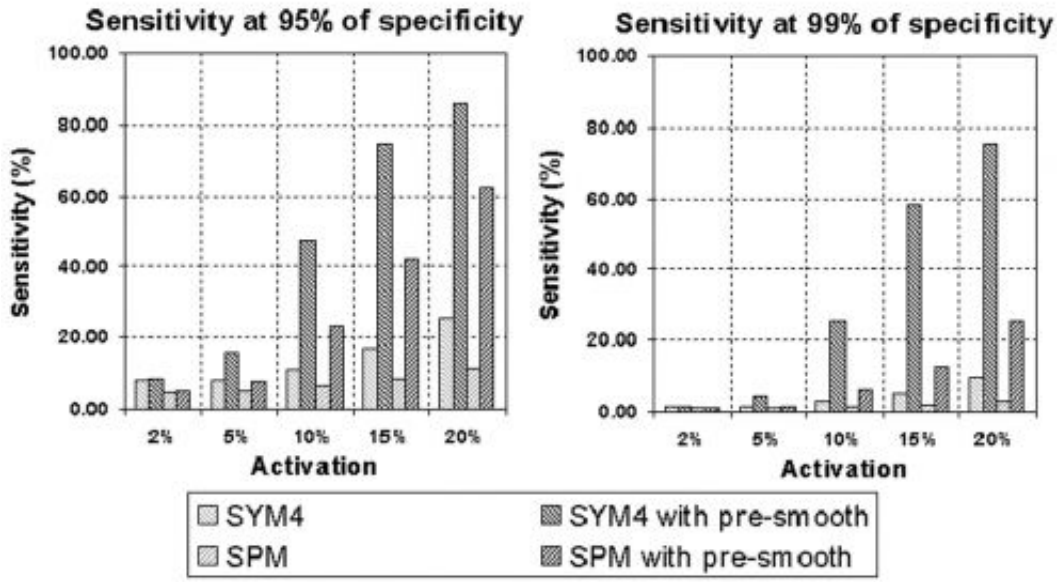

Figure 3. The statistical wavelet-based method substantially outperformed conventional image-domain SPM. When operating on smoothed images, a noticeable increase in performance was observed for both approaches, although the wavelet method still yielded better results.

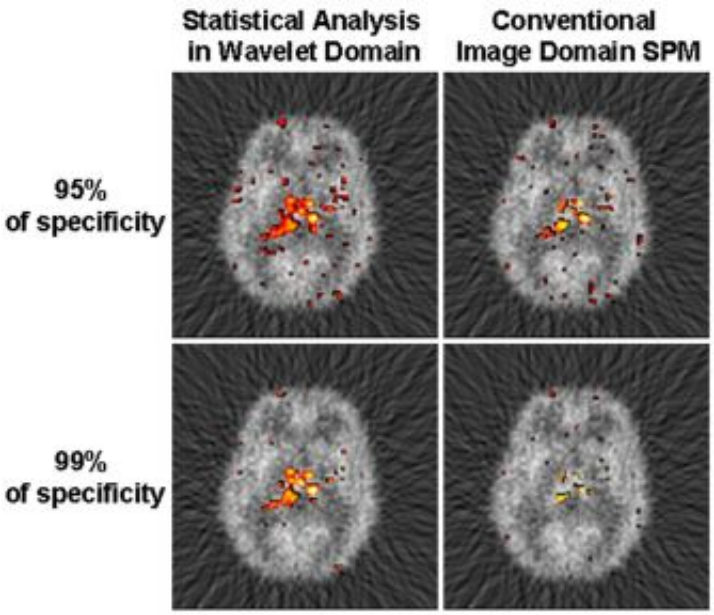

Figure 4. Pre-smoothed study with a 10% of thalamus activation level: at a fixed specificity rate, activation areas are closer in size and shape to real activations with the wavelet method than with SPM.

WE 379
rCBF in Alzheimer‘s disease versus Mild Cognitive Impairment: a SPECT study with Partial Volume Effect correction

Mario Quarantelli[1], Sabina Pappatà[1], Andrea Varrone[1], Carmine Mollica[2], Valeria Sansone[2], Elisa Lorè[2], Alfredo Postiglione[3], Sergio Carlomagno[4], Alessandro Iavarone[5], Bruno Alfano[1], Marco Salvatore[2]
[1]Biostructure and Bioimaging Institute, National Council for Research, Naples, Italy, [2]Department of Diagnostic Imaging, University Federico II , Naples, Italy, [3]Department of Clinical and Experimental Medicine, University Federico II , Naples, Italy, [4]Department of Neurology, University Federico II , Naples, Italy, [5]Institute of Neurological Sciences, Second University of Naples, Italy

Introduction: The progression from Mild Cognitive Impairment (MCI) to Alzheimers Disease (AD) is characterized by the increase in severity and extension of cerebral hypometabolism and regional cerebral blood flow (rCBF) [Nestor 2003], which are already detectable in posterior cingulate, hippocampus and temporal neocortex in MCI patients.
Concurrently, gray matter (GM) loss, essentially limited in MCI to hippocampal cortex [Chetelat 2002], progresses into a more widespread cortical loss.
It is not currently known weather this pattern of progression is characterized by a strict coupling of these two phenomena (i.e. GM loss explains the metabolism reduction as detected by FDG-PET and rCBF-SPET studies), or if metabolic impairment exceeds the rate of GM loss.
Aim of our study was to compare rCBF decrease independently of GM loss in two groups of MCI and AD patients, using a ROI-based method for partial volume effect (PVE) correction which takes into account both WM and CSF.

Material and Methods
12 subjects with Mild Cognitive Impairment (MCI, mean age 74.8 yrs, MMSE 27.8+/-2.0 range 24.9-30.0) and 10 AD patients (NINDS-ADRDA criteria; mean age 79.5 yrs, MMSE 21.2+/-2.4, range 16.9-24.0) underwent rCBF-SPECT and volumetric MRI.
SPECT studies were carried out 20-30 min after an intravenous injection of 740-1110 MBq of [99mTc]HMPAO (Ceretec®, Nycomed Amersham Sorin), using a 64-slice brain-dedicated camera equipped with a circular LEHR collimator (Ceraspect, Digital Scintigraphics, D.S.I, Waltham, MA, USA). Studies were acquired for 30 min in step-and-shoot mode (120 steps, 3° angular step, 15 sec per step, 128 x 128 matrix). Images (pixel size 1.673mm) were reconstructed using a Butterworth filter (cut-off = 0.9 cm^{-1}, order=10) and were corrected for attenuation assuming uniform attenuation within the skull, applying a zero order attenuation factor (0.120 cm-1) and the Changs algorithm [Chang, 1987].
Corresponding MRI volume data (magnetization-prepared 3D T1-weighted fast-GrE images, TR/TE/TI 11/2/600ms, 1.5T, voxel size 0.98x0.98x1.2mm) were segmented into GM, WM and CSF maps by probabilistic MRI segmentation [Ashburner J, 2000] and co-registered to SPECT studies [Friston KJ, 1995].
A set of cortical regions of interest (ROI) including cerebral lobes, hippocampus and posterior cingulate for each side, and a single region for cerebellum, was defined in the MNI space and adapted to each co-registered segmented GM using normalization parameters derived from the SPM99 affine normalization matrix [Berkouk 2003].
For each ROI, uncorrected and PVE-corrected mean tracer concentrations were calculated [Rousset OJ, 1998; Quarantelli M, 2003] and normalized by corresponding cerebellum values.
Comparison between MCI and AD groups was carried out for each region by Student’s T-test. Significance level was set to $P<0.05$.

Results
Before PVE-correction, temporal lobes (both hippocampus and lateral cortices) and posterior cingulate bilaterally ($P<0.01$), as well as right dorso-lateral prefrontal cortex ($P<0.05$), showed a significantly reduced CBF in AD as compared to MCI studies. After PVE-correction, only CBF decreases in left posterior cingulate remained significant ($P<0.05$).

Discussion
As compared to normal subjects, metabolic/CBF changes in AD are paralleled by GM loss [Baron JC, 2001a;

Karas GB, 2003]. Accurate voxel-based comparisons of these changes have shown that the atrophy explains the GM hypometabolism with the exception of the posterior cingulate [Baron JC, 2001b], an area known to be affected precociously in AD [Minoshima S, 2000].
Our results integrate these findings, showing in PVE-corrected rCBF-SPET data from AD patients, as compared to MCI, the same pattern of posterior cingulate involvement independent of GM loss.
Reduced metabolism in these regions may be related to remote functional disruption.
Longitudinal studies are needed to confirm this progression pattern.

Acknowledgments
Support by the EC (contract # QLG3-CT2000-594 and QLG3-CT2000-594) and from the Italian Ministry of Health (Progetto Alzheimer, Attività di ricerca finalizzata D. Lgs. 502/92 e D. Lgs. 229/99, n. ICS150.1/RA00-47) is acknowledged.

References

-Ashburner J, Friston KJ, NeuroImage 2000; 11:805-21
-Baron et al, NeuroImage 2001b; 13:S771
-Baron JC, et al. Neuroimage 2001a ; 14:298-309
-Berkouk K, et al. 2003 HBM meeting; Abs. 1017
-Chang, L. IEEE Trans Nucl Sci 1987;25: 638-643.
-Chetelat G, Baron JC. Neuroimage. 2003;18:525-541.
-Chetelat G, et al. Brain 2003; 126:1955-1967
-Chetelat G, et al. Neuroreport 2002; 13:1939-1943
-Friston KJ, et al. Hum Brain Map 1995; 2:165189
-Karas GB, et al. Neuroimage 2003; 18:895-907
-Minoshima S, et al. Ann Neurol 1997, 42 :85-94.
-Nestor PJ, et al. Ann Neurol 2003;54:343351
-Quarantelli M, et al. 2003 HBM meeting 2003; Abs. 695
-Rousset OG, et al. J Nucl Med 1998;39:904-911

WE 380
Analysis of first-episode schizophrenia patients sMRI and fMRI BOLD activation during the Tower of London Task using cortical pattern matching

Paul E. Rasser[1,2,3], Patrick Johnston[1,3], Jim Lagopoulos[1,2], Philip B. Ward[1,2], Ulrich Schall[1,3], Renate Thienel[1,4], Stefan Bender[1,4], Arthur W. Toga[5], Paul M. Thompson[1,5]

[1]Neuroscience Institute of Schizophrenia and Allied Disorders (NISAD), Australia, [2]School of Psychiatry, University of New South Wales, Australia, [3]Centre for Mental Health Studies, University of Newcastle & Hunter Medical Research Institute (HMRI) , Australia, [4]Clinic for Psychiatry and Psychotherapy, University of Duisburg-Essen, Germany, [5]Laboratory of Neuro Imaging, Department of Neurology, UCLA School of Medicine, USA

The organization of the human neocortex creates a challenge for accurate co-registration of grouped functional brain imaging data. While primary sensory and motor areas are well defined by distinct anatomical landmarks, other areas (such as those involved in complex cognitive processes) are anatomically less well defined and also highly variable between individuals. In addition, data derived from common spatial normalization techniques can be further distorted by brain pathology when investigating clinical populations.

This study addresses some of these limitations by employing cortical pattern matching techniques to derive gyral pattern average (GPA) models of the cerebral cortex for the co-registration of structural and functional brain imaging data. Three objectives were pursued: (1) compare difficulty-dependent Tower of London blood oxygenation level dependent (BOLD) activation represented on an intensity average (IA) model and a GPA model of the cerebral cortex; (2) to compare the cortical BOLD response of 10 first-episode male schizophrenia patients with 10 age and gender-matched healthy control subjects; (3) to analyse regional differences of cortical grey matter thickness between the two groups and its association with BOLD response.

Our results suggest that (1) both models (IA and GPA) generally produce an equivalent representation of BOLD response across hemispheres, cortical regions and groups, when using a deformable Brodmann area atlas as an anatomical reference. However, some closer association of Brodmann areas with primary visual and auditory areas were seen using the GPA model. (2) Analysis of statistically thresholded and clustered BOLD data showed predominantly right-hemispheric activation in healthy control subjects, particularly for the dorsolateral prefrontal and frontal cortex as well as for the temporal lobe. However, more extensive clusters of left-hemispheric activation were confirmed for the occipital lobe. For patients, the hemispheric dominance pattern was significantly diminished or reversed in the temporal, parietal and occipital lobes. The most significant group difference was found for decreasing cortical BOLD response with increasing task difficulty in the left superior frontal and superior temporal gyrus. (3) The assessment of cortical grey matter thickness by group performed on the GPA model suggests predominantly right-hemispheric reduction of grey matter in patients in the prefrontal, frontal and parietal cortex as well as the anterior temporal lobe and the hippocampus. Also for patients, reduced BOLD activation correlated with reduced cortical grey matter thickness, predominantly in the left prefrontal and frontal, as well as bilateral parietal cortex. These findings suggest first-episode schizophrenia patients exhibit an association between the subtle reduction of regional grey matter thickness and impaired brain function when performing the Tower of London task.

WE 381
A MEG/EEG analysis toolbox for BrainVisa

Denis P Schwartz [1,4], Karim N'Diaye [1,4], Anne Bellio [2,4], Jérémie Mattout [2,4], Mélanie Pélégrini-Issac [2,4], Yann Cointepas [3,4], Denis Rivière [3,4], Antoine Ducorps [1,4], Habib Benali [2,4], Line Garnero [1,4]
[1] MEG/EEG Center - LENA CNRS UPR640 - Pitié Salpêtrière - France, [2] INSERM U494 - France, [3] UNAF SHFJ CEA - France, [4] IFR 49 - NeuroImagerie

Introduction : We developed a new set of tools focused on MEG/EEG analysis for the BrainVisa software platform [1]. These tools include anatomical constraint definition and registration, gain matrix computation, inverse solution based on the BrainStorm Toolbox [2], advanced visualization using Anatomist [3] capabilities and statistical processing of MEG/EEG localizations results.
Pre-processing : Using the segmentation tools provided by the standard BrainVisa package, a set of processes (segmentation of scalp, skull, and brain interface, MEG/EEG to MRI registration and mesh decimation) was defined to analyze the structural MRI. White matter surface was used to build anatomical constraints necessary to our advanced localization algorithms. Forward problems (ie computation of MEG/EEG sensors gain matrix) were implemented through the BrainStorm Toolbox : several geometrical models are available : single sphere, multiple spheres and Boundary Element Method using the individual anatomy.
Inverse Procedure: Inverse approaches include classical weighted minimum norm (WMNE), spatio-temporal analysis (music, sptf). All methods work on MEG, EEG or a combination of both measurements. Both of our methods are based on BrainStorm advanced localization capabilities.
Time Frequency Analysis: We provide time-frequency analysis tools allowing computation of evoked and induced time-frequency maps based on wavelets transforms.
Visualization: We used Anatomist [3] to produce high quality visualization of our localization results. Mixing 3D anatomical MRI data and MEG/EEG localization (either simple dipoles or complex results from imaging localization approaches like WMNE), we provide the user the tools necessary to interpret efficiently his data : Visualization of activation on 2D MRI, on 3D surfaces, on inflated brains, movies generations, ROI definition and characterization (ie time course of activation).
Conclusion: Using the flexible framework of BrainVisa, we added the necessary tools allowing a complete analysis of electromagnetic signals from the forward problem computation to high end 3D visualization of the results. Several cognitive and clinical experiments (MEG/EEG CTF data) were analyzed using these developments. The batch processing capabilities built in BrainVisa speed the whole process (pre-processing and localization). These tools added to the existing capabilities of BrainVisa in term of segmentation, morphometry, labeling of the cortical folds, diffusion analysis and functional MRI tools offer a very coherent analysis platform to researcher, especially those working with multimodality functional data.
Futur developments include : non-supervised MEG/EEG artifact correction, inter subjects statistical post-processing and improved multimodality visualization approaches.
References :
[1] BrainVISA: Software platform for visualization and analysis of multi-modality brain data.
Y. Cointepas, J.-F. Mangin, L. Garnero, J.-B. Poline and H. Benali.
Neuroimage 13(6):S98, 2001
[2] Brainstorm . S. Baillet, J. Mosher and R. Leahy. To be published in Proceedings of IEEE Isbi 2004 Meeting
[3] Anatomist: A structural browser of brain anatomy. D. Rivi?re, D. Papadopoulos-Orfanos, J. Régis and J.-F. Mangin. NeuroImage, 11(5), HBM, San Antonio, 2000

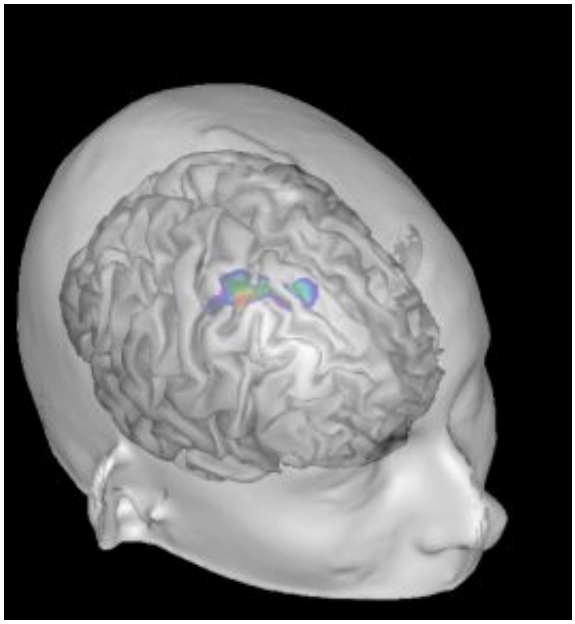

Figure 1 : ***MEG Motor activation (grasping task)***

WE 382
A Voxel-Based Morphometric Study of Alzheimer's Disease and Normal Aging: Evaluation of the Methods

Matthew L. Senjem , Jeffrey L. Gunter , Maria M. Shiung , Clifford R. Jack, Jr.
Mayo Clinic and Foundation, Rochester, MN, USA

Purpose:
Voxel-based morphometry (VBM) is an increasingly popular way to detect differences in brain morphology between different patient groups. The method provides an estimate of inter-group differences in gray matter concentration on a voxel-wise basis in standardized space. The approach is particularly popular in evaluating various neurodegenerative disorders, as a close relationship exists between localized cerebral atrophy and the resulting cognitive disturbances. However, a variety of options exist in implementation of specific steps in VBM. At each possible branch point within the VBM data processing chain, it is not clear which option or options produce better or more accurate results. The purpose of this project was to systematically evaluate the effects of varying certain elements of the VBM processing chain in the context of differentiating cognitively normal elderly subjects from patients with Alzheimers Disease (AD).
Methods:
Fifty-one probable AD and 43 cognitively normal elderly control subjects were selected from the Mayo Alzheimers Disease Research Center (ADRC) and Alzheimers Disease Patient Registry (ADPR). These are IRB approved prospective longitudinal studies of aging and dementia which incorporate MRI in the protocol. MR studies were performed at 1.5T with a standardized imaging protocol that included a T1 weighted 3-dimensional volumetric sequence with 124 contiguous partitions, 1.6 mm slice thickness, 22 x 16.5 cm FOV, 192 views, and 25 degree flip angle. The 51 AD and 43 control MR images were processed in two different ways: 1) standard VBM, 2) optimized VBM. In optimized VBM, spatial normalization of each individual volume is based on matching a gray matter segmentation of that volume with the gray matter template, whereas in standard VBM, spatial normalization is performed without prior segmentation. The two statistic maps produced from the above methods were displayed both corrected for and uncorrected for family-wise error.
Results:
Results of group effect (AD vs. control) voxel-wise analyses of gray matter are illustrated in Figures 1-4. Figure 1 is a tri-planar glass brain display of group effect using standard VBM and Figure 2 is a display of group effect with the same image data using optimized VBM. Figures 3 and 4 are displays of the data in figures 1 and 2, respectively, after correction for family-wise error. Figures 1-2 illustrate that the method of processing the data influences the output. Figures 1-4 illustrate that there is an interaction between the method of data processing and correcting the data for family-wise error. That is, one can draw fundamentally different inferences about how AD differs morphometrically from normal aging, due slight variation within the data processing chain.
Conclusion:
Relatively minor changes in the data processing chain of VBM will noticeably influence the results of intergroup morphometric comparisons. Inferring fundamental principles of biology from apparent intergroup differences in VBM analyses should be approached judiciously.

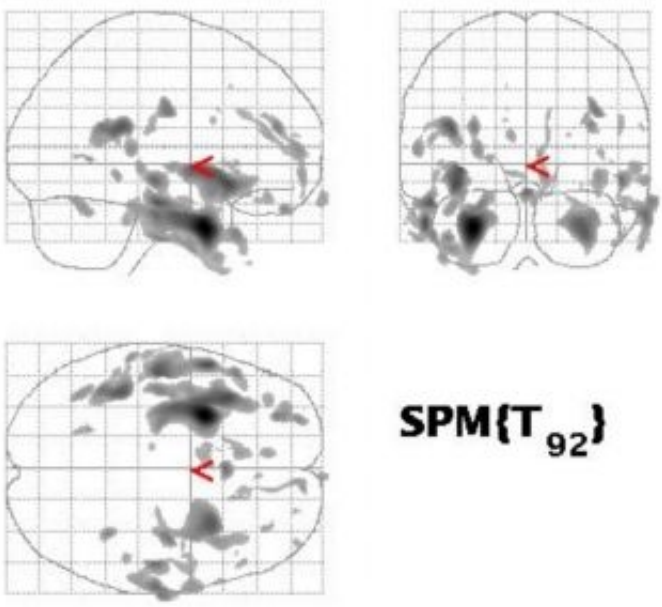

Group effect analysis with standard VBM and no family-wise error correction, control (n = 43) vs. AD (n = 51)

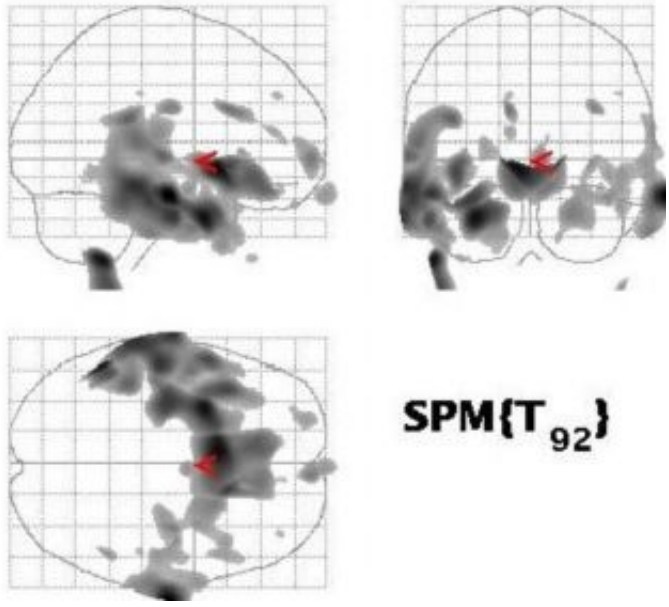

Group effect analysis with optimized VBM and no family-wise error correction, control (n = 43) vs. AD (n = 51)

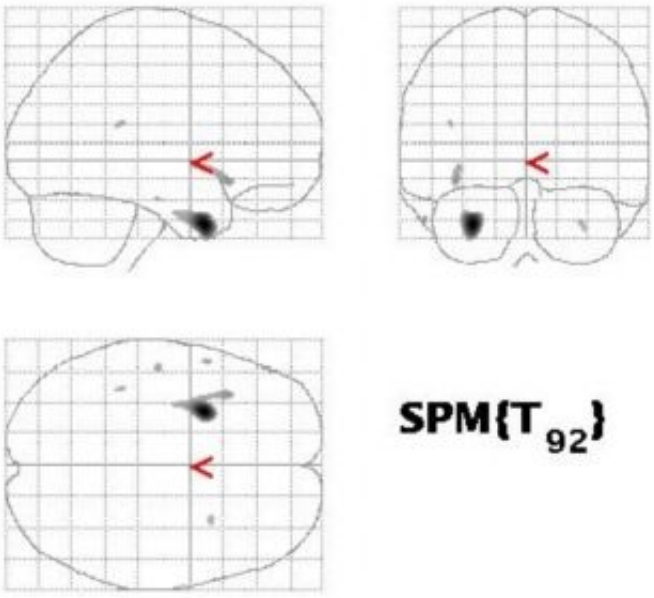

Group effect analysis with standard VBM and family-wise error correction, control (n = 43) vs. AD (n = 51)

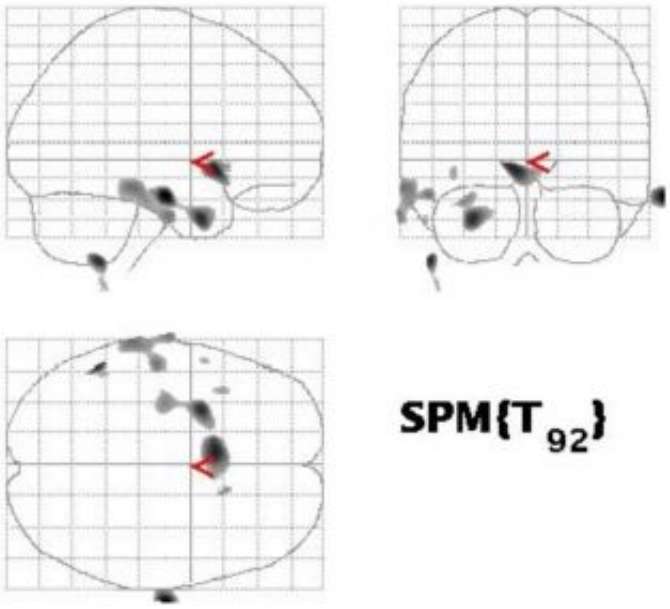

Group effect analysis with optimized VBM and family-wise error correction, control (n = 43) vs. AD (n = 51)

WE 383
FIBRIL POLYMERS AS IMAGING TARGETS IN ALZHEIMERS DISEASE

K Shoghi-Jadid[1], HW Wu[2], CL Yu[2], V Kepe[2], JR Barrio[2], S-C Huang[1,2]
[1]UCLA, Dept. of Biomathematics, [2]UCLA, Dept. of Molecular & Medical Pharmacology

The polymerization of Ab peptides into fibrillary plaques is implicated, in part, in the pathogenesis of Alzheimers disease. Polymers offer a new and unique paradigm for imaging that is conceptually different from current receptor models. In this work, we simulate PET data for binding of hypothetical molecular imaging probes to Ab polymers with an underlying mathematical model for the polymerization of Ab. We offer insight into the molecular requirements of an ideal Ab imaging probe as well as discuss possible limitations in imaging AD progression and (eventual) therapy for a particular probe.

We present a mathematical model for the nuclear dependent polymerization (NDP) of Ab and track the temporal evolution of polymer length as measured by the number of elements in fibrillary form (Figure 1). We hypothesize four types of probes: probe A binds to every fifth element, probe B binds to a fixed number of binding sites irrespective of polymer length, probe C binds to every tenth element, and probe D binds to every twentieth element on a growing fibril. The number of available binding sites at a given time, for a given probe, is meant to portray the progression of disease, for example AD (Figure 2). Based on the temporal availability of binding sites, we select three discrete time points (I, II, III) in the polymerization process (Figure 2, red arrows). The number of binding sites for a particular probe is a measure of the maximum concentration of receptors (Bmax) at a given time point. We use the apparent Bmax, for a given probe at a given time point, with an available input function and typical PET ligand-receptor kinetic parameters (kon, koff) in conjunction with the PET ligand-receptor model to simulate PET time activity curves (TAC) (Figure 3). In simulating the TAC, we are mainly interested in using the kinetics of the TAC to discriminate between stages as well as draw insights for the suitability of a particular probe.

In classical receptor-ligand interactions, the efficacy of a PET probe is judged by its kinetic parameters (e.g., Kd). The number of available binding sites (Bmax) changes with disease progression; however, it is similar for all probes that target a particular receptor. In contrast, when imaging polymers, Bmax is also a characteristic of a probe, as seen in Figure 2. Probes A, B, C, and D have differing sensitivities resulting in different TACs for the same kinetic parameters. These findings will ultimately weigh in when imaging disease progression and therapy. One interesting feature is that although probe A has highest Bmax in all stages, the relative difference between the TAC of stages II and III is not as high as expected. This is due to a lack of free probes to allow binding.

Polymers offer a new environment for in-vivo imaging which is different from classical receptor models. In imaging polymers, the efficacy of a probe needs to be judged by the availability of binding sites for different lengths of polymers, in addition its kinetic parameters.

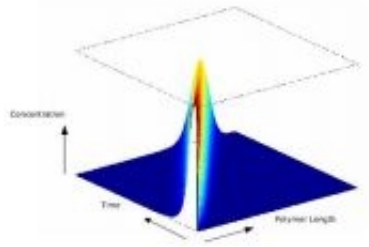

A realization of NDP model parameters for the concentration of polymers as function of time and polymer length.

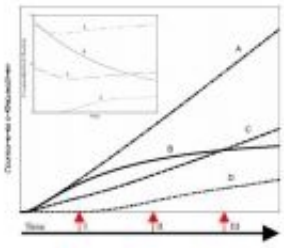

Concentration of binding sites (Bmax) for probes A, B, C, and D as function of disease progression based on the mathematical model of Ab polymerization. Inset depicts percentage of total binding sites for each probe.

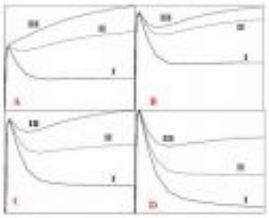

TAC realization of probes A, B, C, and D in binding to Ab polymers at stages I, II, and III.

WE 384

Measuring generalized synchronization and connectivity in MEG or EEG;

Cees J Stam[1], Bob W van Dijk[2]
[1]Dept Clinical Neurophysiology, VUmc , Amsterdam, the Netherlands, [2]MEG centre VUmc, VUmc, Amsterdam, the Netherlands

Cognitive processes require local activation of specialized neural systems as well as some mechanism to integrate the activity of subsystems into a meaningful whole. There is increasing evidence from animal studies, mathematical models and experiments in humans that synchronization of neuronal activity in theta and gamma frequency bands may be the mechanism that brings this integration about. However, information processing requires more than just synchronization of activity. Information processing requires a mechanism for the rapid formation (binding) as well as dissolution (breakdown) of cell assemblies. Thus non-stationarities reflecting alternations between desynchronization and synchronization of neural systems are hypothesized to reflect individual information processing steps in the brain.
We developed a method, Synchronization Likelihood, that makes it possible to estimate changes in general synchronization and changes in functional connectivity in the brain from the macroscopic signals that can be recorded from human subjects.
We define generalized synchronization to exist between two dynamical systems X and Y , when the state of the response system Y is a function of the state of the driving system X: Y=F(X), where F is continuous. It is important to note that in this concept it is not necessary that the signals from the two system resemble each other, or that both systems are in a (near) oscillatory state.
Our synchronization likelihood measure S, is not biased by the dynamical properties of the individual systems and gives a straightforward normalized estimate of the dynamical interdependencies between 2 or more simultaneously recorded time series. The measure is closely related to the concept of generalized mutual information and like this measure can also be computed in a time dependent way, making it suitable for the analysis of non-stationary data. Being able to detect changes in coupling with a high time resolution is very important for the characterization of normal and disturbed brain dynamics.
Synchronization likelihood has been monitored from MEG and EEG resting state recordings in normals and in patients with Alzheimers Disease, Multiple Sclerosis and Parkinsons Disease.
The data from controls show that there is substantial non-linear coupling, which is much more easily detected with MEG than with EEG. MEG data from the patient groups show that for each of these diseases the pattern of generalized synchronization differs from that of the controls in specific frequency bands and for specific cortical regions. Therefore we conclude that non-linear general synchronization can be detected with our method, and reflects the disturbed formation of connected neural ensembles in these patient groups.

WE 385
Assessing functional differences in phonological processing in normal and dyslexic subjects

Larissa Stanberry , Dietmar Cordes , Todd Richards , Rajesh R Nandy , Elizabeth Aylward , Virginia W Berninger
University of Washington, Department of Radiology

The purpose of our imaging research in dyslexia is to describe the brain reading network and identify the deficiencies in cognitive systems leading to the learning disability. The Phoneme Mapping task employed here involved a number of cognitive components and neural connections used in linguistic processing, and was presented in a continuous activation mode and, thus, could not be analyzed by model-driven methods. We used a Hierarchical Clustering method with Dendrogram Sharpening to examine the patterns of correlations between the signal changes across the brain. We hypothesize that associated activation has significant spatial and temporal structure that can be grouped into a few types of responses. Subsequently, temporal and spatial characteristics of the obtained clusters can be analyzed with regard to descriptive parameters.

Dendrogram sharpening is a model free approach without any prior assumptions about the number and location of the clusters. The similarity between two voxels is expressed as a correlation coefficient which is converted into distance as **d(i,j)=1 - cc(i,j)**. Voxels are grouped into a binary tree using the single-linkage method. The tree is pruned by discarding all small-sized children-nodes with a large-sized parent node. Clusters in the modified tree are identified using the value of median edge length of the left(right) subtree plus twice the interhindge spread as a threshold, beyond which an edge is considered inconsistent. Discarded voxels are assigned to the closest cluster group.

FMRI was performed on a 1.5T GE MRI scanner with parameters TR/TE 2s/40ms, FA82deg, FOV24x24, 64x64 imaging matrix, thick 6mm/1mm, 20 axial slices, 453 volumes. Ten healthy adult male subjects were selected for the study, six dyslexics and four controls. A continuous phoneme-matching task is executed as follows.

Word-pairs are visually presented every 6s. In each of the words in a pair, certain letters are colored in pink: TAL**K**, ROC**K**. One has to indicate whether these highlighted letters stand for the same phoneme. Each participant was presented with 50 word-pairs.

Only voxels with correlation coefficient of at least 0.4 were considered. As a consequence, the number of voxels was reduced to about 1000. The dendrogram sharpening was performed twice with (fluff-value, core-value) set to (2,40) and (10,40), where fluff-value is the maximum size of a child cluster discarded if it has a parent node of a size greater than core-value. Activation maps with slight variability were consistent across all four control subjects. We observed much larger variability in the dyslexics. All of the affected participants showed significant underactivation in IFG, STG, FFG and OTC compared to controls. Five dyslexics showed largely uncorrelated activations in the cerebellum and brain stem. These preliminary qualitative results indicate possible functional differences between the control and dyslexic subjects. The results suggest a failure of the language network, perhaps in the very initial stage. The objective of our future work is to quantify the observed differences using ROI analysis. The proposed method might ultimately result in a powerful diagnostic tool for therapeutic interventions.

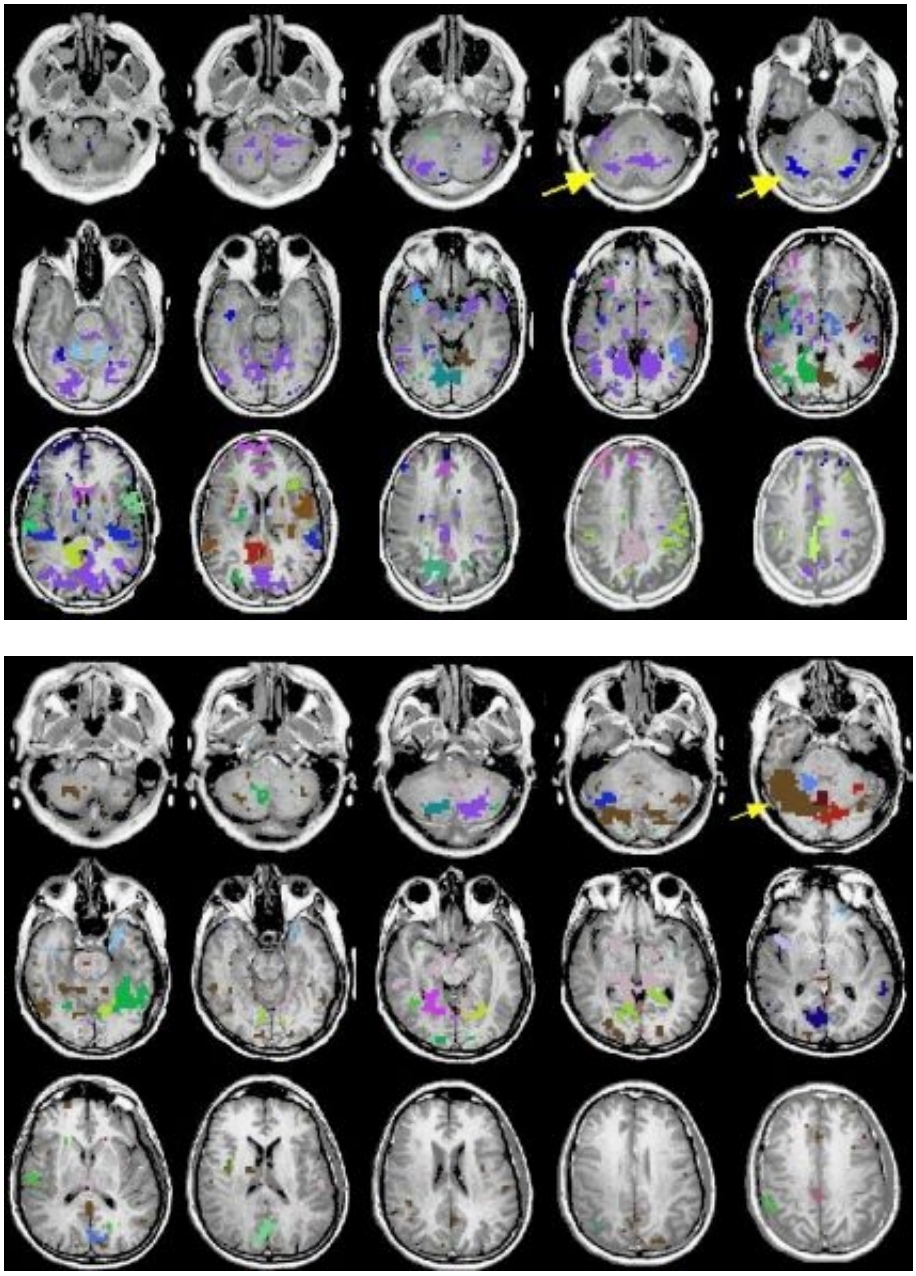

Fig.1 Clustering results for control (top) and dyslexic (bottom) subjects. The control subject shows a symmetrical cluster in the cerebellum that extends to the FFG, lingual gyrus, OTC, and occipital lobe. The map indicates different correlated clusters in the cingulate cortex, Insula, IFG, STG and parietal lobe. The dyslexic reader shows much less correlated clusters in IFG, STG or OTC. However, there is an unproportionally large cluster in the right cerebellum which does not extent any further.

WE 386
Comparison of Accuracy of Clinical Diagnosis by a Support System with Experienced Doctors using Functional Brain Images

Makoto Takahashi[1], Sumiko Murooka[1], Naoki Miura[1], Ryo Matsumoto[1], Masaharu Kitamura[2], Ryuta Kawashima[2], Shigeo Kinomura[3], Goto Ryoi[3], Kentaro Inoue[3], Hiroshi Fukuda[3], Kazunori Sato[3]
[1]Graduate School of Engineering, Tohoku University, [2]New Industry Creation Hatchery Center,Tohoku University, [3]Institute of Development, Aging and Cancer, Tohoku University

The experimental study has been performed to compare the accuracy of clinical diagnosis by newly developed automated support system with that of experienced radiologists. Two diagnosis support systems have been developed, one based on the technique of the inductive learning (C4.5) and the other on the artificial neural network (ANN). These two methods have been applied to the differential diagnosis of Alzheimerfs disease (AD), Depression, and Parkinson disease (PD) and normals using brain perfusion images obtained by single photon emission computed tomography (SPECT). These diseases are characterized by the decrease of the regional blood flow, which is visualized by the SPECT. The average level of perfusion in specific functional areas has been adopted as the features to characterize the SPECT image. The sample data from the database developed at Institute of Development, Aging and Cancer , Tohoku University has been utilized for building decision-tree by inductive learning and also for constructing ANN, both for discriminating the SPECT image of each disease from the image of normal subject. The SPECT images in this database were obtained using 99mTc-HMPAO i99m-Technesium-hexamethyl-propylenamine oximej and were registered to a standard stereotactic space and were anatomically standardized to a template with a voxel size 35x46x37 by using AIR. A total number of samples is 135.
Three experienced radiologists participated in this study in order to evaluate the accuracy of their diagnosis and to compare the accuracy with that by the support systems. They were given the SPECT images for routine reading procedure and were asked to diagnose whether it is normal or abnormal. If it is diagnosed as abnormal, they were asked further to classify it into AD, Depression or PD. They were also asked to specify the regions of decreased perfusion. Three radiologists performed their diagnosis independently and were not given any other clinical information.
The results are summarized as follows:
1. Average diagnosis accuracy (diagnosis performance) by the radiologists did not differ significantly from that by the support systems. (Approximately 70-80%)
2. When the perfusion level of thalamus is lower, the radiologists tended to miss the decrease of perfusion of the functional regions adjacent to the thalamus, which leaded to the misdiagnosis. The support system could diagnose these cases correctly.
The results revealed the characteristics of the diagnosis performance for diverse cases for radiologists and the support systems. They also indicate the necessity of the appropriate combination of the radiologists and support systems taking their specific performance into account in order to increase the overall diagnostic performance.

WE 387
Evaluation of BOLD changes related to interictal epileptic discharges using continuous and simultaneous EEG-fMRI

Fumiko Tanaka[1,2], Kimitaka Anami[1], Takeyuki Mori[1], Takashi Ohnishi[1], Yoshiharu Yonekura[2], Hiroshi Matsuda[1], Osamu Saitoh[1]

[1]National Center Hospital for Mental, Nervous and Muscular Disorders, National Center of Neurology and Psychiatry, [2]Biomedical Imaging Research Center, University of Fukui

Introduction:
Continuous and simultaneous EEG and functional MRI recording (EEG-fMRI) has been used to identify the spike-related BOLD changes that may correspond to an epileptogenic focus. Recent studies and our experiences revealed that even localized epileptic discharges caused multiple BOLD sensitive areas in brain, in many cases with symmetrical distributions. In the present study, by comparing the time course of BOLD response function in each of these BOLD activated areas, we attempted to clarify how an epileptic discharge propagated and left the BOLD traits in multiple areas in the brain.
Methods:
We studied a 45 year old patient with right temporal lobe epilepsy in the interictal state. Structural imaging demonstrated right mesial temporal sclerosis. Routine EEG revealed frequent interictal spikes over the bilateral frontal, central and temporal regions with right hemispheric predominance. fMRI was performed on a 1.5 Tesla MRI scanner (Siemens Vision Plus). 420 EPI volume scans (21-slices volume, 64x64 matrix, 6 mm thickness, 0.6 mm gap, TR: 2000 ms) were acquired over 14 min. 9-channel scalp EEG was recorded using SSS method simultaneously with fMRI acquisition [1]. fMRI data were realigned and smoothed after a slice timing correction using SPM99. EEG data were retrospectively reviewed to identify epileptic discharges and regressors were then constructed for an event-related analysis using SPM99. The result of SPM was thresholded at $P < 0.01$ (uncorrected). The time course of BOLD response was measured at location of a voxel with the highest *t* score in each cluster.
Results:
A total of 11 spikes in the bilateral hemispheres was revealed during an fMRI run. Two clusters of spike-related BOLD activation were revealed in the bilateral temporal lobes. The latent period between spike onset and the peak of BOLD response of the right temporal cluster was shorter than that of the left temporal cluster.
Conclusions:
Our results implicate that the time course of BOLD response in each of the activated areas varies within the same patient. This patient showed the faster and stronger BOLD activation on the focus side than on the non-focus side. In this context, continuous and simultaneous EEG-fMRI has the potential for providing a new insight into how interictal epileptic discharge localizes and/or propagates over the brain.
Reference:
[1] Anami K, et al. NeuroImage 2003; 19:281-95.

WE 388

Non-invasive Measurements of Acetylcholinesterase Activity with Normalized [11C]MP4A-PET Images for Dementia Diagnosis

Noriko Tanaka[1,2], Hajime Matsuura[3], Hitoshi Shinotoh[1], Shin-ichiro Nagatsuka[1], Kiyoshi Fukushi[1], Tsuneyoshi Ota[1], Tetsuo Shiraishi[1], Yasuo Sato[1], Naruki Hirano[1], Toshiaki Irie[1], Shuichi Sendoda[4]
[1]National Institute of Radiological Sciences, [2]Tokyo Women's Medical University, [3]Siemens Asahi Medics Co. Ltd, [4]Toshiba Info. System Co.Ltd

Background: [11C]MP4A-PET images have been employed for diagnosis for dementia with measurement of brain acetylcholinesterase (AChE)activity. Normalization process may enhance the evaluation of PET scans on small-sized ROI. The aim of this study was to develop easily applicable (non-invasive)and reproducible method for determining reduction rate of parameter k3, as an index of AChE activity in patients with Alzheimer disease (AD) and Dementia with Levy Bodies (DLB).
Method: 20 normal controls (mean age ± SD, 56 ± 14y), 20 patients with AD (64 ± 10y) and 10 patients with DLB (73 ± 6y) participated. Their Mini-Mental State Examination (MMSE) scores ranged 28 to 30 (normal), 7 to 22 (AD), 3 to 23 (DLB). Dynamic PET scan in two-dimensional mode were performed over 40 min to acquire a sequence of 14 scans, following [11C]MP4A (about 740MBq/5mL) injection. To normalize MP4A images for standard brain map, the MP4A-specified template model was created using SPM99. Non-linear least square algorithm (NLS) (1) and non-invasive modified Herholz method (2) using cerebellum as a reference region were employed for k3 calculation on MRI-based ROI (neocortex, thalamus, amygdala, and hippocampus).
Results: Modified Herholz method revealed 22% smaller k3 values compared with NLS analysis. Both methods showed the same k3 distributions in normal controls, highest in the sensorimotor area followed by temporal tip, anterior cingulate, posterior cingulate, orbitofrontal, temporal cortex, frontal cortex, superior parietal, supramarginal, angular area, and medial occipital cortex. Coefficient of variations (SD/mean) of the k3 values by both methods were under 15% in all cortical regions, except temporal tip and orbitofrontal. Reduction rate of k3 in AD patients by both methods was over 25% in temporal, 20-25% in parietal, 15-20% in frontal and occipital, and 15% in posterior cingulate cortex. In DLB patients, over 25-30% reduction was shown in frontal, temporal, parietal and occipital cortex.
Conclusions: Normalization process and non-invasive Herholz method make routine data analysis easier.
References: (1) Namba H et al., Eur J Nucl Med 26: 135-143, 1999
(2) Herholz K et al., Eur J Nucl Med 28: 472-7, 2001
Key word: MP4A, Dementia, Normalization

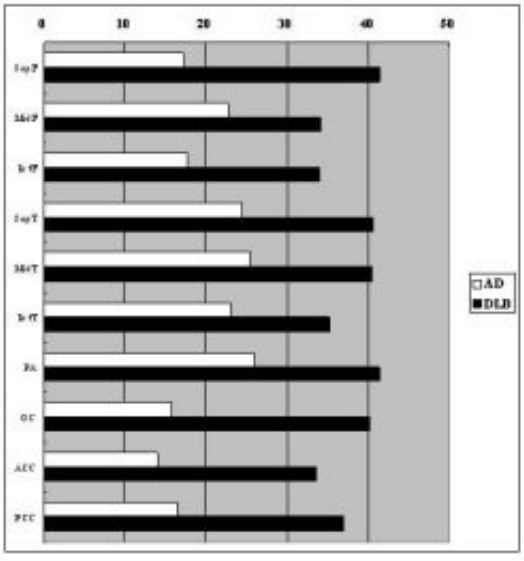

Reduction Rate of AChE Activity (%)

WE 389
FRACTAL COMPLEXITY OF THE HUMAN CORTEX IS INCREASED IN WILLIAMS SYNDROME

Paul M Thompson[1], Agatha D Lee[1], Rebecca A Dutton[1], Jennifer A Geaga[1], Kiralee M Hayashi[1], John D Bacheller[1], Mark A Eckert[2], Arthur W Toga[1], Allan L Reiss[2]
[1]Laboratory of Neuro Imaging, Brain Mapping Division, Dept. Neurology, UCLA School of Medicine, Los Angeles, CA 90095, [2]Stanford Psychiatry Neuroimaging Laboratory, Stanford University School of Medicine, Stanford, CA 94305

We developed a new algorithm to measure the fractal dimension, or complexity, of the human cerebral cortex. Cortical complexity was found to be significantly increased in Williams syndrome, a genetic condition associated with deletion of ~20 contiguous genes on chromosome 7 [cf. 1,2]. Most prior complexity measures such as the gyrification index [2,3] typically measure the cortical contour in a specific image slice. By contrast, the proposed fractal dimension takes into account the full 3D cortical surface geometry, and is independent of brain scale, orientation and the direction of image acquisition.

Methods. 75 T1-weighted MRI scans (256x192x124 SPGR volumes; FOV=24 mm, slice thickness 1.2 mm) were acquired on a GE-Signa 1.5 Tesla scanner from 36 subjects with genetically-confirmed Williams syndrome (mean age: 29.3±1.6SE years, 14M/22F) and 39 age-matched healthy controls (age: 29.3±1.6 years; 16M/23F). All 43 MRI scans were aligned to ICBM space, and 72 sulci per brain were traced on parametric surface models of each subjects cortex. A cortical pattern matching technique [4] then used these sulcal landmarks as anchors to reparameterize the cortex so that corresponding sulci occurred at the same parameter space locations [4]. The resulting deformed spherical parameterization was discretized in parameter space using a hierarchy of quadtree meshes of size NxN, for N=2 to 256. The cortex was remeshed at each spatial frequency and its surface area measured. The rate of increase of surface area with increasing spatial frequency was estimated by least squares fitting of a linear model to the area versus frequency, on a log-log plot [5]. If A{M(N)} represents the surface area of the cortical surface mesh M(N), the fractal dimension or complexity was computed as $DimF=2+\{\delta \ln(A\{M(N)\})/\delta \ln N\}$. The gradient of the multifractal plot is obtained by regressing ln A{M(N)} against ln N. For a flat surface, this slope is zero, and the dimension is 2; representing the surface at a higher spatial frequency adds no detail. Values above 2 indicate increasing surface detail and greater gyral complexity.

Findings. Left hemisphere complexity in the Williams group (2.2509±0.0018SE) was greater than that in controls (2.2450±0.0017SE; $p<0.019$). Right hemisphere complexity was also increased (2.2482±0.0018SE in the Williams group versus 2.2413±0.0015 in controls; $p<0.0019$). Differences were significant with or without adjusting for effects of age and gender.

Interpretation. These results support prior anatomic findings of regional gyral patterning anomalies and polymicrogyria in Williams syndrome [2]. Increased cortical complexity may result from disturbed developmental processes during cortical pattern formation in utero. The fractal dimension measure detects subtle cortical abnormalities that conventional volumetrics and structural brain mapping approaches may miss. We are now analyzing cortical subregions to determine whether these differences are regionally specific.

References.

[1]. Schmitt et al. Arch Neurol. 58(2): 283-7(2001); [2]. Schmitt et al. Dev Med Child Neurol. 44(5):292-5(2002); [3]. Zilles et al. (1988). Anat Embryol 179(2):173-9; [4]. Thompson et al. J Neurosci. 23(3): 994-1005(2002); [5]. Thompson et al. J Neurosci. 16(13): 4261-74(2003).

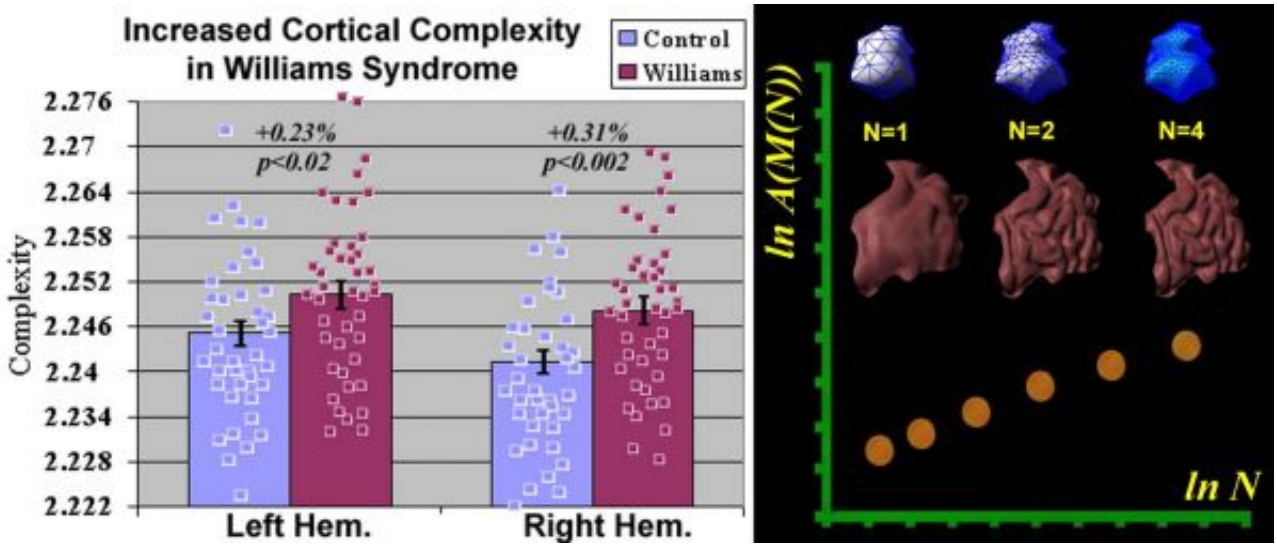

Cortical Complexity in Williams Syndrome (left); Multifractal Plot (right)

WE 390
Functionally connected networks underlying auditory verbal hallucinations in schizophrenia

Vincent G. van de Ven[1,2], Elia Formisano[1], Christian H. Roeder[3], David Prvulovic[2], Anna Rotarska-Jagiela[2], Viola Oertel[2], Matthias G. Dietz[4], Robert Bittner[2], Rainer Goebel[1], David E.J. Linden[2,5,6]
[1]Dept. of Cognitive Neuroscience, Faculty of Psychology, University of Maastricht, The Netherlands, [2]Dept. of Psychiatry, [3]Dept. of Psychosomatic Medicine, Johann Wolfgang Goethe University, [4]Dept. of Psychiatry, Markus Hospital, [5]Max Planck Institute for Brain Research, Frankfurt, Germany, [6]School of Psychology, University of Wales, Bangor, Wales, U.K.

Introduction
Auditory verbal hallucinations (AVH) are a prominent symptom in schizophrenia. Their investigation with fMRI has so far been limited by the need for patients' self-reports [1]. We investigated the functional networks underlying AVH with spatial independent component analysis (sICA). SICA is an explorative, multivariate and data-driven analysis technique that decomposes the functional dataset into a set of spatial components that are as spatially independent from each other as possible [2]. SICA can be used to asses functional connectivity in fMRI [3]. We narrowed our search to components of interest (COIs) of cortical areas that are associated with auditory (left and right auditory cortex) and language processing (left and right inferior frontal gyrus and superior temporal plane). The intra-group consistency of the hallucination COIs was verified, and these COIs were compared to COIs of the non-hallucinating and control groups.
Methods
We studied four paranoid schizophrenia patients who experienced frequent episodes of AVH, using fMRI. In most of the sessions, patients pressed a button to signal hallucinations, in 1 session the patient provided no self-reports but confirmed having experienced hallucinations after the measurement. Five non-hallucinating schizophrenia patients and five healthy controls were measured while no task was performed. To assess patterns of functional connectivity the data were analyzed with sICA. Using the auditory and language-related spatial templates two COIs were selected from each decomposition. The spatial consistency of the COIs was verified within and across subject groups, and the laterality of the clusters of voxels within the COIs was estimated (see Fig. 1).
Results
The first COI contained a variable pattern of primary and secondary auditory areas of both hemisphere in most of the hallucinating patients, as well as in the non-hallucinating patients and controls. The second COI contained a fronto-temporal network in all cases, including bilateral inferior frontal gyrus, superior temporal plane, left dorsolateral prefrontal cortex and middle temporal gyrus. For the hallucination session without self-reports, the findings were similar to those obtained from other sessions. The fronto-temporal COIs for hallucinations showed a stronger orbitofrontal contribution, a lack of supplementary motor area (SMA) contribution, and a significantly decreased laterality as compared to COIs of the non-hallucinating and healthy controls (Fig 1), which were more left lateralized. The decreased laterality of the fronto-temporal hallucination network adheres to models [4] and neuroanatomical findings [5] of a decreased laterality in the schizophrenic brain.
We suggest that AVH may be associated with the interaction of two cortical networks that comprise early auditory processing and language-related areas. The investigation of the brain's activity during hallucinations can greatly benefit from the use of data-driven analyzes that do not necessitate the use of overt self-reports. The neural responses associated with hallucinations may be better studied in terms of connectivity, rather than activity.
[1] T.Dierks et al. (1999).Neuron, 22, 615-621.
[2] M.J.McKeown et al. (1998).Human Brain Mapping, 6, 160-188.
[3] V.G.Van de Ven et al. (in press). Human Brain Mapping.
[4] T.J.Crow (1997).Trends in Neurosciences, 20, 339-343.
[5] J. Shapleske et al. (2002). Cerebral Cortex, 12, 1331-1341.

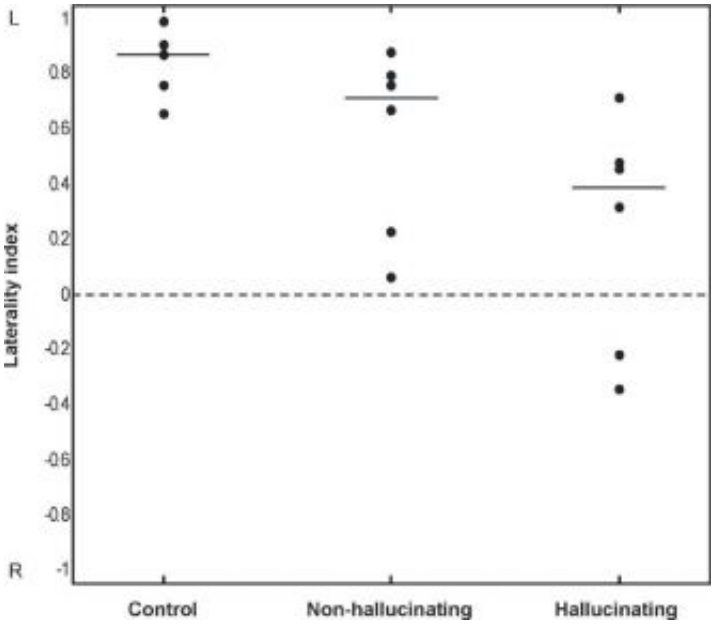

Fig 1. Laterality of the fronto-temporal COI in hallucinating patients is decreased in comparison to non-hallucinating patients and controls. Stripes are medians. Laterality index = (left - right)/(left + right).

WE 391

Near real-time 3-D cortical reconstruction of normal and diseased brains for fMRI

James T. Voyvodic[1,2], Imran Deshmukh[1], Kathryn M. Harris[1], Jeffrey Petrella[2], Timothy M. George[3], Allan H. Friedman[3]

[1]Duke-UNC Brain Imaging & Analysis Ctr., Duke University, Durham NC, USA, [2]Radiology Dept., Duke University, Durham NC, USA, [3]Neurosurgery Dept., Duke University, Durham NC, USA

Clinical applications of functional MRI (fMRI) generate thousands of images for each patient showing brain morphology, areas of task-specific functional activation, tissue pathology, and blood vessels. Interpreting such data sets requires extracting information from multiple sets of MR images and statistical maps, each with different image contrast, voxel resolution, and slice orientation. To address this issue, we have developed a novel, fast, and automated method for converting multiple anatomical MR image volumes into 3-D surface representations. This method produces a multimodal set of 3-D reconstructed surfaces, including brain, blood vessels, functional maps, and tissue pathology, all aligned in space and converted to a common coordinate system. An important advantage of this approach is that it works with both normal and diseased brain tissue and can reconstruct either full or partial brain data sets (Fig 1), all within minutes of image acquisition. The software for generating and viewing the 3-D surfaces has been implemented as extensions to the fScan analysis program (Voyvodic, 1999).

The surface reconstruction algorithm involves a series of image processing steps to segment brain white and gray matter, identify and mask tumor pathology, and tesselate tissue boundaries. For efficiency, the image processing sequence goes back and forth between voxel-based image volumes and vertex-based surface formats to take advantage of computational benefits of each data form. Each reconstructed brain is stored in both a high resolution form (~1mm vertex spacing), along with a low resolution version for fast real-time rendering. Full brain reconstruction is completed within 9 minutes using a 2.4 GHz Pentium 4 PC.

Our approach includes interactive visual validation tools that allow fMRI activation maps, tissue pathology, cranial blood vessels, and brain structural anatomy to be viewed together in accurate 3-D surface-based renderings, even before the patient has left the scanner (Figure 2). To ensure accuracy, image alignment and surface reconstructions can be verified, and if necessary adjusted, on-line by superimposing surface renderings or fMRI activation maps onto the original MR slices. This near real-time surface reconstruction and visualization approach has become a routine part of our functional MRI mapping studies. It is particularly useful for 3-D localization of essential language and motor areas in neurosurgical patients.

This work was supported by US PHS grants NS377456 and IP01NS41328.

Reference: Voyvodic JT (1999) NeuroImage, 10:91-106.

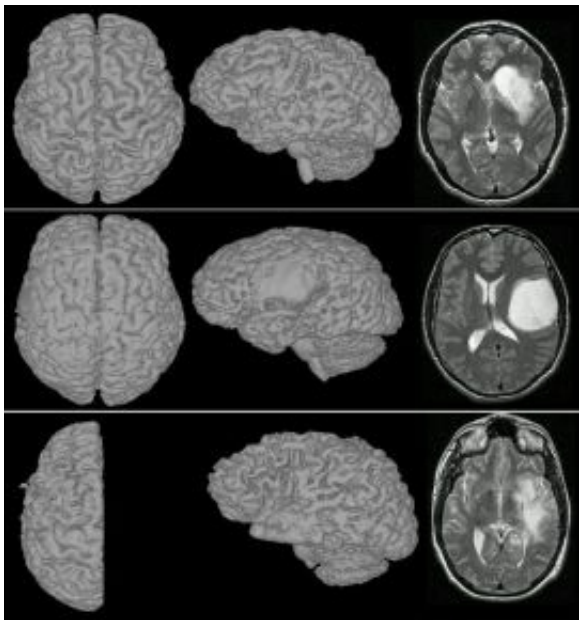

Top and left lateral surface reconstructed views and an axial slice are shown for 3 patients with left hemispherebrain tumors. Bottom reconstruction was from T1 images of left hemisphere only.

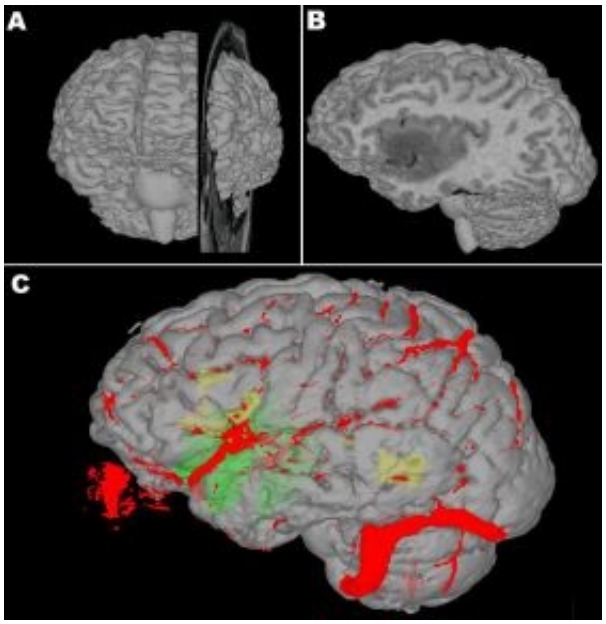

Visualization of multiple 3-D. A cutting plane can be interactively positioned (A) and toggled to reveal the inside of the original MR image volume resliced at that orientation (B). The brain of a 24 year old man with a left anaplastic astrocytoma is shown (C) with the tumor rendered in green, functional activation for language in yellow, and blood vessels in red.

WE 392

A non-parametric framework for assessing the reliability of FMRI/EEG data

Anthony B Waites , Marnie Shaw , Regula s Briellmann , Angelo Labate , Richard Masterton , Graeme D Jackson

Brain Research Institute, Austin Health, Melbourne, Australia

Introduction

Simultaneous acquisition of functional magnetic resonance (fMRI) images and electroencephalograms (EEG) is used to explore the localization of electrical discharges in epilepsy. EEG spikes are typically considered to be 'events' and entered into a typical event related analysis such as implemented in SPM99. Despite burgeoning interest in this technique, little work has been done to objectively validate the method. In this study we use a non-parametric permutation test to assess the reliability of spike-related activation maps. We assess the extent to which the results of fMRI/EEG analysis are sensitive to the analysis strategy chosen.

Methods

Subjects consisted of two patients with epilepsy plus one control. Four methods of analysis of fMRI/EEG data were compared: labelling spike timings as events, and ignoring (1) or modelling (2) all other EEG events, or removing scans associated with artefactual events (3) or all non-spike EEG events (4). For each approach, we considered the effect of using a canonical haemodynamic response function (HRF, method A) versus using a more flexible model consisting of Gamma basis functions (method B). All analyses were performed using SPM99 (http:// www.fil.ion.ucl.ac.uk/spm). To assess the ability of each method to detect cortical activity associated with the spikes, we used a non-parametric permutation test on scan labels to compare the maximum t score obtained using true spike timings with the distribution of maximum t generated by a set of twenty random timings.

Results

Fig.1A shows how many standard deviations (SDs) above the mean of the random distribution the true maximum t lies. For patient 1 (red line), there is a large difference between the true and random 'events', independent of analysis strategy. The second patient (blue line), with lower SNR , shows little difference between true and random labels. It can be seen that the significance level (a measure of true positives) is higher for the flexible model (B) than the canonical HRF (A), and higher for methods 1 and 2 than 3 and 4. False positives (Fig.1B) are however also higher for the flexible model (B), for all subjects, including the control.

Discussion/conclusions

Our findings indicate that fMRI/EEG results are valid given sufficient SNR. Activations with high SNR will be detected independent of analysis strategy, whereas those with low SNR cannot be detected. All subjects show false positives that reach the $p<0.05$ corrected level, including the control subject, suggesting that this may not always be sufficient as a threshold for fMRI/EEG studies. Further, it is found that the non-parametric framework can distinguish between analysis strategies on the basis of their true and false positive levels, making it a powerful tool for optimising fMRI/EEG analysis.

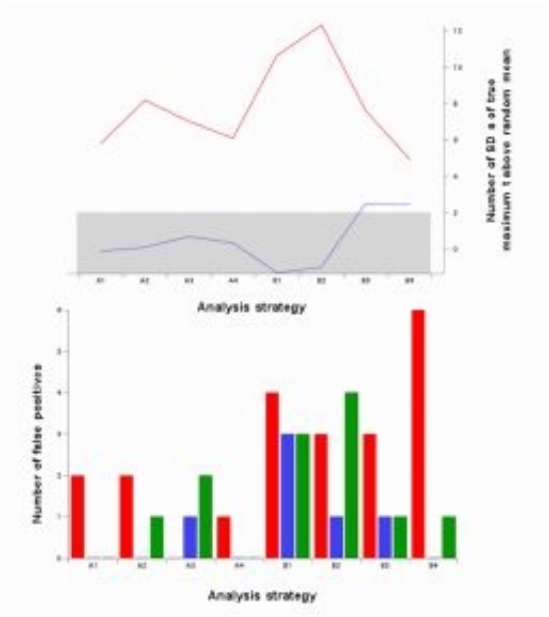
Number of SD a of true maximum t above random mean
Analysis strategy
Number of false positives
Analysis strategy

WE 393

Roy's maximum root and maximum canonical correlation SPMs from multivariate multiple regression analysis of imaging data

Keith J. Worsley[1], Francesco Tomaiuolo[2]
[1]Department of Mathematics and Statistics, and Montreal Neurological Institute, McGill University, Montreal, Canada, [2]IRCCS Fondazione 'Santa Lucia', Roma, Italy

This abstract fills a gap in the random field theory for the P-value of local maxima of SPMs from multivariate linear models. So far results are only available for:
- univariate images, single contrasts (*T* SPM, [1]),
- univariate images, multiple contrasts (*F* SPM, [1]),
- multivariate images, single contrasts (Hotelling's T^2 SPM, [2)].

We report results for
- multivariate images, multiple contrasts.

Examples of multivariate image data are: vector deformations to warp an MRI image to an atlas standard, diffusion tensors, and the HRF sampled at 1s intervals. Examples of multiple contrasts are: several polynomial effects, several performance measures, or differences between several groups.
For multivariate data and multiple contrasts, there are several different test statistics, all based on the eigen values r of $W^{-1}B$, where W is the error mean sum of squares matrix, and B is the regression mean sum of squares matrix. The natural choice is the likelihood ratio test Wilks' Λ, equivalent to the product of $1/(1+r)$, but the random field theory for this has so far proved intractable. However we have succeeded for an alternative, Roy's maximum root $R=\max r$, reported here.
A simpler definition of Roys maximum root is the following. Take a linear combination of the multivariate image data, creating univariate image data. Work out the *F* SPM for relating the univariate image data to the multiple contrasts. Roys maximum root *R* is the maximum *F* SPM over all such linear combinations.
The maximum canonical correlation *C* can be defined analogously as the maximum univariate correlation between all linear combinations of the multivariate data and multiple covariates. The relation between the two is $R=(C/b)/((1-C)/w)$, where *b* and *w* are the degrees of freedom of *B* and *W*. Applications are effective connectivity, detected by the maximum canonical correlation between multivariate image data at a single reference voxel, and that at all other voxels. If the reference voxel is varied as well, the search space is 6D rather than 3D, and the results of [3] have been extended in the same way.
The P-value of local maxima of a smooth SPM in *D* dimensions is well approximated by

$$P(\text{local max} > t) \sim \Sigma_{d=0}^{D} \, Resels_d \, EC_d(t),$$

where $Resels_d$ and $EC_d(t)$ are the resels and Euler characteristic density in *d* dimensions. Figure 1 gives a surprisingly simple expression for the EC density $EC_d{}^R(t)$ of Roys maximum root for *k* components in terms of the EC density $EC_d{}^F(t)$ of the *F* statistic with *b*,*w* df [1]. The EC density of Hotellings T^2 [2] now falls out as a special case when $b=1$.
These results are available in FMRISTAT (www.math.mcgill.ca/keith/fmristat/toolbox/stat_threshold.m) and applied to detecting regions of brain damage of $n=17$ non-missile brain trauma patients compared to $n=19$ age and sex matched controls, using vector deformations images, and correlating the deformations with 6 memory tests.

[1]. Worsley et al. (1996). *Human Brain Mapping*, **4**:58-73
[2]. Cao, Worsley (1999). *Annals of Statistics*, **27**:925-942.
[3]. Cao, Worsley (1999). *Annals of Applied Probability*, **9**:1021-1057.

$$EC_d^R(t) = \sum_{j=0}^{\lfloor \frac{k-1}{2} \rfloor} \left(\frac{\pi}{\log 2} \right)^{\frac{k-1-2j}{2}} \frac{\Gamma\left(\frac{k+1}{2}\right)}{j!(k-1-2j)!} EC_{d+k-1-2j}^F(t)$$

Figure 1: EC density for Roy's maximum root SPM

WE 394
State Space Approach to Dynamical Inverse Problems with an Application to Epilepsy EEG Data

Okito Yamashita[1], Andreas Galka[2], Tohru Ozaki[2]
[1]Department of Statistical Science, The Graduate University for Advanced Studies, Japan, [2]The Institute of Statisitcal Mathematics, Japan

In this work we shall address the inverse problem of estimating electrical sources of EEG/MEG recordings. In particular we will emphasize on the use of dynamical constraints. In the literature (Yamashita et.al 2004, Andreas et.al.), this dynamical inverse problem is regarded as a state estimation problem; the spatio-temporal constraint is incorporated into the system equation of state space representation and then the distributions of electrical sources are obtained as the state estimates.
Unlike most previous approaches for solving the inverse problems, where only one instantaneous measurement is used for a solution, this dynamical state approach can exploit the information contained in multiple instantaneous measurements. As a result, the solution obtained from this approach becomes more reliable as well as more robust to the observation noise. Furthermore this dynamical state space framework provides the chance to model the underlying brain dynamics in the system equation. The use of innovations for detecting unexpected events can also be mentioned as another attractive feature of this dynamical approach.
In this presentation, we shall particularly focus on the use of innovations and the filtered innovation (innovation multiplied by Kalman gain), which can be considered as new information added into evolution of the state. In order to show the possibility of the state space approach, we will present the result of an application to an epilepsy EEG data.

Reference

O. Yamashita et.al. 2004, Recursive Penalized Least Squares Solution for Dynamical Inverse Problems of EEG Generation,Human Brain Mapping, In press
A. Galka et.al, A Solution to the Dynamical Inverse Problem of EEG Generation using Spatio-temporal Kalman Filtering, NeuroImage, to be submitted

WE 395
Classifying Spatial Temporal Multi-frequency Quantitative EEG Brain Oscillations

Chih-Chiang Yang[1], Chih-Chien Yang[2,3]
[1]National Taipei Teachers College, Taipei, Taiwan, [2]L.L. Thurstone Psychometric Laboratory, University of North Carolina at Chapel Hill, Chapel Hill, North Carolina, USA, [3]Graduate School of Educational Measurement & Statistics, National Taichung Teachers College, Taichung, Taiwan

Background and purpose
Clinically recorded quantitative electroencephalograms (QEEG) for brain oscillations have complex formats that are structured by multiple channels, time-points, and bands (electric signal frequencies). Due to the mechanism of EEG, mapping brainŸs cognitive functions has to utilize all possible spatial (channels), temporal (time-points) and bands under an overall model in order to make functioning inference validated and reliable. The aim of the paper is to propose a class of new statistical models to deal with the problems and study the mathematical and statistical properties of the models.
Material and methods
Various extended latent transition analysis (ELTA) models will be proposed in this study. ELTA models are built under the frameworks of maximum likelihood estimation and Gibbs sampling approaches. The two methods will be compared by using both artificially simulated and empirically collected datasets for ELTA illustrations. In particular, inter- and intra-hemispheric coherences and their linkages with behavioral information are to be analyzed. Different assumptions on the distributional forms, including Poisson- and Norm- mixtures, will be examined, respectively. Detailed derivations and estimation procedures will be shown in the paper.
Result and conclusion
Simulation studies showed that both statistical approaches were feasible. The ELTA models are capable to incorporate spatial, temporal and multiple bands into an overall statistical model that can be estimated and justified. Sensitivity analysis and model diagnosis further proved that the models were indeed validated and reliable. To summarize the difference, maximum likelihood estimation enjoys more speedy computations than its competitor while Gibbs sampling might have advantages in incorporating complex model assumptions. Detailed comparisons and further implications on the results are to be discussed.